Predeal International Summer School

Raduta
Delion
Ursu

COLLECTIVE MOTION AND NUCLEAR DYNAMICS

COLLECTIVE MOTION AND NUCLEAR DYNAMICS

Editors

A. A. Raduta
D. S. Delion
I. I. Ursu

World Scientific

COLLECTIVE MOTION
AND
NUCLEAR DYNAMICS

Predeal International Summer School

COLLECTIVE MOTION AND NUCLEAR DYNAMICS

August 28 – September 9, 1995 Predeal, Romania

Organized by: Institute of Physics and Nuclear Engineering
Sponsored by: O.E.A. – I.C.T.P. Trieste, Italy
Romanian Ministry for Research and Technology
Romanian Ministry of Youth and Sport
Romanian Academy

Editors: **A. A. Raduta, D. S. Delion & I. I. Ursu**

Institute of Atomic Physics, Bucharest, Romania

World Scientific
Singapore • New Jersey • London • Hong Kong

Published by

World Scientific Publishing Co Pte Ltd

P O Box 128, Farrer Road, Singapore 912805

USA office: Suite 1B, 1060 Main Street, River Edge, NJ 07661

UK office: 57 Shelton Street, Covent Garden, London WC2H 9HE

British Library Cataloguing-in-Publication Data
A catalogue record for this book is available from the British Library.

COLLECTIVE MOTION AND NUCLEAR DYNAMICS

ISBN 981-02-2528-8

This book is printed on acid-free paper.

Printed in Singapore by Uto-Print

PREFACE

This book contains the lectures given at the International Summer School on Collective motion and Nuclear Dynamics held in Predeal, Romania, in the period of August 28-September 9. The Nuclear Physics Schools, organised by Institute of Physics and Nuclear Engineering are well known to physicists throughout the world due to their long hystory and good reputation. The first edition took place in 1964 in Bucharest and after a break of five years the series has been continued regularly every two years in Predeal. For some administrative reasons in 1978 the location of the school was changed from Predeal to Poiana Brasov. Since 1991 we moved back to Predeal and that happened not only because we wanted to restore the tradition but also to have back the excellent conditions we had before 1978. Unfortunately this revolutionary desire was only partly fulfilled since the new priviledged class of Romania does not yet realise the importance of physics among other intelectual activities.

The school held in 1995 was devoted to the stydy of collective features and dynamics of nuclear system from both theoretical and experimental angles. A large variety of subjects were chosen. Indeed, we aimed at covering fields ranging from classical to pure quantum mechanical formalisms, from standard nuclear structure to nuclear dynamics for finite temperature and relativistic effects of nuclear systems, from deuteron and alpha to heavy clusters, from exotic nuclei lying far away from the stability line to superdeformed nuclei. Outstanding speakers were invited to present an overview of the results in their field and to sketch the most appealing perspectives.

It is well known that nuclear physics "imported" some formalisms from other fields but also "exported" some efficient theoretical tools. Examples of such events were also presented at our school. Thus we had an exhaustive lecture about the use of quantum groups for nuclear structure problems where a completely new mathematical technic is transferred to nuclear physics. On the other hand many theoretical achievements in the description of nuclear systems were borrowed by a relatively new field studying atomic clusters. This field was present at our school through a nice talk about fissioning atomic clusters.

In contradistinction to the previous editions, now we did not accept lectures longer than two hours. Therefore the style of our meeting may be placed between those of conferences and traditional schools. Due to this fact we had a relatively large number of invited lectures (37). All of them were supposed to appear in this volume. We regret very much for being unable to receive two distinguished lectures, in due time. Besides invited lectures many short seminars were given. These will be published in a special issue of Romanian Journal of Physics.

The present edition, like the previous three ones, took place under the special circumstances generated by the so-called transition to the market economy. Due to this social and economical phase transition , our institute, like many other institutions, crosses a very difficult financial crises. In this context organising an international school is an inconsistent and not an opportune social phenomenon. We were able, however, to save the School due to some external grants. Thus, we have received a generous financial help from OAE (office for External Activity) of ICTP Trieste, Ministry for Research and Technology, Ministry for Youth and Sport and from Academy of Romania. We take this opportunity to express our deep gratitude to these International and National organisms.

During the preparation of this School I received a constant help and friendly advices from Director General of IFA Prof. T. Necsoiu, Director of IFIN, Prof. V. Zoran and Deputy Director of IFIN, Prof. A. Calboreanu. I am very grateful to them for their continous support. I shared the work implied by organising this meeting with my collaborators Prof. D. Bucurescu (co-Director of the School), Drs. D. S. Delion and I. I. Ursu (Scientific Secretaries). They were very efficient and contributed substantially to the succes of the school.

I hope this volume will be very useful to a large cathegory of nuclear physicists. Also I am convinced that the scientific level of the lectures, the academic atmosphere and the beauty of the mountain surrounding the place are three strong attractors for participants to the next editions.

A. A. Raduta

CONTENTS

3. NUCLEAR REACTIONS: EXOTIC NUCLEI, FUSION, FISSION

4. NUCLEAR DYNAMICS: NONLINEAR EFFECTS AND FINITE TEMPERATURE

1. NUCLEAR STRUCTURE

PAIRING AND CORIOLIS EFFECTS IN DEFORMED ODD-MASS NUCLEI

A. COVELLO, A. GARGANO, and N. ITACO

Dipartimento di Scienze Fisiche, Università di Napoli Federico II
and Istituto Nazionale di Fisica Nucleare
Mostra d'Oltremare, Pad. 20, 80125 Napoli, Italy

ABSTRACT

The many-particles plus rotor model provides an appropriate framework for the study of strongly deformed nuclei. We discuss here a version of this model in which the pairing correlations between the valence nucleons in the intrinsic deformed field are treated by a new method, the chain-calculation method. This method has the power to reduce the computational work drastically while yielding practically exact results. The model is applied to the two odd-mass nuclei ^{163}Er and ^{165}Er focusing attention on the lowest-lying decoupled band. The role of the recoil term as a mechanism that produces attenuation of the Coriolis coupling is emphasized. The results of our calculations for both nuclei turn out to be in good agreement with experiment.

1. Introduction

The study of pairing and Coriolis effects in strongly deformed nuclei is a central theme in nuclear structure theory. A particularly appropriate theoretical basis for this study is provided by the many-particles plus rotor (MPR) model.[1−3] The main difficulty with this model is the treatment of the pairing correlations between the valence nucleons in the intrinsic deformed field. On the one hand the model space dimensionalities generally preclude a standard diagonalization procedure, on the other hand the use of the BCS approximation may well result in a poor description of the intrinsic structure.[3,4]

We overcome this difficulty by making use of a new method,[5] the chain-calculation method (CCM), which provides a highly effective way for cutting down the size of the energy matrices while yielding extremely accurate results. This opens up the possibility of assessing the real scope of the MPR model.

In this paper, we focus attention on odd-mass nuclei and apply the MPR model to the two isotopes ^{163}Er and ^{165}Er. Of particular interest in these nuclei is the lowest-lying decoupled band which originates from the $i_{13/2}$ shell-model state. The study of this band provides in fact the opportunity to shed light on the role of the various terms of the model Hamiltonian.

In Sec. 2 we give an outline of the MPR model. Our calculations are described in Sec. 3 while the results are presented and discussed in Sec. 4. Sec. 5 presents some concluding remarks.

2. Many-particles plus rotor model

In the strong coupling representation the model Hamiltonian describing a system of N valence particles coupled to an axially-symmetric rotor is written

$$H_{MPR} = H_I + H_{intr} + H_c \,, \tag{1}$$

where

$$H_I = A(\mathbf{I}^2 - I_3^2) \,, \tag{2}$$

$$H_{intr} = H_0 + H_{pair} + H_{rec} \,, \tag{3}$$

$$H_{rec} = A(\mathbf{J}^2 - J_3^2) \,, \tag{4}$$

$$H_c = -A(I_+ J_- + I_- J_+) \,, \tag{5}$$

with standard notation. The recoil term H_{rec} is of particular relevance in the MPR model,[2,6] as it contains both one-body and two-body terms. In fact, the angular momentum $\mathbf{J}$ due to the valence particles has the form

$$\mathbf{J} = \sum_{i=1}^{N} \mathbf{j}(i) \,, \tag{6}$$

which implies that H_{rec} becomes

$$H_{rec} = A \left[\sum_{i=1}^{N} \mathbf{j}^2(i) - \left(\sum_{i=1}^{N} j_3(i) \right)^2 + 2 \sum_{i<k} \mathbf{j}(i) \cdot \mathbf{j}(k) \right] . \tag{7}$$

The eigenstates of $H_I + H_{intr}$ can be written in the form

$$\Psi^I_{M\Omega\tau} = \sqrt{\frac{2I+1}{16\pi^2}} \left[D^I_{M\Omega}(\omega) \chi_{\Omega\tau} + (-)^{I+\Omega} D^I_{M-\Omega}(\omega) \chi_{\overline{\Omega}\tau} \right] , \tag{8}$$

where the intrinsic wave functions $\chi_{\Omega\tau}$ are solutions to the eigenvalue equation

$$(H_0 + H_{pair} + H_{rec})\chi_{\Omega\tau} = \mathcal{E}_{\Omega\tau}\chi_{\Omega\tau}. \tag{9}$$

Once Eq. (9) is solved the Coriolis term can be diagonalized in this representation. In the next section we shall discuss in some detail our treatment of the intrinsic Hamiltonian and of the Coriolis coupling.

3. Calculations

We now describe our calculations for ^{163}Er and ^{165}Er. Let us first consider the Hamiltonian

$$H = H_0 + H_{pair} = \sum_{i=1}^{N} H_{sp}(i) + H_{pair}\,, \tag{10}$$

which in second quantization takes the form

$$H = \sum_{\nu} \epsilon_\nu \hat{N}_\nu - G \sum_{\nu\nu'} A^\dagger_\nu A_{\nu'}\,, \tag{11}$$

where

$$\hat{N}_\nu = a^\dagger_\nu a_\nu + a^\dagger_{\bar{\nu}} a_{\bar{\nu}}\,, \tag{12}$$

$$A^\dagger_\nu = a^\dagger_\nu a^\dagger_{\bar{\nu}}\,. \tag{13}$$

The index ν stands for all quantum numbers specifying the single-particle states while $\bar{\nu}$ denotes the time reversal partner. In cases where Ω is essential, ν will represent only the asymptotic quantum numbers $[Nn_3\Lambda]$.

We describe the intrinsic deformed field H_0 by a nonspheroidal axial and reflection symmetric Woods-Saxon potential.[7] Thus we write

$$H_{sp} = -\frac{\hbar^2}{2m}\,\Delta + V(\mathbf{r}) + V_{so}(\mathbf{r};\mathrm{spin})\,, \tag{14}$$

$$V(\mathbf{r}) = \frac{-V_0}{1 + \exp\left[(r - R(\theta))/a\right]}\,, \tag{15}$$

$$R(\theta) = R_0\left[1 + \beta_0 + \beta_2 Y_{20}(\theta) + \beta_4 Y_{40}(\theta)\right]\,, \tag{16}$$

$$V_{so}(\mathbf{r};\mathrm{spin}) = -\kappa\,\boldsymbol{\sigma}\cdot[\mathrm{grad}\ \mathrm{V}(\mathbf{r}) \times \mathbf{p}/\hbar]\,. \tag{17}$$

For both ^{163}Er and ^{165}Er we have considered nineteen valence neutrons distributed over eighteen levels chosen in such a way that on both sides of the Fermi surface lies the same number of single-particle states. The adopted single-particle level schemes are listed in Table I. The level energies have been calculated using a

Table I. Single-particle energies (MeV).

^{163}Er		^{165}Er	
$\Omega^\pi[Nn_3\Lambda]$	Relative Energy	$\Omega^\pi[Nn_3\Lambda]$	Relative Energy
$\frac{9}{2}^-[514]$	0.0	$\frac{1}{2}^-[530]$	0.0
$\frac{1}{2}^-[530]$	0.469	$\frac{3}{2}^-[532]$	0.202
$\frac{3}{2}^-[532]$	0.838	$\frac{1}{2}^+[400]$	0.707
$\frac{1}{2}^+[400]$	1.080	$\frac{3}{2}^+[402]$	0.986
$\frac{1}{2}^+[660]$	1.322	$\frac{1}{2}^+[660]$	1.032
$\frac{3}{2}^+[402]$	1.471	$\frac{3}{2}^+[651]$	1.592
$\frac{3}{2}^+[651]$	1.858	$\frac{11}{2}^-[505]$	1.901
$\frac{11}{2}^-[505]$	2.175	$\frac{3}{2}^-[521]$	2.240
$\frac{3}{2}^-[521]$	2.523	$\frac{5}{2}^-[523]$	2.552
$\frac{5}{2}^+[642]$	2.896	$\frac{5}{2}^+[642]$	2.682
$\frac{5}{2}^-[523]$	3.203	$\frac{1}{2}^-[521]$	3.458
$\frac{1}{2}^-[521]$	3.798	$\frac{7}{2}^+[633]$	4.207
$\frac{7}{2}^+[633]$	4.356	$\frac{5}{2}^-[512]$	4.563
$\frac{5}{2}^-[512]$	4.757	$\frac{7}{2}^-[514]$	5.264
$\frac{7}{2}^-[514]$	5.921	$\frac{9}{2}^+[624]$	5.968
$\frac{9}{2}^+[624]$	6.071	$\frac{1}{2}^-[510]$	6.186
$\frac{1}{2}^-[510]$	6.380	$\frac{3}{2}^-[512]$	6.559
$\frac{3}{2}^-[512]$	6.837	$\frac{7}{2}^-[503]$	6.700

unique value of the potential depth V_0 and of the radius parameter r_0, namely $V_0 = 43$ MeV and $r_0 = 1.29$ fm. These values are in agreement with those reported in Ref. 8, taking into account that we use a single value of r_0 for the central and

spin-orbit terms. The deformation parameter β_2 is taken to be 0.320 and 0.335 for ^{163}Er and ^{165}Er, respectively.[9-12] The values of the spin-orbit strength κ, the diffuseness a and the deformation parameter β_4 are: $\kappa = 0.425$ fm^2, $a = 0.68$ fm, $\beta_4 = 0.052$ for ^{163}Er and $\kappa = 0.387$ fm^2, $a = 0.65$ fm, $\beta_4 = 0.062$ for ^{165}Er. These values of κ and a are within the range of those reported in the literature,[8,13] while the values of β_4 come quite close to those obtained from the equilibrium shape calculations of Ref. 14 for this region.

It should be noted that in the model spaces used for ^{163}Er and ^{165}Er we include the five lowest-lying states originating from the $i_{13/2}$ level, leaving out the two states $\frac{11}{2}^+[615]$ and $\frac{13}{2}^+[606]$. These latter, lying very high in energy, are not expected to contribute significantly to the wave functions of the lowest positive-parity bands. The only two other positive-parity states, $\frac{1}{2}^+[400]$ and $\frac{3}{2}^+[402]$, that might contribute to this band are also included.

As already mentioned in the Introduction, we treat the pairing correlations between the valence particles by the CCM. A detailed description of this approach as well as a test case evidencing its degree of accuracy are to be found in Refs. 3 and 5. We only emphasize here that our solutions of the pairing Hamiltonian are practically exact. As for the pairing strength G, we use a value of 0.190 MeV for ^{163}Er and 0.189 MeV for ^{165}Er, which give an odd-even mass difference for neutrons in agreement with the experimental values of 0.975 and 0.905 MeV, respectively.

We now turn our attention to the recoil term (7), which in second quantization reads

$$H_{rec} = A\Big[\sum_{\nu\nu'} F_{\nu\nu'} a^\dagger_\nu a_{\nu'} + \sum_{\nu_1\nu_2\nu_3\nu_4} R_{\nu_1\nu_3} R_{\nu_4\nu_2} a^\dagger_{\nu_1} a^\dagger_{\nu_2} a_{\nu_4} a_{\nu_3}\Big], \tag{18}$$

where

$$F_{\nu\nu'} = \langle\nu|\mathbf{j}^2 - j_3^2|\nu'\rangle, \tag{19}$$

$$R_{\nu\nu'} = \begin{cases} \langle\nu|j_-|\nu'\rangle & \text{if } \Omega_\nu < \Omega_{\nu'}, \\ \langle\nu'|j_-|\nu\rangle & \text{if } \Omega_\nu > \Omega_{\nu'}, \\ \langle\bar{\nu}|j_-|\nu'\rangle & \text{if } \Omega_\nu = \Omega_{\nu'} = \frac{1}{2}. \end{cases} \tag{20}$$

Here we are concerned with the treatment of odd-A nuclei. In this case we diagonalize H_{rec} within the set of seniority-one ($v = 1$) states obtained by treating the Hamiltonian (11) by the CCM. The intrinsic wave function has therefore the form

$$\chi_{\Omega\tau} = \sum_{\beta\mu} f^\Omega_{\beta\tau\mu} |\beta, \mu\Omega\rangle. \tag{21}$$

The states $|\beta, \mu\Omega\rangle$ are $v = 1$ eigenstates of the pairing Hamiltonian, the label μ referring (here and in the following) to the quantum numbers of the blocked level and the index β standing for all the other quantum numbers necessary to completely specify the states. In our formalism these pairing eigenstates are expressed[3] as

$$|\beta, \mu\Omega\rangle = \sum_{n_1 \ldots n_l} K^{\mu}_{n_1 \ldots n_l \beta} (A_1^\dagger)^{n_1} \ldots (A_l^\dagger)^{n_l} a^\dagger_{\mu\Omega} |0\rangle. \tag{22}$$

The basis states on the r.h.s. of Eq. (22) contain an odd particle in the level $(\mu\Omega)$ while the remaining $(n_1 + \ldots + n_l)$ pairs are distributed in all possible ways over the chosen l doubly degenerate single-particle levels. As mentioned above, in our case $l = 18$ and $n_1 + \ldots + n_l = 9$.

The matrix elements of H_{rec} between $v = 1$ states are given by

$$\langle \beta, \mu\Omega | H_{rec} | \beta', \mu'\Omega \rangle = A \Bigg\{ \delta_{\mu\mu'} \Big[2 \sum_{\nu>0} F_{\nu\nu} T^{\mu\mu'}_{\beta\beta'\nu} - \sum_{\nu,\nu'>0} R^2_{\nu\nu'} T^{\mu\mu'}_{\beta\beta'\nu\nu'} \Big] +$$

$$[1 - (1 - \delta_{\beta\beta'})\delta_{\mu\mu'}] F_{\mu\mu'} S^{\mu\mu'}_{\beta\beta'} - \sum_{\nu>0} R_{\nu\mu'} R_{\nu\mu} S^{\mu\mu'}_{\beta\beta'\nu} \Bigg\}, \tag{23}$$

where the quantities S and T are expressed in terms of the coefficients K appearing in Eq. (22).

Let us now discuss briefly the effects produced by the recoil term. We first consider the diagonal matrix elements. The first two sums in Eq. (23) are almost independent of the level blocked by the unpaired particle[15] and, as a consequence, do not significantly affect the spectrum of the odd nucleus. The third term reduces to the single-particle matrix element $F_{\mu\mu}$ ($S^{\mu\mu}_{\beta\beta} = 1$). This term may be particularly large for levels originating from the so-called intruder states (in the case considered here this is the spherical $i_{13/2}$ state). It has the effect to push up in energy the band-heads associated with these levels. The last quantity in Eq. (23), $\sum_{\nu>0} R^2_{\nu\mu} S^{\mu\mu}_{\beta\beta\nu}$, represents the correction arising from the other valence nucleons. Through the coefficients $S^{\mu\mu}_{\beta\beta\nu}$ it depends on the pair distribution of particles and in some cases can significantly reduce[2,15] the single-particle contribution, $F_{\mu\mu}$, of the recoil term.

As regards the off-diagonal matrix elements, they may have $\beta \neq \beta'$ and/or $\mu \neq \mu'$. From our study of the Er isotopes it turns out that the matrix elements with $\mu \neq \mu'$ may be particularly significant only in connection with the $\Delta N = 2$ coupling between $N = 4$ and $N = 6$ states. Through the matrix elements with $\beta \neq \beta'$ different eigenstates of the pairing Hamiltonian may be brought into the intrinsic wave function. In this way the recoil term affects the distribution of pairs over the single-particle levels.[16]

As a final step we take into account the Coriolis interaction (5). Its matrix elements are given by

$$\langle \Psi^I_{M\Omega\tau}|H_c|\Psi^I_{M\Omega'\tau'}\rangle = -A\Bigg\{ \sum_{\mu\mu'} \Big[(I+\Omega')(I-\Omega'+1)\Big]^{\frac{1}{2}} R_{\mu\mu'}\delta_{\Omega'\Omega+1}$$

$$+\Big[(I-\Omega')(I+\Omega'+1)\Big]^{\frac{1}{2}} R_{\mu'\mu}\delta_{\Omega'\Omega-1} + (-)^{I+\frac{1}{2}}(I+\frac{1}{2})R_{\mu\mu'}\delta_{\Omega\frac{1}{2}}\delta_{\Omega'\frac{1}{2}}\Bigg\} P^{\Omega\Omega'}_{\tau\mu\tau'\mu'}\,, \quad (24)$$

where

$$P^{\Omega\Omega'}_{\tau\mu\tau'\mu'} = \sum_{\beta\beta'} f^{\Omega}_{\beta\tau\mu} f^{\Omega'}_{\beta'\tau'\mu'} S^{\mu\mu'}_{\beta\beta'}. \quad (25)$$

We see that the matrix elements (24) are written as the product of two factors. The first one corresponds to the contribution of the odd particle while the second takes into account the many-particle correlations induced from both the pairing and the recoil interaction. Since the quantities $P^{\Omega\Omega'}_{\tau\mu\tau'\mu'}$ are all ≤ 1, they produce an attenuation of the Coriolis coupling.

For the rotational parameter A, we take the value 14 keV for ^{163}Er and 13 keV for ^{165}Er. These values are intermediate between the values obtained from the $E_{2+} - E_{0+}$ energy difference in the neighbouring even-even isotopes and those derived from the spectra of the four low-lying negative-parity bands in both ^{163}Er and ^{165}Er.

4. Results

We now come to discuss the results of our calculations for ^{163}Er and ^{165}Er. In both these nuclei there are five low-lying bands, four with negative parity (essentially rotational in character) built on the $\frac{1}{2}^-[521]$, $\frac{3}{2}^-[521]$, $\frac{5}{2}^-[523]$ and $\frac{11}{2}^-[505]$ single-particle states, and one with positive parity originating from the $i_{13/2}$ shell-model state.

It is this experimental situation that we have tried to reproduce within the framework of the MPR model as described in the previous section, concentrating our attention on the decoupled $i_{13/2}$ band for which the recoil term is of particular relevance.

As regards the spectra of the negative-parity bands, which are practically purely rotational, a very good agreement with experiment is obtained up to about 1.5 MeV excitation energy (relative to each bandhead), the largest discrepancy being about 60 keV. It should be stressed that for these bands the calculations with and without

recoil yield practically the same results. By way of illustration, the spectrum of the $\frac{5}{2}^-[523]$ band in ^{163}Er is presented in Fig. 1.

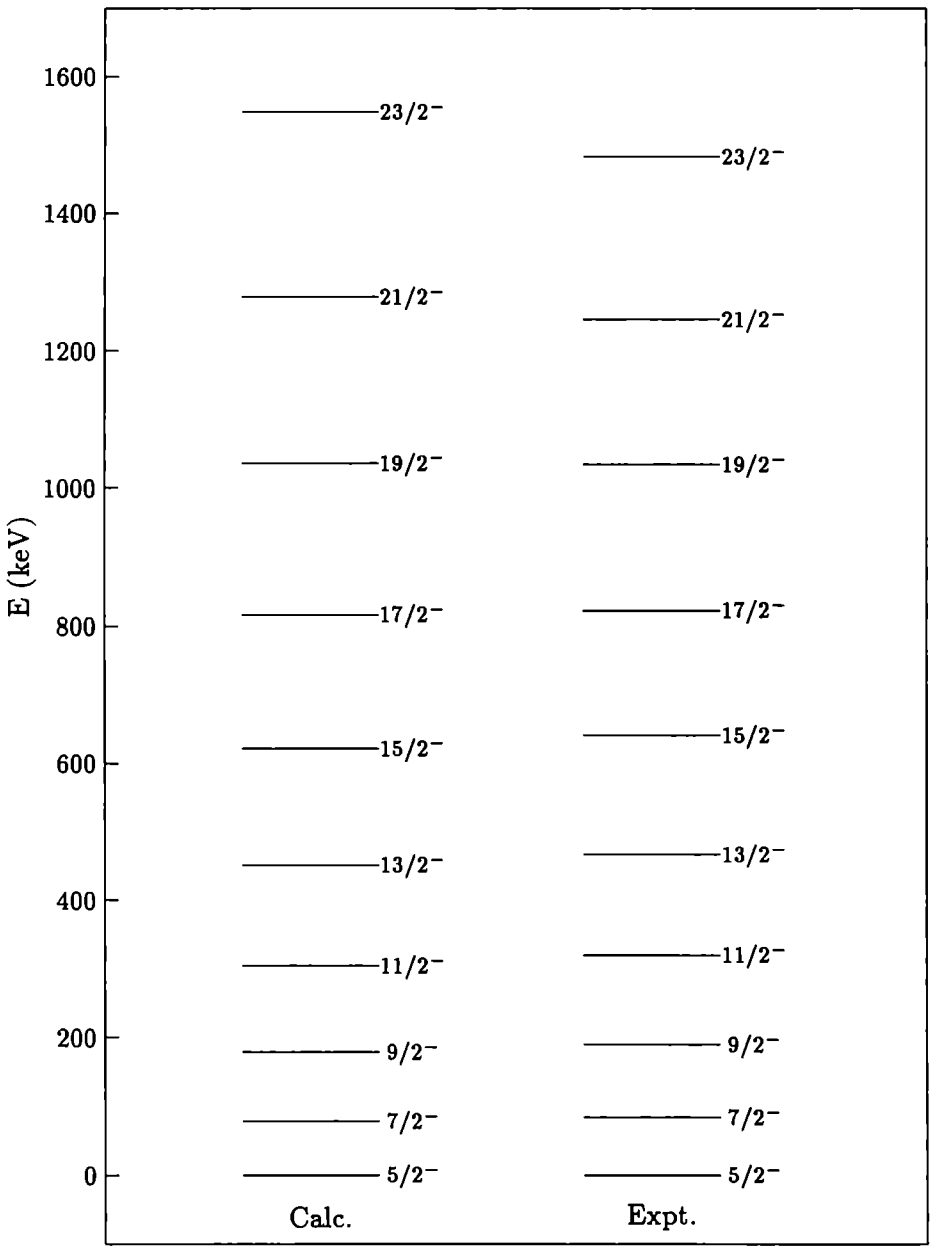

Fig. 1. Experimental and calculated spectrum of the $\frac{5}{2}^-[523]$ band in ^{163}Er. The experimental data are from Ref. 11.

In Fig. 2 we show the spectrum of the lowest positive-parity band of ^{163}Er.

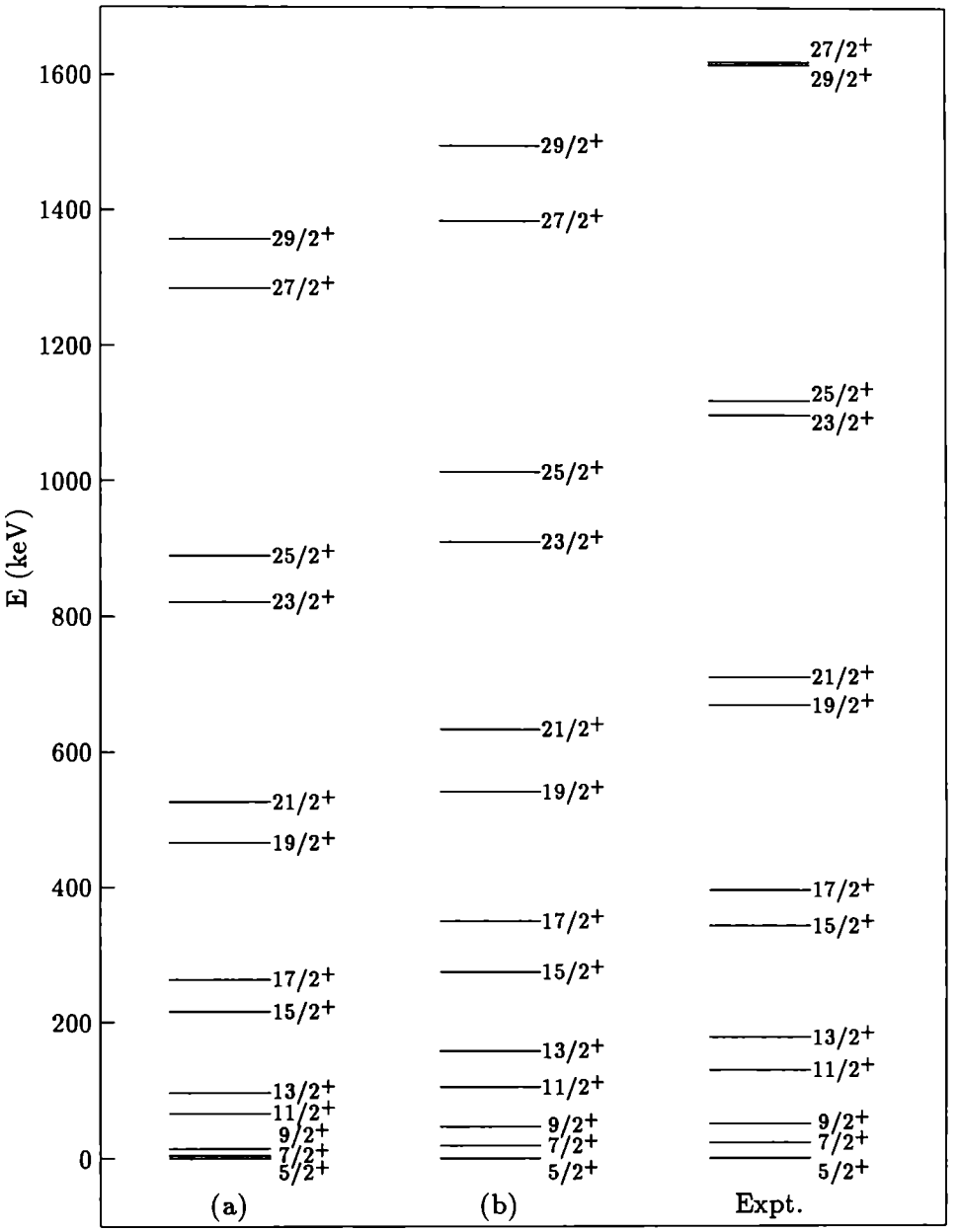

Fig. 2. Experimental and calculated [(a) without recoil; (b) with recoil] positive-parity spectrum of ^{163}Er. The experimental data are from Ref. 11.

We see that the right level ordering and an overall satisfactory agreement with experiment is obtained up to $J = \frac{21}{2}$. It should be stressed that this is not the case

when the pairing correlations are treated by the usual BCS method. In fact, the use of this approximation makes it necessary to introduce an ad-hoc attenuation factor.[3,4] The comparison between case (a) and (b) shows the relevance of the recoil term. Concerning the higher-spin states, which lie above 1 MeV excitation energy, our calculation fails to reproduce the observed pattern. This is certainly a point which deserves further investigation. As a first step, states of seniority higher than one ($v = 3$) should be taken into account.

The origin of the difference in the spectra of the positive parity band is to be found in the strong Coriolis coupling and in the attenuation of such a coupling produced by the recoil term. In Table II we report the values of the intrinsic energies for the positive-parity states originating from the $i_{13/2}$ level (they are characterized by $[Nn_3\Lambda]$ since there is no appreciable mixing of states corresponding to different blocked levels). From this table we see that the recoil term produces an increase in the intrinsic level spacings. In Table III we give the attenuation factors $P^{\Omega\Omega'}_{\mu\mu'}$

Table II. Values of the intrinsic energies $\mathcal{E}_{\mu\Omega} - \mathcal{E}_{[642]5/2+}$ (keV) for ^{163}Er calculated : (a) without recoil; (b) with recoil.

$\mu\Omega$	(a)	(b)
$[660]\frac{1}{2}^+$	1245	1504
$[651]\frac{3}{2}^+$	761	955
$[642]\frac{5}{2}^+$	0	0
$[633]\frac{7}{2}^+$	1032	1054
$[624]\frac{9}{2}^+$	2634	2650

(see Eq. 25), which show the effect of the recoil term on the off-diagonal Coriolis matrix elements. Therefore, we see that both effects produce a reduction of the Coriolis coupling. As regards the wave functions of the states of the decoupled band, they result in a rather complex mixture of the $\frac{1}{2}^+[660]$, $\frac{3}{2}^+[651]$, $\frac{5}{2}^+[642]$ and $\frac{7}{2}^+[633]$ states. This mixture, however, is significantly reduced by the recoil term. Finally, in Table IV we compare with experiment the band-head energies. We see that the agreement is at most within 20 keV.

Table III. Values of the quantities $P^{\Omega\Omega'}_{\mu\mu'}$, as given by Eq. (25), calculated for ^{163}Er : (a) without recoil; (b) with recoil.

$\mu\Omega$	$\mu'\Omega'$	(a)	(b)
$[660]\frac{1}{2}^+$	$[651]\frac{3}{2}^+$	0.99	0.96
$[651]\frac{3}{2}^+$	$[642]\frac{5}{2}^+$	0.95	0.86
$[642]\frac{5}{2}^+$	$[633]\frac{7}{2}^+$	0.91	0.84
$[633]\frac{7}{2}^+$	$[624]\frac{9}{2}^+$	0.99	0.99

Table IV. Experimental (Ref. 11) and calculated band-head energies (keV) for ^{163}Er.

Bandhead	Expt.	Calc.
$\frac{5}{2}^-$	0	0
$\frac{5}{2}^+$	69	85
$\frac{3}{2}^-$	104	96
$\frac{1}{2}^-$	347	367
$\frac{11}{2}^-$	444	434

Fig. 3 and Tables V, VI and VII present the results obtained for ^{165}Er. We see that the situation is quite similar to that which emerged for ^{163}Er, the overall agreement with experiment being of comparable quality. It may be noted, however, that the spectrum of the decoupled band is even better reproduced while the theoretical band-head energy of the $\frac{1}{2}^-[521]$ band lies 170 keV below the experimental value. There are, however, some indications that this state may have a small γ-vibration admixture.[17] As in the case of ^{163}Er, the spectra of the negative-parity bands are also very well reproduced by the theory.

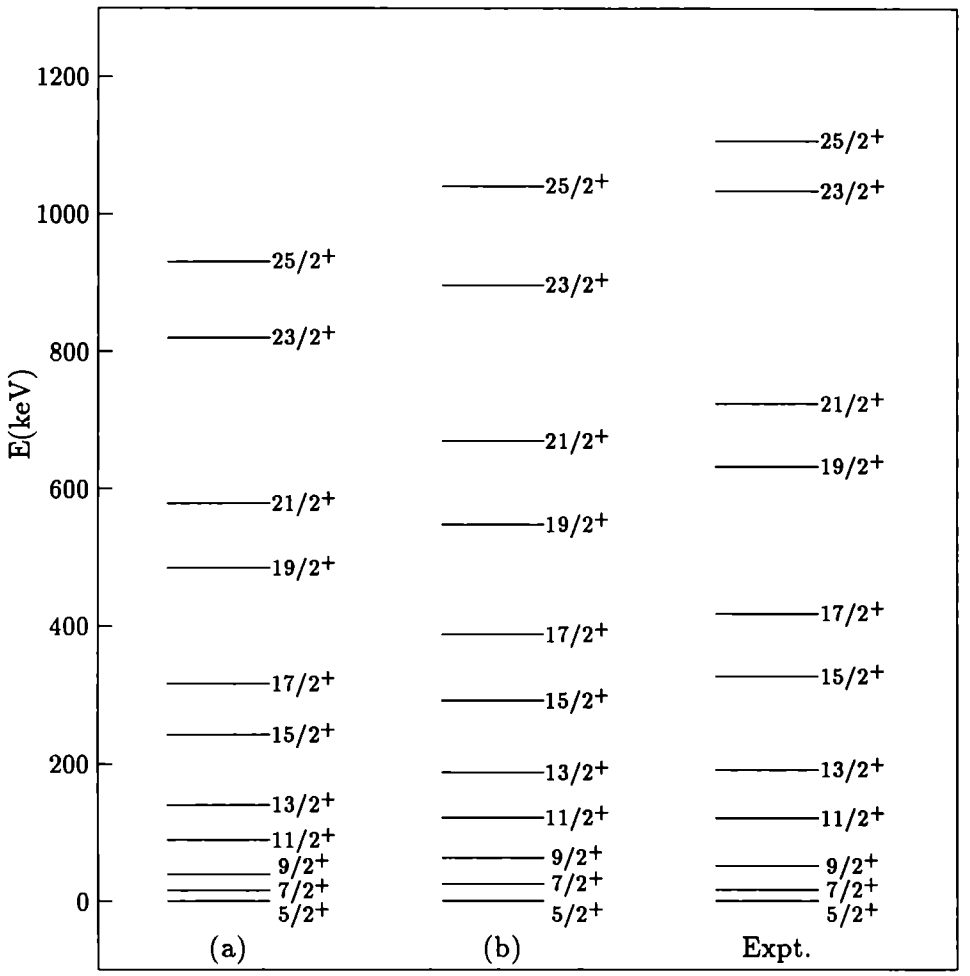

Fig. 3. Experimental and calculated [(a) without recoil; (b) with recoil] positive-parity spectrum of ^{165}Er. The experimental data are from Ref. 12.

Table V. Values of the intrinsic energies $\mathcal{E}_{\mu\Omega} - \mathcal{E}_{[642]5/2+}$ (keV) for ^{165}Er.

$\mu\Omega$	(a)	(b)
$[660]\frac{1}{2}^+$	1502	1798
$[651]\frac{3}{2}^+$	970	1241
$[642]\frac{5}{2}^+$	0	0
$[633]\frac{7}{2}^+$	946	911
$[624]\frac{9}{2}^+$	2593	2604

Table VI. Values of the quantities $P^{\Omega\Omega'}_{\mu\mu'}$, as given by Eq. (25), for ^{165}Er.

$\mu\Omega$	$\mu'\Omega'$	(a)	(b)
$[660]\frac{1}{2}^+$	$[651]\frac{3}{2}^+$	1.00	0.98
$[651]\frac{3}{2}^+$	$[642]\frac{5}{2}^+$	0.99	0.94
$[642]\frac{5}{2}^+$	$[633]\frac{7}{2}^+$	0.82	0.75
$[633]\frac{7}{2}^+$	$[624]\frac{9}{2}^+$	0.99	0.99

Table VII. Experimental (Ref. 12) and calculated band-head energies (keV) for ^{165}Er.

Bandhead	Expt.	Calc.
$\frac{5}{2}^-$	0	0
$\frac{5}{2}^+$	47	51
$\frac{3}{2}^-$	243	242
$\frac{1}{2}^-$	297	127
$\frac{11}{2}^-$	551	530

5. Closing remarks

In this paper, we have discussed the MPR model as a framework for the description of deformed odd-mass nuclei. We have applied this model to the study of the low-energy bands in the strongly deformed nuclei ^{163}Er and ^{165}Er. A salient feature of our calculations is the very accurate treatment of the pairing correlations in the intrinsic deformed field. As a result, the role played by the recoil term has been clearly evidenced.

The results of our calculations for both nuclei have turned out to be in good agreement with experiment. Of particular interest is the fact that the $i_{13/2}$ decoupled band is well reproduced up to rather high values of the angular momentum. In fact, this is not possible with the BCS approximation unless an ad-hoc attenuation factor of the Coriolis term is introduced. This shows that an accurate treatment of the intrinsic structure is essential if one wants to assess the real scope of the MPR model.

Here we have considered odd-A nuclei including in the calculations only $v = 1$ eigenstates of the pairing Hamiltonian. As a next step we intend to take into account the $v = 3$ states as well as to extend our calculations to doubly-even nuclei.

Acknowledgements

This work was supported in part by the Italian Ministero dell'Università e della Ricerca Scientifica e Tecnologica (MURST).

References

1. P. Ring and P. Schuck, *The Nuclear Many-Body Problem* (Springer-Verlag, New York, 1980), Chap. 3, and references therein.
2. T. Engeland, in *International Review of Nuclear Physics*, Vol. 2, edited by T. Engeland, J. Rekstad, and J. S. Vaagen (World Scientific, Singapore, 1984), p. 155, and references therein.
3. A. Covello, A. Gargano, and N. Itaco, in *Proceedings of the Predeal International Summer School, Predeal, Romania, 1993*, edited by W. Scheid and A. Sandulescu (Plenum Press, New York, 1994), p. 207.
4. T. Engeland, *Physica Scripta* **25** (1982) 467.
5. A. Covello, F. Andreozzi, A. Gargano, and A. Porrino, in *Proceedings of the Fourth International Spring Seminar on Nuclear Physics, Amalfi, 1992*, edited by A. Covello (World Scientific, Singapore, 1993), p. 301.
6. E. Osnes, J. Rekstad, and O. Gjøtterud, *Nucl. Phys.* **A253** (1975) 45.
7. F. A. Gareev, S. P. Ivanova, V. G. Soloviev, and S. I. Fedotov, *Sov. J. Particles Nucl.* **4** (1973) 148.
8. J. Dudek and T. Werner, *J. Phys.* **G4** (1978) 1543.
9. R. G. Helmer, *Nucl. Data Sheets* **64** (1991) 79.
10. E. N. Shurshikov and N. V. Tomofeeva, *Nucl. Data Sheets* **65** (1992) 365.
11. T. Burrows, *Nucl. Data Sheets* **56** (1989) 313.
12. L. K. Peker, *Nucl. Data Sheets* **65** (1992) 439.
13. W. Ogle, S. Wahlborn, R. Piepenbring, S. Frederiksson, *Rev. Mod. Phys.* **43** (1971) 424.
14. R. Bengtsson, J. Dudek, W. Nazarewicz, and P. Olanders, *Physica Scripta* **39** (1989) 196.
15. G. Ehrling, and S. Wahlborn, *Physica Scripta* **6** (1972) 94.

16. T. Engeland, and J. Rekstad, *Phys. Lett.* **89B** (1979) 8; J. Rekstad and T. Engeland, *Phys. Lett.* **89B** (1980) 316.
17. A. K. Jain, R. K. Sheline, P. C. Sood, and Kiran Jain, *Rev. Mod. Phys.* **62** (1990) 393.

M1 EXCITATIONS IN DEFORMED NUCLEI: A THEORETICAL SURVEY

N. LO IUDICE
Dipartimento di Scienze Fisiche, Università di Napoli " Federico II" and INFN sez. di Napoli
Mostra d'Oltremare Pad.19, I-80185, Napoli

ABSTRACT

A general definition of the scissors M1 summed strength inspired by the geometrical two-rotor model is given. Such a definition is shown to be consistent with the observed deformation properties of the mode. It is here adopted in the realm of algebraic interacting boson models to study the same deformation properties and then used to produce the results of schematic random-phase approximation. These include the possible existence of a low and high energy mode in deformed as well as superdeformed nuclei. It is pointed out that the harmonic oscillator basis adopted in schematic random-phase approximation plays the role of a Hartree-Bogoliubov basis. In virtue of this properties the M1 states are free of spurious rotational admixture. The effect of selfconsistency on the scissors energy weighted M1 sum rule is also discussed. The problem of spurious rotational admixture is discussed in the context of realistic random-phase approximation. A calculation of this kind formulated in the laboratory frame as a way of avoiding such a problem is discussed.

1. Introduction

Since their first discovery in ^{156}Gd through a high resolution (e,e') experiment[1], the low lying M1 excitations, known as scissors mode according to the picture provided by the the geometrical two-rotor model[2], have been object of extensive experimental and theoretical investigations.

The mode was confirmed in a (γ,γ') experiment[3] and, since then, observed in all deformed nuclei[4]. A fine structure study of the M1 strength made possible by a combined analysis of (e,e') and (γ,γ') experiments[5], has shown that the mode is fragmented into several peaks closely packed around a prominent one. Comparative studies based on (e,e') and (p,p') experiments[6-8] have established the orbital nature.

A renewed interest toward the subject has been stimulated recently by two important discoveries.

Combined (e,e') and (γ,γ') experiments carried out on a chain of even Sm isotopes have shown that the integrated M1 strength depends quadratically on the deformation parameter[9] and is strictly correlated with the strength of the E2 transition to the lowest 2^+ state[10]. The same deformation law was confirmed in Nd isotopes[11] and ascertained by now to hold for all nuclei of the rare earth region[12].

At the same time, inelastic proton scattering experiments on ^{154}Sm and other deformed nuclei[13], have detected a sizeable strongly fragmented M1 spin strength distributed over an energy range of 4 to 10 MeV so as to give rise to a double-hump[14]. Such a pattern is specially pronounced in ^{154}Sm.

The deformation law has been described with different degrees of accuracy in all phenomenological or schematic models adopted in the past to study the mode[15-24] as well as in realistic microscopic calculations[25-30].

The phenomenological descriptions, though successful in the analysis of the gross features of the mode and in giving useful physical insights, cannot account for detailed properties such as the fragmentation of the M1 strength. Moreover, they are completely inadequate for studying spin excitations. A unified and complete analysis of orbital and spin excitations can be made only in a fully microscopic context.

In heavy deformed nuclei, the microscopic studies have been carried out in Tam-Dancoff (TDA) and, mostly, in random phase approximation (RPA). The early RPA calculations[31], being carried out in the intrinsic frame, suffered with uncertainties induced by approximations not completely under control[32]. A notable uncertainty was induced by the occurrence of spurious rotational admixture[33]. This could be removed either by properly modifying the quadrupole-quadrupole interaction[33] or by a Schmidt orthogonalization of the basis states[31] or by adopting a self-consistent basis[34,35]. A RPA calculation formulated in the laboratory frame as an alternative way of avoiding the occurrence of redundant rotational states has been also proposed[28].

Spin excitations have been studied with good success in TDA[36] as well as in RPA[27,28,37,38]. There is however no conclusive answer to the interpretation of the observed two-peak structure. It is indeed not clear whether the two peaks correspond to different proton and neutron excitations[28,36,37] or are of isovector and isoscalar nature[27].

In these lectures we will devote most of our attention to the orbital low $M1$ excitations. We will give a definition of scissors mode which is inspired by the geometrical TRM and study the consistency of such a definition with the observed deformation properties (sect. 2). We will then briefly show (sect.3) how this definition applies to some phenomenological models, namely the generalized coherent state model (GCSM)[39] and to the proton-neutron interacting boson model (IBM-2)[40]. In sect.4 we will study the relation to schematic RPA. In this connection we will see that a new scissors mode at high energy mode is predicted. In sect.5 we will study the problem of selconsistency in proton-neutron schematic RPA and its effects. We will see that its states are free of spurious rotational admixture, a property which will be exploited to compute the scissors energy-weighted M1 sum rule. Sect.6 deals with realistic RPA. Special attention is devoted to the connection between rotational symmetry breaking and spurious admixture in the $M1$ RPA states. An RPA approach formulated in the laboratory frame is discussed as a way of solving the problem. A brief conclusion is drawn in the final section.

2. Definition of Scissors Mode

The definition of the scissors strength proposed here is inspired by the geomet-

rical TRM.

2.1. Semiclassical description and general definition of scissors mode

The basic assumption of the model[2] is that protons and neutrons form two axially symmetric rotors interacting via a potential $V(\vartheta)$ dependent on the angle 2ϑ between the symmetry axes. The Hamiltonian has then the form

$$H_{TR} = \frac{1}{2\Im_p}\vec{J}_p{}^2 + \frac{1}{2\Im_n}\vec{J}_n{}^2 + V(\vartheta), \tag{1}$$

where $\Im_p$ and $\Im_n$ are the proton and neutron moments of inertia, $\vec{J}_p$ and $\vec{J}_n$ their angular momenta. In order to separate the relative motion between the two rotors from the rotation of the whole nucleus one must express the Hamiltonian in terms of the total and relative angular momenta

$$\vec{J} = \vec{J}_p + \vec{J}_n\ , \qquad \vec{S} = \vec{J}_p - \vec{J}_n\ . \tag{2}$$

Apart from a Coriolis-like term which can be neglected, the Hamiltonian decouples into a rotational and an intrinsic part. This, for small values of ϑ, assumes the form of a two-dimensional harmonic oscillator Hamiltonian

$$H = H_{int} = \frac{1}{2\Im_{sc}}(S_1^2 + S_2^2) + \frac{1}{2}C_\vartheta(\vartheta_1^2 + \vartheta_2^2), \tag{3}$$

where ϑ_k $(k = 1, 2)$ play the role of x and y variables and $(k = 1, 2)$

$$S_k = J_k^{(p)} - J_k^{(n)} = i\frac{d}{d\vartheta_k} \tag{4}$$

are their conjugate momenta. The TRM physical constants are

$$\Im_{sc} = \frac{4\Im_p\Im_n}{\Im_p + \Im_n}\ , \qquad C_\vartheta = \Im_{sc}\omega^2 = \frac{4C_\vartheta^{(p)}C_\vartheta^{(n)}}{C_\vartheta^{(p)} + C_\vartheta^{(n)}} \tag{5}$$

where $C_\vartheta^{(\tau)} = \omega^2\Im_\tau$. The same quantities can be defined through the harmonic relation holding for the TRM Hamiltonian, namely

$$\frac{1}{\Im_{sc}} < S^2 >= \frac{1}{\Im_{sc}} \sum_{\mu=\pm1} |\ \langle \mu\ |\ S_\mu\ |\ 0\rangle\ |^2 = \omega, \qquad C = \omega \sum_{\mu=\pm1} |\ \langle \mu\ |\ S_\mu\ |\ 0\rangle\ |^2, \tag{6}$$

The scissors mode is the first excited state, with quantum numbers $n = 0$ and $K^\pi = 1^+$. It falls at an excitation energy given by the frequency ω and is mainly excited by a magnetic dipole operator of the form

$$\begin{aligned} \mathcal{M}(M1,\mu) &= \sqrt{\frac{3}{4\pi}}\,(g_p J_\mu^{(p)} + g_n J_\mu^{(n)})\,\mu_N \\ &= \sqrt{\frac{3}{4\pi}}(g_R J_\mu + \frac{1}{2}g_r S_\mu)\,\mu_N\ , \end{aligned} \tag{7}$$

where

$$g_R = \frac{1}{2}(g_p + g_n), \qquad g_r = g_p - g_n, \tag{8}$$

Making use of the harmonic relations (6) we obtain the $M1$ strength

$$B(M1)\uparrow = \frac{3}{16\pi} \sum_{\mu=\pm 1} |\langle \mu \mid S_\mu \mid 0 \rangle|^2 \, g_r^2 \, \mu_N^2 = \frac{3}{16\pi} \Im_{sc} \, \omega g_r^2 \, \mu_N^2 \, . \tag{9}$$

The defining eq. (6) can be written in the form

$$\Im_{sc} = \sum_{\mu=\pm 1} < 0|S_\mu^\dagger \frac{1}{H - E_0} S_\mu|0 > \, , \qquad C = \frac{1}{2} \sum_{\mu=\pm 1} < 0| \left[S_\mu^\dagger, [H, S_\mu]\right] |0 > \, . \tag{10}$$

These equations, first obtained in a sum rule approach[41] provide a general definition of the TRM constants, valid in any context. By using closure indeed, we obtain

$$\Im_{sc} = \sum_{n\mu} \frac{1}{\omega_n} |< n\mu|S_\mu|0 >|^2 \quad , \qquad C = \sum_{n\mu} \omega_n |< n\mu|S_\mu|0 >|^2 \, . \tag{11}$$

The scissors energy weighted $M1$ sum rule follows now immediately

$$\begin{aligned} \sum_n \omega_n B_n(M1)\uparrow \; &= \; \frac{3}{16\pi} \sum_{n,\mu} \omega_n \, |< n\mu|S_\mu|0 >|^2 \, g_r^2 \, \mu_N^2 \\ &= \; \frac{3}{32\pi} \sum_{\mu=\pm 1} < 0| \left[S_\mu^\dagger, [H, S_\mu]\right] |0 > g_r^2 \, \mu_N^2 \simeq \frac{3}{16\pi} \Im_{sc} \omega^2 g_r^2 \, \mu_N^2 \end{aligned} \tag{12}$$

This sum rule holds in the macroscopic as well as in the microscopic domain. Under the experimentally supported assumption of small fragmentation of the mode, we obtain for the summed strength the expression defining the TRM $M1$ strength (eq. 9). It follows that the TRM formula, with $\Im_{sc}$ and C given by eq. (11), represents a general definition of the scissors $M1$ summed strength.

2.2. Consistency with the deformation properties

It is useful to express all TRM quantities in terms of the shape variables $\alpha_{2\mu}$ instead of the angle ϑ. To this purpose let us consider a proton (neutron) density of the form suitable to an axially deformed shape

$$\varrho_\tau(\vec{r}) = \varrho_\tau \left[r - R(1 + \alpha_{20}^{(\tau)} Y_{20}(\hat{r}))\right] \tag{13}$$

where $\tau = p, n$ and

$$\alpha_{20}^{(\tau)} = \beta_\tau = \sqrt{\frac{16\pi}{45}} \delta_\tau . \tag{14}$$

The proton (neutron) density is subjected to the normalization condition

$$< Q_{\lambda\mu}^{(\tau)} > = \int \varrho_\tau(\vec{r}) r^\lambda Y_{\lambda\mu}(\vec{r}) d\vec{r} = \alpha_{\lambda\mu} \varrho_0^{(\tau)} R^{\lambda+3} \tag{15}$$

where $\varrho_0^{(p)}$ and $\varrho_0^{(n)}$ are normalized to the number of protons and neutrons respectively. Under a rotation by ϑ_τ ($\vartheta_p = \vartheta$, $\vartheta_n = -\vartheta$) around the $x-$axis, the proton ($\tau = p$) and neutron ($\tau = n$) densities undergo the following change

$$\varrho_\tau(R_{\vartheta_\tau}^{-1}\vec{r}) = \varrho_\tau \left[r - R(1 + \sum_{\mu=\pm1} \alpha_{2\mu}^{(\tau)} Y_{2\mu}^*(\hat{r})) \right] \tag{16}$$

where

$$\alpha_{2\mu}^{(\tau)} = D_{0\mu}^{(2)}(\vartheta_\tau)\alpha_{20}^{(\tau)} \simeq -i\sqrt{\frac{3}{2}}\alpha_{20}^{(\tau)}\vartheta_\tau = -i\sqrt{\frac{3}{2}}\beta_\tau\vartheta_\tau \tag{17}$$

to leading order in ϑ_τ . This key relation enables us to express the TRM Hamiltonian (3) in terms of shape variables, namely

$$H = \frac{1}{2\Im_{sc}}S^2 + \frac{1}{2}C_\vartheta\vartheta^2 = \frac{1}{2B_{sc}}\sum_{\mu=\pm1}|\pi_{2\mu}|^2 + \frac{1}{2}C\sum_{\mu=\pm1}|\alpha_{2\mu}|^2 \tag{18}$$

where $\pi_{2\mu}$ are conjugate to $\alpha_{2\mu}$. The new parameters are

$$B_{sc} = \frac{4B_pB_n}{B_p + B_n}\ , \qquad C = \frac{4C_pC_n}{C_p + C_n} \tag{19}$$

Old and new constants are related by

$$\Im_\tau = 3\beta_\tau B_\tau\ , \qquad C_\vartheta^{(\tau)} = 3\beta_\tau C_\tau \tag{20}$$

It follows that the scissors M1 strength has a quadratic dependence. Using indeed the above relations we obtain from eq. (9) for $\beta_p = \beta_n = \beta$

$$B_{sc}(M1)\uparrow = \frac{9}{16\pi}\,B\,\omega\beta^2(g_p - g_n)^2\,\mu_N^2. \tag{21}$$

The δ^2 behaviour of such a scissors $M1$ strength has been studied quantitatively in Ref.[23] by making an empirical estimate of the mass parameter. The following expression was obtained

$$B_{sc}(M1)\uparrow\ \simeq\ 0.004\,\omega A^{5/3}\,\delta^2\,g_r^2\mu_N^2. \tag{22}$$

Numerical calculations carried out by putting $g_n = 0$ and $g_r = g_p = 2g_R = (2Z)/A$ yield results in good agreement with experiments[9-11]. In particular theoretical and experimental summed $M1$ strengths have similar saturation properties (Fig.1). A systematic analysis carried out recently[12] has shown that the $M1$ strengths computed by such an empirical formula are in overall agreement with experiments for all nuclei of the whole rare earth region.

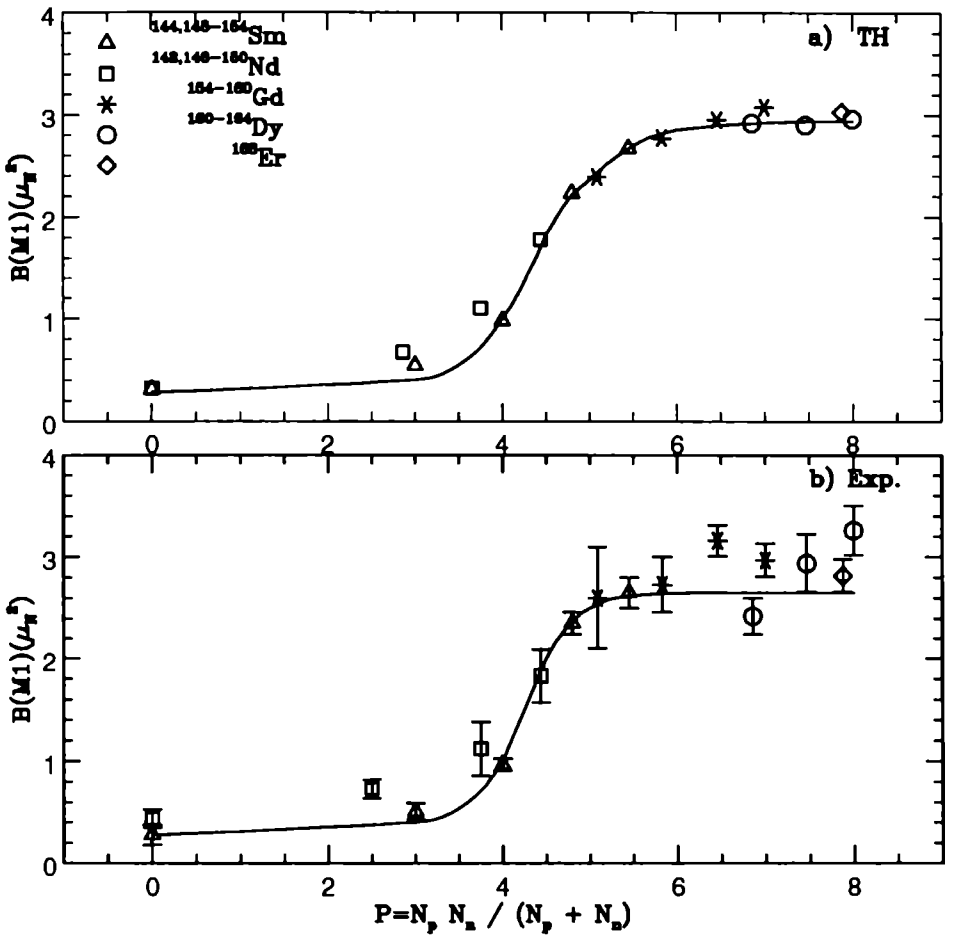

Fig. 1. Summed $M1$ strength computed by the empirical TRM formula versus the fractional number P introduced by Casten[42].

3. Phenomenological descriptions

The TRM $M1$ strength, in the form given by eq. (21), represents the semiclassical limit of several phenomenological models. We will discuss briefly the connection

with GCSM and IBM-2

3.1. Relation to the GCSM

In the GCSM[39] an interacting quadrupole boson hamiltonian which does not preserve the number of bosons is adopted. This Hamiltonian is treated by means of states obtained by projecting the good angular momentum out of intrinsic states constructed by operating with quadrupole bosons on a coherent state representing a boson condensate. The model has been used with success to describe the properties of the low energy levels of spherical, transitional and deformed nuclei.

The $M1$ mode has been described by a state obtained by angular momentum projection from an intrinsic wave function of the form

$$\Phi_{sc} = (b_n^\dagger \otimes b_p)_{J=K=1}\Phi_0 \tag{23}$$

where $b_\tau^\dagger(b_\tau\ ), (\tau = p,n)$ are quadrupole boson creation (annihilation) operators acting on a coherent ground state of the form

$$\Phi_0 = exp[d\sum_\tau (b_{\tau 0}^\dagger - b_{\tau 0})]|0> . \tag{24}$$

Here d is a deformation parameter which can be related directly to the $E2$ strength. In the limit of strong deformation we have indeed

$$d \simeq \frac{1}{\sqrt{2}} k_p \beta \tag{25}$$

where the constant k_p in the harmonic limit becomes

$$k_p = (B_p C_p)^{1/4} \simeq (B_p \omega)^{1/2}. \tag{26}$$

In this limit the GCSM $M1$ strength can be written in the scissors form[22]

$$B(M1)\uparrow \simeq \frac{9}{4\pi} d^2 g_r^2 \mu_N^2 \simeq \frac{9}{8\pi} k_p^2 \beta^2 g_r^2 \mu_N^2 \simeq \frac{9}{8\pi} B\omega\beta^2 g_r^2 \mu_N^2 \tag{27}$$

having used $B_p \simeq B/2 \simeq \Im\beta^2/6$. This is just the TRM eq. (21),

The numerical calculations[22] have been carried out once the model parameters have been fixed so as to reproduce some selected levels of the ground, β and γ bands and the E2 transition strength. The results of such a parameter free calculation are quite good. The $M1$ strength follows closely the observed quadratic law and saturates correctly with deformation.

3.2. Relation to IBM-2

The above strength is consistent with the TRM definition. Since the TRM ground state has vanishing angular momentum, we can indeed write the harmonic relation for the mass parameter (6) in the following way

$$\Im_{sc}\omega = < S^2 > = -\frac{1}{4} < \vec{L}_p \cdot \vec{L}_n > \tag{28}$$

Using now eqs.(4) and (6) of ref.[20] we get

$$\Im_{sc}\omega =< S^2 >= 12P\frac{< N_d >}{N-1} \tag{29}$$

where $N = N_\pi + N_\nu$. Upon insertion into the TRM strength (eq. 9) we get

$$B(M1)\uparrow = \frac{3}{16\pi}\langle 0 \mid S^2 \mid 0\rangle(g_\pi - g_\nu)^2\mu_N^2 \simeq \frac{9}{4\pi}P\frac{< N_d >}{N-1}(g_\pi - g_\nu)^2\mu_n^2, \tag{30}$$

where N_π and N_ν are the number of valence proton and neutron pairs, $< N_d >$ is the average number of quadrupole bosons in the ground state, $P = 2N_\pi N_\nu/N$ the fractional number introduced by Casten[42]. This is the most general IBM-2 $M1$ summed strength consistent with the conservation of $F-$spin symmetry. It yields the expression derived in the $SU(3)$ limit as a special case ($n_d =< N_d > /N = 2/3$).

We can render the relation to the semiclassical scheme more explicit by the following procedure. Let us write

$$N_d = N_d^{(p)} + N_d^{(n)} = d_p^\dagger \cdot d_p + d_n^\dagger \cdot d_n \quad , \tag{31}$$

having denoted by $d_\tau^\dagger$ and d_τ the quadrupole boson creation and annihilation operators respectively. Being a scalar, N_d can be referred to the intrinsic frame. In the classical limit, the harmonic approximation holds. We can then transform to shape variables by means of the canonical transformation

$$\alpha_{2\mu}^{(\tau)} = \alpha_0^{(\tau)}(d_{\tau,\mu}^\dagger + d_{\tau,\mu}) \quad , \qquad \alpha_\tau^{(0)} = \sqrt{\frac{1}{2B_\tau\omega}} \tag{32}$$

The $\mu = 1$ components are the shape variables entering into the TRM Hamiltonian (eq. 18). We can therefore assume ω to be the energy of the scissors mode.

In dealing with an axially symmetric system it is appropriate to take as intrinsic ground state an harmonic oscillator wave function which is coherent only in the proton and neutron $\mu = 0$ components of $\alpha_{2\mu}^{(\tau)}$. We have $d_{\tau,0}\psi_c = \delta_{\mu 0}d'_\tau\psi_c$ where d'_τ are pure c-numbers. It follows that $\beta_\tau =< \alpha_{20}^{(\tau)} >_c = 2\alpha_0^{(\tau)}d'_\tau$ In the strong coupling limit we then obtain

$$< N_d >= \frac{1}{4}\left[\left(\frac{\beta_p}{\alpha_0^{(p)}}\right)^2 + \left(\frac{\beta_n}{\alpha_0^{(n)}}\right)^2\right] = \frac{1}{2}\omega\left(B_p\beta_p^2 + B_n\beta_n^2\right) \tag{33}$$

Putting $\Im_\tau = 3\beta_\tau^2 B_\tau$ as in the TRM approach, we obtain the result

$$< N_d >= \frac{1}{6}(\Im_p + \Im_n)\omega = \frac{1}{6}\Im\omega = \frac{1}{2}B\omega\beta^2 \tag{34}$$

With the help of this equation and eq. (30) we can write the IBM-2 summed strength in the TRM form (9) with a mass parameter given by

$$\Im_{sc} = 2P\frac{\Im}{N-1} \simeq \frac{4\Im_\pi\Im_\nu}{\Im} \quad , \qquad \Im_\tau = N_\tau/N. \tag{35}$$

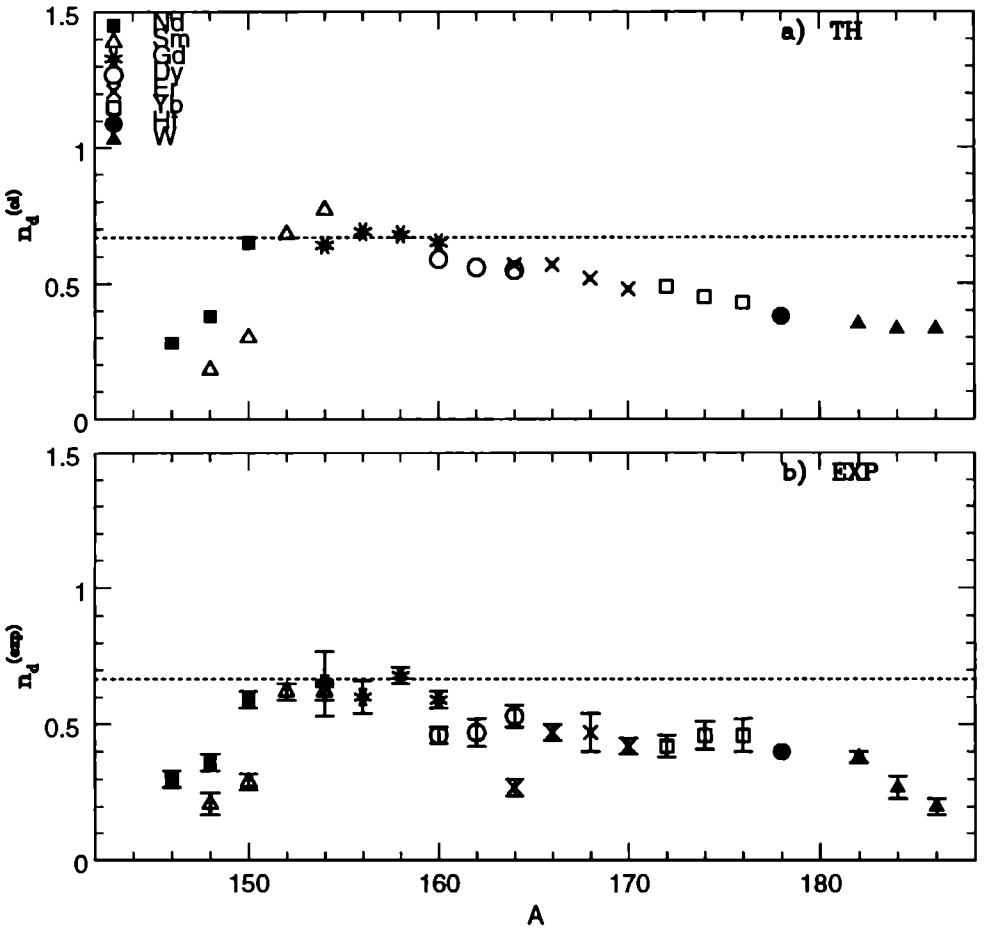

Fig. 2. Fractional number of IBM-2 d bosons versus the mass number.

The procedure just outlined enables us to state an explicit relation between the number of quadrupole bosons in the IBM-2 ground state and the Bohr-Mottelson deformation parameter β. In virtue of this relation, the IBM-2 strength appears to be quadratic in the deformation parameter consistently with experiments. Such a property is hidden when the same strength is expressed in the IBM-2 formalism.

To test the validity of the semiclassical expression of the IBM-2 $M1$ sum rule we use eq. (34) to compute the fraction of quadrupole bosons in the ground state of the nuclei of the whole rare-earth region and compare with the values extracted

from the experimental $M1$ strengths[12] using eq. (30) with$g_\pi = 1$ and $g_\nu = 0$.

In the calculation we assume equal deformation for protons and neutrons and constant B and ω throughout the whole rare-earth region. We choose for the energy the value $\omega = 3MeV$. We fix B by imposing the equality $n_d^{(cl)} = n_d^{(exp)}$ in ^{158}Gd. For this nucleus in fact the experimental $M1$ strengths give almost exactly the $SU(3)$ value $n_d^{(exp)} = 2/3$.

Semiclassical and experimental values of the fraction of quadrupole bosons are plotted versus A in Fig.2. The two quantities have a similar behaviour. The computed fraction of quadrupole bosons increases rapidly up to a maximum value and then decreases slowly with A in good agreement with experiments.

4. From the semiclassical approach to schematic RPA: A low and a high energy mode

The definitions given for the TRM constants in section 2 can be adopted also in a microscopic context. We will actually apply them to get the results of schematic RPA and will show that they coincide with the semiclassical results.

4.1. Semiclassical approach

In the semiclassical approach the restoring force constant can be determined from the symmetry energy mass formula

$$\Delta V = \frac{1}{2} b_s \int \frac{(\delta\varrho)^2}{\varrho_0} d\vec{r} = \frac{1}{2} b_s \int \frac{(\delta\varrho_p - \delta\varrho_n)^2}{\varrho_0} d\vec{r} \tag{36}$$

where $b_s \simeq 50MeV$ and ϱ_0 is the nuclear density normalized to the mass number. The density variation is computed by making use of eqs. (16) with the result

$$\delta\varrho_\tau = \varrho_\tau(\vartheta_\tau) - \varrho_\tau(0) = k_\tau \varrho_0^{(\tau)} \sum_{\mu=\pm 1} \alpha_{2\mu}^{(\tau)} r^2 Y_{2\mu}^*, \tag{37}$$

where the constant k_τ is fixed by the normalization condition (15) and $\alpha_{2\mu}^{(\tau)}$ is given by eq. (17). Upon insertion into eq. (36) we obtain

$$\Delta V = \frac{1}{2} C \vartheta^2, \tag{38}$$

where

$$C \simeq \frac{28}{5} b_s A \delta^2 \ . \tag{39}$$

If the mode is assumed to arise from a relative motion between two irrotational fluids we can attach to each of the two rotors the velocity fields

$$\vec{v}_p = -\vec{\nabla}\chi_p, \qquad \vec{v}_n = -\vec{\nabla}\chi_n \tag{40}$$

where

$$\chi_\tau = \delta\ x_{2_\tau} x_{3_\tau}\ \Omega_{1_\tau} + \delta\ x_{1_\tau} x_{3_\tau}\ \Omega_{2_\tau} \tag{41}$$

where Ω_{i_τ} ($i_\tau = x_\tau, y_\tau$) are the proton and neutron angular velocities. We get a two rotor Hamiltonian of the form given by eq. (1) and therefore an intrinsic one given by eq. (3) with an irrotational moment of inertia

$$\Im_{sc} = \Im_{irr} = \delta^2 \Im_{rig} , \qquad \Im_{rig} \simeq \frac{2}{5} m A R^2 \tag{42}$$

The energy of the mode and the corresponding strength are given by

$$\omega_+ = \sqrt{\frac{C}{\Im_{irr}}} \simeq 139.4\, A^{-1/3}\, MeV, \tag{43}$$

$$B_+(M1)\uparrow = \frac{3}{16\pi} \Im_{irr} \omega\, g_r^2\, \mu_N^2 \simeq 0.12\, \delta^2\, A^{4/3}\, g_r^2\, \mu_N^2. \tag{44}$$

The strength is quadratic in the deformation parameter, but the energy is far higher than the observed one. We obtain indeed for ^{154}Sm $\omega \simeq 26\ MeV$ and $B(M1)\uparrow \simeq 4.7\ \mu_N^2$, having put $g_n = 0$ and $g_p = 2g_R = 2Z/A$. Although the $M1$ strength is reasonably close to the experimental value, the energy lies in the region of the giant isovector quadrupole resonance. It is indeed the energy of the $K^\pi = 1^+$ component of the isovector quadrupole resonance mode.

In order to get a low energy mode as required by experiments, we could use a rigid body moment of inertia as done in the original formulation[2]. We know on the other hand from that paper that the resulting $M1$ strength is six times larger than the experimental summed strength. It seems therefore hopeless to get close to the experimental data if we remain entirely within the classical domain.

4.2. Microscopic approach

Let us assume that nucleons move in a deformed mean field described by an anisotropic harmonic oscillator potential with frequencies ω_1 and ω_3 such that $\omega_1^2 \omega_3 = \omega_0^3$ and $\omega_0 \simeq 41 A^{-1/3} MeV$.

4.2.1. High energy mode

We use now eq. (6) in the specific form

$$\frac{1}{\Im_{sc}} < S^2 > = \frac{1}{\Im_{sc}} \sum_{ph \in 2\omega_0} \sum_{\mu \pm 1} |\langle\, ph \mid S_\mu \mid \rangle|^2 = \omega_1 + \omega_3 \simeq 2\omega_0 \tag{45}$$

where $|\ \rangle$ is the particle-hole vacuum. The sum is restricted to the $\Delta N = 2$ particle-hole excitations. This condition yields

$$\Im_{sc} = \Im_{irr} = \delta^2 \Im_{rig} , \qquad \Im_{rig} = \frac{1}{\delta\omega_0} \sum_{ph \in \delta\omega_0} |(S_+)_{ph}|^2 \simeq \frac{2}{5} m A R^2 , \tag{46}$$

which is the irrotational mass parameter obtained in the semiclassical approach (eq. 42). Let us now decompose the restoring force constant into a kinetic and a

potential component

$$C_+ = C_0^{(+)} + C_1^{(+)} = C_0^{(+)}(1 + a_+) \ , \qquad a_+ = \frac{C_1^{(+)}}{C_0^{(+)}} \tag{47}$$

The unperturbed part can be obtained from the defining eq. (46)

$$C_0^{(+)} \simeq \Im_{irr}(2\omega_0)^2 \simeq \frac{28}{5} b_0 A\delta^2 \tag{48}$$

where $b_0 \simeq 17.5 MeV$. The potential component follows from its relation to the energy symmetry potential $V_1 \simeq 130\ MeV$ which yields $b_1 = V_1/4 \simeq 32.5 MeV$. The total strength is $b_s = b_0 + b_1 \simeq 50 MeV$ exactly as in the semiclassical case. Consequently the total restoring force C_+ coincides with the semiclassical quantity given by eq. (39). It is to be noted that $a_+ = C_1^{(+)}/C_0^{(+)} = b_1/b_0 \simeq 1.9$. This is in complete agreement with the estimate made within the unified theory of Bohr and Mottelson[43] for the isovector quadrupole giant resonance.

Energy and strength are therefore given exactly by the semiclassical eqs. (43) and (44) respectively. The gap between semiclassical and microscopic descriptions is thereby filled.

4.2.2. Low energy scissors mode

For the low energy mode we make use of the defining eq.7 with the following requirement

$$\frac{1}{\Im_{sc}} < S^2 >= \frac{1}{\Im_{sc}} \sum_{ph \in \delta\omega_0} \sum_{\mu=\pm 1} |\langle\ ph \mid S_\mu \mid \rangle|^2 \simeq \delta\omega_0 \tag{49}$$

where the sum is restricted to the $\Delta N = 0$ particle-hole space. This yields a rigid body moment of inertia $\Im_{sc} = \Im_{rig}$. The unperturbed restoring force constant is now

$$C_0^{(-)} \simeq (\delta\omega_0)^2 \Im_{rig} = \frac{28}{5} b_0^{(-)} A\delta^2 \tag{50}$$

with $b_0^{(-)} \simeq b_0/4$. The potential component can be fixed[43] from the ratio between the nuclear isovector and isoscalar average potential strengths V_1 and V_0, $a_- = C_1^{(-)}/C_0^{(-)} = b_1^{(-)}/b_0^{(-)} = -V_1/(4V_0) \simeq 0.6$. The final result is

$$\begin{aligned} \omega_- &= \sqrt{\frac{C_-}{\Im_{rig}}} = \delta\omega_0\sqrt{1 + a_-} \simeq 53\delta A^{-1/3} MeV \ , \\ B_-(M1)\uparrow &\simeq \frac{3}{4\pi}\Im_{rig}\omega_- \simeq 0.045\delta A^{4/3} g_r^2 \mu_N^2 \ . \end{aligned} \tag{51}$$

The strength so determined is close to that derived in the TRM in its original formulation[2] and, as pointed out already, is unrealistically larger than the observed summed strength. It will turn nonetheless useful for superdeformed nuclei.

We may alternatively impose for the low energy mode

$$\frac{1}{\Im_{sc}} < S^2 >= E(\epsilon_{sp}) + E(\epsilon_{sp} + \delta\omega_0) \tag{52}$$

where ϵ_{sp} is the single particle energy referred to the chemical potential λ. It is natural to choose for λ the value $\lambda = (\delta\omega_0)/2$. With this choice the previous equation becomes

$$\frac{1}{\Im_{sc}} < S^2 >= 2E = \sqrt{(\delta\omega_0)^2 + (2\Delta)^2} \tag{53}$$

Using closure we obtain for the mass parameter

$$\Im_{sc} \simeq \Im_{sf} \simeq \frac{\delta\omega_0}{(2E)}(u(\epsilon_{sp})v(\epsilon_{sp} + \delta\omega_0) - (v(\epsilon_{sp})u(\epsilon_{sp} + \delta\omega_0))^2\Im_{rig} \simeq (\frac{\delta\omega_0}{2E})^3\Im_{rig} \ , \tag{54}$$

having made use of the standard expressions of the amplitudes u and v with $\lambda = (\delta\omega_0)/2$. The resulting energy and strength are

$$\omega_- = \sqrt{\frac{C_-}{\Im_{sf}}} \simeq (2E)\sqrt{1 + a_-} \ , \qquad B_-(M1)\uparrow \simeq \frac{3}{16\pi}\omega_-\Im_{rig}(\frac{\delta\omega_0}{2E})^3 g_r^2\mu_N^2 \tag{55}$$

or more explicitly

$$\omega_- \simeq 1.26(2\Delta)\sqrt{1 + x^2}, \qquad B_-(M1)\uparrow \simeq 0.001(2\Delta)A^{5/3}\frac{x^3}{1 + x^2}g_r^2\mu_N^2 \tag{56}$$

where $x = \delta\omega_0/(2\Delta)$. According to these equations the strength goes like δ^3 for small deformations ($x \ll 1$) and becomes linear for very large deformations ($x \gg 1$).

Had we averaged the two quasi-particle energies and the moment of inertia with respect to λ[43] we would have obtained exactly the schematic RPA strength derived by Hamamoto and Magnusson[26] Such a strength is quadratic for weak deformations but deviates from the quadratic law as the deformation parameters increases. Numerically the two procedures lead to very similar results. Putting in fact $g_r = 1$, we obtain in both cases a $M1$ strength approximately quadratic in δ at least in the range of deformations observed in Sm isotopes. In the most deformed nuclei, however, we obtain a value which is about a factor two larger than the experimental summed strength. A quenching gyromagnetic factor is needed. This can be effectively obtained only from realistic RPA calculations, like the one carried out in [26], which account for spin admixture.

4.3. Scissors modes in superdeformed nuclei

We have seen that, in its reformulated version, the TRM predicts a low and a high energy mode. In the first mode protons and neutrons behave approximately as superfluid systems, in the second as irrotational fluids. Being the modes switched by deformation, the predictions of the model should apply in principle to superdeformed nuclei.

If K is a good quantum number, the transition goes from K to $K+1$. The $M1$ operator couples the state $\mid IMK\rangle$ to the states $\mid I'M'K+1\rangle$ with $I' = I-1, I, I+1$. Using the standard expression for the transition matrix elements[43] with the TRM intrinsic wave function[2] and assuming $I \gg K$ we obtain for the summed strength

$$\sum_{I'} B(M1, IK \rightarrow I'K+1) \simeq \frac{3}{16\pi} \Im_{sc}\, \omega \frac{1}{K+1} g_r^2\, \mu_N^2 \,. \tag{57}$$

According to this expression the strength decreases with increasing K. If we assume that the superdeformed state has $K = 0$, we gain the standard scissors expression (eq. 9. We may use eqs. (44) obtaining for the high energy mode of the superdeformed ^{152}Dy ($\delta \simeq 0.62$)

$$\omega_+ \simeq 26\ MeV, \qquad B_+(M1) \uparrow \simeq 26.1\ \mu_N^2 \,, \tag{58}$$

where we have put $g_n = 0$ and $g_p = 2g_R = 2Z/A$.

For the low energy mode we may assume rigid rotors and use eqs. (56) with $g_n = 0$ and $g_p = 1$, obtaining for the same superdeformed nucleus

$$\omega_- \simeq 6.1\ MeV, \qquad B_-(M1) \uparrow \simeq 22.6\ \mu_N^2 \,. \tag{59}$$

The above numbers are in agreement with the RPA results of ref.[44]. They have been obtained under the assumption that, in going from deformed to superdeformed nuclei, protons and neutrons in their relative motion remain irrotational at high energy but undergo a transition from a superfluid to a rigid-body phase at low energy. Such an assumption is fully consistent with the conclusions drawn in ref.[44].

We like to stress that, according to our equations based on the use of the TRM scissors wave function, these strong transitions occur only if the intrinsic superdeformed state has $K = 0$. If such a state has a non vanishing but small K or contains K admixture the corresponding strength should be still sizeable.

4.4. Equivalence with schematic RPA

When expressed in terms of shape variables the intrinsic TRM Hamiltonian coincides with the harmonic Hamiltonian adopted within the unified theory[43] Let us indeed switch from the normalization (15) to the new one

$$< Q_{\lambda\mu} >= \int \varrho(\vec{r}) r^\lambda Y_{\lambda\mu}(\vec{r}) d\vec{r} = \alpha_{\lambda\mu} \,. \tag{60}$$

This induces in turn a renormalization of the mass and restoring force parameters. These assume the form

$$\begin{aligned} \Im_{sc} \quad &\Longrightarrow \quad B_\alpha = \frac{\Im_{sc}}{3\beta^2(\frac{3}{4\pi}AR^2)^2} = \frac{2\pi}{3}\frac{m}{AR^2} \\ C_\vartheta \quad &\Longrightarrow \quad C_\alpha = \frac{C}{3\beta^2(\frac{3}{4\pi}AR^2)^2} = C_\alpha^{(0)} + C_\alpha^{(1)} \,, \end{aligned} \tag{61}$$

where

$$C_\alpha^{(0)} \simeq \frac{8\pi}{3}\frac{m\omega_0^2}{AR^2}\ , \qquad C_\alpha^{(1)} \simeq \frac{7}{3}\frac{\pi V_1}{AR^4}\ . \tag{62}$$

The above quantities are just the mass parameters and coupling strengths derived within the unified theory approach[43] We have indeed adopted effectively the unified theory philosophy already in the description of the mode discussed in sect.3.

The link with schematic RPA is now obtained simply through the standard condition[43]

$$\sum_\mu |\alpha_{2\mu}|^2 = \sum_\mu \sum_{ph} |(Q_{2\mu}(1))_{ph}|^2\ , \qquad Q_{2\mu}(1) = Q_{2\mu}^{(p)} - Q_{2\mu}^{(n)} \tag{63}$$

Useless to say, an explicit RPA calculation would yield exactly the results obtained in the previous subsections.

5. Proton-neutron schematic RPA: Selfconsistent mean fields

Schematic RPA has some virtues which we are going to discuss. Let us assume that Z protons and N neutrons move in a spherical harmonic oscillator mean field and interact through a quadrupole-quadrupole force. The Hamiltonian is therefore of the rotational invariant form

$$H = \sum_i h(i) + \frac{1}{2}\chi \sum_\mu \left(Q_{2\mu}^{(p)*}Q_{2\mu}^{(p)} + Q_{2\mu}^{(n)*}Q_{2\mu}^{(n)}\right) + \frac{1}{2}\chi_{pn}\sum_\mu \left(Q_{2\mu}^{(p)*}Q_{2\mu}^{(n)} + Q_{2\mu}^{(n)*}Q_{2\mu}^{(p)}\right) \tag{64}$$

where $\chi_{pp} = \chi_{nn} = \chi$ and χ_{pn},

$$h = \frac{1}{2m}p^2 \ + \ \frac{1}{2}m\omega_0^2 r^2 \tag{65}$$

and $(\tau = p, n)$

$$Q_{2\mu}^{(\tau)} = \sum_i q_{2\mu}^{(\tau)}(i) \ = \ \sum_i r_i^{(\tau)} Y_{2\mu}^{(\tau)}(i) \tag{66}$$

5.1. Selfconsistent mean field and double-stretched coordinates

In the Hartree approximation we obtain for the i_{th} proton or neutron deformed mean field

$$V_H^{(\tau)} = \frac{1}{2}m\omega_0^2 r^2 - \beta_\tau m\omega_0^2 q_{20}^{(\tau)} \tag{67}$$

having put

$$\chi < Q_{20}^{(p)} > + \chi_{pn} < Q_{20}^{(n)} > = -\beta_p m\omega_0^2\ , \qquad \chi < Q_{20}^{(n)} > + \chi_{pn} < Q_{20}^{(p)} > = -\beta_n m\omega_0^2 \tag{68}$$

The Hartree potential can be written in the form of an anisotropic harmonic oscillator potential

$$V^{(\tau)} = \frac{1}{2}m\omega_1^2(\tau)(x_1^{(\tau)^2} + x_2^{(\tau)^2}) + \frac{1}{2}m\omega_3^2(\tau)x_3^{(\tau)^2} \tag{69}$$

with frequencies

$$\omega_1(\tau) = \omega_0\sqrt{1+\frac{2}{3}\delta_\tau} \simeq \omega_0\left(1+\frac{1}{3}\delta_\tau\right) \ , \qquad \omega_3(\tau) = \omega_0\sqrt{1-\frac{4}{3}\delta_\tau} \simeq \omega_0\left(1-\frac{2}{3}\delta_\tau\right) \quad (70)$$

where $\delta_\tau = \sqrt{45/(16\pi)}\beta_\tau$. The same potential can be put in the "spherical" form

$$V^{(\tau)} = \frac{1}{2}m\omega_0^2\left(\tilde{x}_1^{(\tau)^2} + \tilde{x}_2^{(\tau)^2} + \tilde{x}_3^{(\tau)^2}\right) \quad (71)$$

if we use double stretched coordinates[45,46] $\tilde{x}_i = \omega_i/\omega_0\ x_i$. These are to be used in the quadrupole operator entering into the (QQ) Hamiltonian so as to preserve its spherical character. This transformation indeed insures that the Hartree field is not further distorted once the interaction is switched on. by the quadrupole-quadrupole potential. We have in fact

$$< \tilde{Q}_{20}^{(p)} > = < \tilde{Q}_{20}^{(n)} > = 0 \quad (72)$$

if we impose the conditions

$$\omega_1^{(\tau)} \sum_1^\tau = \omega_2^{(\tau)} \sum_2^\tau = \omega_3^{(\tau)} \sum_3^\tau \quad (73)$$

where $\sum_i^\tau = \sum_i^\tau (n_i + 1/2)$. The explicit form of the $\tilde{Q}$ operators is

$$\begin{aligned} \tilde{Q}_{\pm 1} &= \frac{\omega_1\omega_3}{\omega_0^2} Q_{\pm 1} \\ \tilde{Q}_{\pm 2} &= \frac{\omega_1^2}{\omega_0^2} Q_{\pm 2} \\ \tilde{Q}_{\pm 0} &= \frac{1}{3\omega_0^2}\left(\omega_1^2 + 2\omega_3^2\right) Q_0 - \frac{\sqrt{5}}{3\omega_0^2}\left(\omega_1^2 - \omega_3^2\right) r^2 Y_{00} \end{aligned} \quad (74)$$

Since the double stretched quadrupole operator, contains also a monopole term, the new (QQ) potential results composed of pure quadrupole-quadrupole plus monopole-quadrupole and monopole-monopole terms.

5.2. Consequences of selfconsistency

A quasi-particle RPA calculation formulated in the $\Delta N = 0 + 2$ space has been carried out using these double stretched coordinates[47]. It is shown that, in virtue of the self consistent conditions (eq.68), the schematic quasi-particle RPA gives a vanishing root. This is the eigenvalue of the redundant rotational mode. Such a state results to be completely removed from the intrinsic ones. One obtains indeed

$$< n, K^\pi = 1^+ | L_+ | 0 > \propto P(x) = x^3 + ax^2 + bx + c = 0 \quad (75)$$

where $P(x) = P(\omega^2) = 0$ is the eigenvalue equation giving the roots of the $M1$ physical states.

The calculation gives also the important $M1 - E2$ relation

$$B(M1)\uparrow = \frac{1}{5}m^2\omega^2 \frac{\epsilon_0^{(p)^2}\epsilon_2^{(p)^2}\left[2\omega^2 - \left(\epsilon_0^{(p)^2} + \epsilon_2^{(p)^2}\right)\right]^2}{\left[2\epsilon_0^{(p)^2}\epsilon_2^{(p)^2} - \left(\epsilon_0^{(p)^2} + \epsilon_2^{(p)^2}\right)\omega^2\right]^2} B(E2)\uparrow \tag{76}$$

where ϵ_k denotes the $\Delta N = 0$ (k=0) and $\Delta N = 2$ (k=2) particle-hole energies. The relation can be easily generalized so as to account for pairing.

The above relation shows that the isoscalar state does not carry any $M1$ strength. Its energy is in fact $\omega = \sqrt{\left(\epsilon_0^{(p)^2} + \epsilon_2^{(p)^2}\right)/2}$, The same equation can be used to get an indirect estimate of the $M1$ strength of the high energy mode if the corresponding $E2$ strength is known[49].

For the high energy mode we have

$$\omega^{(+)} \simeq \epsilon_2\sqrt{1 + a_+}. \tag{77}$$

Putting $\epsilon_0 \simeq \delta\omega_0$ and $\epsilon_2 \simeq 2\omega_0$ we obtain

$$B(M1)\uparrow \simeq 1.45\delta^2 A^{-2/3} B(E2)\uparrow \simeq 0.58\delta^2 A^{-2/3} B_{tot}(E2)\uparrow \tag{78}$$

Where we have exploited that the strength of the $K^\pi = 1^+$ mode is 2/5 of the total strength. For ^{154}Sm the experimental $E2$ strength is[49] $B(E2)\uparrow = 2610$. Using $\delta = 0.275$ we get

$$B(M1)\uparrow \simeq 0.0015 B_{tot}(E2)\uparrow \simeq 3.97\mu_N^2 \tag{79}$$

5.3. Double stretched coordinates and scissors sum rule

The double stretched coordinates have been adopted also to compute the scissors energy weighted $M1$ sum rule (eq. 12)[48]. We obtained

$$S_{EW}^{(sc)}(M1) = \frac{3}{16\pi}\left(S_1^{(sc)} + S_{20}^{(sc)} + S_{22}^{(sc)}\right) g_r^2\,\mu_N^2 \tag{80}$$

The first tern comes from the Hartree field and is given by

$$S_1^{(sc)} = \frac{1}{2}\sum_{\mu=\pm1} <0|\left[S_\mu^\dagger, [H_0, S_\mu]\right]|0> = 3m\omega_0^2\left(\beta_p < Q_{20}^{(p)} > + \beta_n < Q_{20}^{(n)} >\right) \tag{81}$$

which is what obtained in ref.[24]. The second piece comes from the two-body interaction which involves the monopole operators. This cancels exactly the one-body contribution. We get indeed

$$S_2^{(0)} = -3m\omega_0^2\left(\beta_p < Q_{20}^{(p)} > + \beta_n < Q_{20}^{(n)} >\right) \tag{82}$$

It remains therefore only the contribution from the pure quadrupole-quadrupole potential, apart from modifications induced by the use of stretched coordinates. This is given to lowest order in δ by

$$S_{EW}^{(sc)}(M1) \simeq -\frac{9}{4\pi}\chi_{pn}\left(\sum_n B_n^{(0)}(E2)\uparrow - \sum_n B_n^{(1)}(E2)\uparrow\right) \tag{83}$$

which is the result of ref.[25]. Stretched coordinates are responsible for higher order terms which however are not negligible[48]. Experimentally[49] the $E2$ strength to the lowest 2^+ state is orders of magnitude larger than the strengths of the other transitions. If these are ignored one gets

$$\omega^{(-)}B(M1)^{(-)} + \omega^{(+)}B(M1)^{(+)} \simeq -\frac{9}{4\pi}\chi_{pn}B_0^{(0)}(E2)\uparrow \tag{84}$$

One may get an indirect estimate of the $M1$ strength of the high energy mode by making use of the $M1 - E2$ relation (78). one may notice that this high energy strength is quadratic in deformation. Since the $E2$ strength depend obviously on δ^2 it follows that

$$B(M1)^{(-)} \propto \delta^2 \tag{85}$$

The sum rule approach presented here gives a quite general theoretical proof of the quadratic deformation law holding for the $M1$ strength of the low-lying scissors mode.

6. Realistic RPA

For a study of the detailed properties of the mode, realistic RPA calculations are required. As already mentioned, many problems have been encountered in the past in carrying out intrinsic RPA calculations[32]. A notable one was the occurrence of spurious rotational admixture[33]. We will discuss this point briefly.

6.1. Spurious rotational admixture

In any calculation carried out in the intrinsic system, including deformed RPA, the unperturbed ground state breaks spherical symmetry so that

$$J_{+1}|0> \neq 0. \tag{86}$$

In RPA, however, this rotational state separates out at zero energy if the starting Hamiltonian is rotationally invariant. In this case we have in fact

$$(H - E_0)J_{+1}|0> = [H, J_{+1}]|0> = 0 \tag{87}$$

Being indeed a solution of the RPA equations, the state given by eq. (86) is orthogonal to the other RPA states.

The problem is therefore solved if the deformed mean field is derived self-consistently from the two-body part of a rotationally invariant Hamiltonian. This

explains why the $M1$ states derived in schematic RPA are free of spurious rotational admixture (sect.5).

In most calculations, however, the deformed field is not obtained selfconsistently. Rotational symmetry is therefore not preserved by these Hamiltonians so that

$$[H, J_{+1}] \neq 0 \tag{88}$$

and therefore

$$< K^{\pi} = 1^{+}|J_{+1}|0 > \neq 0 \tag{89}$$

This point was first pointed out in Ref.[33]. In order to give a clue to the solution of this problem we insert our harmonic oscillator deformed mean field (eq. 67) into eq. (88) obtaining

$$[H_0, J_{+1}] \propto Q_{21}^{(p)} + Q_{21}^{(n)} \tag{90}$$

In order to restore rotational invariance one must modify the isoscalar quadrupole-quadrupole interaction $V^{(\tau=0)}$ so that

$$[H_0 + V^{(\tau=0)}, J_{+1}] = 0 \tag{91}$$

This is what obtained approximately in Ref.[33] following a prescription given by Pyatov et al.[50]. The net result was to fix the coupling constant of the isoscalar quadrupole-quadrupole interaction.

6.2. RPA in the Laboratory frame

A way of avoiding the above difficulties would be to formulate the RPA directly in the laboratory frame. This has been attempted in a recent calculation[28] by using a projected single particle basis which, though reproducing the Nilsson spectra to a good approximation, is composed of states of good angular momentum. The technique for constructing such a basis has been developed elsewhere[51,52]. The underlying ideas will be sketched below.

Let us write the deformed Nilsson Hamiltonian in the form

$$h_{Nils}(\delta) = h_{sph} - m\omega_0^2 \beta Q_{20} \tag{92}$$

where h_{sph} stands for the spherical Nilsson component. Let us now consider the rotational invariant particle-core Hamiltonian:

$$\tilde{H} = h_{sph} + H_{core} - k_c \sum_{\mu} (b_{\mu}^{+} + b_{-\mu}) Q_{2\mu}^{*} \tag{93}$$

where H_{core} is an interacting quadrupole boson Hamiltonian describing a phenomenological core and the third component is a particle-core coupling term. We now use a core coherent state which turns the boson operator b_{μ} into c-numbers, to take the mean value

$$< \psi_g|h|\psi_g > = < \psi_g|(\tilde{H} - H_{core})|\psi_g > = h_{sph} - 2k_c \; d \; Q_{20}. \tag{94}$$

This can be identified with the deformed Nilsson Hamiltonian (33) if we put $2\ d\ k_c = m\omega_0^2\ \beta$. Inspired by this property we consider particle-core angular momentum projected states of the form

$$\Phi_{\alpha IM}(d) = \mathcal{N}_{\alpha I} P^I_{MI}[\varphi_{\alpha I}\psi_g] \tag{95}$$

where $\varphi_{\alpha I} = \varphi_{nljI}$ are spherical single particle states, $\mathcal{N}_{\alpha I}$ is a normalization factor, P^I_{MI} a projection operator of standard form. We then considered these states as eigenstates of an effective Fermionic single particle Hamiltonian h_{eff} whose eigenvalues are assumed to be the mean values

$$\epsilon_{\alpha I} \ = \ \langle \Phi_{\alpha IM}(d) \mid h \mid \Phi_{\alpha IM}(d) \rangle \ . \tag{96}$$

These energies depend not only on (nlj) but also on I which plays here the same role as $|\Omega|$ in the Nilsson basis. The corresponding "eigenstates" are mutually orthogonal with respect to I and M. They are not exact eigenstates of the particle-core Hamiltonian (34) and therefore do no reproduce exactly the Nilsson spectrum. For a given deformation however, it is possible to obtain the Nilsson level scheme to a good approximation by a suitable choice of the strength k_c. The correspondence with the Nilsson states is not one to one. Because of the degeneracy in M, $2I+1$ states of the present basis will correspond to a $|\Omega| = I$ Nilsson state. We can keep however all M-degenerate projected single particle states given by eq. (36) as long as we normalize them to $2/(2I+1)$ rather than 1.

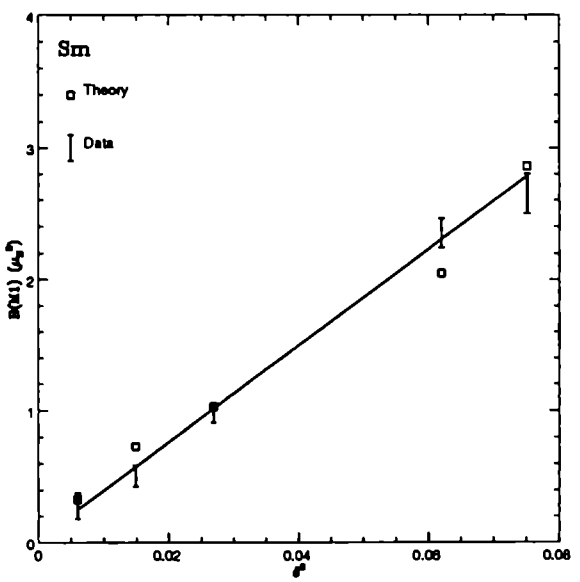

Fig. 3. Summed $M1$ strength versus deformation square for Sm isotopes in RPA with a projected basis.

We adopted these projected basis to carry a QRPA calculation in the laboratory frame using a spherical one body term with single particle energies given by eq. (37) and a two-body potential composed of monopole pairing treated in BCS , quadrupole and spin interactions.

We carried out calculations for *Sm* isotopes. We found that practically all excitations of mainly orbital nature fall below 4 MeV while the spin levels are above. Fig. 3 shows that the summed M1 strength of the orbital excitations below 4 MeV is linear in δ^2, in good agreement with the experimental data. As in the other microscopic approaches the deformation law is obtained only after pairing has been included. Also the $M1$ spin distribution with its characteristic double-hump structure observed recently[13] in ^{154}Sm is fairly well reproduced.

7. Concluding remarks

We have shown that the TRM expression of the $M1$ strength can be taken as the definition of the scissors M1 strength once the parameters entering into the TRM Hamiltonian are properly redefined. Such a definition, which is consistent with the observed deformation properties of the low lying $M1$ excitations on phenomenological ground, applies to several approaches including the interacting boson models like the GCSM and IBM-2. When used in these contexts the TRM definition describes the deformation properties of the mode in good agreement with experiments.

The definition can also be applied to get the $M1$ strength in schematic RPA. In this context a high energy mode in addition to the low energy one observed in all deformed nuclei is predicted. An indirect evidence in favour of this excitation has been found recently[49]. It applies also to super-deformed nuclei for which strongly collective excitations of the same nature are predicted.

We have pointed out that the deformed harmonic oscillator potential in schematic RPA can be considered as a selfconsistent potential in the Hartree approximation. In virtue of such a property, no rotational admixture appears in the states describing the M1 excitations if doubled stretched coordinates are adopted. These new coordinates generate quadrupole-monopole terms in the Hamiltonian which cancel the contribution coming from the deformed mean field to the energy weighted $M1$ sum rule.

For a detailed description of the properties of the $M1$ excitations it is necessary to exploit the full shell model structure as in realistic RPA. These calculations, being carried out in the intrinsic system, have run in the past into difficulties which have been now removed. As an alternative way of avoiding them, a RPA calculation carried out in the laboratory frame using a projected single particle basis has been discussed. This calculation relies on approximations whose validity needs to be studied. The results obtained are however encouraging.

8. References

1. D. Bohle et al. *Phys. Lett.* **B137** (1984) 27.
2. N. Lo Iudice and F. Palumbo, *Phys. Rev. Lett.* **41** (1978) 1532; G. De Franceschi, F. Palumbo and N. Lo Iudice, *Phys. Rev.* **C29** (1984) 1496.
3. U.E.P. Berg, C. Bläsing, J. Drexler, R.D. Heil, U. Kneissl, W. Naatz, H. Ratzek, S. Schennach, R. Stock, T. Weber, H. Wickert, B. Fischer, H. Hollick and D. Kollewe, *Phys. Lett.* **B149** (1984) 59.
4. For a review and references A. Richter in *The building blocks of nuclear structure*, ed. A. Covello, (World Scientific, Singapore, 1992), p. 135.
5. D. Bohle, A. Richter, U.E.P. Berg, J. Drexler, R.D. Heil, U. Kneissl, H. Metzger, R. Stock, B. Fischer, H. Hollick and D. Kollewe, *Nucl. Phys.* **A458** (1986) 205.
6. C. Djalali, N. Marty, M. Morlet, A. Willis, J.C. Jourdain, D. Bohle, U. Hartman, G. Küchler, A. Richter, G. Caskey, G.M. Crawley and A. Galonsky, *Phys. Lett.* **B164** (1985) 269.
7. C. Wesselborg, K. Schiffer, K.O. Zell, P. von Brentano, D. Bohle, A. Richter, G.P.A. Berg, B. Brinkmöller, J.G.M. Römer, F. Osterfeld and M. Yabe, *Z. Physik* **A323** (1986) 485.
8. D. Frekers, D. Bohle, A. Richter, A. Abegg, R.E. Azuma, A. Celler, C. Chan, T.E. Drake, K.P. Jackson, J.D. King, C.A. Miller, R. Schubank, J. Watson and S. Yen, *Phys. Lett.* **B218** (1989) 439.
9. W. Ziegler, C. Rangacharyulu, A. Richter and C. Spieler, *Phys. Rev. Lett.* **65** (1990) 2515.
10. C. Rangacharyulu, A. Richter, H.J. Wörtche, W. Ziegler and R.F. Casten, *Phys. Rev.* **C43** (1991) R949.
11. J. Margraf et al., *Phys. Rev.* **C47** (1993) 1474.
12. P. von Brentano, A. Zilges, R.-D. Herzberg, U. Kneissl, J. Margraf, and H.H. Pitz, Nucl. Phys. **A577**, 191c (1994) and references therein.
13. D. Frekers, H. J. Wörtche, A. Richter, A.Abegg, R.E. Azuma, A. Celler, C. Chan, T.E. Drake, K.P. Jackson, J.D. King, C.A. Miller, R. Schubank, M.C. Vetterli and S. Yen, *Phys. Lett.* **B244** (1990) 178.
14. For a more complete picture see A. Richter, *Nucl. Phys.* **A553** (1993), 417c.
15. S.G. Rohozinski and W. Greiner, *Z. Phys.* **A322** (1985) 271.
16. J.N. Ginocchio, *Phys. Lett.* **B265** (1991) 6.
17. T. Mizusaki, T. Otsuka and M. Sugita, *Phys. Rev.* **C44** (1991) R1277.
18. K. Heyde and C. De Coster, *Phys. Rev.* **C44** (1991) R2262.
19. K. Heyde, C. De Coster, A. Richter, and H.-J. Wörtche, *Nucl. Phys.* **A 549** (1992) 103.
20. K. Heyde, C. De Coster, D. Ooms, and A. Richter, *Phys. Lett.* **B 312** (1993) 267.
21. K. Heyde, C. De Coster, and D. Ooms, *Phys. Rev.* **C 49** (1994) 156.
22. N. Lo Iudice, A.A. Raduta and D.S. Delion, *Phys. Lett.* **B300** (1993) 195;

Phys. Rev. **C50** (1994) 127.
23. N. Lo Iudice and A. Richter, *Phys. Lett.* **B304** (1993) 193.
24. E. Moya de Guerra , and L. Zamick, *Phys. Rev.* C **47** (1993) 2604.
25. Zamick and D.C. Zheng, *Phys. Rev.* **C44** (1991) 2522; **C46** (1992) 2106.
26. I. Hamamoto and C. Magnusson, *Phys. Lett.* **B260** (1991) 6.
27. P. Sarriguren, E. Moya de Guerra, R. Nojarov and A. Faessler, *J. Phys: Nucl. Phys.* **G19** (1993) 291.
28. A.A. Raduta, N. Lo Iudice and I.I. Ursu, *Nucl. Phys.* **A584** (1995) 84.
29. E. Garrido, E. Moya de Guerra, P. Sarriguren and J.M. Udias, *Phys. Rev.* **C44** (1991) R1250.
30. R.R Hilton, W. Höhenberger and H. J. Mang, *Phys. Rev.* C **47** (1993) 602.
31. For early references see C. De Coster and K. Heyde, *Nucl. Phys.* **A524** (1991) 441.
32. N. Lo Iudice and A. Richter, *Phys. Lett* **B228** (1989) 291.
33. R. Nojarov and A. Faessler, *Nucl. Phys.* **A484** (1988) 1.
34. K. Sugawara - Tanabe and A. Arima, *Phys. Lett.* **B206** (1988) 573.
35. R.R Hilton, S. Iwasaki, H.J. Mang, P. Ring, and M. Faber, in *Microscopic Approaches to Nuclear Structure Calculations*, ed. A. Covello (Editrice Compositori-Bologna, 1986) p.357.
36. C. De Coster and K. Heyde, *Phys. Rev. Lett.* **66** (1991) 2456; C. De Coster, K. Heyde and A. Richter, *Nucl. Phys.* **A542** (1992) 375.
37. C. Magnusson, *Phys. Scripta* **43** (1991) 460.
38. D. Zawischa, M. Macfarlane and J. Speth, *Phys Rev.* **C42** (1990) 1461; D. Zawischa and J. Speth, *Phys. Rev. Lett.* **B252** (1990) 4.
39. A.A. Raduta, A. Faessler and V. Ceausescu, *Phys. Rev.* **C36** (1987) 2111.
40. For references see F. Iachello and A. Arima , *The interacting boson model*, (Cambridge University Press, 1987).
41. E. Lipparini and S. Stringari, *Phys. Lett.* **B130** (1983) 139.
42. R.F. Casten, D. S. Brenner and P.E. Haustein,*Phys. Rev. Lett.* **58** (1987) 658.
43. A. Bohr and B.R. Mottelson, *Nuclear Structure* (Benjamin, N.Y., Vol. II, 1975) ch.6.
44. I. Hamamoto and W. Nazarewicz, *Phys. Lett.* **B297** (1992) 25.
45. T. Kishimoto et al., *Phys. Rev. Lett.* **35** (1975) 552.
46. H. Sakamoto and T. Kishimoto, *Nucl. Phys.* **A501** (1989) 205.
47. N. Lo Iudice, to be submitted for publication.
48. N. Lo Iudice, to be submitted for publication.
49. H.-J. Wörtche et al., *Phys. Rev. Lett.* submitted to.
50. M.I. Baznat, N.I. Pyatov, *Sov. J. Nucl. Phys.*, **21** (1975) 365
51. A. A. Raduta and N. Sandulescu, *Nucl. Phys.* **A531** (1991) 299.
52. A.A. Raduta, D.S. Delion and N. Lo Iudice, *Nucl. Phys.* **A551** (1993) 73.

EXTENSION OF MOSZKOWSKI MODEL TO PROTON-NEUTRON SYSTEMS: a) SCISSORS MODE b) GAMOW-TELLER-$2\nu\beta\beta$ DECAY.

A. A. RADUTA
Institute of Physics and Nuclear Engineering
Bucharest, PO Box MG-6, Romania

ABSTRACT

Two extensions of the Moszkowski model to a composite system of protons and neutrons are considered. One is used for describing the scissors mode while with the other one calculates the Gamow-Teller amplitude for the $2\nu\beta\beta$ decay. In both cases, most of results obtained by realistic calculations are recovered. Moreover some new results are pointed out.

1. Introduction

Schematic models are very useful since they allow to simulate the realistic cases. This goal is achieved either by analytical solutions or by minimal computational efforts. Moreover, in realistic calculations some important effects might be hidden by the inherent details. Thus, schematic models might unveil new properties of nuclear systems. On the other hand some approaches aimed at describing a many body system might be easily tested by using such a simplified scheme. To give an example, many features of boson expansion formalisms were studied [1] within the schematic model of Lipkin and Meshkov [2].

All these three virtues -simulation, reveals new aspects of the quantal systems, may serve as testing model-are obvious signatures for the schematic model proposed by Moszkowski [3]. The collective features of a many body system can be described within either a phenomenological or a microscopic formalism. A relation between these methods can be established when a set of collective variables is expressed in terms of single particle coordinates. One of the first attempts along this line was proposed by Moszkowski in Ref. [3]. Therein the connection between the unified model and the nuclear shell model is studied within a schematic approach. A many body system is moving in a mean field consisting of a two dimensional harmonic oscillator plus a spin-orbit term. The particles interact among themselves by a quadrupole-quadrupole force. The quadrupole operator comprises not only the moments of coordinates but also the quadrupole moment of linear momenta. Increasing the strength of the two body interaction, the structure of the eigenstates of the model Hamiltonian varies smoothly from a vibrational to a rotational type.

Moskowski model (MM) was used by several authors with different purposes. Thus the pairing properties of a spinless particle system described by MM were studied in Ref. 4. A different application of the Moszkowski model was proposed by Marshalek [5], who uses a boson expansion preserving the angular momentum at any

stage in order to evaluate perturbatively the first corrections to the vibrational and rotational energies. The temperature effects on the RPA (random phase approximation) states provided by the MM Hamiltonian were studied by J. da Providencia and his coworkers in Ref. [6]. The broken rotational symmetries are restored by a cranking procedure. Replacing the operators involved in MM Hamiltonian by the corresponding q-deformed operators, the resulting Hamiltonian was studied within the RPA approach [7]. It was the first time that a q-deformed many body system was treated by the RPA approach. This is a nice example to show how schematic models are used for developing a new approach for a many body system.

Here I will present two extensions of the MM formalism to a composite system of protons and neutrons. The pairing interaction for like nucleons is also considered.

The quadrupole operator involved in the two body interaction of the model Hamiltonian, is a tensor of rank one with respect to a group $\Re_3$, describing rotations in a fictitious three dimensional space. This observation suggests that the p-n extension of MM (EMM) might be suitable for describing the magnetic "dipole" (M1) states.

Replacing the two body QQ interaction with the Gamow-Teller (GT) proton-neutron interaction one obtains a new model Hamiltonian which is used to describe the $2\nu\beta\beta$ process. As we shall see, this schematic model provides a new explanation for the GT amplitude supression.

The results obtained for the two extensions of Moszkowski model, will be presented according to the following plan. A short review of the MM is given in Section 2. A possible extension of the MM to the proton-neutron (p-n) system is considered in Section 3 where the model Hamiltonian is successively treated by particle-hole RPA and semiclassical procedures. The pairing interaction is introduced in subsection C. Numerical results and the final conclusions for the scissors like excitations are presented in Section 4.

Another extension of the Moszkowski model, which is suitable for the description of the $2\nu\beta\beta$ decay, is described in Section 5. The formalism developed in Section 5 is applied in Section 6 to calculate several observables. Here we also summarise the main results concerning the double beta decay.

2. Mozkowski model: short review

The MM model [1] considers a system of nucleons moving in a mean field consisting of a two dimensional oscillator potential plus a spin orbit term

$$\begin{aligned} H_{sp} &= H_{ho} + H_{so}, \\ H_{ho} &= \frac{1}{2m}(p_x^2 + p_y^2) + \frac{m\omega_0^2}{2}(x^2 + y^2), \quad H_{so} = -C\vec{l}\vec{s}, \end{aligned} \tag{2.1}$$

and interacting among themselves through a quadrupole-quadrupole force H_{QQ}. Here m denotes the nucleon mass and ω_0 is the potential frequency. In order to write H_{QQ} in a convenient form some preliminar remarks are necessary. Since the angular momentum has only one nonvanishing component (l_z) the only effective component

of spin is s_z. The eigenstates of H_{ho} can be writen as follows:

$$|n_x n_y \sigma >= \frac{1}{\sqrt{n_x! n_y!}} (a_x^+)^{n_x} (a_y^+)^{n_y} |0> \chi_\sigma, \quad \sigma = \pm, \tag{2.2}$$

with a_x^+, a_y^+ the creation operators along the x and y axes, respectively. $\chi_\pm$ denotes the eigenstates of s_z corresponding to the eigenvalues $\pm\frac{1}{2}$, respectively. It can be checked that H_{ho} commutes with the quasispin operators

$$\begin{aligned} t_x &= \frac{1}{4}[m\omega_0(x^2 - y^2) + \frac{1}{m\omega_0}(p_x^2 - p_y^2)], \quad t_y = \frac{1}{2}[m\omega_0 xy + \frac{1}{m\omega_0} p_x p_y], \\ t_z &= \frac{1}{2} l_z = \frac{1}{2}(x p_y - y p_x), \end{aligned} \tag{2.3}$$

which are generators of an $\mathfrak{R}_3$ group describing rotations in a fictitious three dimensional space. Consequently, the eigenstates of H_{ho} can be classified by the *irrep* of this group:

$$\begin{aligned} \vec{t}^2 |Nm\sigma> &= \frac{N}{2}(\frac{N}{2} + 1)|Nm\sigma> \equiv t(t+1)|Nm\sigma>, \quad \sigma = \pm, \\ t_z |Nm\sigma> &= \frac{1}{2} m |Nm\sigma>, \quad m = -N, -N+2, ..., +N. \end{aligned} \tag{2.4}$$

The eigenvalues of H_{ho} are *

$$E_N = (N+1)\omega_0, \quad N = n_x + n_y. \tag{2.5}$$

Obviously, the states $|Nm\sigma>$ have the degeneracy $2(N+1)$. This degeneracy is partially removed by switching on the s.o. term which may be written as:

$$H_{so} = -C[t_z(+) - t_z(-)], \tag{2.6}$$

where the argument $\sigma(\pm)$ indicates the fact that the operator should be considered in the space spanned by $|Nm\sigma>$.

The states with the same N form a shell. States from different shells can not be related by any of the generators t_k $(k = x, y, z)$. The operator H_{sp} can be considered as a one body term of a many body Hamiltonian which can be written in the second quantization form:

$$H_{sp} = \frac{1}{2}\omega_0 + \omega_0 \sum_{m,\sigma} c^+_{Nm\sigma} c_{Nm\sigma} - C[T_z(+) - T_z(-)], \tag{2.7}$$

where

$$T_\mu(\sigma) = \sum_{m,m'} < Nm\sigma|t_\mu|Nm'\sigma > c^+_{Nm\sigma} c_{Nm'\sigma}, \quad \mu = \pm, z, \tag{2.8}$$

*Here one uses the units of $\hbar = 1$.

The components of the total quasispin operator are:

$$T_\mu = T_\mu(+) + T_\mu(-), \tag{2.9}$$

It is worth noticing that t_x and t_y are the components of the quadrupole moment depending only on x and y coordinates. Hence the QQ interaction in the (x, y) plane can be written as:

$$H_{QQ} = -\frac{1}{4}X(T_+T_- + T_-T_+) = -\frac{X}{2}(T^2 - T_z^2). \tag{2.10}$$

The MM Hamiltonian is defined by

$$H_{Mos} = H_{sp} + H_{QQ}. \tag{2.11}$$

One distinguishes two limiting cases. When $C = 0$, one obtains the two dimensional version of the Elliot model [8] which is suitable for describing the collective rotations and quadrupole vibrations of a many body system. Indeed, for this case the eigenvalues of H_{Mos} are given by:

$$E_{TM} = \omega_0(N_p + \frac{1}{2}) - \frac{1}{2}XT(T+1) + \frac{1}{8}XM^2, \tag{2.12}$$

where N_p denotes the number of particles in the shell N while M is the eigenvalue of

$$L_z = 2T_z, \tag{2.13}$$

and takes the values $0, \pm 2, \pm 4, ..., \pm 2T$. For a given T, the set $\{E_{T,M}\}_M$ defines a finite rotational band. Consider now an even number of particles $N_p = 2\nu$ filling the oscillator shell in a pairwise fashion in the order: $m = N, N-2, N-4, ...$ The ground state of this system corresponds to the maximum value of T, which is

$$T_0 = \nu(N + 1 - \nu). \tag{2.14}$$

From 2.12, it results that the ground band states are two fold degenerate.

The other regime, when the long range interaction is missing ($X = 0$), simulates the shell model description in realistic situations. One notes that the single particle states belonging to a given shell have the same "t" but different "t_z".The corresponding energies depend on "M" quantum number and therefore the states are "deformed". The rotational symmetry of the many body system is also broken. Since in the two dimensional case there is no spin flip, T_z is conserved. However T is not conserved. For $C > 0$ the lowest energy is reached in the many body state:

$$|\Psi_g> = |\frac{T_0}{2}, \frac{T_0}{2}+> |\frac{T_0}{2}, -\frac{T_0}{2}-> . \tag{2.15}$$

The excited many body states are equally spaced with $\omega = C$.

The case when both terms are present in the model Hamiltonian allows for a transition between vibrational and rotational regimes controlled by the parameter

$$x = \frac{1}{C} X T_0. \tag{2.16}$$

The two limits correspond to $x = 0$ and $x = \infty$ respectively. Whithin the Hartree approximation the phase transition is achieved for $x = 1$.

3. Extended Moszkowski model. Description of scissors mode.

The generators t_k are tensors of rank 2 with respect to the group R_3 while under the $\Re_3$ transformations they behave as tensors of rank one. Here, we shall use the tensorial properties corresponding to the group $\Re_3$. To begin with, let us consider the operators

$$S^+_{+\frac{1}{2}} = \frac{a^+_x + i a^+_y}{\sqrt{2}}, \quad S^+_{-\frac{1}{2}} = \frac{a^+_x - i a^+_y}{\sqrt{2}}, \tag{3.1}$$

and denote by $S_{+\frac{1}{2}}, S_{-\frac{1}{2}}$ their hermitian conjugates, respectively. These operators have some very useful properties which will be enumerated below. a) They are bosons operators, i.e.

$$[S_{\pm\frac{1}{2}}, S^+_{\pm\frac{1}{2}}] = 1. \tag{3.2}$$

b) $S^+_{+\frac{1}{2}}$ and $S^+_{-\frac{1}{2}}$ are the components $+\frac{1}{2}$ and $-\frac{1}{2}$ respectively, of a tensor of rank $\frac{1}{2}$ with respect to the group $\Re_3$. c) This property is not preserved by the hermitian conjugation operation. Indeed, the operators $-S_{+\frac{1}{2}}$, $S_{-\frac{1}{2}}$ are the components $-\frac{1}{2}, +\frac{1}{2}$ of a tensor of rank $\frac{1}{2}$. d) The $\Re_3$ generators can be easily expressed in terms of $S^+_{\pm\frac{1}{2}}$ operators:

$$t_\mu = -\frac{1}{\sqrt{2}}(S^+ S)_{1\mu}, \quad \mu = \pm 1, 0. \tag{3.3}$$

Actually, this is a Schwinger-like boson representation of the $SU2$ quasispin operators[9-11]. The Casimir operator $\vec{t}^2$ is a scalar and can be written as:

$$\vec{t}^2 = \frac{\hat{N}_{+\frac{1}{2}} + \hat{N}_{-\frac{1}{2}}}{2}\left(\frac{\hat{N}_{+\frac{1}{2}} + \hat{N}_{-\frac{1}{2}}}{2} + 1\right), \tag{3.4}$$

with

$$\hat{N}_{\pm\frac{1}{2}} = S^+_{\pm\frac{1}{2}} S_{\pm\frac{1}{2}}. \tag{3.5}$$

The eigenstates $|n_x n_y \sigma>$ with $n_x + n_y = N$ of H_{ho} can be written as linear combinations of the states

$$|mn\sigma> = \frac{(S^+_{+\frac{1}{2}})^m (S^+_{-\frac{1}{2}})^n}{\sqrt{m!n!}} |0>\sigma', \quad m + n = N, \quad \sigma' = \uparrow \delta_{\sigma,+} + \downarrow \delta_{\sigma,-}. \tag{3.6}$$

Thus the N multiplet may be described by $2(N+1)$ states $|m,n,\sigma>$ with $(m,n) \in \{(N,0),(N-1,1),...(0,N)\}$ and σ taking the values $\pm$ for spin up and down, respectively.

If in addition H_{so} is switched on, one obtains a set of $N+1$ energy levels which are equally spaced and doubly degenerate. Such a spectrum is shown in fig. 1. Denoting by $|0>_f$ the fermionic vacuum, the creation operator for one fermionic single particle state is defined by

$$c^+_{i\sigma}|0>_f = |i\sigma>, \quad i=(m,n), \quad \sigma = \pm. \tag{3.7}$$

In order to study the pairing correlations of the particles occupying the single particle states one needs to know how a state $|mn\sigma>$ transforms under the action of the time reversal operator

$$T = KC, \quad K = -i\sigma_y, \quad \mathrm{C} - \text{complex conjugation}. \tag{3.8}$$

It can be easily checked that

$$Tc^+_{mn\sigma}T^+ = (-)^{\frac{1}{2}-\sigma'}c^+_{nm-\sigma} \equiv c^+_{\widetilde{mn\sigma}}; \quad \sigma' = \frac{1}{2}\delta_{\sigma,+} - \frac{1}{2}\delta_{\sigma,-}. \tag{3.9}$$

In fig. 1 one sees that the time reversed states are degenerate. Therefore they may be paired.

The formalism we are going to develop in the next Sections, uses the single particle states $|i\sigma> \equiv |mn\sigma>$ with $m+n=N$. The time reversed corresponding states are $|\widetilde{i\sigma}> = |nm-\sigma>(-)^{\frac{1}{2}-\sigma'}$.

Since H_{Mos} contains, as a two body force, a dipole-dipole interaction (we remind the reader that the tensors are defined with respect to $\Re_3$ group) we believe that by extending H_{Mos} to a proton-neutron system we may easily study the M1 (again M1 is a dipole transition operator under any $\Re_3$ transformation) states and see whether the known features of the realistic case can be simulated by this schematic model.

Thus, we shall suppose [12] that the pn system is described by the following model Hamiltonian:

$$H_{pn} = \sum_{\tau=p,n}[\omega_{0\tau}\hat{N}_\tau - C_\tau(T^{(\tau)}_z(+) - T^{(\tau)}_z(-)] - \frac{1}{2}\sum_{\tau,\tau'}X_{\tau\tau'}[T^{(\tau)}_- T^{(\tau')}_+ + T^{(\tau)}_+ T^{(\tau')}_-], \tag{3.10}$$

where the upper index $(\tau)(=(p),(n))$ suggests that the operator T_k defined by (2.13) is to be considered in the space of τ single particle states. Also, we denoted by $\hat{N}_\tau$ the particle number operator for the τ system. The isovector and isoscalar channels of the two body interaction have the strengths X_1 and X_0, respectively.

$$X_1 = \frac{1}{2}(X_{pp} - X_{pn}), \quad X_0 = \frac{1}{2}(X_{pp} + X_{pn}). \tag{3.11}$$

The components of angular momentum having these symmetries are

$$\vec{T}_1 = \vec{T}^{(p)} - \vec{T}^{(n)}, \vec{T}_0 \equiv \vec{T} = \vec{T}^{(p)} + \vec{T}^{(n)}, \tag{3.12}$$

respectively. The two body interaction term (H_2) can be written in terms of T_1 and T_0 operators, as follows:

$$H_2 = -X_0(T^2 - T_z^2) - X_1(T_1^2 - T_{1z}^2). \tag{3.13}$$

Obviously such a separation can be extended to H_{pn}. Unfortunately, the split of H_{pn} into two pieces, one describing the "intrinsic" motion of the system (depending on T_1) while the other one is associated with the rotational collective motion, has only a formal meaning. Indeed, the operators T_{0k} do not commute with $T_{1k'}$, and consequently one can not construct an $SU2 \times SU2$ basis for studying the eigenstates of H_{pn}. If that were the case, to each intrinsic state one would associate a full rotational band. However, as we shall see later on, the two motions are decoupled for a certain value of the ratio $\frac{X_0}{X_1}$.

A. RPA-particle hole treatment.

Consider now a system of $2\pi_0$ protons and $2\nu_0$ neutrons filling the lowest levels of the major shells N_p, N_n, respectively. Since the operators $T_\pm$ are tensors of rank 1 with respect to the group $\Re_3$, they can relate only adjacent single particle states. Moreover, due to the Pauli principle only particles from Fermi levels can be promoted to the next state. Therefore the operators $T_\pm^{(\tau)}$ have the expressions:

$$T_+^{(\tau)} = a(\tau)[c_{h+}^+(\tau)c_{p+}(\tau) + c_{p-}^+(\tau)c_{h-}(\tau)],\ T_-^{(\tau)} = a(\tau)[c_{p+}^+(\tau)c_{h+}(\tau) + c_{h-}^+(\tau)c_{p-}(\tau)], \tag{3.14}$$

with

$$a(\tau) = \sqrt{\pi_0(N_p - \pi_0 + 1)}\delta_{\tau,\pi} + \sqrt{\nu_0(N_n - \nu_0 + 1)}\delta_{\tau,\nu}. \tag{3.15}$$

Here the index "h" stands for hole while "p" for particle like states. To avoid confusions we use the index "π" for protons and "ν" for neutrons and leave the index "p" for the set of quantum numbers characterising the particle states.

Within the RPA particle-hole approach one defines the operators

$$\begin{aligned}\Gamma_{(\pm)}^+ &= \frac{1}{\sqrt{2}}[X_\pi^{(\pm)}(c_{p+}^+(\pi)c_{h+}(\pi) \pm c_{p-}^+(\pi)c_{h-}(\pi)) \\ &+ X_\nu^{(\pm)}(c_{p+}^+(\nu)c_{h+}(\nu) \pm c_{p-}^+(\nu)c_{h-}(\nu)) + Y_\pi^{(\pm)}(c_{h+}^+(\pi)c_{p+}(\pi) \pm c_{h-}^+(\pi)c_{p-}(\pi)) \\ &+ Y_\nu^{(\pm)}(c_{h+}^+(\nu)c_{p+}(\nu) \pm c_{h-}^+(\nu)c_{p-}(\nu))],\end{aligned} \tag{3.16}$$

so that they satisfy bosonic commutation relations and describe harmonic modes for the model Hamiltonian The phonon states are two fold degenerate ($\omega_+ = \omega_- \equiv \omega$) and the energy is given by the following equation:

$$\begin{aligned}\omega^4 &- \omega^2[C_p^2 + C_n^2 - 2X_{pp}(a^2C_p + b^2C_n) + C_pC_n(C_pC_n \\ &- 2X_{pp}(a^2C_n + b^2C_p))] + 4a^2b^2C_pC_n(X_{pp} + X_{pn})(X_{pp} - X_{pn}) = 0,\end{aligned} \tag{3.17}$$

where the following abreviations have been used

$$a = a(\pi), \quad b = a(\nu). \tag{3.18}$$

Depending on the strengths of the two body interactions, the equation 3.17 may have at most two distinct positive solutions. Two particular cases deserve special attention.

i) $C_n = C_p \equiv C$, $X_{pn} = \pm X_{pp}$ (i.e. one channel is missing).

The equation 3.17 becomes

$$(\omega^2 - C^2)(\omega^2 - C^2 + 2X_{pp}C(a^2 + b^2)) = 0. \tag{3.19}$$

Note that the unperturbed p-h energy is a solution of the RPA equations. The second solution exists provided the following relation is obeyed.

$$X_{pp} \leq \frac{C}{2(a^2 + b^2)}. \tag{3.20}$$

When the equality sign is achieved, $\omega = 0$ is a solution for 3.19. Note that this value of X_{pp} is half of that for which the phase transition, from spherical to deformed shape, takes place in a Hartree-Fock treatment.

ii) Taking for the ratio $k = X_1/X_0$, the particular value

$$k = \frac{-C_pC_n + 2X_0(a^2C_n + b^2C_p)}{2X_0[8a^2b^2X_0 - (a^2C_n + b^2C_p)]}, \tag{3.21}$$

one of the two non-negative solutions (ω_0) is vanishing. The bosons corresponding to the energies ω_k ($k = 0, 1$) are hereafter denoted by $\Gamma_{(\pm)}(k)$. The corresponding amplitudes are also carrying this additional argument. Defining the hermitian variables

$$\theta_k = -\frac{i}{\sqrt{2}}(aX_\pi^{(\pm)}(0) + bX_\nu^{(\pm)}(0))^{-1}\Gamma^+_{(\pm)}(0), \quad k = x,\ y, \tag{3.22}$$

the following relations can be easily checked:

$$[H_{pn}, \theta_k] = 0, \quad [\theta_k, T_k] = i, \quad [\theta_k, T_{k'}] = 0, \quad k \neq k'. \tag{3.23}$$

Therefore θ_k is the conjugate variable of T_k. The model Hamiltonian can be written in terms of the RPA bosons:

$$H_{pn} = \frac{1}{2}\mathcal{C}_x\theta_x^2 + \frac{1}{2}\mathcal{C}_y\theta_y^2 + \omega_1(\Gamma^+_{(+)}(1)\Gamma_{(+)}(1) + \Gamma^+_{(-)}(1)\Gamma_{(-)}(1)), \tag{3.24}$$

where $\mathcal{C}_x, \mathcal{C}_y$ are real numbers and can be determined from the consistency conditions. The bosons $\Gamma^+_{(\pm)}$ satisfy the equations:

$$[\Gamma^+_{(+)}, T_y] = [\Gamma^+_{(+)}, T_z] = 0, \quad [\Gamma^+_{(-)}, T_x] = [\Gamma^+_{(-)}, T_z] = 0. \tag{3.25}$$

Consequently, the following relations hold:

$$[H_{pn}, T_x] \neq 0, \quad [H_{pn}, T_y] \neq 0, \quad [H_{pn}, T_z] = 0. \tag{3.26}$$

Concluding, the present procedure allows for separating the spurious modes. However the RPA states do not have good "angular momentum".

Since $T_\mu(\mu = 0, \pm 1)$ are generators for the group $\Re_3$, they may be considered as components of the operator describing the pseudo M1 transition $0^+ \rightarrow 1^+_{(\pm)}$, where the states 0^+ and $1^+_{(\pm)}$ are associated with the vacuum $|0>$ and the first RPA states $\Gamma^+_{(\pm)}|0>$ respectively, which are to be considered as intrinsic states. The reduced probability for the transition between the states $|0^+)$ and $|1^+_{(\pm)})$, defined in the laboratory frame, is given by:

$$B(M1; 0^+ \rightarrow 1^+_{(\pm)}) = \frac{3}{8\pi} a^2 (\mp X^{(\pm)}_\pi + Y^{(\pm)}_\pi)^2 \mu_N^2. \tag{3.27}$$

Here we accounted for the fact that the m.e. in the laboratory frame is twice as much as in the intrinsic frame. Indeed, the factor two is determined by the contribution of the rotational degrees of freedom to the transition matrix element. The nuclear magneton is denoted by μ_N^2.

B. Semiclassical treatment of scissors mode.

The ground state properties may be alternatively described by solving the equations provided by the variational principle

$$\delta \int_0^t < \psi | H_{pn} - i \frac{\partial}{\partial t'} | \psi > dt' = 0, \tag{3.28}$$

where ψ belongs to the Hilbert space $\mathcal{S}$, associated with the many body system. If ψ spans the whole space $\mathcal{S}$, solving (4.15) is equivalent to solving the Schrodinger equation. Here we confine the variational space to the manifold of states:

$$\psi = \psi_p(\alpha, \beta) \psi_n(\gamma, \delta) \tag{3.29}$$

with

$$\psi_p(\alpha, \beta) = N_p(\alpha, \beta) e^{\alpha T_-(+) + \beta T_+(-)} |j_a, j_a, + >_p \, |j_b, -j_b, - >_p, \tag{3.30}$$

$$\psi_n(\gamma, \delta) = N_n(\gamma, \delta) e^{\gamma T_-(+) + \delta T_+(-)} |j_c, j_c, + >_n \, |j_c, -j_c, - >_n \, . \tag{3.31}$$

The parameters $\alpha, \beta, \gamma, \delta$ are complex functions of time. The variational principle provides a set of differential equations for them and their complex conjugate functions $\alpha^*, \beta^*, \gamma^*, \delta^*$. $N_p(\alpha, \beta), N_n(\gamma, \delta)$ stand for the normalization factors of ψ_p and ψ_n respectively. The many body states $|j_i, \pm j_i, \pm >$ $(i = \alpha, \beta, \gamma, \delta)$ are eigenfunctions for $\vec{T}^2(\pm)$ and $T_z(\pm)$. Since for a vanishing two body interaction, the ground state is

$$|\frac{T_0^{(p)}}{2}, \frac{T_0^{(p)}}{2}, + > |\frac{T_0^{(p)}}{2}, -\frac{T_0^{(p)}}{2}, - > |\frac{T_0^{(n)}}{2}, \frac{T_0^{(n)}}{2}, + > |\frac{T_0^{(n)}}{2}, -\frac{T_0^{(n)}}{2}, - > . \tag{3.32}$$

The pseudo-angular momenta j_a, j_b, j_c, j_d may take the values:

$$j_a = j_b = \frac{T_0^{(p)}}{2}; \quad j_c = j_d = \frac{T_0^{(n)}}{2}. \tag{3.33}$$

It is worth noting that ψ 3.29 is a product of four functions which are coherent states for the SU2 groups associated with the proton and neutron systems with spin up and down respectively. The product of these groups is the dynamical group of the model Hamiltonian. In each of the above mentioned factor states, the product of dispersions of a certain component of angular momentum and its conjugate angle has a minimum value. Due to this fact ψ is a good candidate for describing a ground state which is assumed to have a semiclassical nature. The semiclassical treatment accounts for oscillations around a ground state which has four subsystems with good angular momenta while the p-h formalism has no such restriction for the ground state. Although the procedure is not able to account for the angular momentum fluctuation in the ground state, due to the intuitive meaning of the classical variables, it allows for a better understanding of the nature of the states. In particular one expects a straight connection with the two rotor model [13] which interprets the orbital $M1$ state as a scissors mode.

In Ref. 12 we have shown that the p-h formalism describes the small oscillations of the system around a "spherical" Hartree-Fock ground state. By contrast, as will be shown in this section, the semiclassical treatment is suitable for the description of small oscillations around a static and deformed Hartree-Fock ground state.

In what follows it is convenient to write the equation 3.28 in terms of the conjugate varioables (x_i, φ_i) (with $i = a, b, c, d$) defined by:

$$x_k = \frac{-2j_k}{(1+\rho_k^2)}, k = a, b, c, d; \quad \alpha = \rho_a e^{i\varphi_a}, \ \beta = \rho_b e^{i\varphi_b}, \ \gamma = \rho_c e^{i\varphi_c}, \ \delta = \rho_d e^{i\varphi_d}. \quad (3.34)$$

Indeed, for the new variables the classical equations of motion acquire a canonical form:

$$\frac{\partial \mathcal{H}}{\partial x_i} = -\dot{\varphi}_i; \quad \frac{\partial \mathcal{H}}{\partial \varphi_i} = \dot{x}_i, i = a, b, c, d, \quad (3.35)$$

where "dot" denotes the time derivative operation and $\mathcal{H}$ is the average of H on ψ. The relations 3.35 confer the variables (x_i, φ_i) the role the conjugate phase space coordinates describing the four classical degrees of freedom.

An equivalent form for the equations 3.35 is:

$$\{x_i, \mathcal{H}\} = \dot{x}_i, \quad \{\varphi_i, \mathcal{H}\} = \dot{\varphi}_i \quad i = a, b, c, d, \quad (3.36)$$

where $\{,\}$ denotes the Poisson bracket having the standard definition.

In order to relate the classical and quantal properties of the nuclear system it is useful to introduce the complex coordinates

$$C_k^* = \frac{x_k - i\varphi_k}{\sqrt{2}}, C_k = \frac{x_k + i\varphi_k}{\sqrt{2}}, \quad k = a, b, c, d. \quad (3.37)$$

The new coordinates obey the equations of motion

$$\{C_k^*, C_k\} = i, \quad \{C_k, \mathcal{H}\} = \dot{C}_k, \quad \{C_k^*, \mathcal{H}\} = \dot{C}_k^*. \quad (3.38)$$

The average of any fermionic operator on the trial function ψ 3.29 can be easily expressed in terms of the complex coordinates C_k^*, C_k. The idea of algebras mapping is used not only for dequantising the quantum motion but also for quantising the classical motion of the nuclear system. Indeed, the mapping

$$C_k^* \to b_k^+, \quad C_k \to b_k, \quad i\{\ ,\ \} \to [\ ,\ ] \tag{3.39}$$

of the classical

$$(C_k^*, C_k, I_k, \{\ ,\ \}) \tag{3.40}$$

and boson

$$(b_k^+, b_k, 1_k, [\ ,\ ])$$

Weyl algebras realises a quantization of the classical motion. I_k and 1_k are identity function on the phase space and identity operator in the boson space, respectively. By this mapping any function of the phase space coordinates becomes an operator depending on the bosons b_k^+, b_k. The transformation 3.39 induces a boson mapping for the classical Hamilton function $\mathcal{H}$. Let us denote by $\mathcal{H}_b$ the image of $\mathcal{H}$. Writing $\mathcal{H}_b$ in a normal order with respect to the boson vacuum, one obtains for $\mathcal{H}_b$ a series of bosons b_i^+, b_i whose lowest order has the form:

$$\mathcal{H}_b = \mathcal{H}_0 + \sum_{i=a,b,c,d} \omega_i b_i^+ b_i. \tag{3.41}$$

We do not give here the expressions of $\mathcal{H}_0$ and ω_i. Instead, we shall adopt the harmonic approximation at classical level. Moreover the trial function is considered for $\beta = \alpha^*, \delta = \gamma^*$:

$$\psi = \psi_p(\alpha, \alpha^*)\psi_n(\gamma, \gamma^*). \tag{3.42}$$

Such an expression is suggested by the fact that the unperturbed states

$$|j, m, + >_\tau, |j, -m, - >_\tau,$$

are degenerate. Using then the coordinates (x_i, φ_i), defined by 3.34 with $i = a, c$ the classical energy function becomes

$$\begin{aligned}
\mathcal{H} &= 2C_p j_a + 2C_n j_c - 2X_{pp}(j_a + j_c) + 2x_a(C_p + X_{pp}(4j_a - 1)) \\
&+ 2x_c(C_n + X_{pp}(4j_c - 1)) + (4 - \frac{1}{j_a})X_{pp}x_a^2 + X_{pp}x_c^2(4 - \frac{1}{j_c}) \\
&- 8X_{pn}\cos\varphi_a \cos\varphi_c[x_a x_c(-x_a - 2j_a)(-x_c - 2j_c)]^{\frac{1}{2}}.
\end{aligned} \tag{3.43}$$

This function reaches a minimum value for

$$\breve{x}_a = -j_a(\frac{C_p}{X_{pp}(4j_a - 1)} + 1), \quad \breve{\varphi}_a = 0, \quad \breve{x}_c = -j_c(\frac{C_n}{X_{pp}(4j_c - 1)} + 1), \quad \breve{\varphi}_c = 0. \tag{3.44}$$

The second order expansion of $\mathcal{H}$ around the minimum point can be easily obtained. To save the space we do not give its expression here. Changing the variables,

$$q_1 = x_a - \breve{x}_a, \quad p_1 = \varphi_a - \breve{\varphi}_a, \quad q_2 = x_c - \breve{x}_c, \quad p_2 = \varphi_c - \breve{\varphi}_c, \tag{3.45}$$

the equations of motion preserve the canonical form

$$\dot{q}_k = \frac{\partial \mathcal{H}}{\partial p_k} \equiv \sum_l A_{kl} p_l, \quad \dot{p}_k = -\frac{\partial \mathcal{H}}{\partial q_k} \equiv \sum_l B_{kl} q_l, \tag{3.46}$$

where the nonvanishing matrix elements A_{kl}, B_{kl} have simple expressions of the strengths C_p, C_n, X_{pp}, X_{pn} and j_a, j_c: The normal modes are defined as linear combinations

$$C_k^* = \sum_{k=1,2} (R_k a_k^* - S_k a_k), \tag{3.47}$$

of the complex coordinates

$$a_k^* = \frac{q_k - i p_k}{\sqrt{2}}, \quad a_k = \frac{q_k + i p_k}{\sqrt{2}}, \quad k = 1, 2. \tag{3.48}$$

The amplitudes R_k, S_k are determined so that the following equations hold:

$$\{C^*, \mathcal{H}\} = i\omega C^*, \quad \{C^*, C\} = i. \tag{3.49}$$

The dispersion equation for ω is:

$$\omega^4 + \omega^2 A_{11}(B_{11} + B_{22}) + (B_{11} B_{22} - B_{12}^2) A_{11}^2 = 0. \tag{3.50}$$

As explained before, the classical motion can be quantized by associating to C^* the boson b^+ and to C the hermitian conjugate one, b. To calculate the transition probability between the ground state (which is a vacuum for the RPA bosons b_k (k=1,2) and the first excited state $b_k^+|0>$, one needs to quantize the average $<\psi|T_{-1}^{(p)}|\psi>$. To achieve this aim one expands this quantity around its minimum point and retains only the linear term which is quantised by following the procedure mentioned above.

The states related by the M1 transition operator are defined in the laboratory frame by:

$$|0^+) = (\frac{1}{8\pi^2})^{\frac{1}{2}}|0>, \quad |1_k^+ M) = \frac{\sqrt{3}}{4\pi}(D_{M1}^{1*} + D_{M,-1}^{1*}) b_k^+ |0> . \tag{3.51}$$

The final result for the reduced probability characterising the transition $|0^+) \to |1_k^+ M)$ is:

$$B(M1; 0^+ \to 1_k^+) = \frac{3}{2\pi} j_a^2 (R_1^{(k)} - S_1^{(k)})^2 \mu_N^2, \quad k = 1, 2, \tag{3.52}$$

where the upper index "(k)" accompanying the amplitudes R_1 and S_1 suggests that they correspond to the RPA energy ω_k.

Now let us focus our attention on the isovector-isoscalar admixture in the structure of the normal modes. To this goal we perform the canonical transformation.

$$Q = \frac{q_1 + q_2}{2}, \; q = \frac{q_1 - q_2}{2}, \; P \equiv \phi = \frac{\varphi_a + \varphi_c}{2}, \; p \equiv \varphi = \frac{\varphi_a - \varphi_c}{2}. \tag{3.53}$$

To these degrees of freedom one associate the complex variables

$$A^* = \frac{Q - iP}{\sqrt{2}}, \quad a^* = \frac{q - ip}{\sqrt{2}}, A = \frac{Q + iP}{\sqrt{2}}, \quad a = \frac{q + ip}{\sqrt{2}}. \tag{3.54}$$

The normal modes coordinates are defined by:

$$C^* = RA^* + ra^* - SA - sa, \quad C = (C^*)^*, \tag{3.55}$$

with the amplitudes R, r, S, s determined so that the equations 3.49 are satisfied. The dispersion equation for the mode energies is identical to 3.50. This is a consequence of the fact that the transformation 3.53 is canonical. For a particular value of the ratio X_1/X_0, the dispersion equation 3.50 takes a factorised form:

$$(\omega^2 - \Omega_1^2)(\omega^2 - \Omega_0^2) = 0, \tag{3.56}$$

where Ω_0 and Ω_1 can be analitically expressed in terms of the static values of the phase space coordinates.

The normal coordinates C_0^*, C_0 corresponding to the energy Ω_0 have vanishing r and s amplitudes. On the contrary, the coordinates C_1^*, C_1 are characterised by $R = S = 0$. It can be rigorously proved that the following inequality holds:

$$\Omega_1 > \Omega_0. \tag{3.57}$$

This ordering relation reflects the fact that the isovector interaction is repulsive while the isoscalar one is attractive. We conclude that this schematic model allows for a full separation of the isoscalar and isovector modes. It is worth noting that such a separation does not necessarily mean a vanishing energy for the isoscalar mode. In the previous subsection we have shown that vanishing value for the isoscalar energy is not a sufficient restriction for getting RPA states with good angular momentum.

Now let us see what are in fact the classical coordinates we have used in this subsection. To this aim we calculate the averages of $\vec{T}^{(p)}, \vec{T}^{(n)}$ on the trial function. The results are:

$$< \psi | T_x^{(\tau)} | \psi >= j_k \frac{2\rho_k}{1 + \rho_k^2} \cos\varphi_k \equiv j_\perp^{(\tau)} \cos\varphi_k,$$

$$< \psi | T_y^{(\tau)} | \psi >= j_k \frac{2\rho_k}{1 + \rho_k^2} \sin\varphi_k \equiv j_\perp^{(\tau)} \sin\varphi_k,$$

$$< \psi | T_z^{(\tau)} | \psi >= j_k \frac{1 - \rho_k^2}{1 + \rho_k^2}, \quad \tau = p, n; k = a\delta_{\tau p} + c\delta_{\tau n}. \tag{3.58}$$

From the above relations it results that $\varphi_a(\varphi_c)$ is the angle between the projection of the pseudo-angular momentum of the proton (neutron) system in the (x,y) plane and the Ox axis. The angle $\frac{(\varphi_a + \varphi_c)}{2}$ defines the bisector line of the angle $(\widehat{\vec{j}_\perp^{(p)}, \vec{j}_\perp^{(n)}})$, while $\frac{(\varphi_a - \varphi_c)}{2}$ defines the angle between the above mentioned bisector line and $\vec{j}_\perp^{(n)}$.

Therefore the isovector mode is just the scissors mode as was defined by Lo Iudice and his collaborators in Ref. 13. The quantity $\frac{2\rho_k}{1+\rho_k^2}$ plays the role of deformation.

C. QRPA formalism

In this Section we shall study a system of nucleons interacting among themselves not only by the long range term simulating the QQ interaction but also by a pairing force. Therefore, the Hamiltonian describing such a system will be

$$H = H_{pn} - \lambda_p \hat{N}_p - \lambda_n \hat{N}_n - \frac{G}{4} \sum_{i,j,\sigma\sigma'} c^+_{i\sigma} c^+_{\bar{i}\sigma} c_{j\bar{\sigma}'} c_{j\sigma'} \tag{3.59}$$

where H_{pn} is defined by 3.10, N_τ stands for particle number operator of the system $\tau(= p, n)$ and λ_τ denotes the corresponding chemical potential. We treat first the one body and pairing terms. This piece of H is brought to a diagonal representation by means of Bogoliubov transformation

$$\begin{aligned} a^+_{k\sigma}(\tau) &= U_k(\tau) c^+_{k\sigma}(\tau) - V_k(\tau) c_{\bar{k}\sigma}(\tau),\ a_{k\sigma}(\tau) = U_k(\tau) c_{k\sigma}(\tau) \\ &- V_k(\tau) c^+_{\bar{k}\sigma}(\tau),\quad \tau = p, n;\quad k = (m, n),\quad \sigma = +, -,\quad 0 < m, n < N_\tau. \end{aligned} \tag{3.60}$$

The coefficients U and V are obtained by solving the pairing equations for gap energy and particle number conservation.

The pairing interaction which is introduced here has some distinctive features. The first distinction refers to the fact that the particles have spin and consequently the single particle spectrum is a set of equidistant double degenerate levels. A particularly nice property of the present interaction is that it transforms a set of equidistant energy levels characterizing the noninteracting system into a non-equidistant set of quasiparticle energies. Moreover since pairing correlations smear out the Femi sea, any two successive levels may be related by a dipole transition operator. This is at variance with what happens in the particle representation where the Pauli principle allows only for the transitions involving the Fermi sea and the first level above it. This means that while in the absence of pairing the system behaves like one with only one degree of freedom (relative to the particle-hole excitations), the paired system has several channels open for excitation. Consequently one expects that the QRPA approach produces a fragmentation of the M1 strength which contrasts with what happens for the uncorrellated system where only one dipole state exists.

The QRPA approach defines the operators

$$\begin{aligned} \Gamma^+ &= \sum_{\tau,m,n} [X^{n+1,m-1}_{m,n}(\tau)(a^+_{mn+}(\tau) a^+_{n+1,m-1,-}(\tau) + a^+_{m-1,n+1,+}(\tau) a^+_{nm-}(\tau)) \\ &+ Y^{n+1,m-1}_{m,n}(\tau)(a_{n+1,m-1,-}(\tau) a_{mn+}(\tau) + a_{nm-}(\tau) a_{m-1,n+1,+}(\tau)], \end{aligned} \tag{3.61}$$

so that the following equations are fulfilled

$$[H, \Gamma^+] = \omega \Gamma^+, \quad [\Gamma, \Gamma^+] = 1. \tag{3.62}$$

Table 1. The values of the major shell quantum number for protons (N_p) and neutrons (N_n), the number of protons ($2\pi_0$) and neutrons ($2\nu_0$), the angular momentum (in units of $\hbar$) carried by protons ($j_a = (N_p - \pi_0 + 1)\pi_0$) and neutrons ($j_c = (N_n - \nu_0 + 1)\nu_0$) and the strength of the pairing interaction($G_p = G_n$, in units of MeV) which are used in our applications are listed.

N_p	N_n	$2\pi_0$	$2\nu_0$	j_a	j_c	$G_p = G_n$
6	8	6	8	6	10	0.6

The first equation 3.62 yields an homogenous system of equations for the amplitudes X and Y. The compatibility condition for this system provides a dispersion ecuation for ω.

The QRPA equations have at most $N_p + N_n$ real solutions for ω. These will be distinguished by the label s. Also, the amplitudes X, Y corresponding to the s-th energy will be accompanied by the additional index s. The associated boson Γ^+ 3.61 is denoted by Γ_s^+. The QRPA vacuum and the first excited states are defined by

$$\Gamma_s|0>=0, \quad |1_s^+>=\Gamma_s^+|0> \tag{3.63}$$

These are viewed as intrinsic parts of the ground state $|0^+)$ and the dipole states $|1_s^+)$ defined in the laboratory frame, respectively. The reduced probability for the transition $|0^+) \rightarrow |1_s^+)$ (induced by the intrinsic operator $T_{-\mu}^{(p)}$) has the expression:

$$B(M1; 0^+ \rightarrow 1_s^+) = \frac{3}{4\pi}(\sum_{m+n=N_p} A_{mn}^{(+)}(p)(X_{mn}^{n+1,m-1}(p) - Y_{mn}^{n+1,m-1}(p)))^2 \mu_N^2 \tag{3.64}$$

The distribution of the M1 strength among the states 1_s^+ will be numerically studied in the next section.

4. Numerical results and discussions.

Here we present the results obtained for the input data given in table 1. We performed successively the ph RPA and QRPA for a set of values for the isoscalar interaction strength X_0. For each value of X_0, the strength of the isovector interaction was fixed so that the isoscalar state has the energy equal to zero. The semiclassical treatment was performed by varying the value of the proton-proton two body interaction, i. e. X_{pp}. The strength for the proton-neutron interaction X_{pn} was determined by enforcing the isoscalar energy be equal to zero. The calculated observables are the energies and the reduced probability for exciting the RPA states from the ground state through a M1 transition operator.

The results for energies are presented in fig. 2 while those regarding the reduced M1 probability in figs. 3 and 4. From there one sees that the plotted energies are decreasing functions of the strength X_0. Such a behaviour is in qualitative agreement with the prediction of realistic calculations. For large values of X_0 the semiclassical energy approximates reasonably well the first QRPA energy while the ph-RPA energy is smaller by about 600 keV. The isoscalar energy Ω_0 (see eq.3.56) is almost vanishing.

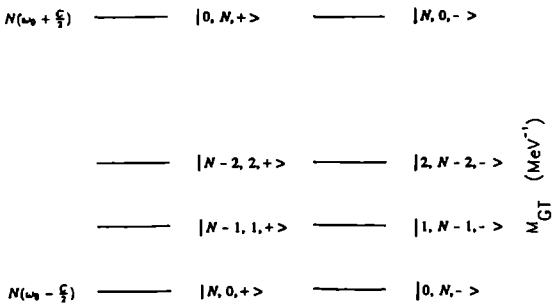

Fig. 1. The single particle spectrum for Nth major shell. It consists of N+1 double degenerate levels.

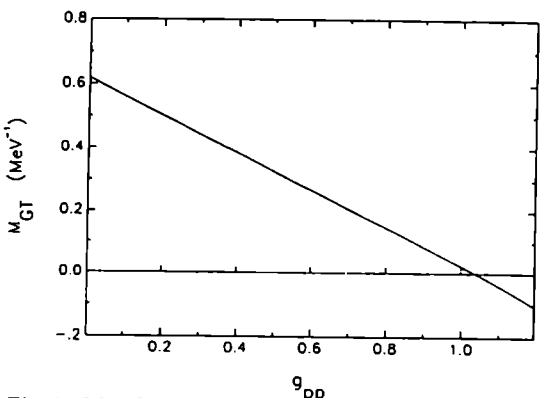

Fig. 5. The Gamow-Teller amplitude M_{GT} characterising $2\nu\beta\beta$. The transition $0_i^+ \rightarrow 0_f^+$ is plotted as function of g_{pp}-the strength of the two body interaction in the particle-particle channel.

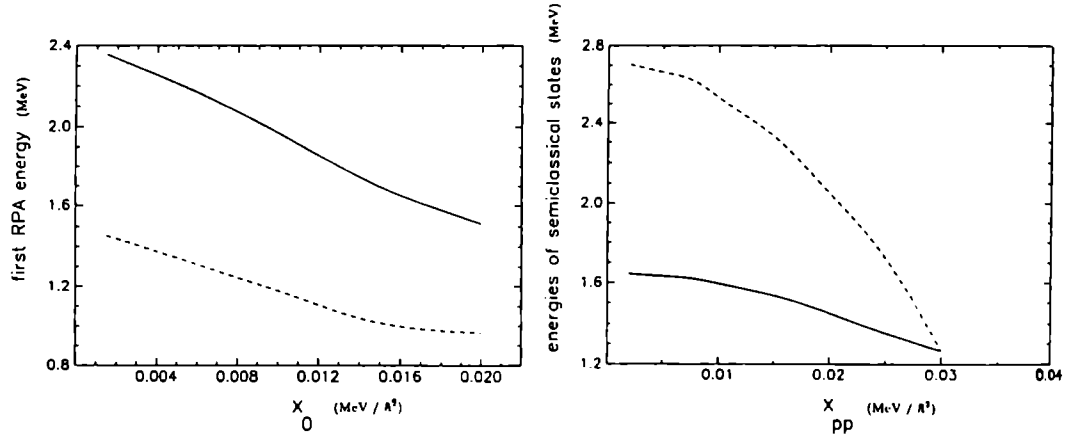

Fig. 2. a) The energies for the first excited QRPA (full line) and the ph-RPA (dash curve) states are given as function of X_0. b) The semiclassical energies ω_1 (full line) and Ω_1 (dash line)(see eqs.3.50 and 3.56) are plotted as function of X_{pp}. The input data are those listed table 1.

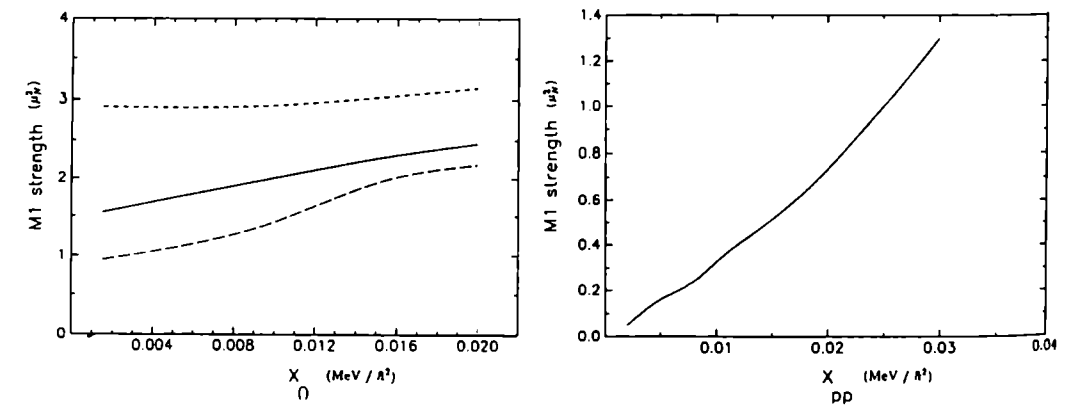

Fig. 3. a) The $BM1$ values characterising the transitions from the ground state to the first QRPA (full) and from the ground state to the ph-RPA (long dash)states are plotted as function of X_0. Also the total M1 strength associated to the full QRPA spectrum is presented by a dash curve. b) The $BM1$ value characterising the semiclassical state of energy ω_1 (eq. 3.50) as function of X_{pp}

If Ω_0 was exactly equal to zero the corresponding RPA boson could have not been defined.

The $BM1$ values characterising the first QRPA, ph-RPA and semiclassical state are increasing functions of the interaction strength. However this feature is not a good signature for the total strength. This is however consistent with the experimental data showing a linear dependence on the nuclear deformation squared in a limited range of the excitation energy. The total strength is however a sensitive increasing function of the pairing strength. As a matter of fact this reflects in that for low values of X_0 the $BM1$ value obtained for the ph-RPA state is smaller than that characterising the first QRPA state. The pairing interaction does not only increase the $M1$ strength but also fragments it as shown in fig. 4. Due to the attractive character of $-X_0$, by incresing it the $M1$ strength is pushed towards the lower energy region.

The main results, presented so far, can be summarised as follows. The schematic model proposed by Moszkowski, many years ago, was extended to an heterogeneous system of protons and neutrons with the scope of studying the the magnetic pseudo-dipole excitations. Within a semiclassical formalism one establishes the conditions under which the scissors mode is fully separated from the isoscalar mode. Such a separation was also possible by using the ph-RPA procedure with the difference that in this case the isoscalar mode is spurious and therefore it can not be quantized. Although the energy of the isoscalar mode, in the latter case is equal to zero the RPA state of the nonvanishing energy has not a good angular momentum. The influence of pairing on the M1 strength consists of fragmenting it.

The conclusion of this analysis is that the main features revealed by realistic calculations are recovered in this schematic model. However there are some differences which should be mentioned. In realistic calculations, using the anisotropic three dimensional oscillator [14], the M1 excitations are obtained by exciting the system by one quanta along two directions. These are z and either y or x direction. By contrast in the EMM the M1 mode is caused by exciting the system along x and y axis. In the former case, when the particle hole states belong to the $\Delta N = 0$ subspace, the quadrupole operators $Q_{2\pm1}$ are (up to a multiplicative constant) equal to the components $L_{\pm1}$ of the angular momentum while in the present case the $Q_{2\pm2}$ components of the quadrupole moment are written as linear combinations of the components $T_{\pm1}$ of the pseudo-angular momentum. According to the semiclassical interpretation, the "$M1$" mode describes the relative angular oscillations of $\vec{T}_{\perp}^{(p)}$ and $\vec{T}_{\perp}^{(n)}$. It can be easily shown that the Hartree-Fock (HF) mean field approximation yields different oscillator frequencies for the axes x and y. This suggests that using the HF states as single particle basis and treating the two body interaction T_z^2 through the ph-RPA method, one of the possible modes could be excited by $T_z^{(p)} - T_z^{(n)}$. Such a mode would be fully analogous to the realistic scissors mode (being excited by $l_z^{(p)} - l_z^{(n)}$) with the difference that the elementary quantas are again in the (x, y) plane and not within the (x, z) or (y, z) as it happens in realistic sitations.

As a final conclusion of Section 3, one may say that Moszkowski model is able to describe not only the E2 features but can also be extended to describe the magnetic

properties of nuclear systems.

5. The cancellation of Gamow-Teller amplitude for $2\nu\beta\beta$ process

We suppose that a composite system of Z protons and N neutrons is distributed from the bottom in the single particle states defined in the previous Section. Protons and neutrons interact among themselves by pairing and Gamow-Teller interaction [15]. Therefore the Hamiltonian describing such a system is:

$$H = \sum_{\tau,i,\sigma}(e_{\tau i} - \lambda_\tau)c^+_{\tau i\sigma}c_{\tau i\sigma} - \sum_\tau G_\tau \sum_{i,\sigma} c^+_{\tau i\sigma}c^+_{\tau\tilde{i}\sigma} \sum_{k,\epsilon} c_{\tau\tilde{k}\epsilon}c_{\tau k\epsilon} - \frac{\chi}{2}\sum_\mu \beta^-_\mu\beta^+_{-\mu}(-)^\mu \quad (5.1)$$

where the single particle energies $e_{\tau i}$ are those from fig. 1. They might be different for protons ($\tau = p$) and neutrons ($\tau = n$) if one takes different values for the parameters ω_0 and C defining the mean fields for protons and neutrons. The operators $\beta^\mp$ are defined by

$$\beta^-_\mu = \sum_{i,\epsilon,\epsilon'} < pi\epsilon|\sigma_\mu|ni\epsilon' > c^+_{pi\epsilon}c_{ni\epsilon'}, \quad \beta^+_\mu = \sum_{i,\epsilon,\epsilon'} < ni\epsilon|\sigma_\mu|pi\epsilon' > c^+_{ni\epsilon}c_{pi\epsilon'} \quad (5.2)$$

where σ_μ denotes the spherical components of the Pauli matrix. The pairing interaction is treated as shown in Section 3. Like in realistic cases we ignored the pairing interaction between protons and neutrons. Indeed, although here the protons and neutrons occupy the same major shells, their Fermi seas are far apart.

Concerning the operators $\beta^\pm$ defining the Gamow-Teller interaction we notice that they flip both the isospin and spin through the spherical components ± 1 and only the isospin by the zeroth component. In principle this should induce a fine structure for the QRPA states each component being determined by a combined effect of isospin and spin flip. In other words if the strengths χ corresponding to the three components ($\mu = \pm 1, 0$) of the interaction were different, then we would expect three different excitation modes determined by the configurations

$$\uparrow_n\downarrow_p, \qquad \downarrow_n\uparrow_p, \qquad \uparrow_p\uparrow_n + \downarrow_p\downarrow_n . \quad (5.3)$$

The pn-QRPA approach defines the operator

$$\Gamma^+ = \sum_{i,\nu\nu'}(X^{\nu\nu'}_{\tilde{i}i}a^+_{p\tilde{i}\nu}a^+_{ni\nu'} - Y^{\nu\nu'}_{\tilde{i}i}a_{ni\nu'}a_{p\tilde{i}\nu}), \quad (5.4)$$

by the requirements

$$[\Gamma, \Gamma^+] = 1, \quad [H, \Gamma^+] = \omega\Gamma^+. \quad (5.5)$$

Conventionally we denoted by $\tilde{i} = (\widetilde{m,n}) = (n,m)$.

The equation 5.5 have at most $4(N+1)$ solutions which are not all distinct. We label the QRPA solutions by an additional index k. Thus the energies are ω_k and the corresponding amplitudes $X^{\nu\nu'}_{\tilde{i}i}(k), Y^{\nu\nu'}_{\tilde{i}i}(k)$. The equations 5.5 comprise not

only the contribution coming from the p-h channel of the two body interaction but also that of the p-p channel. These terms are multiplied by the real factors g_{ph} and g_{pp} respectively. This is done having in view our aim to study the influence of the particle-particle interaction strength g_{pp} on the Gamow-Teller transition rate. Since the RPA uses the output of the BCS calculation and moreover the strength for the pn two body interaction is A (atomic mass) dependent, the results for mother and daughter nuclei are different. In order to distinguish between them we use the label "i" for initial and "f" for the final nucleus. Thus the vacua states are denoted by $|0>_i$ and $|0>_f$ while the first excited states are:

$$\Gamma_s^+(k)|0>_s = |k>_s, \quad s=i,f, \quad k=1,2,...,4(N+1). \tag{5.6}$$

Since the single particle states are deformed, the RPA states are also deformed. However the relations expressing the m.e. of the $\beta^{\pm}$ operators between the vacuum and first excited RPA states suggest a certain selection rule with respect to μ. Supposing that the vacuum state has $M=0$ then these relations recommend the terms of Γ^+ multiplied by $X^{+,-}, X^{-,+}$ and either of $X^{-,-}, X^{+,+}$, as tensorial components having "μ" equal to $+1, -1$, and 0, respectively. These operators are conventionally denoted by Γ_μ^+ with $\mu = \pm 1, 0$.

The QRPA states are to be viewed as intrinsic states. Adopting the strong coupling language the states in the laboratory frame are

$$\begin{aligned} |0>^{(lab)} &= \frac{1}{\sqrt{8\pi^2}}|0>^{(int)}, \quad |k,1M>_s^{(lab)} = \sqrt{\frac{3}{8\pi^2}}\sum_{\mu'} D^{1*}_{M\mu'}(\Omega)|k,\mu'>_s^{(int)}, \\ |k,\mu'>_s^{(int)} &= \Gamma^+_{\mu'}(k)|0>_s^{(int)}, \quad s=i,f. \end{aligned} \tag{5.7}$$

An operator acting on the laboratory states is related with that acting in the intrinsic frame by a rotation

$$\beta_M^{+(lab)} = \sum D^{1*}_{M\mu}(\Omega)\beta_\mu^{+(int)}. \tag{5.8}$$

The intrinsic frame S_{int} is obtained from the laboratory frame by a rotation of Eulerian angles Ω. We recall that here rotation means an element of the group $\mathcal{R}_3$ acting in a fictitious three dimensional space.

The Gamow-Teller matrix elements for the transition $0_i^+ \to 0_f^+$ will be evaluated by using states defined in the laboratory system by the relations 5.6, 5.7. Finally the matrix elements are expressed in terms of the intrinsic states with the result:

$$M_{GT} = \sum_{\mu,\mu',k,k'} \frac{{}_i<0|\beta^+_{-\mu}(-)^{1+\mu}|k\mu>_i \; {}_i<k\mu|k'\mu'>_f \; {}_f<k'\mu'|\beta^+_{\mu'}|0>_f}{E_k + \Delta E} \tag{5.9}$$

The energy denominator is the average of the QRPA energies of the mother and daughter nuclei, normalised to the first QRPA state plus a correction ΔE consisting of summing half of the electron rest-mass plus the Q value for the $2\nu\beta\beta$ process and the experimental energy of the first 1^+ state.

The stability of the mother nucleus against β^- and β^+ decay channels are characterised by the strength for the single beta decay $\beta^{(-)}$ and $\beta^{(+)}$ respectively:

$$ {}_i\beta_k^{(-)} = \frac{1}{3}[\sum_\mu (-)^\mu \, {}_i < 0|\beta^+_{-\mu}|k,\mu >_i]^2, \quad {}_i\beta_k^{(+)} = \frac{1}{3}[\sum_\mu (-)^\mu \, {}_i < 0|\beta^-_{-\mu}|k,\mu >_i]^2. \tag{5.10} $$

These quantities are related by a simple relation which is known under the name of Ikeda sum rule [23]

$$ \sum_k ({}_i\beta_k^{(-)} - {}_i\beta_k^{(+)}) = N - Z. \tag{5.11} $$

Checking this relation is a very good test of the model assumption. Another quantity of interest is

$$ {}_f\beta_k^{(+)} = \frac{1}{3}[\sum_\mu \, {}_f < k\mu|\beta^+_\mu|0 >_f]^2 \tag{5.12} $$

which is related with the second leg of the $2\nu\beta\beta$ process. This is proportional to the $\beta^{(+)}$ strength associated to the daughter nucleus.

6. Numerical results

The formalism which was developed in the previous Sections was applied for the major shell $N_p = N_n = 16$.

Since we want to compare our results with those obtained by a realistic calculation we take as a guide the transition ${}^{82}_{34}Se \rightarrow {}^{82}_{36}Kr$ with the intermediate nucleus ${}^{82}_{35}Br$. Therefore we consider the protons and neutrons lying outside the double magic nucleus with $(N, Z) = (28, 28)$.

On the double degenerate spectrum (see fig. 1) determined by $\omega_0 = 0$ and $C_p = C_n \equiv C = 0.5$ MeV one distributes $2\pi_0 = 6$ protons and $2\nu_0 = 20$ neutrons for the mother nucleus and $2\pi_0 = 8$ protons and $2\nu_0 = 18$ neutrons for the daughter nucleus. Pairing equations were solved for $G_p = 0.39, G_n = 0.34\ MeV$ for the mother nucleus and $G_p = 0.37, G_n = 0.34\ MeV$ for the daughter nucleus. This gives for the gap parameters $\Delta_p = \Delta_n = 2\ MeV$ for both the mother and daughter nuclei.

The QRPA calculations were performed for $\chi = -0.4\ MeV$ and $g_{ph} = 1$ which yields a Gamow-Teller resonance at about 8 MeV.

In what follows we shall discuss the resemblances as well as the differences between the predictions of the present schematic model and those given by realistic calculations [16–23]. The common features will enable us to conclude on the model ability to simulate the realistic situations. Moreover we try to understand whether some of the specific predictions of the schematic model might exist even for realistic cases but at a smaller scale. Indeed some of the inherent details of realistic cases could possibly hide some important effects for the double beta decay process.

The results for M_{GT} are plotted in fig. 5, as a function of g_{pp}. It is worth noticing that M_{GT} cancels at $g_{pp} = 1.02$ as it happens when realistic interactions are used.

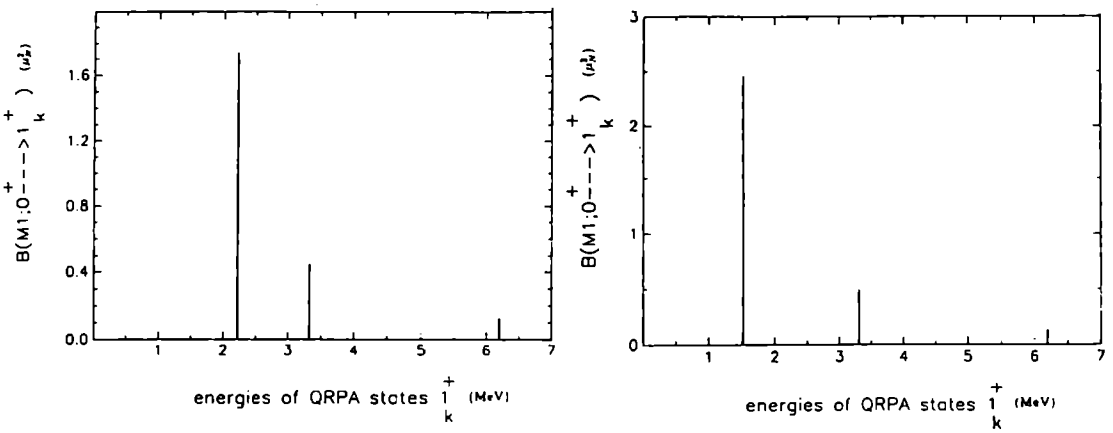

Fig. 4. a) The diagonal terms $(k = k')$ appearing under the sum which define the M_{GT} amplitude for $g_{pp} = 0$. b) The same as in fig. 6 a) but for $g_{pp} = 1$.

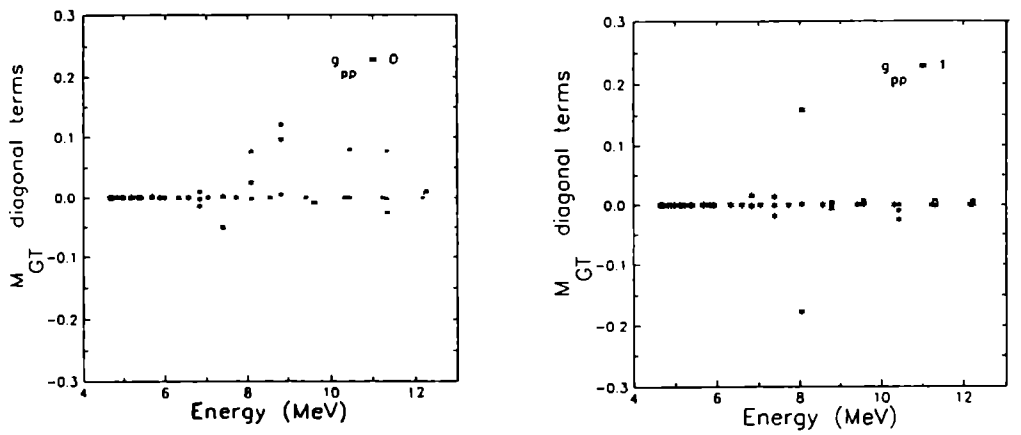

Fig. 6. a)The strength distribution for β^- transition of the mother nucleus for $g_{pp} = 0$. b) The same as in a) but for $g_{pp} = 1$.

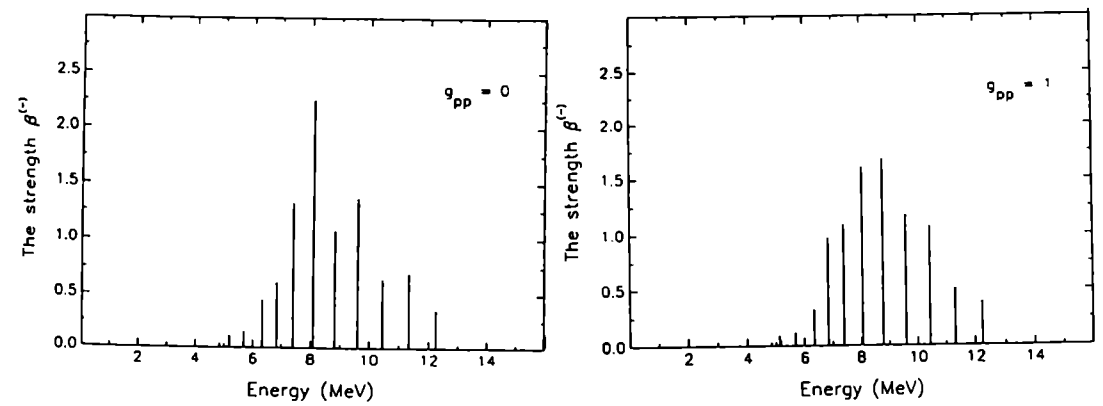

Fig. 7. a) The distribution of the $M1$ strength among the QRPA states is given for $X_0 = 0.005\ MeV$ b) The same as in a) but for $X_0 = 0.02\ MeV$.

However in contrast to the realistic case here M_{GT} does not have a plateau [19] below $g_{pp} = 1$ but it decreases linearly with g_{pp}.

In realistic cases the fall of M_{GT} is attributed to the fact that the contributions of forward and backward RPA amplitudes to the second β^- transition, have an opposite sign. Moreover increasing g_{pp}, the contribution of the back going graphs is increasing and consequently at a certain value of $g_{pp}(\approx 1)$ the total matrix element is vanishing [16-21]. This effect was pointed out by several groups for both realistic [19-20]and Gamow-Teller interactions [17,18,22]. A common feature of realistic calculations consists of that the value of g_{pp} which yields a vanishing M_{GT} amplitude lies close to the critical value (≈ 1.2) where the RPA approach breaks down. Here the value of g_{pp} for which QRPA breaks down is far away ($g_{pp} = 6.75$) from the value for which the M_{GT} amplitude is cancelled.

We now want to ask: what is the mechanism for such a cancellation ? To answer this question we plotted in figs. 6a and 6b, the diagonal terms ($k = k'$) of the sum defining M_{GT}, for g_{pp} equal to zero and one, respectively. The components of M_{GT} are asymmetrically distributed around abscisa axis for $g_{pp} = 0$ while for $g_{pp} = 1$ they have an almost symmetric distribution. The Gamow-Teller giant resonance has a large and positive contribution to M_{GT} but there is another state lying very close to it and having an equally large but negative contribution. As a matter of fact there is still the third quasidegenerate state but, as can be seen from fig. 6b, giving vanishing contribution to M_{GT}. The energies for the three states differ from each other in their 5th or 6th digit and they correspond to the configurations labelled by (5.3). Indeed the state having the largest energy has as dominant component the configuration $\uparrow_p\uparrow_n + \downarrow_p\downarrow_n$ while the other two are described by two independent linear combinations of the terms $\uparrow_p\downarrow_n$ and $\downarrow_p\uparrow_n$. The nondegeneracy of these states is a reflection of the isospin T_3 violation in this process. These states can not be practically distinguished by their energies. However they produce distinguishable contributions to the Gamow-Teller matrix elements. Indeed, the largest contribution of the M_{GT} (=1.534) term corresponding to the highest energy, comes from the $\mu = 0$ term and is 1.6. For the second highest energy state the terms with μ equal to $+1$ and -1 have large contributions but they have oppposite sign. Indeed for this energy M_{GT} is equal to 0.258 and the contributions coming from $\mu = 0, +1, -1$ terms are $+0.058$, $+1.238$ and -0.949 respectively. The lowest state is characterised by a small contribution coming from the $\mu = 0$ term and large and constructively interfering contributions coming from the components with $\mu = +1$ and -1. For this state $M_{GT} = 2.196$ and the partial contributions are -0.027, 1.284 and 0.939 for $\mu = 0, +1, -1$, respectively.

Fig. 6 a) shows that for $g_{pp} = 0$ the Gamow-Teller (GT) double beta decay amplitudes are distributed over many intermediate 1^+ GT states. For $g_{pp} = 1$ (see fig. 6b)) the GT strength is concentrated into two states.

They have the spin and isospin structure:

$$\begin{pmatrix} n^{-1}\uparrow\ p\uparrow \\ n^{-1}\downarrow\ p\downarrow \end{pmatrix} \quad "K" = 0, \quad (\hat{\sigma}_z); \quad \begin{pmatrix} n^{-1}\downarrow\ p\uparrow \\ n^{-1}\uparrow\ p\downarrow \end{pmatrix} \quad |"K"| = 1; \quad (\hat{\sigma}_\pm) \qquad (6.1)$$

These amplitudes have different signs and cancel each other around $g_{pp} = 1$. These

are almost but not completely degenerate in the MM. A third state which is an orthogonal combination of the "K" = 1 state carries no GT strength. The splitting of these states in the MM is caused by the spin-orbit force in the intrinsic system.

We would like to stress on the fact that this picture contrasts the predictions of some realistic calculations where the cancellation of the GT amplitude is caused by the vanishing value of the matrix element describing the second leg of the $2\nu\beta\beta$ transition.

It seems that in realistic three dimensional calculations in spherical nuclei the two states mentioned by 6.1 are all included in a single GT resonance whose amplitude is cancelled arround $g_{pp} = 1$.. Indeed, due to the jj coupling as well as the non-cotact character of realistic calculations the giant resonance components describing spin-isospin flip and isospin flip modes, respectively are not separated.

The $\beta^{(-)}$ strengths characterising the mother nucleus and corresponding to $g_{pp} = 0$ and $g_{pp} = 1$ respectively, are given in figs. 7. One remarks that increasing the particle-particle strength g_{pp}, determines a fragmentation of the $\beta^{(-)}$ strength. This statement holds also for the $\beta^{(+)}$ strength characterising the daugther nucleus. It is worth mentioning that the latter strength is by an order of magnitude smaller than the former one. These features are also seen in realistic calculations.

It is also worth mentioning that the QRPA results for the ${}_i\beta_k^{(-)}$ and ${}_i\beta_k^{(+)}$ obey to alarge accuracy (10^{-3}) the $N - Z$ sum rule [23].

7. Conclusions for Section 6

Most of the features appearing in realistic calculations are nicely reproduced within this schematic model.

Some specific aspects are pointed out. One of these regards the linear dependence of M_{GT} on the strength of the particle-particle channel of the two body interaction. The values of g_{pp} where the GT matrix element M_{GT} goes through zero and that where RPA breaks down are far apart from each other.

The RPA states are clustered in quasidegenerate triplets describing isospin and spin flip and isospin flip modes, respectively. The fine structure of the Gamow Teller giant resonance provides the explanation for the cancellation of the GT matrix element M_{GT}. It seems that in realistic three dimensional calculations in spherical nuclei the three states mentioned above are all included in a single GT resonance whose amplitude is cancelled arround $g_{pp} = 1$. Thus, the present explanation for this cancellation completes the results reported earlier where the cancellation is assumed to be connected with the increasing of the ground state correlations [17–21]. However, in order to confirm this assertion one needs to repeat the realistic calculations and compare the contributions to M_{GT}, coming from the three components associated with spin-isospin flip (2) and isospin flip (1), respectively. Actually such calculations with realistic single particle basis were made [24] and they fully confirm the results presented above. In fact, this confirmation pleads for the beauty of the schematic model.

Practically all features of the $2\nu\beta\beta$ decay which one finds in realistic calculations

are also present in the extension of the Moszkowski model (EMM). But due to its simple structure one obtains a deeper insight into the physics governing the $2\nu\beta\beta$ decay and especially the cancellation around $g_{pp} = 1$, as discussed in this work.

References

1. S.C. Pang, A. Klein and R.M.Dreizler, Ann. Phys. **49** (1968) 467; J. da Providencia, J. N. Urbano and L.S. Ferreira, Nucl. Phys. **A170** (1971) 129.
2. H. J. Lipkin, N. Meshkov and A. J. Glick, Nucl. Phys. **62** (1965), 188.
3. S.A. Moszkovski, Phys. Rev. **110** (1958) 403.
4. H.J. Lipkin, Nucl. Phys. **26** (1961) 147.
5. E.R. Marshalek, Ann. Phys. **143** (1982) 191.
6. Joao da Providencia, Constanca da Providencia and Helena Caldeira, Phys. Rev. **C46** (1992) 2098.
7. Constanca Providencia, Lucilia Brito, Joao da Providencia, Dennis Bonatsos and Debora Peres Menezes, J. Phys. **G20** (1994) 1209.
8. J.P. Elliot, Proc. Roy. Soc. (London) **A245** (1958) 128.
9. J. Schwinger, "On angular momentum" in Quantum Theory of Angular Momentum ed. by L. Biedenharn and H. Van Dam (Academic Press, New York, 1965) p.229.
10. A. Klein and E.R. Marshalek, Rev. Mod. Phys. **63** (1981) 375.
11. A. A. Raduta, V. Ceausescu, A. Gheorghe, M. S. Popa, Nucl. Phys. **A427**(1984) 1.
12. A. A. Raduta, Phys. Rev. **C51** (1995)2973.
13. N. Lo Iudice and F. Palumbo, Phys. Rev. Lett. **74**(1978)1046.
14. A. A. Raduta, I. I. Ursu and Amand Faessler, Nucl. Phys. **A489** (1988) 20.
15. A. A. Raduta, D. S. Delion and A. Faessler, Phys. Rev. **C51** (1995) 3008.
16. T. Tomoda, Amand Faessler, K.W. Schmid and F. Grümmer, Nucl. Phys. **A452** (1986) 591.
17. P. Vogel and P. Fischer, Phys. Rev. **C32** (1985) 1362.
18. P. Vogel and M.R. Zirnbauer, Phys. Rev. Lett. **57** (1986) 3148.
19. A. Faessler, Prog. Part. Nucl. Phys. **21** (1988) 183.
20. W.M. Alberico, M.B. Barbaro, A. Boltino and A. Molinari, Ann. Phys. **187** (1988) 79.
21. K. Muto and H.V.K. Klapdor, Phys. Lett. **200B** (1988) 420
22. A.A. Raduta, Amand Faessler and S. Stoica, Nucl. Phys. **A534**(1991) 149.
23. K. Ikeda, Prog. Theor. Phys. **31** (1964) 434.
24. A. A. Raduta and D. S. Delion to appear in Phys. Rev. C.

The Role of ΔN=2 and Higher Excitations in Nuclear Structure

Larry Zamick (Speaker) and Mohamed S. Fayache
Department of Physics and Astronomy, Rutgers University, Piscataway, NJ 08855

Abstract

Higher shell admixtures in shell model calculations lead to self weakening of the tensor interaction in a nucleus and therefore help to explain many nuclear properties in a systematic way. For highly deformed states such as linear alpha chains, the shell model approach is not practical but the deformed Hartree-Fock method is very useful.

1 Introduction

Most shell model calculations have been performed in a single major shell for positive-parity states (ΔN=0) or in two adjacent major shells for negative-parity states (ΔN=1). With the advent of better computers and better shell model codes, it is now possible to enlarge the spaces considerably. We wish to show here that calculations in larger spaces e.g. ΔN=2 and beyond can remove discrepancies which are present in the small space calculations and can considerably clarify the systematic behaviours.

In this context we have considered the following problems:

(a) Self Weakening of the Tensor Interaction in a Nucleus.

(b) Resistance to Phase transitions when a strong interaction is applied.

(c) Ground State Corrections in Closed Shell Nuclei and Magnetic Dipole Excitations (this includes a surprising symmetry in ^4He).

(d) ΔN=2 Admixtures and Scissors Mode States.

We will next consider highly deformed states, in particular the linear chain states in nuclei. At present, these cannot be handled by the shell model so we will use the deformed Skyrme Hartree-Fock approach.

2 The Interactions Used

We have performed calculations with currently fashionable realistic interactions such as Bonn A (4.4 % D-state admixture in the deuteron)[1], Bonn C (5.6 %)[1] and Nijmegen (5.7 %)[2]. These interactions are very hard to handle. To cut things down to size, we have also used a simplified '(x, y)' interaction which is of the form

$$V = V_c + xV_{so} + yV_t$$

with $c \equiv$ central, $s.o. \equiv$ spin-orbit, and $t \equiv$ tensor. For $x = 1$, $y = 1$ we obtain a good fit to bare G matrix elements of Bonn A in ^{16}O. We can study the effects of the spin orbit and tensor interaction by varying x and y e.g. $x = 0$ means no spin-orbit is present, $y = 2$ means we double the the strength of the tensor interaction relative to Bonn A etc. The details of the interaction are given by Zheng and Zamick[3].

When dealing with collective behaviour, we will compare the realistic interaction with schematic ones like $-\chi Q \cdot Q$ or $-\chi Q \cdot Q(1 + B\vec{\tau}(1) \cdot \vec{\tau}(2))$.

3 Self Weakening of the Tensor Interaction in the Nucleus

Let us first list some properties of the tensor interaction in a nucleus:

(1) It gives a small positive contribution to the Quadrupole Moment of the deuteron by admixing $(L=0\ S=1)^{J=1}$ and $(L=2\ S=1)^{J=1}$.

(2) In a nucleus, the tensor interaction gives *zero* for the binding energy of a closed LS shell *in first order*. It also contributes nothing to the single-particle energies of a closed LS shell $\pm$ one nucleon.

(3) Therefore, to see the effects of the tensor interaction, we must look beyond single-particle energies. The tensor interaction causes a shift in the energies of particle-hole states with $S=1$ e.g. in ^{16}O, it causes a large energy splitting between the $T=1$ and $T=0$ $J=0^-$ states whose main configuration is $(1s_{1/2}0p_{1/2}^{-1})^{0^-}$.

(4) The tensor interaction causes the quadrupole moment of ^6Li $(J=1^+, T=0)$ to be negative i.e. with only a central and spin-orbit interaction the quadrupole moment would be positive.

(5) The most famous case is the $A=14$ system. The near vanishing of the Gamow-Teller decay matrix element from the $J=0^+$ $T=1$ state of ^{14}O or ^{14}C to the $J=1^+$ $T=0$ state of ^{14}N.

(6) In a closed minor shell e.g. ^{12}C, the tensor interaction acts as a spin-orbit interaction of the opposite sign to the basic spin-orbit interaction as noted by C.W. Wong[4]; e.g. it can cause an inversion bringing the $p_{1/2}$ single-particle energy to come below the $p_{3/2}$.

(7) For a closed L S shell plus or minus one nucleon, the second-order corrections to the isoscalar magnetic moment would vanish unless there is a tensor interaction. This will not be discussed here.

The main point in this section is that if we carry out a calculation of the properties 3 to 5, using *realistic matrix elements* in the minimum model space e.g. ΔN=0 for the ^6Li quadrupole moment, ΔN=1 for the $J=0^-$ splittings in ^{16}O there is an overshoot, the tensor interaction appears to be too strong. However, when we allow higher shell admixtures the effect is always the same as if we had used a weaker tensor interaction in the smaller space.

3.1 The Energy Splitting of $J=0_1^-$ $T=1$ and $T=0$ States in ^{16}O

Let us first consider the $J=0_1^-$ $T=0$ and $T=1$ states in ^{16}O which are at 10.952 MeV and 12.797 MeV respectively. We focus on the energy splitting $\Delta E = 1.845\ MeV$. It has been shown by Blomquist and Molinari[5] and Millener and Kurath[6] that without a tensor interaction, and with realistic exchange mixtures, ΔE is very close to zero. (However, as shown by Elliott and Flowers[7], this is not true for a non-realistic interaction like Rosenfeld).

The main $\Delta N=1$ configuration for $J=0^-$ in ^{16}O is $(1s_{1/2}0p_{1/2}^{-1})$ but there is also a small admixture of $(0d_{3/2}0p_{3/2}^{-1})$.

We now show results[8,9] for $\Delta E = E(0^-, T=1) - E(0^-, T=0)$ in different model spaces and for different interactions:

Interaction	Space		
	$1p-1h$	$1p-1h\ +\ 3p-3h$	$1p-1h\ +\ 3p-3h\ +2p-2h$
$(x=1,\ y=0)$	0.046	-0.036	0.156
$(x=1,\ y=1)$	2.932	2.900	2.002
Bonn A	3.08	3.20	1.87
Bonn C	2.72	2.87	1.65

In the above, for the $\Delta N = 1$ $1p-1h$ calculation, with the tensor off ($x = 1,\ y = 0$) $\Delta E = 0.046\ MeV$ -very small. With the tensor on ($x = 1,\ y = 1$) ΔE is much larger (2.932 MeV). In fact, it is *too large* compared with the experimental splitting of 1.85 MeV. This is but one example of *many* in which the tensor interaction appears to be too strong inside the nucleus.

When we enlarge the model space to include $3p-3h$ configurations nothing much changes. But when we allow $2p-2h$ admixtures there is a significant drop in ΔE to a value much closer to experiment -i.e. for the ($x,\ y$) interaction with ($x = 1,\ y = 1$), ΔE changes from 2.932 MeV to 2.002 MeV. Thus we conclude that higher shell admixtures can make the tensor interaction appear to be weaker in agreement with experiment.

We get similar results for Bonn A where the change is from 3.08 MeV ($\Delta N = 1$) to 1.87 MeV when $2p-2h$ admixtures are allowed. There is one subtlety however. Bonn C with a 5.6 % D-state admixture gives a smaller splitting than Bonn A which has only 4.4 % D-state admixture (2.72 MeV vs. 3.08 MeV for $\Delta N = 1$). This tells us that the D-state admixture is not the only criterion for the strength of the tensor interaction -in the problem considered here, we are sampling a different region in r of this interaction.

We analyze the results via perturbation theory. We show the 2-particle 2-hole diagrams and their effects:

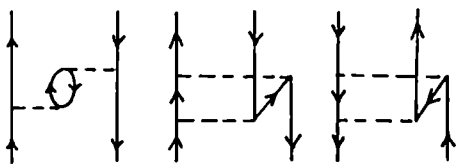

Interaction ($x,\ y$)		Particle-Hole	Particle-Particle	Hole-Hole	Total
Spin-Orbit	Tensor				
OFF	OFF	0.012	0.252	0.049	0.312
ON	OFF	-0.024	0.249	0.057	0.282
OFF	ON	-1.739	0.639	0.385	-0.714
On	ON	-1.728	0.593	0.308	-0.826

Notice that only when the tensor interaction is ON do we get a large desired negative effect. This justifies the phrase we use -*self weakening*. At the one particle-one hole level the tensor interaction gives too large a splitting for $\Delta E = E(0^-,\ T = 1) - E(0^-,\ T = 0)$. In second order, only if the tensor interaction participates is the correction $\delta(\Delta E)$ large and negative. The tensor interaction must be present both in first order and second order to achieve the desired effect.

3.2 The Quadrupole Moment of ^6Li

Whereas the quadrupole momemt of the deuteron is positive ($Q = 0.2860\ e\ fm^2$), that of the $J = 1^+$ ground state of ^6Li (which can be lossely considered to be an alpha particle and a deuteron) is negative ($Q = -0.082\ e\ fm^2$). A striking fact is that in a p-shell calculation i.e. one involving a valence neutron and a valence proton, the quadrupole moment in the absence of a tensor interaction is positive e.g. for the ($x,\ y$) interaction we obtained $Q = 0.106\ e\ fm^2$ for $x = 1,\ y = 0$ (tensor off) and $Q = -0.358\ e\ fm^2$ for $x = 1,\ y = 1$ (tensor on).

As in the previous problem of $J = 0^-$ states, the tensor interaction appears to be too strong. However, here are results when we we enlarge the model space (in the following table we are using the Nijmegen II potential -not ($x,\ y$)):

Space	Q	μ
0 $\hbar\omega$	-0.360	0.866
2 $\hbar\omega$	-0.251	0.848
4 $\hbar\omega$	-0.0085	0.846
Exp't	-0.082	0.822

We see that for Q we get the magnitude of Q decreasing i.e. Q becomes less negative as we increase the size of the model space. We would get the same effect in the small space by decreasing the strength of the tensor interaction.

It should be noted that we can also decrease the magnitude of Q by increasing the spin-orbit interaction. Skouras and Müther[10] noted that in a relativistic theory they can get Q become less negative by using a Dirac effective mass $\frac{m_D}{m}$ less than one. This can be interpreted as making the spin-orbit interaction stronger i.e. $V_{s.o}$ is proportional to $\frac{m}{m_D}$. The tensor interaction however is not affected.

3.3 Gamow-Teller Transitions for $A = 14$

The most famous example of where one needs a tensor interaction in the nucleus is the case of the allowed Gamow-Teller transitions for $A = 14$ systems i.e. the beta decay ^{14}C ($J = 0^+$, $T = 1$) $\rightarrow^{14} N$ ($J = 1^+$, $T = 0$) (and also the mirror transition ^{14}O ($J = 0^+$, $T = 1$) $\rightarrow^{14} N$ ($J = 1^+$, $T = 0$). All the quantum numbers are correct for an allowed transition via the operator $\sum \sigma_\mu t_+$ where $t_+|n\rangle = |p\rangle$. However the Gamow-Teller matrix element A_{GT} is essentially zero. Inglis[12] showed that this could not occur in a 2-hole calculation with just a central and spin-orbit interaction. Then Jancovici and Talmi[13] showed that one could get the matrix element to vanish if one introduced a tensor interaction.

With the (x, y) interaction we find that for $y = 0$ (tensor off) we get a large matrix element $B(GT) = |A_{GT}|^2 \approx 4$. If we put $y = 1$ (Bonn A-type tensor interaction) we get almost the same value. This is at first puzzling. However, if we plot the amplitude A_{GT} as a function of y, we find that for $y = 0$ it is large and positive. It decreases almost linearly with y going to zero around $y = 0.5$, as we continue A_{GT} becomes negative and for $y = 1$ it is almost equal and opposite to what it was for $y = 0$. Again there is an overshoot.

In a $0\hbar\omega$ calculation the Nijmegen II interaction[2] gives $B(GT, 0^+\ T = 1 \rightarrow 1^+\ T = 0) = 3.97$. When we allow $2\hbar\omega$ admixtures the result decreases to $B(GT) = 1.80$. This is in the right direction but not enough. Again higher shell admixtures make the tensor interaction look weaker. A further examination shows that the realistic interactions give too small a spin-orbit splitting for $A = 15$ i.e. the $p^{-1}_{3/2} - p^{-1}_{1/2}$ splitting is calculated to be 4 MeV but from experiment it is 6 MeV. If we somehow increase the spin-orbit interaction as well as invoking the self weakening mechanism for the tensor interaction, we can get A_{GT} to become very small.

One way of increasing the the spin-orbit interaction is to use a Dirac effective mass $\frac{m_D}{m}$ less than one[11]. As mentioned before, the one-body spin-orbit interaction is proportional to $\frac{m}{m_D}$.

4 Trying to Induce Phase Transitions by Increasing y, the Strength of the Tensor Interaction

Consider again 0^- states but this time in ^4He. The $1p-1h$ $\Delta N = 1$ configuration is $(0p_{1/2}0s^{-1}_{1/2})^{J=0^-,T}$ with $T = 0$ or 1. The tensor interaction causes some unnatural parity states to come down in energy. Bleuler[14] noted that in a $1p-1h$ calculation (or $R.P.A.$) one could get the unnatural parity states to come down to

zero energy with a sufficiently strong tensor interaction. This leads to a phase transition. Curves showing this behaviour are contained in textbooks of Ericson and Weiss[15] and Eisenberg and Koltun[16], as simulations of pion condensation.

We have examined this[17] with the $OXBASH$ program[18], plotting the excitation energies of $J = 0^-$ $T = 0$ states as a function of y, the strength of the tensor interaction for the $(x,\ y)$ interaction. As shown in figure 1, the solid line is the $1p - 1h$ $\Delta N = 1$ calculation, and indeed it goes down linearly to zero energy as y is increased. However, when we allow more configurations ($\Delta N = 3$ and beyond) in $OXBASH$, there is a completely different behaviour. The best calculation is the dashed line in which all four nucleons are allowed to roam in the four major shells ($S,\ P,\ SD,\ PF$). This is both for the $J = 0^+$ ground state and $J = 0^-$ excited state. The dashed line starts going down with increasing y, but there is a quick turnaround and the curve actually rises beyond about $y = 1$. The 0^- states do not collapse to zero energy. Of course the nature of the wave function changes in a smooth way as we increase y.

This simple example indicates, at least to us, that one must reconsider and study more carefully the topics of precursors to condensation and condensation itself.

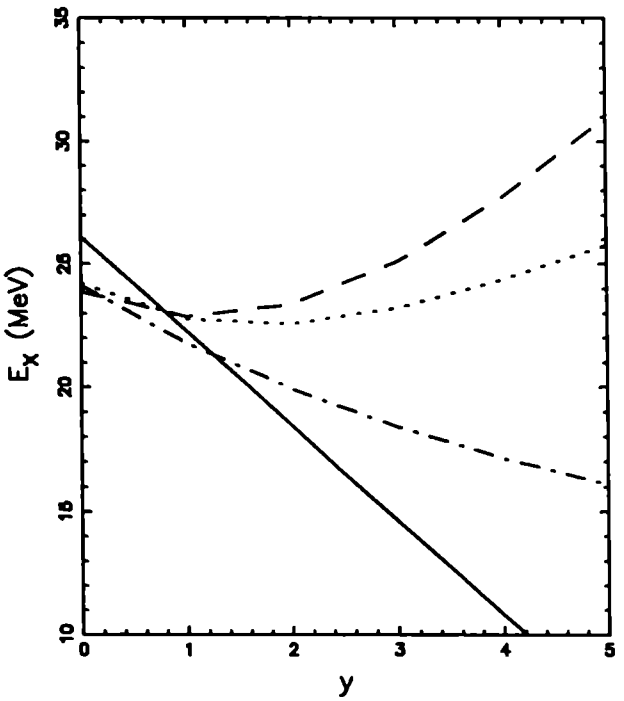

Figure 1: Excitation energy of the $J = 0^-$ T=0 state in ^4He as a function of the strength of the tensor interaction

4.1 Ground State Correlations in ^4He and Magnetic Dipole Excitations

For a closed LS shell e.g. ^4He, ^{16}O, ^{40}Ca there can be no $M1$ transitions to excited states unless there are ground state correlations. Using our $(x,\ y)$ interaction we can calculate ground state correlations by simply

running the $OXBASH$ code with more and more configurations. The $M1$'s are very weak so we use as units $(10^{-3}\mu_N^2)$.

The $M1$ operator is $g_l\vec{L} + g_s\vec{S}$. The bare operator has $g_l = 1$, $g_s = 5.586$ for the proton (π) and $g_l = 0$, $g_s = -3.826$ for the neutron (ν). In this section though, we want to keep spin and orbit on an even footing, and we are interested in the isovector operators so we will use the following:

Isovector Orbital: $g_{l,\pi} = 0.5\ g_{l,\nu} = -0.5\ g_{s,\pi} = 0\ g_{s,\nu} = 0$
Isovector Spin: $g_{s,\pi} = 0.5\, g_{s,\nu} = -0.5\, g_{l,\pi} = 0\ \ g_{l,\nu} = 0$

In the following table we allow only 2 $\hbar\omega$ excitations. We calculate the *isovector* $B(M1)_{spin}$ and $B(M1)_{orbital}$. The results are as follows:

Interaction		$B(M1)\ 10^{-3}\mu_N^2$	
x	y	SPIN	ORBITAL
0	0	0.855	0.855
1	0	0.857	0.857
0	1	3.824	3.824
1	1	3.395	3.395

We get the remarkable result[19] that the isovector spin $B(M1)$ and isovector orbital $B(M1)$ are the same for all (x, y) combinations. After some thought one can explain this. The components of the wave function of the $J = 0^+$ correlated ground state can be classified by the L S labels L_π, L_ν, S_π, S_ν. It can be shown that in the restricted space $\Delta N = 2$, the wave function is *invariant* under the interchange of the spin and orbital labels. One counter example is the component $[(L_\pi = 1, L_\nu = 1)^{L=0}(S_\pi = 0, S_\nu = 0)^{S=0}]^{J=0}$. This is not invariant under the interchange of L and S. However, this state is completely spurious i.e. the center-of-mass operator creates a state with $L = 1^-$ $S = 0$.

In more detail, we get for the case $x = 0$, $y = 0$ (central interaction) only three states excited as follows:

Energy	$B(M1)\ 10^{-3}\mu_N^2$	
(MeV)	SPIN	ORBITAL
45.3	0.855	0
56.4	0	0.855
439.0 (Spurious)	0	13.07

Note that the spin state and the orbital state are not at the same energy but they have the same strength. The spurious 1^+ state has artificially been put up at a high energy (439 MeV) using the Gloeckner-Lawson technique[20] in $OXBASH$[18]. Note that the spurious state carries a lot of orbital strength so it is essential that it be removed. Note that a $2p-2h$ spurious 1^+ state can be obtained by combining a $1p-1h$ state (spurious or non-spurious) with the 1^- spurious state $\vec{R}|0\rangle$ where $\vec{R}$ is the center-of-mass operator. (The spuriosity we are talking about here should not be confused with the spurious state obtained with the operator J_+ acting on a deformed intrinsic state). It should be remarked that this symmetry does not hold when we allow more than 2 $\hbar\omega$ excitations, and it does not hold for heavier nuclei like ^{16}O. Another point of interest in the above table is the big rise in $B(M1)$ when we turn on the *tensor* interaction. For ($x = 1$, $y = 0$), the sum $B(M1)_{spin}$ is 0.857 but with ($x = 1$, $y = 1$) it jumps to 3.395 (the same is true for the orbital transition). This shows that the tensor interaction is of extreme importance for ground state correlations.

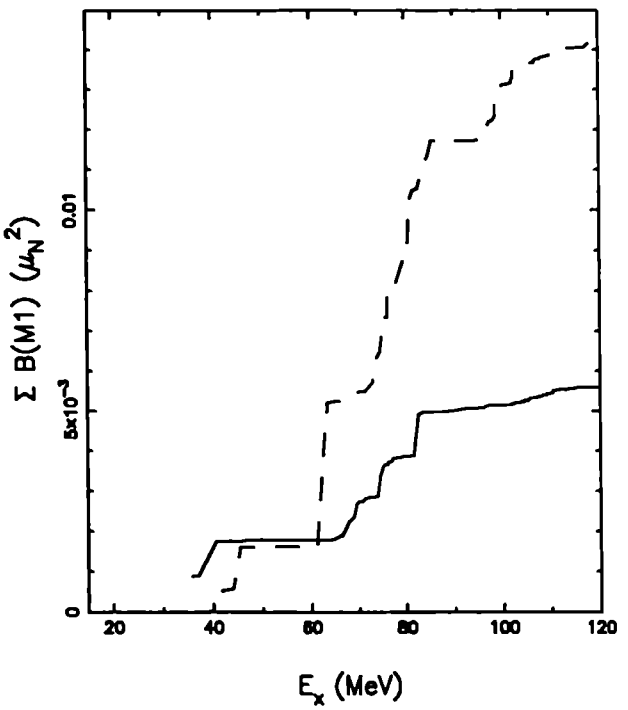

Figure 2: Summed strengths of the spin (solid line) and orbital (dashed line) magnetic dipole transitions $J = 0_1^+ \; T = 0 \; \rightarrow \; J = 1^+ \; T = 1$ in ^4He

Figure 2 shows the isovector spin and orbital cumulative strength when we allow up to 6 $\hbar\omega$ excitations. The solid line is for spin and the dashed line for orbital. Consistent with the previous discussion, the two curves become almost equal in the 2 $\hbar\omega$ region but then beyond 60 MeV excitation energy they diverge, with the orbital sum becoming large.

These $M1$'s are in principle a signature of ground state correlations, although in practice it may be impossible to observe them in ^4He (the situation is more favorable in heavier nuclei like ^{16}O or ^{40}Ca). Note the slow convergence in the figure, especially for the orbital case. We have gone up to 6 $\hbar\omega$ and the curve keeps rising. If we include 8 $\hbar\omega$, the curve might increase even more.

5 Collective Behaviour: Scissors Modes

Thus far, we have dealt with closed shells or closed shells plus or minus two nucleons. To get more collective behaviour, one needs more valence protons and neutrons. In this section, we will consider the light deformed nuclei ^8Be and ^{10}Be in the context of scissors mode behaviour. In a p shell calculation ($\Delta N = 0$), ^8Be has two valence protons and two valence neutrons. The nucleus ^{10}Be has four valence neutrons and two valence potons. Our motive for considering light nuclei is that we can perform shell model calculations which include $\Delta N = 2$ configurations. It should be noted that these nuclei are strongly deformed.

Although we have studied these nuclei with the realistic (x, y) interaction, here we will discuss these nuclei using the schematic quadrupole-quadrupole interaction $-\chi Q \cdot Q$. With this interaction, of the four

types of magnetic dipole excitations isoscalar spin, isoscalar orbital, isovector spin, isovector orbital, only the last one will have non-zero strength from the ground states of ^8Be or ^{10}Be i.e. the only surviving operator is $L_\pi - L_\nu$. Since $\vec{L}$ is a generator for rotations, this operator includes a scissors mode excitation, with neutrons and protons oscillating in opposite directions -hence the name scissors modes. As shown by one of the founders of this subject -N. LoIudice[21], the proper milieu for the existence of these modes is a strongly deformed nucleus. He has performed calculations in the intrinsic frame where it is easier to visualize the scissors mode as a vibration of the deformed proton symmetry axis against that of the neutrons. However, we shall here perform calculations in the laboratory frame.

In $L\ S$ coupling we can have the following magnetic dipole ($J = 1^+$) excitations:

1. $L = 0\ S = 1\ T = 0$
2. $L = 0\ S = 1\ T = 1$
3. $L = 1\ S = 1\ T = 0$
4. $L = 1\ S = 1\ T = 1$
5. $L = 1\ S = 0\ T = 0$
6. $L = 1\ S = 0\ T = 1$

The first two states can be excited by the spin part of the magnetic dipole operator, but for a spin-isospin independent interaction, of which $Q \cdot Q$ is a special case, they will not be excited. The states 3 and 4 cannot be excited from an $L = 0\ S = 0$ ground state. You cannot simultaneously change L and S with a one-body operator. The state 5. cannot be excited form an $L = 0$ ground state because $(L_\pi + L_\nu)|L = 0\rangle = 0$. Thus, the only state excited is 6. -the scissors mode: $(L_\pi - L_\nu)|L = 0,\ S = 0\rangle = |L = 1,\ S = 0,\ T = 1\rangle$.

In the $0p$ shell, one can classify the states according to Wigner's Supermultiplet Scheme[22], and for a $Q \cdot Q$ interaction one can use the Elliott formula for the energies[23]. The results are shown in the following table taken essentially from Hammermesh's book on Group Theory[24]. To find the scissors mode, one simply looks for an $L = 1\ S = 0$ state. First, for ^8Be note that the ground band is $[4\ 0\ 0]^{L=0,2,4}$. If one has any spin-isospin independent interaction is the p shell one necessarily gets a rotational spectrum (if one does not change the interaction from one nucleus to the next, one gets *identical bands* for all nuclei in the p shell).

The scissors mode has orbital symmetry [4 0 0]. The scissors band has orbital symmetry and has an energy $54\bar{\chi}$, and if $\bar{\chi}$ is chosen to fit the lowest 2^+ state, the excitation energy is 9.12 MeV. This is too low -the experimental value is 17.6 MeV.

In ^{10}Be, the first 2^+ state is two-fold degenerate with a $Q \cdot Q$ interaction at 3.37 MeV. The first two $L = 1$ states are also two-fold degenerate with orbital symmetries [4 1 1] and [3 3 0]. However, these are not scissors modes because they have quantum numbers $L = 1\ S = 1$. The scissors modes have orbital symmetry [3 2 1] at $60\bar{\chi}$=12.35 MeV and there is a degeneracy of the $T = 1$ and $T = 2$ scissors modes in ^{10}Be. The energy is again too low in this model -almost by a factor of two.

One point worthy of note is that in this supermultiplet scheme, there are many degenerate states with various S and T shown in the right hand column. This shows right away why there is intermediate structure in the scissors modes both here and in heavier nuclei. With more realistic interactions, the strength gets fragmented amongst the nearly degenerate $J = 1^+$ states. The IBA-2 may predict the centroids of the scissors mode strength but does not give the intermediate structure that is observed.

A. ^8Be				
$[\ f_1 f_2 f_3]^a$	L	$\frac{E^*}{\tilde{\chi}}{}^b$	E^*(MeV)	(S T)
[400]	0	0	0	(0 0)
	2	18	3.04	
	4	60	10.13	
[310]	1	54	9.12	(0 1)^c (1 0)(1 1)
	2	66	11.15	
	3	84	14.18	
[220]	0	72	12.16	(0 0)(0 2)(2 0)(1 1)
	2	90	15.20	
[211]	1	102	17.23	(0 1)(1 0)(1 1)(1 2)(2 1)
B. ^{10}Be				
[420]	0	0(-96)	0	(0 1)
	$2_1, 2_2$	18	3.37	
	3	36	6.74	
	4	60	11.23	
[411] + [330]	1	30	5.61	(1 1)
	3	60	11.23	
[321]	1	66	12.35	(0 1)^d (0 2)^d (1 1)(2 1)
[222]	0	96	17.96	(0 1)(1 2)(2 1)
				(0 3)(3 0)

[a] $\lambda = f_1 - f_2$, $\mu = f_2 - f_3$, $\frac{E^*}{\tilde{\chi}} = -4(\lambda^2 + \mu^2 + \lambda\mu + 3(\lambda + \mu)) + 3L(L+1)$.

[b] $\tilde{\chi}$ was chosen so that the energies of the 2_1^+ states in ^8Be and ^{10}Be agreed with the experimental values of 3.04 MeV and 3.368 MeV respectively.

[c] Scissors mode state in ^8Be.

[d] Scissors mode states in ^{10}Be.

5.1 Energy Weighted Sum Rule with the $Q \cdot Q$ Interaction

We should mention that we are taking a rather unusual approach to the scissors mode problem by examnining these very light nuclei. The proper milieu for these scissors modes is generally considered to be heavy deformed nuclei with $156Gd$ being the classic example. This is the nucleus where the Darmstadt group[25], by a combination of inelastic electron scattering and inelastic proton scattering, was able to ascertain that they had excited a $J = 1^+$ state at about 3 MeV which was mainly an orbital excitation with $B(M1) \uparrow \approx 3\ \mu_N^2$.

This prompted many other theoretical works besides the previously mentioned works of Loludice and Palumbo[21]. An important contribution was made by Iachello[26] in the context of IBA-II, namely that the collectivity of the mode does not come from all the nucleons in the nucleus but rather from the valence nucleons. At this summer school, we have the coherent state approach of Raduta et. al. applied to the scissors mode problem by Loludice, Raduta and Delion[27]. The shell model approach was used by Zamick and Liu[28,29] in the $f - p$ shell and by the Madrid group in the $s - d$ shell[30,31].

The collective nature of the scissors mode was made much more apparent by the Darmstadt group when they noted that in the Samarium isotopes the summed orbital $B(M1)$ strength was proportional to $B(E2)$

from the ground state to the first 2^+ state (alternately to δ^2)[32,33]. This stimulated more theoretical activity -especially sum rule approaches- either energy weighted[34,35] or non-energy weighted[28,36,37].

We are here motivated by the above mentioned empirical observation that $B(M1)_{orbital}$ appears to be proportional to $B(E2)$ i.e. is larger the more deformed the nucleus is[32,33]. The energy weighted sum rule for the scissors mode operator $(L_\pi - L_\nu)/2$ is proportional to the double commutator of this operator with the Hamiltonian. With the interaction $-\chi Q \cdot Q$ one can evaluate the double commutator analytically, and one obtains the following result[34]:

$$(EWSR) \qquad \sum_n (E_n - E_0) B(M1)_{v,o} = \frac{9\chi}{16\pi} \left\{ \sum_i [B(E2, 0_1 \rightarrow 2_i)_{isosca.} - B(E2, 0_1 \rightarrow 2_i)_{isovec.}] \right\}$$

where $B(M1)_{v,o}$ is the value for the *isovector orbital* $M1$ operator ($g_{l\pi} = 0.5$ $g_{l\nu} = -0.5$ $g_{s\pi} = 0$ $g_{s\nu} = 0$) and the operator for the $E2$ transitions is $\sum_{protons} e_p r^2 Y_2 + \sum_{neutrons} e_n r^2 Y_2$ with $e_p = 1$, $e_n = 1$ for the isoscalar (isosc.) transition, and $e_p = 1$, $e_n = -1$ for the isovector (isovec.) transition.

This differs from other peoples' results which on the right hand side have only $B(E2)$ to the first excited state (mainly isoscalar)[35]. To see how this sum rule works, we give a breakdown in both a small space ($0p$ shell) and large space $0p$ + all $\Delta N = 2$ excitations[38] in the following table.

The fact that $B(E2)_{isoscalar}$ increases almost by a factor of 4 in going to the large space ($0p + \Delta N = 2$) is consistent with the fact that the effective charge of a proton is 1.5 and of a neutron is 0.5 i.e. $B(E2)_{isoscalar} \propto (e_p + e_n)^2$. This factor is unity for $e_p = 1$, $e_n = 0$ but is 4 for $e_p = 1.5$, $e_n = 0.5$.

Note that the isovector $B(E2)$ is very large for ^{10}Be and therefore causes $EWSR$ to be much smaller in ^{10}Be than in ^{8}Be. Indeed the the strength is much weaker in ^{10}Be than in ^{8}Be. One can show that for ^{8}Be $B(M1) = \frac{2}{\pi} \mu_N^2$ in the $0p$ shell and is $\frac{3}{4\pi} \mu_N^2$ in ^{10}Be[38]. This is only 3/8 of what it is in ^{8}Be. On the other hand, the $B(E2)$'s are about the same in the two nuclei. Thus we have a deviation from the 'universal' systematic that $B(M1)_{orbital}$ is proportional to $B(E2)$.

	$0p$ space	$0p + \Delta N = 2$ space
^{8}Be		
$EWSR\ M1_{orb.}$	6.411	14.04
$B(E2)_{isoscalar}$	72.54	237.5
$B(E2)_{isovector}$	10.37	89.6
Right Hand Side	6.411	15.25
^{10}Be		
$EWSR\ M1_{orb.}$	2.026	6.413
$B(E2)_{isoscalar}$	68.31	251.4
$B(E2)_{isovector}$	37.00	142.8
Right Hand Side	2.026	7.029

On can obtain the one-body Nilsson deformation potential from the two-body quadrupole-quadrupole interaction by replacing $-\chi Q \cdot Q$ by $-\chi \langle Q \rangle \cdot Q$ where $\langle Q \rangle$ is the expectation value in a deformed intrinsic state. In this simple model, it was shown by de Guerra and Zamick[39] that besides the usual low energy isovector orbital scissors mode strength, there is also strength in the $2\hbar\omega$ region. Moreover, if χ is chosen self-consistently, one obtains the result that the energy-weighted scissors mode strength in the high energy region is equal to that in the low energy region. This result is also true when a pairing interaction (between like particles only) is included.

In figure 3 -taken from the work of Fayache, Sharma and Zamick[38,40]- we show the cumulative energy-weighted strengths for ^8Be ($T = 0 \rightarrow T = 1$). ^{10}Be ($T = 1 \rightarrow T = 1$) (solid line) and ^{10}Be ($T = 1 \rightarrow T = 2$) (dashed line) coming, not from the Nilsson model, but from a shell model diagonalization with the interaction $-\chi Q \cdot Q$. The space is the $0p$ shell plus all $\Delta N = 2$ excitations.

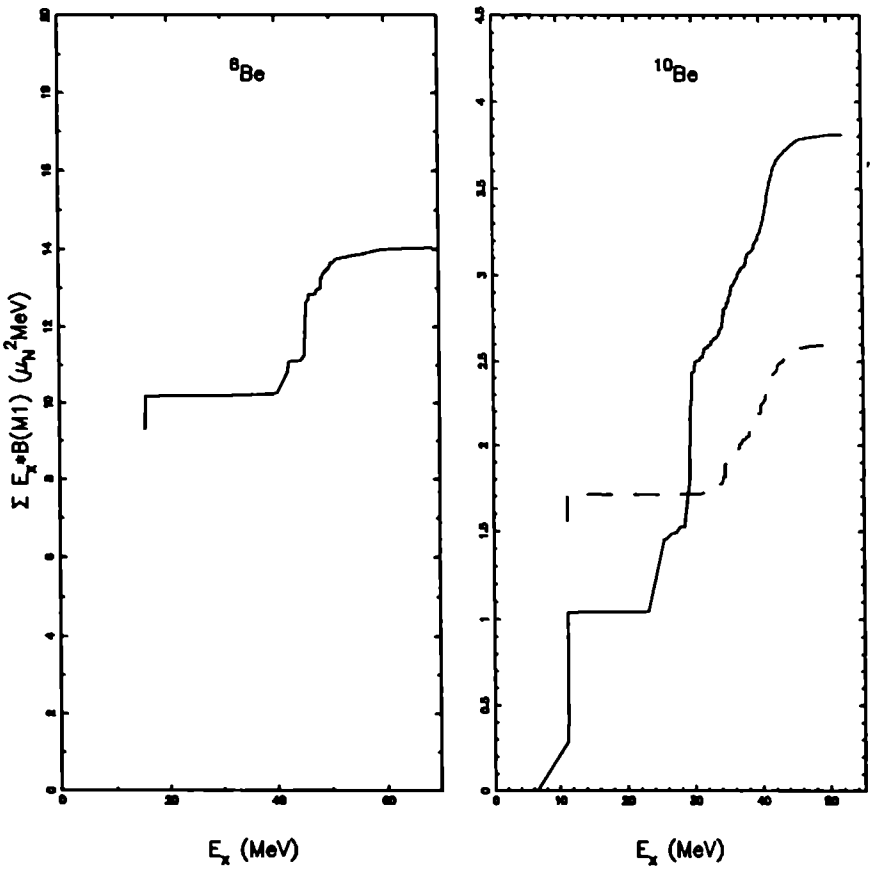

Figure 3: Energy-weighted summed strength of the isovector orbital magnetic dipole transition $J = 0_1^+ \; T = 0 \rightarrow J = 1^+ \; T = 1$ in ^8Be (left figure), and for the $J = 0_1^+ \; T = 1 \rightarrow J = 1^+ \; T = 1$ transition (solid line) and $J = 0_1^+ \; T = 1 \rightarrow J = 1^+ \; T = 2$ transition (dashed line) in ^{10}Be (right figure), using the $-\chi Q \cdot Q$ interaction

In the ^8Be figure, as in the ^{10}Be figure, there is a sudden rise followed by a flat plateau followed by a second rise. Had we only done the calculation in the $\Delta N = 0$ space, we would not get the second rise.

The high lying energy-weighted strengths are not precisely twice the low lying strengths, as would be given by the self-consistent Nilsson model[39]. In fact the ratios of high to low are as follows:

^8Be ($T = 0 \rightarrow T = 1$)	1.37
^{10}Be ($T = 1 \rightarrow T = 1$)	3.68
^{10}Be ($T = 1 \rightarrow T = 2$)	1.52

Hence for ^{10}Be ($T = 1 \rightarrow T = 1 + T = 2$) the ratio is 2.33. We see that replacing $-\chi Q \cdot Q$ by $-\chi(Q) \cdot Q$ does not give the correct results in detail but as a crude average, it may be correct. The large ratio in ^{10}Be ($T = 1 \rightarrow T = 1$) is due to a suppression of the low lying strength as discussed before.

Let us briefly mention some results with the realistic (x, y) interaction for $x = 1$, $y = 1$. We give the mean energy of the $M1$ orbital strength in the $\Delta N = 0$ region in the small $0p$ space and the large $0p + \Delta N = 2$ space.

		Mean Energy	
Nucleus	Mode	Small Space	Large Space
^{8}Be	$0^+ T = 0 \rightarrow 1^+ T = 1$	15.9	20.1
^{10}Be	$0^+ T = 1 \rightarrow 1^+ T = 1$	18.7	24.6
	$0^+ T = 1 \rightarrow 1^+ T = 2$	19.8	25.1

We see that including $\Delta N = 2$ excitations raises the energy of the scissors mode. The results are in better agreement with experiment.

5.2 Isovector $Q \cdot Q$

One can generalize from $-\chi Q \cdot Q$ to an interaction

$$V = -\chi Q \cdot Q[1 + B\vec{\tau}(1) \cdot \vec{\tau}(2)]$$

where $\vec{\tau}(1) \cdot \vec{\tau}(2) = 1$ for $T = 1$ states and -3 for $T = 0$ states. A large negative B of the order of -3.6 has been needed to fit the separation of the isoscalar and isovector giant quadrupole states. That is to say one wants the isoscalar quadrupole state to come to an energy of $\sqrt{2}\hbar\omega$ and the isovector to come at about 2.6 $\hbar\omega$. To do this requires $-\chi B$ to be positive and hence B to be negative.

It has been pointed out[41,42] that a large value of B causes the $EWSR$ orbital $M1$ strength at high energies to be much more than that at low energies (the equality of the two comes in the Nilsson model as shown by de Guerra et. al.[39]). Indeed at this conference Loludice gets the result[42] -not that the *energy weighted strengths* at low and high energies are the same- but rather that the strengths themselves are almost the same at least for superdeformed states. He may well be correct. What we will now do is to throw the subject into a state of confusion (confusing ourselves as well) by noting the dire consequences of a large B for low lying spectroscopy.

M.S. Fayache, S. Shelly Sharma and the speaker[43] have recently investigated the B dependence of the spectrum of ^{10}Be. The results as a function of B are shown in figure 4.

One gets very strange results for negative B. For $B = 0$, we recall that the 2_1^+ and 2_2^+ states are degenerate. As we make B negative this degeneracy is removed. We get a downgoing line (solid). This is a 2^+ state with the *strange* property that it cannot be reached from the ground state by an isoscalar $E2$ probe -only by the isovector probe $\sum e_p r^2 Y_2 + e_n r^2 Y_2$ with $e_p = 1$, $e_n = -1$. This 'isovector' 2^+ state becomes the ground state for $B < -0.68$. Also coming down (dash-dot line) is an $L = 1$, $S = 1$ triplet of states i.e. $J = 0^+$, 1^+ and 2^+ corresponding to some linear combination of states of orbital symmetry [4 1 1] and [3 3 0]. This triplet becomes the ground state for $B < -0.82$. Clearly these results are very unphysical. It would appear that an interaction chosen to fit one problem -isospin splitting of giant resonances- gives difficulties when applied to another problem -low lying spectroscopy e.g. in ^{10}Be.

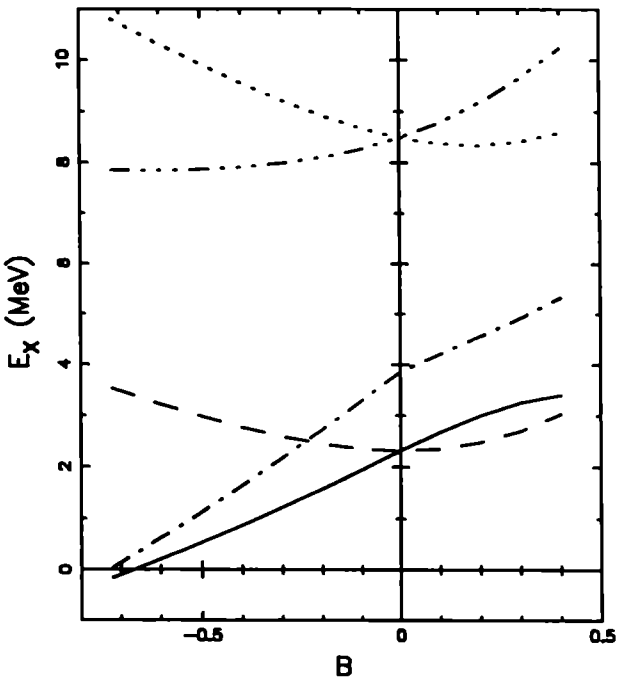

Figure 4: The excitation energies of selected states in ^{10}Be as a function of the isovector quadrupole interaction parameter B. The solid line is for the isovector 2^+ state, the dashed line is for the isoscalar 2^+ state and the dot-dashed line for the $S = 1$ $L = 1$ triplet ($J = 0^+$, 1^+, 2^+). The upper two curves are for the scissors modes. The dotted line is for the $J = 1^+$ $T = 1$ scissors mode branch, and the dash-triple-dot line is for the $J = 1^+$ $T = 2$ scissors mode branch.

We should add that figure 4 corresponds to a $0p$ shell calculation. In a large space $0p + 2\ \hbar\omega$ we no longer get the curves to go below zero, but still in detail the results are very different from experiment.

Higher up in the figure we show the 1^+ scissors modes in ^{10}Be. The $T = 1$ branch is represented by the dotted line and the $T = 2$ by the dash-triple dot line. Recall again that for $B = 0$ these two states are degenerate. As we make B increasingly negative we find that the $T = 2$ state comes below the $T = 1$ state. We have at present no experimental evidence whether this is right or wrong.

6 Linear α-Chain States

In this last section we treat highly deformed states in nuclei -in particular linear α-chain states. This topic fits well into our title "$\Delta N = 2$ and Beyond", but we find it currently impossible to carry out the calculations with shell model codes. We will rather use the Skyrme Hartree-Fock approach[44,45,46].

A two-alpha chain state corresponds to the ground state of ^8Be. The three-alpha chain state is identified with a $J = 0^+$ bandhead in ^{12}C at 7.65 MeV excitation, barely above the threshold for decay into three alpha particles.

Let us say at the outset that with respect to linear chain states beyond ^{12}C there are still many ambigu-

ities, both experimental and theoretical. There may be a 4α linear chain in ^{16}O with the $J = 0^+$ bandhead at 16.7 MeV but the evidence is not definitive according to Hodgson[47]. As another example, perhaps the most promising, Wuosmaa[48,49] reports reports strong evidence for a 6α linear chain state in ^{24}Mg. His group obtains a strong peak in the excitation function of $^{12}C\ (0_2^+)\ +\ ^{12}C\ (0_2^+)$ at an excitation energy of 46.4 MeV in ^{24}Mg. The experimental results are very beautiful. Presumably the peak corresponds to the breakup of a 6α chain into two 3α chains. The 3α chain is identified with the 7.65 MeV 0^+ excited state in ^{12}C. The excitation energy in ^{24}Mg is in good agreement with calculations of Marsh and Rae[50]. However, those authors point out that in their calculation they ignore the Coulomb interaction. In our Skyrme Hartree-Fock approach we find that the Coulomb energy of the Chain state in ^{24}Mg is 9.5 MeV less than for the ground state[46]. This is not surprising -in an elongated chain state the charges are further apart than in a less deformed state. Furthermore, Marsh and Rae[50] use an interaction (Brink-Boecker B1)[51] which does not fit the binding energies of ground states. Thus, we feel that close agreement between theory and experiment may be fortuitous. Also, at Santorini, as reported in the conference summary by Greiner[52], Horiuchi presented an alternate mechanism to explain Wuosmaa's data. We are frankly not expert enough to judge the relative merits of the two models. Nevertheless, we will here present some calculations and ideas concerning these fascinating states.

It is easiest to picture the linear α-chain states in the context of the deformed oscillator (DO) model. The Hamiltonian is

$$H_{\rm DO} = H_x + H_y + H_z = \left(\frac{p_x^2}{2m} + \frac{1}{2}m\omega_x x^2\right) + \left(\frac{p_y^2}{2m} + \frac{1}{2}m\omega_x y^2\right) + \left(\frac{p_z^2}{2m} + \frac{1}{2}m\omega_z z^2\right).$$

We assume axial symmetry: $\omega_x = \omega_y \equiv \omega_\perp$. The energy is

$$E = \hbar\omega_x\Sigma_x + \hbar\omega_y\Sigma_y + \hbar\omega_z\Sigma_z\ ,$$

where $\Sigma_x = \sum(N_x + \frac{1}{2})$ with N_x the number of quanta in the x direction, *etc.*.

The ground state, say, for ^{16}O, is obtained by filling the lowest four levels: $(N_x, N_y, N_z) = (0,0,0), (1,0,0), (0,1,0), (0,0,1)$. The linear chain state is obtained by Brink's prescription[53] of "putting all the quanta in the z direction", so for ^{16}O, the occupying states are (0,0,0), (0,0,1), (0,0,2) and (0,0,3). To get the deformation we must supplement the above with the Mottelson condition:

$$\frac{\omega_x}{\omega_z} = \frac{2\Sigma_z}{\Sigma_x + \Sigma_y}.$$

This condition leads to a minimization of the energy provided that the volume is conserved, i.e., $\omega_0^3 = \omega_x\omega_y\omega_z$ is fixed.

For the chain states, it is easy to show that

$$E_{\rm chain} = \hbar\omega_\perp A + \hbar\omega_z\frac{A^2}{8} = \frac{2A^{4/3}}{2^{5/3}}\hbar\omega_0\ ,$$

and that $\omega_x/\omega_z = A/4$, where A is the mass number. The above energy is interpreted as an intrinsic state energy from which we must project out the states of good angular momentum. If we assume that $\hbar\omega_0 = 45A^{-1/3} - 25A^{-2/3}$ MeV, the above procedure yields intrinsic state energies of 9.8 MeV, 29.2 MeV and 102.2 MeV for ^{12}C, ^{16}O and ^{40}Ca respectively.

6.1 The Skyrme Hartree-Fock Methods

6.1.1 General Skyrme Interactions

The Skyrme (Vautherin and Brink) interaction can be written as[54]:

$$V_{\text{Skyrme}} = \sum_{i<j} V_{ij} + \sum_{i<j<k} V_{ijk} + V_{\text{Coulomb}}$$

where

$$\begin{aligned} V_{12} &= -t_0(1 + x_0 P^\sigma)\delta(r_1 - r_2) + \frac{1}{2}t_1[k'^2\delta(r_1 - r_2) + \delta(r_1 - r_2)k^2] \\ &\quad + t_2 k'\delta(r_1 - r_2)k + iWk' \cdot \delta(r_1 - r_2)\sigma \times k, \end{aligned}$$

and

$$V_{123} = t_3\delta(r_1 - r_2)\delta(r_1 - r_3).$$

In the above, the t_0 term is attractive to hold the nucleons and the t_3 term is repulsive to prevent nuclear collapse. The W term is the spin-orbit interaction which causes a $j = l + \frac{1}{2}$ orbit to be lower in energy than the $j = l - \frac{1}{2}$ orbit. The t_1 and t_2 terms are finite-range terms. In Hartree-Fock calculations, V_{123} is equivalent to a density-dependent interaction $\frac{t_3}{6}\rho(R)\delta(r_1 - r_2)$.

6.1.2 Zero-Range Skyrme Interactions and Oscillator Trial Wave Functions

One can achieve saturation with just the zero-range t_0 and t_3 terms of the Skyrme interaction[45]. So we have a simplified Hamiltonian:

$$H = \sum_i \frac{p_i^2}{2m} - \sum_{i<j} t_0\delta(r_i - r_j) + \sum_{i<j<k} t_3\delta(r_i - r_j)\delta(r_i - r_k).$$

We use a single Slater determinant involving harmonic oscillator trial single-particle wave functions expressed in terms of a harmonic oscillator length parameter $b = \sqrt{\frac{\hbar}{m\omega}}$. The value of b for mass number A is roughly $1.0A^{1/6}$ fm.

The trial energy has the structure

$$E_{\text{trial}} = \frac{\hbar^2}{2mb^2}\Sigma - t_0\frac{|A|}{b^3} + t_3\frac{|B|}{b^6},$$

where $|A|$ and $|B|$ do not depend on b, and Σ is the oscillator sum $\Sigma = \sum_i^A(2n + l + \frac{3}{2})$. The minimum condition is $\frac{dE}{db} = 0$. The nuclear incompressibility is $b^2\frac{d^2E}{db^2}$.

For the deformed oscillator, the trial wave function, assuming axial symmetry, is a Slater determinant involving states $|N_x, N_y, N_z\rangle$. The general structure of the b_x, b_z dependence of the trial energy can be obtained by a dimensional analysis as:

$$E_{\text{trial}} = \frac{\hbar^2}{2mb_x^2}(\Sigma_x + \Sigma_y) + \frac{\hbar^2}{2mb_z^2}\Sigma_z - t_0\frac{|A|}{b_0^3} + t_3\frac{|B|}{b_0^6},$$

where $b_0^3 = b_x b_y b_z$ and where $|A|$ and $|B|$ are independent of b_x and b_z.

Note that the potential energy depends only on b_0; there is no explicit dependence on b_z. We therefore have to minimize only the kinetic energy. The minimum condition $\left[\frac{\partial E_{\text{trial}}}{\partial b_z}\right]_{b_0} = 0$ leads again to the Mottelson conditions, the same ones of the deformed oscillator model:

$$\frac{b_z^2}{b_0^2} = \frac{\omega_\perp}{\omega_z} = \frac{2\Sigma_z}{\Sigma_x + \Sigma_y}.$$

We thus have a close connection between the Skyrme model and the previously considered Deformed Oscillator or Nilsson model.

6.2 Results

We go beyond the simple deformed oscillator model for the linear chain states by expanding the single-particle orbitals:

$$\Psi = \sum_{n_z,n_\perp} C_{n_z,n_\perp}\phi_{n_z}(z/b_z)\phi_{n_\perp}(\rho/b_\perp).$$

We include 14 major shells.

The results are presented in the following table (where 'Diff' means the difference in the results between the ground state (G) and the chain state (C)). We give the intrinsic energies and the $J^\pi = 0^+$ bandhead energies. The latter are obtained by the Villars result[55]

$$E_{0+} = E_{\rm int} - \frac{\hbar^2}{2\mathcal{I}}\langle J_\perp^2\rangle,$$

where we take for $\mathcal{I}$ (and this point deserves further attention) the *rigid-body* moment of inertia.

The calculated $J^\pi = 0^+$ bandhead excitation energies for ^{12}C, ^{16}O, ^{20}Ne and ^{24}Mg are respectively 12.3 MeV, 25.8 MeV, 37.2 MeV and 58.6 MeV. The experimental values are 7.65 MeV for ^{12}C and 47.8 and from the Wuosmaa experiment about 40 MeV for ^{24}Mg.

Nucl.	State	β	$E_{\rm K}$	$E_{\rm V}$	$E_{\rm S}$	$E_{\rm so}$	$E_{\rm C}$	$E_{\rm int}$	$\langle J_\perp^2\rangle$	$\mathcal{I}_{\rm rigid}$	$-\frac{\langle J_\perp^2\rangle}{\mathcal{I}_{\rm rigid}}$	E_{0+}
^{12}C	G	0.00	183.4	-312.3	51.0	-23.5	8.1	-93.21	—	—	0.00	-93.21
	C	1.03	150.6	-269.2	47.5	-6.1	6.5	-70.71	58.7	2.88	-10.19	-80.90
	Diff		-32.8	43.1	-3.6	17.4	-1.6	22.50			-10.19	12.31
^{16}O	G	0.00	220.3	-413.3	53.1	-1.2	13.5	-127.59	—	—	0.00	-127.59
	C	1.25	204.0	-358.9	61.4	-7.7	10.2	-90.93	143.9	6.65	-10.82	-101.75
	Diff		-16.3	54.5	8.3	-6.5	-3.3	36.66			-10.82	25.84
^{20}Ne	G	0.37	298.2	-530.4	65.5	-11.0	20.3	-157.44	17.22	3.04	-2.83	-160.26
	C	1.36	258.3	-449.3	75.3	-9.5	14.4	-110.88	311.3	12.76	-12.20	-123.08
	Diff		-39.9	81.1	9.7	1.6	-5.9	46.56			-9.37	37.18
^{24}Mg	G	0.39	383.3	-663.7	80.1	-25.3	28.6	-196.95	19.32	3.88	-2.49	-199.44
	C	1.42	320.7	-549.5	93.6	-12.3	19.1	-128.34	520.6	20.89	-12.46	-140.80
	Diff		-62.6	114.2	13.5	13.0	-9.5	68.6			-9.97	58.64

Also of interest in the breakdown of the difference in the energy of the linear chain states and the ground state into various parts. For example, in ^{16}O, the Coulomb energy difference is -3.3 MeV, i.e., there is less Coulomb repulsion in the chain state than in the ground state because the nucleons are further apart. The difference in the surface energy is 8.3 MeV because the deformed linear chain state has a larger surface area than the ground state. The spin-orbit interaction helps lower the energy of the chain state by 6.5 MeV.

For ^{24}Mg the Coulomb energy difference is -9.5 MeV. Unlike ^{16}O, the spin-orbit difference for ^{24}Mg is positive, +13 MeV. Note that for all nuclei considered the kinetic energy of the chain state is less than that of the ground state. This might at first seem puzzling because to form the chain state we put nucleons into higher shells. However, the kinetic energy of the chain state is lowered sufficiently by deformation (one can have a long wavelength along the z direction) to overcome this.

Our bandhead energies for ^{12}C, ^{16}O, ^{20}Ne and ^{24}Mg are 12.3, 25.8, 37.2 and 58.6 MeV respectively. These appear to be much too high in energy. The corresponding results of Marsh and Rae are 7.9, 18.9, 31.7 and 45.5 MeV. However, as was mentioned before, Marsh and Rae use an interaction which does not fit the binding energies of ground states and they ignore Coulomb effects.

How can we lower the energy of the chain states in the context of Skyrme interactions? It was noted by Zamick, Zheng and Sprung[45] that this could be achieved by making the finite-range terms t_1 and t_2 smaller with the constraint that one obtains the correct ground state energy and radius of a given nucleus. Indeed with a zero-range Skyrme interaction ($t_1 = 0$, $t_2 = 0$, $t_0 \neq 0$, $t_3 \neq 0$) one gets the chain states too low in energy. In some sense, the zero-range Skyrme and the Nilsson model have a close association, so this explains why the naive Nilsson model seems to give the correct energy for the linear alpha chain state.

On the other hand, we have at present no justification for making the parameters of the Skyrme interaction different for the chain states than for the ground state. There is clearly much work to be done both experimentally and theoretically on this very interesting topic.

This work was supported by the U.S. Department of Energy Grant No. DE-FG05-86ER-40299. The speaker thanks A. Raduta and S. Delion, M. Grigorescu, M. Petrascu, A. Sandulescu and others for their kind hospitality in Romania. Also to be thanked are the collaborators in the topics which were discussed here -D.C. Zheng, E. Moya de Guerra, H. Müther, S.J. Lee, A. Richter, N. Auerbach and J.A. Caballero, D.W.L. Sprung and S. Shelly Sharma. We are also greatful for comments and help from B.A. Brown and M. Horoi.

References

1. R. Machleidt, Adv. Nucl. Phys. **19**, (1989)189; R. Machleidt, K. Holinde and Ch. Elster, Physics Reports **149**, (1987)1

2. V.G.J. Stoks, R.A.M. Klomp, C.P.F. terheggen and J.J. De Swart, Phys. Rev. C **49**, (1994)2950.

3. D.C. Zheng and L. Zamick, Annals of Physics **206**, (1991)106.

4. C.W. Wong, Nucl. Phys. **A 108**, (1968)481

5. J. Blomqvist and A. Molinari, Nucl. Phys. **A 106**, (1968)545

6. D.J. Millener and D. Kurath, Nucl. Phys. **A 255**, (1975)315

7. J.P. Elliott and B.H. Flowers, Proc. Roy. Soc. London **242**, (1957)57

8. D.C. Zheng, L. Zamick, M.S. Fayache and H. Müther, Ann. Phys. (N.Y.) **230**, (1994) 118

9. D.C. Zheng, L. Zamick and M.S. Fayache, Phys. Rev. C **51**, (1995)1253.

10. L.D. Skouras and H. Müther, Nucl. Phys. **A534**, (1991)128

11. L. Zamick, D.C. Zheng, and H. Müther, Phys. Rev. **C45**, (1992)2763

12. D. R. Inglis, Rev. Mod. Phys. **25**, (1953)390

13. B. Jancovici and I. Talmi, Phys. Rev. **95**, (1954)289

14. K. Bleuler, Proceedings of the International School of Physics "Enrico Fermi", Course XXXVI, edited by C. Bloch, Academic Press, New York (1966)

15. T. Ericson and W. Weiss, *Pions and Nuclei*, Clarendon Press, Oxford (1988)

16. J.M. Eisenberg and D. Koltun, *Theory of Meson Interaction with Nuclei*, John Wiley and Sons, New York (1980)

17. M.S. Fayache and L. Zamick, Phys. Rev C **51**, (1995)160

18. B. A. Brown, A. Etchegoyen and W. D. M. Rae, The computer code OXBASH, MSU-NSCL report number 524 (1988).

19. M.S. Fayache and L. Zamick, Phys. Rev. C **51**, (1995)1580

20. D.H. Gloeckner and R.D. Lawson, Phys. Lett. **53B**, (1974)313

21. N. Loludice and F. Palumbo, Phys. Rev. Lett. **41**, (1978)1532

22. E.P. Wigner, Physical Review **51**, (1937)107

23. J.P Elliot, Proc. Royal Soc. **A 405**, (1958)128 and 562

24. M. Hammermesh, *Group Theory and its Applications to Physical Problems*, Addison-Wesley, Reading MA (1962)

25. D. Bohle et. al., Phys. Lett. **137 B**, (1984)27

26. F. Iachello, Nucl. Phys. **358**, (1981)890

27. N. LoIudice, A.A. Raduta and D.S. Delion, Phys. Rev. **C 50**, (1994)127

28. L. Zamick, Phys. Rev. **C 31** (1985)1555; Phys. Rev. **C 33** (1986)691

29. H. Liu and L. Zamick, Phys. Rev. **C 36**, (1987)2064

30. I. Chaves and A. Poves, Phys. Rev. **C 34**, (1986)1137

31. J. Retamosa, J.M. Udias, A. Poves and E. Moya de Guerra, Nucl. Phys. **A 511**, (1990)221

32. W. Ziegler, C. Rangacharyulu, A. Richter and C. Spieler, Phys. Rev. Lett. **65**, (1990)2515

33. C. Rangacharyulu et. al. Phys. Rev. **C 43**, (1991)R949

34. L. Zamick and D.C. Zheng, Phys. Rev. **C 44**, (1991)2522; **C 46**, (1992)2106

35. K. Heyde and C. de Coster, Phys. Rev. **C 44**, (1991)R2262

36. J.N. Ginocchio, Phys. Lett. **B 265**, (1991)6

37. B.R. Barrett, E.D. Davis and A.F. Diallo, Phys. Rev. **C 50**, (1994)1917

38. M.S. Fayache, S. Shelly Sharma and L. Zamick, submitted for publication.

39. E. Moya de Guerra and L. Zamick, Phys. Rev. **C 47**, (1993)2604

40. M.S. Fayache and L. Zamick, Phys. Lett. **B 338**, (1994)421

41. I. Hamamoto and W. Nazarewicz, Phys. Rev. **C 49**, (1994)3352

42. N. LoIudice, these proceedings.

43. M.S. Fayache, S. Shelly Sharma and L. Zamick, Phys. Lett. **B 357**, (1995)1

44. L. Zamick, D.C. Zheng, S.J. Lee, J.A. Caballero and E. Moya de Guerra, Annals of Physics **212**, (1991)402

45. L. Zamick, D.C. Zheng and D.W.L. Sprung, Phys. Lett. **B 293**, (1992)1

46. L. Zamick and D.C. Zheng, Z. Phys. **A 349**, (1994)255

47. P.E. Hodgson, Z. Phys. **A 349**, (1994)197

48. A.H. Wuosmaa et. al., Phys. Rev. Lett. **68**, (1992)1295

49. A.H. Wuosmaa, Z. Phys. **A 349**, (1994)249

50. S. Marsh and W.D.M. Rae, Phys. Lett. **B 180**, (1986)185

51. D.M. Brink and E. Boeker, Nucl. Phys. **A 91**, (1967)1

52. W. Greiner, Z. Phys. **A 349**, (1994)349

53. D.M. Brink, in *Many-Body Description of Nuclear Structure and Reactions*, International School of Physics Enrico "Enrico Fermi", Course XXXVI, Varenna 1966, edited by C. Bloch, Academic Press, New York (1966)

54. D. Vautherin and D.M. Brink, Phys. Rev. **C 5**, (1972)626

55. F. Villars, in *Nuclear Physics*, Proceedings of the International School of Physics Enrico "Enrico Fermi", Course XXXVI, Varenna 1966, edited by C. Bloch, Academic Press, New York (1966)

SHELL-MODEL STUDY OF PROTON RICH NUCLEI IN THE ^{100}Sn REGION

P. DIVARI, L.D. SKOURAS
Institute of Nuclear Physics, NCSR Demokritos
GR-15310, Aghia Paraskevi, Greece

and

I.P. JOHNSTONE
Department of Physics, Queen's University
Kingston, Ontario, K7L 3N6, Canada

ABSTRACT

The structure of the proton-rich nuclei with $47 \leq Z \leq 50$ and $47 \leq N \leq 51$ is determined in two shell-model calculations which differ in the definition of model space and in the manner the effective interaction is determined. The results of the calculation are found to be in satisfactory agreement with the existing experimental data. In addition the calculation makes a series of predictions about the spins and decay properties of the low lying states of several *exotic* nuclei, including the recently observed $^{94-97}$Ag, ^{97}Cd and ^{100}Sn.

1. Introduction

One of the new and exciting fields of research in nuclear structure physics appears to be the study of the *exotic* nuclei. These are nuclei for which the proton to neutron number ratio Z/N deviates strongly from the values characterizing nuclei near the stability valley. Exotic nuclei exhibit unusual properties such as new decay modes, very large decay energies (Q values) and *halo* structures of loosely bound particles [1,2]. The understanding of these properties presents a strong challenge to nuclear structure models.

Among the exotic nuclei, the proton-rich nuclei ($Z \simeq N$) in the mass $A \sim 100$ region provide an excellent ground for testing the nuclear shell-model. In this region one can use the doubly-magic ($Z = N = 50$) state of ^{100}Sn as a core and consider configurations with few valence particles and holes outside it. Due to the shell closure, the number of shell-model configurations is not too large, so the effects of variation of the model space can be studied systematically. Of particular interest in such a study is to investigate the effects of configuration mixing on the nuclear decay properties such as Fermi and Gamow-Teller β-decay and to draw conclusions about the quenching of the Gamow-Teller strength [3,4].

In this work we present a shell-model study of the properties of nuclei with proton number $47 \leq Z \leq 50$ and neutron number $47 \leq N \leq 51$. From the shell-model point of view, these nuclei need to be separated into two groups. Thus nuclei with $N < 50$

are conveniently described in terms of neutron holes outside a suitable $N = 50$ core, like $^{88}_{38}Sr_{50}$ or $^{100}_{50}Sn_{50}$. The other group contains the $N \geq 50$ nuclei, i.e nuclei with valence neutrons beyond the $N = 50$ core. Fig. 1 shows the single-particle orbitals which enter in the description of nuclei in the $A \sim 100$ region.

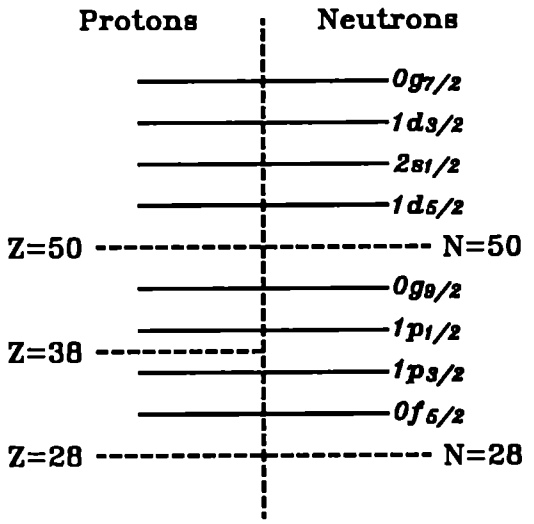

Figure 1: Single-particle states considered in the calculation

Until recently experimental investigations were concentrated on the β-decay of the $N \geq 50$ nuclei [5]. The dominant mechanism in this decay is the Gamow-Teller transition $\pi g_{9/2} \rightarrow \nu g_{7/2}$. A comparison of the observed data with the results of shell-model calculations [6,7,8] suggests a strong quenching of the Gamow-Teller strength. However, the agreement between experiment and theory drastically improves by introducing effective Gamow-Teller operators [4,6,7] which take into account the effects of breaking the $N = 50$ core. Due to the experimental difficulties in observing transitions to states just below the Q_{EC} value [5], one cannot be certain whether this simple renormalization of the operator is alone sufficient to account for the quenching of the Gamow-Teller strength.

Recently, experimental information regarding the β-decay of the $N \leq 50$ nuclei $^{94-97}$Ag, ^{95}Pd and ^{97}Cd has become available [9,10]. In addition there is evidence that ^{100}Sn itself has been observed by experimental groups at GANIL [11] and GSI [12]. A shell-model study of these nuclei is the main topic of the present work.

Normally, the aim of a calculation is to interpret the experimental data. In the case of the exotic nuclei, however, where experimental data are scarce, the main aim of a calculation is to make predictions about the properties of these nuclei. Such predictions are often useful to the experimentalists in analysing their data. For these predictions to be reliable, one has to employ a model which has been tested to describe satisfactorily the observed properties of neighbouring nuclei. Of course, there is no guarantee that a model will be succesful outside the region in which has been tested.

A more safe approach, therefore, is to determine the properties of the exotic nuclei using different models and to compare their predictions.

In our calculations we consider two models, which differ in the definition of model space but also in the manner the effective interaction is determined. A detailed description of these two models is given in sect. 2 of this paper. Sect. 3 contains a brief review on the β-decay of the $N = 50$ nuclei and a description of the renormalization of the Gamow-Teller operator. The results of the calculation are presented in sect. 4, while the conclusions are drawn in sect. 5.

2. Details of the calculation

As discussed above, in our calculations we need to describe two groups of nuclei, namely $N < 50$ and $N \geq 50$ nuclei. For the nuclei in each of these groups, we have performed two different shell-model calculations. A brief description of these two calculations, to be hereafter distinguished as *Model-1* and *Model-2*, is given in the following sections.

2.1. Description of Model-1

In the Model-1 approach we consider $^{88}_{38}Sr_{50}$ as inert core and place the n_π valence protons ($n_\pi = Z - 38 \leq 12$) in the $p_{1/2}$ and $g_{9/2}$ orbitals (see fig. 1). In this picture the $N < 50$ nuclei are described in terms of neutron holes which are also placed in the $g_{9/2}$ and $p_{1/2}$ orbitals. On the other hand, nuclei with $N > 50$ have valence neutron particles which are distributed in the $d_{5/2}$, $s_{1/2}$, $d_{3/2}$ and the $g_{7/2}$ orbitals. The definition of model spaces employed in the Model-1 calculations is summarized in Table 1. H and P in this table denote the use of hole and particle formalism, respectively.

Table 1: Model spaces used in the study of the exotic nuclei in the $A \sim 100$ region

Model	Core	Case	Proton Space		Neutron Space	
Model-1	$^{88}_{38}$Sr	$N \leq 50$	$(p_{1/2}g_{9/2})$	P	$(g_{9/2}p_{1/2})$	H
		$N > 50$	$(p_{1/2}g_{9/2})$	P	$(d_{5/2}s_{1/2}d_{3/2}g_{7/2})$	P
Model-2	$^{100}_{50}$Sn	$N \leq 50$	$(g_{9/2}p_{1/2}p_{3/2}f_{5/2})$	H	$(g_{9/2}p_{1/2}p_{3/2}f_{5/2})$	H
		$N > 50$	$(g_{9/2}p_{1/2}p_{3/2}f_{5/2})$	H	$(d_{5/2}s_{1/2}d_{3/2}g_{7/2})$	P

The effective hamiltonians required for Model-1 calculations have been determined following the *Talmi approach* [13]. In this approach the single-particle energies and the

two-body matrix elements of the shell-model hamiltonian:

$$H_{sm} = \sum_i \epsilon_i a_i^\dagger a_i + \frac{1}{2} \sum_{ijkl} \langle ij | \, V_{eff} | kl \rangle a_i^\dagger a_j^\dagger a_l a_k \, , \tag{1}$$

are treated as parameters which are determined by a least-square fit to the spectra of a series of neighbouring nuclei. The manner in which this approach was applied in the present calculation is described below.

2.1.1. $N = 50$ nuclei

These nuclei have only valence protons in the $p_{1/2}$ and $g_{9/2}$ orbitals. The effective hamiltonian for this model space contains 11 parameters, i.e the 2 single-particle energies and the 9 two-body matrix elements. These have been determined [14,15,16] by a least-square fit to levels of the $A \sim 90$ nuclei. In our calculations we use the values determined by Gloeckner and Serduke [15], although we have repeated their fit using a larger set of experimental data than was available to them [17].

There have been other shell-model studies of the $N = 50$ nuclei following the Talmi approach [17,18]. These, however, employed larger model spaces than the $(p_{1/2} g_{9/2})$ space considered in our approach.

2.1.2. $N < 50$ nuclei

As Table 1 shows, these nuclei are described in terms of proton-particles and neutron-holes placed in the $p_{1/2}$ and $g_{9/2}$ orbitals. Effective hamiltonians for this model space have been derived by Serduke, Lawson and Gloecker [19] (SLG) and by Gross and Frenkel [20] by least-square fits to the levels of the $N = 50$ and $N = 49$ nuclei. The matrix elements of these two interactions are very similar, so it is a matter of choice which of the two interactions one should use in Model-1 calculations.

2.1.3. $N = 51$ nuclei

A complete determination of the effective hamiltonian using the Talmi approach is in this case very difficult due to the large number of parameters involved (60 two-body matrix elements and 6 single-particle energies). In order to reduce the number of parameters, Johnstone [6] adopted the following procedure:

- The proton-part of the hamiltonian is taken from Gloeckner and Serduke [15].
- The three neutron single-particle energies of the $s_{1/2}$, $d_{3/2}$ and the $g_{7/2}$ orbitals relative to the $d_{5/2}$ together with the six matrix elements $\langle g_{9/2} d_{5/2}; J | V | g_{9/2} d_{5/2}; J \rangle$ where $J = 2, \ldots 7$ are considered as parameters.
- The other proton-neutron matrix elements are detemined using a volume- delta interaction. The $T = 1$ and $T = 0$ strengths of this interaction are also considered as parameters.

- The 11 parameters of the calculation were determined by a least-square fit to 65 levels of $N = 51$ nuclei. This fit produced a rms error of only 67 keV. From this fit one obtains the following values (in MeV) of neutron single-particle energies

$$\epsilon_{5/2} = 0, \quad \epsilon_{1/2} = 1.17, \quad \epsilon_{3/2} = 2.15, \quad \epsilon_{7/2} = 2.98, \tag{2}$$

  which reproduce satifactorily the low-lying spectrum of ^{89}Sr.

As may be evident from the above discussion, the effective interactions used in the Model-1 calculations have all been derived and tested in systematic shell-model studies of nuclei in the mass $A \sim 90$ region. As an example of the applicability of Model-1, we list in Table 2 the results of a recent calculation [17] on the binding energies of the $N = 50$ and $N = 51$ nuclei. As table 2 shows, discrepancies between theory and mass table values are small for those nuclei whoce binding energies have been determined by experiment, but become very large for several of those estimated from systematic trends. However, as Table 2 also shows, in these last cases the errors in the experimental estimates are also very large.

Table 2: Binding energies of nuclei in the ^{100} region

$N = 50$			$N = 51$		
Nucleus	Calc	Mass Tables	Nucleus	Calc	Mass Tables
^{90}Zr	783.87	783.894(2)	^{91}Zr	791.00	791.089(2)
^{91}Nb	789.10	789.053(3)	^{92}Nb	796.97	796.936(3)
^{92}Mo	796.46	796.509(4)	^{93}Mo	804.53	804.579(4)
^{93}Tc	800.64	800.596(4)	^{94}Tc	809.25	809.219(4)
^{94}Ru	806.81	806.843(13)	^{95}Ru	815.77	815.797(12)
^{95}Rh	809.93	809.900(150)	^{96}Rh	819.35	819.261(13)
^{96}Pd	814.99	815.030(150)	^{97}Pd	824.67	824.720(300)
^{97}Ag	817.12	816.940(400)	^{98}Ag	827.19	827.090(150)
^{98}Cd	821.14	820.890(210)#	^{99}Cd	831.09	831.360(210)#
^{99}In	822.38	821.640(500)#	^{100}In	832.94	832.530(400)#
^{100}Sn	825.39	824.480(450)#	^{101}Sn	836.03	835.650(500)#

Estimated from systematic trends

2.2. Description of Model-2

As Table 1 shows, in the Model-2 approach we consider the doubly closed ($Z = N = 50$) ^{100}Sn as core. In this approach the $N \leq 50$ nuclei are described in terms of proton and neutron holes which are distributed in the $g_{9/2}$, $p_{1/2}$, $p_{3/2}$ and $f_{5/2}$ orbitals of the harmonic oscillator potential. On the other hand, the $N \geq 50$ nuclei are described in terms of proton holes in the $(g_{9/2}p_{1/2}p_{3/2}f_{5/2})$ space and neutron particles in the $(d_{5/2}s_{1/2}d_{3/2}g_{7/2})$ space.

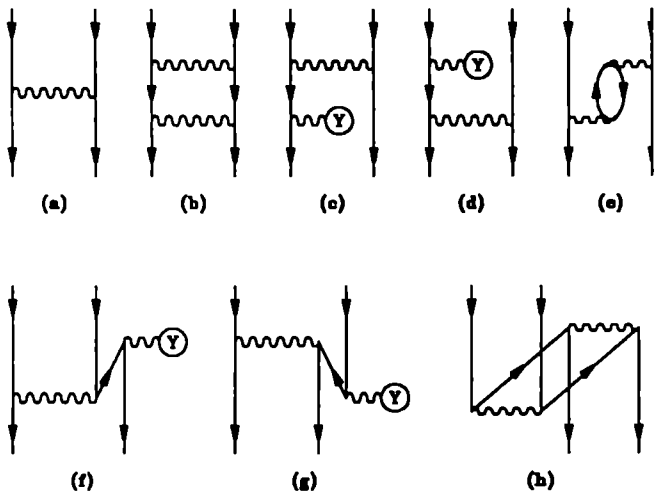

Figure 2: Diagrams considered in the determination of the two-hole effective interaction

An effective interaction which is suitable for the description of the $N, Z \leq 50$ nuclei has recently been derived by Sinatkas et al [21,22]. In this calculation the Kuo-Brown approach [23] was adopted, i.e the matrix elements of the two-hole effective interaction were determined by considering 2nd-order corrections to the G-matrix. Fig. 2 shows the diagrams involved in the calculation of the two-hole effective interaction [21]. These diagrams were calculated using the *Sussex* [24] interaction as G-matrix and considering up to $4\hbar\omega$ excitations for the intermediate states.

Normally in the Kuo Brown approach [23] single-particle energies are taken directly from experiment. This, however, is not possible in the case of the $Z, N \leq 50$ nuclei since the one-hole nuclei $^{99}_{49}$In and $^{99}_{50}$Sn are far from the stability line and their spectra have not yet been observed. For this reason the hole energies of the $p_{1/2}$, $p_{3/2}$ and $f_{5/2}$ orbitals relative to the $g_{9/2}$ were treated as parameters and their values were deduced by least-square fit to 68 excitation energies of $N = 50$ nuclei. The following values (in MeV) were obtained from this fitting procedure:

$$\epsilon_{9/2} = 0, \quad \epsilon_{1/2} = 1.85, \quad \epsilon_{3/2} = 3.45, \quad \epsilon_{5/2} = 6.32. \tag{3}$$

The procedure of Sinatkas et al [21,22] has been adopted in our study of the $N > 50$ nuclei [25]. Here the proton part of the hamiltonian is taken to be the one determined by Sinatkas et al [21] in their study of the $N = 50$ nuclei. The two-body matrix elements of the proton-hole neutron-particle and neutron-neutron effective interactions have been determined following the Kuo-Brown approach [23]. Finally, the single-particle energies of the $s_{1/2}$, $d_{3/2}$ and $g_{7/2}$ orbitals relative to the $d_{5/2}$ have been deduced by a fitting to the excitation energies of $N = 51$ nuclei. The following values (in MeV) were obtained from this last procedure:

$$\epsilon_{5/2} = 0, \quad \epsilon_{1/2} = 1.66, \quad \epsilon_{3/2} = 2.19, \quad \epsilon_{7/2} = 0.01\,. \tag{4}$$

The differences in the single-particle energies listed in Eqs (2) and (4) should mainly be attributed to the fact that they refer to different core states, i.e ^{88}Sr and ^{100}Sn. It is interesting to observe that the additional 12 protons have little effect on the energies of the $s_{1/2}$ and $d_{3/2}$ orbitals but lower the energy of the $g_{7/2}$ state by about 3 MeV and make it almost degenerate to the $d_{5/2}$.

The space employed in Model-2 calculations contains many orbitals so that, in principle, a very large number of nuclei can be described in it. However, due to this large space, the energy matrices have very large dimensions. The problem is already serious when only the proton shell is open ($N = 50$ nuclei), where in the middle of the shell one encounters dimensions of about 8500 for each J state. The problem becomes, however, really prohibiting when both proton and neutron shells are open. In this case one has to introduce suitable truncation schemes.

A suitable scheme for describing nuclei with n_π valence protons and n_ν valence neutrons is the *weak-coupling* approximation. To apply this scheme we separate the effective hamiltonian into three parts:

$$H = H_\pi + H_\nu + V_{\pi\nu}. \tag{5}$$

The proton and neutron parts of the hamiltonian are then diagonalized separately

$$\begin{aligned} H_\pi|n_\pi J_\pi \mu_\pi\rangle &= E_{n_\pi J_\pi \mu_\pi}|n_\pi J_\pi \mu_\pi\rangle \\ H_\nu|n_\nu J_\nu \mu_\nu\rangle &= E_{n_\nu J_\nu \mu_\nu}|n_\nu J_\nu \mu_\nu\rangle\ , \end{aligned} \tag{6}$$

where $|nJ\mu\rangle$ denotes the μth eigenvector of those having spin J. We consider only those vectors $|n_\pi J_\pi \mu_\pi\rangle$ and $|n_\nu J_\nu \mu_\nu\rangle$ which correspond to the lowest eigenvalues. Then $V_{\pi\nu}$ is diagonalized in the basis

$$|n_\pi J_\pi \mu_\pi, n_\nu J_\nu \mu_\nu; J\rangle$$

One has to apply this truncation scheme carefully since $V_{\pi\nu}$ is strong, specially when protons and neutrons occupy the same orbitals. In our Model-2 calculations, to be described in sect. 4, the weak coupling approximation was only employed in the determination of the ^{94}Ag and ^{94}Pd wavefunctions. In all other cases the number of shell-model configurations was not too large so that exact diagonalization could be performed.

Before concluding this section let us make the following remarks about the applicability of Model-2.

- Model 2 type of calculations have been performed [21,22,25] for a large number of nuclei in the ^{100}Sn region. Specifically, this model has been applied to describe the spectroscopic properties of the following groups of nuclei:

$$\begin{aligned} &34 \leq Z \leq 46 \qquad && N = 50 \\ &38 \leq Z \leq 46 \qquad && N = 48, 49 \\ &39 \leq Z \leq 46 \qquad && N = 51, 52 \end{aligned}$$

  and to study the $\beta\beta$ decay of the Kr, Se and Ge nuclei [26].

- The calculations describe satisfactorily the energy spectra and decay properties of all nuclei with

$$38 < Z \leq 46 \qquad 48 \leq N \leq 52$$

However, the agreement with experiment deteriorates for nuclei with $Z \leq 38$. Possibly this disagreement is caused by *intruder states* which are created by breaking the $N = 50$ inert core. Calculations investigating this subject are now in progress.

3. Gamow-Teller decay of the $N = 50$ nuclei

The β-decay of the $N = 50$ nuclei has been the subject of several experimental [5] and theoretical investigations [4,6,7,8]. In this section we review briefly the results of these investigations.

In the model spaces considered in both Model-1 and Model-2 calculations the decay of the $N = 50$ nuclei can only proceed via the Gamow-Teller transition:

$$\pi g_{9/2} \longrightarrow \nu g_{7/2} \ , \tag{7}$$

However, there are other configurations, like those which describe the breaking of the $N = 50$ core or the presence of a proton in the $g_{7/2}$ orbital, which also contribute to the Gamow-Teller decay of the $N = 50$ nuclei. These configurations are outside the model space considered in both Model-1 and Model-2 calculations. However, the effects of such configurations can be taken into account, at least in lowest-order of perturbation, by introducing effective Gamow-Teller operators. The manner in which these effective operators may be determined in Model-1 and Model-2 calculations is demonstrated in fig. 3.

The diagrams shown in fig. 3 contain both one-body and two-body corrections. There are two interesting features to be noticed in this figure. The first arises from the selectivity of the Gamow-Teller operator. Due to this selectivity all one-body terms can connect only a proton in the $g_{9/2}$ orbital to a neutron in the $g_{7/2}$. On the other hand, the two body corrections are less restrictive and can involve all orbitals in the model space. The other interesting feature in fig. 3 arises from the fact that different core states are considered in Model-1 and Model-2 calculations. Due to this difference, there is no one-to-one correspondence between the diagrams of the two calculations and, as a consequence, all diagrams should be considered for a meaningful comparison of the two models. Another related reason to consider all diagrams is that in this way there is complete cancellation of the Pauli violating terms that each diagram introduces [4].

In a quantitative comparison between measured Gamow-Teller strength and model predictions the most important quantity is

$$B = \frac{1}{2J_i + 1} \langle J_f || GT || J_i \rangle^2 \ . \tag{8}$$

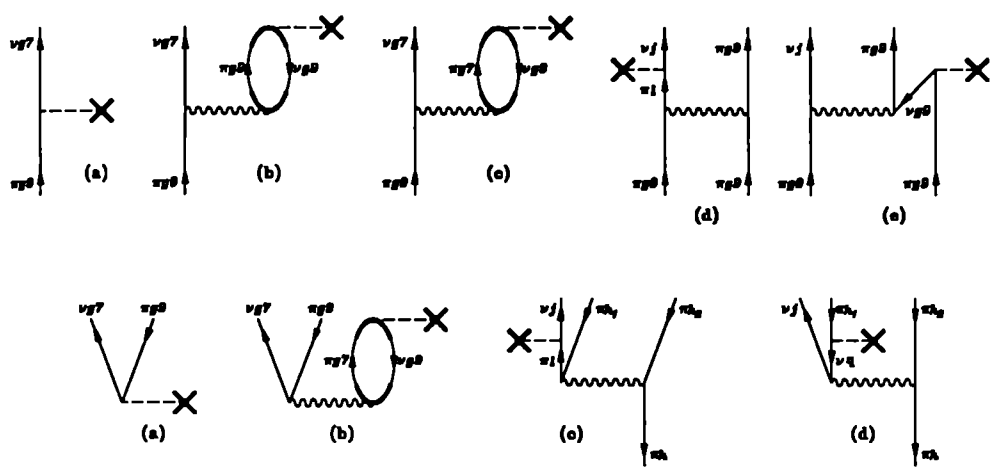

Figure 3: Diagrams considered in the determination of the effective Gamow-Teller operator. The diagrams in the upper row correspond to Model-1 while those of the lower row to Model-2 calculations. ν and π denote neutron and proton while $g7$ and $g9$ stand for $g_{7/2}$ and $g_{9/2}$, respectively.

This is related to the *comparative half-life*, or ft value, of the transition

$$ft = \frac{6160}{(g_a/g_v)^2 B} = \frac{3862}{B}(s), \tag{9}$$

where t is the half-life of the transition, $f = f(Z, E)$ is the phase space factor [27] and (g_a/g_v) is the ratio of the axial to vector coupling constants which, for free-nucleon decay, has the value of 1.263 [28].

Suppose now that the initial state decays to N final states. Then the *summed strength* is defined as

$$B_\Sigma = \sum_{i=1}^{N} B_i = \sum_{i=1}^{N} 3862/ft_i \,, \tag{10}$$

where B_i is the strength corresponding to final state i. From an experimental point of view, N in the above relation denotes all states observed in experiment. On the other hand, one can consider two theoretical B_Σ values. The first is determined by summing the strengths to final states predicted to be below the Q_{EC} limit. This is the summed strength which should be compared with the one observed in experiments. However, in many cases the observed strength is compared with the total theoretical strength. The latter arises if we take N in Eq. (10) to represent all states accounted by the calculation.

The summed strength B_Σ is usually compared to the *extreme single-particle value* B_{ref} [4]. In the case of the $N = 50$ nuclei this is calculated from

$$B_{ref} = \frac{\langle (\pi g_{9/2})^n v_f, \nu g_{7/2}; J_f || GT_{bare} || (\pi g_{9/2})^n v_i; J_i \rangle^2}{2J_i + 1} \,, \tag{11}$$

where the seniority number v is 0 or 1 depending on whether the particle number n is even or odd, respectively. The *hindrance factor* is then defined as

$$h = \frac{B_{ref}}{B_{\Sigma}} , \tag{12}$$

and a large value of h denotes a strong *quenching* (reduction) of the Gamow-Teller strength from the value predicted by the mechanism of Eq.(7).

The effects produced by the renormalization of the Gamow-Teller operator are best studied by determining the total Gamow-Teller strength in the same model space as that considered for the evaluation of B_{ref}. Table 3 lists hindrance factors obtained from three different calculations in the $(\pi g_{9/2}, \nu g_{7/2})$ space. To make the comparison complete, we also include in table 3 the experimental estimates for the hindrance factors. However, it should be remembered that the experimental values correspond to the observed decay and do not, necessarily, represent the total strength.

Table 3: Hindrance factors for the total Gamow-Teller Strength in the ($\pi g9/2$, $\nu g7/2$) space

Parent	B_{ref}	Ref. [7]	Ref. [6]	Ref. [4]	Experiment	Ref.
^{98}Cd	14.22	1.50	2.08	1.6-2.2	$4.1^{+1.0}_{-0.8}$	29
^{96}Pd	10.67	1.79	2.61	2.0-2.9	$4.6^{+1.7}_{-1.2}$	30
^{94}Ru	7.11	2.17	3.22	2.6-4.0	$7.2^{+0.6}_{-0.7}$	31

As table 3 shows, there is a wide range of values in the theoretical hindrance factors. Since all calculations are performed in the same space and consider the same type of corrections, these differences are due to the use of different hamiltonians in the calculation of the effective Gamow-Teller operator.

The summed strength obtained in the Model-2 calculation of Skouras and Manakos [7] is compared in Table 4 with the experimental estimates. N in this table denotes number of final states.

Table 4: Hindrance factors for the Summed Gamow-Teller Strength in the even N = 50 nuclei

Parent	Experiment			Total Strength		Strength below Q_{EC}	
	N	h	Ref.	N	h	N	h
^{98}Cd	4	$4.1^{+1.0}_{-0.8}$	29	27	1.46	12	1.54
^{96}Pd	4	$4.6^{+1.7}_{-1.2}$	30	176	1.65	11	2.05
^{94}Ru	2	$7.2^{+0.6}_{-0.7}$	31	404	1.93	3	6.35

There are two interesting features to be observed in table 4. The first is that the total strength obtained in the Model-2 space is larger than the one contained in $(\pi g_{9/2} \nu g_{7/2})$ space (see column 3 of Table 3). An explanation of this behaviour

may be found in in Ref. [7]. The other interesting feature in Table 4 is that, with the exception in the decay of ^{94}Ru, the calculation predicts that most of the Gamow-Teller strength goes to states below the Q_{EC} limit. However, as Table 4 shows, the calculated Gamow-Teller strength is substantially larger than the one observed in experiments.

For many years this reduction (*quenching*) of the Gamow-Teller strength has been one the open problems in nuclear physics [3,4]. It is attributed to one or more of the following reasons, some of which have been discussed above:

1. Strength goes to states above the Q_{EC}.
2. Strength going to states below Q_{EC} but which is not detected in the experiments [5,8].
3. Configuration mixing which results in an effective GT operator.
4. Non-nucleonic contributions [32].

4. Recent Results

In this section we describe the results of a calculation on proton-rich nuclei which have only recently been observed in experiments. In this calculation we have determined energy spectra and β-decay properties for the nuclei involved in the following decays:

$$
\begin{array}{lll}
^{100}_{50}Sn \longrightarrow {}^{100}_{49}In \longrightarrow {}^{100}_{48}Cd \\
^{98}_{48}Cd \longrightarrow {}^{98}_{47}Ag \\
^{97}_{48}Cd \longrightarrow {}^{97}_{47}Ag \longrightarrow {}^{97}_{46}Pd \\
^{96}_{47}Ag \longrightarrow {}^{96}_{46}Pd \longrightarrow {}^{96}_{45}Rh \\
^{95}_{47}Ag \longrightarrow {}^{95}_{46}Pd \longrightarrow {}^{95}_{45}Rh \\
^{94}_{47}Ag \longrightarrow {}^{94}_{46}Pd \\
^{94}_{45}Rh \longrightarrow {}^{94}_{44}Ru
\end{array}
$$

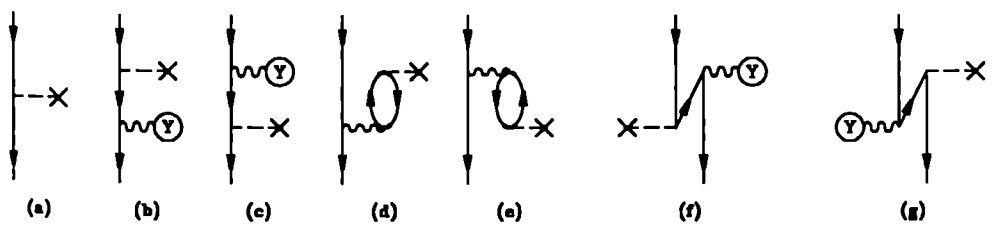

Figure 4: Diagrams involved in the determination of an effective Gamow-Teller operator describing the decay of $N < 50$ nuclei.

In our calculation of the β-decay of proton-rich nuclei we consider effective Gamow-Teller operators. In the previous section we discussed the construction of such operators for the decay of $N \geq 50$ nuclei. However, different operators are involved

in the decay of nuclei with $N < 50$. In this case, using Model-2 description, the Gamow-Teller operator destroys a neutron-hole in the $(g_{9/2}p_{1/2}p_{3/2}f_{5/2})$ space and creates a proton-hole in the same space. Fig. 4 shows the diagrams involved in the determination of such an effective operator.

Table 5: Gamow-Teller lifetimes (s)

Nucleus	Model 1	Model 2	Experiment	Ref.
^{97}Ag	10.7	3.3	25.2	10
^{97}Cd	1.1	0.9	2.8	10
^{96}Ag	6.9	5.2	4.5	10
^{95}Ag		1.26	1.74	9
^{95}Pd	7.6	7.7	$1.7 \leq t_{1/2} \leq 4.3$	10
^{94}Rh	22		26	33
^{94}Ag		0.55	0.42 ± 0.05	9
^{100}Sn	0.7			
^{100}In	2.4		6.1 ± 0.9	12

In table 5 we list β-decay half-times obtained from our calculation in comparison with the measured values. As may be seen in this table, with the exception of the Model-2 result on the decay of ^{97}Ag, the calculated lifetimes are generally in satisfactory agreement with the experimental data. The decay of ^{97}Ag and some other interesting results of our calculation are discussed in more detail in the remainder of this section.

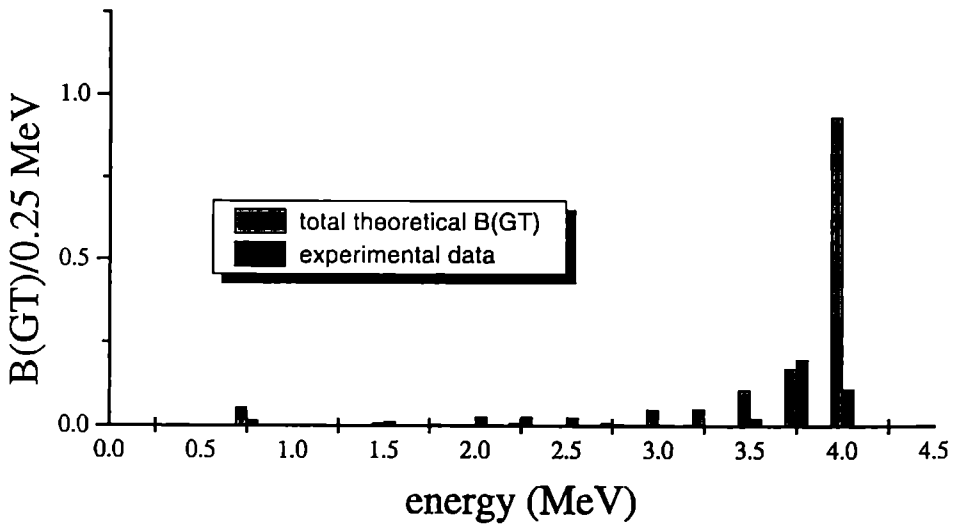

Figure 5: Experimental and theoretical distribution of Gamow-Teller strength in the decay of ^{97}Ag.

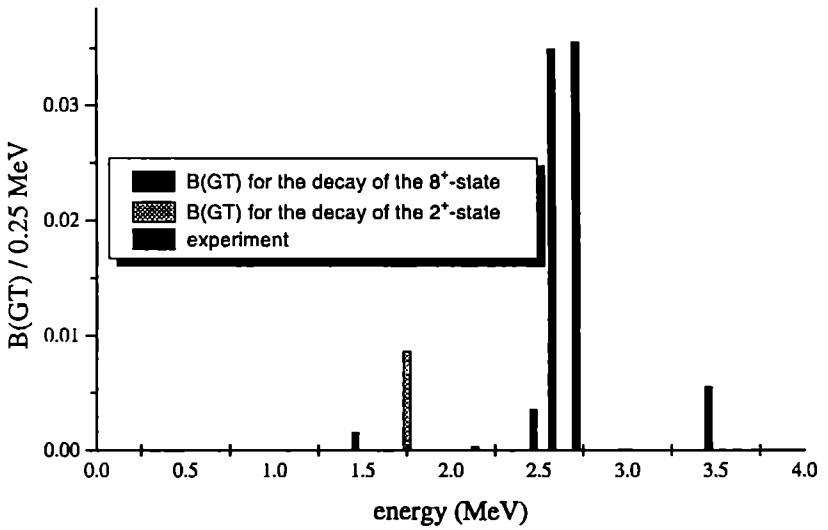

Figure 6: Experimental and theoretical distribution of Gamow-Teller strength in the decay of ^{96}Ag.

The experimental data [10] from the decay ^{97}Ag $\rightarrow$^{97}Pd are shown in fig. 5 in comparison with the predictions of Model-2 about the Gamow-Teller decay of the ground state $(9/2^+)$ of ^{97}Ag. As may be seen in this figure, the calculation reproduces quite accurately, up to about 4 MeV, the position of the states of the daughter nucleus which are fed in the decay. However, the Gamow-Teller strength predicted by the calculation is not observed in the experiment. In addition the calculation predicts that many other states of ^{97}Pd in the energy interval 4 to 7.5 MeV are strongly fed in the decay of the ground state of ^{97}Ag. These transitions have not been observed and this accounts for the disagreement between the experimental and theoretical values of the half-life of ^{97}Ag.

In contrast to the ^{97}Ag case, there is very good agreement between the observed [10] and calculated Gamow-Teller strength distributions in the decay of ^{96}Ag (figure 6). The Model-2 calculation on ^{96}Ag predicts that the ground state of this nucleus is an 8^+ state but that there is an excited 2^+ state at 19 keV. Model-1, on the other hand, predicts the 2^+ to be the ground state and the 8^+ to be the first excited state at 25 keV. In either case, the first excited state of ^{96}Ag is predicted to be an isomeric state. For this reason it was considered necessary to determine the Gamow-Teller decay of both the 8^+ and 2^+ states. As fig. 6 shows, the observed strength distribution is in very good agreement with the one predicted for the decay of the 8^+ state. It should be noted that the calculation predicts that most of the Gamow-Teller strength in the decay of this state goes to the states shown in fig. 6. This feature accounts for the very good agreement, shown in Table 5, between experimental and calculated lifetimes.

As table 5 shows, there is very good agreement between calculated and experimental [9] lifetimes for the decay of ^{95}Ag. The theoretical value corresponds to the

ground state decay of this nucleus. The interesting question with respect to ^{95}Ag is, however, whether there exist low-lying isomeric states whose Gamow-Teller decay can also be observed. This question was first raised by Ogawa [34], who made a Model-1 type of calculation on ^{95}Ag using the Gross and Frenkel effective hamiltonian [20]. The results of Ogawa's calculation are compared to the Model-2 predictions in fig. 7.

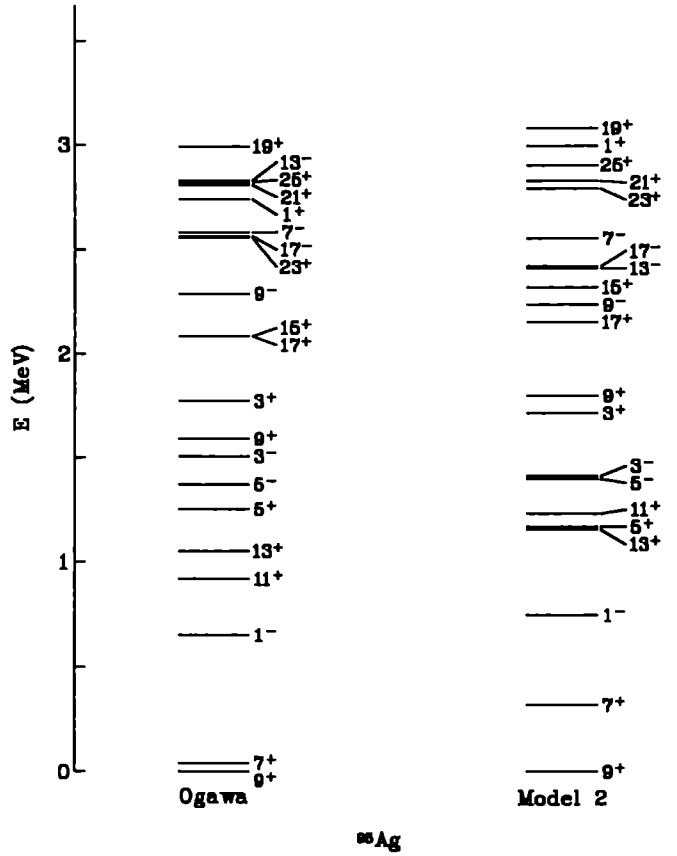

Figure 7: Low-lying states of ^{95}Ag. The number on the right of each level stands for $2J^{\pi}$.

As fig. 7 shows the energy spectra predicted by the two calculations are in very close agreement. Thus all levels predicted by Ogawa [34] to be below 3 MeV are accounted for by the Model-2 calculation and the excitation energies produced by the two calculations do not differ by more than 250 keV. On the other hand, there are significant differences in the predictions of the two calculations about the decay properties of the ^{95}Ag levels. The main reason for these differences arises from the fact that Ogawa's calculations are performed in a small model space, consisting of only the $p1/2$ and $g9/2$ orbitals, in which certain decay modes, as for example the E3 decay, cannot be described. Thus the prediction of Ogawa'a model that the first $1/2^-$ state of ^{95}Ag is deexcited by M4 decay to the $9/2^+$ and $7/2^+$ states below is not confirmed

by the results of our calculation, which predict that the E3 decay $1/2^- \longrightarrow 7/2^+$ has a rate about 2500 times faster than the two M4 decays. Another interesting case is the deexcitation of the $23/2^+$ state of ^{95}Ag. Our calculation predicts this state to be at 2.78 MeV, above a $17/2^+$ state at 2.15 MeV and a $17/2^-$ level at 2.40 MeV. The excitation energies obtained in Ogawa's calculation are 2.56, 2.07 and 2.57 MeV for the $23/2^+$, $17/2^+$ and $17/2^-$ states, respectively. Using our results on the excitation energies, we estimate the partial half-life corresponding to γ-decay of the $23/2^+$ state to be about 2 ms with a 97% branch populating the $17/2^-$ state. This estimate is by a factor of 200 smaller than the value obtained in Ogawa's calculation [34], in which, of course, only the M3 decay mode was considered. It should also be noted that our calculation predicts a value of 410 ms for the β^+-decay half-life of the $23/2^+$ level which is also smaller than the value of 1 s predicted by Ogawa.

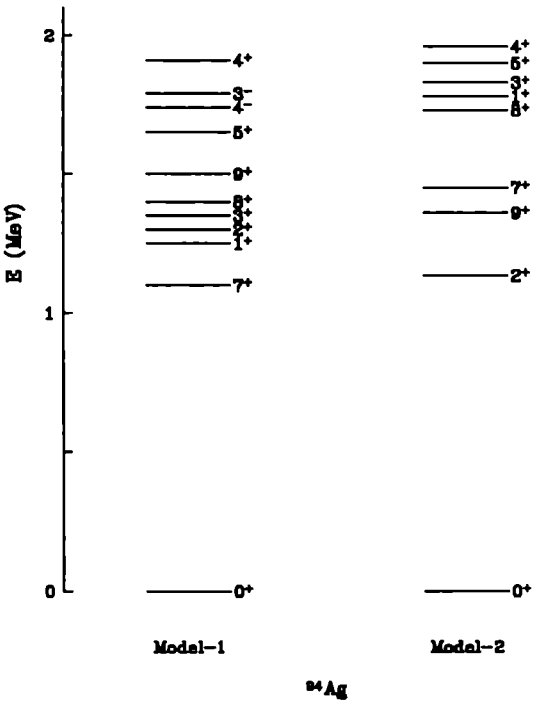

Figure 8: Spectrum of ^{94}Ag

Figure 8 shows the predictions of Model-1 and Model-2 calculations on the low-energy spectrum of ^{94}Ag. Both calculations predict the ground state of this nucleus to be a 0^+ state, which is separated by over 1 MeV from the other states. The Model-2 prediction for the half-life of this state is about 10 ms . The decay of this 0^+ is dominated by the Fermi transition to the ground state of ^{94}Pd.

It is interesting to observe in fig. 8 that the two calculations agree on the number and spins of excited positive parity states of ^{94}Ag up to about 2 MeV of excitation, although they disagree on their position in the spectrum of this nucleus. Anyway, as

may be concluded from fig. 8, either the 9^+ or the 7^+ represents an isomeric state which can only be de-excited by β^+-decay. The Model-2 prediction for the half-life of the 9^+ state is 550 ms and for that of the 7^+ 300 ms. Both these values are close to the measured half-life of ^{94}Ag of 420 ± 50 ms [9].

^{94}Ag and ^{95}Ag are not the only nuclei for which the calculation predicts the presence of isomeric states. A very interesting situation appears also in the case of ^{94}Rh where Model-1 calculations predict the presence of two isomeric states with spins 2^+ and 4^+ instead of a 3^+ suggested by experiment.

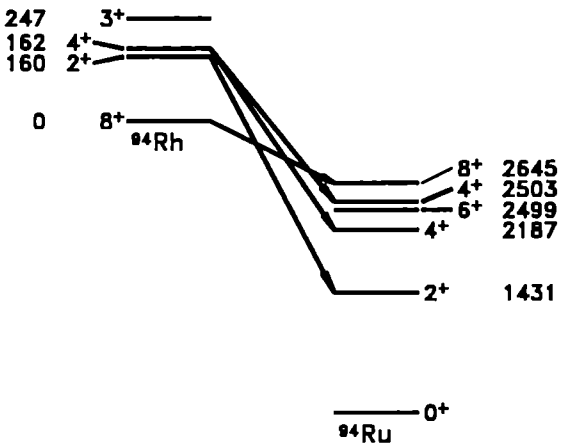

Figure 9: Isomeric states in ^{94}Rh

The experimental work of interest is by Oxom et al [33]. ^{94}Rh was produced by the $(p, 3n)$ reaction, and the time variation of gamma rays following beta decay was examined. One time constant ($26s$) was attributed to the decay of the 8^+ state of ^{94}Rh, since it is associated with gammas de-exciting the 8^+ state of ^{94}Ru. The other time constant ($71s$) was attributed to the decay of a 3^+ isomer in ^{94}Rh, since both 2^+ and 4^+ states in ^{94}Ru are fed.

^{94}Rh was studied in two shell-model calculations. The first of these is a standard Model-1 calculation (see sect. 2) using the SLG interaction [19]. The second calculation, to be referred for brevity as Model-1a, uses the model space of Model-1 but with the addition of the $g_{7/2}$ proton orbital. The inclusion of this orbital was deemed necessary in view of the large effects it produces in the renormalization of Gamow-Teller matrix elements. The effective interaction used in this Model-1a calculation was the SLG interaction, supplemented by a Yukawa force with Rosenfeld exchange mixture to give $g_{7/2}$ matrix elements.

Logft values calculated in the two models are given in Table 6. The Model-1a results have been obtained using the bare Gamow-Teller operator while in those of Model-1 the effect of the $g_{7/2}$ orbital was included in the renormalization of the operator.

The calculated values for the $8^+ \rightarrow 8^+$ decay, arising from the ground state of

Table 6: Calculated logft values for ^{94}Rh $\longrightarrow$ ^{94}Ru.

Decay			Model-1	Model-1a	Exp. [33]
8^+	$\rightarrow$	8_1^+	5.27	5.05	5.13
3^+	$\rightarrow$	2_1^+	5.29	5.04	6.67
	$\rightarrow$	4_1^+	5.41	5.10	6.27
2^+	$\rightarrow$	2_1^+	5.59	5.44	
4^+	$\rightarrow$	4_1^+	6.53	6.25	
	$\rightarrow$	4_2^+	6.02	5.80	

^{94}Rh, are in good agreement with experiment. However, there is no agreement for the transitions attributed to the $3^+ \rightarrow 2_1^+$ and $3^+ \rightarrow 4_1^+$ decays. Inspection of the calculated spectrum of ^{94}Rh, shown in fig. 9, suggests an explanation for this discrepancy. Model-1a gives the lowest 3^+ at 247 keV above the 8^+ ground state but it predicts two almost degenerate 2^+ and 4^+ states at 160 and 162 keV. If this is correct, the 3^+ will gamma decay to the 2^+ and 4^+ states (with a lifetime of less than $1ns$), while the 2^+ and 4^+ will have extremely long gamma lifetimes and will beta decay. The 2^+ is calculated to decay 95% to the 2_1^+ state of ^{94}Ru and to have a half-life of 31s (Model-1) or 22s (Model-1a). This additional component in the time variation of the 1431 keV gamma ray would have been difficult to detect in the experiment. The 4^+ is calculated to have strong decay branches to the 4_1^+ and 4_2^+ states of ^{94}Ru and to have a half-life of 109s (Model-1) or 62s (Model-1a). This should be compared to the empirical value of 71s.

In the calculations described so far ^{100}Sn was assumed to represent an inert core state. This is, of course, only an approximation. ^{100}Sn, in similarity to ^{16}O and ^{40}Ca, is expected to have excited states of complicated structure as well as ground state correlations.

The spectrum and decay of ^{100}Sn were determined in a recent shell-model calculation by Johnstone and Skouras [35]. In this calculation the $N = Z = 50$ closed shell was used as a core and ^{100}Sn was described in terms of particle-hole excitations with respect to this core. The particles were placed in the $g_{7/2}$, $d_{5/2}$, $s_{1/2}$, $d_{3/2}$ orbitals while the holes in the $g_{9/2}$ and $p_{1/2}$ orbitals. Johnstone and Skouras [35] determined the spectrum of ^{100}Sn in two different shell-model calculations, to be denoted hereafter as JS1 and JS2. The model space used in the JS1 calculation was restricted to contain only 1p1h excitations. The 1p1h spectrum was determined using a variety of phenomenological interactions, like the Perez interaction [36] or a Yukava force with a Rosenfeld exchange mixture. A different approach was used in the JS2 calculation. In this case there were no restrictions imposed on the particle-hole excitations. The JS2 effective interaction was determined in the Model-2 manner, i.e by considering second-order corrections to the *Sussex* matrix elements [24].

The energy spectra obtained in the JS1 and JS2 calculations are shown in fig. 10. Spectrum (a) in this figure represents the JS1 result, while spectrum (b) the result obtained in a JS2 calculation in which only 1p1h excitations were considered. As

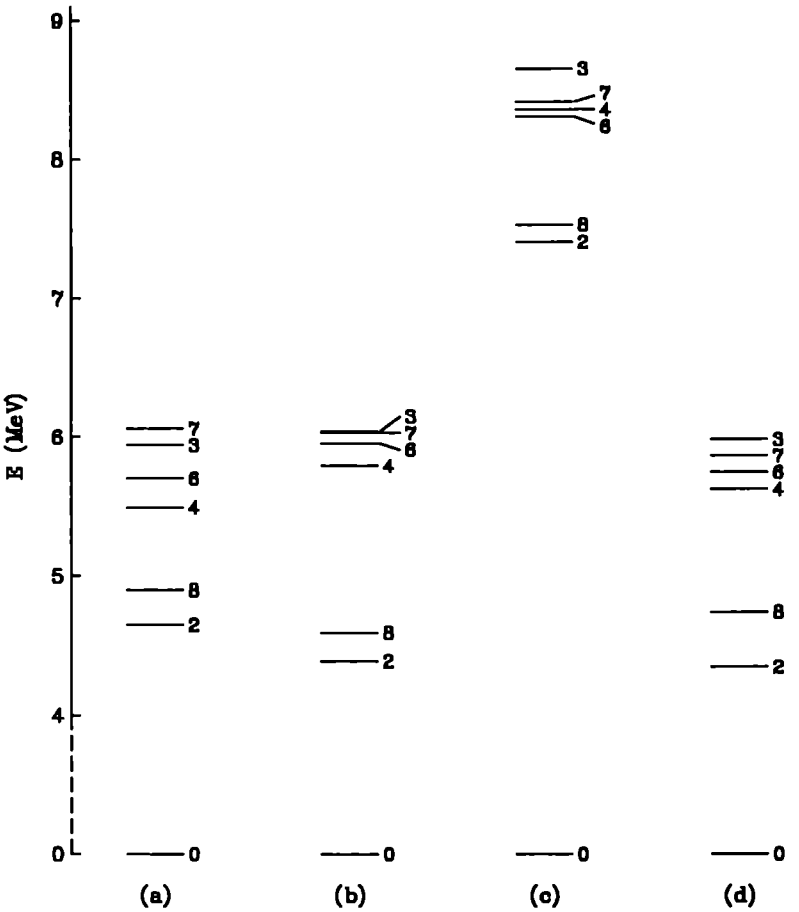

Figure 10: Calculated spectra of ^{100}Sn (see text).

fig. 10 shows, the predictions of the two models are in close agreement up to about 6 MeV. This agreement is, however, totally distroyed by the inclusion in the model space of 2p2h configurations (spectrum (c)). These configurations are found to interact strongly with the closed core state and weakly with the 1p1h configurations. The effect of this mixing is that the ground state of ^{100}Sn, which now contains about 21% 2p2h admixtures, is pushed down by over 3.5 MeV relative to the low-lying excited states, which remain of almost pure 1p1h character. The agreement between the JS1 and JS2 results is, however, restored by including in the model space the 3p3h configurations (spectrum (d)). These configurations cannot interact directly with the closed-core state and thus their effect on the ground state of ^{100}Sn is to lower it by less than 200 keV. On the other hand, there is a strong mixing between 1p1h and 3p3h configurations with the result that spectra (b) and (d) become almost identical. Due to exceedingly large dimensions, it is practically impossible to study the effects of 4p4h

configurations on the energy spectum of ^{100}Sn. However, from the results obtained so far one can safely predict that the effect of such 4p4h configurations on the low-lying states of ^{100}Sn would be rather small, since these states are predominantly of 1p1h character.

A large-scale calculation of the decay of ^{100}Sn would use configurations of up to 2p2h for ^{100}Sn, 3p3h for ^{100}In and 4p4h for ^{100}Cd. It is very difficult to attempt such a calculation due to the exceedingly large dimensions of the energy matrices. We have taken, therefore, a more conservative approach and consider only the 0p0h, 1p1h and 2p2h configurations for these nuclei, respectively. The results of this simple calculation are shown in Table 5.

5. Conclusions

In this paper we presented a shell-model study of proton-rich nuclei in the ^{100}Sn region. Two main conclusions may be drawn from this study.

- The theoretical results are in satisfactory agreement with experiment regarding the β-decay of the $N < 50$ nuclei, provided one uses renormalized Gamow-Teller matrix elements. This situation is contrary to what was observed in earlier investigations [4,6,7] of the decay of the $N = 50$ nuclei, and also here in the case of ^{97}Ag $\rightarrow$ ^{97}Pd, where the calculated Gamow-Teller strength is consistently larger than the one observed in experiments.

- The results on ^{100}Sn suggest that particle-hole excitations probably play an important role in the properties of other nuclei in the $A \sim 100$ region.

Acknowledgments

We are grateful to Karsten Schmidt for communicating to us results of his Thesis investigation and for providing us with figures 5 and 6. We are also grateful to E. Roeckl, O. Klepper, K. Rykaczewski and C. Kalfas for many useful discussions.

References

1. E. Roeckl, *Rep. Prog. Phys.* **55** (1992) 1661
2. E. Roeckl in *Europhysics News* **25** (1994) No 3.
3. O. Klepper and K. Rykaczewski in *Recent Advances in Nuclear Structure*, ed. D. Bukuresku, C. Cata-Danil and N.V. Zamfir (World Scientific, Singapore, 1990) p.45 and references therein
4. I. S. Towner, *Nucl. Phys.* **A444** (1985) 402
5. K. Rykaczewski in *Proc. of 6th Int. Conf. on Nuclei far from Stability and 9th Int. Conf. on Atomic Masses and Fundamental Constants*, ed. R. Neugart and A. Wöhr, *IOP Conf. Ser.* **132** (Inst. of Physics, Bristol, 1993) p. 517 and references therein.

6. I. P. Johnstone, *Phys. Rev.* **C44** (1991) 1476
7. L. D. Skouras and P. Manakos, *J. Phys.* **G44** (1993) 731
8. B. A. Brown and K. Rykaczewski, *Phys. Rev.* **C50** (1994) 2270
9. K. Schmidt et al, *Z. Phys.* **A350** (1994) 99
10. K. Schmidt, PhD thesis, University of Frankfurt, in preparation
11. M. Lewitowicz et al, *Phys. Lett.* **332B** (1994) 20
12. R. Schneider et al, *Z. Phys.* **A348** (1994) 241
13. I. Talmi and I. Unna, *Nucl. Phys.* **19** (1960) 225
14. J. B. Ball, J. B. McGrory and J. S. Larsen, *Phys. Lett.* **41B** (1972) 581
15. D. H. Gloeckner and F. J. D. Serduke, *Nucl. Phys.* **A220** (1974) 477
16. J. Blomquist and L. Rydstrom *Phys. Scr.* **31** (1985) 31
17. I. P. Johnstone and L. D. Skouras, *Phys. Rev.* **C51** (1995) 2817
18. X. Ji and B. H. Wildenthal, *Phys. Rev.* **C37** (1988) 1256
19. F. J. D. Serduke, R. D. Lawson and D. H. Gloeckner, *Nucl. Phys.* **A256** (1976) 45
20. R. Gross and A. Frenkel, *Nucl. Phys.* **A267** (1976) 85
21. J. Sinatkas, L. D. Skouras, D. Strottman and J. D. Vergados, *J. Phys.* **G18** (1992) 1377
22. J. Sinatkas, L. D. Skouras, D. Strottman and J. D. Vergados, *J. Phys.* **G18** (1992) 1400
23. T. T. S. Kuo and G. E. Brown, *Nucl. Phys.* **85** (1966) 40 ; *Nucl. Phys.* **A114** (1968) 241
24. J. P. Elliott, A. D. Jackson, H. A. Mavromatis, E. A. Sanderson and B. Singh *Nucl. Phys.* **A121** (1968) 241
25. P. Divari, L. D. Skouras and I. P. Johnstone, to be published.
26. J. Sinatkas, L. D. Skouras and J. D. Vergados, *Phys. Rev.* **C37** (1988) 1229
27. D. H. Wilkinson and B. E. F. Macefield, *Nucl. Phys.* **A232** (1974) 58
28. P. J. Brussaard and P. W. M. Glaudemans, *Shell-Model Applications in Nuclear Spectroscopy* (North-Holland Publishing Co., Amsterdam, 1977)
29. A. Plochoski et al and the ISOLDE collaboration, *Z. Phys.* **A342** (1992) 43
30. K. Rykaczewski et al, *Z. Phys.* **A232** (1985) 263
31. P. Graf and H. Münzel *Radiochim. Acta* **20** (1987) 140
32. E. Ericson and W. Weise *Pions and Nuclei* (Clarendon Press, Oxford, 1988)
33. K. Oxom, B. Singh, S. K. Mark, *Z. Phys.* **A294** (1980) 389
34. K. Ogawa, *Phys. Rev.* **C28** (1983) 958
35. I. P. Johnstone and L. D. Skouras, *J. Phys.* **G21** (1995) 63
36. S. Perez, *Nucl. Phys.* **A136** (1969) 599

DESCRIPTION OF NONROTATIONAL STATES IN DEFORMED NUCLEI

V.G. SOLOVIEV, A.V. SUSHKOV and N.YU. SHIRIKOVA

Bogoliubov Laboratory of Theoretical Physics,
Joint Institute for Nuclear Research
141980 Moscow region, Dubna, Russia
E-mail: soloviev@thsun1.jinr.dubna.su

ABSTRACT

Basic assumptions of the quasiparticle-phonon nuclear model (QPNM) and the PRA equations for the $K^\pi = 1^+$ states with isoscalar and isovector quadrupole and spin-spin interactions are presented. The QPNM equations for doubly even and odd mass deformed nuclei are given. The energies and wave functions of the $K^\pi = 1^+$ states and M1 transition rates were calculated with approximate exclusion of the spurious state. It is shown that the scissor state is strongly fragmented and the overlapping between the scissor state and any 1^+ state is less than 0.1. The orbital motion accounts for 60% of the total M1 strength at the excitation energy below 4 MeV. The E1 and E3 transition rates from the ground to the excited states with $K^\pi = 0^-$ and 1^- were calculated. The correlation between B(E1) and B(E3) values was observed. The total E1 strength for excitation of the $K^\pi = 0^-$ is three times as larger as for the $K^\pi = 1^-$ states. One-phonon states below 2.5 MeV are slightly fragmented. The fragmentation of one-phonon states with energy above 3 MeV strongly affects the E1 and M1 strength distribution in doubly even deformed nuclei.

1. Introduction

The Quasiparticle-Phonon Nuclear Model (QPNM) [1-7] is used for a microscopic description of excited states in spherical nuclei not far from closed shells and well-deformed nuclei. The QPNM calculations have been made for nuclei with small ground state correlations. The ground state correlations increase with the collectivity of the first one-phonon states. Particle-particle interactions reduce the ground state correlations. They are small in well-deformed nuclei. According to the calculation in [8], the maximum average values of quasiparticles in the ground states in ^{168}Er, ^{158}Gd and ^{156}Gd equal 0.017, 0.035 and 0.040, respectively. Therefore, the RPA phonons are used as a basis in the QPNM. The ground state correlations are to be taken into account in several spherical nuclei. For example, an effect of the ground state correlations on the energies, transition probabilities and transition densities of the quadrupole and octupole vibrational states in $^{64-70}$Zn has been studied in [9].

In the framework of the QPNM we have calculated low-lying excited states, the fragmentation of deep-hole and high-lying one-quasiparticle states, the s-, p- and d- wave neutron strength functions and the widths of different types of giant

resonances in many spherical nuclei and in well-deformed nuclei.

The low-lying states in deformed nuclei have been studied experimentally and theoretically. Experimental data on the excited states above the lowest two-quasiparticle and first quadrupole and octupole vibrational states are still fragmentary. These states have a more complex structure than the one-phonon states. Their experimental investigation is very important. The study of the γ-ray transition rates provides new information on the nuclear structure in addition to that from inelastic scattering, one- and two-nucleon transfer reactions and β-decays.

The energies and wave functions of nonrotational states in ^{166,168}Er, ^{156,158,160}Gd, and ^{160,162,164}Dy have been calculated [9,10–14] within the QPNM. A fairly good description of the energies, structure and γ-ray transition rates has been obtained and the predictions have been made. All nonrotational states of excitation energy less than 2.3 or 2.5 MeV have been calculated. The $K^\pi = 1^+$, 0^- and 1^- states have been calculated up to an energy of 4 MeV

In this paper we expound the basic assumptions of the QPNM and give the description of nonrotational states in well-deformed nuclei.

2. Quasiparticle-Phonon Nuclear Model

2.1. Basic assumptions

The initial QPNM Hamiltonian contains the average field of a neutron and a proton system in the form of the axial-symmetric Woods-Saxon potential, monopole pairing, isoscalar and isovector particle-hole (ph), as well as particle-particle (pp) multipole, spin-multipole and tensor interactions between quasiparticles. The effective interactions between quasiparticles are expressed as a series of multipoles and spin-multipoles. It is essential that the interaction between quasiparticles is presented in a separable form. In this paper, we used only the multipole and spin-spin interactions.

We now transform the initial QPNM Hamiltonian. For this purpose we perform a canonical Bogolubov transformation

$$a_{q\sigma} = u_q \alpha_{q\sigma} + \sigma v_q \alpha^+_{q-\sigma} \tag{1}$$

in order to replace the particle operators $a_{q\sigma}$ and $a^+_{q\sigma}$ by the quasiparticle operators $\alpha_{q\sigma}$ and $\alpha^+_{q\sigma}$. We introduce the phonon operators of two types. If we take into account only interactions of the electric type, the phonon creation operator has the following standard form:

$$Q^+_{\lambda\mu i_1\sigma} = \frac{1}{2}\sum_{qq'}\{\psi^{\lambda\mu i_1}_{qq'} A^+(qq';\mu\sigma) - \phi^{\lambda\mu i_1}_{qq'} A(qq';\mu-\sigma)\}. \tag{2}$$

If we take into account electric and magnetic interactions, we write the phonon operator [6,15] in the form

$$Q^{+}_{\lambda\mu i_1\sigma} = \frac{1}{2\sqrt{2}}\sum_{qq'}\{\psi^{\lambda\mu i_1}_{qq'}(1+i\sigma)A^{+}(qq';\mu\sigma) - \phi^{\lambda\mu i_1}_{qq'}(1-i\sigma)A(qq';\mu-\sigma)\}. \quad (3)$$

The coefficients of the electric part are real and of the magnetic part imaginary. Here $i_1 = 1,2,3\ldots$ is the root number of the RPA secular equation. The quantum numbers of the single-particle states are denoted by $q\sigma$, where $\sigma = \pm 1$; q equals K^{π} and asymptotic quantum numbers $Nn_z\Lambda\uparrow$ at $K = \Lambda + 1/2$ and $Nn_z\Lambda\downarrow$ at $K = \Lambda - 1/2$. The operator $A(qq';\mu\sigma)$ is given in Appendix. The RPA one-phonon state is described by the wave function

$$Q^{+}_{\lambda\mu i\sigma}\Psi_0, \quad (4)$$

where Ψ_0 is the ground state wave function of a doubly even nucleus which is determined as a phonon vacuum. The normalization condition of the wave function (4) has the form

$$\frac{1+\delta_{\mu 0}}{2}\sum_{qq'}[(\psi^{\lambda\mu i_1}_{qq'})^2 - (\phi^{\lambda\mu i_1}_{qq'})^2] = 1. \quad (5)$$

After some transformation, the QPNM Hamiltonian becomes

$$H_{QPNM} = \sum_{q\sigma}\epsilon_q\alpha^{+}_{q\sigma}\alpha_{q\sigma} + H_v + H_{vq}, \quad (6)$$

where the first two terms describe quasiparticles and phonons, and H_{vq} describes the quasiparticle-phonon interaction. We shall use isoscalar and isovector ph and pp quadrupole and spin-spin interactions for describing one-phonon states with $K^{\pi} = 1^{+}$ and isoscalar and isovector ph and pp octupole and isovector ph dipole interactions for describing one-phonon states with $K^{\pi} = 0^{-}$ and 1^{-}. In this paper, we shall use only the following terms of the Hamiltonian:

$$H_v = H_v^{00} + H_v^{21\sigma} + H_v^{22} + H_v^{d-o} + \sum_{\substack{\lambda=3;\mu=2,3\\ \lambda=4,\mu=3,4\\ \lambda=5,\mu=4,5}} H_v^{\lambda\mu}, \quad (7),$$

$$H_v^{21\sigma} = H_v^{21} - \sum_{ii'\sigma} W^{011}_{ii'}Q^{+}_{21i\sigma}Q_{21i'\sigma}, \quad (8)$$

$$W^{011}_{ii'} = \frac{1}{4}\sum_{\tau}\sum_{\rho=\pm 1}(\kappa_0^{011} + \rho\kappa_1^{011})D_{\tau}^{011i}D_{\rho\tau}^{011i'} \quad (8')$$

$$H_v^{d-o} = \sum_{K=0,1}\sum_{ii'\sigma} W^{K}_{ii'}Q^{+}_{Ki\sigma}Q_{Ki'\sigma}, \quad (9)$$

$$W^{K}_{ii'} = \frac{(1+\delta_{K0})^2}{4}\sum_{\tau}\sum_{\rho=\pm 1}(\kappa_0^{3K} + \rho\kappa_1^{3K})D_{\tau}^{3Ki}D_{\rho\tau}^{3Ki'} +$$

$$+G^{3K}[D^{3Ki}_{g\tau}D^{3Ki'}_{g\tau}+D^{3Ki}_{w\tau}D^{3Ki'}_{w\tau}]+\sum_{\rho=\pm1}\rho\kappa_1^{1K}D^{1Ki}_{\tau}D^{1Ki'}_{\rho\tau}\},\tag{9'}$$

$$H_v^{\lambda\mu}=-\sum_{ii'}W^{\lambda\mu}_{ii'}Q^{+}_{\lambda\mu i\sigma}Q_{\lambda\mu i'\sigma},\tag{10}$$

$$W^{\lambda\mu}_{ii'}=\frac{1+\delta_{\mu0}}{4}\sum_{\tau}\{\sum_{\rho=\pm1}(\kappa_0^{\lambda\mu}+\rho\kappa_1^{\lambda\mu})D^{\lambda\mu i}_{\tau}D^{\lambda\mu i'}_{\rho\tau}+$$

$$+G^{\lambda\mu}[D^{\lambda\mu i}_{g\tau}D^{\lambda\mu i'}_{g\tau}+D^{\lambda\mu i}_{w\tau}D^{\lambda\mu i'}_{w\tau}]\},\tag{10'}$$

$$H_{vq}=H^{00}_{vq}+H^{21\sigma}_{vq}+H^{22}_{vq}+H^{d-o}_{vq}+\sum_{\substack{\lambda=3;\mu=2,3\\ \lambda=4,\mu=3,4\\ \lambda=4,\mu=4,5}}H^{\lambda\mu}_{vq},\tag{11}$$

$$H^{21\sigma}_{vq}=-\frac{1}{4}\sum_{i_0\sigma\tau}\sum_{qq'}V^{21i_0}_{\tau}(qq')[\frac{1-i\sigma}{\sqrt{2}}(Q^{+}_{21i_0\sigma}+Q_{21i_0-\sigma})B(qq';1-\sigma)+h.c.]$$

$$+f^{011}(qq')v^{(+)}_{qq'}\sum_{\rho=\pm1}(\kappa_0^{011}+\rho\kappa_1^{011})D^{011i_0}_{\rho\tau}$$

$$\times[\frac{\sigma-i}{\sqrt{2}}(Q^{+}_{21i_0\sigma}-Q_{21i_0-sigma})\mathcal{B}(qq';1-\sigma)+h.c]\}\tag{12}$$

$$H^{d-o}_{vq}=-\frac{1}{4}\sum_{\mu=0,1}\sum_{i\tau\sigma}\sum_{qq'}^{\tau}\{V^{3\mu i}(qq')$$

$$+f^{1\mu}(qq')\sum_{\rho=\pm1}\rho\kappa_1^{1\mu}v^{(-)}_{qq'}D^{1\mu i}_{\rho\tau}]$$

$$\times Q^{+}_{3\mu i\sigma}B(qq';\mu-\sigma)+h.c.\},\tag{13}$$

$$H^{\lambda\mu}_{vq}=-\frac{1}{4}\sum_{i\tau\sigma}\sum_{qq'}^{\tau}V^{\lambda\mu i}_{\tau}(qq')Q^{+}_{\lambda\mu i\sigma}B(qq';\mu-\sigma)+h.c.\}.\tag{14}$$

$$V^{\lambda\mu i}_{\tau}(qq')=f^{\lambda\mu}(qq')\{\sum_{\rho=\pm1}(\kappa_0^{\lambda\mu}+\rho\kappa_1^{\lambda\mu})v^{(-)}_{qq'}D^{\lambda\mu i}_{\rho\tau}-G^{\lambda\mu}u^{(+)}_{qq'}D^{\lambda\mu i}_{g\tau}\}\tag{15}$$

Here ϵ_q is the quasiparticle energy with the monopole and quadrupole pairing; H_v^{00} and H^{00}_{vq} are given in [6,7]. The functions $D^{\lambda\mu i}_{\tau}$, $D^{\lambda\mu i}_{g\tau}$, $D^{\lambda\mu i}_{w\tau}$, $D^{011i_0}_{\tau}$,the operator $B(qq';\mu\sigma)$, $\mathcal{B}(qq';\mu\sigma)$ and the matrix element of $f^{\lambda\mu}(qq')$ and $f^{011}(qq')$ are given in Appendix. Further, $g^{\lambda\mu i}_{qq'}=\psi^{\lambda\mu i}_{qq'}+\phi^{\lambda\mu i}_{qq'}$, $w^{\lambda\mu i}_{qq'}=\psi^{\lambda\mu i}_{qq'}-\phi^{\lambda\mu i}_{qq'}$, $u^{(\pm)}_{qq'}=u_qv_{q'}\pm u_{q'}v_q$, $v^{(\pm)}_{qq'}=u_qu_{q'}\pm v_qv_{q'}$. Summation over single-particle states of the neutron and proton system is denoted by $\sum^{\tau}_{qq'}$ at $\tau=n$ or $\tau=p$, respectively; $\kappa_0^{\lambda\mu}$ and $\kappa_1^{\lambda\mu}$ are the isoscalar and isovector constants of ph and $G^{\lambda\mu}=G_0^{\lambda\mu}+G_1^{\lambda\mu}$ represents the pp multipole interactions; κ_0^{011} and κ_1^{011} are the isoscalar and isovector constants of the ph spin-spin interaction.

The one-phonon states form the basis of the QPNM. We, therefore, pay much attention to the solution of the RPA equations. At the next stage the interaction of quasiparticles with phonons is taken into account. The wave function of the excited

state is represented as a series with respect to the number of phonon operators; in odd-mass nuclei the wave function consists of the sum of one-quasiparticle, one-quasiparticle $\otimes$ phonon, etc., terms. The approximation consists of the truncation of this series.

2.2. RPA equation

The interactions between quasiparticles in the ground and excited states are taken into account in the RPA. The ground state wave function Ψ_0 of a doubly even nucleus is defined as the vacuum relative to various phonons. In addition to the quasiparticle term, it contains four – eight- and more-quasiparticle terms. A two-quasiparticle state is treated as a specific case of an one-phonon state when the root of the RPA secular equation is very close to the relevant pole. The RPA is valid when the mean number $< \alpha^+_{q\sigma}\alpha_{q\sigma} >$ of the quasiparticles in the ground state is small.

The one-phonon states with $K^\pi = 0^+$ (denoted by $(\lambda\mu)_i = (20)_i$) are calculated in the RPA with monopole and quadrupole pairing and monopole and ph and pp isoscalar and isovector quadrupole interactions. The relevant RPA equation is given in [6,7].

The one-phonon states with $K^\pi = 1^+$ (denoted by $(21)_i$) are calculated with ph and pp isoscalar and isovector quadrupole and spin-spin interactions. The RPA equations for the $K^\pi = 1^+$ one-phonon states have the following form:

$$\epsilon_{qq'}g^{21i}_{qq'} - \omega_{21i}w^{21i}_{qq'} - f^{21}(qq')[u^{(+)}_{qq'}\sum_{\rho=\pm1}(\kappa^{21}_0 + \rho\kappa^{21}_1)D^{21i}_{\rho\tau} + v^{(-)}_{qq'}G^{21}D^{21i}_{w\tau}] = 0, \quad (16)$$

$$\epsilon_{qq'}w^{21i}_{qq'} - \omega_{21i}g^{21i}_{qq'} - f^{011}(qq')\chi(qq')u^{(-)}_{qq'}\sum_{\rho=\pm1}(\kappa^{011}_0 + \rho\kappa^{011}_1)D^{011i}_{\rho\tau} -$$

$$-G^{21}f^{21}(qq')v^{(+)}_{qq'}D^{21i}_{w\tau} = 0, \quad (16')$$

where $\epsilon_{qq'} = \epsilon_q + \epsilon_{q'}$. From eqs. (16) and (16') we got the function $g^{21i}_{qq'}$ and $w^{21i}_{qq'}$ and substitute them into the formulae for D^{21i}_τ, $D^{21i}_{g\tau}$, $D^{21i}_{w\tau}$ and $D^{011_i}\tau$. The secular equation for the energies ω_{21i} has the form of the determinant of rank 8.

In the previous calculations of the $K^\pi = 1^+$ states, the spurious state was not excluded. In the new calculations [14,16], the spurious state is excluded approximately by choosing the constant $\kappa^{21}_0 > (\kappa^{21}_0)_{\rm cr}$. The first root of the RPA secular equation equals zero at $(\kappa^{21}_0)_{\rm cr}$. The overlap between the one-phonon and the spurious states is given by

$$N^i_{\rm sp} = \frac{1}{< j_-j_+ >} < j_-Q^+_{21i} >< Q_{21i}j_+ >= \frac{1}{< j_-j_+ >} I^{21i}_- I^{21i}_+, \quad (17)$$

$$I^{21i}\pm = \sum_\tau I^{21i}_\pm(\tau),$$

$$I_{\pm}^{21i}(\tau) = \sum_{\substack{q_1>q_2 \\ K_1 \geq K_2}}{}^{\tau} < q_1|j_{\pm}|q_2 > u_{q_1q_2}^{(-)}\psi_{q_1q_2}^{21i}. \qquad (17')$$

$$\sum_i N_{\rm sp}^i = 1. \qquad (18)$$

The sum (18) over the first twenty states up to 4 MeV is equal to 0.010– 0.025 in ^{156,158,160}Gd and ^{160,162,164}Dy. For any nonrotational state with $K^\pi = 1^+$ the $N_{\rm sp}^i$ value is smaller than 0.005. Therefore, the approximate exclusion of the spurious state is reasonably good.

The modified one-phonon states with $K^\pi = 0^-$ and 1^- are calculated in the RPA with the ph and pp isoscalar and isovector octupole and ph isovector dipole interactions. The relevant RPA equations are given in [7,11]. Other phonons ($\lambda\mu$=22, 32, 33, 43, 44, 54, 55 etc.) are calculated with the ph and pp isoscalar and isovector interactions. The RPA equations have the form (15) and (16) with $\kappa_0^{011} = \kappa_1^{011} = 0$.

2.3. The QPNM equations for doubly even nuclei

For describing nonrotational states in the QPNM we used a wave function consisting of a sum of one- and two-phonon terms

$$\Psi_n(K_0^{\pi_0}\sigma_0) = \{\sum_{i_0} R_{i_0}^n Q_{g_0}^+ + \sum_{\substack{g_1g_2 \\ \sigma_1\sigma_2}} \frac{(1+\delta_{g_1g_2})^{1/2}}{2[1+\delta_{\mu_0 0}(1-\delta_{\mu_1 0})]^{1/2}} \times$$

$$\times \delta_{\sigma_1\mu_1+\sigma_2\mu_2,\sigma_0\mu_0} P_{g_1g_2}^n Q_{g_1\sigma_1}^+ Q_{g_2\sigma_2}^+\}\Psi_0 \qquad (19)$$

Here $g_0 = \lambda_0\mu_0 i_0$, $\mu_0 = K_0$ or $g_0 = K_0 i_0$, $n = 1, 2, 3\ldots$ is the number of the K_0^π state. To take the Pauli principle into account regarding the two-phonon terms of the wave function (19), we introduce the function

$$\mathcal{K}^{K_0}(g_2, g_1'|g_1, g_2) = (1+\delta_{g_1,g_2})^{-1} \sum_{\sigma_1\sigma_2} \delta_{\sigma_1\mu_1+\sigma_2\mu_2,\sigma_0 K_0} \times$$

$$\times (\Psi_0^* Q_{g_2\sigma_2}[[Q_{g_1'\sigma_1}, Q_{g_1\sigma_1}^+], Q_{g_2\sigma_2}^+]\Psi_0) \qquad (20)$$

$$\mathcal{K}^{K_0}(g_1g_2) \equiv \mathcal{K}^{K_0}(g_2, g_1|g_1, g_2).$$

Its explicit form is given in [6,7]. If we use only the diagonal terms of the function $\mathcal{K}^{K_0}(g_2, g_1|g_1, g_2)$, the normalization condition of the wave function (17) has the form

$$\sum_{i_0}(R_{i_0}^n)^2 + \sum_{g_1 \geq g_2} (P_{g_1g_2}^n)^2[1 + \mathcal{K}^{K_0}(g_1g_2)] = 1. \qquad (21)$$

Now we find the average value of H_{QPNM} over the state (19) and using the variational principle we get the following equations:

$(\omega_{g_0} - E_n)R_{i_0}^n -$

$$-\sum_{g_1\geq g_2}(1+\delta_{g_1g_2})^{-\frac{1}{2}}[1+\delta_{K_0 0}(1-\delta_{\mu_1 0})]^{-\frac{1}{2}}P^n_{g_1g_2}U^{g_0}_{g_1g_2}[1+\mathcal{K}^{K_0}(g_1g_2)]=0, \qquad (22)$$

$$[\omega_{g_1}+\omega_{g_2}+\Delta\omega(g_1,g_2)-E_n]\,P^n_{g_1g_2}-$$

$$-\sum_{i_0}(1+\delta_{g_1g_2})^{-\frac{1}{2}}[1+\delta_{K_0 0}(1-\delta_{\mu_1 0})]^{-\frac{1}{2}}R^n_{i_0}U^{g_0}_{g_1g_2}=0, \qquad (23)$$

where

$$U^{g_0}_{g_1g_2}[1+\mathcal{K}^{K_0}(g_1g_2)]=-\frac{1}{2}\sum_{\sigma_1\sigma_2}\delta_{\sigma_1\mu_1+\sigma_2\mu_2,\sigma_0K_0}\times$$

$$\times\{(\Psi^*_0Q_{g_0\sigma_0}H_{\nu q}Q^+_{g_1\sigma_1}Q^+_{g_2\sigma_2}\Psi_0)+h.c.\}. \qquad (24)$$

The function $\Delta\omega(g_1g_2)$ is given in Appendix. Inclusion of the Pauli principle in the two-phonon terms (19) generates in Eqs. (22) and (23) the factor $1+\mathcal{K}^{K_0}(g_1g_2)$, and the shift $\Delta\omega(g_1g_2)$ of the two-phonon pole to higher energies.

In [7], the three-phonon terms have been added to the wave function (19) and their influence on the contribution of the two-phonon configuration to the low-lying states has been investigated. In the approximation used in [7], the three-phonon terms led to a shift of the two-phonon poles which we denote by $\Delta(g_1g_2)$. This shift differs from zero if the Pauli principle in the three-phonon terms of the wave functions is not taken into account. A secular equation for calculating the energies E_n of the excited states has the following form:

$$\det||(\omega_{g_0}-E_n)\delta_{i_0i'_0}-\sum_{g_1\geq g_2}\frac{1+\mathcal{K}^{K_0}(g_1g_2)}{1+\delta_{g_1g_2}}[1+\delta_{K_0 0}(1-\delta_{\mu_1 0})]^{-1}\times$$

$$\times\frac{U^{g_0}_{g_1g_2}U^{g'_0}_{g_1g_2}}{\omega_{g_1}+\omega_{g_2}+\Delta\omega(g_1,g_2)-\Delta(g_1,g_2)-E_n}||=0, \qquad (25)$$

The rank of the determinant (25) equals the number of one-phonon terms in the wave function (19).

The form of Eqs. (22) and (23) and the rank of the determinant (25) are independent of the ph and pp multipole and spin-multipole interactions which are taken into account, and are independent of the rank of a separable interaction. Equations (22), (23) and (25) coincide in form with the equations in the previous papers in which only the ph multipole interactions were taken into account. All the complications caused by the form of interactions were concentrated in the RPA equations. This means that calculations using the QPNM can be made with any complex interactions presented in a separable form.

We calculate in this paper the energies and wave functions of the excited states and the reduced probabilities of Eλ and Mλ transitions from the ground state to the excited ones and E1 and M1 transitions between excited states. The reduced

probability of Eλ transition from the ground state $0^+_{g.s.}$ to the excited state with the fixed values of $I^\pi K_n$ is written as

$$B(E\lambda\mu; 0^+0_{g.s.} \to I^\pi K_n) = (2-\delta_{\mu 0}) < 00\lambda\mu|IK >^2 e^2 \times$$

$$\times|\frac{1+\delta_{\mu 0}}{2}\sum_{\tau}\sum_{q_1q_2}{}^{\tau} e^1_{eff}(\tau) p^{\lambda\mu}(q_1q_2)\{\sum_{i_0} R^n_{i_0} u^{(+)}_{q_1q_2} g^{\lambda\mu i}_{q_1q_2} +$$

$$+\delta_{\lambda,1}\sum_{g_3g_4\sigma_3\sigma_4}(1+\delta_{g_3g_4})^{1/2}\delta_{\sigma_3\mu_3+\sigma_4\mu_4,\sigma_0 K}\tilde{P}^n_{g_3g_4} v^{(-)}_{q_1q_2}\tilde{T}^{g_3,g_4}_{q_1q_2K}\}|^2, \qquad (26)$$

where $p^{\lambda\mu}(q_1q_2)$ is the single-particle matrix element of an operator of the electric transition. The second term in Eq. (26) describes the Eλ transition from the ground state to the two-phonon terms of the wave function (19). The E1 effective charge is given by

$$e^{(1)}_{eff}(\tau_z) = -\frac{e}{2}(\tau_z - \frac{N-Z}{A}). \qquad (27)$$

We used the truncated space of the single-particle levels and, therefore, we calculated B(Eλ) values for $\lambda = 2, 3$ and 4 with the effective proton and neutron charge $e^{(\lambda)}_{eff}(p) = 1.2$ and $e^{(\lambda)}_{eff}(n) = 0.2$. The function $\tilde{T}^{g_3,g_4}_{q_1q_2K}$ is given in Appendix.

It is known that there are no one-phonon 1^- states below a partial threshold in spherical nuclei. The quasiparticle-phonon interaction is responsible for the shift of a part of the E1 strength from GDR to a lower energy region. Nevertheless, the E1 strength below 5 MeV is practically absent in spherical nuclei. The 1^- states with an energy around 4 MeV have been described as two-phonon quadrupole-octupole $[2^+_1 \oplus 3^-_1]$ states [6,17]. The influence of a term like that on B(E1) values has been considered in [18]. Therefore, we include in Eq. (26) the term describing the transition from the ground state to the two–phonon components of the 1^- state wave function . The reduced probability of the Eλ and Mλ transition between excited states are given in [6,7,10,11].

2.4. The QPNM equation for odd-mass nuclei

The equation for describing nonrotational states with the wave function consisting of a sum of one-quasiparticle and quasiparticle $\otimes$ phonon terms have been derived in [19]. For describing nonrotational states in odd-mass nuclei in the QPNM we used a wave function in the form

$$\Psi_n(K^{\pi_0}_0\sigma_0\tau_0) = \{\sum_{q_0}{}^{\tau_0} C^n_{q_0}\alpha^+_{q_0\sigma_0} + \sum_{\substack{q_3q_2\\ \sigma_3\sigma_2}}{}^{\tau_0} D^n_{q_3q_2}\alpha^+_{q_2\sigma_3} Q^+_{g_2\sigma_2}\delta_{\sigma_3 K3+\sigma_2\mu_2,\sigma_0 K_0}\}\Psi_0. \qquad (28)$$

To take the Pauli principle into account in quasiparticle $\otimes$ phonon terms, we used the function [19]

$$\mathcal{L}^{K_0}(q_3g_2, i') = -\sum_{q_4}\psi^{\lambda_2\mu_2 i_2}_{q_3q_4}\psi^{\lambda_2\mu_2 i'}_{q_3q_4}[\delta_{K_3+K_4,\mu_2}\delta_{K_3+\mu_2,K_0} +$$

$$+\delta_{K_3-K_4,\mu_2}\delta_{K_3+\mu_2,K_0}+\delta_{K_4-K_3,\mu_2}\delta_{|K_3-\mu_2|,K_0}], \tag{29}$$

We used the notation $\mathcal{L}^{K_0}(q_3g_2)$ for $i'=i_2$. The normalization condition of the wave function (28) takes the form

$$\sum_{q_0}^{\tau_0}(C_{q_0}^n)^2+\sum_{q_3g_2}^{\tau_0}(D_{q_3g_2}^n)^2[1+\mathcal{L}^{K_0}(q_3g_2)]=1. \tag{30}$$

If the violation of the Pauli principle is maximal, then $\mathcal{L}^{K_0}(q_3^0g_2^0)=-1$ and the corresponding term drops out of the sum over q_3g_2.

Now we find the average value of H_{QPNM} over the state (28) and using the variational principle we get the following equation [6]:

$$(\epsilon_{q_0}-E_n)C_{q_0}^n-\frac{1}{2}\sum_{q_3g_2}^{\tau_0}V_{\tau_0}^{g_2}(q_0q_3)[1+\mathcal{L}^{K_0}(q_3g_2)]=0, \tag{31}$$

$$[\epsilon_{q_3}+\omega_{g_2}+\Delta^{K_0}(q_3g_2)-E_n]D_{q_3g_2}^n-\frac{1}{2}\sum_{q_0'}^{\tau_0}C_{q_0'}^nV_{\tau_0}^{g_2}(q_0'q_3)=0, \tag{31'}$$

where

$$\Delta^{K_0}(q_3g_2)=-\sum_{i_2'}W_{i_2i_2'}^{\lambda_2\mu_2}\mathcal{L}^{K_0}(q_3g_2), \tag{32}$$

$W_{i_2i_2'}^{\lambda_2\mu_2}$ and $V_{\tau_0}^{g_2}(q_0q_3)$ are given by (10') and (15). If one-quasiparticle $\otimes$ two-phonon terms are added to the wave function (28), then in the diagonal approximation we get an additional shift of the quasiparticle $\otimes$ phonon poles which we denote by $\delta(q_3g_2)$. A secular equation for calculating the energies E_n has the following form:

$$det||(\epsilon_{q_0}-E_n)\delta_{q_0q_0'}-\frac{1}{4}\sum_{q_3g_2}^{\tau_0}\frac{V_{\tau_0}^{g_2}(q_0q_3)V_{\tau_0}^{g_2}(q_0'q_3)[1+\mathcal{L}^{K_0}(q_3g_2)]}{\epsilon_{q_3}+\omega_{g_2}+\Delta^{K_0}(q_3g_2)-\delta(q_3g_2)-E_n}||=0. \tag{33}$$

The reduced probability of Eλ transitions between the states described by the wave function (28) was given in [6].

3. Nonrotational states in doubly even well-deformed nuclei

3.1. Details of calculation

A specific feature of deformed nuclei is the explicit role of the degrees of freedom connected with the rotation of the nucleus as a whole. According to the axial rotor model the wave function of an excited state can be written in the form

$$\Psi_{M\sigma K}^I(\Theta_l,n)=\sqrt{\frac{2I+1}{16\pi^2}}[D_{M\sigma K}^I(\Theta_l)\Psi_n(K^\pi\sigma)+(-)^{I+K}D_{M-\sigma K}^I(\Theta_l)\Psi_n(K^\pi-\sigma)],$$

$$\Psi^I_{M0}(\Theta_l, n) = \sqrt{\frac{2I+1}{8\pi^2}} D^I_{M0}(\Theta_l)\Psi_n(0^\pi), \tag{34}$$

where the generalized spherical functions $D^I_{M\sigma K}(\Theta_l)$ describe rotation.

We restrict our investigation to an internal wave function $\Psi_n(K^\pi\sigma)$ with a good quantum number K (all $K > 0$), parity π, and $\sigma = \pm 1$ is related to the time-reversal symmetry. We do not consider the Coriolis interaction that mixes states with different K and the same π. The Coriolis coupling calculations have been carried out in [8], where its influence on energies of $K^\pi_n = 0^-_1$ and 1^-_1 and B(E1) values in ^{156,158}Gd is very strong. It is possible to use our wave functions $\Psi_n(K^\pi\sigma)$ for Coriolis coupling calculations.

The calculations are made with the Woods-Saxon potential with quadrupole β_2 and hexadecapole β_4 and $\gamma = 0$ equilibrium deformations. The single-particle spectrum is taken from the bottom of the potential well up to +5 or +15 MeV. The parameters of the Woods-Saxon potential have been fixed in 1968. The energies and wave functions of the single-particle levels of the Woods-Saxon potential in the rare-earth region and the energies and structure od odd-mass nuclei have been published in [21].

The isoscalar constants $\kappa_0^{\lambda\mu}$ of ph interactions are fixed so as to reproduce experimental energies of the first $K^\pi_{n=1}$ nonrotational states. The calculations were made with the isovector constant $\kappa_1^{\lambda\mu} = -1.5\kappa_0^{\lambda\mu}$ for ph interactions and the constant $G^{\lambda\mu} = \kappa_0^{\lambda\mu}$ for pp interactions. The monopole pairing constants were fixed by pairing energies at $G^{20} = \kappa_0^{20}$. The radial dependence of the multipole interactions has the form $dV(r)/dr$, where $V(r)$ is the central part of the Woods-Saxon potential. The phonon basis consists of ten ($i_0 = 1, 2, \ldots, 10$) phonons of each multipolarity: $\lambda\mu = 20, 22, 32, 33, 43, 44, 54, 55$ and 65. We used twenty phonons with $\lambda\mu = 21, 30, 31$. The energies of the two-quasiparticle poles were calculated by taking into account the blocking effect and the Gallagher-Moszkowski correction.

3.2. 1^+ states and M1 transition rates

The results of calculations within the QPNM of nonrotational states with $K^\pi = 0^+, 2^+, 4^+, 2^-$ and 3^- have been published in many papers. Now we consider only the $K^\pi = 1^+, 0^-$ and 1^- states and M1 and E1 transition rates.

A strongly collective scissor mode was predicted by the classical picture of the two-rotor model [22] by assuming that neutrons and protons perform out-of-phase rotational oscillations around the axis perpendicular to the nuclear symmetry axis. The collective properties of the mode have been studied in the RPA [23–26].

We calculated in the RPA and QPNM the energies up to 4 MeV and wave functions of the $K^\pi = 1^+$ states and B(M1)↑ values in ^{156,158,160}Gd and ^{160,162,164}Dy and the overlapping with the spurious and scissor states. The overlap of the wave function (19) with the spurious state and with the scissor-type state, in the form of

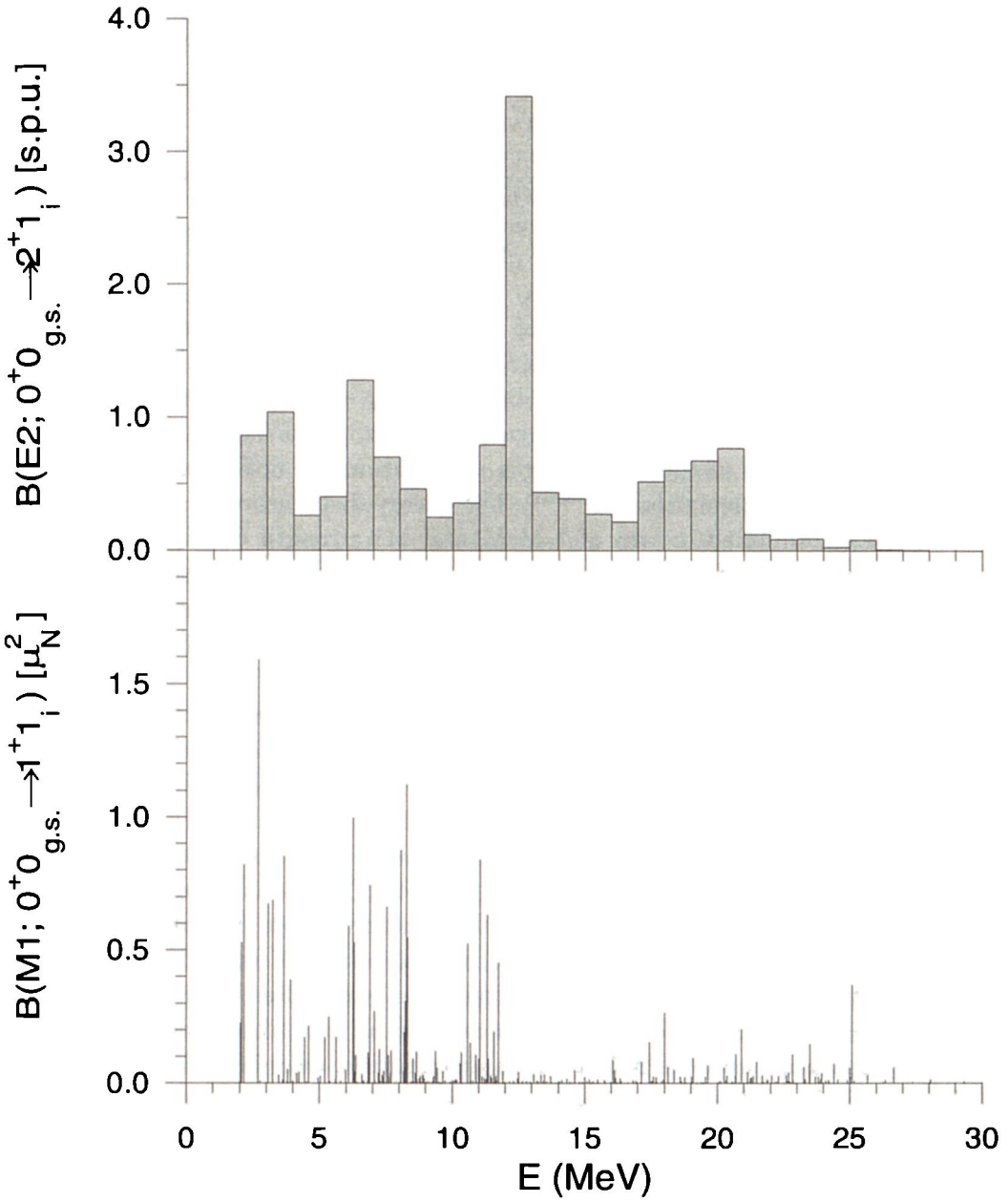

Fig. 1. B(E2) and B(M1) values in ^{164}Dy, calculated in the QPNM.

eq.(4) in [25], has the following form:

$$N_{sp}^{n} = \frac{1}{< j_{-}j_{+} >} \sum_{ii'} R_{i}^{n} R_{i'}^{n} I_{-}^{21i} I_{+}^{21i'}, \tag{35}$$

$$Sc^{n} = \frac{1}{< j_{-}j_{+} >< j_{-}j_{+} >_{\nu} < j_{-}j_{+} >_{\pi}} \sum_{ii'} R_{i}^{n} R_{i'}^{n} [< j_{-}j_{+} >_{\pi} I_{+}^{21i}(\nu) -$$

$$- < j_{-}j_{+} >_{\nu} I_{+}^{21i}(\pi)][< j_{-}j_{+} >_{\pi} I_{+}^{21i'}(\nu) - < j_{-}j_{+} >_{\nu} I_{+}^{21i'}(\pi)], \tag{36}$$

where $I_{\pm}^{21i}(\tau)$ is given by eq. (17').

The energies and wave functions of the 1^+ states are calculated in the RPA with $\kappa_0^{011} = 0.0024$, $\kappa_0^{011} = 0.024$ fm^{2}MeV^{-1}, and $\kappa_0^{21} = 0.147$ for ^{160,162,164}Dy and 0.0160 fm^{2}MeV^{-1} for ^{156,158,160}Gd. The B(M1; $0^+0_{g.s.} \rightarrow 1^+1_n$) values are calculated with bare orbital and effective gyromagnetic factors, $g_s^{eff} = 0.8 g_s^{free}$. The results of the RPA calculations of the M1 strength distribution are not practically different compared with the calculations in [23–26]. The energy distribution of the E2 strength with $K^{\pi} = 1^+$, summed in bins of 1 MeV, and M1 strength distribution in ^{164}Dy are shown in Fig. 1. It is seen from Fig. 1 that we correctly described the low-energy E2 strength and the positions of the isoscalar and isovector giant quadrupole resonances. The high-energy M1 strength is purely orbital, the spin contributions are dominant between 6–12 MeV.

According to our investigation, the equilibrium quadrupole deformation gives rise to the low energy magnetic dipole excitations in deformed nuclei. This statement is in agreement with the correlation between the B(M1)↑ and B(E2;$0^+0_{g.s.} \rightarrow 2^+0_{g.s.}$) values [27].

The scissor mode fragments over both the low- and high-energy orbital M1 excitations. The sum over the first twenty states $\sum_{n=1}^{20} Sc^n$ is equal to 0.4. The scissor state is strongly fragmented in the low-energy region. For any 1_n^+ state the Sc^n value is smaller than 0.1. The orbital motion accounts for $\approx 60\%$ of the total strength in the RPA and QPNM at the excitation energy less than 4 MeV.

The wave function of the first 3–5 states with $K^{\pi} = 1^+$ has a dominating one-phonon component, and the M1 strength distribution, calculated in the RPA and QPNM, is similar. The fragmentation of one-phonon states increases with excitation energy. It splits the most collective M1 peaks into two or more of weaker intensity. The fragmentation of one-phonon states should be taken into account in the description of the M1 strength distribution at energies above 3 MeV. The result of calculation of the energies of 1^+ states and B(M1)↑ values are in reasonable agreement with experimental data.

3.3. $K^{\pi} = 0^-$ and 1^- states and E1 transition rates

Octupole interactions between quasiparticles lead to the formation of octupole states with $K^{\pi} = 0^-, 1^-, 2^-$ and 3^-. The energies, B(E3) values for the transition to

the ground states and the two-quasiparticle structure of the dominant one-phonon component of the wave functions of the low-lying octupole states are reasonably well described in the QPNM.

The origin of E1 strength in the low-energy region in deformed nuclei has been investigated in [28]. It is known that there are no one-phonon 1^- states below the particle threshold in spherical nuclei. Quadrupole deformation is responsible for the splitting of the subshells of a spherical basis into twice-degenerate single-particle states. Due to this splitting, part of the E1 strength is shifted to low-lying states. An octupole isoscalar interaction between quasiparticles leads to the formation of collective octupole states. Due to octupole interaction, the summed E1 strength for the transition to $K^\pi = 0^-$ and 1^- states in the (0–4) MeV energy region increases by two orders of magnitude. An isovector dipole ph interaction shifts the largest part of E1 strength from the low-lying states to the region of the isovector GDR.

The B(E1) values for a transition from the ground state to the excited states 1^-K_ν with $K^\pi = 0^-$ and 1^- were calculated [10–14,28] with the effective charge (27) and $\kappa_1^{1K} = -1.5\kappa_0^{3K}$. According to the calculation of the B(E1) values in ^{160}Gd in the excitation region up to 25 MeV, the energy centroids of the $K^\pi = 0^-$ and 1^- states equal 13.0 and 14.8 MeV, respectively. The total cross section of the photoabsorption equals 2.45 b·MeV. These results are in agreement with the experimental data and the results of earlier calculations in ref [29]. The summed B(E1) strength for the $K^\pi = 0^-$ and 1^- states equals 13.6 and 29.2 e^2fm^2, respectively. The energy centroids, calculated with $\kappa_1^{1K} = -2\kappa_0^{3K}$, are shifted to higher energies by about 3 MeV and , therefore, contradict the experimental data on the GDR. The quasiparticle-phonon interaction leads to the fragmentation of one-phonon states due to the coupling with two-phonon configurations. We are studying the E1 strength distribution at energies below 4 MeV as a result of the fragmentation of one-phonon states. The quasiparticle-phonon interactions almost do not influence the first five states with the same K^π. The one-phonon states with energy larger than 3 MeV are fragmented. Some of them are strongly and others are weakly fragmented. Nevertheless, there are states in the energy range 3–4 MeV which are strongly excited by E1 transitions. Influence of the fragmentation of the one-phonon states on the E1 strength distribution in ^{160}Gd is demonstrated in Fig. 2. It is seen from Fig. 2 that the B(M1) values, calculated in the RPA, are strongly fragmented at energies above 3 MeV.

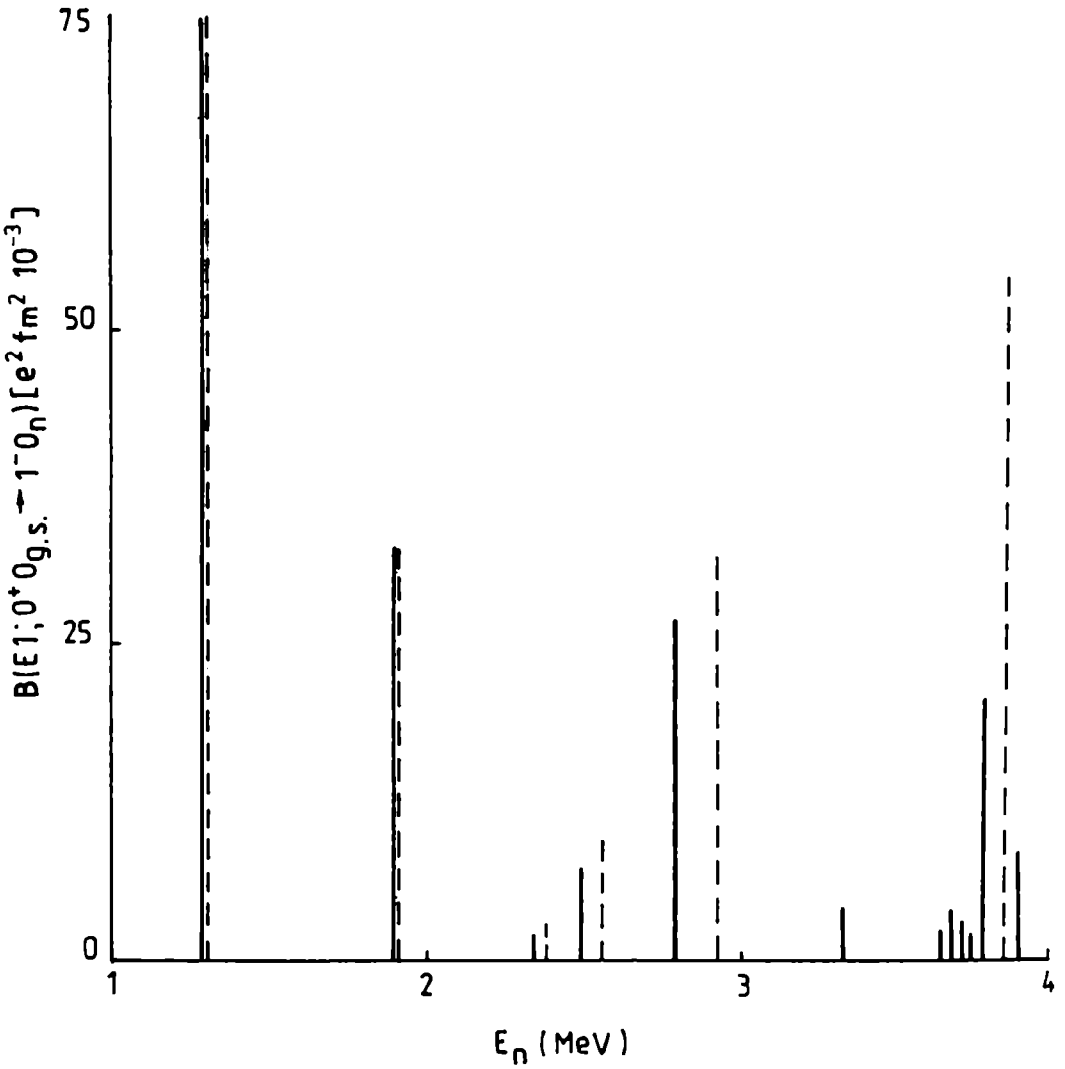

Fig. 2. The E1 strength distribution in ^{160}Gd. Dashed lines refer to RPA, full-lines to QPNM.

The calculated B(E1) values with the effective charge (27) for the excitation of $I^\pi K = 1^-0$ are approximately 3–5 times as large as the experimental ones. By using the renormalized effective charge we improve the agreement with experimental data. But this improvement is very artificial. The calculated and experimental B(E1) values for the excitation of the first $K^\pi_\nu = 0^-_1$ state are larger as compared with higher-lying 0^- states. In agreement with experimental data, the B(E1) values for the 0^-_1 state in ^{166,168}Er are larger than in ^{162,164}Dy and ^{158,160}Gd. According to calculation in the QPNM, the concentration of the E1 strength takes place at 2.6–3.5 MeV in ^{168}Er, at 3.2–3.8 MeV in ^{164}Dy and at 3.75–3.85 MeV in ^{160}Gd. It is possible to expect that the E1 transition to the $K^\pi = 0^-$ states in this region will be observed experimentally. The calculated B(E1) values for the transition to the $K^\pi = 1^-$ states are as large as experimental ones. There are no data on the B(E1) values for transitions to $K^\pi = 1^-$ states experimentally observed by the Nuclear Resonance Fluorescence method except ^{160}Gd [30]. According to our calculations, B(E1) values for the excitation of the $K^\pi = 0^-$ states with an energy below 3 MeV are 3–4 times as large as for the excitation of the $K^\pi = 1^-$ states. Nevertheless, the B(E1) values for the excitation of the $K^\pi = 1^-$ states are large enough. They can be observed experimentally.

The correlation between the E1 and E3 reduced transition probabilities from the ground state to the same rotational bands has been analyzed in [31]. The B(E3) value is the coherent sum over the two-quasiparticle states qq' of many terms. The B(E1) is a noncoherent sum but it contains the same amplitude $\psi^{3K_i}_{qq'} + \phi^{3K_i}_{qq'}$. According to calculation in [31], there is a strong correlation between B(E3) and B(E1) values. The correlation coefficients were calculated over all $K^\pi = 0^-$ and 1^- levels up to 4 MeV in ^{160}Gd, ^{160}Dy, ^{162}Dy and ^{164}Dy. They are equal to 0.987 and 0.910 respectively.

It is possible to state that the QPNM can be served as a basis for description of all nonrotational states below 4 MeV in well-deformed nuclei.

The research was supported in part by grant N6N000 for the International Science Foundation and by grant RFFR 95-02-05701 from Russian Foundation for Fundamental Research.

Appendix

$$A^+(q_1q_2;\mu\sigma) = \begin{cases} \sum_{\sigma'} \delta_{\sigma'(K_1-K_2),\sigma\mu}\sigma'\alpha^+_{q_1\sigma'}\alpha^+_{q_2-\sigma'}, & \text{if } |K_1-K_2| = \mu, \\ \delta_{(K_1+K_2),\mu}\alpha^+_{q_1\sigma}\alpha^+_{q_2\sigma}\chi(q_1q_2), & \text{if } K_1+K_2 = \mu; \end{cases}$$

$$\delta_{\sigma_1K_1+\sigma_2K_2,\sigma K} = \begin{cases} 1, & \text{if } \sigma_1K_1+\sigma_2K_2 = \sigma K, \\ 0, & \text{if } \sigma_1K_1+\sigma_2K_2 \neq \sigma K. \end{cases}$$

with all $K \geq 0$, $\mu \geq 0$, $\sigma = \pm 1$.

$$f^{\lambda\mu}(q_1q_2) = \begin{cases} < q_1 + |\frac{\partial V(r)}{\partial r}Y_{\lambda\mu}(\theta\phi)|q_2+ >, & \text{if } |K_1-K_2| = \mu; \\ < q_1 + |\frac{\partial V(r)}{\partial r}Y_{\lambda\mu}(\theta\phi)|q_2- > .\chi(q_1q_2). & \text{if } K_1+K_2 = \mu; \end{cases}$$

$$\chi(q_1q_2)=1,\quad \chi(q_2q_1)=-1,\quad \chi^2(q_1q_2)=1,$$

$$f^{011}(q_1q_2)=<q_1|\frac{\partial V(\tau)}{\partial r}\sigma|q_2>$$

$$D^{\lambda\mu i}_{\tau}=\sum_{qq'}{}^{\tau} f^{\lambda\mu}(qq')u^{(+)}_{qq'}g^{\lambda\mu i}_{qq'},$$

$$D^{\lambda\mu i}_{g\tau}=\sum_{qq'}{}^{\tau} f^{\lambda\mu}(qq')v^{(-)}_{qq'}g^{\lambda\mu i}_{qq'},$$

$$D^{\lambda\mu i}_{w\tau}=\sum_{qq'}{}^{\tau} f^{\lambda\mu}(qq')v^{(+)}_{qq'}w^{\lambda\mu i}_{qq'}.$$

$$D^{011i}_{\tau}=\sum_{qq'}{}^{\tau} f^{011}(qq')u^{(-)}_{qq'}\chi(qq')w^{21i}_{qq'}.$$

$$B(q_1q_2;\mu\sigma)=\begin{cases}\sum_{\sigma'}\delta_{\sigma'(K_1-K_2),\sigma\mu}\alpha^{+}_{q_1\sigma'}\alpha_{q_2\sigma'}, & \text{if } |K_1-K_2|=\mu,\\ \delta_{(K_1+K_2),\mu}\sigma\alpha^{+}_{q_1\sigma}\alpha_{q_2-\sigma}, & \text{if } K_1+K_2=\mu.\end{cases}$$

$$\mathcal{B}(q_1q_2;\mu\sigma)=\begin{cases}\sum_{\sigma'}\delta_{\sigma'(K_1-K_2),\sigma\mu}\sigma'\alpha^{+}_{q_1\sigma'}\alpha_{q_2\sigma'}, & \text{if } |K_1-K_2|=\mu,\\ \sum_{\sigma'}\delta_{\sigma'(K_1+K_2),\sigma\mu}\alpha^{+}_{q_1\sigma'}\alpha_{q_2-\sigma'}, & \text{if } K_1+K_2=\mu.\end{cases}$$

$$\Delta\omega(g_1g_2)=-[\frac{1-\delta_{K_00}}{1+\delta_{g_1g_2}}+\frac{\delta_{K_00}}{1+\delta_{g_1g_2}\delta_{\mu_10}}]$$

$$\times\sum_{i'}\{\mathcal{K}^{K_0}(g_2,g_1'|g_1,g_2)W^{\lambda_1\mu_1}_{i_2i'}+\mathcal{K}^{K_0}(g_2',g_1|g_1,g_2)W^{\lambda_2\mu_2}_{i_1i'}\},$$

the function $W^{\lambda\mu}_{ii'}$ is given by Eq. (10'). For $K^{\pi}=0$ and 1^{-} states the function $W^{\lambda_1\mu_1}_{ii'}$ is replaced by the function $W^{K_1}_{ii'}$ in the form (9').

$$T^{g_2,g_0}_{qq';\mu_1}=\sum_{q_3}{}^{\tau}(\psi^{g_0}_{q_3q'}\phi^{g_2}_{q_3q}+\phi^{g_0}_{q_3q'}\psi^{g_2}_{q_3q})\theta^{\mu_1\mu_2K_0}_{KK'K_3}(1+\delta_{K_00})(1+\delta_{K_00}(1-\delta_{\mu_10})),$$

where $\theta^{\mu_1\mu_2K_0}_{KK'K_3}$ equals -1, if $K+K'=\mu$, or $K_3+K'=\mu$, or $\mu_1+\mu_2=K_0$, or $\mu_1-\mu_2=K_0$, and equals 1 in other cases.

References

1. V.G. Soloviev, *Sov. J. Part. Nucl.* **2** (1978) 343.
2. A.I. Vdovin and V.G. Soloviev, Sov. *Sov. J. Part. Nucl.* **14** (1983) 99.
3. V.V. Voronov and V.G. Soloviev, *Sov. J. Part. Nucl.* **14** (1983) 583.
4. A.I. Vdovin et al., *Sov. J. Part. Nucl.* **16** (1985) 105.
5. V.G. Soloviev, *Progr. Part. Nucl. Phys.* **19** (1987) 107.
6. V.G. Soloviev, *Theory of Atomic Nuclei. Quasiparticle and phonons.* (Institute of Physics Publishing,Bristol and Philadephia, 1992).
7. V.G. Soloviev, A.V. Sushkov and N.Yu. Shirikova, *Part.Nucl.* **25** (1994) 377.

8. V.G. Soloviev, A.V. Sushkov and N.Yu. Shirikova, *Nucl.Phys.* **A568** (1994) 244.
9. D. Karadjov, V.V. Voronov and F. Catara, *J. Phys. G* **20** (1994) 1431.
10. V.G. Soloviev and A.V. Sushkov and N.Yu. Shirikova, *J. Phys. G* **20** (1994) 113.
11. V.G. Soloviev, A.V. Sushkov and N.Yu. Shirikova, *IJMP* **E3** (1994) 1227.
12. V.G. Soloviev, A.V. Sushkov and N.Yu. Shirikova, *Phys. Rev.* **C51** (1995) 551.
13. J. Berzins et al., *Nucl. Phys.* **A584** (1995) 413.
14. V.G. Soloviev, A.V. Sushkov and N.Yu. Shirikova, *Yad. Fiz.* (in press).
15. V.G. Soloviev,*In: Recent Advances in Nuclear Structure ed. D Bucurescu, G. Cata-Danil, N.V. Zampfir* (Singapure, World Scientific, 1990) 215.
16. V.G. Soloviev, A.V. Sushkov and N.Yu. Shirikova, *In: 5th Int. Spring Seminar "New perspectives in nuclear structure" ed. A. Covello* (Singapure, World Scientific, 1995) (in press)
17. Dao Tien Khoa, V.Yu. Ponomarev and V.V. Voronov,*Izv. AN USSR ser. fiz.* **48** (1984) 1846.
18. U. Kneissl et al., *Phys.Rev.Lett.* **71** (1993) 2180.
19. V.G. Soloviev, *Phys. Lett.* **16** (1965) 308.
20. V.G. Soloviev, V.O. Nesterenko and S.I. Bastrukov, *Z. Phys.* **A309** (1983) 353.
21. F.A. Gareev, S.P. Ivanova, V.G. Soloviev and S.I. Fedotov, *Sov. J. Part. Nucl.* **4** 1973 148.
22. N. Lo Iudice and F. Palumbo, *Phys. Rev. Lett.* **41** (1978) 1532.
23. I. Hamamoto and C. Magnusson, *Phys. Lett.* **B312** (1992) 267.
24. R.Nojarov and A. Faessler, *Nucl. Phys.* **A484** (1988) 1.
25. A. Faessler, R. Nojarov and T. Taigel, *Nucl. Phys.* **A492** (1989) 105.
26. R. Nojarov, A. Faessler and M.Dingfelder, *Nucl. Phys.* **C51** (1995) 2449.
27. C. Rangacharyulu, A. Richter et al., *Phys. Rev.* **C43** (1991) R949.
28. V.G. Soloviev and A.V. Sushkov, *Physics of Atomic Nuclei* **57** (1994) 1304.
29. L.A. Malov and V.G. Soloviev, *Part.Nicl.* **11** (1980) 301.
30. H. Friederichs et al., *Nucl. Phys.* **A567** (1994) 266.
31. V.G. Soloviev and A.V. Sushkov and N.Yu. Shirikova, *J. Phys. G* (in press)

SEMICLASSICAL DESCRIPTION OF FERMI SYSTEMS

JOÃO DA PROVIDÊNCIA JR.
Departamento de Física, Universidade de Coimbra
P-3000 Coimbra, Portugal

ABSTRACT

Collective motion of Fermi systems is described in terms of collective coordinates defined by means of a polynomial expansion of the generator of the fluctuations in powers of the momentum. The dynamics are determined by the variational principle. The volume plasmon in metals is described in the framework of a simple variational model. Sum rules consistent with the variational formalism are analysed.

1. Introduction

In the present note we will be concerned with the semiclassical description of collective modes in Fermi systems. The method we follow is closely related to Time Dependent Hartree-Fock [TDHF] and to the Random Phase Approximation [RPA]. Slater determinants are the wave functions which describe, approximately, the quantal states of the system. Collective coordinates which parametrize the Slater determinants or the distribution function are chosen according to intuitive criteria and their dynamics is determined by means of the variational principle.

A possible way of defining a suitable variational space is to approximate the generator of the fluctuations by a polynomial in the particle momentum (or in the particle momentum and coordinate). This approximation is attractive due to its simplicity. In section 2 we apply such an approximation to an infinite homogeneous system of nuclear matter. Using a variational method we derive approximate eigenmodes of the system which we compare with the exact eigenmodes.

As an example we consider (section 3) the collective modes of the valence electrons in a metal. The generator of the fluctuations is approximated by a linear function of the momentum and we evaluate the volume plasmon identifying the contributions which have semiclassical and quantum origin. In section 4 we relate the approximate eigenmode (volume plasmon), obtained from the variational principle, with the linear and cubic energy weighted sum rules. In section 5 we derive, within the semiclassical approach, the equilibrium condition for a finite Fermi system and we review some possible choices of the generator of the fluctuations. In section 6 we draw conclusions.

2. Solution of the Vlasov Equation in the Polynomial Approximation

In transport theory one deals with non-equilibrium states. The physical properties such as the density, the current density and the pressure tensor may all be evaluated

once we know the distribution function $f(\vec{x},\vec{p},t)$ which denotes the average density of particles with momentum $\vec{p}$ at a given point $\vec{x}$ in space at a given instant t. The aim of transport theory is to obtain the distribution function $f(\vec{x},\vec{p},t)$ which requires that we solve the Boltzmann equation. According to this equation, the total derivative of the distribution function is equal to the rate of change of f due to the collisions. The Boltzmann equation is an integro-differential equation which involves the scattering probabilities. One has to resort to approximate schemes in order to obtain manageable solutions. There are different methods to obtain approximate solutions. A possible way is to relate the equation we wish to solve to a variational principle. This method has the advantage that the results may be improved in a systematic way.

The Vlasov equation is obtained when, in the Boltzmann equation, the collision terms are neglected. If the Pauli principle is incorporated into the Vlasov equation, then this equation is identified with the classical limit of TDHF. The Vlasov equation is of great interest because it provides a most appealing and intuitive picture.

We investigate the validity of the polynomial approximation[1] to the generator of the distribution function fluctuations in the context of the Vlasov equation applied to extended nuclear matter[2,3]. The description of the properties of finite nuclei may be achieved if the generating function $S(\vec{x},\vec{p},t)$ of small amplitude oscillations is approximated by a polynomial in the momentum variables.

The nuclear Vlasov equation describes the time evolution of the classical distribution function $f(\vec{x},\vec{p},t)$ for a system of interacting nucleons. The generator of the time evolution $h(\vec{x},\vec{p},t)$ is a functional of the distribution function. We have

$$\frac{\partial f}{\partial t}+\frac{\partial f}{\partial \vec{x}}\cdot\frac{\partial h}{\partial \vec{p}}-\frac{\partial f}{\partial \vec{p}}\cdot\frac{\partial h}{\partial \vec{x}}=0, \tag{1}$$

$$h[f](1)=\frac{p_1^2}{2m}+\int d\Gamma_2 v_{12} f(2)+\frac{1}{2}\int\int d\Gamma_2 d\Gamma_3 v_{123} f(2) f(3), \tag{2}$$

where h stands for the single particle hamiltonian. Here $d\Gamma$ is the volume element in phase space

$$d\Gamma = g\frac{d^3x d^3p}{(2\pi\hbar)^3}, \tag{3}$$

g is the spin-isospin multiplicity and v_{12} and v_{123} stand for the two-body and three-body interactions. We choose a short-range effective interaction $v_{12}=2a_2\delta(\vec{x}_1-\vec{x}_2)$, $v_{123}=6a_3\delta(\vec{x}_1-\vec{x}_2)\delta(\vec{x}_2-\vec{x}_3)$. The energy functional may be written

$$\begin{aligned} E[f] = &\int d\Gamma\frac{p^2}{2m}f+\frac{1}{2}\int\int d\Gamma_1 d\Gamma_2 v_{12} f(1) f(2) \\ &+\frac{1}{6}\int\int\int d\Gamma_1 d\Gamma_2 d\Gamma_3 v_{123} f(1) f(2) f(3). \end{aligned} \tag{4}$$

The Vlasov equation admits time-independent solutions $f_0(\vec{x},\vec{p})$ such that

$$\frac{\partial f_0}{\partial \vec{x}}\cdot\frac{\partial h_0}{\partial \vec{p}}-\frac{\partial f_0}{\partial \vec{p}}\cdot\frac{\partial h_0}{\partial \vec{x}}\equiv\{f_0,h_0\}=0, \tag{5}$$

where $h_0(\vec{x},\vec{p}) = h[f_0]$. By $\{A,B\}$ we denote the Poisson bracket of A and B. The linearized Vlasov equation describes the time evolution of systems close to the equilibrium state f_0. We find

$$\partial_t \delta f + \{\delta f, h_0\} + \{f_0, \delta h\} = 0, \tag{6}$$

where

$$\delta f = \delta f(\vec{x},\vec{p},t), \tag{7}$$

and

$$\delta h(\vec{x}_1,\vec{p}_1,t) = \int d\Gamma_2 v_{12}\delta f(2) + \int\int d\Gamma_2 d\Gamma_3 v_{123} f_0(2)\delta f(3). \tag{8}$$

The linearized Vlasov equation may be replaced by an equation for the generator S of fluctuations

$$\delta f = \{f_0, S\}. \tag{9}$$

We have

$$\{f_0, (\partial_t S + \{S, h_0\} + \delta h)\} = 0. \tag{10}$$

In order to determine the normal modes of the system we take

$$S(\vec{x},\vec{p},t) = S_\omega(p,u)\exp[i(\vec{q}\cdot\vec{x} - \omega t)], \tag{11}$$

where $u = \cos\theta$, being θ the angle between $\vec{p}$ and $\vec{q}$. Since we are only interested in describing longitudinal modes we have assumed that S_ω only depends on $\vec{p}\cdot\vec{q}/q$. Then, for an homogeneous system, we obtain from Eq. (10),

$$\left\{(\frac{\vec{p}\cdot\vec{q}}{m} - \omega)S_\omega(p,u) + 2\pi g\frac{F_0 p_F^4}{3m\rho_0}q\int\frac{du'}{(2\pi\hbar)^3}u' S_\omega(p_F,u')\right\}\vec{q}\cdot\frac{\partial f_0}{\partial\vec{p}} = 0, \tag{12}$$

where

$$F_0 = \frac{3m}{p_F^2}\sum_{\nu=2,3} a_\nu \nu(\nu-1)\rho_0^{\nu-1}. \tag{13}$$

From Eq. (12) it follows that

$$(u - \frac{m\omega}{p_F q})S_\omega(p_F,u) + \frac{F_0}{2}\int du' u' S_\omega(p_F,u') = 0. \tag{14}$$

It is convenient to express the time in units of $m/p_F q$, $t' = t p_F q/m$, and to express the frequency ω in units of $p_F q/m$, $\omega' = m\omega/p_F q$, so that $\omega t = \omega' t'$. In what follows, and in order to keep the notation simple, we replace ω' and t' respectively by ω and t. Then the previous equation may be written as follows

$$-i\partial_t S(u,t) + uS(u,t) + \frac{F_0}{2}\int du' u' S(u',t) = 0, \tag{15}$$

where

$$S(u,t) = S_\omega(u)\exp(-i\omega t). \tag{16}$$

In order to obtain approximation schemes for this equation we observe that it may be derived from the following lagrangian,

$$\mathcal{L} = i\int_{-1}^{+1} S^*\dot{S}udu - \int_{-1}^{+1} S^*Su^2du - \frac{F_0}{2}\left|\int_{-1}^{+1} Sudu\right|^2, \tag{17}$$

where the dot stands for a derivative with respect to t. The system described by Eq. (14) is stable provided $F_0 > -1$. The choice given by Eq. (16) defines the normal mode solutions. It is found[2,3,4] that for $\omega \in]-1,+1[$

$$S_\omega(u) = \delta(\omega - u) + \frac{\lambda_0(\omega)}{\omega - u}, \tag{18}$$

where $\lambda_0(\omega)$ is such that

$$\frac{\omega}{\lambda_0(\omega)} = \frac{2}{F_0} + 2 + \omega \ln\frac{1-\omega}{1+\omega}. \tag{19}$$

If $F_0 > 0$ we also have, for $|\omega_z| > 1$ such that

$$\frac{2}{F_0} + 2 + |\omega_z| \ln\frac{|\omega_z| - 1}{|\omega_z| + 1} = 0, \tag{20}$$

isolated modes given by

$$S_{\omega_z}(u) = \frac{1}{\omega_z - u}, \tag{21}$$

for $\omega_z = \pm|\omega_z|$.

We wish to investigate the validity of a polynomial approximation to the functions $S(u)$

$$S^{(N)}(u) = \sum_{j=0}^{N} a_j u^j, \tag{22}$$

for low values of N.

Inserting the polynomial (22) into the lagrangian (17) we find

$$\begin{aligned}\mathcal{L} = \sum_{j,n=0}^{N}\left(ia_j^*\dot{a}_n\frac{1-(-1)^{j+n}}{j+n+2} - a_j^*a_n\frac{1+(-1)^{j+n}}{j+n+3}\right)\\ -\frac{1}{2}F_0\left(\sum_{j=0}^{N} a_j^*\frac{1-(-1)^j}{j+2}\right)\left(\sum_{n=0}^{N} a_n\frac{1-(-1)^n}{n+2}\right).\end{aligned} \tag{23}$$

Allowing for arbitrary variations of the variational parameters we obtain the following system of equations

$$\begin{aligned}\sum_{n=0}^{N}\left\{i\dot{a}_n\frac{1-(-1)^{j+n}}{j+n+2} - a_n\frac{1+(-1)^{j+n}}{j+n+3}\right.\\ \left.-\frac{1}{2}F_0a_n\left(\frac{1-(-1)^j}{j+2}\right)\left(\frac{1-(-1)^n}{n+2}\right)\right\} = 0,\\ j = 0,1,2,....N.\end{aligned} \tag{24}$$

For normal modes, the coefficients a_n have a harmonic time dependence. Then, from the system of equations represented by Eq. (24), we obtain a set of eigenpolynomials $P_n^{(N)}$ of a degree not greater than N. For odd N, the eigenpolynomials are conveniently labeled by positive and negative integers $\pm 1, ..., \pm\frac{1}{2}(N+1)$ and the corresponding frequencies satisfy the relation $\omega_n = -\omega_{-n}$. These eigenpolynomials fulfill the set of integral equations

$$\int_{-1}^{+1} duu^{j+1} \left\{ (\omega_m - u) P_m^{(N)}(u) - \frac{1}{2} F_0 \int_{-1}^{+1} du' u' P_m^{(N)}(u') \right\} = 0$$
$$j = 0, 1, ..., N. \tag{25}$$

The eigenpolynomials satisfy the following orthogonality relation

$$\int_{-1}^{+1} duu P_n^{(N)*}(u) P_m^{(N)}(u) = \delta_{mn} M_n, \tag{26}$$

where M_n is a constant determined by the normalization chosen for the polynomials. Besides the orthogonality relations these eigenpolynomials fulfill appropriate sum rules[1]. We assume that at $t = 0$ the generator $S(u,t)$ is some polynomial $H(u)$ of degree not greater than N so that it may be expanded in the polynomials $P_n^{(N)}$,

$$S(u,0) = H(u) = \sum_{n=-(N+1)/2, n\neq 0}^{(N+1)/2} d_n P_n^{(N)}(u,0). \tag{27}$$

Then the approximate variational solutions fulfill an energy-weighted sum rule[1],

$$2 \sum_{n=1}^{(N+1)/2} \omega_n d_n d_n^* M_n, = \int_{-1}^{+1} duu^2 S^*(u,0) S(u,0) + \frac{1}{2} F_0 \left| \int_{-1}^{+1} duu S(u,0) \right|^2 \equiv m_1 \tag{28}$$

which corresponds to the energy-weighted sum rule for the exact solutions[2].

Since the exact eigenmodes are known, we can compare the exact results with the approximate results obtained from the polynomial approximation for a given truncation scheme (N). The exact solutions lead to a continuous frequency region $]-1,1[$ and if $F_0 > 0$ also to two discrete frequencies $\pm\omega_z$ with $|\omega_z| > 1$. In ref.[1] we arbitrarily take as an example $N = 31$. For $F_0 = 0.656872$ we find 30 eigenfrequencies in the interval $]-1,1[$ and two eigenfrequencies equal to ± 1.01390 which are very close to the exact results $\pm\omega_z = \pm 1.01391$.

The simplest scheme arises for $N = 1$ which corresponds to considering a polynomial of first order. We obtain the eigenfrequencies

$$\omega_1^{(1)} = \sqrt{\frac{3}{5} + \frac{F_0}{3}}$$
$$\omega_{-1}^{(1)} = -\omega_1^{(1)} \tag{29}$$

and the eigenpolynomials

$$P_1^{(1)}(u,t) = \left(\sqrt{\frac{3}{5}+\frac{F_0}{3}}+u\right) a_{1,1}^{(1)}(t), \tag{30}$$

$$P_{-1}^{(1)}(u,t) = \left(-\sqrt{\frac{3}{5}+\frac{F_0}{3}}+u\right) a_{-1,1}^{(1)}(t). \tag{31}$$

These approximate eigenmodes fulfill an energy weighted sum rule (see Eq. (28))for any operator $H(u)$ which may be expanded in the eigenpolynomials of the scheme N under consideration. For $N = 1$ it follows from Eqs. (30) and (31) that we may choose the operators $H(u) = 1$ or $H(u) = u$. Next, we will compare the strength distribution obtained in the approximate scheme with the exact results. As a choice we consider $H(u) = 1$ which corresponds to the excitation operator

$$Q = \exp(i\vec{q}\cdot\vec{x}) + \exp(-i\vec{q}\cdot\vec{x}). \tag{32}$$

For this operator we can analyse how the strength is distributed for different truncation schemes (different values of N) and in particular we can compare with the strength distribution corresponding to the exact eigenmodes. If we plot, for the operator $H(u) = 1$, the exact strength distribution $s(\omega)$ divided by the total value of the strength, m_1, the area under the curve between any two frequencies ω' and ω'' gives the fraction of the sum rule which is exhausted by the frequencies in the interval $[\omega', \omega'']$. Therefore, if $F_0 < 0$, since there is no discrete eigenmode (see ref.[1]), the area under the continuous curve is 1. In the case of $F_0 = 0.6569$ the discrete eigenfrequencies $\pm\omega_z$ exhaust together 0.41815 of m_1. The strength distribution has two δ-functions centered at $\pm\omega_z$. For convenience, we represent the strength of this state by the area of a rectangle with lower abcissa given by $\omega = 1$. Its width has no real meaning. In order to compare the exact results with the results obtained by the polynomial approximation we consider the example $N = 31$. In fig. 1 we represent the approximate eigenstates by adjacent rectangles, where each rectangle covers an area equal to the fraction of the sum rule exhausted by the corresponding state. It is found that the set of rectangles obtained in this way matches very well with the exact results (continuous curve). This fact supports the polynomial approximation. We are also able to describe the discrete eigenmode. Therefore the numerical results show that the polynomial approximation leads to results which become exact when the degree of the polynomial increases indefinitely.

3. Variational Description of the Volume Plasmon in a Metal

As an application[5] we now consider the plasma of valence electrons in a metal, within the variational approximation with $N = 1$, taking into account the quantum corrections and using determinants of plane waves. The Coulomb interaction is considered. We approximate the positive ionic background by a uniform density of positive charge (jellium approximation).

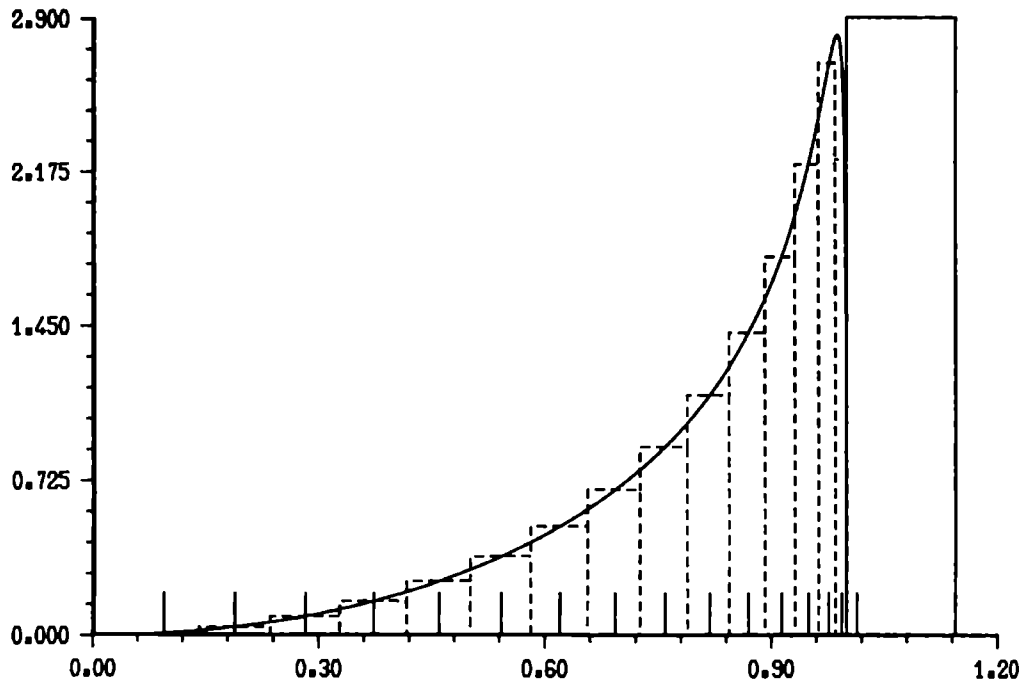

Figure 1: Comparison between the exact strength distribution (continuous line), as a function of ω (in units of qp_F/m), and the respective polynomial approximation for $N = 31$. These results correspond to $F_0 = 0.6569$. The positions of the variational eigenfrequencies are indicated by short vertical lines. The strength associated with the frequency $\omega_i^{(31)}$ has been uniformly distributed over the interval $[\alpha_{i-1}, \alpha_i]$ with $\alpha_i = (\omega_i^{(31)} + \omega_{i+1}^{(31)})/2$ for $1 \leq i \leq 14$ and $\alpha_0 = 0$, $\alpha_{15} = 1$ and $\alpha_{16} = 1.14$ (dashed lines).

The operator $H = T+V$ stands for the hamiltonian of an electron gas in a uniform positive background (jellium model) and T and V are, respectively,

$$T = \sum_{i=1}^{N} \frac{p_i^2}{2m}, \tag{33}$$

$$V = \sum_{i<j} \frac{e^2}{|\vec{x}_i - \vec{x}_j|} + \sum_{i=1}^{N} U(\vec{x}_i) + W, \tag{34}$$

where $U(\vec{x})$ is the potential energy due to the uniform positive density distribution and W is the electrostatic energy of the positive background.

We begin by considering the general quantum mechanical lagrangian which is given by

$$L = i\hbar < \phi|\dot{\phi} > - < \phi|H|\phi > . \tag{35}$$

As a variational wave function we choose the Slater determinant $|\phi>$ which is related to the Slater determinant $|\phi_0>$, describing the ground state, by means of the unitary transformation

$$|\phi>=\exp(\frac{i}{\hbar}S)|\phi_0>, \tag{36}$$

where S is a hermitian one–body operator. For small amplitude deviations from the equilibrium state, we obtain the following harmonic lagrangian which describes the time evolution of the generator S,

$$L^{(2)}=\frac{i}{2\hbar}<\phi_0|[S,\dot{S}]|\phi_0>-\frac{1}{2\hbar^2}<\phi_0|[S,[H,S]]|\phi_0>. \tag{37}$$

If we allow for arbitrary variations of the generator S we obtain the RPA equations. As an alternative we consider a restricted RPA by constraining the generator S. We use a variational method, based on a generator S linear in the momentum. It is convenient to express S as the sum $Q+P$ where Q is independent of momentum and P is linear. The operator Q is a local time-even operator,

$$Q=\sum_j\left[\alpha e^{i\vec{q}\cdot\vec{x}_j}+\alpha^* e^{-i\vec{q}\cdot\vec{x}_j}\right], \tag{38}$$

while P is time-odd,

$$P=\sum_j\left[\vec{p}_j\cdot\vec{q}\left(\gamma e^{i\vec{q}\cdot\vec{x}_j}+\gamma^* e^{-i\vec{q}\cdot\vec{x}_j}\right)+\left(\gamma e^{i\vec{q}\cdot\vec{x}_j}+\gamma^* e^{-i\vec{q}\cdot\vec{x}_j}\right)\vec{p}_j\cdot\vec{q}\right]. \tag{39}$$

Here $\vec{p}_j$ stands for the momentum operator $-i\hbar\nabla_j$, acting on the particle j.

It is convenient to specify explicitly the phases of the collective variables. Therefore we write $\alpha=\tilde{\alpha}\exp(i\phi)$ and $\hbar q^2\gamma=\tilde{\gamma}\exp(i\theta)$ where $\tilde{\alpha}$ and $\tilde{\gamma}$ are real functions of time. Then we obtain the following lagrangian,

$$L^{(2)}(\alpha,\gamma)=-\frac{4N}{\hbar}\left[\dot{\tilde{\alpha}}\tilde{\gamma}\sin(\phi-\theta)+\dot{\phi}\tilde{\alpha}\tilde{\gamma}\cos(\phi-\theta)\right]-T^{(2)}(\alpha)-E^{(2)}(\gamma), \tag{40}$$

$$T^{(2)}(\alpha)=N\frac{q^2}{m}\tilde{\alpha}^2, \tag{41}$$

$$E^{(2)}(\gamma)=\frac{N}{2\hbar^2}\tilde{\gamma}^2\left[\frac{\hbar^2q^2}{m}\left(\frac{24}{5x^2}+2\right)+n_0e^2\frac{32\pi}{q^2}+e^2q\zeta(x)\right]. \tag{42}$$

Allowing for arbitrary variations of the phases ϕ and θ we find that $\dot{\phi}=\dot{\theta}=0$ and $\cos(\phi-\theta)=0$. Therefore in what follows we will arbitrarily choose the phases of the collective variables as $\phi=0$ and $\theta=\pi/2$. The function $\zeta(x)$ ($x=q/k_F$ is the

reduced momentum) is related to the exchange contribution of $< \phi_0|[P,[V,P]]|\phi_0 >$ and has the following expression

$$\zeta(x) = \frac{12}{\pi x^3}\left\{\left(\frac{x^3}{36} - \frac{x}{15} + \frac{4}{35x} - \frac{16}{189x^3}\right)\ln\left|\frac{x+2}{x-2}\right| + \frac{4}{189}\left[-\frac{x^4}{20} - \frac{71x^2}{20} - \frac{76}{15} + \frac{4}{x^2} + \left(\frac{36x^4}{80} - \frac{x^6}{80}\right)\ln\left|1 - \frac{4}{x^2}\right|\right]\right\}. \tag{43}$$

Requiring the action integral to be stationary for arbitrary variations of the variables $\tilde{\alpha}$ and $\tilde{\gamma}$ the following equations are obtained

$$\dot{\tilde{\gamma}} + \frac{\hbar q^2}{2m}\tilde{\alpha} = 0, \tag{44}$$

$$-4\hbar\dot{\tilde{\alpha}} + \tilde{\gamma}\left[\frac{\hbar^2 q^2}{m}\left(\frac{24}{5x^2} + 2\right) + n_0 e^2 \frac{32\pi}{q^2} + e^2 q\zeta(x)\right] = 0. \tag{45}$$

We assume harmonic time dependence for the variables $\tilde{\alpha}$, and $\tilde{\gamma}$ ($\ddot{\tilde{\alpha}} = -\omega^2\tilde{\alpha}$). Requiring that the determinant of the 2×2 matrix associated to the equations (44) and (45) for a normal mode is zero we obtain

$$\omega_1^2 = \frac{\hbar^2 q^4}{m^2}\left(\frac{3}{5x^2} + \frac{1}{4}\right) + n_0 e^2 \frac{4\pi}{m} + \frac{1}{8m}e^2 q^3 \zeta(x). \tag{46}$$

In Eq. (46) the term with coefficient 3/5 is due to the kinetic energy and is the same which we have obtained from the Vlasov equation making the polynomial approximation with $N = 1$ (see Eq. (29)). The term with coefficient 1/4 is also related to the kinetic energy but has quantum origin since it does not appear if we make the semiclassical approximation leading to the Vlasov equation. Instead of the term with coefficient F_0 (see Eq. (29)) which is connected with the local short range interaction, we now find different contributions since we are considering a long range interaction. We find a direct term ($4\pi n_0 e^2/m$) associated with the Coulomb interaction, which also appears in the semiclassical limit and additionally we have an exchange contribution ($e^2 q^3 \zeta(x)/8m$) which obviously does not appear if we consider the semiclassical limit. In the semiclassical limit one finds the following expression for the frequency,

$$(\omega_1^2)_{CL} = \frac{3\hbar^2 q^4}{5m^2 x^2} + n_0 e^2 \frac{4\pi}{m}. \tag{47}$$

In fig. 2 we plot $\hbar\omega_1$ as a function of q^2. The continuous line refers to the quantum result as given by Eq.(46), the dashed line refers to the semiclassical result given by Eq. (47) and the dots are the experimental points[6]. We incorporate band effects through an effective band mass m^* and the ionic polarizability by means of an ionic dielectric constant ϵ. We use $\epsilon = 1.05$ and $m^* = 1.05$ a.u., obtained from the calculated shifts of the plasmon energies at $q = 0$ due to the inhomogeneity and core polarization effects by Sturm[7].

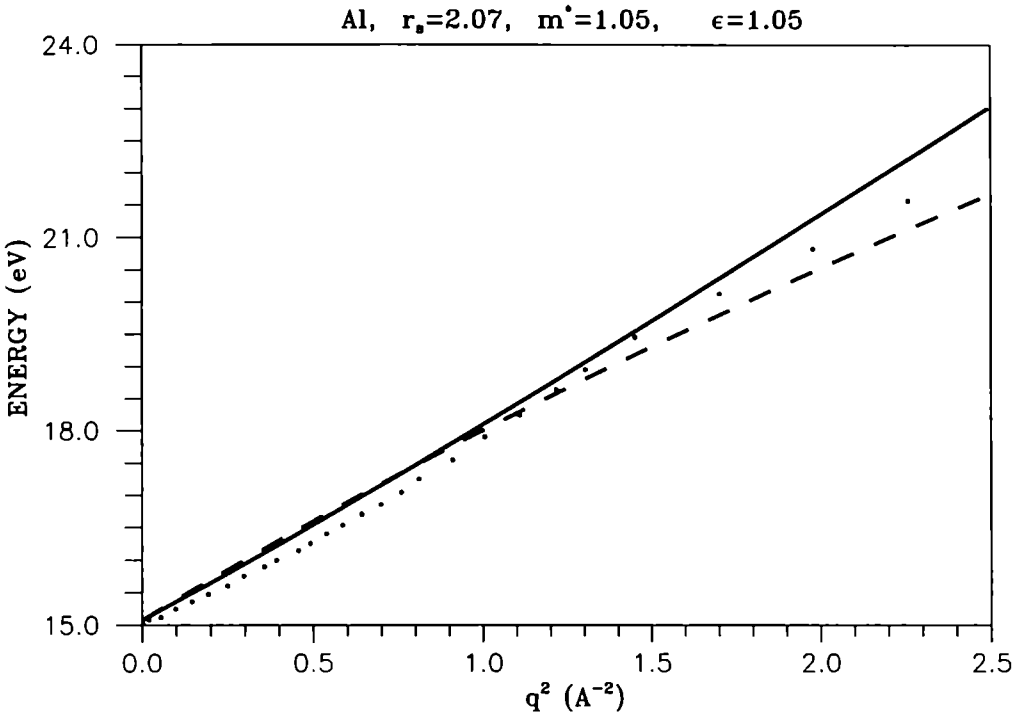

Figure 2: Quantum (full line) and semiclassical results (dashed line) for the bulk dispersion relation for aluminium (r_s = 2.07) obtained from Eqs. (46) and (47) compared with the experimental data from ref.[6] (dots).

The transition probability corresponding to the only eigenmode is characterized by the quantities $\overline{\alpha}^{(1)}$ and $\overline{\gamma}^{(1)}$ which are obtained from the equations (44) and (45) and from the normalization condition (56). As we will see in the next section this eigenmode satisfies the linear energy weighted sum rule (m_1) and the cubic energy weighted sum rule (m_3). As only one eigenmode is obtained within this parametrization it follows that $\hbar\omega_1 = \sqrt{m_3/m_1}$.

4. Sum Rules

We consider again Eq. (37). If a general variation of the one-body operator S is performed, the following equation is obtained

$$i\hbar < \phi_0|[\delta S, \dot{S}]|\phi_0 >=< \phi_0|[\delta S, [H, S]]|\phi_0 > . \tag{48}$$

In general a one-body operator may be expanded in the normal modes

$$S = \sum_r \left(\eta_r \Theta_r e^{i\omega_r t} + \eta_r^* \Theta_r^\dagger e^{-i\omega_r t}\right), \tag{49}$$

where the operators Θ_r are normalized according to the condition

$$< \phi_0|[\Theta_r, \Theta_s^\dagger]|\phi_0 >= \delta_{rs}. \tag{50}$$

Then, if we replace in Eq. (48) δS, which is arbitrary, by the expansion (49) we obtain the energy weighted sum rule,

$$\sum_r \hbar\omega_r |\eta_r|^2 = \frac{1}{2} < \phi_0|[S,[H,S]]|\phi_0 >, \tag{51}$$

where the quantities η_r are interpreted as the transition amplitudes $(r|S|0)$.

In our model we are considering a restricted RPA and therefore our equations of motion are not obtained by requiring an arbitrary variation of the generator S, but instead, we consider a restricted variation of the action integral which is achieved by performing arbitrary variations of the collective coordinates α and γ. We obtain for each value of the transferred momentum $\vec{q}$ one eigenmode which is characterized by the generator S_1 specified by $\alpha^{(1)}$, and $\gamma^{(1)}$. We present the energy weighted sum rule for two types of excitation operators, $G = \sum_i [\vec{p}_i \cdot \vec{q} \sin(\vec{q} \cdot \vec{x}_i) + \sin(\vec{q} \cdot \vec{x}_i)\vec{p}_i \cdot \vec{q}]$ and $D = \sum_i \cos(\vec{q} \cdot \vec{x}_i)$. The operators D and G are proportional to the generators Q and P. We will prove that, for these specific generators, the equation (51) is fulfilled where the sum on the l.h.s. now only refers to one eigenmode. We refer to such an equation as the energy weighted sum rule and the coefficients of the expansion of the excitation operator in the generators which correspond to the eigenmodes are interpreted as the transition amplitudes. To prove the results concerning the sum rules we have to resort to the equations of motion for the collective variables.

It is convenient to express the normalization condition in terms of the variables α and γ. Therefore we assume a time dependence of the form

$$\tilde{\gamma}(t) = \overline{\gamma}^{(1)} \sin(\omega_1 t + \lambda_1), \tag{52}$$

and

$$\tilde{\alpha}(t) = \overline{\alpha}^{(1)} \cos(\omega_1 t + \lambda_1). \tag{53}$$

This implies that for the generators P and Q we have

$$P(t) = \overline{P}^{(1)} \sin(\omega_1 t + \lambda_1), \tag{54}$$

$$Q(t) = \overline{Q}^{(1)} \cos(\omega_1 t + \lambda_1). \tag{55}$$

In order to impose the normalization analogous to Eq. (50) we express the normalization condition as follows

$$\overline{\alpha}^{(1)}\overline{\gamma}^{(1)} = -\frac{1}{2N}, \tag{56}$$

which implies that

$$< \phi_0|[\overline{P}^{(1)}, \overline{Q}^{(1)}]|\phi_0 >= 2i. \tag{57}$$

We will now show that the present model satisfies the sum rules m_1 and m_3 associated with the operator

$$D = \sum_{j=1}^{N} (\exp(i\vec{q}\cdot\vec{x}_j) + \exp(-i\vec{q}\cdot\vec{x}_j)). \tag{58}$$

The operator D is proportional to $\overline{Q}^{(1)}$

$$D = c_1 \overline{Q}^{(1)}. \tag{59}$$

In Eqs. (52) and (53) λ_1 is taken to be zero in agreement with the initial condition $Q(0) = D$ and $P(0) = 0$ (this means $S(0) = D$). From the orthogonality relation (57) it follows that

$$< \phi_0|[\overline{P}^{(1)}, D]|\phi_0 >= 2ic_1 = -i4N\overline{\gamma}^{(1)}. \tag{60}$$

Therefore,

$$c_1 = -2N\overline{\gamma}^{(1)}. \tag{61}$$

We note that the coefficient c_1 represents the transition amplitude $(1|D|0)$. For t=0 we find

$$\begin{aligned} m_1 \equiv \frac{1}{2} < \phi_0|[D,[H,D]]|\phi_0 >= \frac{1}{2}c_1 < \phi_0|[D,[H,\overline{Q}^{(1)}]]|\phi_0 > \\ = N\frac{\hbar^2}{m}q^2 c_1 \overline{\alpha}^{(1)} = N\frac{\hbar^2}{m}q^2 c_1 \tilde{\alpha}^{(1)} = -N\frac{\hbar^2}{m}q^2 c_1 \left(\frac{2m}{\hbar q^2}\right)\dot{\tilde{\gamma}}^{(1)} \\ = -2Nc_1\hbar\omega_1^{(1)}\overline{\gamma} = \hbar\omega_1 c_1^2. \end{aligned} \tag{62}$$

We have proved that the sum rule m_1 (Energy Weighted Sum Rule) is fulfilled. We have used the following relations, $\tilde{\alpha}^{(1)}(0) = \overline{\alpha}^{(1)}$, and $\dot{\tilde{\gamma}}^{(1)}(0) = \omega_1\overline{\gamma}^{(1)}$. The equations (44) and (61) were taken into account.

We will now be concerned with the sum rule m_3 (Cubic EWSR). We consider $\lambda_1 = \pi/2$ in agreement with the initial conditions $Q(0) = 0$ and $P(0) = G$ (therefore $S(0) = G$) where

$$G = i\frac{m}{2\hbar^2}[H, D]. \tag{63}$$

We consider the expansion

$$G = d_1 \overline{P}^{(1)}, \tag{64}$$

where the coefficients d_1 are obtained from the orthogonality relation (57). We have

$$< \phi_0|[G, \overline{Q}^{(1)}]|\phi_0 >= 2id_1 = -iNq^2\overline{\alpha}^{(1)}, \tag{65}$$

and therefore the coefficient d_1 is

$$d_1 = -\frac{1}{2}q^2 N\overline{\alpha}^{(1)}. \tag{66}$$

Then we find, also for t=0, that

$$m_3 \equiv -\frac{1}{2} < \phi_0|[[H,D],[H,[H,D]]]|\phi_0 >$$

$$= \frac{1}{2}\left(\frac{2\hbar^2}{m}\right)^2 < \phi_0|[G,[H,G]]|\phi_0 >= \frac{1}{2}\left(\frac{2\hbar^2}{m}\right)^2 d_1 < \phi_0|[G,[H,\overline{P}_1]]|\phi_0 >$$

$$= \frac{1}{2}\left(\frac{2\hbar^2}{m}\right)^2 \frac{N}{4} d_1 q^2 \tilde{\gamma}^{(1)} \left[\frac{\hbar^2 q^2}{m}\left(\frac{24}{5x^2}+2\right) + n_0 e^2 \frac{32\pi}{q^2} + e^2 q \zeta(x)\right]$$

$$= \left(\frac{2\hbar^2}{m}\right)^2 \frac{N}{2} d_1 q^2 \hbar \dot{\bar{\alpha}}^{(1)} = -\left(\frac{2\hbar^2}{m}\right)^2 \frac{N}{2} d_1 \hbar q^2 \omega_1 \overline{\alpha}^{(1)} = \left(\frac{2\hbar^2}{m}\right)^2 \hbar\omega_1 d_1^2. \qquad (67)$$

We have used the following relations, $\tilde{\gamma}^{(1)}(0) = \overline{\gamma}^{(1)}$ and $\dot{\bar{\alpha}}^{(1)}(0) = -\omega_1 \overline{\alpha}^{(1)}$. The equations (45) and (66) were taken into account. We now consider Eq. (44) in order to relate the coefficients d_1 and c_1. From Eqs. (44), (52) and (53) it follows that

$$\omega_1 \overline{\gamma}^{(1)} + \frac{q^2\hbar}{2m}\overline{\alpha}^{(1)} = 0, \qquad (68)$$

Thus, from Eqs. (61), (66) and (68) we have

$$d_1 = -\frac{m}{2\hbar}\omega_1 c_1. \qquad (69)$$

Finally we obtain the m_3 sum rule

$$m_3 \equiv \frac{1}{2} < \phi_0|[[H,D],[H,[D,H]]]|\phi_0 >= (\hbar\omega_1)^3 c_1^2 \qquad (70)$$

We remark that Eq. (67) may also be regarded as the m_1 sum rule corresponding to the transition operator $(2\hbar^2/m)G = i[H,D]$. Then d_1 is the corresponding transition amplitude.

5. Semiclassical Description of Collective Modes in a Finite Fermi System

We are interested in applying the variational formalism to study the collective modes in a finite system, such as an atomic nucleus or a metal cluster. Since we are considering small amplitude vibrations around the equilibrium state we have first to derive the equilibrium condition.

As an example of a finite system we consider an atomic nucleus at finite temperature T. To describe this system we consider effective local short range forces which are consistent with equilibrium properties such as the binding energy, nuclear matter compressibility and the nuclear matter equilibrium density. Since we are considering the classical limit only the lowest order terms in an expansion of the energy in powers of $\hbar$ are taken into account. Therefore, we are neglecting terms with derivatives of the density in the energy density for the equilibrium state. Such a choice implies that the

equilibrium density is constant inside the boundaries of the system. Since the terms with derivatives of the density are responsable for a surface energy, we additionally include by hand a surface tension σ.

As a trial distribution function we consider a Fermi type distribution function,

$$f = \frac{\Theta(R-r)}{1+\exp[(\frac{p^2}{2m}-\zeta)/T]}. \tag{71}$$

where $\zeta = \mu - U$, being $U = \sum_{\nu=2,3} a_\nu \nu \rho^{\nu-1}$ the potential energy. Starting from the distribution function f the density ρ and the kinetic energy density τ are computed,

$$\rho = g\int \frac{d^3p}{(2\pi\hbar)^3} f, \tag{72}$$

$$\tau = g\int \frac{d^3p}{(2\pi\hbar)^3} f\frac{p^2}{2m}. \tag{73}$$

We find the following expression for the energy,

$$E[f] = \frac{4\pi}{3}R^3(\tau + \sum_{\nu=2,3} a_\nu \rho^\nu) + \sigma 4\pi R^2, \tag{74}$$

where we have assumed a spherical shape (R stands for the nuclear radius). The parameter ζ in Eq. (71) is a constant macroscopic parameter. If in (71) we replace the parameter ζ by a field $\zeta(\underline{x},t)$ and R by a function $R(\theta,\phi)$ of the angles θ and ϕ, the distribution f will describe a non-equilibrium state.

The equilibrium condition is obtained if the free energy $F = E - TS$ is minimized with respect to ζ and R taking into account the subsidiary condition $\int d^3x\rho = A$. Allowing for a variation of ζ and also for a displacement of the surface, we have

$$\int_V d^3x\delta\zeta[\frac{\partial\tau}{\partial\zeta} + \frac{\partial\rho}{\partial\zeta}(\sum_\nu a_\nu\nu\rho^{\nu-1} - \mu) - T\frac{\partial s}{\partial\zeta}]$$
$$+ \oint_\Sigma d\Sigma\delta\underline{R}\cdot\hat{\underline{n}}(\tau + \sum_\nu a_\nu\rho^\nu + \frac{2\sigma}{R} - \mu\rho - Ts) = 0, \tag{75}$$

where V is the domain $r \le R$, Σ the boundary of V and s is the entropy density. The Lagrange multiplier μ assures the conservation of the particle number. Allowing for arbitrary variations $\delta\zeta$ and $\delta\underline{R}\cdot\hat{\underline{n}}$ we find two equations,

$$[\frac{\partial\tau}{\partial\zeta} + \frac{\partial\rho}{\partial\zeta}(\sum_\nu a_\nu\nu\rho^{\nu-1} - \mu) - T\frac{\partial s}{\partial\zeta}]_{\zeta=\zeta_0} = 0, \tag{76}$$

$$[\tau + \sum_\nu a_\nu\rho^\nu + \frac{2\sigma}{R} - \mu\rho - Ts]_{r=R} = 0. \tag{77}$$

From the Eqs. (76) and (77) and knowing the particle number we determine the chemical potential μ and also the radius R. Therefore we have evaluated the distribution function which determines the equilibrium state. Any distribution function which may be obtained from f_0 by means of a canonical transformation should lead to a higher energy. The static Vlasov equation,

$$\{f_0, h_0\} = 0, \tag{78}$$

is trivially satisfied since f_0 is a function of h_0.

The time dependent distribution function f describing some type of motion of the system is related with the equilibrium distribution function f_0 by means of a time dependent canonical transformation,

$$f = f_0 + \{f_0, \mathcal{G}\} + \frac{1}{2}\{\{f_0, \mathcal{G}\}, \mathcal{G}\} + ... \tag{79}$$

Therefore the time dependent generator $\mathcal{G}$ determines the type of motion that the system is undergoing. Such a generator appears as a solution of the Vlasov equation. Since we will be considering small amplitude vibrations we will be concerned with the linearized Vlasov equation which may be derived from the following lagrangian[12],

$$L^{(2)} = \frac{1}{2}\int d\Gamma_1 f_0(1)\{G(1), \dot{G}(1)\} - \frac{1}{2}\int d\Gamma_1 f_0(1)\{G(1), \{G(1), h_0(1)\}\}$$
$$-\frac{1}{2}\int d\Gamma_1 \int d\Gamma_2 \{f_0(1), G(1)\}_1 \{f_0(2), G(2)\}_2 v(1,2). \tag{80}$$

If we allow for arbitrary variations of $\mathcal{G}$ the following equation is obtained

$$\{f_0(1), \dot{\mathcal{G}}(1)\} + \{\{f_0(1), \mathcal{G}\}, h_0(1)\} + \{f_0(1), \int d\Gamma_2 v(1,2)\{f_0(2), \mathcal{G}(2)\}_2\}_1 = 0, \tag{81}$$

which is the linearized Vlasov equation for $\delta f = \{f_0, \mathcal{G}\}$,

$$\delta\dot{f}(1) + \{\delta f(1), h_0(1)\} + \{f_0(1), \int d\Gamma_2 v(1,2)\delta f(2)\} = 0. \tag{82}$$

The Vlasov equation is not easy to solve. We use approximation methods based on the variational principle related to the lagrangian (80). The variational approach allows for a systematic improvement of the approximation procedure, according to the variational choices for the generator $\mathcal{G}$. On the other hand such a procedure may be controled by relevant sum rules which are fulfilled by the approximate eigenmodes.

The generator $\mathcal{G}$ may be decomposed into a time-even part Q and a time-odd part P,

$$\mathcal{G}(\vec{x}, \vec{p}, t) = Q(\vec{x}, \vec{p}, t) + P(\vec{x}, \vec{p}, t) \tag{83}$$

$$Q(\vec{x}, -\vec{p}, t) = Q(\vec{x}, \vec{p}, t) \tag{84}$$

$$P(\vec{x}, -\vec{p}, t) = -P(\vec{x}, \vec{p}, t) \tag{85}$$

The approximate procedure consists in considering restricted variational spaces for the generator $\mathcal{G}$ and to obtain approximate solutions by means of the variational principle. Within this spirit several variational ansatzes for the generator $\mathcal{G}$ have been explored,

$$P + Q = \psi(\vec{x},t) + p_\alpha s_\alpha(\vec{x},t) + \frac{1}{2}p_\alpha p_\beta \phi_{\alpha\beta}(\vec{x},t) + \frac{1}{6}p_\alpha p_\beta p_\gamma \theta_{\alpha\beta\gamma}(\vec{x},t) + ... \qquad (86)$$

In sections 2 and 3 we have given explicit expressions for both the generators P and Q. Such a method has been followed in refs.[1,5,8,9,10,11]. As an alternative we may define explicitly the generator Q and implicitly the generator P through a parametrization of the distribution function. A variational scheme which allows for the introduction of transverse components in the current is considered. A large fragmentation of the strength is obtained if a parametrization by means of a scalar field $\psi(\vec{x},t)$ and a tensor field $\phi_{\alpha\beta}(\vec{x},t)$ is chosen for the generator Q,

$$Q = \psi(\vec{x},t) + \frac{1}{2}p_\alpha p_\beta \phi_{\alpha\beta}(\vec{x},t), \qquad (87)$$

while P is the generator of a canonical transformation such that the following equation is approximately satisfied

$$f_0 + \{f_0, P\} + \frac{1}{2}\{\{f_0, P\}, P\} + ... = \frac{\Theta(R_0 + R_1(\theta,\phi,t) - r)}{1 + \exp[(\frac{p^2}{2m} - \varsigma_0 - \varsigma_1(\vec{x},t) + \frac{p_\alpha p_\beta}{2m}\chi_{\alpha\beta}(\vec{x},t))/T]}. \qquad (88)$$

In table 1 we give the energies (in MeV) and the percentages of the sum rule m_1 corresponding to different electric eigenmodes for a nucleus with A=208. These results refer to the model of ref.[13] which is based on the equations (87) and (88). We have considered a potential energy density of the form $u = a_2\rho^2 + a_{2+1/6}\rho^{2+1/6}$ where $a_2 = -(3/8) \times 3075.8$ MeV fm^3, and $a_{2+1/6} = (1/16) \times 20216.4$ MeV fm$^{3+1/2}$. Since the surface of the nucleus becomes more diffuse when the temperature increases, we assume that the surface tension σ decreases with temperature according to $\sigma(T) = \sigma(0)(1 - aT^2)$ (see ref.[15]), where $\sigma(0) = 1.0$ MeV fm^{-2} and $a = 6 \times 10^{-3}$ MeV^{-2}. We have considered the transition operators $D(\vec{x}) = r^2$ for $\ell = 0$ and $D(\vec{x}) = r^\ell Y_{\ell 0}$ for $\ell > 1$.

This scheme has been studied in refs.[12,13,14]. As a remark we note that from Eqs. (87) and (88) a simpler scheme may be considered if we neglect the tensor fields $\phi_{\alpha\beta}$ and $\chi_{\alpha\beta}$. This variational scheme has been studied in ref.[16] and leads to the equations of motion which characterize the liquid drop model[17,18], since it assumes a local equilibrium assumption for the time-even distribution function.

Table 1: Energies (in MeV) and percentages of the energy weighted sum rule are given (for different values of the temperature T) for the electric modes listed in the first column and calculated according to the model of ref.[13]. A nucleus with A=208 was considered.

	T=0 MeV		T=3 MeV		T=5 MeV	
ℓ^π	$\hbar\omega_i$	m_1 [%]	$\hbar\omega_i$	m_1 [%]	$\hbar\omega_i$	m_1 [%]
0_1^+	—	—	13.62	9.752	12.90	23.13
0_2^+	15.87	95.15	15.65	84.05	15.25	68.07
0_3^+	18.95	2.256	18.75	3.566	18.16	6.261
0_4^+	—	—	26.62	4.789×10^{-1}	25.13	6.550×10^{-1}
0_5^+	28.14	2.838×10^{-1}	28.46	4.940×10^{-2}	27.86	5.977×10^{-2}
0_6^+	36.83	3.428×10^{-1}	36.39	2.801×10^{-1}	35.02	2.496×10^{-1}
2_1^+	3.473	30.90	3.641	35.23	3.810	40.73
2_2^+	11.70	64.19	11.99	59.55	12.33	53.00
2_3^+	17.45	2.165	17.28	2.525	16.80	3.680
2_4^+	20.54	1.094	20.53	1.209	20.40	1.213
2_5^+	21.12	1.002	21.36	8.183×10^{-1}	21.70	6.560×10^{-1}
2_6^+	—	—	24.75	9.638×10^{-5}	23.49	6.407×10^{-3}
3_1^-	2.923	34.10	2.960	37.24	2.931	40.95
3_2^-	8.428	2.879×10^{-4}	8.724	6.333×10^{-3}	9.083	2.035×10^{-1}
3_3^-	18.53	43.44	18.72	38.08	18.73	27.93
3_4^-	22.80	10.88	22.68	13.58	22.37	20.00
3_5^-	25.15	3.847	25.43	3.428	25.81	2.916
3_6^-	26.87	5.178	26.99	5.300	27.02	5.185
3_7^-	—	—	29.65	1.958×10^{-1}	28.03	3.874×10^{-1}
4_1^+	4.505	33.85	4.581	37.45	4.557	41.78
4_2^+	12.26	2.046	12.62	1.008	13.07	2.428×10^{-1}
4_3^+	23.36	22.39	23.35	18.16	22.96	11.97
4_4^+	27.64	8.859	27.78	11.82	27.89	16.63
4_5^+	29.67	17.10	29.90	15.22	30.21	11.96
4_6^+	33.45	8.450	33.49	4.588	32.13	2.033×10^{-3}
4_7^+	35.38	4.184	34.43	7.182	34.10	10.27
4_8^+	—	—	36.21	1.434	35.46	3.949
5_1^-	6.208	33.18	6.319	36.88	6.293	41.41
5_2^-	15.82	2.880	16.23	1.667	16.74	6.312×10^{-1}
5_3^-	27.24	13.11	27.13	10.64	26.54	7.286
5_4^-	31.63	2.676	31.93	3.661	32.29	5.602
5_5^-	34.76	22.45	34.92	20.41	34.92	14.16
5_6^-	38.96	3.778×10^{-6}	38.27	7.887×10^{-1}	36.55	4.140
5_7^-	40.75	20.08	40.70	5.370	39.72	1.855×10^{-1}
5_8^-	—	—	41.17	15.01	41.38	20.93

6. Conclusion

Semiclassical methods are a possible way of studying collective modes in many body systems. In such methods the dynamics of the system is described by collective coordinates which should be conveniently chosen. Different types of generators and therefore different types of variational spaces may be considered. The chosen parametrization depends on the type of modes we are interested in describing.

The meanfield methods give good results because the force we use incorporates renormalization effects. Indeed, our calculations are based on effective forces which reproduce equilibrium properties. On the other hand, the fact that we consider restricted generators implies that we have a discrete set of eigenmodes which simulate a quantal situation. In this way we compensate for the semiclassical approximations. Finite systems exhibit discrete spectra.

Semiclassical models are able to describe the main features of the cluster excitations, giving a good forecast of the excited energies, specially for larger systems, where microscopic calculations are almost impossible, and semiclassical aspects play a dominant role. Besides yielding the excitation energies and the exhausted fractions of the main sum rules these methods also bring a deeper insight on the physical processes responsable for the transitions since they yield the transition densities and the currents.

7. Acknowledgements

The author would like to thank Fundação Calouste Gulbenkian for financial support.

1. J.P. da Providência, *Nucl. Phys.* **A489** (1988) 111.
2. D. M. Brink and J. da Providência, *Nucl. Phys.* **A500** (1989) 301.
3. M. C. Nemes, A. F. R. de Toledo Piza and J. da Providência, *Physica* **146A** (1987) 282.
4. N. G. van Kampen, *Physica* **21** (1955) 949.
5. J. da Providência Jr. and N. Barberán, *Phys. Rev. B*45, 6935 (1992); J. da Providência Jr., *Solid State Communications* **86** 573 (1993).
6. J. Sprsser-Prou, A. vom Felde and J. Fink, *Phys. Rev.* **B40** 5799 (1989).
7. K. Sturm, *Z. Physik* **B29** 27 (1978).
8. K. Andō and S. Nishizaki, *Prog. Theor. Phys.* **68** (1982) 1196.
9. J.P. da Providência, *Prog. Theor. Phys.* **75** (1986) 862.
10. J. da Providência Jr. and R. de Haro Jr., *Phys. Rev.* **B49** 2086 (1994).
11. J. P. da Providência and G. Holzwarth, *Nucl. Phys.* **A398** (1983) 59; J.P. da Providência, J. Phys. **G13** (1987) 783.
12. J. da Providência, L. Brito and C. Providência, *Nuovo Cimento* **87** (1985) 248.
13. J. da Providência Jr. *Nucl. Phys.* **A582** (1995) 23.

14. L. Brito and C. da Providência, *Phys. Rev.* **C32** (1985) 2049; L. Brito, *Phys. Lett.* **B177** (1986) 251; L. Brito, *Ph. D. Thesis* Coimbra 1986.
15. C. Guet, Strumberger and M. Brack, *Phys. Lett.* **B205** (1988) 427.
16. J. da Providência Jr., *Nucl. Phys.* **A523** (1991) 247.
17. G. Eckart, G. Holzwarth and J.P. da Providência, *Nucl. Phys.* **A364** (1981) 1.
18. A. Bohr and B. Mottelson, *Nuclear Structure* (Benjamin, NY, 1975) vol. 2, ch. 6A.

TRIAXIALITY IN ODD AND EVEN NUCLEI OF THE A=130 MASS REGION

P. VON BRENTANO, O. VOGEL, I. WIEDENHÖVER, R. KÜHN,
AND A. GELBERG
Institut für Kernphysik, Universität zu Köln
D-50937 Köln, Germany

ABSTRACT

Analogous low lying collective states in ^{125}Xe and ^{127}Xe are presented. Triaxial Rotor plus particle calculations for ^{125,127,129}Cs and the recently measured ^{129}La are examined. Effective γ–deformations are extracted for these nuclei from the calculations. For even-even nuclei of the $A \approx 130$ mass region the effective γ-deformation is calculated in the framework of the Rigid Triaxial Rotor Model and the Interacting Boson Model. Transition strengths in even Ba nuclei are interpreted in framework of Q–phonon scheme. The structure of 3_1^+ state in the IBM is discussed in the scheme.

1. Introduction

In recent years several investigations on the structure of odd and even nuclei in the $A \approx 130$ mass region have been made.[1–23] It has been shown that these nuclei show many different excitations corresponding to different shapes.[24] The rich spectrum of low lying positive parity states corresponds to shapes with a a near maximum triaxiality.[13,17,18] Core polarizations leading to prolate or oblate deformations occur due to broken proton and neutron quasi particle pairs.[24,25] In this work we will concentrate on the triaxial features of the low lying collective states in odd and even nuclei.

For the low lying collective levels in odd nuclei, Triaxial Rotor plus Particle (TRP) calculations have been performed for several neutron odd Xe and Ba nuclei[26,14] and for proton odd Cs and La nuclei.[15,30] The calculations for the neutron odd nuclei showed that these nuclei indeed display a triaxial deformation with $\gamma = 20° - 30°$. These values have the meaning of an effective triaxial deformation resulting from the averaging of the dynamical variable γ.[1,31] Another interesting question is whether the proton-odd nuclides of the same region are also triaxial. This is not at all obvious, since we have good reasons to believe that the odd-proton and the odd-neutron will polarize the even-even core in opposite ways.[24] In the present work we compare the low lying negative-parity states of proton-odd nuclei with TRP calculations and extract from the fit the values of the deformation parameters β and γ. Since the observable which is most sensitive to the γ deformation is the signature splitting, yrast states with both favoured and unfavoured signatures must be known.

For the even–even nuclei the collective low lying positive parity states are well described by the Interacting Boson Model (IBM),[32–34] the General Collective Model (GCM),[35] the Rotation Vibration Model (RVM),[36] the Fermion Dynamical Symmetry Model(FDSM),[37] or the Zelevinsky Model.[38] Typical for the structure of triaxial

nuclei, is the low lying quasi-γ-band.[9,10,39] It is possible to distinguish between γ–rigid and a γ–soft models by examining the odd–even staggering in the quasi-γ-band. This excludes a rigid triaxial deformation as in the Davydov–Fillipov Model.[39] This is consistent with the good description of these in nuclei by O(6) dynamical symmetry of the IBM,[8] which corresponds in its classical limit with the γ-unstable rotor of Wilets and Jean.[40] In order to get a better description of the nuclei investigated, one has to break the O(6) symmetry.[17,18] This can be done in the framework of the Consistent Q Formalism (CQF),[41]by introducing a non vanishing value for the parameter χ in the quadrupole operator Q if the IBM. This leads to two very interesting questions:

1. How strong is the effective triaxiality in these nuclei with (slightly) broken O(6) symmetry?

2. What is the structure of the wavefunctions of the collective states observed in these nuclei?

The first question can be answered by using an approach introduced by Elliott *et al.* [42] which allows to introduce an effective triaxial deformation for an IBM state. The results of this calculation will be compared with an earlier approach using the rigid triaxial rotor model. This calculation was performed for even–even Xe and Ba nuclei.[17,18] The second questions can be answered in the framework of the multiple Q–phonon scheme as introduced by T. Otsuka *et al.* .[43–46] It allows a consistent description of low lying positive parity collective yrast states in the whole model space of the IBM.

2. Analogous states in ^{125}Xe and ^{127}Xe

For the investigation of the structure of the nuclei, the in–beam–γ-spectroscopy allows two different approaches, namely *vertical* and *horizontal* spectroscopy:

Vertical spectroscopy:
The study of high spin near yrast states. In order to study the lifetimes in the ground and quasi-γ band fusion reactions with heavy projectiles are very useful. With such fusion reactions the identification of the yrast band in this region up to high spins e.g. $I = 34\hbar$ in ^{128}Ba and $I = 32\hbar$ in ^{126}Xe has been accomplished.

Horizontal spectroscopy:
The study of low spin states above the yrast line. The heavy ion induced fusion reactions are not very suitable for the spectroscopy of the low lying non yrast collective states however. Useful tools to investigate the non yrast collective states are fusion reactions with light projectiles as e.g. (p,n), (α, n), $(\alpha, 2n)$, and (^{13}C,3n) reactions which populate low spins levels far above the yrast line with reasonable cross sections.

A very good examples for the *horizontal* spectroscopy is a recent experiment, were excited states in ^{127}Xe were populated using the ^{125}Te(α,2n)^{127}Xe reaction at the Cologne FN Tandem accelerator with beam energies of 23, 25 and 27 MeV. The $\gamma\gamma$–coincidences were measured the Osiris-cube-spectrometer, equipped with 6 high-purity germanium detectors with asymmetrical anti-Compton-shields. Over 200 Million $\gamma\gamma$ events were acquired during 7 days of beam time and sorted in to $4k \times 4k$

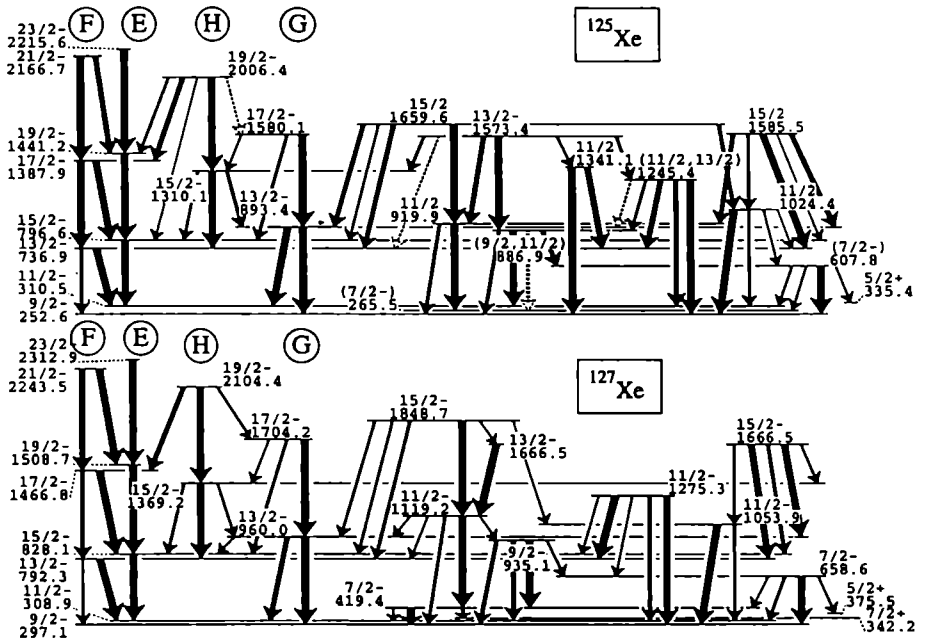

Fig. 1. Partial level scheme of negative parity states in ^{125}Xe(top) ,taken from[22] and ^{127}Xe(bottom).[21] The data of both nuclei are experiments of the Cologne group. The arrow widths are proportional to the branching ratios.

matrices. In the analysis of the data more than 300 transitions were found connecting 180 levels. This allowed us to expand the level scheme known from a previous experiment[47] by over 100 new levels. The spin and parity of the excited states and the multi-polarities of the γ–transitions was investigated with the angular correlation intensities of the coincidence experiment and with a separate angular distribution experiment. Furthermore, the side-feeding–cross section was analyzed from $\gamma\gamma$ coincidence spectra at the 3 beam energies and used for the spin assignments as well.

The resulting spectrum of negative parity levels of ^{127}Xe and their branched γ–decay are compared in fig. 1 with the corresponding data of ^{125}Xe.[22] The results of Urban et al.[47] for ^{127}Xe, which cover the Yrast and Yrare bands (E,F,G,H) could be confirmed. A curious feature found in our experiment is the existence of two states at 1666.5 keV with spins $13/2^-$ and $15/2^-$. Within an uncertainty of $\approx$ 0.1 keV no energy difference could be observed, but the branching ratios and the unambiguous spin assignments from the angular correlation analysis imply two separate states.

One notes a striking similarity of the two level spectra, which is a clear indication for the collective character of the observed levels. The favoured and unfavoured Yrast Bands (E,F) show a similar 'decoupled' staggering pattern for both nuclei ^{125}Xe and ^{127}Xe. The branching ratios of the unfavoured Yrast band are slightly weaker for the in-band E2 transitions in ^{127}Xe. The branchings of the Yrare Bands (G,H) are very similar for both nuclei.

Quite clearly the similarity goes much beyond the Yrast and Yrare bands. The spectrum of both nuclei are very rich. It contains four $11/2^-$, and $15/2^-$ states, three $13/2^-$ and two $7/2^-$ and $9/2^-$ states. One interesting feature is the decay of the individual $7/2_2^-$ states in both nuclei. Even the weak decay to the positive parity $5/2_1^+$ state exists with about the same branching in both nuclei.

In establishing the detailed similarity of the two decay schemes one has to consider besides the excitation energies also the decay branching. As an example we associate the $11/2_2^-$ state at 919.9 keV in ^{125}Xe and the $11/2_3^-$ state at 1119.2 keV in ^{127}Xe, which both show a dominant branching towards the $7/2_1^-$ state. In both nuclei, the $15/2_4^-$ state decays mainly towards these $11/2^-$ states. Furthermore we compare the $11/2_2^-$ state at 1024.4 keV in ^{125}Xe and the corresponding $11/2_3^-$ state at 1053.9 keV in ^{127}Xe, which have a dominant decay to the individual $9/2_1^-$ states.

In[22] the different decay patterns of the $11/2^-$ states could be reproduced for ^{125}Xe by the RTRP and IBFM model calculations. It was attributed to the the γ–soft character of the core. The band–like decay of the $15/2_4^-$ state could however not be reproduced by either of the models, although it seems to be an important feature of the collective non-yrast excitations and exists in both nuclei.

The analogous character of the spectra is a challenge for the theoretical collective models, as it implies the collective nature of the newly established Non-Yrast states, which thus should be within reach of the simple "core plus particle" picture.

3. TRP description of proton odd La and Cs nuclei

In the Triaxial Rotor plus Particle Model the particle moves in a mean field produced by a core with fixed triaxial deformation characterized by the deformation parameters ϵ and γ.[27] Since the model has been previously described in detail[28,29] we will give here only a brief review.

The Hamiltonian of the coupled system is

$$\begin{aligned} H &= H_{sp} + H_{pair} + H_{rot} \\ &= H_{sp} + H_{pair} + \sum_k \frac{\hbar^2}{2}\Theta_k(I_k - j_k)^2 \end{aligned} \tag{1}$$

where Θ_k are the moments of inertia and I_k and j_k are the projections on the intrinsic quantization axis of the total and particle angular momenta respectively. The moments of inertia are given by the hydrodynamic formula (see eq. 4 below). The interaction between particle and rotational motion contained in H_{rot} can be decomposed into the Coriolis term $-\sum_k I_k j_k/\Theta_k$ and the recoil term $\sum_k j_k^2/2\Theta_k$. The Coriolis interaction can be modified by the so called Coriolis attenuation factor ξ.

A particular aim of the Triaxial Rotor plus Particle (TRP) calculations done by the Cologne group was to describe the negative-parity yrast states of the proton-odd nuclei with TRP calculations and to extract the values of the deformation parameters ϵ and γ for these nuclei. Since the observable which is most sensitive to the γ deformation is the signature splitting, yrast states with both favoured and unfavoured

Table 1. Parameters used in the calculations. (ϵ, γ) are the deformation parameters, ξ is the Coriolis attenuation factor, A00 is an inertial factor, #orb gives the number of orbits in the deformed potential used for the TRP calculation and GSFAC is the spin quenching factor.

	^{125}Cs	^{127}Cs	^{129}Cs	^{129}La
ϵ	0.26	0.22	0.20	0.255
γ	21°	22°	22°	16
ξ	1.0	1.0	1.0	0.8
A00	0.0335	0.0375	0.0425	0.0270
#orb	7-21	7-21	7-21	7-21
GSFAC	1.0	0.9	1.0	1.0

signatures must be known. Besides the nucleus ^{129}La, which has been recently investigated in Cologne.[30] we also choose to investigate the nuclei ^{125,127,129}Cs which have been recently investigated by the group of D. Fossan at Stony Brook. The used parameters of the TRP calculation are given in table 1.

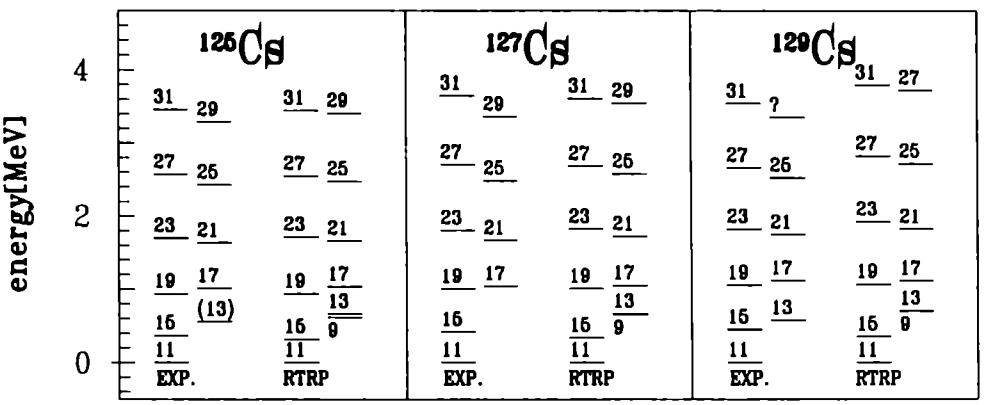

Fig. 2. Experimental and TRP calculated negative parity yrast states for ^{125,127,129}Cs. The experimental data are from Stony Brook. They were taken from ref..[48-52]

The results of our calculations are shown in fig. 3 for the negative parity states in ^{129}La. In fig. 2 the yrast bands of ^{125}Cs,[48,49,52] ^{127}Cs[50] and ^{129}Cs[51] are shown. As one can see, the agreement with the experimental data is quite good: in particular the staggering between the favored and unfavored bands, which depends strongly on γ, is quite well reproduced. One also notes that the staggering is very similar in all three nuclei, the $13/2^-$ level is well above the $15/2^-$ one , the $17/2^-$ and the $19/2^-$ levels are nearly degenerated, and for higher spins the unfavored states lies below the next favored states (e.g the $25/2^-$ level below the $27/2^-$ one). One can see in fig. 3, that the overall reproduction of the bands in ^{129}La by the TRP is quite good, although the staggering in the lower part of the the band is not well reproduced. While the fitted

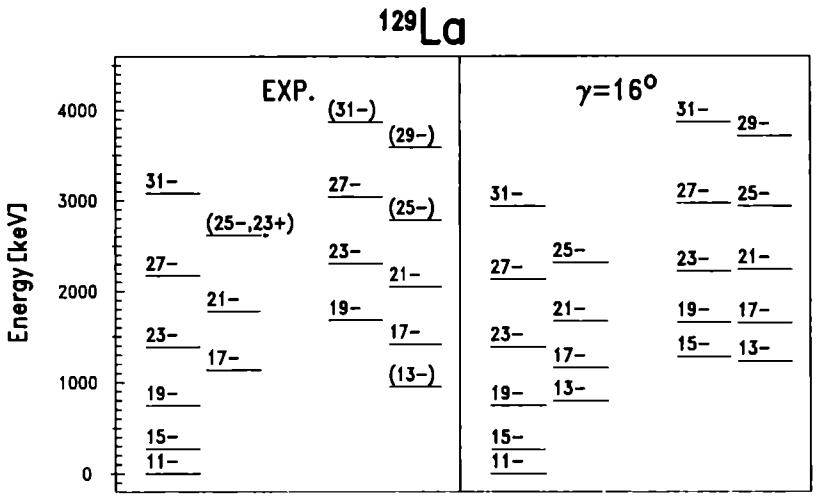

Fig. 3. Experimental and TRP calculated negative parity states for ^{129}La. The experimental data are from Cologne and were taken from ref..[30]

γ values for ^{125,127,129}Cs are rather similar, the value for ^{129}La $\gamma = 16°$ is definitely smaller. A convenient way to describe the staggering has been introduced by Zamfir and Casten[10] by the following function $S(I)$:

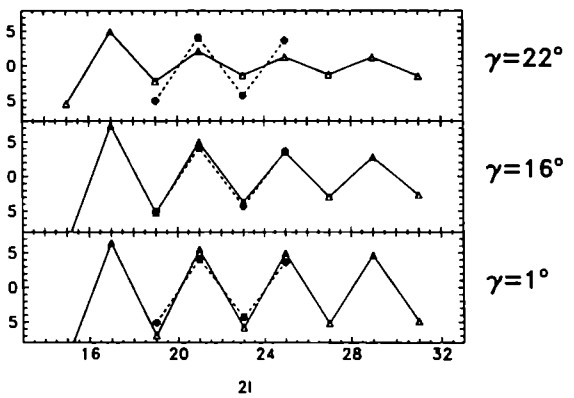

Fig. 4. Experimental signature splitting $S(I)$ for ^{129}La compared with the theoretical one for $\gamma = 1, 16, 22°$.

$$S(I) = \frac{E(I) - E(I-1)}{E(I) - E(I-2)} \frac{I(I+1) - (I-2)(I-1)}{I(I+1) - I(I-1)} - 1 \qquad (2)$$

In fig. 4 we have calculated the staggering function $S(I)$ of ^{129}La for several values of γ with the TRP model and compared them to the experimental values. One

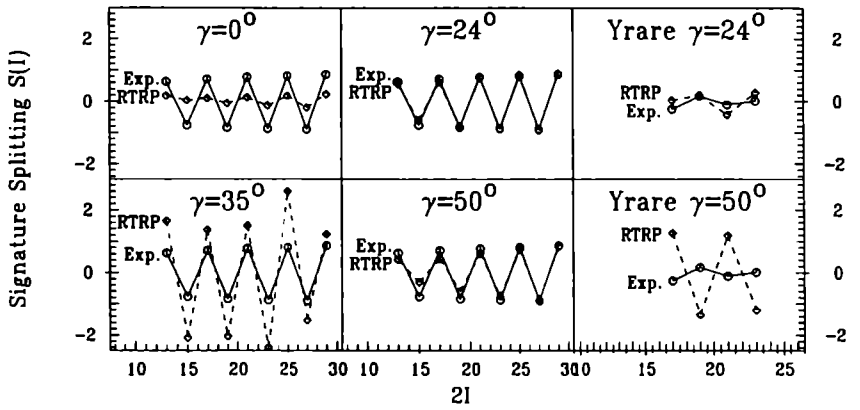

Fig. 5. Signature splitting S, as defined by eq. 4, versus spin calculated for a few γ values for yrast levels of ^{125}Xe versus the experimental data from the Cologne group. Also shown are signature splittings for yrare levels at $\gamma = 24°$ and $50°$.[26,22]

sees immediately that no fit can be obtained with an axially symmetric prolate core ($\gamma = 1°$), but also no fit is possible if we use the γ value of the ^{128}Ba core, which is about $22°$.[13] Our best result was for $\gamma = 16°$, as can be seen in fig. 4. This is a marked deviation from the value of $\gamma = 22°$.

Table 2. Some experimental and TRP calculated branching ratios in the yrast band of ^{129}La.[30]

Level			Energy		Branching	
I_i	→	I_f	E_i	E_γ	Exp	TRP
$17/2_1$	→	$15/2_1$	1305.1	862.9	100	100
	→	$19/2_1$		388.4	22(5)	18
$21/2_1$	→	$19/2_1$	1949.8	1033.0	100	100
	→	$17/2_1$		644.7	41(13)	15
	→	$23/2_1$		391.3	21(8)	12
$25/2_1$	→	$23/2_1$	2789.8	1231.4	100	100
	→	$21/2_1$		840.2	97(25)	41

4. Effective gamma deformation in even-even Xe and Ba nuclei

The experimental information accumulated in recent years has provided compelling evidence of dynamic triaxial deformation of transitional nuclei in the mass

region $A \approx 130$.[8] In this work we show two approaches to determine the effective γ–deformation of these nuclei. The first approach by Yan *et al.*[13] uses the rigid triaxial rotor model (RTRM) and the second one by Vogel *et al.*[17,18] which follows the suggestions by Elliott *et al.* [42] is based on the IBM.

A simple description of a nucleus whose shape deviates from axial symmetry is provided by the RTRM of A. Davydov and G. Filippov.[39] In this model the nucleus has a rigid shape characterized by definite values of the deformation parameters β and γ. On the contrary , the Interacting boson Model (IBM)[32] and the General Collective Model (GCM)[35] treat β and γ as dynamical variables. Even though the $O(6)$ symmetry provides only an approximate description of the considered nuclei , it constitutes a good reason to consider these nuclei as being gamma–soft. The RTRM constitutes an approximation in which the vibrational variables β and γ are replaced by fixed effective values.[31,53]

Nevertheless most properties of the ground and quasi-gamma bands can also be well described described by the RTRM. An exception are in particular the energy staggering in the quasi gamma band. The relationship between the IBM and the RTRM have been investigated in ref..[54] As shown above calculations of odd–A nuclei in this region by means of the TRP model have been quite successful. Roughly speaking, it seems that the value of γ which has to be used in the RTRM corresponds to the average value $< \gamma >$ of the wave-function of the IBM. The main aim of the present work is to see whether we can get a consistent set of (β,γ) deformation parameters for even–even Xe, and Ba nuclei by using the RTRM. For this purpose we will use the energies and decay properties of the ground bands and quasi-gamma bands as described by the RTRM.

The Hamiltonian of the RTRM can be written as

$$H = \frac{\hbar^2}{2}\Sigma\frac{I_i^2}{\Theta_i} \tag{3}$$

where I_i are the projections of the angular momentum on the intrinsic axes. The moments of inertia of the Davydov–Fillipov model are given by the hydrodynamical formula

$$\Theta_\kappa = \frac{4}{3}\Theta_0 \sin^2(\gamma - \frac{2\pi}{3}\kappa) \tag{4}$$

where Θ_0 depends only on β.

In the RTRM analytical formulas for reduced $E2$ transition probabilities from the $2^+_{1,2}$ states are given by

$$B(E2; 2^+_{1,2} \rightarrow 0^+_1) = \frac{1}{16\pi^2}Q_0^2(1 + (-)^{1,2}\chi(\gamma)) \tag{5}$$

and where

$$\chi(\gamma) = \frac{3 - 2\sin^2(3\gamma)}{\sqrt{9 - 8\sin^2(3\gamma)}} \tag{6}$$

Furthermore Q_0 is defined as in the axially symmetric case by the approximate relation

$$Q_0 = \frac{3}{\sqrt{5\pi}} Z R_0^2 \beta \tag{7}$$

which is valid to the first order in beta. The ratio of the two $B(E2)$ values from the two 2_2^+ state depends only on γ and it is independent of Q_0 and β. It is given by[39,59]

$$R_B(\gamma) = \frac{B(E2; 2_2^+ \to 2_1^+)}{B(E2; 2_2^+ \to 0_1^+)} = \frac{20}{7} \frac{\sin^2(3\gamma)}{9 - 9\sin^2(3\gamma) - (3 - 2\sin^2(3\gamma))\sqrt{9 - 8\sin^2(3\gamma)}} \tag{8}$$

This formula allows us to to determine the effective value of γ directly from the branched decay of the 2_2^+ state.

As stated above, the RTRM cannot reproduce all spectroscopic features of the even-even nuclei of this mass region. It thus seems appropriate to seek a more realistic description of these nuclei as e.g. the IBM model. A problem is that the parameters β and γ are not parameters of the IBM. Thus one has to devise a method by which one can define effective value $\langle\gamma\rangle$ $\langle\beta\rangle$ in the IBM.

In the approach of Elliott *et al.* ,[42] the following association between the invariants constructed from the quadrupole operator Q and the deformation parameters (β, γ) is proposed by analogy with the geometrical model[55]:

$$(Q \times Q)_{00} \quad \to \quad \beta^2/\sqrt{5}, \tag{9}$$

$$(Q \times Q \times Q)_{00} \quad \to \quad -\beta^3 \sqrt{\frac{2}{35}} \cos 3\gamma. \tag{10}$$

This allows to define an expectation value of $\cos 3\gamma$, by the following equation:

$$\langle \cos 3\gamma \rangle = -\sqrt{\frac{7}{2\sqrt{5}}} \frac{\langle (Q \times Q \times Q)_{00} \rangle}{\langle (Q \times Q)_{00} \rangle^{3/2}}. \tag{11}$$

So the effective γ deformation of the ground state is defined as

$$\gamma_{\text{eff}} = 1/3 \cdot \arccos \langle 0_1^+ | \cos 3\gamma | 0_1^+ \rangle. \tag{12}$$

In order to describe the Ba nuclides, we use the following simple Hamiltonian:

$$H = -\kappa Q(\chi) \cdot Q(\chi) + \kappa' L \cdot L, \tag{13}$$

with

$$Q_\mu = d_\mu^\dagger s + s^\dagger \tilde{d}_\mu + \chi (d^\dagger d)_{2\mu}, \tag{14}$$

was used. It allows us to interpolate to move between the O(6) limit ($\chi = 0$) and the SU(3) limit ($\chi = -\sqrt{7}/2$) of the IBM. In the consistent-Q formalism[41] (CQF) the same value of χ is used in the Hamiltonian and in the E2 transition operator. The resulting wave functions and transition rates are thus totally determined by the one

Table 3. Experimental B(E2) ratio R_B from refs.,[43,58,57] boson number N, deduced parameter χ, the derived values of $\gamma_{\rm eff}$ in the IBM ground state,[17,18] and the γ from the RTRM.[13]

Nucleus	^{124}Ba	^{126}Ba	^{128}Ba	^{130}Ba	^{132}Ba	^{134}Ba
R_B	6.0(14)	7.7(12)	8.8(3)	16.1(18)	35.7(64)	176(9)
N	10	9	8	7	6	5
χ	-0.189(38)	-0.189(20)	-0.209(5)	-0.181(11)	-0.150(14)	-0.088(3)
$\gamma_{\rm eff}$	19.4(15)°	20.4(8)°	20.7(2)°	22.8(4)°	24.8(5)°	27.3(1)°
$\gamma_{\rm RTRM}$	20.6(14)°	21.8(8)°	22.3(2)°	24.4(4)°	26.2(4)°	28.3(1)°

parameter χ and the boson number N. Due to our choice of the CQF Hamiltonian, the average γ deformation is a function of χ and N only.

In order to derive the parameter χ for a given nucleus we follow the same approach as above, deducing the parameter χ from the ratio R_B.

In the case of the IBM, R_B is a monotonous function of χ (for fixed N) and can be used to determine the parameter χ. In table 1 the values for the parameter χ are given together with the effective γ deformation in the ground state from equation 12 and the γ from the RTRM fit. One can see that the deduced value of the γ deformation, and therefore the triaxiality, decreases with increasing boson number. It is remarkable that the agreement between the effective γ calculated with IBM and the parameter γ from RTRM is very good.

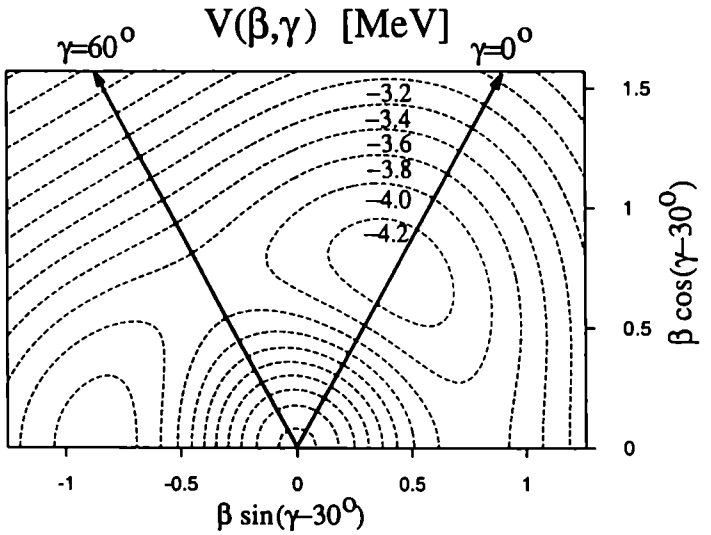

Fig. 6. Contour plot of $V(\beta,\gamma)$ for ^{130}Ba, calculated with the parameters $\kappa = -0.0606$ MeV, $\kappa' = 0.0125$MeV and $\chi = -0.181$.[17,18]

To better understand the calculated values of $\gamma_{\rm eff}$, it is useful to examine the

energy surfaces $V(\beta,\gamma)$.[56] As an example, $V(\beta,\gamma)$ is shown for ^{130}Ba in figure 6, with the same parameters as in the energy fit below. Although $V(\beta,\gamma)$ has a minimum at the prolate side, the effective γ deformation is very large due to the softness of the potential $V(\beta,\gamma)$ in γ.

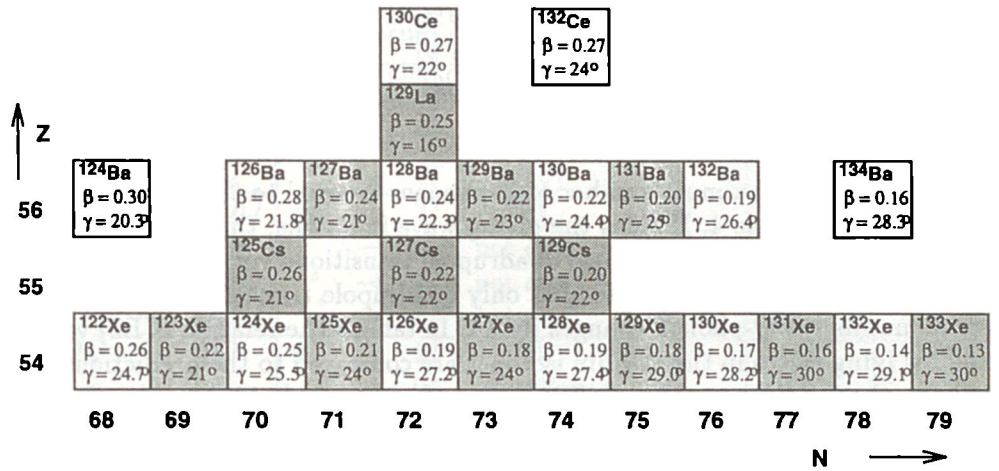

Fig. 7. Systematics of deformation parameters (β,γ) for even and odd Xe, Ba and odd Cs, La nuclei. The deformation parameters were taken from TRP and RTRM calculations.[26,14,13,30]

5. Multiple Q-phonon scheme for the low lying states in dynamical symmetry O(6) of the IBM

We noted that the collective positive parity states in the Barium and Xenon isotopes with masses around $A = 130$ are well described by a near O(6) Hamiltonian of the IBM. This answers many questions but not all. Interesting questions are e.g.

1. What is the structure of the second 0^+ state? Is it a double gamma vibration?
2. What is the structure of the wave function of the IBM states relative to the ground state?

For the discussion of these questions the Q-phonon scheme as proposed by Otsuka, Siems et al.[43] and by Otsuka and Kim[46] is very useful. One should note that this scheme is exactly valid only for the O(6) symmetry. In the Q-Phonon scheme the wave functions of the low lying O(6) eigenstates can be expressed by multiple applications of the quadrupole operator Q on the ground state, This is shown in table

Table 4. Q-phonon configurations of low lying O(6) states.

$\|I^\pi, \tau, \nu_\Delta\rangle$		
$\|0_1^+, 0, 0\rangle$		$\|0\rangle$
$\|2_1^+, 1, 0\rangle$	Q	$\|0\rangle$
$\|4_1^+; 2, 0\rangle$	$[QQ]^{(4)}$	$\|0\rangle$
$\|6_1^+, 3, 0\rangle$	$[QQQ]^{(6)}$	$\|0\rangle$
$\|2_2^+, 2, 0\rangle$	$[QQ]^{(2)}$	$\|0\rangle$
$\|4_2^+, 3, 0\rangle$	$[QQQ]^{(4)}$	$\|0\rangle$
$\|3_1^+, 3, 0\rangle$	$[QQQ]^{(3)}$	$\|0\rangle$
$\|5_1^+, 4, 0\rangle$	$[QQQQ]^{(5)}$	$\|0\rangle$
$\|0_2^+, 3, 1\rangle$	$[QQQ]^{(0)}$	$\|0\rangle$

4. We note that the maximum number of Q-phonons is equal to the τ quantum number, as is shown in table 4. Besides the giving wave functions, the Q-phonon scheme makes the selection rules for electrical quadrupole transitions very transparent in the O(6) limit. The selection rules state that only quadrupole transitions are allowed for which the number of Q-phonon changes by ± 1. In table 5 the relative B(E2) values of several low lying states in the Barium isotopes are compared to the predictions of the Q-phonon scheme. We note that B(E2) ratios which are forbidden in the Q-phonon scheme are indeed very small, typically less than 10%. For the Xenon isotopes the agreement is even better, since they are closer to the O(6) symmetry. The small deviation from the Q-phonon scheme is mainly due to the admixture of several Q-phonon configurations, since the O(6) symmetry is broken by the non vanishing value of χ.

As stated above the structure of the 0_2^+ state and of the 4_3^+ state a very interesting. The decay properties of the 0_2^+ state with its strong relative B(E2) to the 2_2^+ suggest an interpretation as a double γ vibration. With the Q-phonon scheme this interpretation can be ruled out for O(6) like nuclei, since a double γ vibration must have a four Q-phonon configuration, whereas the structure of the 0_2^+ state has only 3 Q–phonons as shown in table 4.

6. Extension of the Q-phonon scheme to nuclei outside the O(6) symmetry

Since the Q-phonon scheme applies beside the O(6) limit also to the vibrational nuclei of the U(5) symmetry and to the ground band of the SU(3), the question arises how pure are the Q-phonon configuration of the IBM eigenstates outside the symmetries.

In order to investigate this problem numerical calculations of the wave functions were done for several low lying states. In particular the following 3 states were investigated:

$$|2_1^+\rangle = \alpha_2 [Q]^{(2)} |0_1^+\rangle + |r_2\rangle \tag{15}$$

Table 5. Experimental relative B(E2) ratios for ^{130,132}Ba and a comparison to the IBM. Also shown are the Q-phonon configurations to illustrate the selection rules. The data are from the Cologne group and taken from refs.[60,43]

						^{130}Ba		^{132}Ba	
						exp.	IBM $\chi = -0.18$	exp.	IBM $\chi = -0.14$
QQ	$\rightarrow$	Q	2_2^+	$\rightarrow$	2_1^+	100	100	100	100
	$\not\rightarrow$			$\rightarrow$	0_1^+	6.2(7)	6.2	2.8(5)	2.8
QQQ	$\rightarrow$	QQ	3_1^+	$\rightarrow$	2_2^+	100	100	100	100
	$\not\rightarrow$	Q		$\rightarrow$	2_1^+	4.5(6)	6.1	3.5(4)	3.3
	$\rightarrow$	QQ		$\rightarrow$	4_1^+	22(3)	28	30(6)	35
QQQ	$\rightarrow$	QQ	4_2^+	$\rightarrow$	2_2^+	100	100	100	100
	$\not\rightarrow$	Q		$\rightarrow$	2_1^+	2.3(4)	0.1	1.8(3)	0.03
	$\rightarrow$	QQ		$\rightarrow$	4_1^+	54(10)	58	82(15)	73
$QQQQ$	$\rightarrow$	QQQ	5_1^+	$\rightarrow$	3_1^+	100	100	100	100
	$\not\rightarrow$	QQ		$\rightarrow$	4_1^+	not obs.	2.6	2.7(5)	1.2
	$\rightarrow$	QQQ		$\rightarrow$	4_2^+	not obs.	46	45(5)	45
	$\rightarrow$	QQQ		$\rightarrow$	6_1^+	not obs.	36	32(5)	41
QQQ	$\rightarrow$	QQ	0_2^+	$\rightarrow$	2_2^+	100	100	100	100
	$\not\rightarrow$	Q		$\rightarrow$	2_1^+	3.3(2)	2.5	0.20(5)	1.6

$$|3_1^+\rangle = \alpha_3[QQQ]^{(3)}|0_1^+\rangle + |r_3\rangle \quad (16)$$
$$|4_1^+\rangle = \alpha_4[QQ]^{(4)}|0_1^+\rangle + |r_4\rangle \quad (17)$$

The eigenfunctions $|I_i^\pi\rangle$ are normalized by the constants α_k and the rest wave function $|r_I\rangle$ is orthogonal to the Q-phonon configuration, i.e.

$$\langle r_2|[Q]^{(2)}|0_1^+\rangle = 0 \quad (18)$$
$$\langle r_3|[QQQ]^{(3)}|0_1^+\rangle = 0 \quad (19)$$
$$\langle r_4|[QQ]^{(4)}|0_1^+\rangle = 0. \quad (20)$$

These investigations were done using the generalized CQF Hamiltonian :

$$H = \kappa(\frac{\epsilon}{\kappa}\hat{n}_d - Q(\chi).Q(\chi)) \quad (21)$$

The wave functions of this CQF Hamiltonian are determined by the two structural parameters ϵ/κ and χ. By varying these two parameters one can interpolate between the three symmetries. A nice overview of the parameter space is given by the symmetry triangle proposed by Casten given in fig. 8 . In order to display the purity of the states, we show the value of the rest wave function $\langle r_I|r_I\rangle$ in the symmetry triangle.

In this work we will concentrate on the phonon structures of the on the 3_1^+ state. The corresponding square modules of the rest term in the Casten triangle are shown in figs. 9. We note that the maximum phonon impurity $\langle r|r\rangle$ of the 3_1^+ state from the simple Q-phonon configurations given in eq. 16 is less than 8%.

7. Conclusion

1. The low lying negative parity collective states of ^{125}Xe and ^{127}Xe exhibit a striking similarity. This is valid not only for the yrast band but extends to about four collective bands. It is a challenge for theoretical collective models.

2. The negative parity states of odd Cs and La nuclei can be fitted with the Triaxial Rotor plus Particle Model, where the signature splitting of the yrast band allows us to determine the γ–deformation. An axially symmetric fit could be excluded.

3. A consistent set of deformation parameters (ϵ, γ) in the $A \approx 130$ region has been obtained. These fit into our systematics of (ϵ, γ) for even and neutron odd Xe and Ba nuclei. A core polarization in γ due to the odd particle has been established.

4. The RTRM and the IBM calculations of the Ba-nuclei indicate a large effective γ deformation. In contrast to the RTRM, the IBM is not characterized by a rigid γ, but by a softness in the γ direction.

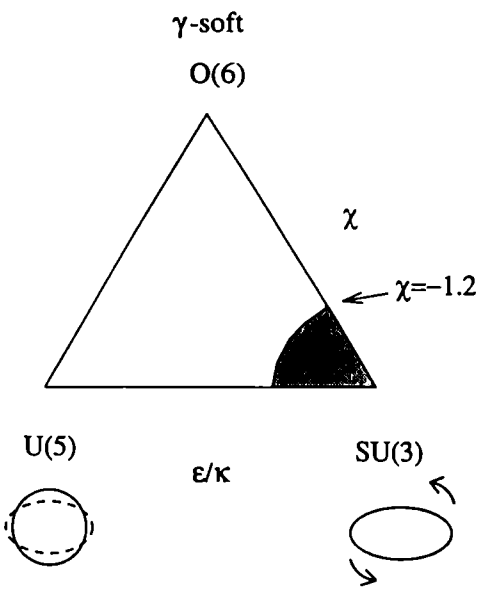

Fig. 8. Symmetry triangle of the three dynamical symmetries of the IBM as proposed by Casten.[59] The area which does not correspond to existing nuclei is shaded

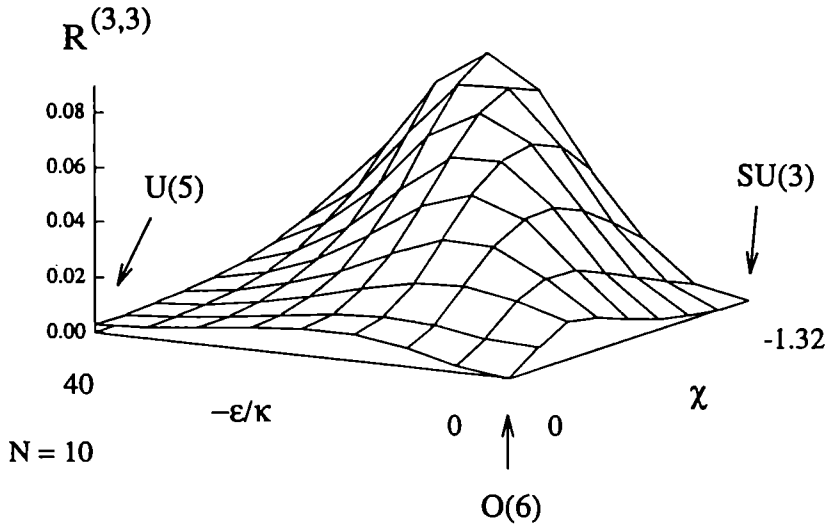

Fig. 9. Q-phonon purity of the 3_1^+ state of the IBM. Calculated for a boson number $N = 10$. From N. Pietralla *el al.* .[45]

5. The selection rules of the Q-phonon scheme for electromagnetic quadrupole transitions are valid near the O(6) symmetry to a very good accuracy.

6. The yrast states of collective nuclei have a rather pure Q-phonon configuration in the IBM.

The authors would like to thank R.F. Casten, R.V. Jolos, T. Otsuka and N. Pietralla for the joint work and discussions on the Q phonon model. We want to thank P. Van Isacker for the joint work and discussions on the effective γ–deformation in the IBM. For the collaboration on the experiments in Cologne we want to thank in particular A. Dewald, T. Diefenbach, S. Kasemann, K. Kirch, M. Luig, H. Meise, U. Neuneyer, N. Nicolay, M. Wilhelm, and K.O. Zell. This work was supported in part by the *Deutsche Forschungsgemeinschaft* under contract Br 799/5-2.

References

1. P. von Brentano, O. Vogel, N. Pietralla, A. Gelberg, and I. Wiedenhöver. *Inv. paper to the 5th Int. Spring Sem. on Nuclear Physics*, Ravello, Italy 1995, World Scientific (Singapore 1996).
2. P. von Brentano, A. Gelberg, O. Vogel, A. Dewald, and I. Wiedenhöver, *Int. Conf. High Spin Physics and Gammasoft Nuclei,* 1990, University of Pittsburgh, eds. J.X. Saladin et al. , World Scientific, (Singapore) p. 344.
3. P. von Brentano, A. Gelberg, O. Vogel, A. Dewald, and O. Stuch, *Inv. talk to the Summer School on Recent Advances in Nuclear Structure,* Predeal, 1990, eds. D. Bucurescu et al., World Scientific, (Singapore 1991) p. 129.
4. P. von Brentano, A. Dewald, A. Gelberg, P. Sala, G. Siems, I. Wiedenhöver, R. Wirowski, and J. Yan, *Int. Symp. on the Frontier of Nuclear Spectroscopy* ,

Kyoto, Japan, October 23-24 (1992), ed. H. Eijri, World Scientific, (Singapore 1994).
5. P. von Brentano, O. Vogel, A. Dewald, A. Gelberg, and N. Pietralla, *Int. Symp. on the Frontiers of nuclear structure Physics,* Tokyo, Japan, 1994. eds. T. Otsuka and K. Yasakai, World Scientific, (Singapore 1994).
6. P. von Brentano, O. Vogel, N. Pietralla, A. Gelberg, and I. Wiedenhöver, *Inv. talk to the Int. Conf. on Perspectives for the Interacting Boson Model, Padova, Italy,* World Scientific, (Singapore 1995) p. 397.
7. P. von Brentano, K. Kirch, U. Neuneyer, G. Siems, and I. Wiedenhöver, *Proc. Summer School on Frontier Topics in Nucl. Phys.,* Predeal, Romania, 1993, eds. A. Sandulescu, W. Scheid, Plenum Press (1994).
8. R. F. Casten and P. von Brentano, *Phys. Lett.* **B 152** (1985) 22.
9. F. Seiffert, W. Lieberz, A. Dewald, S. Freund, A. Gelberg, A. Granderath, D. Lieberz, R. Wirowski, and P. von Brentano, *Nucl. Phys.* **A 554**(1993) 287.
10. N.V. Zamfir and R. Casten, *Phys. Lett.* **B260** (1991) 265.
11. A. Arima and F. Iachello, *Annals of Phys.* **123** (1979) 468.
12. A. Leviathan, A. Novoselsky, and I. Talmi, *Phys. Lett.* **B172** (1986) 144.
13. J. Yan, O. Vogel, P. von Brentano, and A. Gelberg, *Phys. Rev.* **C48** (1993) 1046.
14. A. Gelberg, D. Lieberz, P. Brentano, I. Ragnarsson, P.B. Semmes, and I. Wiedenhöver, *Nucl. Phys.* **A557** (1993) 439c.
15. O. Vogel, A. Gelberg, R.V. Jolos, and P. von Brentano, *Nucl. Phys.* **A576**(1994) 109.
16. D. Lieberz, A. Gelberg, P. von Brentano, I. Ragnarsson and P.B. Semmes, *Phys. Lett.* **B282** (1992) 7.
17. O. Vogel, A. Gelberg, P. von Brentano, and P. Van Isacker, *Inv. talk to the Int. Conf. on Perspectives for the Interacting Boson Model, Padova, Italy,* World Scientific, (Singapore 1995) p. 397.
18. O. Vogel, P. Van Isacker, A. Gelberg, P. von Brentano, A. Dewald, to be published.
19. R.F. Casten, P. von Brentano, K. Heyde, P. Van Isacker and J. Jolie, *Nucl. Phys.* **A439** (1985) 289.
20. N. Yoshida, A. Gelberg, T, Otsuka, and H. Sagawa, Int. Conf. on Perspectives for the Interacting Boson Model, Padova, Italy, 13-17 June 1994.
21. I. Wiedenhöver, C. Kerskens, S. Albers, M. Eschenauer, and P. von Brentano, *Z. Phys.* **A350** (1995) 287.
22. I. Wiedenhöver, J. Yan, U. Neuneyer, R. Wirowski, P. von Brentano, A. Gelberg, N. Yoshida, T. Otsuka, *Nucl. Phys.* **A582** (1995) 77.
23. I. Wiedenhöver, U. Neuneyer, C. Kerskens, J. Altmann, O. Stuch, J. Theuerkauf, G. Siems, R. Wirowski, M. Eschenauer, P. von Brentano, R. Schubart, H. Kluge and K.H. Mayer. *Z. Phys.* **A347** (1993) 71.
24. R. Wyss, A. Granderath, R. Bengtsson, P. von Brentano, A. Dewald, A. Gelberg, A. Gizon, J. Gizon, S. Harissopulos, A. Johnson, W. Lieberz, W. Nazarewicz, J. Nyberg and K. Schiffer, *Nucl. Phys.* **A 505** (1989) 337.
25. A. Granderath, P.F. Mantica, R. Bengtsson, R. Wyss, P. von Brentano, A. Gelberg, and F. Seiffert, Nucl. Phys. **A**.

26. D. Lieberz, A. Gelberg, A. Granderath, P. von Brentano, I. Ragnarsson and P.B. Semmes, Nucl. Phys. **A529** (1991) 1.
27. A. Bohr and B.R. Mottelson, Nuclear Structure Vol. II (W.A. Benjamin Inc., Reading MA, 1957).
28. S.E. Larsson, G. Leander and I. Ragnarsson, Nucl. Phys. **A307** (1978) 189.
29. I.Ragnarsson and P.B. Semmes, Hyp. Int. **43** (1988) 425.
30. R. Kühn, L. Eßer, A. Gelberg, O. Vogel, I. Wiedenhöver, and P. von Brentano, Nucl. Phys. **A** , to be published.
31. T. Yamazaki, H. Nakayma, T. Numao and T. Shibata Journ. Phys. Loc. Jap. **44**, 1421 (1978)
32. F. Iachello and A. Arima, *The Interacting Boson Model,* Oxford Univ. Press, Cambridge, 1987, and refs. given therein.
33. R.F. Casten, J.P. Draayer, K. Heyde, P.O. Lipas, T. Otsuka, and D.D. Warner, *Algebraic Approaches to Nuclear Structure,* Harwood Publ., Chur, Switzerland, 1993, and refs. given therein.
34. I. Talmi, *Simple Models of Complex Nuclei,* Harwood Publ., Chur, Switzerland, 1993.
35. J.M. Eisenberg and W. Greiner, *Nuclear Theory Vol. I,* North Holland Publ., (Amsterdam 1987).
36. A. Faessler, W. Greiner, and R.K. Sheline, *Nucl. Phys.* **80** (1965) 417.
37. C.-L. Wu, D.-H. Feng, and M. Guidry, *Advances in Nuclear Physics Vol. 21: The Fermion Dynamical Symmetry Model,* Plenum Press, (New York 1994).
38. O.K. Vorov and V.G. Zelevinsky, *Nucl. Phys.* **A439** (1985) 207.
39. A.S. Davydov and G.F. Filippov, *Nucl. Phys.* **8** (1958) 237.
40. L. Wilets and M. Jean, *Phys. Rev.* **102** (1956) 3.
41. R.F. Casten and D.D. Warner, *Phys. Rev.* **C28** 1798 (1983).
42. J.P. Elliott, J.A. Evans, and P. Van Isacker, *Phys. Rev. Lett.* **57** (1986) 1124.
43. G. Siems, U. Neuneyer, I. Wiedenhöver, S. Albers, M. Eschenauer, R. Wirowski, A. Gelberg, P. von Brentano and T. Otsuka, *Phys. Lett.* **B320** (1994) 1.
44. N. Pietralla, P. von Brentano, R.F. Casten, T. Otsuka, and N.V. Zamfir, *Phys. Rev. Lett.* .**73** (1994) 1940.
45. N. Pietralla, P. von Brentano, T. Otsuka, and R.F. Casten *Phys. Lett.* **B349** (1995) 1.
46. T. Otsuka and K.-H. Kim, *Phys. Rev.* **C50** (1994) R1768.
47. W. Urban, T. Morek, Ch. Droste, B. Kotlinski, J. Srebrny, J. Wrzesinski, J. Styczen, Z. Phys. **A320** (1985) 327.
48. Ch. Droste, D. Chlebowska, J. Dobaczewski, F. Dönau, A. Kerek, G. Leander, J. Srebny and W. Walus, Nucl. Phys. **A341** (1980) 98.
49. J.P. Martin, V. Barci, H. El–Samman, A. Gizon, J. Gizon, W. Klamra and B.M. Nyakò, Nucl. Phys. **A489** (1988) 169.
50. Y. Liang, R. Ma, E.S. Paul, N. Xu, D.B. Fossan and R.A. Wyss, Phys. Rev. **C42** 890 (1990).
51. L. Hildingsson, W. Klamra, Th. Lindblad, F. Lidén, Y. Liang, R. Ma, E.S. Paul, N. Xu, D.B. Fossan and J. Gascon, Z. Phys. **A340** 33 (1991).
52. J.R. Hughes, D.B. Fossan, D.R. LaFosse, Y. Liang, P. Vaska and M.P. Waring, Phys. Rev. **C44** 2390 (1991).

53. G. Leander, Nucl Phys. **A 273**, 286 (1976)
54. M. Sugita, T. Otsuka and A. Gelberg, Nucl. Phys. **A 493**, 350 (1989)
55. K. Kumar, *Phys. Rev. Lett.* **28** (1972) 249.
56. J. Ginocchio and M.W. Kirson *Phys. Rev. Lett.* **44** (1980) 1744.
57. NNDC online data bank, National Nuclear Data Center, Brookhaven, New York.
58. N. Idrissi, A. Gizon, J. Genevey, P. Paris, V. Barci, D. Barnéoud, J. Blachot, D. Bucurescu, R. Duffait, J. Gizon, C.F. Liang and B. Weiss, Z. Phys. **A341** 427 (1992).
59. R.F. Casten, *Nuclear Structure from a Simple Perspective*, Oxford Univ. Press (1990).
60. K. Kirch, G. Siems, M. Eschenauer, A. Gelberg, R. Kühn, A. Mertens, U. Neuneyer, O. Vogel, I. Wiedenhöver, P. von Brentano, and T. Otsuka, *Nucl. Phys.* **A587** (1995) 211.

MIXED SYMMETRY STATES AND ELECTROMAGNETIC MOMENTS IN EVEN-EVEN Pd NUCLEI

ADRIAN GELBERG[a,b], KA-HAE KIM[a], TAKAHIRO MIZUSAKI[a]

TAKAHARU OTSUKA[a] and PETER VON BRENTANO[b]

a. Department of Physics, University of Tokyo, Hongo, Tokyo 113, Japan

b. Institut für Kernphysik der Universität zu Köln, 50937 Köln, Germany

ABSTRACT

Excitation energies and electromagnetic transition strengths in even-even Pd nuclei have been calculated by using the Proton- Neutron Interacting Boson Model (IBM-2). Mixed symmetry 2^+ states have been identified. A comparison of fitted parameters with estimations based on microscopic calculations has been carried out.

1. Introduction

Pd even-even nuclei have in recent years been the object of extensive investigations by means of in beam gamma ray spectroscopy, Coulomb excitation and inelastic scattering, as well as by transfer reactions. It is therefore interesting to carry out a systematic comparison of the experimental data with model calculations. Since the A=100 - 120 region has transitional character, the Interacting Boson Model [1] should provide a suitable description. Recent experimental data seem to indicate the existence of states with mixed proton- neutron symmetry. Consequently one should use the Proton-Neutron Interacting Boson Model (IBM-2)[2]. Such an investigation has been carried out in ref [3], but the rich experimental information which appeared in the meantime requires a new theoretical assessment. Besides, progress has been achieved in recent years in estimating the IBM-2 parameters by microscopic calculations [4].

The aims of this lecture are the following:

1. To review the basic concepts of the IBM-2, particularly the concept of F-spin.
2. To describe systematic IBM-2 calculations of even-even Pd with $102 \leq A \leq 112$, special attention been paid to the identification of mixed symmetry states.
3. To show how to choose the IBM-2 parameters so as to keep them close to the values obtained by microscpic calculations based on the shell model.

2. The model

The microscopic picture of the IBM is given in terms of collective pairs of nucleons [5]. The S and D pairs of valence nucleons have angular momentum J=0 and J=2 respectively. These pairs correspond intuitively to the s and d bosons respectively. The building blocks of the IBM-2 are the proton bosons s_π, d_π and the neutron bosons s_ν, d_ν.

We used a Hamiltonian similar to the one of ref.[6]

$$H = \epsilon_\pi n_{d_\pi} + \epsilon_\nu n_{d_\nu} + \kappa Q_\pi \cdot Q_\nu + M_{\pi\nu} + V_{\pi\pi} + V_{\nu\nu} \tag{1}$$

where

$$Q_\rho = (d^\dagger \times s + s^\dagger \times \tilde{d})^{(2)}_\rho + \chi_\rho (d^\dagger \times \tilde{d})^{(2)}_\rho, \qquad \rho = \pi, \nu \tag{2}$$

$$M_{\pi\nu} = \xi_2 (s^\dagger_\nu \times d^\dagger_\pi - d^\dagger_\nu \times s^\dagger_\pi)^{(2)} \cdot (s_\nu \times \tilde{d}_\pi - \tilde{d}_\nu \times s_\pi)^{(2)} - 2 \sum_{k=1,3} \xi_k (d^\dagger_\nu \times d^\dagger_\pi)^{(k)} \cdot (\tilde{d}_\nu \times \tilde{d}_\pi)^{(k)} \tag{3}$$

and

$$V_{\rho\rho} = \sum_{L=0,2,4} \frac{1}{2} c^\rho_L (d^\dagger_\rho \times d^\dagger_\rho)^{(L)} \cdot (\tilde{d}_\rho \times \tilde{d}_\rho)^{(L)}, \qquad \rho = \pi, \nu \tag{4}$$

We will halve the number of the free parameters c^ρ_L by requiring

$$c^\pi_L = c^\nu_L = c_L \tag{5}$$

The E2 transition strengths were calculated by using the operator

$$T(E2) = e_\pi Q_\pi + e_\nu Q_\nu \tag{6}$$

where e_π and e_ν are effective boson charges. The M1 operator is given by

$$T(M1) = \sqrt{\frac{3}{4\pi}} (g_\pi \hat{L}_\pi + g_\nu \hat{L}_\nu) \mu_N \tag{7}$$

where $\hat{L} = \sqrt{10} (d^\dagger \times \tilde{d})^{(1)}$ is the angular momentum operator and g_π and g_ν are the proton and neutron boson g-factors respectively.

The numerical diagonalization has been carried out by using an improved version of the NPBOS code [7]. As noticed in previous calculations, the general features of the excitation spectra are mainly determined by the parameters ϵ, κ and $\chi_s = (\chi_\pi + \chi_\nu)/2$. These quantities generally depend on the proton and neutron boson numbers N_π and N_ν. In particular we assumed [2] that χ_π and χ_ν depend only on N_π and N_ν respectively.

3. F-spin

The concept of F-spin was introduced by A.Arima,F.Iachello, T.Otsuka and I.Talmi in the framework of the IBM-2 [1,2,8]. The F-spin is the analog of isospin for bosons. A boson has $F = 1/2$ and the projection 1/2 and -1/2 for a proton or neutron boson respectively. The $F_\pm$ operators transform proton and neutron bosons into each other. A basis state is characterized by two quantum numbers: the F-spin F and the projection $F_0 = (N_\pi - N_\nu)/2$. N_π and N_ν are the proton and neutron boson numbers respectively. The $\hat{F}^2$ operator has the eigenvalue $F(F+1)$. The values of F are

$$F_0 \leq F \leq (N_\pi + N_\nu)/2 = F_{max} \tag{8}$$

The states with $F = F_{max}$ are totally symmetric and they have the lowest energy. States with $F < F_{max}$ are mixed symmetry states [2].

Obviously the Hamiltonian (2) is not an F-spin scalar. This is mainly due to the quadrupole term, which has scalar, vector and tensor components. Therefore H does not commute with $F_{\pm}$. However,the empirical evidence shows that the F-spin splitting is large in comparison with the splitting arising from other degrees of freedom. Therefore in many cases F is an approximately good quantum number [9 2]

The magnetic dipole operator of eq. (7) can be rewritten as

$$T(M1) = \sqrt{\frac{3}{4\pi}}[g_s\hat{L} + g_v(\hat{L}_\pi - \hat{L}_\nu)]\mu_N \tag{9}$$

with $g_s = (g_\pi + g_\nu)/2$, $g_v = (g_\pi - g_\nu)/2$ and $\hat{L} = \hat{L}_\pi + \hat{L}_\nu$. Since the total angular momentum is diagonal, the M1 transitions will be generated only by the second term, i.e.

$$B(M1; a \to b) \propto < b|\hat{L}_\pi - \hat{L}_\nu|a >^2 \tag{10}$$

The general F-spin selection rule is

$$\Delta F = 0, \pm 1 \tag{11}$$

Besides, M1 transitions between two totally symmetric states ($F = F_{max}$) are forbidden [9]. Therefore, if M1 transitions occur between low-lying collective states, these states must contain components with mixed symmetry ($F < F_{max}$). This allows to use the strength of M1 transitions between low-lying collective states as an indicator of F-spin mixing. As far as geometrical models are concerned, the M1 transitions have been explained in the so-called two-fluid model [10,11]

4. General features of even even Pd nuclei

In order to locate the Pd nuclei on the map of the IBM-2 parameters, we must first examine a few characteristic features. We will start with the frequently used excitation energy ratios $E(4_1^+)/E(2_1^+)$ displayed in Table 1. They are rather narrowly spread around the value 2.4, and this is typical for the O(6) - U(5) transition region [12]. We must also examine the B(E2) ratios [1]

$$R(2_2) = \frac{B(E2; 2_2 \to 2_1)}{B(E2; 2_2 \to 0_1)} \quad \text{and} \quad R'(2_2) = \frac{B(E2; 2_2 \to 2_1)}{B(E2; 2_1 \to 0_1)} \tag{12}$$

$R(2_2)$ becomes infinite at both limits. The observed values are typical for the U(5) to O(6) transition region. The values of $R'(2_2)$ for a large boson number are 2 and 10/7 for U(5) and O(6), respectively. The experimental values of R' come close to what we can expect in the transition region. However, they are much smaller than expected in ^{102}Pd and ^{104}Pd. This could be due to an intruder admixture into the 2_2 state.

We used a Hamiltonian similar to the one of ref.[6]

$$H = \epsilon_\pi n_{d_\pi} + \epsilon_\nu n_{d_\nu} + \kappa Q_\pi \cdot Q_\nu + M_{\pi\nu} + V_{\pi\pi} + V_{\nu\nu} \tag{1}$$

where

$$Q_\rho = (d^\dagger \times s + s^\dagger \times \tilde{d})^{(2)}_\rho + \chi_\rho (d^\dagger \times \tilde{d})^{(2)}_\rho, \qquad \rho = \pi, \nu \tag{2}$$

$$M_{\pi\nu} = \xi_2 (s^\dagger_\nu \times d^\dagger_\pi - d^\dagger_\nu \times s^\dagger_\pi)^{(2)} \cdot (s_\nu \times \tilde{d}_\pi - \tilde{d}_\nu \times s_\pi)^{(2)} - 2 \sum_{k=1,3} \xi_k (d^\dagger_\nu \times d^\dagger_\pi)^{(k)} \cdot (\tilde{d}_\nu \times \tilde{d}_\pi)^{(k)} \tag{3}$$

and

$$V_{\rho\rho} = \sum_{L=0,2,4} \frac{1}{2} c^\rho_L (d^\dagger_\rho \times d^\dagger_\rho)^{(L)} \cdot (\tilde{d}_\rho \times \tilde{d}_\rho)^{(L)}, \qquad \rho = \pi, \nu \tag{4}$$

We will halve the number of the free parameters c^ρ_L by requiring

$$c^\pi_L = c^\nu_L = c_L \tag{5}$$

The E2 transition strengths were calculated by using the operator

$$T(E2) = e_\pi Q_\pi + e_\nu Q_\nu \tag{6}$$

where e_π and e_ν are effective boson charges. The M1 operator is given by

$$T(M1) = \sqrt{\frac{3}{4\pi}} (g_\pi \hat{L}_\pi + g_\nu \hat{L}_\nu) \mu_N \tag{7}$$

where $\hat{L} = \sqrt{10}(d^\dagger \times \tilde{d})^{(1)}$ is the angular momentum operator and g_π and g_ν are the proton and neutron boson g-factors respectively.

The numerical diagonalization has been carried out by using an improved version of the NPBOS code [7]. As noticed in previous calculations, the general features of the excitation spectra are mainly determined by the parameters ϵ, κ and $\chi_s = (\chi_\pi + \chi_\nu)/2$. These quantities generally depend on the proton and neutron boson numbers N_π and N_ν. In particular we assumed [2] that χ_π and χ_ν depend only on N_π and N_ν respectively.

3. F-spin

The concept of F-spin was introduced by A.Arima,F.Iachello, T.Otsuka and I.Talmi in the framework of the IBM-2 [1,2,8]. The F-spin is the analog of isospin for bosons. A boson has $F = 1/2$ and the projection 1/2 and -1/2 for a proton or neutron boson respectively. The $F_\pm$ operators transform proton and neutron bosons into each other. A basis state is characterized by two quantum numbers: the F-spin F and the projection $F_0 = (N_\pi - N_\nu)/2$. N_π and N_ν are the proton and neutron boson numbers respectively. The $\hat{F}^2$ operator has the eigenvalue $F(F+1)$. The values of F are

$$F_0 \leq F \leq (N_\pi + N_\nu)/2 = F_{max} \tag{8}$$

The states with $F = F_{max}$ are totally symmetric and they have the lowest energy. States with $F < F_{max}$ are mixed symmetry states [2].

Obviously the Hamiltonian (2) is not an F-spin scalar. This is mainly due to the quadrupole term, which has scalar, vector and tensor components. Therefore H does not commute with $F_{\pm}$. However,the empirical evidence shows that the F-spin splitting is large in comparison with the splitting arising from other degrees of freedom. Therefore in many cases F is an approximately good quantum number [9 2]

The magnetic dipole operator of eq. (7) can be rewritten as

$$T(M1) = \sqrt{\frac{3}{4\pi}}[g_s\hat{L} + g_v(\hat{L}_\pi - \hat{L}_\nu)]\mu_N \tag{9}$$

with $g_s = (g_\pi + g_\nu)/2$, $g_v = (g_\pi - g_\nu)/2$ and $\hat{L} = \hat{L}_\pi + \hat{L}_\nu$. Since the total angular momentum is diagonal, the M1 transitions will be generated only by the second term, i.e.

$$B(M1; a \to b) \propto < b|\hat{L}_\pi - \hat{L}_\nu|a >^2 \tag{10}$$

The general F-spin selection rule is

$$\Delta F = 0, \pm 1 \tag{11}$$

Besides, M1 transitions between two totally symmetric states ($F = F_{max}$) are forbidden [9]. Therefore, if M1 transitions occur between low-lying collective states, these states must contain components with mixed symmetry ($F < F_{max}$). This allows to use the strength of M1 transitions between low-lying collective states as an indicator of F-spin mixing. As far as geometrical models are concerned, the M1 transitions have been explained in the so-called two-fluid model [10,11]

4. General features of even even Pd nuclei

In order to locate the Pd nuclei on the map of the IBM-2 parameters, we must first examine a few characteristic features. We will start with the frequently used excitation energy ratios $E(4_1^+)/E(2_1^+)$ displayed in Table 1. They are rather narrowly spread around the value 2.4, and this is typical for the O(6) - U(5) transition region [12]. We must also examine the B(E2) ratios [1]

$$R(2_2) = \frac{B(E2; 2_2 \to 2_1)}{B(E2; 2_2 \to 0_1)} \quad \text{and} \quad R'(2_2) = \frac{B(E2; 2_2 \to 2_1)}{B(E2; 2_1 \to 0_1)} \tag{12}$$

$R(2_2)$ becomes infinite at both limits. The observed values are typical for the U(5) to O(6) transition region. The values of $R'(2_2)$ for a large boson number are 2 and 10/7 for U(5) and O(6), respectively. The experimental values of R' come close to what we can expect in the transition region. However, they are much smaller than expected in ^{102}Pd and ^{104}Pd. This could be due to an intruder admixture into the 2_2 state.

Table 1: Excitation energy ratios and the $R(2_2)$ and $R'(2_2)$ B(E2) ratios (see eq.8)

Nucleus	$E(4_1^+)/E(2_1^+)$	$R(2_2)$	$R'(2_2)$
^{102}Pd	2.29	8.8	0.460
^{104}Pd	2.38	18	0.606
^{106}Pd	2.40	37	1.162
^{108}Pd	2.41	95	1.526
^{110}Pd	2.46	70	0.983
^{112}Pd	2.53	56	

What are the consequences of this simple observation? First, we must reckon with a relatively large value of ϵ, in comparison to typical O(6) nuclei such as those in the A=130 region [13]. The ratios $R(2_2)$ tell us that we will need a negative $\chi_s = (\chi_\pi + \chi_\nu)/2$ with a moderately large absolute value. The complementary $\chi_\nu = (\chi_\pi - \chi_\nu)/2$ has a direct influence on the strength of M1 transitions between low lying collective states [9]. The values of $B(M1; 2_2 \rightarrow 2_1)$ are given in Tables 3, 4. The M1 strength decreases with increasing mass, nearly vanishes for ^{106}Pd, and then increases again. This shows that for ^{106}Pd $\chi_\pi \approx \chi_\nu$.Therefore we can expect that both χ_π and χ_ν are mostly negative for $^{102-112}$Pd.

One salient feature of the low energy level scheme of the investigated nuclei is the crossing of the 4_1^+ and 2_2^+ levels which approximately happens for ^{106}Pd. This inversion of the pattern of the so-called two-phonon multiplet will oblige us to make use of the c_L parameters of eq. (1).

Another interesting problem is that of the mixed symmetry states. The experimental data on (p,p') and (d,d') reactions suggest the existence of such states in ^{106}Pd [14] and ^{110}Pd [15]. We will further use M1 transition strengths for identifying states with less than maximum F-spin [9].

The comparison with experimental data must be carried out with care, owing to the possible presence of intruder states. The latter occur through the excitation of two-particle two-hole states accross the Z=50 closed shell [16]. Such intruder states are well known in Cd and Sn, and a few of them have been identified also in Pd nuclei. For example, the $0_2 \rightarrow 2_1$ transition in ^{102}Pd is extremely hindered, while the E0 transition to the ground state is very strong [17]. This is a typical signature of an intruder state. Before carrying out the IBM-2 fit, the intruder states must be removed. However, the exisiting data hardly allow a quantitative treatment of the mixing of intruder and normal states.

The experimental data used during the fit were taken from the following references: ^{102}Pd [18],^{104}Pd [19], ^{106}Pd [20 21], ^{108}Pd [21 22], ^{110}Pd,[23] and ^{112}Pd [24].They have been updated by making use of the Brookhaven Nuclear Data Base.

5. Microscopic parameters

The microscopic study of the IBM in realistic nuclei has been investigated in the

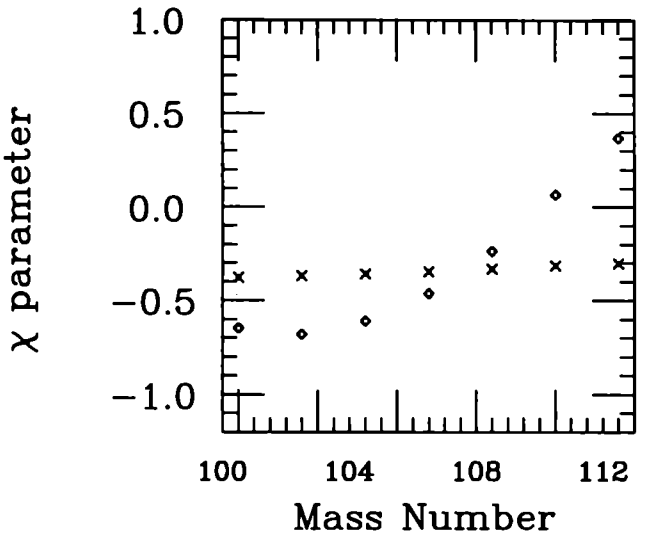

Figure 1: Microscopically calculated χ_π (crosses) and χ_ν (squares) parameters

framework of the Otsuka-Arima-Iachello (OAI) mapping[4]. It is based on the generalized seniority scheme and is expected to be valid for the spherical and nearly spherical nuclei. For instance, the Te, Xe and Ba regions have been studied[4]. From these results, in practical applications, the OAI mapping makes it possible to obtain quantitative results for nearly spherical nuclei. However, the renormalization method of the non-collective degrees of freedom is not sufficient for nuclei with many valence particles (holes). Besides, there is no unambiguous mapping method for the Majorana interactions, which are important for discussing the mixed-symmetry states investigated in the present paper. Therefore, in the following study we consider the microscopic results only as a a first approximation for certain IBM parameters .

The underlying shell model hamiltonian is assumed to be $H_\pi + H_\nu + H_{\pi\nu}$ where H_π (H_ν) are like-nucleon hamiltonians for protons (neutrons), and $H_{\pi\nu}$ is a proton-neutron interaction which we considered of being of quadrupole-quadrupole type. The like-nucleon Hamiltonian H_π or H_ν is composed of the single particle energies, monopole, quadrupole, hexadecapole pairing interactions and quadrupole-quadrupole, hexadecapole-hexadecapole interactions. Their parameters are determined so as to reproduce the spectra of Sn isotopes and N=50 isotones. The strength of the proton-neutron interaction is the same as the one in ref.[25]. The proton configuration space consists of the $1g_{9/2}, 2p_{1/2}, 1f_{5/2}$ and $2p_{3/2}$ orbitals. The neutron configuration space comprises the $2d_{5/2}, 1g_{7/2}, 3s_{1/2}, 1h_{11/2}$ and $2d_{3/2}$ orbitals. The structure of S pairs has been determined by projecting from the intrinsic state which is obtained by the number conserved Hartree-Fock-Bogoljubov (HFB) method. The structure of D pairs has been obtained by the proton-neutron Tamm-Dankov-Approximation(TDA). The OAI mapping requires that the matrix elements between the collective fermion states

spanned by the S and D pairs are equal to those between the corresponding boson states[2]. This requirement determines the parameters of the IBM Hamiltonian[4]. The details of the calculation are the same as in ref[4].

Here we show the results for χ_π and χ_ν. The χ parameter reflects the underlying shell structure. In the S_π pair, the ($g_{9/2}$, $g_{9/2}$) component is dominant and its occupation probability is about 87%. In the D_π pair, the probability of the same configuration reaches about 98% due to the angular momentum coupling. Although in the calculation we assume 4 orbits, the structure of the proton holes is nearly pure $g_{9/2}$. In turn, in the neutron case, as the number of the valence neutron increases, the neutrons fill successive orbits starting from $d_{5/2}$. Around the nuclei with 14 valence nucleons, the $d_{5/2}$ and $g_{7/2}$ orbits are nearly filled. This pattern is reflected in the behaviour of the χ_ν parameter. In fig.1, we show χ_ν as a function of the valence neutron number. The general trend of the microscopic calculation follows the one of the single orbit approximation, but the effect of the underlying shell structure is also visible.

Next we consider the results for g_π and g_ν. The boson g factor can be evaluated by equating the matrix elements both of the boson and nucleon M1 transition operators. The nucleon M1 transition operator is given by,

$$T(M1) = \sqrt{\frac{3}{4\pi}}(g_{L,\pi}\hat{L}_\pi + g_{S,\pi}\hat{S}_\pi + g_{L,\nu}\hat{L}_\nu + g_{S,\nu}\hat{S}_\nu) \qquad (13)$$

where the g's are nucleon g-factors and L and S denote the orbital and spin angular momentum operators. According to the OAI mapping, the boson g-factor contains contributions from both nucleon orbital and spin g-factors. A preliminary microscopic calculation shows that the spin and orbital contributions to the boson- g_π are 0.35 and 0.9, respectively; a spin quenching factor 0.7 has been used. Then the boson g_π is about 1.25. In constrast to this, the boson g_ν's are reduced due to the lack of the orbital part and are comprised between -0.05 to -0.002 for the considered Pd isotopes. The calculation of the g-boson factors is still in progress.

6. Results

6.1. Parameters

As a starting point we used parameters extrapolated from the IBM-2 calculation of Cd isotopes [25]. At a first stage we set $\epsilon_\pi = \epsilon_\nu = \epsilon$. The latter parameter, as well as κ and $\chi_s = (\chi_\pi + \chi_\nu)/2$ were fitted to the experimental excitation energies and B(E2) values. The parameters c_0, c_2 and c_4 were fitted to the energy splitting of the "2-phonon" triplet. Up to this point the calculation is still equivalent to using an IBM-1 Hamiltonian.

The quantity $\chi_v = (\chi_\pi - \chi_\nu)/2$ was fitted to $B(M1; 2_2 \rightarrow 2_1)$, which nearly vanishes for $\chi_v = 0$. The parameter χ_π was kept constant for all the nuclei investigated.

Table 2: The IBM-2 parameters.All parameters in MeV, with the exception of χ_ν. For all isotopes $\chi_\pi = -0.3$

Nucleus	ϵ	ϵ_π	ϵ_ν	κ	χ_ν	c_0	c_2	c_4	ξ_1	ξ_2
^{102}Pd	0.940	0.985	0.910	-0.2	-0.497	-0.1	-0.03	-0.2	0.2	0.05
^{104}Pd	0.900	0.830	0.935	-0.18	-0.48	-0.39	-0.13	0	0.2	0.05
^{106}Pd	0.820	0.720	0.860	-0.16	-0.22	-0.45	-0.2	0.1	0.2	0.05
^{108}Pd	0.800	0.650	0.850	-0.14	-0.05	-0.325	-0.25	-0.01	0.2	0.04
^{110}Pd	0.740	0.545	0.805	-0.125	0.0	-0.26	-0.29	-0.03	0.2	0.04
^{112}Pd	0.630	0.79	0.59	-0.1	0.1	-0.05	-0.15	0.10	0.2	0.05

As it can be seen from Fig. 1, this is a quite acceptable approximation. The quantity $\epsilon_\upsilon = \epsilon_\pi - \epsilon_\nu$ was fitted to the g-factor of the 2_1^+ state. This parameter does not affect other physical quantities significantly.

Howevere, $B(M1; 2_2 \rightarrow 2_1)$ is weakly sensitive to ϵ_υ, so that we had to readjust χ_υ afterwards. Since there is only scarce knowledge of the excitation energies of the mixed symmetry 2^+ states in even even Pd, and none for the 1^+, an accurate fit of the Majorana parameters was not possible. We mostly took the same values for ξ_1, ξ_2 for all nuclei and we set $\xi_3 = 0$. The fitted values of the parameters are given in Table 2.

6.2. Excitation energies

The calculated excitation energies for ^{102}Pd - ^{112}Pd as well as the experimental ones are shown in Figs. 2 and 3. The general agreement between experiment and model is quite satisfactory. The even-spin yrast sequence is quite well reproduced in all investigated nuclei. The calculated yrast 6^+ and 8^+ excitation energies are slightly higher than the experimental ones, which is a general feature of this type of model. The latter deviations are smaller than in deformed nuclei, owing to the predominant role played by the ϵn_d term in the Hamiltonian.

The inversion of the 4_1^+ and 2_2^+ levels starting from ^{104}Pd is well described by the model. The splitting of the "two phonon multiplet" is rather small. It has been necessary to use the c_L parameters of eqs (4,5).

The 2_3^+ states have also been quite well reproduced by the calculation. As it will be shown in subsection 6.4, these states are assumed to have mixed proton-neutron symmetry. On the contrary, the agreement is not so good for the 3_1^+ and the 0_3^+ states. A possible reason could be a mixing with intruder states.

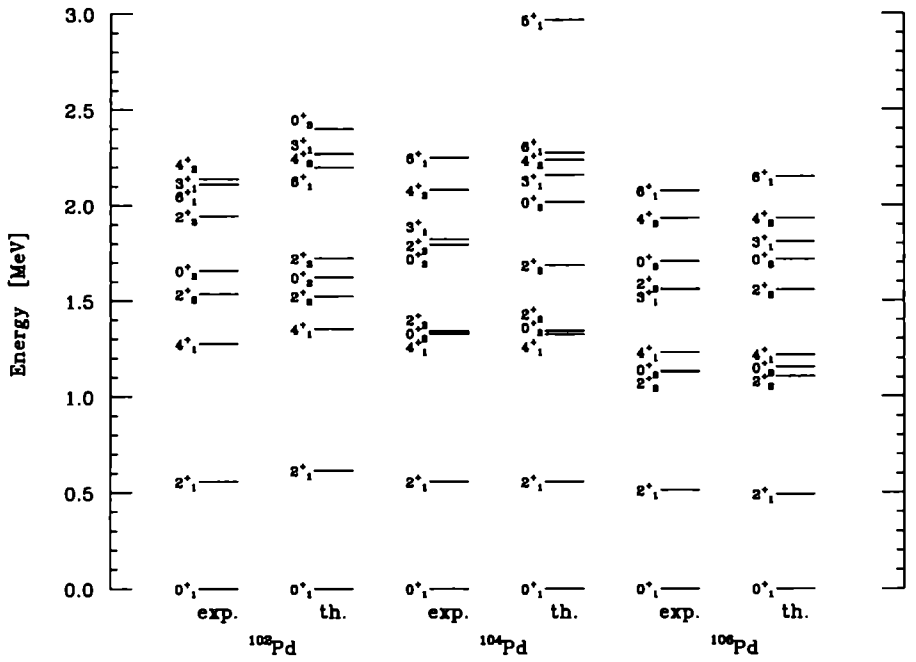

Figure 2: Experimental and calculated excitation energies in ^{102}Pd,^{104}Pd and ^{106}Pd

6.3. Electromagnetic transition rates and moments

The matrix elements of the E2 operator of eq. (6) have been calculated by using the same effective charges for all the nuclei, namely

$$e_\pi = 0.12 \qquad \text{and} \qquad e_\nu = 0.1 \tag{14}$$

The units are e^2fm^4.

Some important reduced E2 transition probabilities are given in Tables 3 and 4. The effective charges (9) were chosen so as to obtain a satisfactory agreement with the experimental $B(E2;2_1^+ \rightarrow 0_1^+)$ throughout the investigated region. The deviations from the experimental values are smaller than $2-3\%$, with the exception of ^{104}Pd. The fit of $B(E2;4_1^+ \rightarrow 2_1^+)$ is also satisfactory. The theoretical $B(E2;2_2^+ \rightarrow 2_1^+)$ is overvalued in ^{102,104}Pd but, as noticed in section 3, the corresponding experimental values are abnormally small. The transitions from 2_2^+ to the ground state are weak, with B(E2)'s 6-10 times smaller than the yrast ones. This feature is well described by the model.

The M1 transitions have been calculated by using the boson g-factors given in Table 5. While g_π was kept constant, g_ν was fitted to $B(M1;2_2^+ \rightarrow 2_1)$ and to $g(2_1^+)$. As it can be seen from Tables 3 and 4, $B(M1;2_2^+ \rightarrow 2_1^+)$ is quite well reproduced by the model. As expected, this reduced transition probability nearly vanishes for ^{106}Pd, in which $\chi_\nu = (\chi_\pi - \chi_\nu)/2$ reaches its smallest absolute value, namely $|\chi_\nu| = 0.04$. We

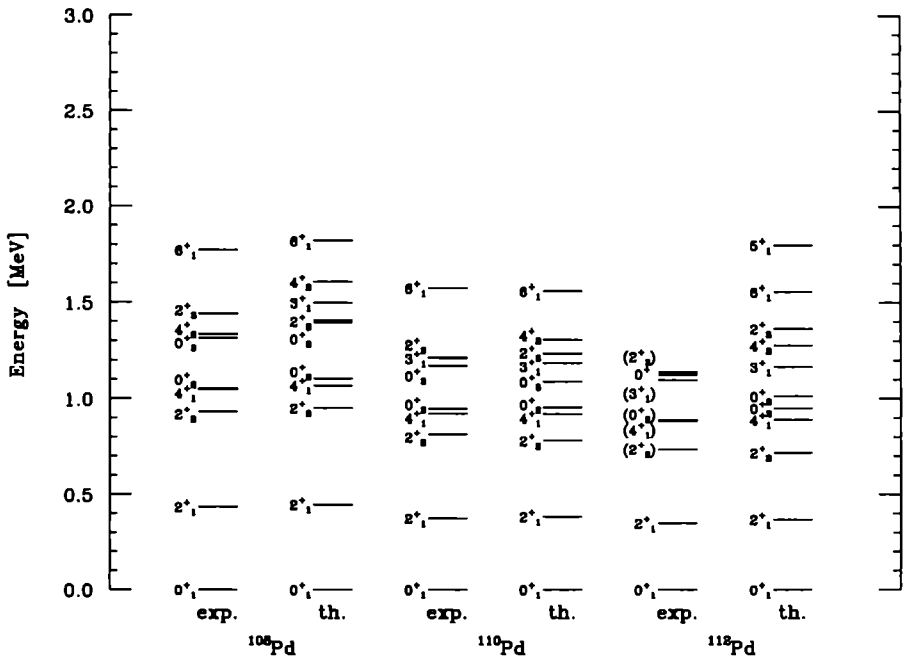

Figure 3: Experimental and calculated excitation energies in ^{108}Pd,^{110}Pd and ^{112}Pd

Table 3: E2 and M1 reduced transition probabilities; B(E2) in e^2fm^4, B(M1) in μ_N^2 (^{102,104,106}Pd).

	^{102}Pd		^{104}Pd		^{106}Pd	
	exp.	th.	exp.	th.	exp.	th.
$B(E2;2_1^+ \rightarrow 0_1^+)$	923(65)	899	1045(58)	1157	1332(45)	1328
$B(E2;2_2^+ \rightarrow 2_1^+)$	425(57)	959	633(49)	1211	1548(140)	1311
$B(E2;2_2^+ \rightarrow 0_1^+)$	48(24)	9	35(4)	25	34(3)	13
$B(E2;4_1^+ \rightarrow 2_1^+)$	1440(71)	1225	1423(203)	1690	2175(297)	1897
$B(E2;2_3^+ \rightarrow 2_1^+)$	-	3	<32	1	-	10^{-4}
$B(M1;2_2^+ \rightarrow 2_1^+)$	0.0036(6)	0.0037	0.0017	0.0021	0.0001	0.0004
$B(M1;2_3^+ \rightarrow 2_1^+)$	-	0.629	<0.013	0.584	-	0.3713

Table 4: E2 and M1 reduced transition probabilities; B(E2) in e^2fm^4, B(M1) in μ_N^2 (^{108,110,112}Pd).

	^{108}Pd		^{110}Pd		^{112}Pd	
	exp.	th.	exp.	th.	exp.	th.
$B(E2;2_1^+ \to 0_1^+)$	1561(40)	1613	1711(118)	1858	1315(224)	1949
$B(E2;2_2^+ \to 2_1^+)$	2383(214)	2083	1681(294)	2399	-	2861
$B(E2;2_2^+ \to 0_1^+)$	25(3)	14	24(3)	21		<1
$B(E2;4_1^+ \to 2_1^+)$	2810(366)	2363	2920(383)	2762		
$B(E2;2_3^+ \to 2_1^+)$	-	2	-			
$B(M1;2_2^+ \to 2_1^+)$	0.0024(6)	0.0017	0.0011(5)	0.0010		
$B(M1;2_3^+ \to 2_1^+)$	-	0.3928	-	0.260		

would like to point out that this behaviour of $B(M1;2_2^+ \to 2_1^+)$ can thus be explained in a natural way as due to the variation of χ_ν, while otherwise it could loook quite arbitrary.

It is difficult to carry out an objective comparison of theoretical and experimental values of the spectroscopic quadrupole moments, because the latter are usually quite widely scattered [26]. Since the deviations are sometimes due to systematic errors, taking weighted averages does not make sense. However, static quadrupole moemnts have been recently measured in ^{106,108}Pd by state of the art Coulomb excitation [21]. The experimental values are $(Q(2_1^+))_{106} = -0.55 \pm 0.05$ and $(Q(2_1^+))_{108} = -0.61^{+.03}_{-.07}$. The theoretical ones are $(Q(2_1^+))_{106} = -0.319$ and $(Q(2_1^+))_{108} = -0.294$. So far we have no explanation for this discrepancy, since most E2 transition rates have been correctly predicted by the model.

A comparison of experimental and calculated g-factors of the 2_1^+ states is given in Table 5. In fact, g_π and g_ν have been simultaneously fitted to $B(M1;2_2^+ \to 2_1^+)$ and $g(2_1^+)$, so as to achieve a consistent description of M1 transition rates and magnetic moments. In older g-factor calculations it has been assumed that the 2_1^+ state is F-spin pure [27]. This allows to calculate g-factors by using a simple analytical formula [1]. As it has been shown in ref.[28], even small F-spin impurities at percentage level can influence the g-factors. This can be seen in fig 4, in which g-factors are plotted vs. the ratio

$$\frac{F_0}{F_{max}} = \frac{N_\pi - N_\nu}{N_\pi + N_\nu} \tag{15}$$

In the case of F-spin purity, if we assume that the boson g-factors have the same value for an isotope series, the values of $g(2_1^+)$ should lie on a straight line given by

$$g = \frac{g_\pi + g_\nu}{2} + \frac{g_\pi - g_\nu}{2}\frac{F_0}{F} \tag{16}$$

In Fig. 4 the straight line corresponds to $g_\pi = 1.2$ and g_ν=-0.1. As a matter of fact, g_ν experiences slight variations from nucleus to nucleus, but this cannot explain the large deviations from the straight line. If we fit a straight line to the g-factor

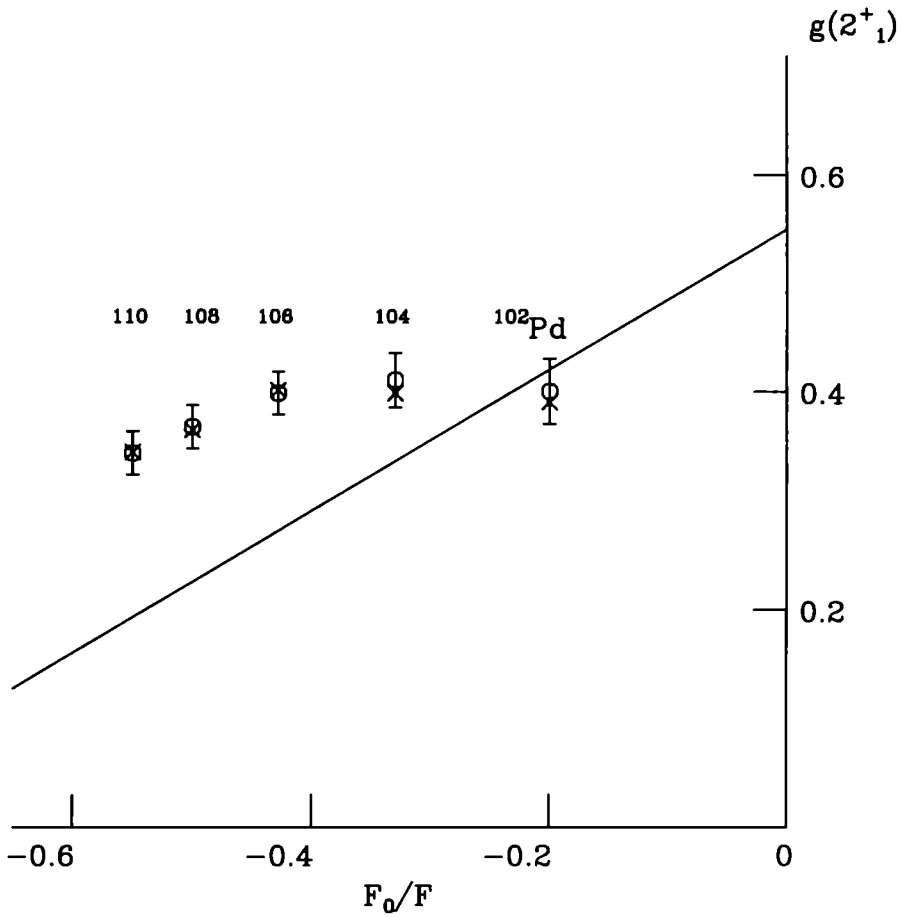

Figure 4: g-factors of 2_1^+ states vs. F_0/F. Circles=calculation;crosses=experiment. The straight line was calculated using eq. (16) with $g_\pi = 1.2$ and $g_\nu = -0.1$

values, the effective boson g-factors obtained in this way lead to reduced values of $B(M1; 2_2^+ \to 2_1^+)$ which are incompatible with the experimental ones. One can see that the fitted values of the boson g-factors are very close to the ones calculated in Section 4 on a microscopic basis.

It is clear that a consistent treatment of both M1 rates and static moments can not be achieved in the hypothesis of an F-spin pure 2_1^+ state. In order to achieve a good agreement for $g(2_1^+)$ we assumed that besides $\chi_\nu \neq 0$ also $\epsilon_\nu \neq 0$ [28] [29]. The F-spin breaking by means of ϵ influences mainly the g-factor. This is due to the large difference of the proton and neutron boson g-factors. On the contrary, χ_ν mainly influences the B(M1)'s. The F-spin mixing will be discussed in a more quantitative way in the next subsection.

Table 5: Boson g-factors; g-factors of the 2_1^+ states.

Nucleus	g_π	g_ν	$g(2_1^+)_{exp.}$	$g(2_1^+)_{th.}$
^{102}Pd	1.2	-0.10	0.40(3)	0.39
^{104}Pd	1.2	-0.15	0.41(3)	0.398
^{106}Pd	1.2	-0.095	0.398(21)	0.401
^{108}Pd	1.2	-0.15	0.367(20)	0.364
^{110}Pd	1.2	-0.16	0.343(17)	0.344

6.4. Mixed symmetry states

One of the important feats of the IBM-2 was the prediction of the mixed symmetry states (MSS) [5]. While states with $F = F_{max}$ [2] are completely symmetric with respect to the exchange of any two bosons, states with $F < F_{max}$ contain also antisymmetric boson pairs. The latter states are those with mixed symmetry. The existence of MSS was confirmed by the discovery of the so called scissors mode with $I^\pi = 1^+$ in electron scattering experiments [30] [31].

The 1^+ states have the peculiar feature of being practically pure. Since for $F = F_{max}$ there is no 1^+ state, there is no symmetric state they could mix with. This makes the scissors mode relatively accessible to experiment. Moreover, in deformed nuclei, which are close to the SU(3) limit of the IBM, the 1^+ state is the lowest MSS. In more vibrational nuclei, such as Pd for example, the lowest MSS have $I^\pi = 2^+$.This state can of course mix with the totally symmetric ones, provided the Hamiltonian of eq.(1) is not an F-spin scalar.

The M1 transitions from the MSS to the totally symmetric states are characterized by large values of B(M1), while the E2 transitions are weak. One type of mixed M1+E2 transitions which has been widely investigated is the $2_2^+ \rightarrow 2_1^+$ transition. In most of the nuclei investigated in this work $B(M1; 2_2^+ \rightarrow 2_1^+)$ is known. The values of the latter, as well as those of the fitted B(M1)'s are given in Tables 3 and 4.

The M1 transition strength is proportional to $(g_\pi - g_\nu)^2$ [9]. While the excitation energies and the B(E2)'s are dependent on $\chi_s = (\chi_\pi + \chi_\nu)/2$, it is the size of the parameter $\chi_v = (\chi_\pi - \chi_\nu)/2$ which determines the F-spin breaking responsible for the M1 transition. In other words, we need know something about the M1 transition strength in order to be able to determine both χ_π and χ_ν. In our case it is the $2_2^+ \rightarrow 2_1^+$ transition which provides this information. As an example, squared amplitudes of several 2^+ states of ^{104}Pd and ^{106}Pd are shown in Table 6.

One can see that while the 2_1^+ and 2_2^+ eigenstates are strongly dominated by the $F = F_{max}$ component, the strongest contribution to the 2_3^+ state is the one with $F = F_{max} - 1$. Since the probability for the latter is at least 0.6, we can describe the 2_3^+ states as having mixed symmetry.

This implies that the 2_3^+ states must be connected to the symmetric ones through strong M1 transitions. In ^{104}Pd the experiment provides only a lower limit $B(M1; 2_3^+ \rightarrow 2_1^+) \geq 0.013$, which is one order of magnitude larger than a "normal" B(M1). The

Table 6: Squared F-spin amplitudes of 2^+ states in ^{104}Pd and ^{106}Pd.

Nucleus	state	F=F_{max}	F=F_{max}-1	F=F_{max}-2
^{104}Pd	2_1^+	0.978	0.006	0.016
	2_2^+	0.871	0.067	0.061
	2_3^+	0.097	0.881	0.022
^{106}Pd	2_1^+	0.950	0.042	0.008
	2_2^+	0.959	0.025	0.016
	2_3^+	0.356	0.602	0.041

$2_3^+ \rightarrow 2_1^+$ transition in ^{106}Pd is characterized as M1+E2 with $\delta(E2/M1) = 0.24$. Obviously further experiments are needed, in particular on lifetimes, in order to obtain absolute values of B(M1).

An additional information can be obtained from inelastic scattering. By comparing the (p,p') and (d,d') cross sections, the isoscalar and isovector parts of the quadrupole transition matrix elements can be deduced. In this way, states which are being described as F-vector (scissors) states in a geometric model [30] and which correspond to the mixed symmetry states can be identified. The results of an inelastic scattering experiment on ^{106}Pd [14] indicate that the 2_3^+ state has mixed symmetry indeed. A 2^+ state at 3.07 MeV is also assumed to be a MSS. However, due to both the large level density and to ambiguous spin assignments, it is difficult to identify it to a definite IBM-2 state. Indications about possible MSS in ^{104}Pd and ^{110}Pd can be found in ref. [15] but again, it is difficult to identify specific individual states. Also in this respect better data are needed. In particular, the ambiguous spin assignments make a comparison with experiment quite risky.

7. Discussion

The fit of excitation energies and B(E2) in $^{102-110}$Pd can be considered as successfull. It would be premature to make a definite statement on ^{112}Pd, since most spin assignments are only tentative.

As it can be seen in Table 2, the parameter $\chi_s = (\chi_\pi + \chi_\nu)/2$ changes from about -0.4 in ^{102}Pd to -0.1 in ^{112}Pd.This shows that we deal with a typical U(5) to O(6) transition indeed.

Another important matter is that of the mixed symmetry states. Since we are able to fix $\chi_v = (\chi_\pi - \chi_\nu)/2$ by fitting $B(M1; 2_2^+ \rightarrow 2_1^+)$, we can obtain the distribution of the M1 strength over 2^+ states, i.e. to find likely candidates for mixed symmetry states. In light Pd nuclei this strength is concentrated in the 2_3^+ state, but the M1 strength gets fragmented and shifted with increasing neutron boson number. In ^{112}Pd it is the 2_5^+ state which has the largest M1 transition to 2_1^+. This shows that accurate enough inelastic scattering experiments are desirable in order to identify mixed symmetry states.

This investigation has confirmed the assumption of ref. [28] that the g-factors are

quite sensitive to F-spin mixing. As a consequence, we had to use different energies of the d_π and d_ν bosons.

A final remark on the general behaviour of the parameters. ϵ_π, ϵ_ν, and κ should be only weakly dependent on N_ν, as requested by the microscopic theory [2]. On the contrary, χ_ν changes rapidly with N_ν and the fitted values should be as close as possible to the microscopically calculated ones. If we compare Table 2 and fig. 1, we see thast these conditions are met.

8. Acknowledgements

The authors would like to thank Profs. H. Ejiri, M. Fujiwara and R. V. Jolos for stimulating discussions. This work has been partly supported by the Deutsche Forschungsgemeinschaft under contract Br.799/5-1 and by the Grant-in-Aid for Scientific Research on Priority Areas (N0.05243102) by the Ministery of Education, Science and Culture of Japan.

1. F. Iachello and A. Arima, The Interacting Boson Model (Cambridge University Press, Cambridge, UK, 1987)
2. T. Otsuka in Algebraic Approaches to Nuclear Structure, ed. R. F. Casten (Harwood Academic, Langhorne, USA, 1993)
3. P. van Isacker and G. Puddu, Nucl. Phys. **A348**, (1980) 125
4. T. Otsuka, Nucl. Phys. **A557**, (1993) 531c; T. Mizusaki and T. Otsuka, to be published
5. T. Otsuka, A. Arima and F. Iachello, Nucl. Phys. **A309**, (1978) 1
6. G. Puddu, O. Scholten and T. Otsuka, Nucl. Phys. **A348**, (1980) 109
7. T. Otsuka and N. Yoshida, User's Manual of the Program NPBOS, JAERI-M report 85-094 (Japan Atomic Energy Research Institute, 1985)
8. A. Arima, T. Otsuka , F.Iachello, and I. Talmi, Phys. Lett.**B66** (1977) 205
9. P. O. Lipas,P. von Brentano and A. Gelberg, Rep. Progr. Phys. **53**,(1990) 1355 and references within
10. W. Greiner, Phys. Rev. Lett. **14** (1965) 599
11. A. Faessler, Nucl. Phys. **85** (1966) 653
12. N. V. Zamfir, R. F. Casten and D. S. Brenner, Phys. Rev. Lett. **71**, (1993) 227
13. R. F. Casten and P. von Brentano, Phys. Lett. **152B**, (1985) 22
14. R. De Leo, L. Lagamba, N. Blasi, S. Micheletti, M. Pignanelli, M. Fujiwara, K. Hosono, I. Katayama, N. Matsuoka, S. Morinobu, T. Noro, S. Matsuki, H. Okamura, J. M. Schippers, S. Y. van der Werf, and M. N. Harakeh, Phys. Lett. **B226** , (1989) 5
15. M. Pignanelli, S. Micheletti, N. Blasi, R. de Leo, W. T. A. Borghols, J. M. Schippers, S. Y. van der Werf, M. N. Harakeh, Phys. Lett. **B202**, (1988) 470
16. K. Heyde in Perspectives of the Interacting Boson Model, ed. R. F. Casten et al. (World Sientific, Singapore, 1994)

17. M. Luontama, R. Julin, J. Kantele, A. Passoga, W. Trzaska, N. -G. Jonsson and L. Westerborg, Z.Phys. **A324**, (1986) 317
18. D. de Frenne and E. Jacobs,NDS *63 (1991) 373
19. J. Blachot, NDS **64**, (1991) 1
20. D. de Frenne and E. Jacobs, NDS **72**, (1994) 1
21. L. E. Svensson, C. Fahlander, L. Hasselgren, A. Bäcklin, L. Westerberg, D. Cline, T. Czosnyka, C. Y. Wu, R. M. Diamond, H. Kluge, Nucl. Phys. **A584**, (1995) 547
22. J. Blachot, NDS **62**, (1991) 803
23. D. de Frenne and E. Jacobs , NDS **67** (1992) 809
24. D. de Frenne, E. Jacobs and M. Verboven, NDS **57**, (1989) 443
25. M. Deleze, S. Drissi, J. Kern, P. A. Tercier, J. P. Varlet, J. Rikovska, T. Otsuka, S. Judge and A. Williams, Nucl. Phys. **A551**, (1993) 269
26. P. Raghavan, At. Data and Nucl. Data Tables, **42**, (1989) 189
27. A. Wolf, R. F. Casten and D. Warner, Phys. Lett. **B190**, (1987) 19
28. A. Wolf, R. F. Casten, O. Scholten and D. Warner, Phys. Lett. **B132**, (1993) 372
29. E. D. Davis and P. Navrátil, Phys. Rev. **C50**, (1994) 2362
30. D. Bohle, A. Richter, W. Steffen, A. E. L. Dieperink, N. Lo Judice, F. Palumbo, and O. Scholten, Phys. Lett. **B137**, (1984) 27
31. A. Richter Nucl. Phys. **A522**, (1991) 139c

*Nuclear Data Sheets

RADIOACTIVE NUCLEAR BEAMS AND THE EVOLUTION OF COLLECTIVITY IN NUCLEI

R.F. CASTEN
Yale University, New Haven, Connecticut 06520, USA
Brookhaven National Laboratory, Upton, New York 11973, USA

N.V.ZAMFIR
Brookhaven National Laboratory, Upton, New York 11973, USA
Clark University, Worcester, Massachusetts 01610, USA
Institute of Atomic Physics, Bucharest-Magurele, Romania

ABSTRACT

The advent of Radioactive Nuclear Beams (RNBs) has opened up new nuclear territories to exploration. Recent theoretical work suggests that nuclear structure in these new regions may be unlike anything observed to date and that its study may substantially alter our concepts of shell structure, collectivity and the evolution of nuclear behavior. To face the challenge of inevitably low RNB intensities, new, more efficient signatures of structure and new experimental techniques are being developed. We discuss these topics and also summarize the current status of RNB facilities and facility planning in North America.

1. Introduction

Nuclear structure physics is entering a new era and enjoying a dramatic renaissance. This is being driven by the new experimental capabilities embodied in the use of radioactive nuclear beams (RNBs) which are opening up for us realms of heretofore unaccessible nuclei in exotic regions. These nuclei include medium mass $N = Z$ nuclei and neutron-rich species, where there is every likelihood of discovering nuclear behavior and structure unlike anything observed to date.

Aside from extensive work on developing the facility concepts to produce RNBs in the first place, the dawning of the RNB age has engendered at least four major new thrusts in nuclear physics. Nuclear astrophysics is entering a new phase where critical nuclei and critical reactions will finally be accessible to direct study. The opportunities offered by RNBs, combined with the fact that, initially, RNB intensities will be orders of magnitude lower than the stable beam intensities we are accustomed to, has led to twin efforts to develop, on the one hand, new and much more efficient instruments and measuring techniques and, on the other, simple empirical signatures of structure based on the easiest-to-obtain data. Finally, the

possibility to access truly exotic, near-drip-line nuclei has led to a major upheaval in our theoretical understanding of the properties of these nuclei. With this has come the recognition that the traditional underpinnings of nuclear structure in a more or less standard Shell Model Hamiltonian acting on single particle states occurring in familiar shells with familiar sequences of single particle energies (s.p.e.'s) and familiar residual interactions is not, in fact, an immutable edifice. Rather, the Shell Model near stability is likely to be only a particular reflection of a richer and more general framework.

The excitement engendered by the opportunities for research with RNBs is widely recognized worldwide. Major RNB facilities (primarily of projectile fragmentation type—see Section 4) already exist in North America, Europe and Japan and most of these facilities have major upgrade initiatives approved or in the planning stages. Wholly new first-generation facilities of ISOL-type (see also Section 4) are being built, and advanced ISOL facilities are being proposed.

The growing momentum embodied in this groundswell was recently reflected in the Long Range Plan (LRP) for Nuclear Science carried out in the first half of 1995 in the United States. In this document, a very strong endorsement of RNB science was made. The LRP Interim Report[1] stated that "The scientific opportunities made available by world-class radioactive beams are extremely compelling and merit very high priority." The first recommendation for new construction initiatives in the LRP states that "We strongly recommend the immediate upgrade of the MSU facility to provide intense beams of radioactive nuclei via fragmentation", and that "We strongly recommend development of a cost-effective plan for a next generation ISOL-type facility and its construction when RHIC construction is substantially complete." This recommendation explicitly recognizes the complementary role of the two principal approaches to the production and use of RNBs.

The remainder of the present discussion will focus on three of the four thrusts cited above, namely a qualitative summary of some of the new theoretical ideas and concepts for exotic nuclei; the development of new signatures of structure (exploiting a different framework for *viewing* nuclear structure); and the adaptation of experimental techniques to the challenges offered by RNBs. We will also include a brief summary of the current (late 1995) status of RNB facilities in North America.

2. Structure of Exotic Nuclei

Recently, there has been a growing recognition that the exotic nuclei made accessible with RNBs may have structure and properties quite different from anything observed to date. Radical changes in shell structure, residual interactions, symmetries, collective modes and the evolution of structure are envisioned. Even the basic concepts of nuclear shape and surface and shell structure themselves are being re-evaluated. Coupling to the continuum must be taken seriously. New forms of nuclear matter(e.g., halo nuclei) have already been observed, and their study expands the horizons of our science. It is therefore useful to review a few of the concepts motivating, and resulting from, recent pioneering theoretical efforts to understand

exotic near-drip-line nuclei.

2.1. Proton Rich Nuclei—the $N = Z$ Line

On the proton rich side, for example, the heavy $N = Z$ nuclei from ^{80}Zr to ^{100}Sn will become accessible to serious study. ^{80}Zr is known to be deformed. (In itself, this is an interesting phenomena in that N, Z values of 40 are, in some nuclei, magic numbers.) ^{100}Sn is expected to be the heaviest bound self-conjugate nucleus and is thought to be itself doubly magic. In $N = Z$ nuclei the $T = 0$ residual interaction dominates. As can be easily understood[2] from Wigner's supermultiplet theory, this dominance is essentially a singularity: even at $N = Z \pm 2$, the $T = 1$ interaction has already assumed its traditional advantage. Therefore, $N = Z$ nuclei form a unique "trajectory" through the nuclear chart. The ^{80}Zr to ^{100}Sn region may therefore constitute an isolated spherical-deformed transition region, which is effectively a 1-dimensional slice through the N/Z plane, and the only new shape transition we will ever be able to study that is controlled by the $T = 0$ interaction. A slice perpendicular to the $N = Z$ line could show the most rapid and dramatic phase transitions yet observed. Of course, if ^{100}Sn turns out to be deformed, the consequences are even greater and strike at the heart of our understanding of the underlying shell structure of nuclei. There are many other features of interest in $N \sim Z$ nuclei. For example, with a strong $T = 0$ residual interaction, the coupling and alignment of high j orbits due to the Coriolis force is likely to be quite different than in other nuclei. Backbending and band crossings may be delayed.

2.2. Neutron Rich Nuclei—New Manifestations of Structure and Collectivity

The neutron rich side of stability, which we focus on in this paper, is even more interesting. In part this is due to the longer "lever arm" from the valley of stability, and hence the greater uncertainty in extrapolation, but, in greater measure, it is due to the wealth of exotic phenomena expected near the neutron drip line. The rationale for this is simple. Near the edges of stability on this side, the outer realms of nuclei are comprised, essentially, of an extended, diffuse, low-density region of nearly-pure neutron matter. As suggested in recent studies[3], such a diffuse density distribution is unlikely to be able to support a shell model potential with sharp contours. Hence, even the traditional form of the Shell Model Hamiltonian itself, long cherished as the underlying basis for nuclear structure, may be radically altered. Its Woods-Saxon form may go over into a more rounded harmonic oscillator shape. In the language of the Nilsson model, this corresponds to the vanishing of the "l^2" term.

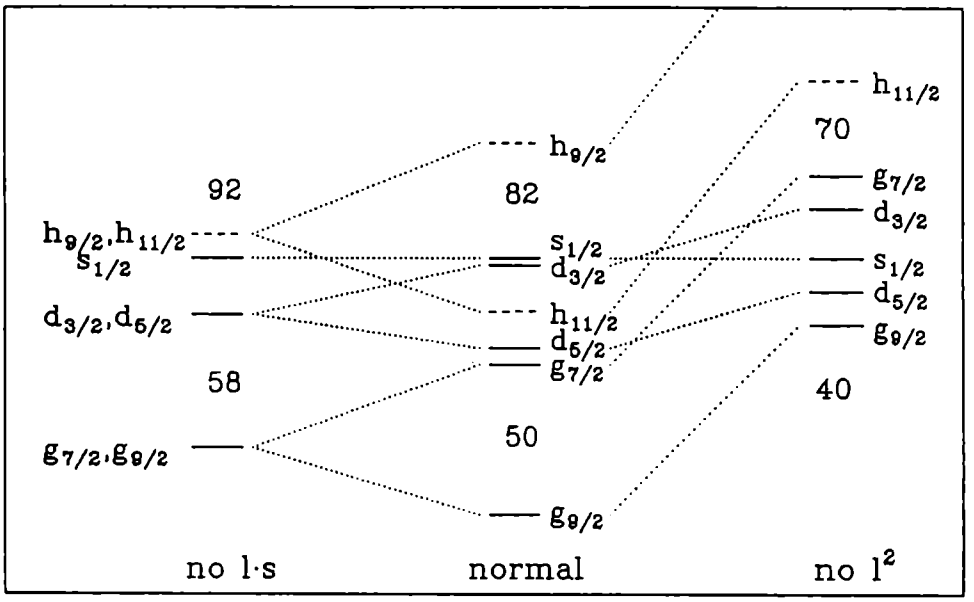

Fig. 1. Single particle energies in the standard Shell Model (middle), in a scenario with no $l \cdot s$ term (left), and with no "l^2" term (right).

The consequences of this are hard to overestimate. Consider the single particle levels that would result in such a scenario. These are illustrated on the right in Fig. 1. The effects of the no-l^2 scenario are to drastically raise the energy of the unique parity orbits which return to their parent shells. Hence, the magic numbers change. Naturally, high spin phenomena and octupole correlations will also be dramatically altered since they depend in essential ways on the location of these special orbits. But, more profound changes occur. The traditional order (see Fig. 1, center) of the normal parity orbits, namely monotonically decreasing in j by $\Delta j = -1$ as their energy increases is completely upset. Instead, one encounters a "nested" pattern of j orbits with the highest j orbits surrounding the middle j, which in turn enclose still lower j orbits, and so on. Moreover, the j spin sequence is now $\Delta l = \Delta j = -2$ throughout (recall that $1/2 \rightarrow 3/2$ is also "$\Delta j = 2$"). It can easily be imagined that the manifestations of collectivity, and especially its evolution with N and Z, could be significantly different than near stability since the quadrupole force specifically favors the coupling of orbits with $\Delta l = \Delta j = 2$. Figure 1 also illustrates an alternate possibility, equally intriguing, namely the absence of the spin orbit interaction. There are suggestions that this could characterize some neutron rich nuclei or perhaps only the proton orbits inside the diffuse neutron skin.

The effects on structure near the neutron drip line go beyond such scenarios,

however. The weak binding of the outermost neutrons and the proximity of quasi-bound levels means that coupling to the continuum must be considered. Moreover, as the uppermost orbits in a shell merge into the continuum (perhaps as quasi-bound levels) the remaining bound levels no longer constitute a complete sequence of j values from some j_{max} down to $j = 1/2$. In the example in Fig. 1 (right), for example, the first orbit into the continuum would be $j = 7/2$. The distorted single j-shell sequences, and the merging into and coupling with the continuum, could easily change the symmetries [such as SU(3) or pseudo-SU(3)] associated with the fermionic states.

Beyond this, residual interactions will also be different. The pairing interaction near the drip line, where wave functions are greatly extended, could become significantly stronger. The neutron excess, leading to a difference in proton and neutron orbits, will alter the p-n interaction as well.

Finally, geometrical concepts of the nucleus are unlikely to survive intact. Just as the diffuse outer zones of neutron rich nuclei may not support sharply defined shell model potentials, they may not support strongly defined surfaces. For example, the outer boundries of such nuclei may be, in effect, spherical. Yet the well-defined inner core may be deformed and might even rotate or vibrate relative to the neutrons. Exotic isovector collective modes might occur.

3. Simple Signatures of Structure: Universal Correlations of Collective Observables

Traditionally, nuclear structure is viewed in a "vertical" sense in terms of the excitations in a specific nucleus or in a small region of nuclei. Virtually all models and experiments are designed to look at nuclear structure in this way. Yet, the present situation in nuclear physics offers an alternative approach.

Over the years, a tremendous body of nuclear structure data has been built up through countless experiments and a number of different types of structure have been identified such as nuclei near closed shells, vibrational nuclei, rotational nuclei, and many varieties of intermediate forms. The vast reservoir of data now offers a unique opportunity to explore nuclear structure in a *horizontal or evolutionary* way.

This can be done by studying *correlations* of collective observables either with external quantities or with other collective observables. From such studies a growing realization has emerged that the seemingly-complex evolution of structure across the nuclear chart can in fact be viewed very simply.

Fascinating as the concepts of structure for exotic nuclei discussed above may be, they will be of little use if we cannot identify new manifestations of structure from the limited data that will be obtained with RNBs. Of course, in many cases, detailed spectroscopy will be necessary, including nucleon transfer reactions and γ-ray spectroscopy. However, frequently, insights into exotic nuclei can be provided by exploiting these correlations to provide new signatures of structures based on the easiest-to-obtain data. Of course, correlations such as these may or may not apply in new regions. If they do, they provide an evolutionary paradigm. If they do not,

their breakdown will itself signal the radical kinds of structural and evolutionary changes we have been discussing. In this section, we will discuss a few of these signatures. Others have also been developed, and work is continuing on new ones.

The N_pN_n scheme[4] (recently reviewed in ref. 5), in which collective observables are plotted against the product of the number of valence protons and the number of valence neutrons, has been a valuable method to disclose the underlying simplicity that is normally hidden in the complexity of nuclear data. The scheme is based, of course, on the assumption that the evolution of collectivity is largely controlled by the residual valence $p-n$ interaction and that the integrated $p-n$ interaction strength, averaged over all occupied valence orbits, approximately scales as N_pN_n. It is fitting to show some recent results of the N_pN_n scheme (and the related P-factor[6]) here since it was at the 1984 School in Poiana Brasov that the concept was first introduced.

A fascinating aspect of the N_pN_n scheme is that N_pN_n values for many nuclei far from stability are actually less than for known nuclei closer to stability. For example, N_pN_n for ^{166}Dy is 288 while N_pN_n values for ^{146}Xe, ^{150}Ba and ^{160}Sm are only 40, 72 and 192, respectively. Thus the properties of many exotic nuclei can be predicted in the N_pN_n scheme by *inter*polation rather than *extra*polation.

We illustrate the idea in Figs. 2 and 3. Figure 2 shows normal and N_pN_n plots for $E(2_1^+)$ in the $A=150$ region. The enormous simplification in the N_pN_n scheme is typical. Note that, in using the scheme, it is, of course, necessary to know the nearest magic numbers in order to properly count N_p and N_n and to take account of important spherical subshell gaps. Indeed, we shall see that the N_pN_n scheme can be used to give information on the underlying shell structure. For now, we just note that, in Figs. 2,3, $Z=64$ is taken as a subshell gap for $N<90$ but not for $N\geq 90$.

Using the N_pN_n plots in Fig. 2, it is trivial to make predictions for $E(2_1^+)$ in unknown nuclei simply by reading off the curve in Fig. 2b at the appropriate N_pN_n value. Such predictions are shown in Figs. 2a,3. The spread of the data in Fig. 2b suggests that these predictions are accurate to about $\pm$ 15%. The reader is encouraged to attempt to use the systematics of Fig. 2a to make similar predictions. The uncertainties will often be much larger and the results sometimes simply wrong. To illustrate this, Fig. 2a shows (as dashed curves) the N_pN_n predictions taken from the right side. Clearly, the predictions from Fig. 2b are hardly what one would have predicted if one had only traditional types of systematics like those shown in Fig. 2a. ^{142}Xe provides a nice example where the $N=88$ and $Z=54$ trendlines in Fig. 2a suggest quite different extrapolations. When the idea of Fig. 2b was first proposed, ^{142}Xe was unknown. Subsequently, it has been studied[7] with the result $E(2_1^+)=0.287$ MeV compared to the N_pN_n prediction of 0.300(40) MeV.

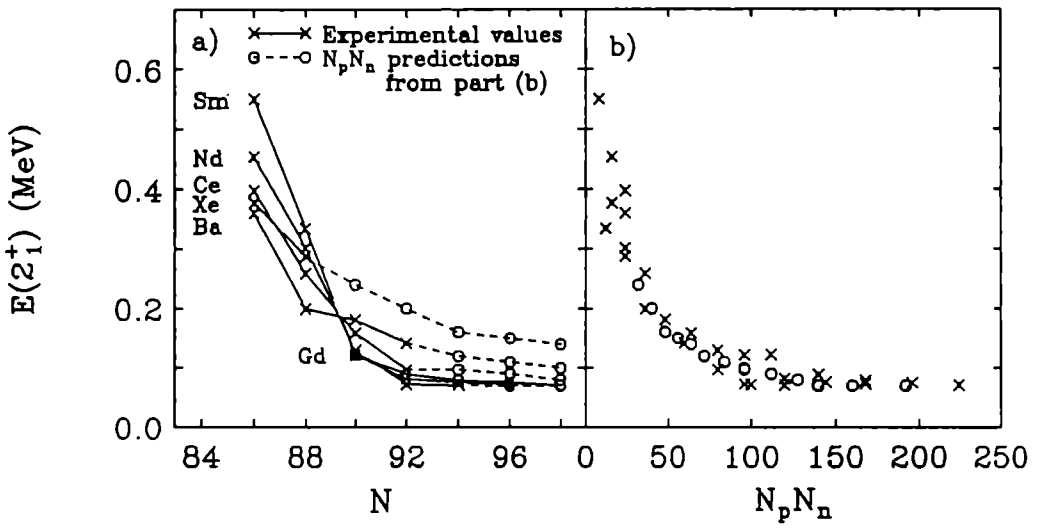

Fig. 2. Correlation of $E(2_1^+)$ with N and with N_pN_n in the $A \sim 150$ region. On the left, the dashed lines are the predictions given by the N_pN_n scheme of Fig. 2b. They are not the most obvious extrapolations one would make if guided only by the trends in Fig. 2a itself.

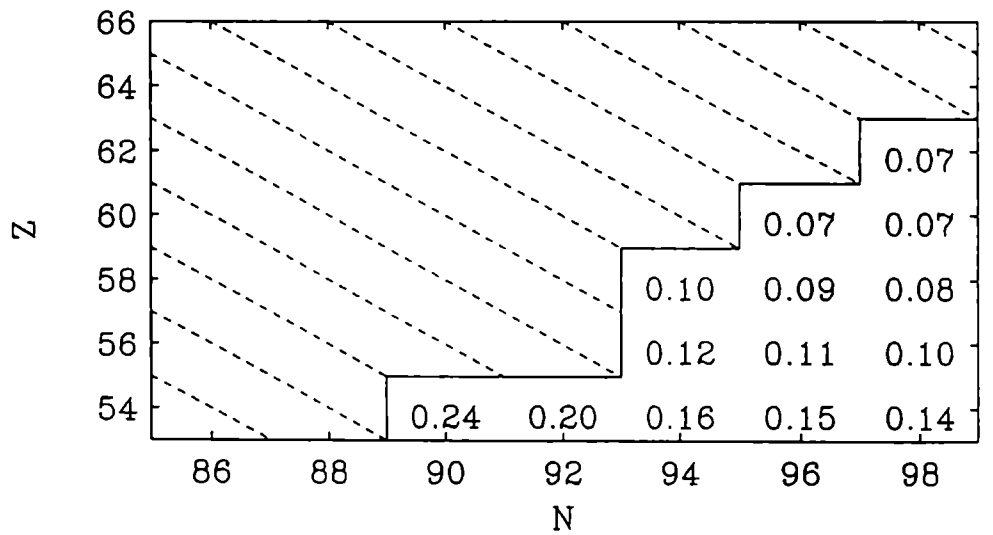

Fig. 3. Predictions of the N_pN_n scheme for $E(2_1^+)$ (in MeV) in the $A \sim 150$ region. Based on Fig. 2b.

Despite the obvious utility of N_pN_n, its actual numerical value is not too meaningful due to different shell sizes. A useful quantity whose absolute value conveys a more precise physical idea is the $P - factor$,[6] defined as

$$P = \frac{N_pN_n}{N_p + N_n} \tag{1}$$

P is a "normalized" N_pN_n giving the number of $p - n$ interactions per valence nucleon. More significantly, it is the number of valence $p - n$ interactions divided by the number of pairing interactions and is therefore related to the ratio of the integrated strengths of these interactions. Since typical $p - n$ matrix elements are ~ 0.2 MeV, and the pairing interaction strength is ~ 1 MeV, $P \sim 5$ corresponds to the point at which the $p - n$ interaction strength begins to dominate the pairing strength. It is hardly surprising that nuclei become deformed for P values near 5.

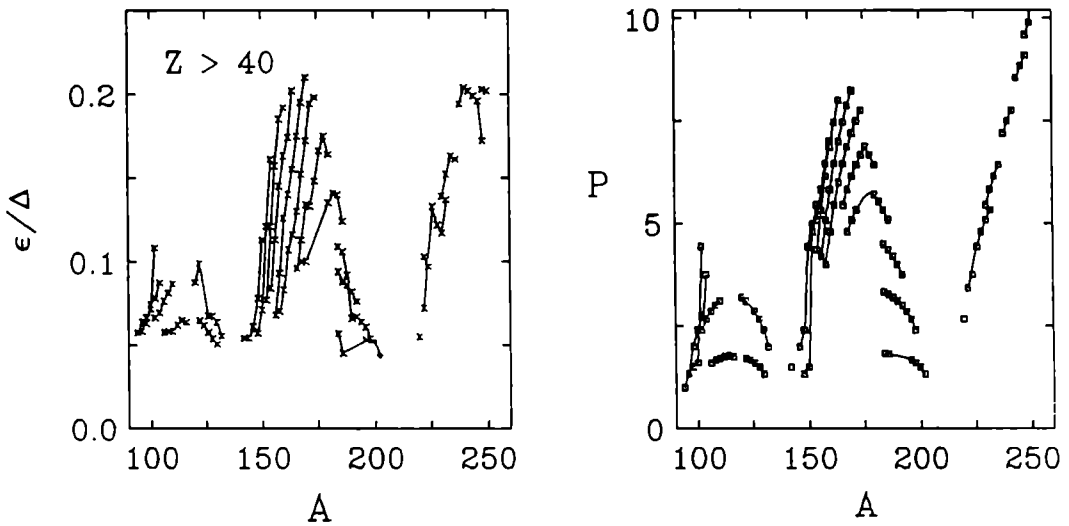

Fig. 4. Comparison of empirical ϵ/Δ and P values. Ref. 8.

There is an elegant way of demonstrating that P senses the competition between $p-n$ and pairing interactions. An empirical measure of this competition, the ratio ϵ/Δ, where ϵ is the usual quadrupole deformation and Δ is the average pairing gap [$\Delta = (\Delta_p + \Delta_n)/2$], can be empirically extracted from $B(E2)$ values and odd-even mass differences. A nearly global comparison of ϵ/Δ values with P is shown in Fig. 4 [8]. The match is excellent, even in fine details.

The significance of this is worth stressing: it is possible to account for the evolution of collectivity and the competition between deformation and spherical-driving forces without resorting to complex microscopic calculations or to multi-parameter phenomenological schemes. Instead, reproduction of the behavior of

virtually all nuclei from $Z = 40-100$ is obtained merely by multiplying two numbers and dividing by their sum.

3.1. B(E2) values and magic numbers

We mentioned above that the N_pN_n scheme can be useful in identifying magic numbers and hence in elucidating the underlying shell structure. We give two illustrations of this.

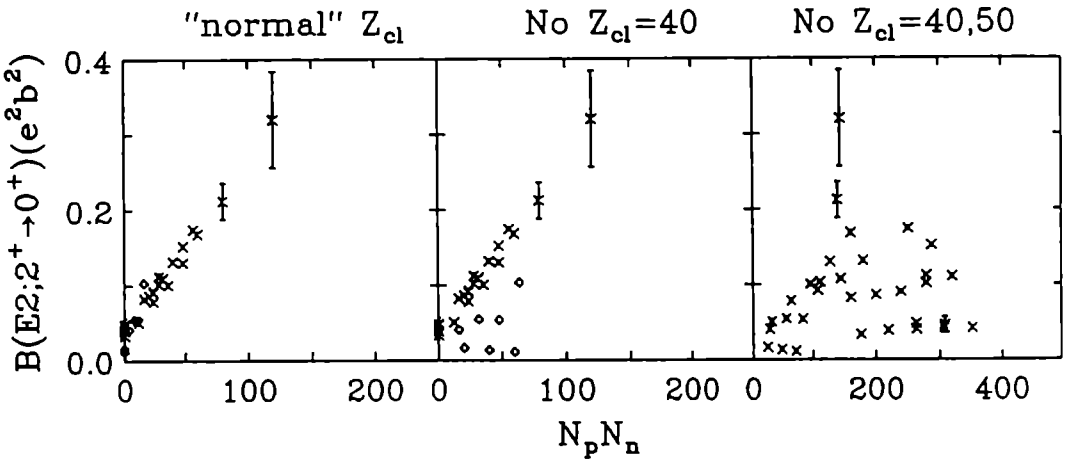

Fig. 5. $B(E2)$ values as a function of N_pN_n for the $A \sim 100$ region under three assumptions concerning magic numbers and shell gaps. (See text.)

The basic idea is that $B(E2 : 2_1^+ \rightarrow 0_1^+)$ values (hereafter "$B(E2)$ values") behave simply in N_pN_n plots. Of course, a previso for this is an accurate counting of N_pN_n. If shell structure is altered from that defined by the traditional magic numbers, or is unknown, the use of incorrect N_p and N_n values can generate large deviations from simple patterns. Figure 5 illustrates this for the $A \sim 100$ region. On the left, standard magic numbers are used, namely $Z = 40, 50$ for $50 < N < 60$, $Z = 28, 50$ for $N \geq 60$. A compact, indeed linear, correlation is achieved. If the well known subshell at $Z = 40$ for $N < 60$ were *not* assumed, however, the correlation becomes messy (Fig. 5, middle). Suppose further that $Z = 50$ is not taken as a magic number. Then the plot on the right of Fig. 5 is obtained. Clearly, the compact correlation for $B(E2)$ values against N_pN_n is destroyed. Even in advance of specific level scheme data on ^{100}Sn, this certainly suggests that the $Z = 50$ proton shell closure is intact, at least for nuclei within a few proton or neutron numbers of 50.

A second example concerns ^{32}Mg. Although it has $N = 20$, it is a quasi-deformed nucleus. This suggests that $N = 20$ is not magic. We can test this notion using the $B(E2)$ value. If $N = 20$ were magic, then N_n would be zero as would N_pN_n, giving a near-vanishing $B(E2)$ value. If $N = 20$ is not magic, then the nearest closed neutron shell is $N = 28$, and $N_pN_n = 4x8 = 32$. This N_pN_n value gives

$B(E2: 2_1^+ \rightarrow 0_1^+)_{N_pN_n} \sim 0.04e^2b^2$ in good agreement with the measured value of 0.045(8) e^2b^2.[9]

3.2. Hexadecapole Deformations and $B(E2)$ Values

Finally, we show one more illustration[10] of the use of the N_pN_n scheme. In this case, it (or, equally well, the P factor) provides semi-quantitative information on subtle aspects of nuclear shape, in particular on hexadecapole deformations (β_4).

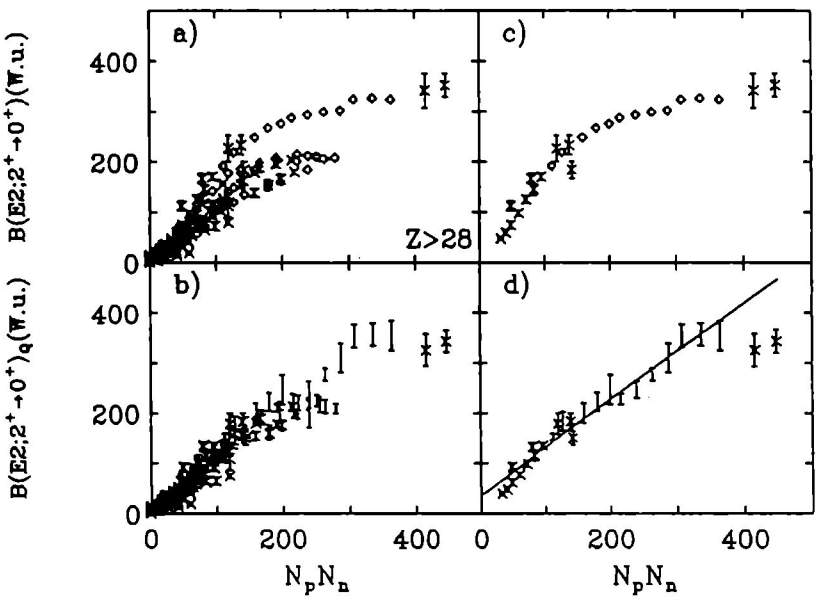

Fig. 6. (Top) $B(E2)$ values against N_pN_n. (Bottom) $B(E2)_Q$ values [i.e., $B(E2)$ values corrected for β_4—see text] against N_pN_n. Based on ref. 10. Crosses denote nuclei where β_2, β_4 values from ref. 11 were used to correct $B(E2)$ values: in all other cases, empirical β_2, β_4 values were used.

Figure 6a shows $B(E2)$ values against N_pN_n for all even nuclei with $Z > 28$. Although the correlation is simpler than one against N or Z, it seems to show several branches. To understand the origin of this phenomenology, note that the quadrupole moment

$$Q(2^+) \sim \beta_2(1 + 0.3604\beta_2 + 0.9672\beta_4 + 0.3277\frac{\beta_4^2}{\beta_2} + ...) \qquad (2)$$

depends on β_4 and on its sign. Since $\sqrt{B(E2)} \propto Q$, the $B(E2)$ values do also. In any major shell β_4 deformations have a characteristic systematics. They are large and positive early in a shell, cross zero near mid-shell and then turn large

and negative. Thus, from eq. 2, $B(E2)$ values are increased by the effects of hexadecapole deformations early in a shell and decreased later on. This leads to the curvatures evident in Fig. 6a. If, however, the effects of β_4 deformations are *removed* from the $B(E2)$ values (by moving the β_4 terms to the left hand side of eq. 2), giving the values that *would* arise if β_4 were zero, the resulting $B(E2)$ values (which we call "$B(E2)_Q$" values since they reflect the contributions from quadrupole deformations alone) are nearly straight against N_pN_n as shown in Fig. 6b.

The linear trajectory means that if $B(E2)$ values are measured in new nuclei, deviations from such trajectories can be used to estimate unknown β_4 values. Figures 6c,d illustrate this by showing $B(E2)$ and $B(E2)_Q$ values for actinide nuclei. Clearly the $B(E2)_Q$ values lie on a nearly straight line trajectory. We note that, at the far right of Fig. 6d, the $B(E2)_Q$ values for ^{250,252}Cf (obtained with theoretical β_2, β_4 from ref. 11) fall well below the trendline. One can estimate the required β_4 to move these two points to the line. We obtain $\beta_4 \sim -0.07$. Interestingly, theoretical calculations do not give a negative value. Thus, not only do we extract a semi-quantitative estimate of β_4, but we can address possible improvements to calculations of the heaviest elements.

3.3. $R_{4/2}$ values and underlying shell structure

In Section 2, we discussed possible scenarios for new shell structure near the neutron drip line that have recently been discussed[3], including the so-called "no-l^{2}" case. Though it is hardly likely that this scenario will be realized in the extreme limit shown in Fig. 1, it is interesting to ask if clues to such changes in shell structure could be obtained from simple observables. This has recently been discussed in ref. 12 where we proposed that the simple ratio $R_{4/2} \equiv E(4_1^+)/E(2_1^+)$ is sensitive to the j and Δj shell sequences.

Consider two like nucleons in a single-j configuration, $\mid j^2 J >$, under the influence of a short range interaction (surface δ force). Then, $R_{4/2} \sim 1.2$. Similar $R_{4/2}$ values arise for $\mid j^n J >$, and for a multi-j configuration of the type $\mid j_1^{n_1} J_1, j_2^{n_2} J_2 ..... J >$ where n_1, n_2 ..... are even. Consider, however, a two particle system with a particle in each of two orbits, that is, $\mid j_1 j_2 J >$. If $\mid j_1 - j_2 \mid \neq 2$, then the 2^+ state is formed by a non-co-planar alignment of angular momenta. Hence, with a short range interaction, the 2^+ state will not be lowered substantially relative to the 4^+ state: $R_{4/2}$ remains near 1.2. However, suppose $\mid j_1 - j_2 \mid = 2$. Then the 2^+ state requires *co-planar* alignment of the two angular momentum vectors and hence a large overlap and interaction, and thus the 2^+ state is strongly lowered. This gives larger $R_{4/2}$ values, which can even attain magnitudes of ~ 1.8 for a 2-particle system. These simple ideas may account for the existing phenomenology of $R_{4/2}$ values in magic nuclei and may provide a signature for "$\Delta j = 2$" j-shell structure near the neutron drip line. Figure 7 shows that, in the $s-d$ and $p-f$ shells, where, in fact, $\Delta j = 2$, empirical $R_{4/2}$ values rise even above 1.5. Only in heavy nuclei, where the j_{max} state has descended to the next lower shell (where it is the unique parity orbit), and the remaining j-sequence is $\Delta j = 1$ (see Fig. 1, middle panel)

does $R_{4/2}$ approach $\sim$ 1.2. These empirical systematics are easily reproduced by schematic calculations with a surface δ-force as shown on the right (solid line) in Fig. 7. However, superposed in this figure are two calculations of $R_{4/2}$ using the $\Delta j = 2$ no-l^2 scenario of Fig. 1[13]. Clearly, the $R_{4/2}$ values calculated with no l^2 term are anomalous, and such large $R_{4/2}$ values in new regions made accessible with RNBs could signal major changes in underlying j-structure.

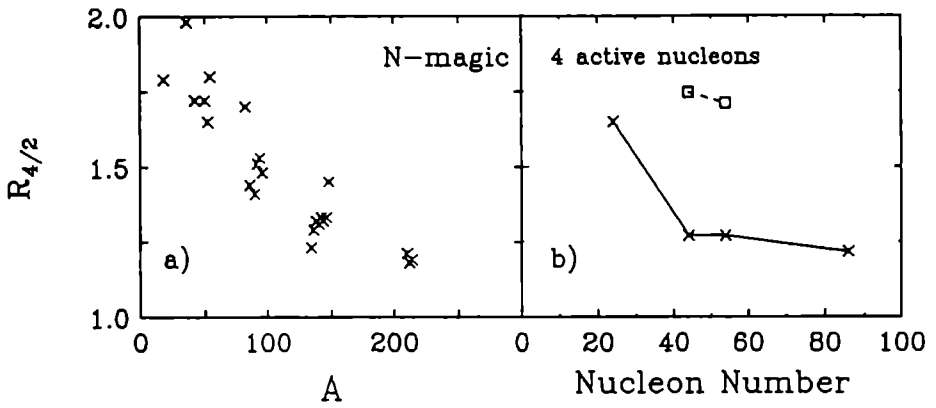

Fig. 7. (Left) Empirical $R_{4/2}$ values for neutron magic nuclei. (Right) Calculations of $R_{4/2}$ with a δ-function interaction using "normal" single particle energies and smoothly decreasing interaction strength (solid line) and for the "no-l^2" scenario of shell model s.p.e.'s in Fig. 1 (two upper points). Based on refs. 12,13.

3.4. Correlations between Collective Observables

We now discuss another kind of correlation, in this case *between* collective observables themselves, $E(4_1^+)$ and $E(2_1^+)$. Considering that the ratio $R_{4/2}$ varies from $\sim$ 1.2 for some magic nuclei to $\sim$ 3.33 for good rotors, it might seem unlikely that $E(4_1^+)$ would be simply correlated with $E(2_1^+)$. Yet it is, and the correlation is simpler, more universal, and more informative than could possibly have been expected[14,15].

We show this in Fig. 8 which includes *all* even-even nuclei with Z between 50 and 82 regardless of $R_{4/2}$ value. The data display a tight correlation characterized by three linear segments. Each segment has a specific, physically meaningful slope, and the transitions between segments are extremely rapid. At the lowest 2_1^+ energies, the data are well reproduced by a slope of 3.33. This segment is the rotor region and is not unexpected. The next segment, though, certainly is. All the nuclei from $E(2_1^+) \sim 150$ keV to ~ 500 keV lie on a linear trajectory with a least squares fitted slope of 2.00. That is

$$E(4_1^+) = 2E(2_1^+) + \epsilon_4 \qquad (3)$$

This is the equation for an anharmonic vibrator (AHV). The remarkable point

is not that the AHV can reproduce the energies of any *individual* nucleus, but rather that *all* these nuclei are fit with a constant intercept $\epsilon_4 = 0.16(1)$ MeV. Physically, in the AHV, ϵ_4 is the anharmonicity and can be viewed as reflecting the phonon-phonon interaction. Clearly, from the $R_{4/2}$ values (approximate $R_{4/2}$ values are given at the top of the figure), the structure of the nuclei in the AHV region is changing continuously. Nuclei in this segment of the plot range from near rotors, to transitional nuclei, to γ-soft structures to traditional anharmonic vibrators and to near harmonic vibrators. Yet, somehow, they all display nearly the same ϵ_4 value. A microscopic understanding of this has not yet been found, but IBA calculations[16] do reproduce it automatically. Analysis of these calculations (see the analytic derivation in ref. 17) shows that they inherently embody a good phonon structure[18] and that the near-constant anharmonicity emerges naturally for a wide variety of parameter values. Evidently, eq. 3 with constant ϵ_4 must result from rather general features of shell structure and residual interactions. In passing, we note that many other features of nuclear excitations are also described well by the AHV. These include yrast $B(E2)$ values and energies extending to much higher spins, and γ- and $K = 0^+$-band energies as well[19,20].

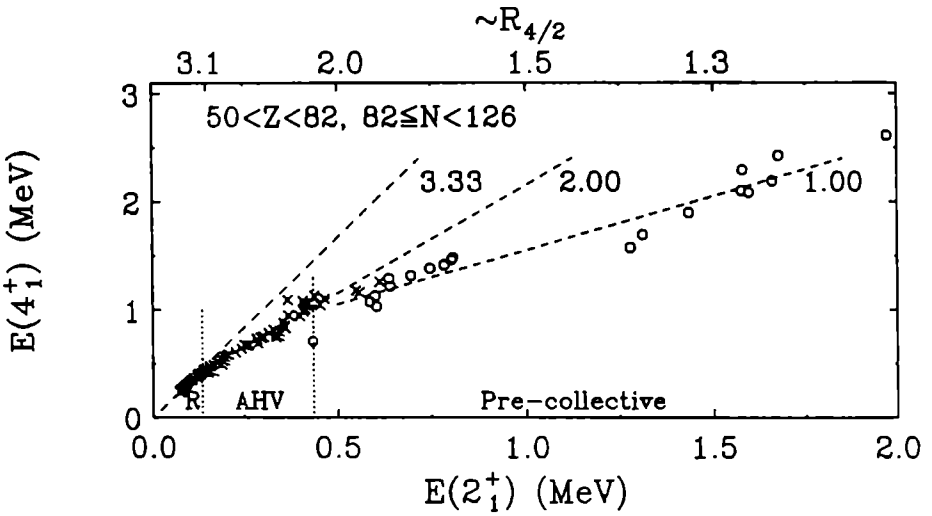

Fig. 8. Correlations of $E(4_1^+)$ with $E(2_1^+)$ for $Z = 50$-82.

The third segment of Fig. 8 is the pre-collective regime with $R_{4/2} < 2$. Herein, again, a linear behavior is noted and the slope is unity. This value also has a simple explanation. It is not, as might first be thought, a reflection of the seniority scheme in which all yrast [$|| j^n J >$] energies are constant. This is generally not the case empirically. Indeed, it is a rare occurrence, the Sn isotopes being the best case.

However, if the wave functions of the n-particle nucleus are constructed from those of the $(n-2)$-particle nucleus by addition of the $(n = 2)$-particle wave function

of the 0^+ state, then the excitation energies of the 2_1^+, 4_1^+, ... levels will change identically since they differ, in the n- and $(n-2)$-particle nuclei, by exactly the same 2-particle wave function[15]. Hence $E(4_1^+) - E(2_1^+)$ will be constant. But this is equivalent to $E(4_1^+) = E(2_1^+)$ + *constant* throughout or, in other words, to a linear relation with slope of unity and constant intercept as observed.

We thus see from Fig. 8 that the entire, seemingly complex, evolution of structure across major shells can be subsumed into a *"tri-partite" classification* of rotor, AHV, and pre-collective regimes. The persistence of these linear regimes forces a squeezing of the span of 2_1^+ energies where the transition from one structural paradigm to another occurs. Hence these transition regions become very rapid and, indeed, seem to be describable in terms of the same critical phase transitional behavior (and power law equations) that have been used to describe phase transitions in magnetic and thermodynamic systems. Thirdly, the 2_1^+ energy takes on a new role, namely that of a kind of critical parameter, and the phase transitional behavior lies not in the behavior of a single nuclear species but in the *relative* behavior of nuclei as N and Z change. These conclusions suggest a re-examination of the applicability of phase transition concepts to nuclei, even though the structure of these nuclei is dominated by a few valence nucleons. These concepts have recently been shown[21] to apply to odd-A nuclei as well.

4. RNB Facilities and Experiments

4.1. Status of North American RNB Activities

Worldwide interest in RNBs has grown enormously in the last five years. There are two complementary approaches to the production and use of RNBs—projectile fragmentation (PF) and the ISOL (Isotope-Separator-On-Line) technique. These are illustrated in Fig. 9. In this section we summarize these production methods and the status of North American RNB activities. The reader is referred to the recent update of the ISL (IsoSpin Laboratory) White Paper[22] and to individual facility proposals[23,24,25,26].

In PF, heavy ion projectiles impinge on a thin light target. The collisions lead to the production of a large variety of exotic species which exit the target at nearly the incident beam velocity. Downstream, the RNBs are separated, and can be focused onto a target for the study of secondary reactions, perhaps leading to even more exotic nuclei. The PF approach produces RNBs virtually immediately and at high energies, typically 50-200 MeV/A. All reaction products are available but, of course, careful separation is necessary. With beam energies well above the Coulomb barrier, the technique is best suited to reaction studies, although a wealth of exciting structure studies (e.g., of halo nuclei) have been performed at such facilities.

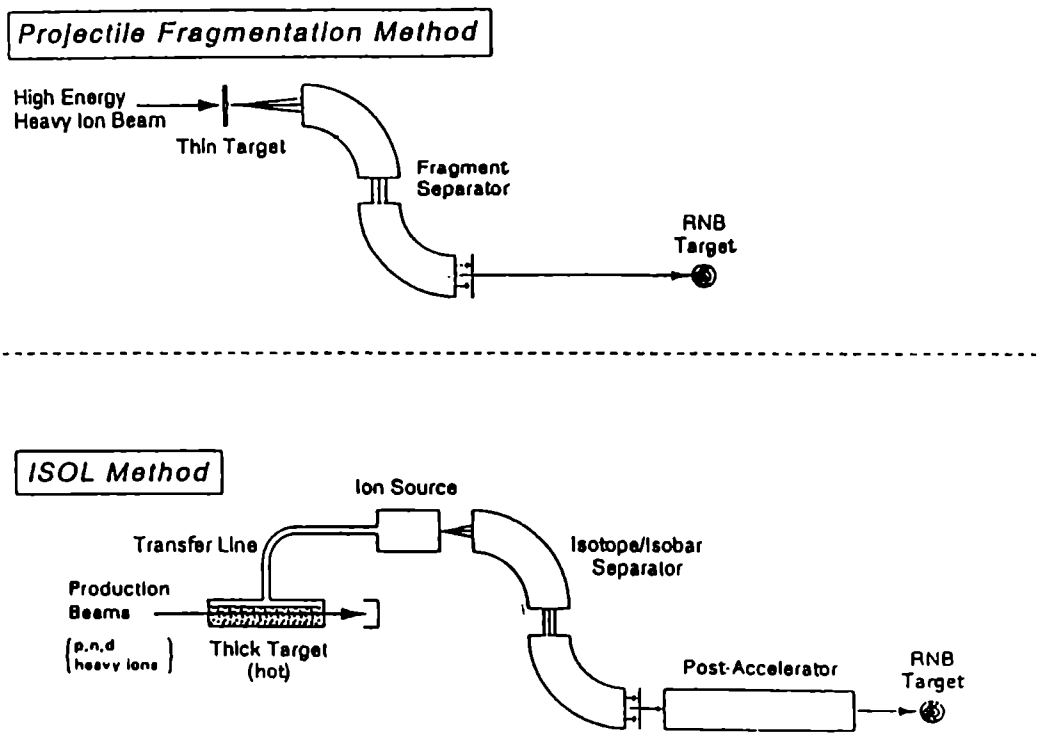

Fig. 9. Comparison of the Projectile Fragmentation and ISOL Methods for the Production of RNBs.

The ISOL technique is very nearly the inverse: light projectiles (p, n,He) or light heavy ions (e.g., ^{12}C) bombard a heavy, thick target. The reaction products are produced at low velocity, diffuse to the surface, are ionized, and accelerated in a post-accelerator. The technique in chemically selective and inherently involves a delay—between production and ionization—which depends sensitively on diffusion, desorption and ionization rates. On one hand, this can be an advantage—a given element is selected before acceleration, but it is also a disadvantage in that some elements cannot be easily produced, and delay times for others are long enough that decay intensity losses are large. With final energies up to $\sim$ 10 MeV/A, this method is ideal for most nuclear structure and nuclear astrophysics experiments.

Most existing RNB facilities are of PF type. The principal ones worldwide are at RIKEN, GSI, MSU, and GANIL. They have been among the pioneers in developing the field of RNB physics and in revealing the exciting research opportunities it provides. RIKEN, MSU and GANIL all have proposed upgrades. That at MSU

involves the coupling of the K500 and K1200 cyclotrons, and an improved RNB separation system. Improvements in RNB intensities will often be 3 orders of magnitude. For example, ^{11}Li beams should increase from $\sim 10^3 p/s$ to $\sim 10^6 p/s$ and ^{132}Sn beams from a couple of particles per sec to $\sim 10^4 p/s$.

In the ISOL approach, an existing facility at Louvain-la-Neuve, Belgium, is aimed primarily at the study of astrophysically important reactions. In North America, two first-generation ISOL initiatives have been approved, HRIBF at Oak Ridge and ISAC-1 in Vancouver, Canada. Construction of the former is nearing completion and an experimental program focusing on nuclear astrophysics and nuclear structure should be in place in 1996. The facility utilizes the ORIC K105 cyclotron as driver and the 25 MV Tandem as re-accelerator. Initially, the focus will be on light and medium mass neutron-deficient RNBs. Initial beams of F, As and Ga are likely. The maximum RNB energies will be 20 MeV/A for $A = 10$ and 5 MeV/A for $A = 90$. There are plans for the use of actinide targets to produce a wide range of neutron-rich fission-product RNBs.

The ISAC-1 facility will use 200-500 MeV protons from TRIUMF. After ionization and separation, the exotic nuclei can be used at low energies in trapping experiments, or accelerated to the 100 keV/A range for low-energy astrophysics experiments. It is planned to build a linear post-accelerator for RNB energies up to $\sim$ 1.5 MeV/A. Initially, beams will be limited to $A/q < 30$.

Several North American laboratories are interested in second generation ISL-like RNB facilities. Both the HRIBF and ISAC-1 installations could be upgraded. In the former case, an upgraded driver cyclotron and a booster linac after the Tandem are envisioned. In the latter case, further linac sections would boost the final energy. Argonne National Laboratory is also actively developing a proposal for an advanced ISOL facility using the existing ATLAS machine as post-accelerator along with its beam line and instrumentation infrastructure. The driver would be a 215 MeV linac that would produce intense beams of protons (1 mA), d, ^{3}He and α particles. Light-heavy ions such as ^{12}C would also be available. An innovative concept is to use 200 MeV deuterons from the driver to bombard a ^{238}U target in order to produce a 0.1 pmA neutron beam that would then bombard a second (e.g., U) target to produce exotic nuclei. The use of neutrons as production beam has the intriguing advantage of much lower heat generation in the production target. The heat that is produced essentially all comes from nuclear reactions that produce exotic nuclei as well. Due to slower energy loss of the neutron beam compared to protons, quite thick targets can be used.

4.2. Low Energy Coulomb Excitation with RNBs

Of course, an extremely wide range of experimental approaches to the use of RNBs are possible. They may be used at low energies in atomic physics experiments. Many critical astrophysics experiments will rely on them. Exotic nuclei produced at RNB facilities can be studied in their own right through decay or scattering experiments. Finally, RNBs can be used to initiate *secondary* reactions that

can lead to even more exotic nuclei. The recent study by Dasso et al.[27] highlights, for example, some of the extremely neutron-rich nuclei that can be produced with reactions of very neutron-rich RNBs on stable heavy targets. Access to the superheavy region should also be possible. It is, of course, impossible to summarize all applications here. The reader is referred to a number of recent overviews[22,23,24,25,26].

Here we discuss only one application, *low* energy Coulomb excitation (CE) in inverse kinematics since it is ideally suited to obtaining the kind of basic nuclear structure information (e.g., $E(2_1^+)$, $R_{4/2}$ and $B(E2: 2_1^+ \rightarrow 0_1^+)$ values) that provides the new signatures of structure discussed above. The use of inverse kinematics–bombardment of light targets by heavy nuclei—allows the RNBs to exit the target region in a narrow forward cone, taking their radioactive background radiation with them. With, for example, an $A \sim 150$ RNB on a light ^{12}C target ($\sim$ 1 mg/cm^2) all beam particles exit the target region in a cone of $\lesssim$5 deg. The other critical element in the technique is to use *low* energy RNBs, of about 1.5-3.5 MeV/A, so that only the lowest 2^+ state (and, perhaps the 4^+) is excited. This enormously simplifies the analysis since real and virtual CE of other states can be neglected and the data reduction involves only one $E2$ matrix element. There are several methods that can be used to measure the CE yields. If the $2_1^+ \rightarrow 0_1^+$ transition is highly converted, Si PIN diode electron detectors can be used. Also, plunger techniques, taking advantage of the Doppler shifts, can be exploited. Here, we will discuss extraction of the yields from direct measurement of the de-excitation γ rays.

Given the low beam energy, the deexcitation spectra following CE of even-even nuclei are very simple. Aside from x-rays, they only contain a single peak. Hence Doppler broadening ($\sim$ 5% at 1.5 MeV/A) and energy resolution are not issues of concern, and NaI(Tl) detectors may be used (along with a Ge monitor detector). There are two approaches depending on the lifetime of the 2_1^+ state. These techniques involve observation of the absolute yield or measurement of the in-flight decay curve and are applicable to lifetimes in the ps or ns regimes, respectively. In the former method, the CE target is placed in the central bore tube of a (say) $3''x3''$ through-well NaI(Tl) detector that has about 90% geometrical coverage. The high efficiency of this device allows rapid accumulation of sufficient statistics so that $E(2_1^+)$ and the $B(E2)$ value can be measured in about a day even at RNB intensities of only $10^5 p/s$. Of course, with this method, one must know the RNB intensity, which can be measured, for example, with a downstream scintillator that can also serve as a trigger on the NaI detector if background from scattered upstream RNBs is large.

For larger 2_1^+ state halflives, decay will occur in flight downstream from the target. In this case, one mounts a linear array of NaI detectors along the beam tube as illustrated in Fig. 10. Each detector sees a certain time window depending on its downstream distance. Their respective counting rates then directly give the lifetime via a measurement of the decay curve. It is not necessary to know the beam intensity.

In an instrument of this type that we have developed, and tested with stable Os beams ($A \sim 190$), we have used semi-annular NaI detectors surrounding a 1"

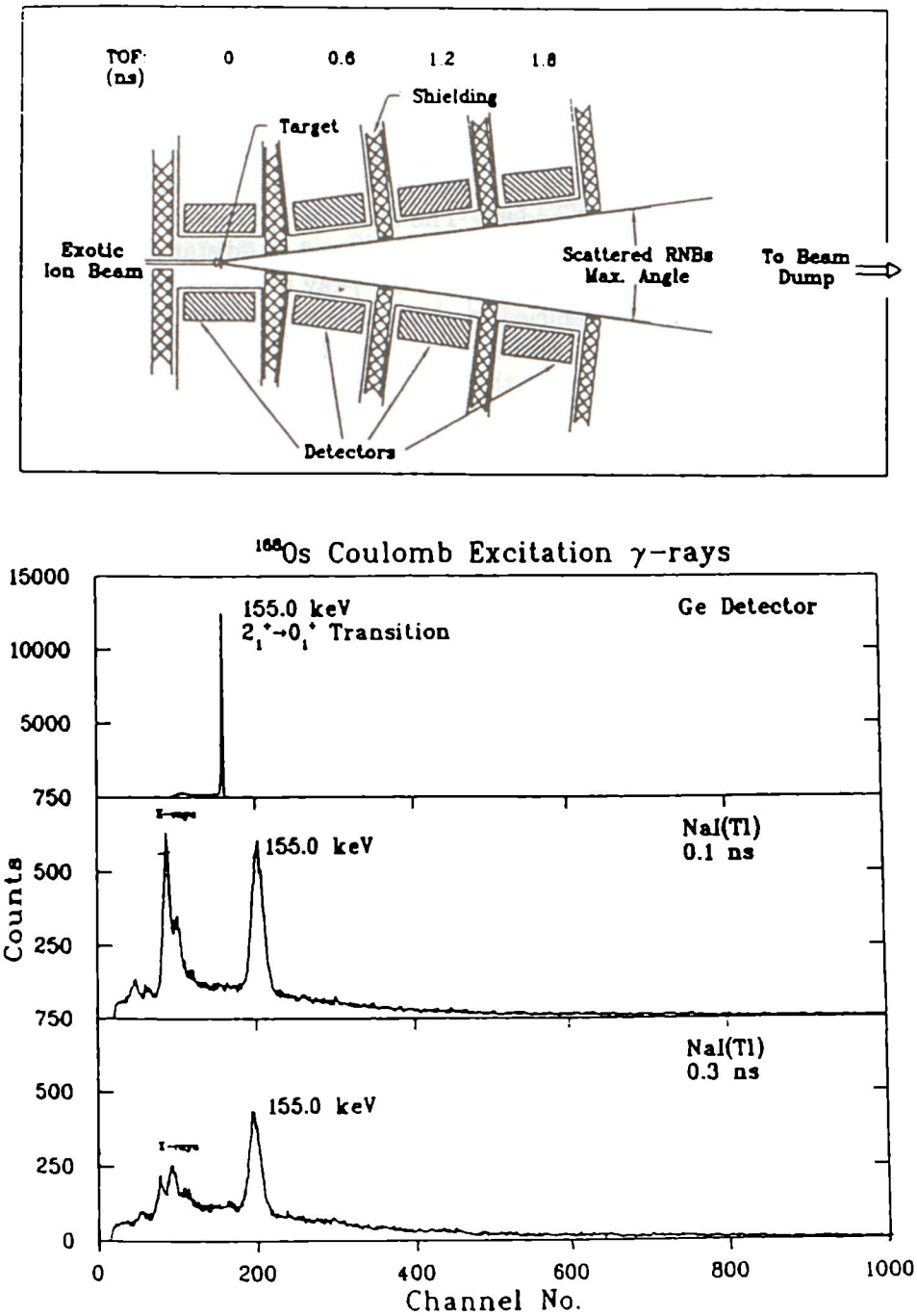

Fig. 10. Top) Schematic depiction of the CE technique discussed in the text; Bottom) Ge and NaI spectra taken with an ^{188}Os beam at $\sim$ 267 MeV incident on a $\sim$ 1 mg/cm^2 ^{12}C target.

diameter beam tube. This is the minimum diameter that permits all scattered RNB particles to exit the beam tube downstream without landing on its walls. (If they did there could be a buildup of unwanted radioactivity.) The cross sections are typically large ($10s$ to $100s$ of mb) for heavy mass RNBs, and hence the count rates are reasonable even with weak beams. A typical set of spectra taken with a stable test beam of ^{188}Os on a ^{12}C target at 267 MeV is shown in the lower part of Fig. 10. The simplicity of the spectra is evident. The lower two panels show the spectra for two NaI detectors located downstream from the target at "distances" of 0.1 and 0.3 ns. The lower intensity of the 155 keV $2_1^+ \rightarrow 0_1^+$ γ-ray in the latter case is clear.

Clearly, with this simple and efficient technique, series of isotopes, extending closer and closer to the drip line, can be measured efficiently and under uniform conditions in rapid succession, allowing the evolution of structure in exotic regions to be readily mapped.

5. Summary

We have discussed aspects of nuclear structure far from stability in regions that will become accessible with RNBs. Exploiting a "*horizontal*" approach, we analyzed several signatures of structure that are based on the simplest data. These signatures exploit remarkably simple, often universal, correlations of collective observables, either with N_pN_n (or P) or among themselves. An important point resulting from this work is that horizontal correlations of nuclear observables are not merely an exercise in "systematics" or "phenomenology", in the zoological sense, but can provide real, new, and otherwise hidden, insights into nuclear behavior and the microscopic underpinnings of nuclear structure. Finally, the status of RNB facilities in North America was reviewed and a particular technique, low energy Coulomb excitation in inverse kinematics, was described.

6. Acknowledgments

We are grateful to our collaborators and colleagues for many contributions and discussions. In particular, we acknowledge with thanks the help of W. Nazarewicz, D.D. Warner, D.S. Brenner, W.-T. Chou, B. Foy, R.L. Gill and C. Barton. Research supported by the USDOE under contracts DE-AC02-76CH00016, DE-FG02-88ER40417 and DE-FG02-91ER40609.

7. References

1. Long Range Plan for Nuclear Science. Interim Report, April 1995. DOE/NSF NSAC Report.
2. P. Van Isacker, D.D. Warner and D.S. Brenner, Phys. Rev. Lett. **74** (1995) 4607.

3. J. Dobaczewski et al., Phys. Rev. Lett. **72** (1994) 981; W. Nazarewicz et al., Phys. Rev. C50 (1994) 2860.
4. R.F. Casten, Nucl. Phys. A443 (1985) 1.
5. R.F. Casten and N.V. Zamfir, Physics Reports, to be published.
6. R.F. Casten, D.S. Brenner, P. Haustein, Phys. Rev. Lett. **58** (1987) 658.
7. A.S. Mowbray et al., Phys. Rev. C42 (1990) 1126.
8. B. Foy et al., Phys. Rev. C49 (1994) 1224.
9. T. Motobayashi et al., Phys. Lett. B346 (1995) 9.
10. N.V. Zamfir et al., Phys. Lett. B (in press).
11. P. Möller et al., At. Data Nucl. Data Tables A59 (1995) 185.
12. R.F. Casten, N.V. Zamfir, D.S. Brenner, Phys. Lett. B324 (1994) 267; B342 (1995) 451.
13. W.-T. Chou, R.F. Casten, N.V. Zamfir, Phys. Rev. C51 (1995) 2444.
14. R.F. Casten, N.V. Zamfir, D.S. Brenner, Phys. Rev. Lett. **71** (1993) 227.
15. N.V. Zamfir, R.F. Casten, D.S. Brenner, Phys. Rev. Let. **72** (1994) 3480.
16. N.V. Zamfir and R.F. Casten, Phys. Lett. B341 (1994) 1.
17. R.V. Jolos et al., Phys. Rev. C51 (1995) R2298.
18. N. Pietralla et al., Phys. Rev. Lett. **72** (1994) 2962.
19. N.V. Zamfir and R.F. Casten, Phys. Rev. Lett. **75** (1995) 1280.
20. W.-T. Chou et al., Nucl. Phys. A580 (1994) 33.
21. D. Bucurescu et al., to be published.
22. Overview of Research Opportunities with Radioactive Nuclear Beams—An Update–1995. ISL Steering Committee.
23. A Proposal for Physics with Exotic Beams at the Holifield Heavy Ion Research Facility, eds. J.D. Garrett and D.K. Olsen, Physics Division, ORNL Report, 1991.
24. Proceedings of the ISAC Workshop, Lake Louise, February 1994, ed. J.M. D'Auria, Report TRI-94-1.
25. MSU-NSCL Coupled Cyclotron Proposal, 1995.
26. Concept for an Advanced Exotic Beam Facility based on ATLAS. A Working Paper, Physics Division, Argonne National Laboratory Report, February 1995.
27. C.H. Dasso, G. Pollarolo and A. Winther, Phys. Rev. Lett. **73** (1994) 1907.

GLOBAL SYSTEMATICS OF NUCLEAR OBSERVABLES IN ODD-A NUCLEI

D. BUCURESCU
Institute for Atomic Physics, P.O. Box MG-6, Bucharest, Romania

ABSTRACT

Different correlations between observables related to the unique parity orbital structures in the odd-A nuclei are studied. It is shown that the correlations between excitation energies within the unique parity orbital quasibands allow a tripartite classification of the evolution of the nuclear structure, similar to that observed in the adjacent even-even nuclei: all nuclei can be assigned to three different regimes, the precollective, anharmonic vibrator and strong coupling, respectively, interconnected by fast, critical phase-like transitions. It is also shown that both an index which characterizes the signature splitting, and the B(E2) values within the quasibands can be organized in terms of a valence correlation scheme.

1. Introduction

There is now a rich collection of nuclear structure data concerning the characteristics of low-energy levels in many nuclei. This allows to observe the evolution of nuclear properties, and, especially, of the nuclear collectivity, over practically the entire nuclide chart. Of course, the use of empirical global correlations is not new. But, most of the correlations usually investigated, such as those of different observables (excitation energies, energy ratios, $B(E2)$ values, etc.) versus A, Z or N are not particularly relevant; rather, they evidence the complexity of the general evolution of the nuclear structure.

On the other hand, during the last years, new correlations between simple observables have been discovered, which suggested an unexpected simplicity of the evolution of the nuclear structure. Most of these global correlations have been investigated for the even-even nuclei. This is understandable, since just the 'standard' structure of these nuclei (e.g., the occurence of the yrast $0^+, 2^+, 4^+$,... sequence of the ground state quasiband in practically all nuclei) provides simple quantities (like $E(2_1^+)$) which can be followed accross the nuclear chart.

There are, basically, two kinds of approach which evidence global systematics of the nuclear structure. The first is to study the correlations between two nuclear observables. For the even-even nuclei, a very simple correlation, that between $E(2_1^+)$ and $E(4_1^+)$, provided a remarkable, completely unexpected result: all nuclei, from magic to deformed, covering an extreme diversity of structures, lie on a universal pattern formed by three linear segments of different slopes, each representing a general regime: precollective, anharmonic vibrator and rotational [1,2], respectively, linked by narrow zones of rapid transitions.

Another very successful approach are the so-called valence correlation schemes (VCS) by which one correlates a nuclear observable with a variable which is a simple function on the numbers of valence protons and neutrons. The most widely used is the N_pN_n scheme [3,4].

The present discussion will focus on recent results concerning universal correlations of nuclear structure observables in odd-A nuclei, some of them published [5,6].

2. Correlations between Excitation Energies

In the odd mass nuclei, the low energy structure varies widely, reflecting the occupation, by the odd particle, of different shell model orbitals close to the Fermi surface, when the mass number is changed. There is, however, a kind of analogue of the g.s. quasiband in the even-even nuclei, which can be followed in practically all the odd-A ones. These are the structures determined by the unique parity orbitals (*upo*'s). There are more than 200 nuclei with mass between $\approx$60 and $\approx$200 in which such structures due to three *upos*, $g_{9/2}, h_{11/2}, i_{13/2}$ have been evidenced and characterized in some detail. Since these structures do not mix significantly with other orbitals, they probe the mean field of the nucleus in the same way, irrespective of the *upo* considered; therefore, one can hope to find universal correlations, just as in the case of the g.s.b. in even-even nuclei.

Before proceeding, we define a few conventions and notations. For an *upo* of spin j (e.g., for $g_{9/2}$, j=9/2) we shall follow the states in the *upo* structure with spin larger than $j-1$. The sequence of spins $j, j+2, j+4$,... will be called 'favored' quasiband, whereas that of spins $j-1, j+1, j+3$,... will be called 'unfavored' quasiband. Within each quasiband we consider excitation energies with respect to the lowest one. Thus, in the favored quasiband the energies of the states with spins $j+2, j+4$, ... relative to the state j are denoted by $E(j+2), E(j+4)$,... For each odd-A nucleus we define as its core the adjacent even-even nucleus that is closest to the closed shell.

2.1. Collective Nuclei: Anharmonic Vibrator and Strong Coupling

Consider first the collective nuclei which are not deformed, defined as those with cores satisfying the relation $2.0 \leq R(4/2) = E(4_1^+)/E(2_1^+) \leq 3.1$. Fig. 1 shows that there are linear correlations between the excitation energies within the two quasibands. We thus have $E(j+4) = \alpha E(j+2) + \epsilon_4$, with $\alpha \simeq 2.0$ (experimental value 1.99±0.03) and ϵ_4=182±19 keV. This is the expression for an anharmoniv vibrator (AHV) [7] *with constant anharmonicity* ϵ_4: for all these nuclei we find practically the same value ϵ_4. For the higher states we find experimental fits in agreement with the general AHV formula $E(J) = nE(J') + \frac{n(n-1)}{2}\epsilon_4$, with $J' = j+2$ (or $j+1$); $n = (J-j)/2$ (or $(J-j+1)/2$) for the favored (or unfavored) quasibands, respectively, where n signifies the number of phonons and ϵ_4 is seen to have the meaning of the phonon-phonon interaction energy. These results are similar to those obtained for the g.s. quasiband in the adjacent even-even nuclei [1]: the same AHV behaviour is present in both cases (there, one finds a value ϵ_4=156±10 keV, which might be

slightly lower than in the odd-A case).

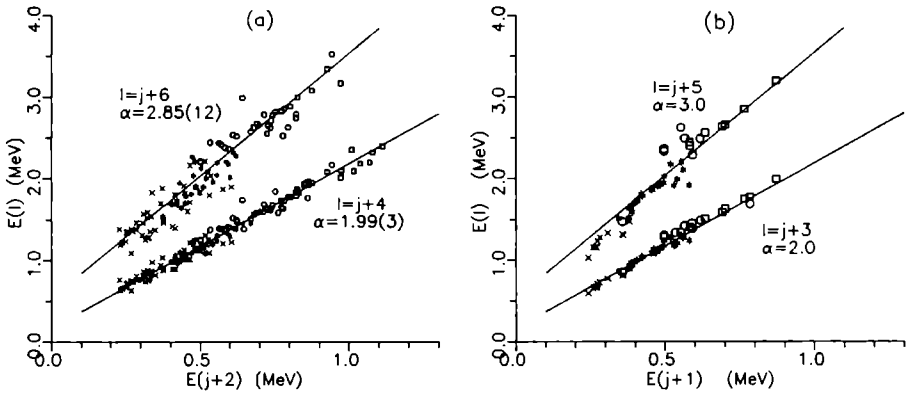

Fig. 1. Correlations between excitation energies within the favored (a) and unfavored (b) quasibands for the $\pi g_{9/2}, \nu g_{9/2}, \pi h_{11/2}, \nu h_{11/2}$ *upos*. The slopes of the straight lines are indicated.

Thus, a large number of nuclei, with rather different structural characteristics, many of them labelled loosely as 'transitional', belong in fact to a regime described by a universal phonon structure. Since the AHV regime in the even-even nuclei is reproduced by the IBA model [8], it is likely that the odd-A result is also automatically provided by the IBFM model, and it is of interest for which domain of the boson-fermion interaction parameters. Such an investigation is in progress. However, this general relevance of the AHV picture is not yet understood microscopically. We add now to the nuclei represented in Fig. 1, the nuclei with deformed cores ($R(4/2) > 3.1$). As obvious from Fig. 2, these nuclei define a second branch in the correlation, which is also a segment of straight line. The slope of this line is the one expected in the strong coupling (SC) limit: $\alpha = (4j + 10)/(2j + 3)$, which is $\approx$2.3 for the j values of interest to us. This value corresponds to the slope $R(4/2)$=3.33 in the core nuclei.

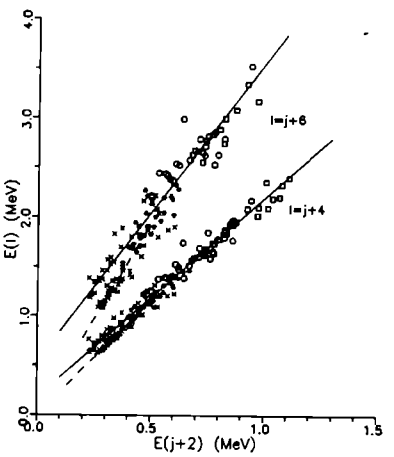

Fig. 2. Same as Fig. 1, but with deformed nuclei added.

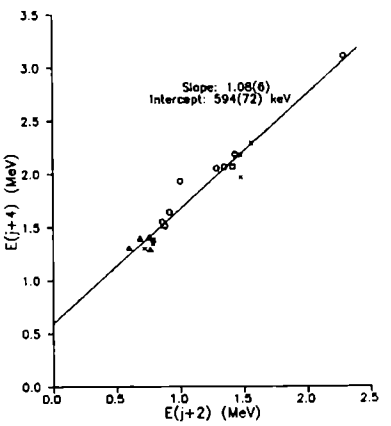

Fig. 3. Same correlation as in Fig. 1(a), for precollective nuclei.

The way the transition between the AHV and SC regimes takes place is not obvious in Fig.2 ; it will be discussed later on the particular case of the $\nu i_{13/2}$ *upo*, where nuclei which make this transition are well represented.

2.2. Precollective nuclei

We investigate now the nuclei in the vicinity of the closed shells. These have cores of the 'precollective' type [2], with $R(4/2) < 2.0$. Fig. 3 shows the correlation between their $E(j+4)$ and $E(j+2)$ values. It is again linear, $E(j+4) = \alpha E(j+2) + \epsilon$, with α=1.08±0.06 and $\epsilon = 594 \pm 72$, values practically identical with those found for the $E(4_1^+)$ versus $E(2_1^+)$ correlation [2]. The value of the slope $\alpha \simeq 1.0$ has the meaning that the energy difference between the states $j+2$ and $j+4$ remains practically constant, in spite of the fact that $E(j+2)$ and $E(j+4)$ may vary considerably from nucleus to nucleus. As in the case of the even-even nuclei [2], this effect was automatically reproduced (for singly magic nuclei) by simple shell model calculations with a surface δ residual interaction [9]. The main ingrediend suggested by these calculations appears to be the validity of a 'pair addition mode': the states of n particles are composed by those of $(n-2)$ particles to which one adds one pair of particles copupled to 0^+ (which is always the same). It is interesting that, although the energies $E(j+4), E(j+2)$ in the odd-A nuclei behave exactly like $E(4_1^+), E(2_1^+)$, respectively, in the cores, and one finds that the pair addition mode works in both cases, the odd-A wavefunctions have not a 'weak coupling' character [9].

2.3. Tripartite classification and phase transition

Fig. 4 collects together all the previously discussed correlations, for all nuclei between As and Au, and the three *upos* ($g_{9/2}, h_{11/2}$ and $i_{13/2}$) evidenced in this mass region. One finds a situation which parallels that for the even-even nuclei [2]. All the nuclei can be classified into three regimes, characterized, in the $E(j+4)$ versus $E(j+2)$ correlation, by straight lines of different slopes: $\simeq$1.0 for the precollective (PC) regime, $\simeq$2.0 for the anharmonic vibrator (AHV) regime, and $\simeq$2.3 for the strong coupling (SC) regime. This is analogous with the tripartite classification of the even-even nuclei into the PC, AHV and rotor regimes. However, while in the e-e case the three regimes are separated in the range of the $E(2_1^+)$ values, here the three regimes span the same range of $E(j+2)$ values. In the even-even case, the transition from one regime to another took place in a narrow zone of $E(2_1^+)$ values, and it was shown to have the features of a critical phase transition [1]. For the odd-A nuclei we also have rapid transitions (in a narrow zone of $E(j+2)$ values), but with different features. Fig. 5 shows in detail the AHV→SC transition for the $\nu i_{13/2}$ case. There is a 'turning point' (TP) in $E(j+2)$, at which the derivative $dE(j+4)/dE(j+2)$ is discontinuous and varies very quickly: its two branches behave like those of a 'λ-anomaly' [10], although one of them is inverted here. Thus, the transition AHV-rotor in the even-even nuclei, and the corresponding one, AHV-SC in the odd-A nuclei, appear, unexpectedly, very similar with the critical phase transitions in macroscopic systems [10], and this behaviour represents a challenge for the nuclear theory.

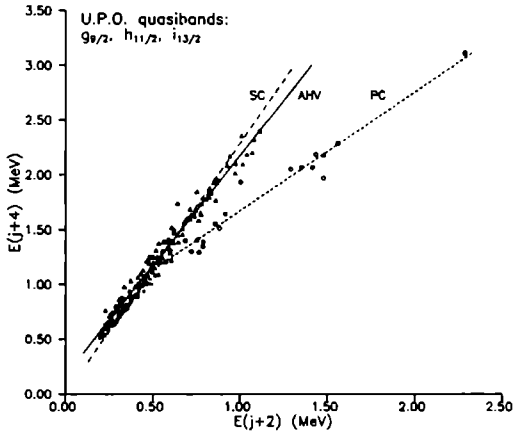

Fig. 4. Tripartite classification of the structural evolution of the *upos* in odd-A nuclei.

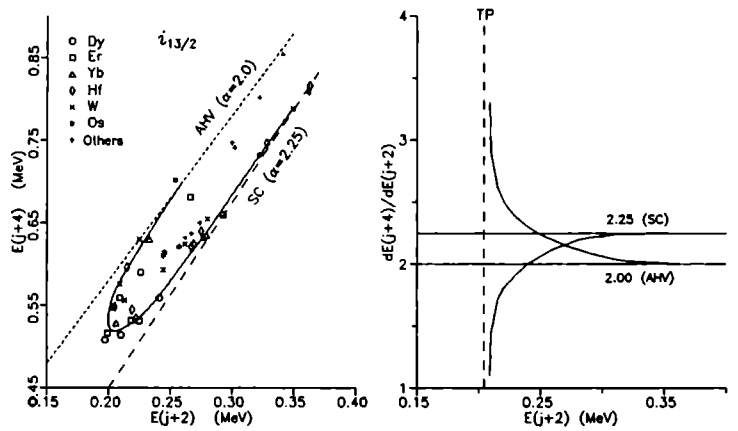

Fig. 5. Illustration of the AHV→SC transition for the $\nu i_{13/2}$ *upo*. The continuous curve in the left side plot is drawn by eye; its derivative is shown in the right side plot.

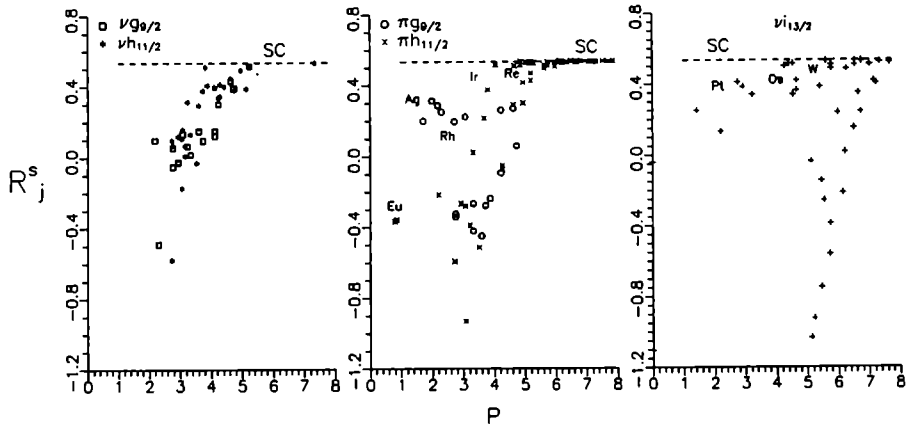

Fig. 6. Evolution of the signature splitting index R^s_j (see text) versus $P(= N_p N_n/(N_p + N_n))$.

3. Valence Correlation Schemes

3.1. Signature Splitting

In the even-even nuclei the universal correlations between the energies of the yrast (g.s.) states give a complete description of the evolution of this structure. The similar universal correlations discussed above, for the energies within the *upo* quasibands are not sufficient to describe entirely the evolution of the *upo* structures. One needs an additional quantity, which characterizes the relative position of the two quasibands. The description of this energy splitting, named signature splitting in the deformed nuclei, is a delicate problem in many structure models. In order to study the splitting between the two quasibands, we have defined [5,9] the following 'signature splitting index': $R_j^s = \frac{E(j+2)-E(j+1)}{E(j+2}$. It has a well defined value in the SC limit, $R_{j,SC}^s = (j+2)/(2j+3) \simeq 0.54$, is positive for partial deformation alignment and may be negative in the weak coupling or decoupling limit. We have investigated the correlation between this quantity and others, and found that it displays a systematic variation in terms of a VCS. Fig. 6 shows its variation as a function of $P(\equiv N_p N_n/(N_p+N_n))$ (valence particles counted according to the general scheme of ref. [3]). One sees that, in general, R_j^s increases with P, from negative values, up to the saturation positive SC value. Strong exception from this rule are the nuclei towards the closed shell. The signature splitting is usually described by another quantity, which (for the rotational sequences) is the true energy difference between the favored and unfavored routhians. Fig. 7 shows the quantity Δe', the signature splitting at a rotational frequency $\hbar\omega$=0.2 MeV, for the $\nu i_{13/2}$ bands (determined in ref. [11]). One sees that most of the points define an almost linear correlation of Δe' with P, the same exceptions being again those noticed in Fig. 6.

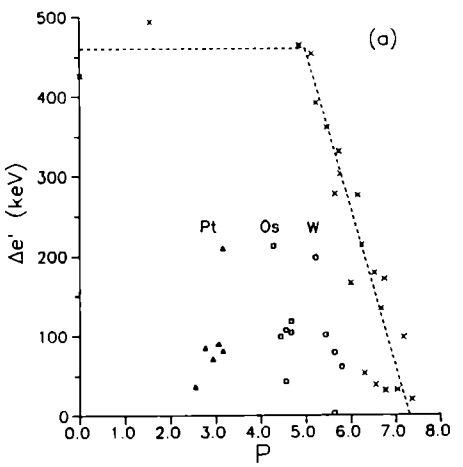

Fig. 7. The same as Fig. 6, but for the true signature splitting $\Delta e'$ at a rotation frequency $\hbar\omega$=0.2 MeV, for the $\nu i_{13/2}$ quasibands [11].

The deviating nuclei (e.g., Pt, Os and W for $\nu i_{13/2}$ can be moved closer to the general trend, if one considers that one feels strongly the effect of 2p-2h neutron excitations above the N=126 shell gap (analogous to the effect seen in the even-even nuclei in this region [13]). In this case, one has to recalculate the P values with a value for N_n increased by 4 for these nuclei, which largely reduces the discrepancy with the other points. Since both R_j^s and Δe' behave smoothly with P, and show the same deviating cases, one deduces that there must be a well defined relation between them. Fig. 8 shows that there is indeed a nice correlation.

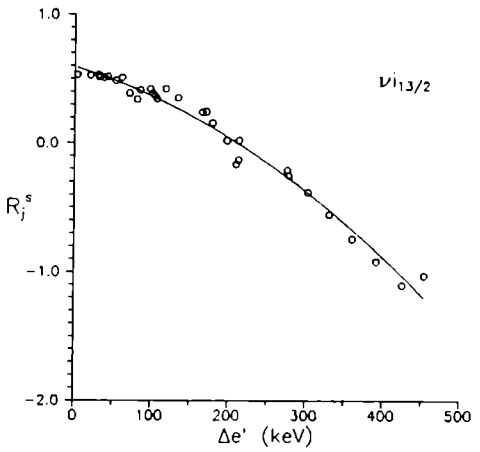

Fig. 8. Correlation between the signature splitting index R_j^s defined in the text and the true signature splitting $\Delta e'$ at $\hbar\omega$=0.2 MeV [11] for the $\nu i_{13/2}$ quasibands. The solid line is a parabola fitted to the points.

Thus, the index R_j^s, which is much easier to determine than Δe' and can be defined for any nucleus, allows a generalization of the study of the 'signature spliting' of the *upo* structures to all nuclei.

3.2. B(E2) Values

The $B(E2)$ values within the g.s. quasiband of the even-even nuclei have been shown to obey very interesting correlations, and to be able to provide useful information on more than merely the quadrupole deformation β_2 [4,13]. We have analyzed the known values of the electromagnetic transition probability $B(E2; j+2 \rightarrow j)$ from the favored *upo* quasibands. Although there are much less values determined experimentally (we have found only 57 cases), an interesting correlation has been evidenced. Fig. 9 shows the correlation of these B(E2) values, normalized by the mass number, with $N_p N_n$. In part (a) of the figure, all experimental points are shown. There are some nuclei (highlighted by filled symbols) which deviate from the general pattern, and have been removed in part (b). The group of nuclei with unusually high values is in the region of light Br, Rb,Y, where phenomena such as very large deformations and prolate-oblate coexistence are known. The second group, of lower points, is largely characterized by predominantly single particle character of this transition. The re-

maining nuclei in Fig. 9(b), which are tightly correlated, resemble the same kind of correlation with that observed for the $B(E2; 2_1^+ \rightarrow 0_1^+)$ in the even-even nuclei, which is indicated by the bilinear pattern shown by full line in part (a) of the figure.

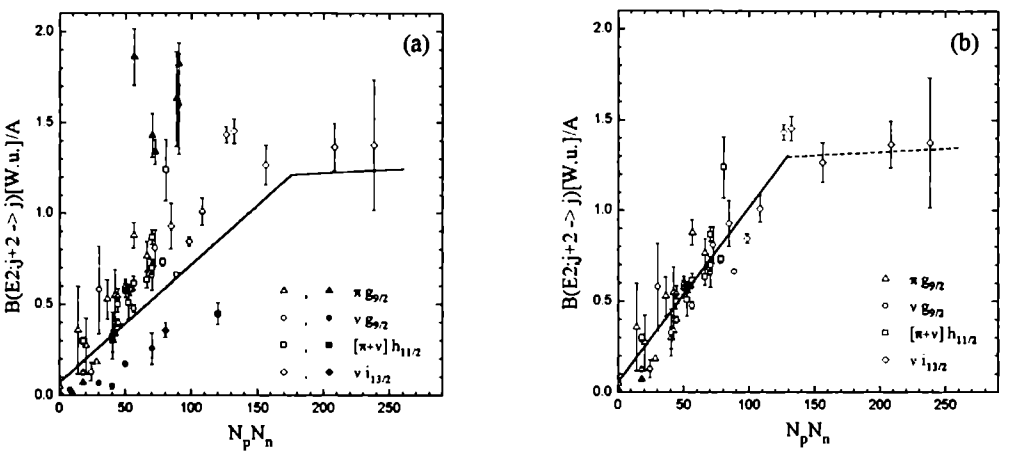

Fig. 9. Normalized $B(E2; j+2 \rightarrow j)$ values in odd-A nuclei. The deviating nuclei (black symbols in part (a), discussed in the text) have been removed in part (b). The bilinear function fitted to the data points in part (b) is similar to that which describes the $B(E2; 2_1^+ \rightarrow 0_1^+)$ values in the even-even nuclei [13] (shown as solid line in part (a)).

One sees that the odd-A pattern lies well above the even-even one (the odd-A nuclei have, in average, larger $B(E2)$ values), and also that the 'saturation' effect occurs earlier in the odd-A case. Recently, it has been shown that this 'saturation' of the B(E2) values, believed to occur towards the middle of the shell, is in fact due to unaccounted for effects of higher order nuclear deformation (hexadecapole) [4]. In our case, there is a hint of 'saturation' at larger N_pN_n values, and it is very interesting to investigate a similar possibility; the role of the hexadecapole deformation in the *upo* structures of the odd-A nuclei is, to our knowledge, very little discussed. For the time being, the well correlated pattern visible in Fig. 9(b) remains an interesting correlation, and as such constitutes a practical guide which can be used to plan further experimental measuremenets of special interest.

4. Conclusions

We have shown that the *upo* structures in the odd-A nuclei obey interesting universal correlations. The evolution of these structures can be cast into a tripartite classification, the three general structural regimes being linked by rapid transitions, similar to the critical phase transitions known in macroscopic systems. As such, all these simple correlations constitute a formidable challenge for the microscopic nuclear theory. On the other hand, they are tools of pragmatic value: they can be used to predict properties of nuclei which are unknown yet. One should emphasize that these

correlations are based on the simplest nuclear observables, which one can hope to be accessible for nuclei farther off stability in the first generation of experiments with the radioactive beam facilities. The question whether the nuclei in the new regions will obey or not these correlations remains, of course, a major one. If the new nuclei will deviate from these patterns, that will be a clear sign of new physics.

1. R. F. Casten, N. V. Zamfir and D. S. Brenner, *Phys. Rev. Lett.* **71** (1993) 227.
2. N. V. Zamfir, R. F. Casten and D. S. Brenner, *Phys. Rev. Lett.* **72** (1994) 3480.
3. R. F. Casten, Nucl. Phys. **A443** (1985) 1.
4. R. F. Casten and N. V. Zamfir, these Proceedings.
5. D. Bucurescu, G. Cata-Danil, M. Ivascu, L. Stroe and C. A. Ur, *Phys. Rev.* **C49** (1994) R1759.
6. D. Bucurescu, G. Cata-Danil, M. Ivascu, L. Stroe and C. A. Ur, in *Perspectives of the Interacting Boson Model on the Ocasion of its 20th Anniversary*, ed. R. F. Casten *et al* (World Scientific, Singapore, 1994), pp. 389.
7. D. M. Brink, A. F. R. de Toledo Piza and A. K. Kerman, *Phys. Lett.* **19** (1965) 413.
8. N. V. Zamfir and R. F. Casten, *Phys. Lett* **B341** (1994) 1.
9. D. Bucurescu et al, to be published.
10. M. F. Collins, *Magnetic Critical Scattering* (Oxford Univ., New York, 1989), pp. 3.
11. W. F. Mueller, H. J. Jensen, W. Reviol, L. L. Riedinger, C. H. -Yu, J. -Y. Zhang, W. Nazarewicz and R. Wyss, *Phys. Rev.* **C50** (1994) 1901.
12. W. -T. Chou, R. F. Casten, R. L. Gill and N. V. Zamfir, *Int. J. Mod. Phys.* **E2** (1993) 821.
13. R. F. Casten and N. V. Zamfir, *Phys. Rev. Lett.* **70** (1993) 402.

NEW SUPERDEFORMED BANDS IN THE A∼130 MASS REGION OBSERVED WITH EUROGAM

JEAN GIZON
Institut des Sciences Nucléaires, IN2P3-CNRS/ Université Joseph Fourier, 53 Avenue des Martyrs, 38026 Grenoble Cedex, France

ABSTRACT

The main properties of the superdeformed bands in the A∼130 mass region are reviewed. Results concerning the first observation of excited and identical superdeformed bands in Ce and Pr isotopes with EUROGAM are presented and discussed. New data on ΔI=2 staggering found in superdeformed bands of Ce isotopes are also shown and commented.

1. Introduction

Many methods and techniques are used for nuclear structures studies. Those based on the detection of γ-rays or conversion electrons emitted during radioactive decay or compound nucleus reaction are particularly powerful. They make possible the determination of *e.g.* level energies, spins, parities, multipole orders of the electromagnetic radiations, transition probabilities, lifetimes, moments... necessary to understand the collective behaviour and the single particle modes appearing in nuclei at various excitation energies and spins.

Methods combining the use of heavy ion induced reactions to excite the nucleus and the use of large germanium arrays to detect γ-rays are very powerful to investigate nuclei at very high angular momentum. For example superdeformed (SD) states produced with low cross-sections are now accessible which was impossible a few years ago. The superdeformation, a strongly collective mode, is now actively explored by many experimentalists and theorists.

This lecture concentrates on the phenomenon of superdeformation and mainly on the A∼130 mass region. After a general description of the properties of SD states, I describe briefly the EUROGAM and EUROBALL arrays. Then I present the main results obtained for nuclei in the cerium region during the last two years with EUROGAM and discuss excited and identical SD bands as well as the staggering recently observed in cerium isotopes.

2. Discovery and Properties of Superdeformed Nuclei

2.1. First Observation of Superdeformed Shapes

The first indication of very large deformation ($\beta_2 \approx 0.6$) in nuclei was found in fission isomers of actinides by S. Polikanov *et al.*[1] in 1962. Their long lifetimes were explained by Strutinsky[2] as originating from superdeformation associated with a second minimum in the potential energy surfaces.

More than twenty years after, in 1984, measurements of dynamic moments of inertia $\mathcal{J}^{(2)}$ from the γ-ray continuum by H. El-Samman *et al.*[3] indicated the existence of large deformation in the A$\sim$130 transitional region. This was confirmed by the observation of a highly collective band in ^{132}Ce by P. Nolan *et al.*[4] in 1985. The corresponding states have a large quadrupole moment[5] Q_0=8 eb and the nucleus is strongly prolate with axis ratios close to 3:2:2 and deformation $\beta_2\approx$0.4.

At the same period, in 1984, by studying γ-γ energy correlations B. Nyakó *et al.*[6] deduced a very large deformation in ^{152}Dy. This was also confirmed by P. Twin *et al.*[7] in 1986 who found in this nucleus a long cascade of γ-rays associated with a very elongated shape having axis ratios of 2:1:1 *i.e.* a quadrupole deformation $\beta_2\approx$0.6.

The existence of a second minimum at large or very large deformation in the potential energy surfaces of the nuclei is predicted in several regions of the periodic table by many theoretical approaches (e.g. see references[8–16]).

Since the first discoveries mentioned above many other SD bands have been observed in several mass regions, *e.g.* with A$\sim$80,130,150,190. In the region we are dealing with *i.e.* from La to Pm nuclei, more than 25 highly deformed bands are known at present.

2.2. Typical Characteristics of Superdeformed States

There are several characteristics typical for SD bands which can be summarized as follows:

The superdeformed nuclei emit long cascades of γ-rays producing spectra with equally spaced lines.

The dynamic moment of inertia $\mathcal{J}^{(2)}\equiv dI/\hbar d\omega$, where $\hbar\omega=E_\gamma/2$ is the rotational frequency, is large. In the A$\sim$130 mass region the energy difference between two consecutive γ-rays is $\Delta E_\gamma\approx$70 keV and $\mathcal{J}^{(2)}\equiv 4/\Delta E_\gamma\approx$55 $\hbar^2$MeV^{-1}. For A$\sim$150 the spacing between adjacent lines in a spectrum is smaller ($\approx$50 keV) and the dynamic moment of inertia larger ($\approx$80 $\hbar^2$MeV^{-1}).

The SD levels decay by collective E2 transitions which are stongly enhanced (several thousands of W.u.) and their lifetimes are very short (<1 ps). The SD shape is associated with a large quadrupole moment ($Q_0\approx$ 8 and 20 eb for mass 130 and 150 regions, respectively).

In the Ce region, the SD bands become yrast above spin I$\approx$30-40$\hbar$ while this happens only above I$\approx$50-60$\hbar$ in the A$\sim$150,190 mass regions.

Superdeformed bands are also characterized by low population. In most cases the yrast bands are fed by only $\approx$1% of the total cross section of production of the nucleus and the excited ones 10 times less. Nuclei in the A$\sim$130 region are exceptions. Indeed their yrast and excited bands receive $\approx$5% and $\approx$1% of the intensity, respectively.

The decay patterns (fig.1) are very similar within most of the SD bands which loose their intensity over a few transitions only.

The linking transitions between SD and normally deformed (ND) states are still unknown in La, Ce, Pr nuclei and in other mass regions. In consequence the spin values and excitation energies of the SD states and the kinematic moments of inertia $\mathcal{J}^{(1)}$ are undetermined. The situation is different in Nd, Sm and light Gd isotopes

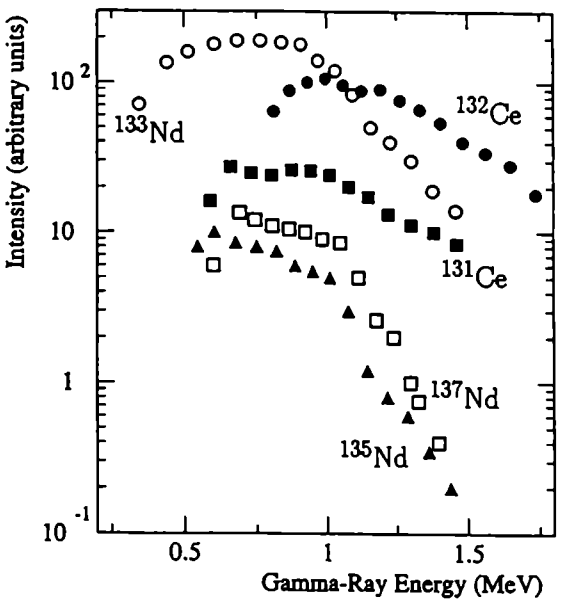

Fig.1:Population of yrast SD bands in ^{131}Ce[ref.[17]], ^{132}Ce[ref.[4,18]], ^{133}Nd[ref.[19,20]], ^{135}Nd[ref.[21,22]], ^{137}Nd[ref.[23,24]] as a function of γ-ray energies.

where the links have been found (see *e.g.* ^{133}Nd [ref.[20]], ^{135}Nd [ref.[22]], ^{137}Nd [ref.[24]]). This comes from the fact that both the first and second energy minima persist and are well separated at high spin in the former nuclei while the first energy minimum gradually evolves towards high deformation with increasing angular momentum in the latter ones. The question related to links between SD and ND states is treated by Santo Lunardi in a talk given at this Summer School.

For very large deformations which appear at very high spins one can expect very weak pairing correlations. One observes that the $\mathcal{J}^{(2)}$ dynamic moments of inertia in SD bands of A$\sim$130,150 nuclei are close to their rigid body values.

2.3. Conditions for the Existence of Superdeformed Shapes

The presence of high-j intruders originating from the $g_{9/2}$, $h_{11/2}$, $i_{13/2}$, $j_{15/2}$ shells and having low Ω, strongly down-sloping orbitals is necessary for the existence of SD shapes. Indeed these high-j orbitals carry very large quadrupole moments and polarize strongly the core of the nucleus. The difference between the quadrupole deformations in the different regions is associated with the number of valence high-j intruders[25].

The stabilization of SD shapes is ensured by gaps at various typical deformations in the level spectra of the deformed harmonic oscillator. For nuclei in the A$\sim$130 region, large gaps appear in the spectra of single-proton and -neutron orbitals at $\beta_2\approx$0.4, Z$\approx$58, N$\approx$72. For nuclei around A=150 gaps are situated at $\beta_2\approx$0.6, Z$\approx$64, N$\approx$84.

An analysis of the combined existence of intruder orbitals and gaps around mass 130 has been made by R. Wyss *et al.*[26]. Single-neutron Routhians indicate the presence of $i_{13/2}(\Omega=1/2)$ orbitals which induce a large deformation in this mass region and both the single-proton and -neutron Routhians exhibit low level densities at Z=58 and N=72, respectively which stabilize the shape of the nucleus at $\beta_2 \approx 0.40$ (fig.2).

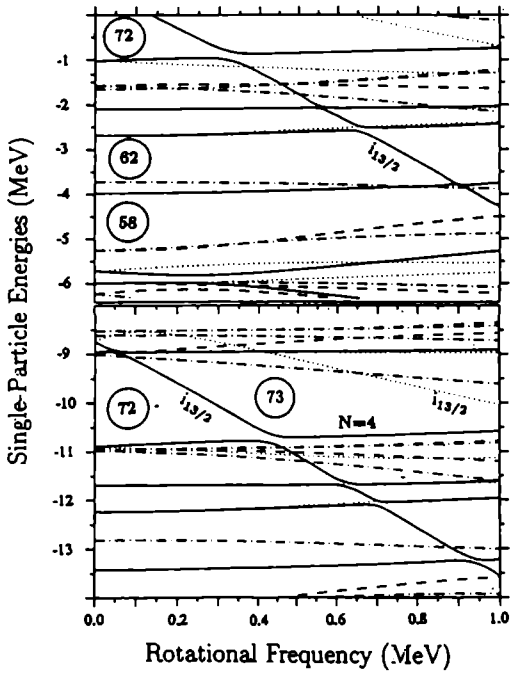

Fig.2: Proton (top) and neutron(bottom) single particle energies for the A$\sim$130 region calculated with β_2=0.38, β_4=0.014, γ=2.8°[ref.[26]].

If one considers only the amplitude of the quadrupole deformation, it is obvious to use the word "superdeformed" for nuclei having an axis ratio of 2:1 and the words "highly deformed" for nuclei with smaller axis ratio like Ce and Nd isotopes. However after consideration of the general properties, main characteristics and conditions described above one can also assign "superdeformed" to nuclei in the cerium region.

3. The New Generation of Multidetectors

3.1. Design of Large Arrays of γ-Ray Detectors

The study of weak amplitude phenomena requires high performances arrays of γ-ray detectors. Good energy resolution, large detection efficiency and large resolving power are the main conditions to fulfil.

The germanium detectors associated with efficient Compton suppressors satisfy the first condition. The detectors must be grouped in large number to detect high multiplicity events and must have reduced solid angles to limit broadening of the γ-lines due to the Doppler effect produced in heavy-ion induced reactions. The large

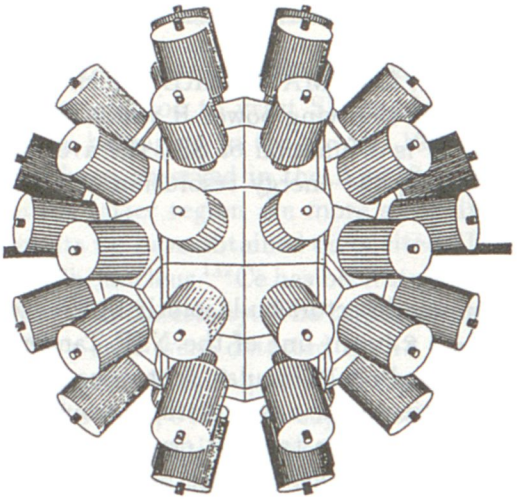

Fig.3: The structure of EUROGAM2. The central part is made of 24 clover detectors.

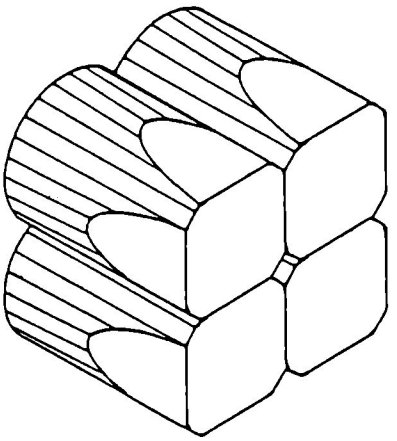

Fig.4: A schematic view of the four crystals constituting a clover detector.

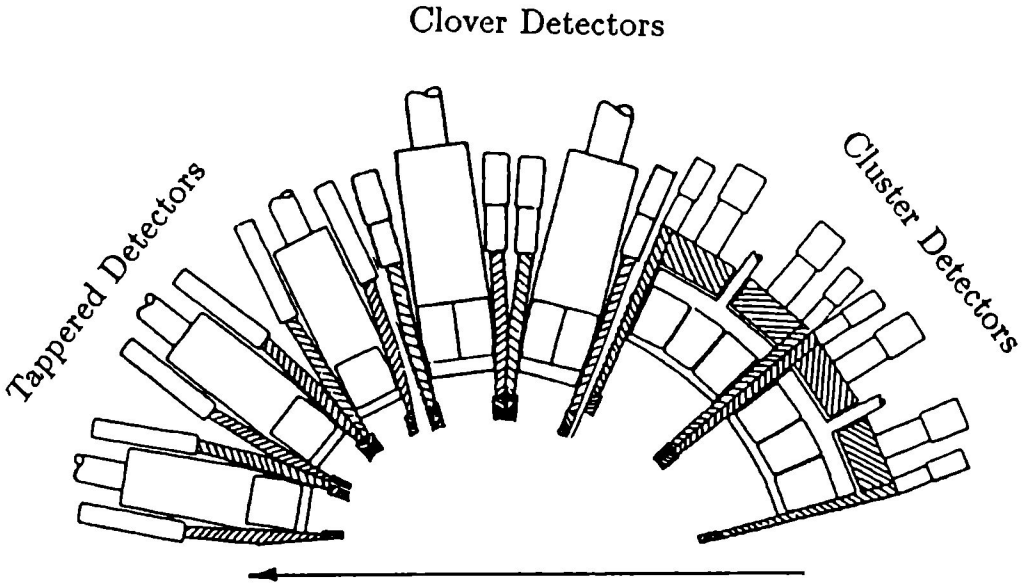

Fig.5: Partial structure of Euroball showing three different types of Ge detectors.

efficiency is obtained by increasing the number of detectors in order to cover the maximum solid angle around the target.

The new generation arrays (EUROGAM, GASP, GAMMASPHERE) which have at least 40 Ge detectors are characterized by a large resolving power R which determines the limit of observation. $R=(SE_\gamma/\Delta E_\gamma).PT$ is a function of SE_γ the average separation between γ-rays in a collective band, ΔE_γ the energy resolution and PT the peak to total ratio.

3.2. The Multidetector EUROGAM

EUROGAM is an array of suppressed germanium detectors built jointly by France and UK. In the first phase which was installed on a beam line of the NSF Tandem at Daresbury the multidetector had a geometry based on 12 regular pentagons, each containing 6 detectors[27,28]. Each detector was constituted of a Ge crystal surrounded by a BGO anti-Compton shield[29]. The Ge detectors were tapered crystals with a volume larger than 250 cm^3 and efficiency of $\approx$65-75%. The distance between their front face and the target was 20.5 cm. Instead of having the maximum number of detectors, EUROGAM1 had only 45 detectors covering 65% of 4π with a total peak efficiency of 5% at 1.33 MeV γ-ray energy. The number of detectors was reduced in order to install the first elements of the beam line to the recoil mass spectrometer. The limit of observation was $\approx 5.10^{-4}$. The electronics was designed with a high degree of integration. The signals from the detectors are processed in VXI based electronics. The data are controlled by a VXI trigger card and processed by an event builder in VME. All the electronic parameters are controlled by software.

For EUROGAM phase 2 (fig.3) the total efficiency is increased to $\approx$8% and the observational limit reduced to $\approx 10^{-4}$ using 24 clover detectors added to 30 detectors from phase 1. A clover detector (fig.4) is made of four 5 cm diameter and 7 cm length coaxial Ge detectors housed in a single BGO shield. The Doppler broadening of the γ-rays is reduced by means of these clover detectors which can be used also as Compton polarimeters to measure the γ-ray linear polarisation. EUROGAM2 is installed on a beam line of the Vivitron at Strasbourg.

3.3. The Future: The European Array EUROBALL

As shown by recent calculations, one of the best option for EUROBALL (fig.5) could consist of 15 cluster detectors in the backward end, 26 clover detectors from EUROGAM2 in the central section and 30 detectors from EUROGAM1 and GASP in the forward part, each detector having an appropriate BGO anti-Compton shield.

A cluster detector consists of 7 hexagonal cross-section tapered Ge detectors mounted in a common cryostat and surrounded by a BGO suppression shield[30]. With Ge detectors having a relative efficiency of $\approx$60%, a cluster detector has a total absorption efficiency of $\approx$0.30.

EUROBALL is expected to have a total peak efficiency of 9.8% and a detection limit of 10^{-5}. It will be placed at Legnaro(Italy) and should be operational at the beginning of 1997.

4. First Observation of Excited SD Bands in the A~130 Mass Region

4.1. Identification of the Excited Superdeformed Bands

In addition to yrast SD bands, excited SD bands had been identified in several nuclei belonging to the A~150,190 regions since several years whilst no such bands had been observed in the A~130 region. This was surprising since the yrast bands in the latter region are more strongly populated. In this section I present the first results we have obtained on excited SD bands in the A~130 region with EUROGAM.

The nucleus ^{132}Ce has been studied using the ^{100}Mo(^{36}S,4n) reaction at 155 MeV at the NSF, Daresbury. The target was self-supporting with a thickness of 625 μg.cm^{-2}. The γ-rays were detected by 42 Ge detectors of EUROGAM1. Only events with unsuppressed fold greater or equal to 7 were written to Exabyte tapes. A total of 7.10^8 events, 84% with suppressed fold $\geq$3, were recorded.

Two transitions have been added to the yrast SD band which extend now over $\approx$28.2 MeV till spin $\approx 62\hbar$.

Two excited SD bands have been identified[18] (fig.6): ^{132}Ce(2) is composed of 13 transitions with energies from 794 to 1687 keV and ^{132}Ce(3) of 12 transitions from

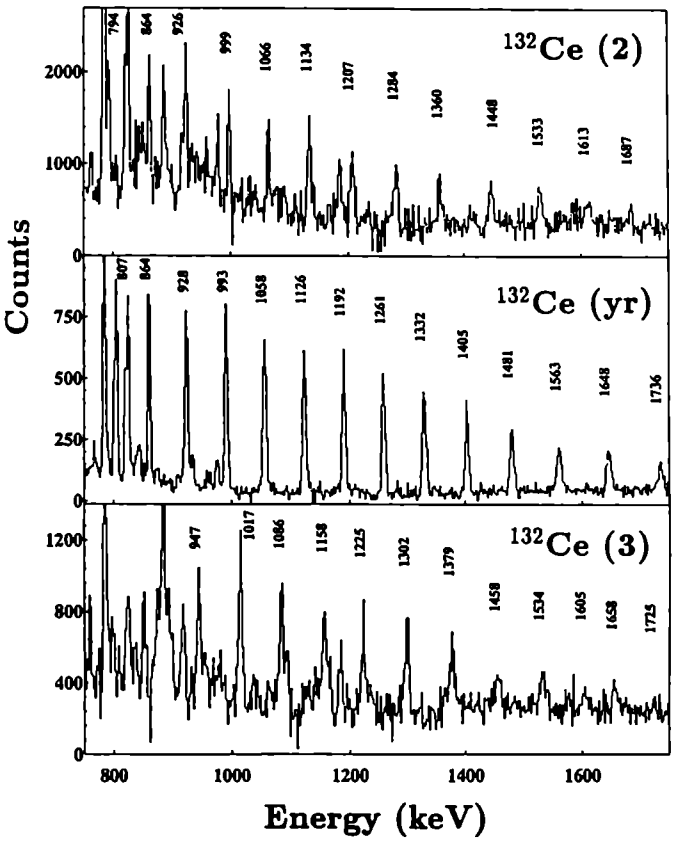

Fig.6: The two excited SD bands (top and bottom) and the yrast SD band (middle) in ^{132}Ce.

947 to 1725 keV. Their intensities correspond to 1% of the ^{132}Ce yield. Their $\mathcal{J}^{(2)}$ moments of inertia which are compared to that of the yrast SD band are shown in fig.7. The spins of the highest levels observed in these two excited bands are close to $48\hbar$ and $50\hbar$, respectively.

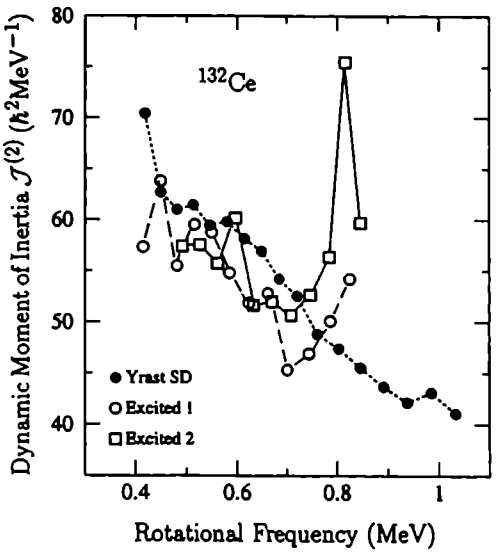

Fig.7: The $\mathcal{J}^{(2)}$ moments of inertia of the SD bands in ^{132}Ce.

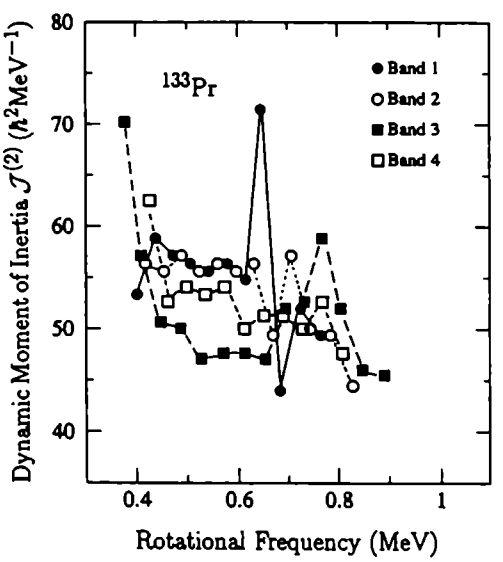

Fig.8: The $\mathcal{J}^{(2)}$ moments of inertia of the SD bands in ^{133}Pr.

In the ^{131}Ce nucleus produced also at high angular momentum in the above mentioned reaction, an excited SD band with 14 transitions ranging from 793 to 1717 keV has been seen[31] up to an estimated spin of $99/2\hbar$.

Another experiment has been performed using EUROGAM1 to search for excited SD bands in Pr isotopes. The main exit channel of the ^{100}Mo+^{37}Cl reaction at 155 MeV corresponds to ^{133}Pr in which no SD band was previously known. Four bands have been discovered in this nucleus[32] with transitions ranging from $\approx$0.8 to $\approx$1.6 MeV. Their $\mathcal{J}^{(2)}$ moments of inertia (fig.8) and experimental Routhians show that bands 1 and 2 on the one hand and bands 3 and 4 on the other hand are signature partners. The highest populated level has a spin of the order of $113/2\hbar$.

It is important to underline that linking transitions have been identified between bands 1 and 2. This is the first observation of dipole links between SD bands in the A$\sim$130 region.

4.2. Configurations of the Excited Superdeformed Bands

The very large deformation in the yrast bands of ^{131}Ce and ^{132}Ce is associated with one and two $i_{13/2}$ neutrons in the [660]1/2 orbitals, respectively.

The excited bands originate also from neutron configurations. In ^{132}Ce (fig.9) the excited bands are very likely due to the promotion of a neutron from any of the

three orbitals ν[411]1/2(α=+1/2) and ν[523]7/2(α=±1/2) to any of the three orbitals ν[530]1/2(α=±1/2) and ν[651]3/2(α=+1/2).

The theoretical $\mathcal{J}^{(2)}$ moments of inertia of these configurations calculated with a model based on the cranking approximation with the Woods-Saxon deformed potential have been compared to the experimental ones (fig.10). The band ^{132}Ce(2) could originate from a neutron excitation from [411]1/2(α=+1/2) to [530]1/2 (α=-1/2) at β_2=0.40, γ=0° or from [523]7/2(α=+1/2) to [530]1/2(α=-1/2) at β_2=0.41, γ=10°. The $\mathcal{J}^{(2)}$ moment of inertia of ^{132}Ce(3) is also well reproduced by the neutron excitation from [523]7/2(α=-1/2) to [530]1/2(α=-1/2) at β_2=0.43, γ=10°. The agreement between calculated and experimental $\mathcal{J}^{(2)}$ moments of inertia is good but the criterion based on these moments of inertia is not sufficient to unambiguously assign a configuration to a band.

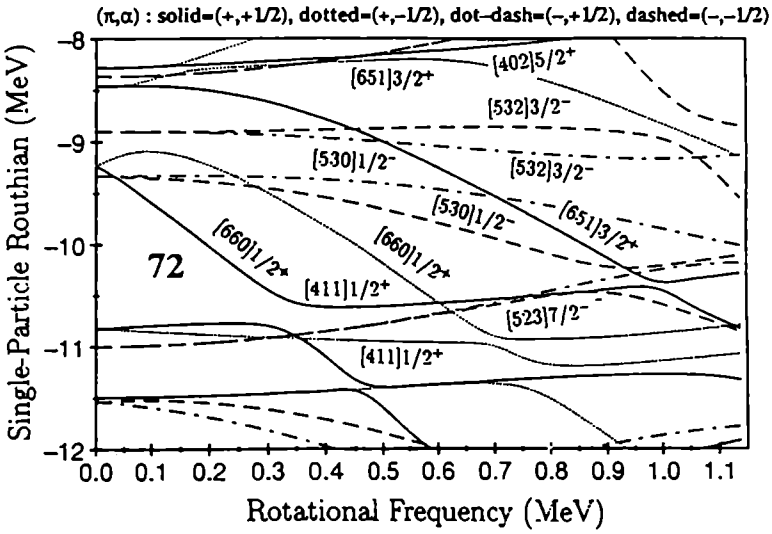

Fig.9: Neutron single particle energies calculated for N=74, β_2=0.43, γ=0°.

I must point out that the experimental moments of inertia of the excited bands in ^{132}Ce are well reproduced by the calculations without including pairing while the agreement is obtained for the yrast SD band only if some pairing is kept at low rotational frequency.

The similarity of the $\mathcal{J}^{(2)}$ moments of inertia of ^{131}Ce(2) and ^{132}Ce(yrast) suggests that the excited band in ^{131}Ce results from the promotion of a neutron to the [660]1/2(α=-1/2) orbital.

In ^{133}Pr(Z=59) the configurations of the SD bands are associated with proton orbitals. Bands 1 and 2 which have no signature splitting up to band interaction at $\hbar\omega$=0.65 MeV (fig.8) are very likely generated by $g_{9/2}$ protons from the [404]9/2$^+$ orbitals. The two other bands could originate from the [532]5/2$^-$ protons of the $h_{11/2}$ shell as suggested by the observed signature splitting (fig.8).

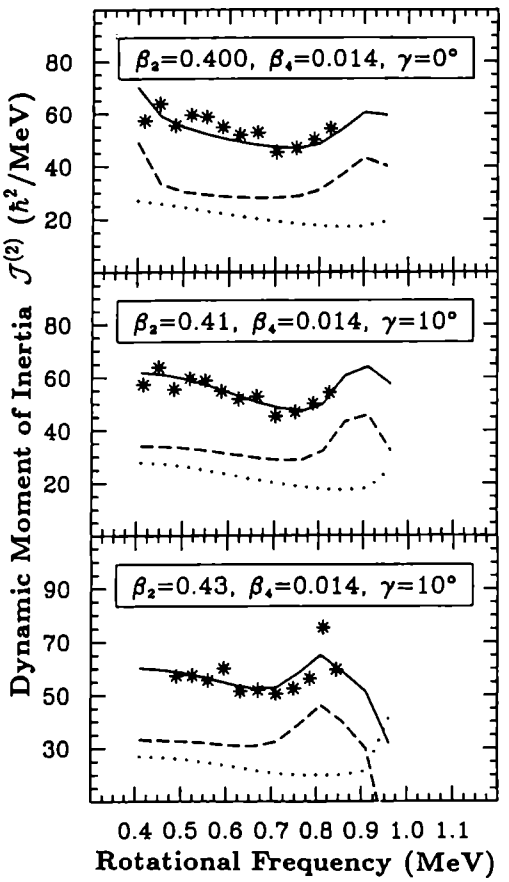

Fig.10: Comparisons of the experimental (*) and calculated (full solid lines) $\mathcal{J}^{(2)}$ dynamic moments. The long-dashed (dotted) lines correspond to the neutron (proton) contribution to the calculated moments. Top: ^{132}Ce(2) compared to the excitation from [411]1/2(α=+1/2) to [530]1/2(α=−1/2) at γ=0°. Middle: ^{132}Ce(2) compared to the excitation from [523]7/2(α=+1/2) to [530]1/2(α=−1/2) at γ=10°. Bottom: ^{132}Ce(3) compared to the excitation from [523]7/2(α=−1/2) to [530]1/2(α=−1/2) at γ=10°.

5. First Evidence for Identical SD Bands in the A∼130 Mass Region

Superdeformed bands in which transition energies are almost equal have been found in the A∼150 region[33]. These SD bands, called identical, could reveal interesting properties of the SD nuclei in question. Identical bands were unknown in the A∼130 region before our experiments with EUROGAM. In this section I present the first experimental evidence of the existence of such bands in this mass region. Some of the results have already been reported elsewhere[34].

The concept of identical bands is not totally accepted. However it is usually recognized that there exist correlations between bands with closely related γ-ray energies, similar dynamic moments of inertia and constant effective alignments.

5.1. Gamma-Ray Energies

The identity between bands is not limited to the domain of SD states but exists also for normally deformed states. For example one can have in mind the well known decoupled bands in odd-A La isotopes[35] where the γ-ray energies are equal or very close to those in the even-even Ba nuclei. This is well explained in the frame of the rotation-alignment model[36] by the coupling of a high-j valence particle oriented perpendicular to the symmetry axis of the core. Other bands having similar γ-ray energies can be found in the literature.

To understand the mechanism of identity between SD bands, it is useful to start first with some analogies existing between even-even and odd-A adjacent nuclei at low and medium spins.

In the strong coupling limit, the energy spectrum of an axial system having an angular momentum R and a moment of inertia $\mathcal{J}$ is given by:

$$E_K(I)= \varepsilon_K + 1/2\mathcal{J}[I(I+1)-K^2 + a(I+1/2)(-1)^{I+1/2}\delta_{K,1/2}]$$

where K=Ω is the projection of j on the symmetry axis, I the total angular momentum of the nucleus, ε_K the intrinsic excitation energy, a the decoupling parameter.

The γ-ray energies in the odd-A nucleus are $E^0_\gamma(I)=E_K(I) - E_K(I-2)$. They are expressed from the γ-ray energies in the even-even core and depend on the decoupling parameter "a" for which 3 particular values can be examined:

1) a=0 (*i.e.* K$\neq$1/2)

The coupling of the odd particle to the core generates a Δ=1 rotational band without signature splitting. The γ-ray energies are determined by

$$E^0_\gamma(I=R\pm1/2)=\tfrac{3}{4}\, E^c_\gamma(R) + \tfrac{1}{4}\, E^c_\gamma(R\pm2).$$

2) a=+1 (*i.e.* K=1/2)

In this case, a j=1/2 particle is coupled to the core and the states E(I=|R$\pm$1/2|) are degenerate . Thus the two sets of E2 γ-rays in the favoured r=$-i$ (I+1/2 odd) and unfavoured r=$+i$ (I+1/2 even) signature branches are identical. The degeneracy is represented by

$$E^0_\gamma(I=|R\pm1/2|)= E^c_\gamma(R).$$

3) a=$-$1 (*i.e.* K=1/2)

As for the preceding case, the levels are degenerate but here, the r=$+i$ signature branch becomes favoured. The γ-rays in the odd-A system are equal to arithmetic average in the core:

$$E^0_\gamma(I=R\pm1/2)=\tfrac{1}{2}\, [E^c_\gamma(R\pm2) + E^c_\gamma(R)].$$

Introducing a pseudo-angular momentum $\tilde{R}$=R+1, the energy relation becomes similar to that found for a=+1 *i.e.*

$$E^0_\gamma(I=|\tilde{R}\pm 1/2|)= E^c_\gamma(\tilde{R}).$$

From the three limits considered above, the γ-ray energies in a band relative to a reference band can be described by the general formula

$$E_\gamma(I')=(1-X)E^{ref}_\gamma(I) + XE^{ref}_\gamma(I+2) \text{ with } X=0,1/4,\ 1/2,\ 3/4.$$

Several SD bands identified in ^{131}Ce, ^{132}Ce, ^{133}Pr have γ-ray energies closely correlated following the above general formulas[18,34] (fig.11). For example, for the ^{132}Ce(yrast) band relative to ^{131}Ce(2), the mean value of the differences ΔE_γ between their γ-ray energies is $\approx$(-2.3$\pm$2.0) keV for 13 transitions when X=1/4. For ^{132}Ce(2) relative to ^{131}Ce(yrast) this mean value is $\approx$(2.5$\pm$2.0) keV with X=3/4.

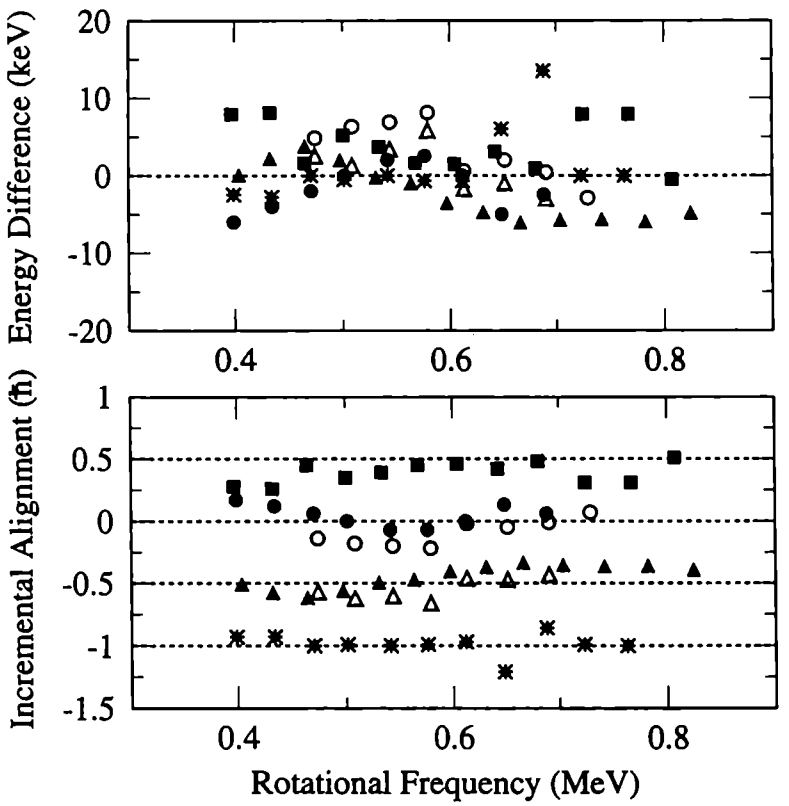

Fig.11: Energy differences (top) and incremental alignments(bottom) for correlated SD bands in in ^{131,132}Ce and ^{133}Pr. ^{132}Ce(2) (■),^{132}Ce(3) (○),^{133}Pr(2) (●) relative to ^{131}Ce(yr). ^{132}Ce(yr) (▲) relative to ^{131}Ce(2). ^{132}Ce(3) (△) relative to ^{132}Ce(2). ^{133}Pr(2) (*) relative to ^{133}Pr(1).

I must point out an interesting feature of the excited SD band in ^{131}Ce. A careful analysis of the data show that the γ-ray peaks in this band are broader than those in other bands produced in the same reaction[31]. The full widths at half maximum of γ-rays in bands of ^{131,132}Ce displayed in fig.12 demonstrate that band2 in ^{131}Ce is double. The two overlaping bands are identical.

It has been found also that ^{132}Ce(yr) and an excited band in ^{133}Ce[ref.[37]] have identical γ-ray energies.

The above discussed results show that, as in other regions, there exist SD bands in the vicinity of A=130 whose γ-ray energies are strongly correlated.

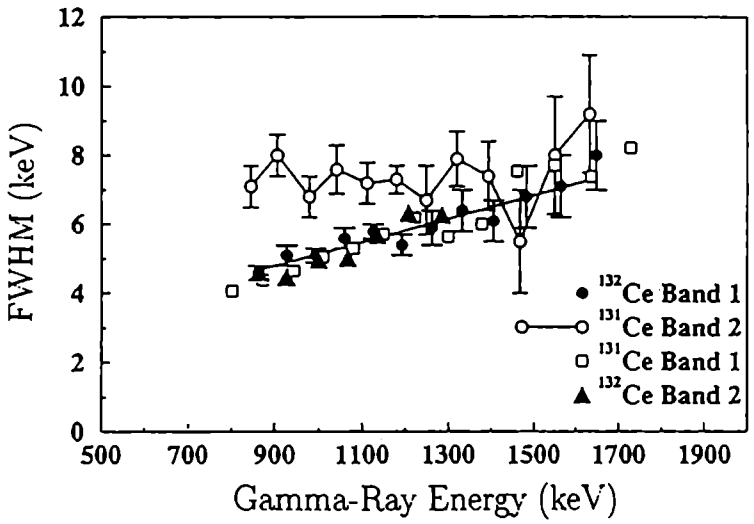

Fig.12: Full Width at Half Maximum of SD bands in ^{131}Ce and ^{132}Ce[ref.[31]].

5.2. Dynamic Moments of Inertia

The moment of inertia $\mathcal{J}^{(2)}$ of bands having correlated γ-ray energies have common features. Their amplitudes as a function of $\hbar\omega$ are sometimes very close to each other as illustrated in fig.13 by the cases of the ^{132}Ce(yrast) and ^{131}Ce(2) bands.

Equivalent $\mathcal{J}^{(2)}$ moments of inertia imply that the configurations of the bands are very likely similar. For the two above mentioned SD bands the configurations are mainly based on two $i_{13/2}$ neutrons.

5.3. Effective and Incremental Alignments

The aligned angular momentum (i=-de/dω) is characteristic of each quasiparticle orbital (see fig.9). Then the study of alignment process can possibly bring information about the configuration of a given band and be helpful for relating the spin and configuration of one band with respect to another.

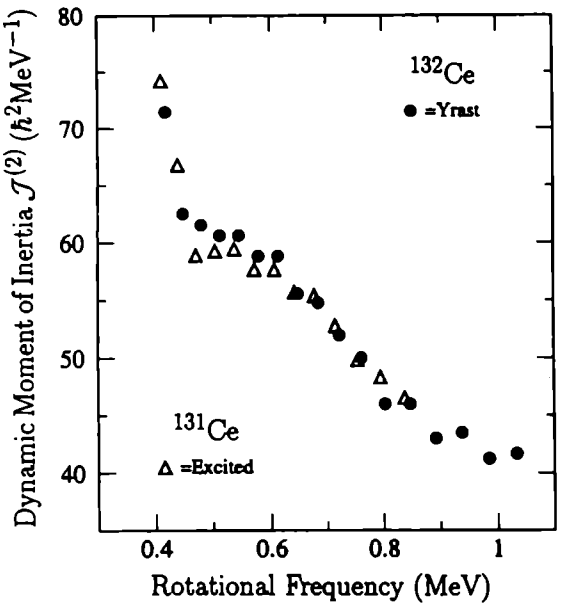

Fig.13: Comparison of the $\mathcal{J}^{(2)}$ moments of inertia of the yrast SD band in ^{132}Ce and excited SD band in ^{131}Ce.

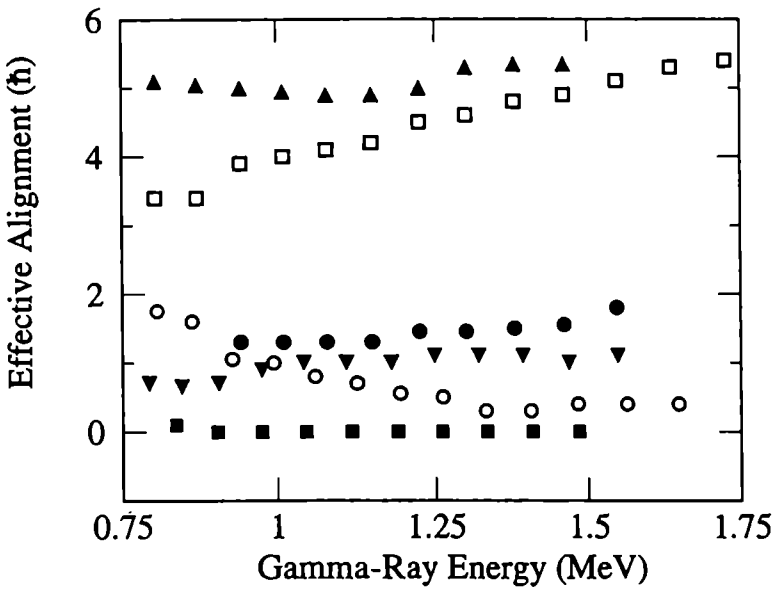

Fig.14: Effective alignment as a function of the γ-ray energy. Correlated bands: ^{132}Ce(3) (•) and ^{133}Pr(1) (▲) relative to ^{131}Ce(yr). ^{132}Ce(yr) (▼) relative to ^{131}Ce(2). ^{133}Pr(2) (■) relative to ^{133}Pr(1). Uncorrelated bands: ^{132}Ce(yr) (□) relative to ^{131}Ce(yr). ^{133}Pr(2) (o) relative to ^{132}Ce(yr).

The alignment of one band relative to another can be extracted from the two curves representing the variations of spin I as a function of γ-ray energy E_γ. The effective (or relative) alignment i_{eff} of two bands[38] at a given rotational frequency is the difference between their two spin values at this rotational frequency. It is plotted in fig.14 for several pairs of SD bands in the Ce and Pr isotopes. As the exact spins of the SD states are unknown the effective alignments are determined within several $\hbar$ units. Two groups of curves show up in fig.14: the first one with constant i_{eff} corresponds to correlated bands while the second one with large variations of i_{eff} as a function of E_γ corresponds to pairs of bands having uncorrelated γ-ray energies. A constant effective alignment between two correlated bands implies that the Routhian of the additional particle is constant with $\hbar\omega$. This can help for selecting the corresponding proton or neutron orbital.

Relating transition energies to aligned spins, Stephens *et al.*[39] have shown that identical bands in Hg nuclei have quantized aligned spins which was discussed in terms of aligned pseudo-spin[40]. Then it was suggested that the incremental alignment Δi must be also quantized[41] *i.e.* $\approx k1/2$ where k is an integer. Δi is defined by the relation $\Delta i = 2\Delta E_\gamma / \Delta E_\gamma^{ref}$ where ΔE_γ is obtained by subtracting the transition energy $E_\gamma(I')$ from the closest transition energy ($E_\gamma^{ref}(I)$ or $E_\gamma^{ref}(I+2)$) in the reference band. The energy difference between the closest two transitions is $\Delta E_\gamma^{ref} = E_\gamma^{ref}(I+2) - E_\gamma^{ref}(I)$.

As shown in fig.11, incremental alignments Δi calculated for several pairs of bands in ^{131}Ce, ^{132}Ce, ^{133}Pr take discrete values which depend on the relation existing between the γ-ray energies.

The question of quantized alignment which has been discussed by many authors is still open.

5.4. Configurations of the Identical Superdeformed Bands

Sometimes the correlations between γ-ray energies, moments of inertia and aligned spins between two bands can be used to deduce their relative configurations. For example, for two nuclei differing by one mass unit, this indicates that these two bands have common properties which are not appreciably influenced by the addition or subtraction of a quasiparticle.

The yrast band ^{132}Ce(1) which has a two $i_{13/2}$ neutron configuration and ^{131}Ce(2) are correlated. Then ^{131}Ce(2) which has one neutron coupled to ^{131}Ce(2). Then ^{131}Ce(2) which has one neutron less than ^{132}Ce(1) could be obtained by promoting the [411]1/2(α=+1/2) neutron to the $i_{13/2}$ [660]1/2(α=−1/2) neutron orbital. Indeed the [411]1/2 orbital which has a flat Routhian brings almost no energy and only a very weak aligned angular momentum to the nucleus (fig.9).

Similar arguments hold when considering the two excited bands in ^{132}Ce relative to the yrast one ^{131}Ce(1). The bands ^{132}Ce(2) and ^{132}Ce(3) which have two [660]1/2 neutrons are very likely produced by the excitation of a neutron close to the Fermi energy such as *e.g.* [411]1/2 or [523]7/2. Energy and aligned angular momentum criteria are slightly in favour of the promotion of a [411]1/2 neutron which could explain the first excited band, the second being produced by the excitation of a [523]7/2 neutron. This is in agreement with the proposition made in section 4.2.

The conclusions that one can draw from the observed correlations are limited and it is impossible so far to go further in this type of analysis.

The first observed identical bands[33] were discussed in terms of the strong-coupling approach and pseudo SU(3) symmetry[42]. The identities were satisfied by considering particular configurations having decoupling parameters a=0 and +1 corresponding to X=1/4 and 3/4, and 0, respectively. In the cerium region there is no $[\tilde{N}\tilde{n}_z\tilde{\Lambda}]$ orbital in the pseudo-spin scheme with decoupling parameters satisfying an interpretation similar to that proposed in the A$\sim$150 region. At present the pseudo-spin scheme seems not to be accepted unanimously.

As a general remark I should mention that the mechanism of identical bands is in fact not yet explained.

6. ΔI=2 Staggering in $^{131-133}$Ce and Possible C_4 Symmetry

6.1. Experimental Data

If we exclude band crossings and band interactions, the collective bands of rigid rotors are characterized by smooth variations of their γ-ray energies and moments of inertia. However, it has been recently observed that the $\mathcal{J}^{(2)}$ moments of inertia of the yrast SD band of ^{149}Gd[ref.[43]] and of three bands of ^{194}Hg[ref.[44]] exhibit a ΔI=2 staggering, $\mathcal{J}^{(2)}$ being related to γ-ray energies by the relation $\mathcal{J}^{(2)}=4\hbar^2/\Delta E_\gamma(I)$ with $\Delta E_\gamma(I)=E_\gamma(I+2) - E_\gamma(I)$. This effect is due to perturbations of the ΔI=2 collective sequence which bifurcates into two separate subsets of ΔI=4 levels. These perturbations of the energy levels induce deviations of the γ-ray energies in the band relative to those in the regular or unperturbed one.

An oscillation of $\mathcal{J}^{(2)}$ was already known at low spin in octupole bands of ^{236,238}U, ^{218}Ra and in the ground state band of ^{218}Ra, as analyzed by Peker *et al.*[45] but in these nuclei the staggering develops over a much shorter range of rotational frequency.

The staggering is obtained by subtracting a reference ΔE_γ^{ref} to the energy difference ΔE_γ between two consecutive γ-rays. For ^{149}Gd it is of the order of 230 eV for $\hbar\omega\geq$0.5 MeV. The effect of the perturbation is rather weak on the γ-ray energies and to extract a significant quantitative result, the experimental data must be analyzed very carefully. In particular the γ-ray energies and uncertainties must be determined very precisely. This supposes that they do not depend on the way the final spectra are produced *i.e.* on background subtractions in multifold gated coincidence spectra.

Recently[46] a staggering has been found in the $\mathcal{J}^{(2)}$ moment of inertia of the yrast SD bands in ^{131,132}Ce and of two SD bands in ^{133}Ce. It is the first observation of this phenomenon in the A=130 region. The results for ^{131,132}Ce were obtained from the EUROGAM1 experiment described in section 2.2. and those for ^{133}Ce from an experiment with GAMMASPHERE.

Deviations of γ-ray energies from the regular behaviour are extracted as a function of $\hbar\omega$ (fig.15). The unperturbed reference is deduced from a quadratic fit of the

variations of E_γ with spin. Several methods[43,44,46] have been introduced to calculate the staggering and/or the reference. They have been applied to ^{131,132,133}Ce and all show that deviations from an unperturbed regime persist. There are only differences in the amplitudes of the staggering.

As shown in fig.15 the staggering between two consecutive ΔI=2 points in ^{132}Ce(1) reaches $\approx$600$\pm$300 eV at $\hbar\omega\approx$0.9 MeV. This corresponds to transition energies shifted up and down by $\approx$300$\pm$150 eV and levels pushed up and down by $\approx$150$\pm$75 eV relative to their unperturbed positions. As for ^{194}Hg there is a phase change in ^{131,132}Ce *i.e.* the deviations have different signs at low and high rotational frequencies.

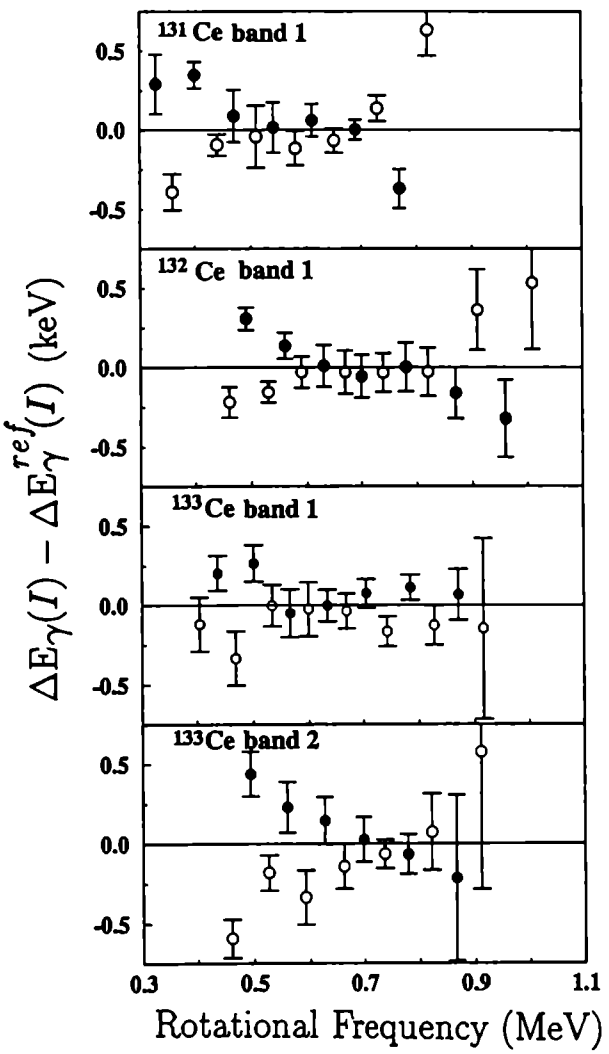

Fig.15: Energy differences ΔE_γ between adjacent γ-rays in ^{131,132,133}Ce as a function of $\hbar\omega$ minus a reference $\Delta E\gamma^{ref}$ [ref.[46]].

6.2. Proposed Explanations

The $\Delta I=2$ staggering observed in the γ-ray spectra of SD bands suggests the existence of a slight perturbation of the SD prolate shape by a Y_{44} hexadecapole term. Several interpretations are proposed for this phenomenon.

Hamamoto and Mottelson[47] explain that the perturbation of the rotational energy of the axially symmetric rotator could be due to a tunneling effect between the four minima of the potential energy surface induced by the Y_{44} deformation. The 4-fold axis of the C_4 symmetry is parallel to the long prolate axis of the nucleus.

The rotational Hamiltonian of the nucleus as proposed by Pavlichenkov and Flibotte[48] has two different regimes suggesting two different microscopic origins for the $\Delta I=2$ staggering associated with two different regions of the angular momentum space. For $I<I_c$ (I_c is a critical value of the angular momentum I) the staggering originates from the tunneling of I between the four minima produced by the static hexadecapole deformation as described by Hamamoto and Mottelson[46]. At the critical angular momentum I_c, the four minima transform into a single one and then, in the region $I>I_c$, the staggering could be produced by a dynamical effect related to the alignment of the total angular momentum along the C_4 symmetry axis.

To interpret the staggering, the mixing of multiple K bands[49] and an intrinsic uniform vortical motion in the nucleus[50] have also been considered.

There is no clear answer so far concerning the validity of these approaches to explain the phenomenon. Nevertheless on can try to relate the observed staggering to the internal structure of the nuclei. In the A=150 region, the effect has been observed in nuclei having an odd N=7 neutron and not in nuclei having even N=7 neutrons. In the A=130 region where the N=6 neutrons play a major role the oscillations exist in both odd and even Ce isotopes and seem to depend neither on the quasiparticle configurations nor on the quadrupole deformations which are different ($\beta_2\approx0.35$ for ^{131}Ce and $\beta_2\approx0.40$ for ^{132}Ce).

The staggering effect in ^{132}Ce appears clearly in two regions of rotational frequency: below $\hbar\omega\approx0.6$ MeV and above $\hbar\omega\approx0.8$ MeV. The existence of two ranges with staggering separated by a region where it dies out is an interesting feature predicted by several theoretical approaches[46,47]. I must indicate that the phase change expected from these theories is observed in the cerium isotopes.

7. Conclusion

By means of the large γ-ray detector array EUROGAM new results have been obtained for superdeformed states in nuclei of the A$\sim$130 region. Excited and identical bands which were unknown in this mass region have been observed for the first time in ^{131,132}Ce and ^{133}Pr isotopes. Propositions are made for the nature of the configurations of the excited bands while the correlations found between identical bands are not well understood. It has been also found for the first time in this region that the dynamic moment of inertia of some bands in $^{131-133}$Ce exhibit a staggering which could be

related to a possible C_4 symmetry in these nuclei.

These results bring new insight on the superdeformation in the A$\sim$130 region. This has been possible only thanks to a very powerful instrument able to detect low intensity phenomena. One can expect new findings in this domain of very large deformations by means of the new array EUROBALL which is under construction.

8. Acknowledgements

The experimental results presented in this lecture have been obtained in the frame of a collaboration between groups at ISN Grenoble, University of Liverpool, University of York and ATOMKI Debrecen. I thank the members of these groups who participate to this research programme. I also thank J. Dudek for discussions relative to the theoretical part of our common work. I acknowledge the Ministry of Education and Research for financial support from the PARCECO Programme.

9. References

1. S.M. Polikanov *et al.*, *Sov. Phys. JETP* **15** (1962) 1016.
2. V.M. Strutinsky, *Nucl. Phys.* **A122** (1968) 1.
3. H. El-Samman *et al.*, *Nucl. Phys.***A427** (1984) 397.
4. P.J. Nolan *et al.*, *J. Phys. G* **11** (1985) L17.
5. A.J. Kirwan *et al.*, *Phys. Rev. Lett.* **58** (1987) 467.
6. B.M. Nyakó *et al.*, *Phys. Rev. Lett.* **52** (1984) 507.
7. P.J. Twin *et al.*, *Phys. Rev. Lett.* **57** (1986) 811.
8. K. Neergård and V.V., Pashkevich, *Phys. Lett.* **59B** (1975) 218.
9. R. Bengtsson *et al.*, *Phys. Lett* **57B** (1975) 301.
10. C.G. Andersson *et al.*, *Phys. Scripta* **24** 1981 266.
11. J. Dudek *et al.*, *Phys. Lett.* **112B** (1982) 1.
12. S. Åberg, *Phys. Scripta* **25** (1982) 23.
13. I. Ragnarsson and S. Åberg, *Phys. Lett.* **B180** (1986) 191.
14. R.R. Chasman, *Phys. Lett.* **B187** (1987) 219.
15. W. Nazarewicz, in *Recent Advances in Nuclear Structure*, ed. D. Bucurescu, G. Cata-Danil and N.V. Zamfir (World Scientific, 1990).
16. J. Dudek, *Prog. Part. Nucl. Phys.* **28** (1992) 131.
17. Y.X. Luo *et al.*, *Z. Phys.* **A329** (1988) 125.
18. D. Santos *et al.*, *Phys. Rev. Lett.* **74** (1995) 1708.
19. R. Wadsworth *et al.*, *J. Phys. G* **13** (1987) L207.
20. D. Bazzaco *et al.*, *Phys.Rev.* **C49** (1994) R2281.
21. E.M. Beck *et al.*, *Phys. Rev. Lett.* **58** (1987) 2182.
22. M.A. Deleplanque, private communication.
23. E.M. Beck *et al.*, *Phys. Lett.* **195B** (1987) 531.
24. S. Lunardi *et al.*, *Phys. Rev.* **C52** (1995) R1.
25. T. Bengtsson, I. Ragnarsson and S. Åberg, *Phys. Lett.* **208B** (1988) 39.

26. R. Wyss *et al.*, *Phys. Lett.* **215B** (1988) 211.
27. P.J. Nolan, *Nucl. Phys.* **A520** (1990) 657c.
28. F.A. Beck, *Prog. Part. Nucl. Phys.* **28** (1992) 443.
29. C.W. Beausang *et al.*, *Nucl. Inst. and Methods* **A313** (1992) 37.
30. J. Eberth, *Conf. on Physics from Large γ-ray Detector Arrays*, Berkeley, USA, (1994), report LBL-35687, vol.2, p.160.
31. P.J. Nolan *et al.*, *ibid.* p.99.
32. J.N. Wilson *et al.*, *Phys. Rev. Lett.* **74** (1995) 1950.
33. T. Byrski *et al.*, *Phys. Rev. Lett.* **64** (1990) 1650.
34. J. Gizon, *XIth Internat. School on Nuclear Physics, Neutron Physics and Nuclear Energy*, Varna, Bulgaria, ed. W. Andrejtscheff and E. Elenkov (1993).
35. J.R. Leigh *et al.*, *Nucl. Phys.* **A213** (1973) 1.
36. F.S. Stephens and R.S. Simon, *Nucl. Phys.* **A183** (1972) 257.
37. K. Hauschild *et al.*, *Phys. Lett.* **353B** (1995) 438.
38. I. Ragnarsson, *Nucl. Phys.* **A557** (1993) 167c.
39. F.S. Stephens *et al.*, *Phys. Rev. Lett.* **64** (1990) 2623.
40. A. Bohr, I. Hamamoto and B.R. Mottelson, *Phys. Scripta* **26** (1982) 267.
41. F.S. Stephens *et al.*, *Phys. Rev. Lett.* **65** (1990) 301.
42. W. Nazarewicz, *Phys. Rev. Lett.* **64** (1990) 1654.
43. S. Flibotte *et al.*, *Phys. Rev. Lett.* **71** (1993) 4299.
44. B. Cederwall *et al.*, *Phys. Rev. Lett.* **72** (1994) 3150.
45. L. Peker *et al.*, *Phys. Rev. Lett.* **50** (1983) 1749.
46. A.T. Semple *et al.*, to be published.
47. I. Hamamoto and B. Mottelson, *Phys. Lett.* **B333** (1994) 294.
48. I.M. Pavlichenkov and S. Flibotte, *Phys. Rev.* **C51** (1995) R460.
49. A.O. Macchiavelli *et al.*, *Phys. Rev.* **C51** (1995) R1.
50. I.N. Mikailov and P. Quentin, *Phys. Rev. Lett.* **74** (1995) 3336.

Nuclear Structure Studies with GASP

Santo Lunardi

Dipartimento di Fisica and INFN, Sezione di Padova, Padova, Italy

ABSTRACT

The GASP array has been used extensively for the study of superdeformation in nuclei as well as for the investigation of various other aspects of nuclear structure. Concerning superdeformation, in this paper results will be given on the decay of SD bands in the mass A=130 region and on the properties of the doubly magic ^{144}Gd nucleus. As an example of the performances of the GASP array for studying neutron-rich nuclei produced in deep-inelastic heavy ion collisions, data will be also presented on a new exotic nucleus ^{68}Ni, which shows characteristics of a doubly-magic shell model nucleus.

1. Introduction

Nuclear structure studies using γ-ray spectroscopy methods have made an impressive advance in the last few years with the advent of the new γ-ray detector arrays like GASP which started operation in 1992. Since then, many experiments have been performed with that array covering a large variety of subjects, such as the study of the properties of the nucleus at very elongates shapes (SD and hyperdeformed shapes), the spectroscopy of nuclei far from stability both on the proton- and on the neutron-rich side and various aspects of heavy-ion reaction mechanisms.

One of the questions left open by the first generation experiments on superdeformation was related to the decay-out of the SD bands into the normal-deformed (ND) states of a nucleus. Whereas in the mass A=150 and A=190 region no transitions linking the SD states to the ND states have been identified, in the mass A=130 region this has been now achieved allowing a better understanding of the structure of the SD bands in this mass region.

The improved sensitivity of GASP has lead also to the discovery of superdeformation in the nucleus ^{144}Gd which was since long predicted to be one of the most favorable cases were to observe the phenomenon. Excited SD bands have been

discovered in ^{144}Gd, as well as in neighboring nuclei, so that a detailed characterization of the single-particle excitations at extreme deformation is now possible also in this rather new region of superdeformation.

In order to illustrate the capabilities of the new generation arrays for spectroscopic studies different from superdeformation, results will be presented on a new exotic isotope ^{68}Ni which shows properties characteristic of a doubly magic shell model nucleus. The observation of excited states in this nucleus has been possible thanks to the great sensitivity of GASP for very weak reaction channels like those following deep-inelastic reactions between heavy ions.

2. The array GASP

The GASP spectrometer[1] is a general purpose 4π detector for advanced γ-ray spectroscopy which is located at the Tandem+Linac accelerator of the Laboratori Nazionali di Legnaro. The array consists of 40 Compton suppressed, large volume germanium detectors and of a 4π calorimeter composed of 80 BGO crystals. The detector houses a reaction chamber of 34 cm diameter where a charged particles detector array (named ISIS) composed of 40 ΔE-E Si-telescopes has been installed (its efficiency for protons is $\approx$ 70%). Evaporation residues produced in the centre of GASP can be injected into the recoil mass spectrometer CAMEL for mass selection. The coupled operation of GASP, CAMEL and the Si-ball gives a powerful instrument for identification and study of weak reaction channels. The absolute photopeak efficiency of GASP at 1332 keV is about 3% but reaches $\approx$ 6% if the BGO inner ball is removed and the 40 Ge detectors are positioned at $\approx$ 20 cm from the target. This second configuration is being used when the detection efficiency, and not the resolving power, is the relevant figure in an experiment.

3. Decay-out of the superdeformed bands in the mass A=130 region: the odd-even Nd nuclei

3.1 Decay-out of SD bands

After the discovery[2] of superdeformation in 1986, it was immediately realized that the decay of SD bands into the ND states was a complicated process not easy to detect. In fact, all SD bands found in many nuclei were not connected with the states at lower energy of a specific nucleus but instead lying "in the air". The construction of the new big arrays (GAMMASPHERE, GASP and EUROGAM) was

partly motivated also by the prospect to discover the missing connection between the states in the two minima (normal- and super-deformed) in the potential nuclear energy surface. Only knowing the transitions linking the SD states to the normal deformed ones it is in fact possible to fix excitation energy, spins and parities of the superdeformed bands and to compare therefore experimental data with theoretical calculations. Even with the great sensitivity of the new big γ-arrays it has not been possible to find such linking transitions for SD nuclei in the A=150 and A=190 mass regions. Nevertheless important steps in characterizing the decay-out process have been achieved[3,4]. It is generally accepted that the connection between the lowest SD states (lying several MeV above the yrast line) and the normal deformed ones proceed through a quasi-continuum of intermediate states. The systematics[5] of the average decay-out spins and the average entry spins into normal-deformed states indicates that they are correlated with the high-N (being N the main oscillator quantum number) configurations of the SD bands and speak in favour of some specific deexcitation pathways, maintaining therefore the hope of experimentally observing the individual linking transitions.

The situation is somehow different in the mass A=130 region where many rotational SD bands have been reported, which have been interpreted as being built on a second minimum in the nuclear potential energy surface. The deformation associated with those SD bands is smaller ($\beta_2 = 0.3$-0.4) than that of SD bands in the higher mass regions ($\beta_2 = 0.5$-0.6). Furthermore, the nuclei in this region have prolate shapes at low spin with a quadrupole deformation $\beta_2 = 0.2$ whereas the nuclear shape in the mass A=150 and 190 regions is oblate with $\beta_2 = -0.1$. The decay out of SD bands in the A=150 and 190 regions is therefore highly fragmented also because of the great difference in the single-particle configuration of the states (SD and ND) involved in the process. In the path from high to low deformation a large number of level crossings occurs, implying the rearrangement of more than 20 nucleons. In the A=130 nuclei the lowest SD states lie around 1 MeV above the yrast line and the transition between the two deformations can be performed through only few level crossings (one or two), which implies a much less fragmentation of the decay out. Through experiments performed at GASP we have been able to identify discrete linking transitions connecting the SD bands in the odd-even ^{133,137}Nd whereas at GAMMASPHERE the same result has been achieved for the ^{135}Nd nucleus. In the next sections the experimental evidence of the decay-out

process will be given together with a theoretical interpretation of its mechanism.

3.2 The decay-out of the SD band in ^{133}Nd: accidental mixing of superdeformed with normal-deformed states.

By means of a high statistics and high resolution backed target experiment using the reaction ^{104}Pd $+^{32}$S at 135 MeV we could establish a detailed level scheme of ^{133}Nd at low excitation energy and identify at the same time all the transitions which depopulate the SD band[6].

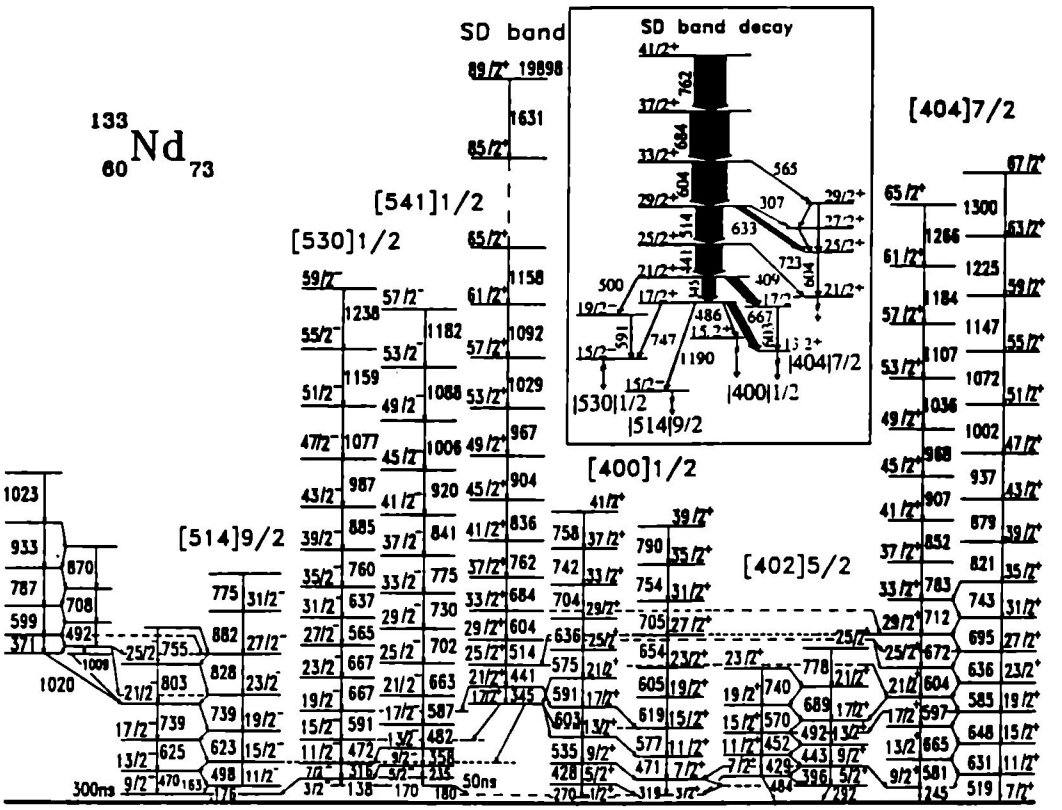

Fig. 1. Level scheme of ^{133}Nd resulting from the GASP experiments. The inset shows the decay out of the SD band.

The full SD band intensity has been found to divide into ten different paths which bridge the band to levels of different structure at lower spin. A complete level

scheme of ^{133}Nd, comprising seven bands built on different Nilsson orbitals, has also been established and it is shown in Fig. 1 together with the part relevant for the decay-out of the SD band. The experimental determination of the spins and parity of the SD band levels confirms that the SD band is based on the N=6 $i_{13/2}$ orbital [660]1/2 whose occupation drives the nucleus to a larger deformation according to cranked deformed shell-model calculations[7].

The SD band, being yrast above spin $29/2^+$, is the most strongly populated discrete structure at high spin (up to $I^\pi=89/2^+$)[8]. Below $29/2^+$ the band is no more yrast and when it disappears (at spin $17/2^+$) it is the furthest from yrast of all the observed bands of the nucleus. The decay of the SD band to the other nuclear states is occurring in the spin interval ($17/2^+$–$29/2^+$) where the band is crossing levels of similar spin and parities and can mix with them.

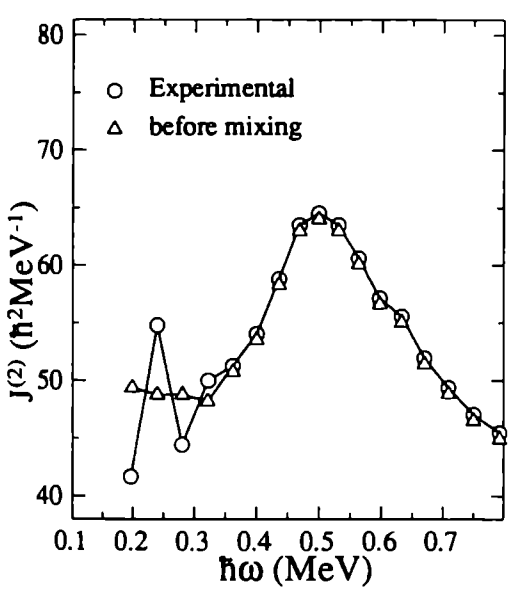

Fig. 2. Experimental (◯) $J^{(2)}$ moment of inertia for the SD band of ^{133}Nd compared with the one obtained (△) when the mixing with normal deformed states is taken into account.

A feature which is immediately clear from the inset in Fig. 1 is that three strong transitions (409, 633 and 667 keV) are responsible for almost 70% of the decay-out whereas the other seven are much weaker. We can relate this fact to a level mixing phenomenon. In fact the $29/2^+$ level of the SD band ($29/2^+_{SD}$), which decays through the strong 633 keV transition to the $25/2^+_{[404]7/2}$, lies only 39 keV apart from the $29/2^+_{[404]7/2}$. Furthermore a weak transition of 553 keV is observed to decay from the $29/2^+_{[404]7/2}$ to the $25/2^+_{SD}$. These facts are a clear indication of a level mixing occurring between levels differing by two major oscillator quantum numbers (N=6 and N=4). Analogously, the mixing of the $17/2^+_{SD}$ with the $17/2^+_{[400]1/2}$ (ΔE=64 keV) can explain the strong transitions linking the $21/2^+_{SD}$ to the $17/2^+_{[400]1/2}$ (409 keV) and the one from the $17/2^+_{SD}$ to the $13/2^+_{[400]1/2}$ (667 keV). Also in this

case the decay of the [400]1/2 band into the SD band is observed ($21/2^+_{[400]1/2} \rightarrow 17/2^+_{SD}$, 527 keV).

In order to extract the interaction matrix elements and the mixing amplitudes of the states, a simple two–band mixing calculation[9] has been performed. From the experimental branching ratios we derive the interaction matrix elements at spin $29/2^+$ and $17/2^+$ (11 and 22 keV respectively) as well as the expected branchings of the $33/2^+$ and $25/2^+$ states of the SD band into the [404]7/2 band. A remarkable agreement between the experimental and calculated branching ratios is found. From this analysis we can derive also the unperturbed energies of the SD band and hence recalculate its dynamic $J^{(2)}$ moment of inertia. Fig. 2 shows the moments of inertia derived, as usual, from the expression $J^{(2)}=4/\Delta E_\gamma$ using both the experimental energy differences between two consecutive transitions, and the ΔE_γ which result when the level shifts due to the mixing with normal states are removed. The irregular behaviour of $J^{(2)}$, typical of the SD bands in the mass 130 region at the decay-out, disappears when the new energy values are used. This result clearly shows that the mixing with normal deformed states is the most likely interpretation of the strange $J^{(2)}$ behaviour at lower frequency, seen also in many other SD bands in the region.

3.3 The decay-out of the SD band in ^{137}Nd.

In ^{133}Nd, as discussed above, the decay out of the SD band can be explained, in a quantitative way, in terms of an accidental mixing of super-deformed and normal-deformed states. Within this approach it is also understood why the band in ^{133}Nd ends at spin $17/2^+$. In order to achieve a more comprehensive understanding of the decay-out mechanism of SD bands in the mass A=130 region we have extended our investigation to the heavier odd Nd isotope ^{137}Nd where a SD band was known since long[10].

From lifetime measurements using the Doppler Shift Attenuation Method[11] a quadrupole moment Q=*4.0 eb* for the SD band of ^{137}Nd has been measured. Under the assumption of an axially symmetric shape, a deformation parameter $\beta_2 =$ *0.22* is extracted which is the smallest among the known SD bands in the A=130 mass region (the normal deformation is here $\beta_2 =$ *0.10-0.15*). The measured quadrupole moment can be anyway equally well explained through a triaxial shape of the nucleus with a larger deformation ($\beta_2 =$ *0.28*, $\gamma \sim 10^0$-20^0). We will see later that this last one

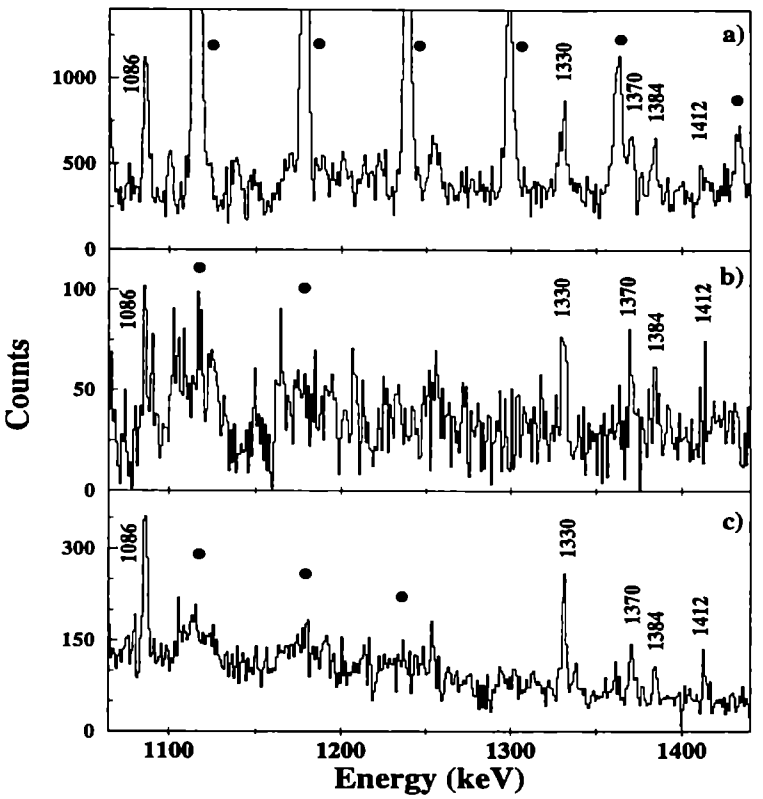

Fig. 3. a) High energy part of a doubly-gated spectrum, with gates set on transitions in the SD band of ^{137}Nd, obtained using the ^{110}Pd + ^{30}Si reaction with thin self-supporting targets. b) Same as a) but with a gold-backed target and gates set on transitions in the SD band below E_γ= 900 keV. c) Same as b) but for the ^{123}Sb + ^{19}F reaction. Transitions belonging to the SD band are labeled with full dots; transitions connecting the SD band to the ND states are labeled with their energies.

is the shape predicted by cranked shell model calculations for an highly-deformed band in ^{137}Nd. The ^{137}Nd nucleus has been populated via the ^{110}Pd(^{30}Si,3n) and the ^{123}Sb(^{19}F,5n) reactions at beam energies of 125 and 97 MeV, respectively. Two different experiments have been performed using the ^{30}Si beam, one with a stack of thin ^{110}Pd foils (2×0.5mg/cm^2) and one with a gold-backed ^{110}Pd target (1.5 mg/cm^2 of ^{110}Pd on 10 mg/cm^2 of gold). The experiments with backed targets had the two-fold goal of obtaining a detailed level scheme of ^{137}Nd at low excitation energy and of identifying the transitions which depopulate the SD band. In fact, only a few levels at low spin were known in the literature for this nucleus[12];

however, in order to study the decay out of the SD band into the ND levels, one needs a detailed level scheme at medium and high spins. The second and important reason (which applies also to the previous ^{133}Nd case) to choose a backed target for the study of the decay out comes from the knowledge of the lifetimes of the band levels. From the previous backed-target experiment[11] it results that the transitions of the SD band with energies higher than $E_\gamma \approx 800$ keV suffer from the Doppler broadening effect; on the contrary, the transitions deexciting the lowest levels of the SD band appear as sharp lines in the γ-ray spectrum, which means that they are emitted from states with lifetimes longer than the stopping time of the recoiling nuclei in the backing. As the transitions which link the SD band to the states of normal deformation are expected to have similar lifetimes but also to be very weak, it is easily realized that one can enhance their detection by taking advantage of the much better energy resolution achieved in a backed-target experiment.

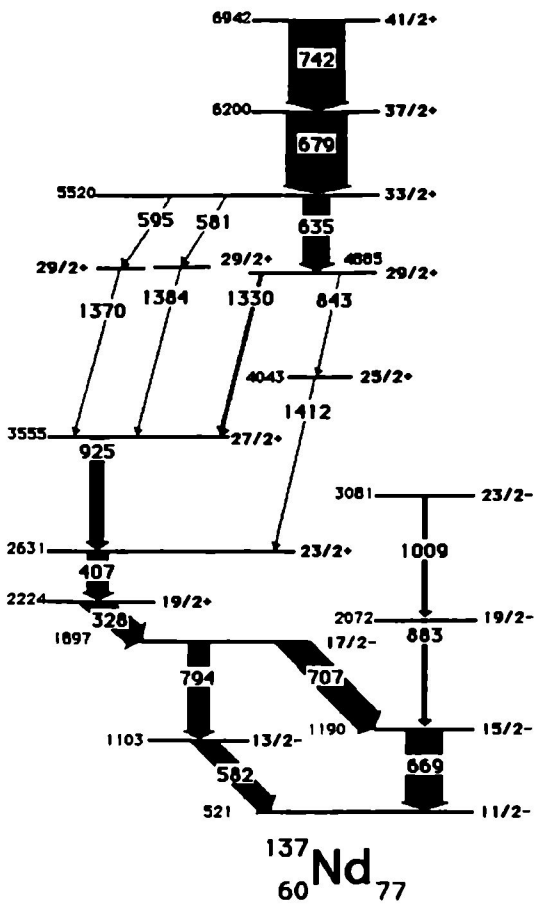

Fig. 4. Partial level scheme of ^{137}Nd showing the bottom of the SD band and the part relevant for the decay-out process of the SD band.

Figure 3 shows nicely how, for our case, the use of a backed target helped to find the decay out of the SD band. In the upper part of the figure, the region above 1 MeV is displayed of a doubly-gated spectrum obtained bombarding a thin ^{110}Pd target with a ^{30}Si beam. The gates are set on all transitions assigned to the SD band in ^{137}Nd. It is evident from this spectrum that the band is in coincidence with

a few other transitions in the energy range 1-1.5 MeV. A striking effect is observed in the two analogous spectra obtained in the backed-target experiments (middle and lower part of the figure for the ^{30}Si + ^{110}Pd and the ^{19}F + ^{123}Sb reactions, respectively). The new transitions in coincidence with the SD band appear as sharp lines, like the low-lying transitions in the SD band (not shown in the figure), whereas the transitions of the SD band above 1 MeV are completely smeared out by the Doppler broadening. This fact strongly suggests that the transitions of 1086, 1330, 1370, 1384 and 1412 keV are related to the decay-out process of the band.

After a detailed analysis of the γ-γ coincidence data a complete level scheme of ^{137}Nd has been obtained[13]. In Fig. 4 only the part relevant to the decay out of the SD band is drawn. In this case only $\approx$ 20% of the intensity of the SD band is carried out by the observed linking transitions.

3.4 Cranked shell model calculations.

In a recent experiment at GAMMASPHERE the decay-out of the SD band in ^{135}Nd has been investigated[14] and some discrete linking transitions have been found which account for $\approx$ 70% of the intensity of the SD band. With respect to ^{133}Nd a different interpretation of the decay-out has been given in ^{135}Nd where the SD band ends at spin $25/2^+$ and no mixing with ND levels has been observed; the sudden disappearance of the band has been here related to the disappearance of the SD potential energy minimum as indicated by Total Routhian Surface (TRS) calculations.

For all three Nd isotopes here discussed, spins and parity of the SD band levels are now experimentally determined which are in agreement with the theoretical interpretation given some time ago[7] for the SD bands of odd-even nuclei in this mass region. They are associated with a quasi-particle $i_{13/2}$ neutron excitation with signature $\alpha = +1/2$.

The different behaviour in the decay-out region of the SD bands in the three odd Nd isotopes with A= 133-137 can now be compared and this is shown in Fig. 5 where the excitation energies of the SD band levels of ^{133}Nd, ^{135}Nd and ^{137}Nd are reported as a function of spin and, for comparison, the yrast lines of the three nuclei are also drawn. One can immediately see that the SD bands, which are yrast and therefore populated preferentially at higher spins, cross the ND yrast line at different points of the I-E* plane and that they continue down to lower spins until

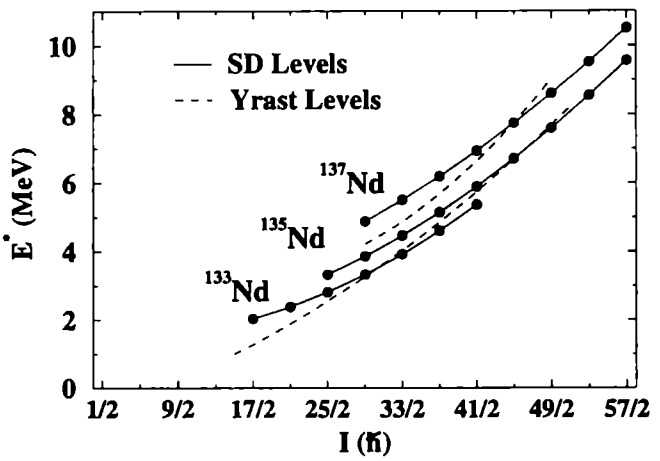

Fig. 5. Excitation energy versus spin for the SD bands of ^{133}Nd, ^{135}Nd and ^{137}Nd. The yrast lines, which for ^{133}Nd and ^{135}Nd are almost coincident, are also drawn.

$\approx$ 700 keV above the yrast lines where they suddenly disappear.

We have performed for the three nuclei ^{133}Nd, ^{135}Nd and ^{137}Nd TRS calculations based on a Woods-Saxon potential including monopole pairing correlations[7,15]. The shape of the nucleus is minimized with respect to the deformation parameters β_2, β_4 and γ for different rotational frequencies and quasi-particle configurations. The results are shown in Fig. 6 for the configuration (+,+1/2) at two relevant rotational frequencies for each nucleus. At the higher frequency a secondary minimum is present at $\beta_2 = 0.90$-0.96 which has been associated with the occupation by the odd neutron of the strongly down-sloping $i_{13/2}$ intruder orbital. This minimum persists also at higher frequencies continuing to be prolate in the ^{133}Nd and ^{135}Nd nuclei and becoming triaxial in the case of ^{137}Nd. The calculations shown in Fig. 6 clearly demonstrate that at the lower frequency the minimum in the potential energy surface moves from the high β_2 deformation to a lower deformation, which is associated with a configuration having the odd neutron placed in a N=4 Nilsson orbital. The frequency where the second minimum becomes energetically unfavoured is different for the three nuclei and is very close to the experimental value of half the energy of the lowest transition observed in the band. At those frequencies (see Fig. 6) almost no barrier exists between the two minima and therefore the configuration mixing between the SD and the ND states may be significant. The decay prefers

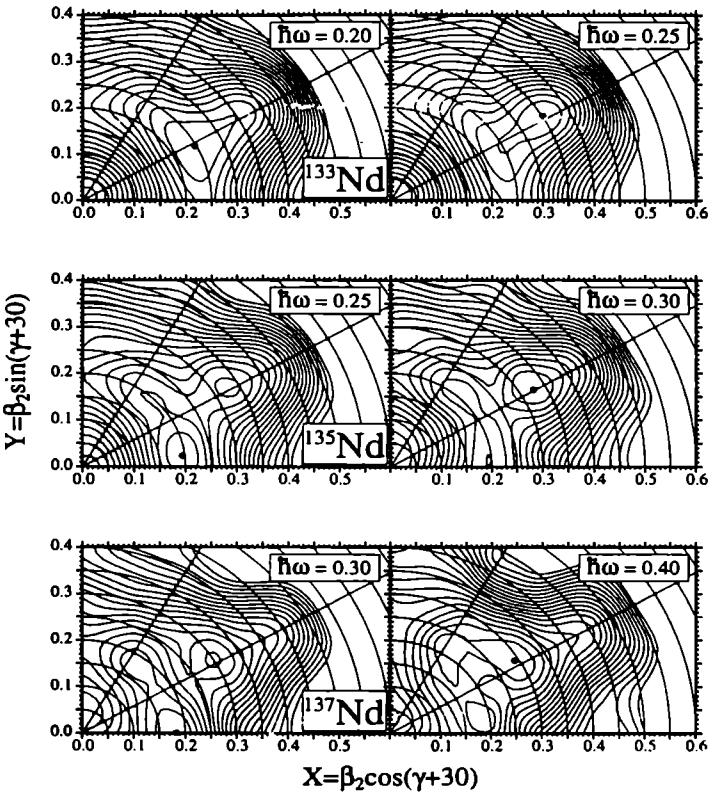

Fig. 6. Total routhian surface calculations for the lowest $(\pi,\alpha)=(+,+1/2)$ configuration in ^{133}Nd, ^{135}Nd and ^{137}Nd at two rotational frequencies. The prolate minimum at β_2=*0.30-0.36* is associated with the $i_{13/2}$ configuration. At the lower frequency a less deformed minimum (β_2=0.18-0.25) associated with the odd neutron in a N=4 configuration appears.

then to go to the yrast levels of the normal deformed, energetically favoured minimum instead of continuing along the SD band. This behaviour seems to be general and to occur in all three Nd nuclei discussed here, as well as in the odd-even Sm and Gd nuclei[16]. The case of ^{133}Nd is peculiar in that there is a strong, accidental mixing of the $17/2^+$ SD state with the $17/2^+$ state of the N=4 $[400]1/2^+$ band, which drives the major part of the decay-out flux towards the $[400]1/2^+$ band. This band is built on the minimum at deformation β_2= *0.25* shown in Fig. 6 (top left). The other decay branches from the lowest SD band members ($17/2^+$ and $21/2^+$) in ^{133}Nd have much lower intensities, being similar to those of the linking transitions in ^{135}Nd and ^{137}Nd.

It seems therefore that the decay-out process in the three Nd nuclei can be

described in the same way. The lowest observed spin of the SD bands in the three nuclei ($17/2^+$, $25/2^+$ and $29/2^+$ respectively) is related to the frequency at which the change of the nuclear shape occurs. The TRS calculations predict in each nucleus such a shape change to occurs, exactly at the frequency value which correspond to the lowest transition of the SD band.

4. Shell structure at superdeformed shapes: the nucleus ^{144}Gd

The discovery of multiple superdeformed bands within a single nucleus has allowed to study in detail the microscopic structure of the nucleus in the second minimum in terms of proton and neutron single particle excitations. It exists by now in the mass A=150 and A=190 regions a wealth of data on excited SD bands which are well described through the excitation of a single proton or neutron in the Nilsson orbitals available at such high (β_2=*0.5-0.6*) deformation. Some nuclei like ^{152}Dy and ^{192}Hg are considered doubly-magic at SD shapes since their proton and neutron numbers correspond to SD shell closures. In these nuclei it becomes more difficult to observe experimentally excited SD bands since a large excitation energy is required to overcome the gap. The intensity of excited SD bands, based on either proton or neutron single particle excitations, reflects indeed the size of the shell gaps at high rotational frequencies. In fact, the measured intensity of excited SD bands in ^{152}Dy and ^{192}Hg is much lower [17,18] than in the neigh-

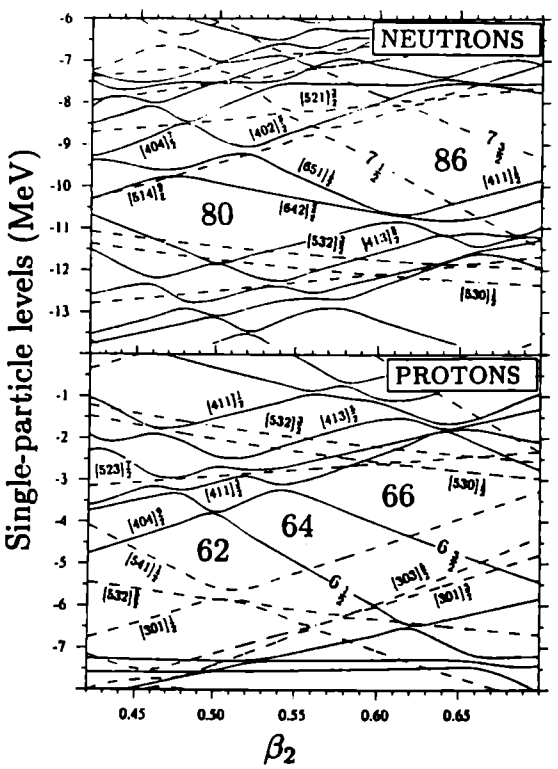

Fig. 7. Single-particle Woods-Saxon levels for neutrons and protons as a funcion of the deformation β_2 (from ref. 15).

boring nuclei with a proton or a neutron above or below the shell closure. This experimental fact has given further support to the idea of doubly-magic superdeformed nuclei. Only very recently a SD band has been identified [19] at GASP in the nucleus ^{144}Gd, which was predicted to be a doubly-magic SD nucleus corresponding to sizable gaps in the single particle energies at Z=64 and N=80 (see Fig. 7). The SD band shows a backbending at $\hbar\omega$=0.45 MeV, which is interpreted as a band crossing due to the alignment of a proton pair in the strong deformation driving $i_{13/2}$ orbital intruding from the higher N=6 oscillator shell.

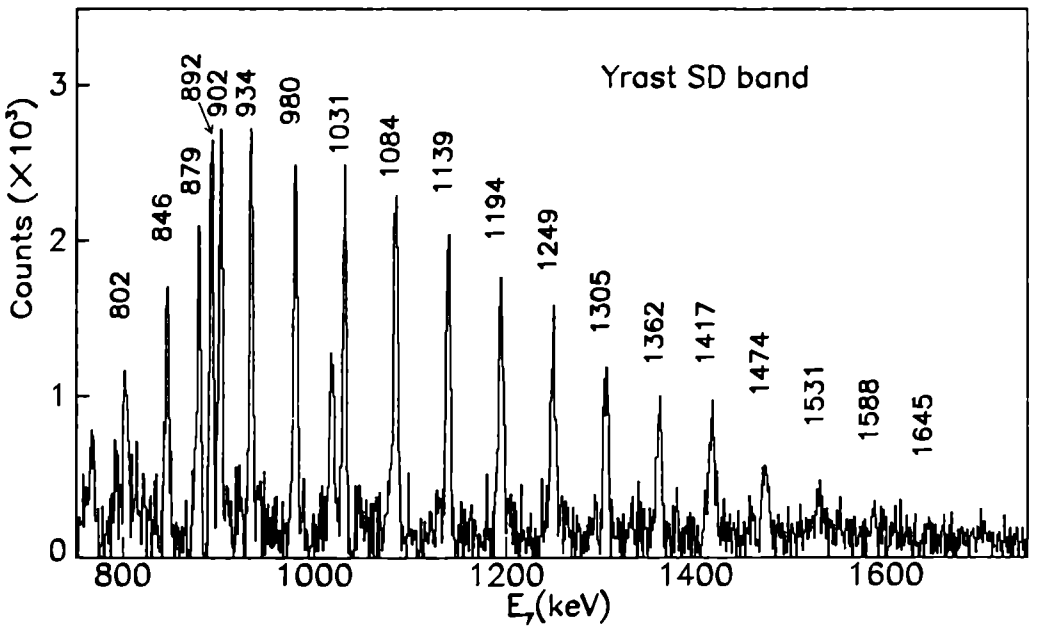

Fig. 8. The yrast SD band in ^{144}Gd as obtained from a sum of doubly-gated coincidence spectra. The backbending due to the alignment of two $i_{13/2}$ neutrons is clearly visible at $E_\gamma \approx$ 900 keV.

A spectrum of the yrast SD band of ^{144}Gd is shown in Fig. 8, where the backbending at $E_\gamma \approx$ 900 keV is clearly visible. New experiments have been performed in order to learn more about the shell structure in this rather poorly explored region of superdeformation around ^{144}Gd. By means of the reactions ^{100}Mo + ^{48}Ti at a beam energy of 215 we have populated the high-spin states of the ^{144}Gd nucleus. Four new SD bands have been found in ^{144}Gd: their dynamic moment of inertia is plotted in Fig. 9 together with that of the yrast band. The intensity of the yrast

SD band is $\approx$ 1.2% of the total population of the ^{144}Gd nucleus, whereas the four excited bands have intensities ranging from 0.2 to 0.3%. The extracted dynamical moments of inertia of the excited SD bands are constant over the full observed frequency range and are slightly lower than that of the yrast SD band, for which a 6^2 proton configuration has been assigned. Furthermore, the transition energies of bands 1 and 2 as well as those of bands 3 and 4 satisfy the characteristic relation for signature partner bands, i.e. the transitions of one band are arithmetic averages of the near-lying transitions of the other band (see Fig. 10). We suggest therefore $6^1 \otimes [404]9/2^+$ (α=$\pm$1/2) and $6^1 \otimes [411]3/2^+$ (α=$\pm$1/2) configurations respectively for the first and second couple of SD excited bands in ^{144}Gd. Those are in fact the lowest excited proton configurations for a Z=64 nucleus at high deformation (β_2=*0.5*). The first excited SD band in ^{144}Gd has transition energies very close to those of an excited SD band recently identified[20] by the Mc Master-Chalk River group in the odd-odd nucleus ^{144}Eu. This nucleus is populated in our reaction but we do not observe any of its SD bands; we are therefore facing a case of identical bands in two nuclei with the same mass number. The interpretation given to the two bands in terms of single particle excitations involve very different configurations which do not favour the identity of the transitions energies. This case of "identical bands" is therefore not yet understood and deserves further theoretical investigations. The observed excited SD bands are all explained through proton excitations across the

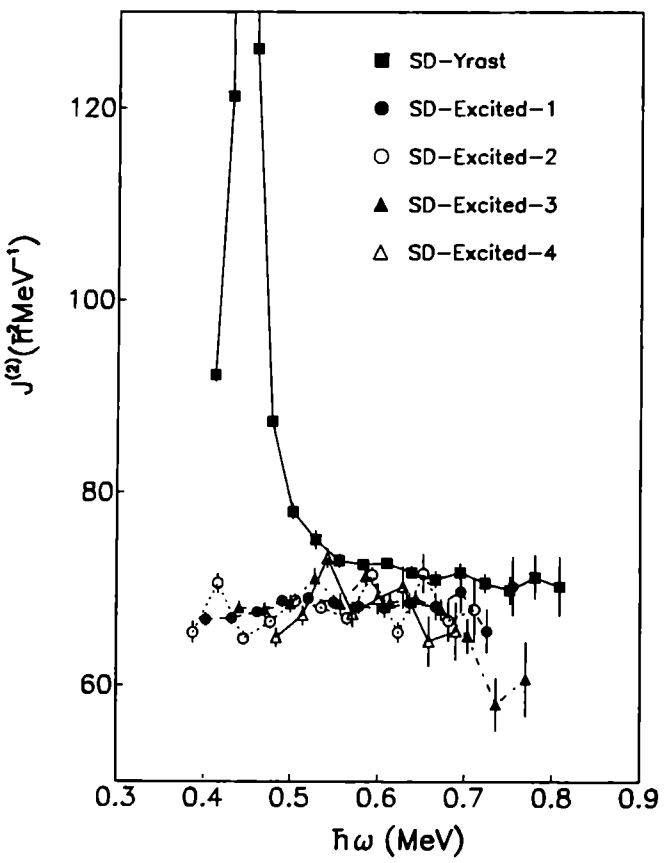

Fig. 9. Dynamic moments of inertia for the five SD bands identified in ^{144}Gd.

Z=64 gap whereas no excited SD bands have been identified in ^{144}Gd which would correspond to neutron excitations across the N=80 gap. In this second case the dynamic moment of inertia would be much different since an N=7 neutron would be involved in the SD band configuration. The fact that excited neutron bands are not observed in ^{144}Gd points to the higher stability of the N=80 shell closure with respect to the Z=64 closure at SD shapes. The absolute intensity of the excited SD bands due to proton excitations, if compared with that of the analogous bands in ^{152}Dy and ^{192}Hg, tell us that the superdeformed Z=64 gap is less pronounced than the well known Z=66 and Z=80 gaps, a fact which is somehow not predicted by the deformed shell model results of Fig. 7.

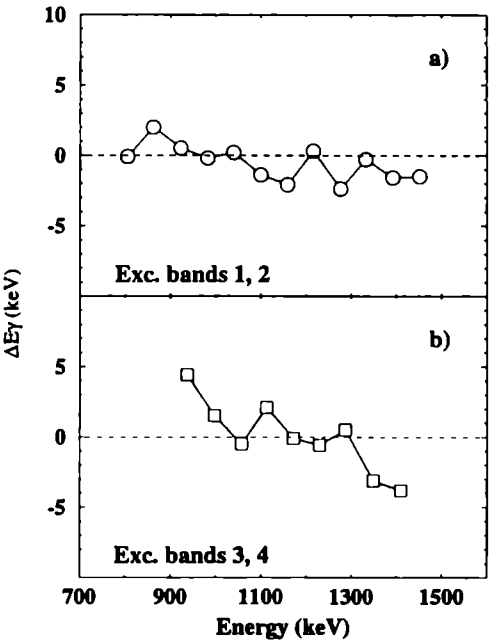

Fig. 10. Energy difference between the transition energies of excited band 2 and the half-points energies of excited band 1 (top). The same is plotted for band 4 and 3 at the bottom.

5. Deep-inelastic reactions as a tool for spectroscopic studies of nuclei far from stability.

With the new γ-detector arrays one generally emphasizes the improved prospects for studying, at high spin and/or far from stability, nuclei produced in compound nucleus reactions. Studies of nuclei produced in non-fusion channels are comparatively neglected. In particular the undeveloped field of spectroscopy of neutron rich nuclei, which are major products of deep-inelastic heavy-ion collisions, remains open for exploration. Since the production method unavoidably delivers many products nuclei with similar yields, such an exploration is a formidable task which takes full advantage of the sensitivity and selectivity of detector systems like GASP.

Only when radioactive beams will be available one can presumably enlarge the

region of nuclei which can be produced in compound nucleus reactions. In the present days, the only possibility to reach some particularly interesting neutron-rich nuclei lying far from stability is to use deep inelastic reactions at energies slightly above the Coulomb barrier. This method has been used at GASP for the spectroscopic study[21] of the neutron rich nucleus ^{68}Ni. In spherical nuclei the $1g_{9/2}$ orbital is well separated in energy from all other single-particle levels. This gives rise to the well established magicity of the neutron and proton numbers N, Z = 50 and points towards a somewhat less pronounced closure at N,Z=40. The Z=40 subshell closure is clearly demonstrated by the well known level structure of the ^{90}Zr nucleus[22], for which the lowest excitation is the 1.76 MeV 0^+ state, the first 2^+ state appears at 2.19 MeV and the lowest lying particle-hole $(p^{-1}_{1/2}g_{9/2})$ excitation produces the long-lived 5^- isomer. The study of similar features in magic nuclei

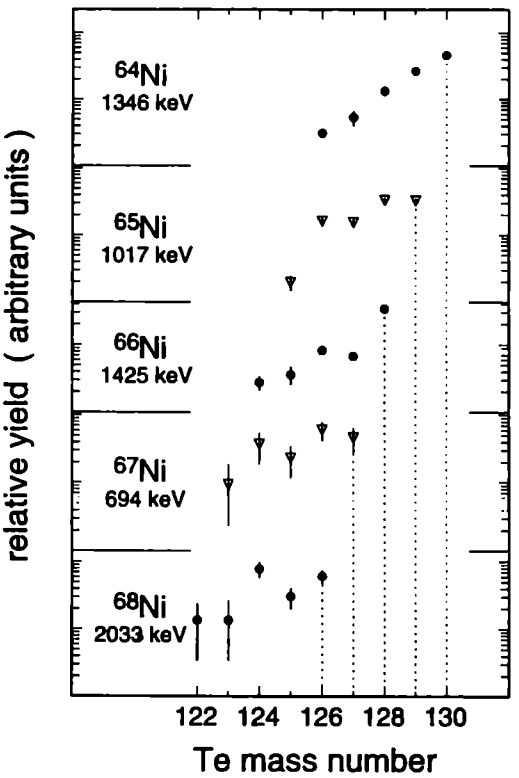

Fig. 11. Distribution of Te isotopes established from γ cross coincidences with indicated lines from ^{64}Ni to ^{68}Ni.

with N=40 is more complicated as it involves nuclei very far from the stability line. The extremely neutron deficient N=Z=40 ^{80}Zr nucleus has been found to be strongly deformed[23] with no trace of shell closure signature. The only other candidate with N=40 and closed proton shell is the ^{68}Ni nucleus which has been populated at GASP using a 275 MeV ^{64}Ni beam on a thin ^{130}Te target which was placed on a thick ^{208}Pb backing. The γ–γ coincidences were stored without any restriction on the multiplicity and the beam was pulsed with 200 ns repetition time in order to separate the prompt and delayed events. In the search for high spin states we were guided by the simple shell model expectation that the ^{68}Ni level spectrum, like that of ^{90}Zr, should feature a long-lived 5^- isomer as well as a significant increase of the 2^+ excitation energy as

compared to the lighter Ni isotopes. The γ–γ data revealed a cascade of two coincident transitions of 814 keV and 2033 keV energy, which fit well to the expectations of a $5^- \rightarrow 2^+ \rightarrow 0^+$ cascade. Both transitions follow the decay of a long–lived isomer and have an intensity consistent with the expected production yields of the ^{68}Ni isotope. Their isotopic identification comes from the γ–γ cross–coincidence analysis whose results are presented in Fig. 11. The coincidence spectra obtained setting gates on known strong transition of a specific Ni product, not only show other γ–rays of that Ni nucleus but also contain known γ–rays belonging to various tellurium partners occurring simultaneously in the exit channel. The yields of these Te products are estimated from the γ–ray intensities and it is clear from the obtained distributions that processes involving the evaporation of up to four neutrons contribute substantially to the production of each Ni isotope.

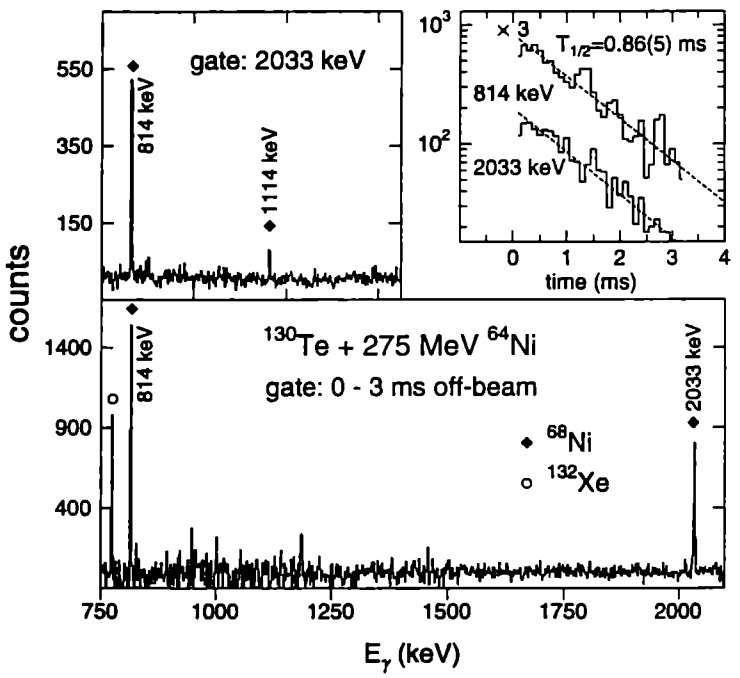

Fig. 12. A part of the off–beam single gamma spectrum, taken in the time range enhancing the ^{68}Ni isomer decay, is shown at the bottom. The prompt coincidence spectrum with the 2033 keV gate (upper-left) shows the 1114 keV line, which establishes the 3147 keV level. The time decay of the two gamma transitions from the 5^- isomer is shown in the upper-right part.

The long–lived isomer complicates somehow the identification of the cross–coincidences of the 2033 keV transition; the extracted intensity pattern, which is shown in the

lower part of the figure, is however good enough to assign it to the ^{68}Ni nucleus which is apparently formed by a transfer of at least four neutrons to the ^{64}Ni projectile and by the subsequent evaporation of zero to four neutrons from the primary Te products.

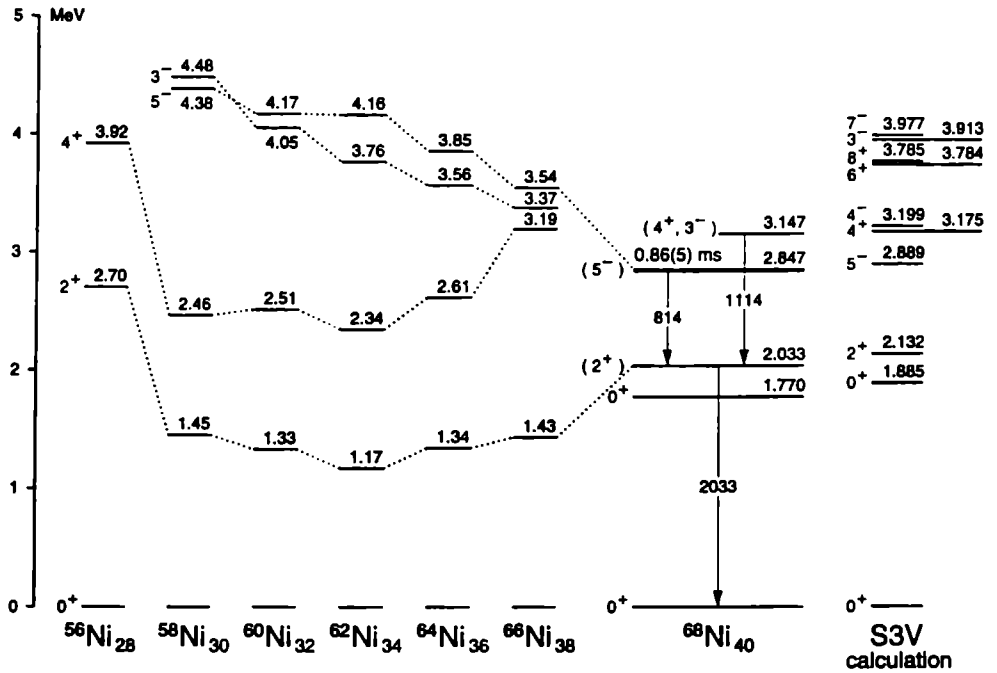

Fig. 13. Systematics of selected states in even Ni isotopes. The ^{68}Ni results are prominently displayed and compared with the shell model calculations of Ref. 24.

The half–life of the isomer was determined in an experiment using a beam pulsing in the range from micro– to milliseconds where, along with the γ–γ coincidence data, also single counts seen by the detectors in the off–beam periods were stored as a function of time. An off–beam spectrum enhancing the isomeric decay is displayed in the lower part of Fig. 12. The 814 keV and 2033 keV lines appear with a similar intensity, and both show the same decay curve as displayed in the upper part of the figure. The extracted lifetime of $T_{1/2}$ = 0.86(5) ms gives a 46 times retarded 814 keV E3 transition and practically excludes other multipolarity assignments. Therefore we conclude that the present results establish the expected 5^- isomer in ^{68}Ni. The high energy section of the prompt coincidence spectrum taken with a gate at 2033 keV contains, as shown in the upper part of the same figure, a weak 1114 keV line. This transition establishes a state lying 300 keV above the isomer

which, from systematics, is assigned tentatively as a 4^+. In Fig. 13 the systematics of the lowest excited states in even nickel isotopes is displayed. For the ^{68}Ni isotope the present results are compared with the shell model calculations shown to the right[24] . The observed increase of the ^{68}Ni 2^+ state energy, by more than 600 keV compared to the ^{66}Ni isotope, indicates a significant subshell closure at neutron number $N = 40$. The 5^- excitation, attributed predominantly to the $p_{1/2}^{-1} g_{9/2}$ configuration, moves down in energy when the subsequent neutron pairs shift the Fermi level towards the $g_{9/2}$ orbital. As expected it reaches the minimum energy at $N = 40$ and becomes isomeric, which is very well reproduced by the calculations. From the measured half-life of the 5^- isomer we get for the 814 keV transition B(E3)=0.022 W.u.; the equivalent E3 transition in ^{90}Zr is 10 times faster and this difference is not reproduced by the calculations.

Further analysis of this data is in progress and experiments are now directed towards a search for higher lying states in ^{68}Ni in the attempt to locate the 8^+ $g_{9/2}^2$ excitation. The perspectives to extend the search to the ^{70}Ni isotope, which would give us the complete set of the $g_{9/2}$ matrix elements, look also promising. With this goal experiments are in progress at Legnaro using heavier beams (e.g. ^{76}Ge, ^{81}Br) provided by the new superconducting Linac.

6. Conclusions.

Some of the results obtained at GASP in its first three years of operation have been presented. The detector is presently taking data for ≈60% of the beam time available at the XTU Tandem of Legnaro. In order to improve its observational limits experiments requiring the coincidence with ancillary devices, like ISIS and CAMEL are becoming more frequent. The physics problems we are attaching now are in any case at the limits of its detection capabilities. Only much more efficient new arrays will give soon qualitatively better data. The next generation detector is EUROBALL III, a common project of the european γ-ray spectroscopy community, which should start operation at Legnaro at the beginning of 1997. With its ≈ 10% photopeak efficiency and with the improved granularity provided by its composite detectors, EUROBALL should bring a solution to some open problems in the field of superdeformation and open new opportunities like the spectroscopy of the third (hyperdeformed) minimum.

7. Acknowledgements.

The results presented here have been obtained thanks to the hard work of all the members of the GASP collaboration and especially of D. Bazzacco and C. Rossi Alvarez. I would like to thank in particular, for the contribution to some parts of my talk, C. Petrache, R. Venturelli and L. H. Zhu. The data on ^{68}Ni come from experiments performed in collaboration with the Cracow group leaded by R. Broda.

References

1. D. Bazzacco, Workshop on large gamma-ray detector arrays, Chalk River 1992, Proceedings Vol. 2, AECL 10613, p. 376.
2. P. Twin et al., *Phys. Rev. Lett.* **57** (1986) 811.
3. R. G. Henry et al., *Phys. Rev. Lett.* **73** (1994) 777.
4. C. M. Petrache et al., *Nucl. Phys.* **A579** (1994) 285.
5. D. Curien et al., *Phys. Rev. Lett.* **71** (1993) 2559.
6. D. Bazzacco et al., *Phys. Rev.* **C49** (1994) R2281.
7. R. Wyss et al., *Phys. Lett.* **B215** (1988) 211.
8. D. Bazzacco et al., *Phys. Lett.* **B309** (1993) 235.
9. R. Bengtsson and S. Frauendorf, *Nucl. Phys.* **A314** (1979) 27.
10. R. Wadsworth et al., *J. Phys.* **G13** (1987) L207.
11. S. Mullins et al., *Phys. Rev.* **C45** (1992) 2683.
12. J. Gizon et al., *Nucl. Phys.* **A222** (1974) 557.
13. S. Lunardi et al., *Phys. Rev.* **C52** (1995) R6; C. M. Petrache et al. to be published.
14. M. A. Deleplanque et al., to be published.
15. W. Nazarewicz, R. Wyss and A. Johnson *Nucl. Phys.* **A503** (1989) 285.
16. C. Rossi Alvarez et al., *Acta Phys. Pol.* **B26** (1995) 237.
17. P. J. Dagnall et al., *Phys. Lett.* **B335** (1994) 313.
18. P. Fallon et al., *Phys. Rev.* **C51** (1995) R1609.
19. S. Lunardi et al., *Phys. Rev. Lett.* **72** (1994) 1427.
20. S. Mullins et al., Conference on Physics from large γ-ray detector arrays, Berkeley 1994, Proceedings Vol. 2, p. 24 and private communication.
21. R. Broda et al., *Phys. Rev. Lett.* **74** (1995) 868.
22. L. P. Ekstrom and J. Lyttkens-Linden,, *Nucl. Data Sheets* **67** (1992) 579.
23. C. J. Lister et al., *Phys. Rev. Lett.* **59** (1987) 1270.
24. J. Sinatkas et al., *J. Phys.* **G18** (1992) 1377, 1401.

DESCRIPTION OF NUCLEAR COLLECTIVE MOTION BY WIGNER FUNCTION MOMENTS

E. B. Balbutsev
JINR, Dubna, Russia

Abstract

The method is presented in which the collective motion is described by the dynamic equations for the nuclear integral characteristics. The "macroscopic" dynamics is formulated starting from the equations of the microscopic theory. This is done by taking the phase space moments of the Wigner function equation. The theory is applied to the description of collective excitations with multipolarities up to $\lambda = 5$.

1 Introduction

Integral characteristics such as the electromagnetic moments are very important elements of nuclear theory. Being the physical observables not only in formal sense of quantum mechanics but also the observables which determine the magnitude of the cross sections of various nuclear reactions and the probability of processes important for nuclear structure studies, such nuclear characteristics are widely used as building blocks for nuclear collective models. Most of these models are formulated phenomenologically to describe a certain type of nuclear excitation and operate using parameters that are loosely related to the nucleon-nucleon interaction and the global properties of nuclear matter [1].

A powerful method for studying the dynamics of nuclear integral characteristics may be constructed on the basis of the time-dependent Hartree-Fock theory. As is well known, this theory is applied with great success to describe nuclear vibrational excited states. In a way, the solutions of the time-dependent Hartree-Fock equations determine the dynamics of all the nuclear collective variables. However, the time evolution of small number of nuclear integral characteristics may be determined in a much simpler way without really solving the Hartree-Fock equations, provided these equations are transformed in a suitable way.

2 Formulation of the method

The basis of our method of describing collective nuclear dynamics is the equation for the one-body density matrix $\rho(\mathbf{r}_1, \mathbf{r}_2, t) = \hat{\rho}$:

$$i\hbar \frac{\partial \hat{\rho}}{\partial t} = \left[\hat{H}, \hat{\rho}\right] \tag{1}$$

where $\hat{H}$ is the one-body Hamiltonian depending implicitly on the density matrix. Equation (1) with a precise definition of the one-body Hamiltonian appears in the Hartree-Fock theory; it is currently used also within the so called energy-functional approach leaving more possibilities for the choice of the one-body Hamiltonian and in addition giving some grounds to believe equation (1) to be rather general [2].

It is convenient to reformulate equation (1) by introducing the Wigner transformations of the density matrix [3]

$$f(\mathbf{r}, \mathbf{p}, t) = \frac{1}{(2\pi\hbar)^3} \int \exp(-i\mathbf{p} \cdot \mathbf{s}/\hbar) \rho(\mathbf{r} + \frac{\mathbf{s}}{2}, \mathbf{r} - \frac{\mathbf{s}}{2}, t)\, d\mathbf{s}. \tag{2}$$

and of the Hamiltonian

$$H^W(\mathbf{r}, \mathbf{p}) = \int \exp(-i\mathbf{p} \cdot \mathbf{s}/\hbar) (\mathbf{r} + \frac{\mathbf{s}}{2} \left| \hat{H} \right| \mathbf{r} - \frac{\mathbf{s}}{2})\, d\mathbf{s}. \tag{3}$$

Using (2,3) one arrives at [4]

$$\frac{\partial f}{\partial t} = \frac{2}{\hbar} \sin\left(\frac{\hbar}{2} (\nabla^H_{\mathbf{r}} \cdot \nabla^f_{\mathbf{p}} - \nabla^H_{\mathbf{p}} \cdot \nabla^f_{\mathbf{r}}) \right) H^W \cdot f. \tag{4}$$

The approximation in which only the first term of the series expansion of the sine is retained is known as the semiclassical approximation of Hartree-Fock theory – the corresponding equation is known as the Vlasov equation for a distribution function [5].

If the Hamiltonian is a sum of a kinetic energy and a local potential $V(\mathbf{r})$, its Wigner transformation is just a classical version of the same Hamiltonian:

$$H^W = p^2/2m + V(\mathbf{r}).$$

The generalization for nonlocal potentials is straightforward and can be found in [6].

To make a step towards the description of the dynamic of nuclear collective characteristics we introduce the moments of the Wigner function $f(\mathbf{r}, \mathbf{p}, t)$ as follows:

$$\begin{aligned}
n(\mathbf{r}, t) &= \int f(\mathbf{r}, \mathbf{p}, t)\, d\mathbf{p} \\
\mathbf{u}(\mathbf{r}, t) &= \int \mathbf{p} f(\mathbf{r}, \mathbf{p}, t)\, d\mathbf{p} \,/\, n(\mathbf{r}, t) m \\
\mathcal{A}_{ij}(\mathbf{r}, t) &= \int p_i p_j f(\mathbf{r}, \mathbf{p}, t)\, d\mathbf{p} \\
\mathcal{A}_{i_1 \ldots i_n}(\mathbf{r}, t) &= \int p_{i_1} p_{i_2} \ldots p_{i_n} f(\mathbf{r}, \mathbf{p}, t)\, d\mathbf{p}.
\end{aligned} \tag{5}$$

The physical meaning of the first three moments is quite clear: n is the density of nucleons, $\mathbf{u}$ is the collective velocity field and $\mathcal{A}_{ij}/2m$ is the component of the kinetic energy (or pressure) tensor.

Now it would be rather natural to integrate equation (4) over the momenta with the weights $1, p_i, p_i p_j$ etc. and to get as a result [5] dynamical equations for $n(\mathbf{r},t)$ (a continuity equation), for $\mathbf{u}(\mathbf{r},t)$ (Euler equation),for $\mathcal{A}_{ij}(\mathbf{r},t)$ and so on. Being very fruitful in the classical hydrodynamics this way leads to the deadlock in the case of nuclear dynamics. The infinite system of coupled equations arises in such a way and one doesn't see any small parameter which allows to decouple them in a mathematically (physically) correct way.

Thus, the problem of truncation of this system arises. It has already been discussed in the literature [7]. The method that we take here to close the system of equations was suggested in [8] and is described in detail in reference [9]. Its idea is based on the virial theorems of Chandrasekhar and Lebovitz [10]. It is shown in [9], that integrating equation (4) over the phase space $\{\mathbf{p},\mathbf{r}\}$ with the weights $x_{i_1} x_{i_2} \cdots x_{i_k} p_{i_{k+1}} \cdots p_{i_{n-1}} p_{i_n}$, where k runs from 0 to n, one can obtain a closed finite subsystem of dynamical equations for multipole moments and other integral characteristics of a nucleus. Taking different values of n $(0,1,2,3$ and so on) one gets subsystems for different multipoles. Let us consider several most simple cases.

$n = 0$. The integration of the equation (4) with unit weight gives one equation for zero rank tensor which is an obvious constant of motion:

$$\frac{d}{dt}\int f(\mathbf{r},\mathbf{p},t)d\mathbf{p}d\mathbf{r} = \frac{d}{dt}\int n(\mathbf{r},t)d\mathbf{r} = \frac{d}{dt}A(t) = 0, \tag{6}$$

i.e. the number of nucleons A is conserved.

$n = 1$. Integrating (4) with the weights x_i and p_i one gets the system of equations for two first rank tensors:

$$\frac{d}{dt}J_i(t) - M_i(t) = 0, \tag{7}$$

$$\frac{d}{dt}M_i(t) - \int n(\mathbf{r},t)\frac{dV(\mathbf{r})}{dx_i}d\mathbf{r} = 0, \tag{8}$$

where $M_i(t) = m\int n(\mathbf{r},t)u_i(\mathbf{r},t)d\mathbf{r}$ is a nucleus momentum, $J_i(t) = m\int n(\mathbf{r},t)x_i d\mathbf{r}$ is a center of mass coordinate. In the absence of external fields the integral in (8) is the sum of all internal forces acting in the nucleus, and it must vanish. In this case, equation (8) expresses the law of conservation of the momentum $\mathbf{M}$ of the nucleus, and equation (7) gives trivial information about the uniform and rectilinear motion of the nucleus as a whole.

$n = 2$. The integration of (4) with the weights $x_i x_j, x_i p_j, p_i p_j$ yields:

$$m\frac{d}{dt}J_{ij}(t) - M_{i,j}(t) - M_{j,i}(t) = 0, \tag{9}$$

$$\frac{d}{dt}M_{i,j}(t) + \int x_i n(\mathbf{r},t)\frac{\partial V}{\partial x_j}d\mathbf{r} - \frac{1}{m}\Pi_{ij}(t) = 0, \tag{10}$$

$$\frac{d}{dt}\Pi_{ij}(t) + m\int n(\mathbf{r},t)\left[u_i(\mathbf{r},t)\frac{\partial V}{\partial x_j} + u_j(\mathbf{r},t)\frac{\partial V}{\partial x_i}\right]d\mathbf{r} = 0. \tag{11}$$

Here we have introduced the notations: $J_{ij}(t) = \int x_i x_j n(\mathbf{r},t)d\mathbf{r}$ for an inertia tensor, $M_{i,j}(t) = m\int x_i u_j(\mathbf{r},t)n(\mathbf{r},t)d\mathbf{r}$ for a moment of a nucleus momentum and $\Pi_{ij}(t) = \int \mathcal{A}_{ij}(\mathbf{r},t)d\mathbf{r}$ for an integral kinetic energy tensor. So, one want to say, that we have derived the system of three dynamical equations for three collective variables $J_{ij}(t), M_{i,j}(t)$ and $\Pi_{ij}(t)$. To make this statement true one must represent the integrals containing derivatives of the potential $V(\mathbf{r})$ in terms of these three variables.In the case of an arbitrary potential this problem (we will call it the representation problem) can not be solved without approximations, although it is possible to find several exact solutions for comparatively simple potentials. For example, in the case of a harmonic oscillator with quadrupole-quadrupole residual interaction $V(\mathbf{r},t) = \frac{1}{2}m\omega^2 r^2 + \lambda\, q(t)Q(\mathbf{r})$, where $Q(\mathbf{r}) = x_1^2 + x_2^2 - 2x_3^2$, $q(t) = \mathrm{tr}\, Q\rho = \int d\mathbf{r}\, d\mathbf{p}\, Q(\mathbf{r})f(\mathbf{r},\mathbf{p},t) = J_{11}(t) + J_{22}(t) - 2J_{33}(t)$, the system (9)-(11) acquires the following form [11]:

$$\begin{aligned}
&m^2\ddot{Q}_{00} + 2m^2\omega^2 Q_{00} + 4m\lambda Q_{20}^2 - 2\Pi_{00} = 0,\\
&m^2\ddot{Q}_{20} + 2m^2\omega^2 Q_{20} + 4m\lambda Q_{20}(2Q_{00} - Q_{20}) - 2\Pi_{20} = 0,\\
&\dot{\Pi}_{00} + m^2\omega^2\dot{Q}_{00} + 2m\lambda Q_{20}\dot{Q}_{20} = 0,\\
&\dot{\Pi}_{20} + m^2\omega^2\dot{Q}_{20} + 2m\lambda Q_{20}(2\dot{Q}_{00} - \dot{Q}_{20}) = 0.
\end{aligned} \tag{12}$$

We have introduced here the component of the quadrupole moment $Q_{20} = J_{11} + J_{22} - 2J_{33}$, the mean square radius $Q_{00} = J_{11} + J_{22} + J_{33}$ and the irreducible tensors $\Pi_{20} = \Pi_{11} + \Pi_{22} - 2\Pi_{33}$ and $\Pi_{00} = \sum_{s=1}^{3}\Pi_{ss}$. It is known [12] that the cartesian tensor of second rank may be represented by a sum of irreducible tensors - one zero rank tensor (monopole moment), one first rank pseudotensor (angular momentum) and one second-rank tensor (quadrupole moment):

$$T_{ij} \Rightarrow \mathcal{T}_{00} + \mathcal{T}_{1\mu} + \mathcal{T}_{2\mu}.$$

So it is natural that we have got the coupled dynamical equations for quadrupole and monopole multipole moments. The angular moment of a nucleus doesn't enter this equations because it is an integral of motion. The system (12) was solved numerically [11]. The Fourier analysis of its solutions shows that this simple model reproduces very well the experimental values of the energies of giant monopole and giant quadrupole resonances (GMR and GQR). More of it, there appear the multiphonon states builded out of these two resonances. The amplitudes of vibrations may be rather large - the maximal possible amplitude corresponds to the deformation parameter $\beta = 0.29$.

In the general case of an arbitrary potential the representation problem may be solved using very popular in nuclear physics small amplitude approximation. Introducing the small deviations of the collective variables from their equilibrium values

$\delta J_{ij}(t), \delta M_{i,j}(t)$ and $\delta \Pi_{ij}(t)$ one may linearise the equations (9)-(11) in delta's. Taking after it more or less evident assumptions on the character of collective motion one arrives finally to the system of linear algebraical equations, their coefficients being the simple combinations of integrals over the nuclear volume of different powers of $n^{(0)}(\mathbf{r})$, $\mathcal{A}_{ii}^{(0)}(\mathbf{r})$ and their derivatives (equilibrium or ground state values are marked by an upper index (0)). Precisely this procedure was developed in [8] when describing the quadrupole modes of nuclear excitations in rotating nuclei.

The above procedure may be used to obtain dynamical equations for the tensors $J_{i_1 \ldots i_n}$ with any number of indices. Proceeding in this way, one introduces into the equations the integrals

$$\Pi_{i_1 \ldots i_k}^{i_{k+1} \ldots i_n} = \int \mathcal{A}_{i_1 \ldots i_k} x_{i_{k+1}} \ldots x_{i_n} \mathrm{d}\mathbf{r}. \tag{13}$$

Such integrals with all values of k in the interval $2 \leq k \leq n$ play the role of some new collective variables. It turns out that one can formulate the next rule: for the consistent treatment of the tensor $J_{i_1 \ldots i_n}$ it is necessary to consider also tensors (13) up to $\Pi_{i_1 \ldots i_n}$. This observation may be formulated more physically but less precisely using the language of the paper [13]: to describe an evolution of the density moment of multipolarity λ, one must take into account the Fermi surface deformations (FSD) with all multipolarities up to λ.

3 Applications, results of calculations

The method was applied to the description of a variety of nuclear properties. The dynamical equations for cartesian tensors of the ranks $n = 1, 2, 3, 4, 5$ were derived using different forces.

3.1 Calculations with surface tension

First calculations [8], [14], [15] were done in the approximation of a sharp edge of a nucleus with a surface tension and a homogeneous density, treating the nuclear matter as incompressible. This enable one to obtain practically all the results analytically; moreover such an approximation is entirely adequate for many physical problems. The equations for second rank tensors were used to describe the shape of rotating nuclei and their vibrational spectrum. The dependence of GQR on the rotation velocity was studied, the low-lying rotational-vibrational modes and bifurcation points were predicted. The widths of these modes and GQR were studied taking into account the collision integral in the τ-approximation [16]. The classical Hamiltonian corresponding to the dynamical equations (9)-(11) was constructed and quantized. The procedure was developed to calculate excitation probabilities of vibrational modes with the help of linear response theory.

The negative parity excitations were considered on the basis of the equations for third rank tensors. The giant octupole resonance (GOR) and the low energy octupole resonance (LEOR) are described rather well. Results on the magnetic quadrupole excitation (2^-) are in qualitative agreement with experimental data. Rather exotic 1^- state of a toroidal type (this type of motion was discussed in [17]) was predicted in the energy region $E \simeq 65.6A^{-1/3}$ (see below).

The equations for fourth rank tensors together with the ones for second rank tensors were used to study the positive-parity collective modes with the multipolarities up to $\lambda = 4$. The theory gives four 2^+ states at the energies $E^{(1)}_{2^+} = 23.7A^{-1/3}MeV$, $E^{(2)}_{2^+} = 65.9A^{-1/3}MeV$, $E^{(3)}_{2^+} = 87.3A^{-1/3}MeV$ and $E^{(4)}_{2^+} = 174.7A^{-1/3}MeV$. The $E^{(2)}_{2^+}$ level is just the GQR exhausting about 79% of the energy weighted sum rule (EWSR). Let us note that the calculations with the aid of a system of equations only for 2nd rank tensors gave for this level $64.7A^{-1/3}MeV$. It is obvious that the extension of the calculation scheme to 4th rank tensors had practically no effect on the GQR energy, indicating that the method is stable.

One may think that the lowest 2^+ excitation mode in our theory describes the centroid off all the 2^+ exited states lying below the GQR. It exhausts about 20% of the EWSR that coincide with the experimental value for ^{208}Pb and don't contradict to the ones for other nuclei. For the present, let us note that of fundamental importance for our method is the very fact of appearance of a low-lying 2^+ state, which is obtained in microscopic calculations [18] and is not reproduced by the nuclear fluid dynamic [19]. Two high lying 2^+ states contribute only 1% to the EWSR. Their nature can apparently be attributed to the dynamics of the toroidal quadrupole moment [17]. This assumption is supported by a simplified RPA calculation [20], which predicts a 2^+ level of an addy nature at the energy $\sim 93A^{-1/3}$ Mev.

The theory gives two 4^+ states: $E^{(1)}_{4^+} = 70A^{-1/3}MeV$ and $E^{(2)}_{4^+} = 212A^{-1/3}MeV$ They yield about 50% to the EWSR each and together exhaust it completely. The lower 4^+ excitation explains well the experimental results on the $\lambda = 4$ giant resonance in heavy nuclei (the calculations must be corrected for the diffuseness of the nuclear surface in order to be applied quantitatively to light nuclei). The second 4^+ excitation lies essentially higher in energy than $4\hbar\omega_{osc}$ as predicted by most of the RPA calculations and agrees with the experimental results from [21] .

The magnetic octupole resonance is predicted at the energy $E_{3^+} = 116A^{-1/3}MeV$. The position of 1^+ state of the complicate nature, discussed in [22] (relative vibrations of an outside layer of a nucleus and its internal part), is predicted at $E_{1^+} = 132.6A^{-1/3}MeV$.

The dynamical equations for fifth rank tensors were used to study the collective states 5^- and 4^-. The theory predicts two isoscalar 5^- states at the energies $E^{(1)}_{5^-} = 137A^{-1/3}MeV$, $E^{(2)}_{5^-} = 293A^{-1/3}MeV$ and two 4^- states at the energies $E^{(1)}_{4^-} = 60A^{-1/3}MeV$, $E^{(2)}_{4^-} = 185A^{-1/3}MeV$. Both 5^- states contribute about 50% to the EWSR each and exhaust it completely. The position of the low-lying 5^- state is in accordance with the experiment [23].

We stress here the large importance of FSD of all the multipolarities up to $\lambda = 5$ for the correct description of nuclear dynamics. The neglect of FSD with $\lambda > 2$ leads not only to appreciable numerical errors in the calculation of the excitation energies, but also (and more importantly) simply to the loss of certain modes (low-lying 2^+ in particular).

3.2 Calculations with Skyrme forces

Later the dynamical equations for 2nd rank tensors and for 1st+3rd rank tensors were derived and solved with Skyrme forces SKM*. Due to the nonlocality of the interaction equations become more complicate. Moreover, the number of equations is doubled, because in this case it is necessary to solve the coupled systems of equations for protons and neutrons.

The 2nd rank tensors allow us to describe monopole and quadrupole modes, the isovector modes as well as isoscalar ones. The results of calculations [6] are in good agreement with experimental data. The strong mixing of the monopole excitation and the quadrupole K=0 branch is found. Experimentally it manifests itself as the "splitting" of the GMR in deformed nuclei [21].

As was mentioned before, the angular moment of nucleus (proton+neutron) is conserved. However, the relative motion of the proton and neutron angular moments generates the low-lying 1^+ mode, known as the "scissor mode" or, maybe more precisely, the "giant angle dipole mode", because of its coupling with quadrupole vibrations. The calculated excitation energies and B(M1) factors are in qualitative agreement with experimental values in a number of rare-earth nuclei.

The calculations with third rank tensors give very good description of isoscalar and isovector GOR. The qualitative agreement with experimental data is obtained for isoscalar LEOR. The isovector LEOR is predicted [24].

Very interesting results are obtained for 1^- collective states. The solution of the system of equations for 1st+3rd rank tensors gives seven 1^- levels (fig.1). The analysis of their excitation probabilities and EWSR shows [25],[26], that: 1) two of them (4 and 5) can be regarded as the splitted giant dipole resonance (GDR); their centroid (dashed line) practically coincides with the experimental value, the energy interval between them being in agreement with the measured width, 2) the two highest resonances (6 and 7) correspond to isoscalar and isovector compressional modes, the isoscalar one being in qualitative agreement with the experiment, 3) the two lowest levels (1 and 2) can be interpreted as the compressional isoscalar excitations in agreement with the scarce experimental data [27], 4) it turns out that the third level has a toroidal nature, because it can be excited only by the toroidal operator [17] $O_{tor} = e_q(\mathbf{r}(\mathbf{rp}) - 2r^2\mathbf{p})$, where e_q is an effective charge; not very definite experimental indications of its existence can be found in [28].

The method was also applied to the description of nuclear reactions. The role of giant and low-lying resonances of different multipolarities in the polarization potential

was investigated in [29]. The contribution of low-lying compressional 1^- states has been estimated being of the order of 10-20% of the total. Formulae for transition densities of 0^+ , 2^+ , 1^- and 3^- collective states were derived with the help of linear response theory [30].

4 Concluding Remarks

The above presentation of the method and its application is far from being complete. We did not discuss the role of the quantum corrections to the Vlasov equation and a number of other important problems and also the comparison of this method with the different approaches are also left out of consideration. More detailed information may be found in [6],[8],[9],[14]-[16], [24]-[26],[29].

Our results speak quite persuasively for the advantages of the method of moments. Indeed, in the framework of a unified approach it is possible to describe the static and dynamical properties of the nuclei and the isoscalar and isovector excitations; besides giant resonances, low-lying modes are obtained. Despite the rather complicated realistic interaction, the computational work is comparatively simple, namely, one finds roots of polynomials whose coefficients are ordinary one-dimensional integrals. The nonlocality of the interaction does not lead to any additional difficulties. A very interesting fact is the appearance of low-lying modes; this fact offers hope of a more detailed description of the low-lying part of the spectrum as the number of degrees of freedom is increased (as study is extended to the dynamics of the tensors of higher and higher rank).

The theory predicts the resonances of a new type. Thus, it has some prognostic value. The results of preliminary study of the large amplitude vibrations are very hopeful. If to modify the method to take into account spin degrees of freedom it will be possible to study a large amplitude motion with the rather realistic Nilsson potential. It is obvious that the inclusion of spin degrees of freedom should not lead to serious difficulties - it is simply necessary to double the number of all possible equations of motion. It would be interesting to take into account elements of the density matrix nondiagonal with respect to the spin and isospin, since this would make it possible to describe spin-flip and charge-exchange processes.

We think that our approach will be useful for the studies of the nuclear fission and fusion also.

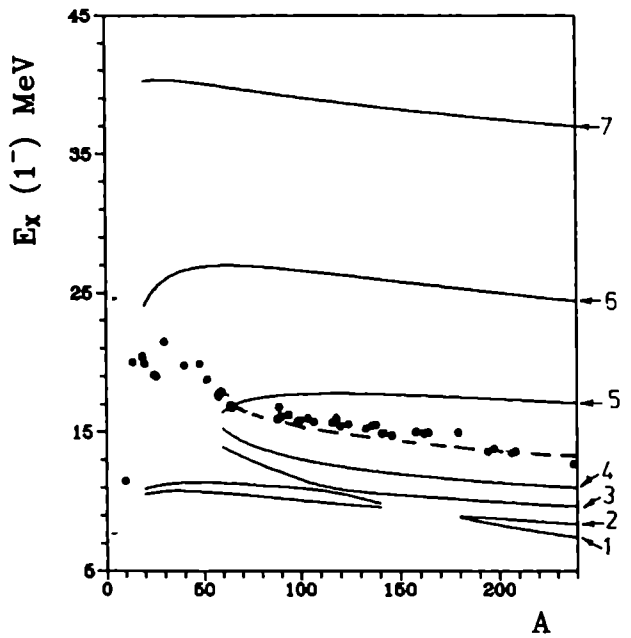

Fig.1. Energies of 1^- excitatoins as a function of the mass number calculated with SkM* force for nuclei on the beta stability line. Solid points correspond to experimental GDR centroids [1]. Dashed line: centroid of E_4 and E_5.

References

[1] Å. Bohr and B. R. Mottelson, *Nuclear Structure* (Benjamin, NY, 1977), v. 2.

[2] P. Hohenberg and W. Kohn, *Phys. Rev.* **136** (1964) 1384.

[3] E. Wigner, *Phys. Rev.* **40** (1932) 749.

[4] D. M. Brink and M. Di Toro, *Nucl. Phys.* **A372** (1981) 151.

[5] R. Balescu, *Equilibrium and Nonequilibrium Statistical Mechanics* (Wiley-Interscience, New York, 1975), v. 2.

[6] E. B. Balbutsev and J. Piperova, *Sov. J. of Nucl. Phys.* **50** (1989) 599.

[7] R. W. Hasse et al., *Phys. Rev.* **C25** (1982) 2771.

[8] E. B. Balbutsev et al., *Nucl. Phys.* **A457** (1986) 222.

[9] E. B. Balbutsev, *Sov. J. Part. Nucl.* **22** (1991) 159.

[10] S. Chandrasekhar, *Ellipsoidal Figures of Equilibrium* (Yale University Press, New Haven, Conn., 1969).

[11] E.B.Balbutsev, I.V. Molodtsova, P. Schuck, in *Collective Nuclear Dynamics, Proc. 4th Int. School on Nucl. Phys., Kiev, Ukraine, 1994*, ed. F. A. Ivanyuk (Vneshtorgizdat, Kiev, 1994) p. 92.

[12] D. A. Varshalovitch, A. N. Moskalev and V. K. Khersonski, *Quantum Theory of Angular Momentum* (Nauka, Leningrad, 1975).

[13] G. F. Bertsch, *Nuclear Physics with Heavy Ions and Mesons, 1977 Les Houches Lectures*, v.1, ed. R.Balian et al. (North-Holland, Amsterdam, 1978), p. 175.

[14] E. B. Balbutsev et al., *J. Phys.* **G14** (1988) 545.

[15] E. B. Balbutsev et al., *Sov. J. of Nucl. Phys.* **50** (1989) 788.

[16] E. B. Balbutsev and J. Piperova, *Izv. Akad. Nauk SSSR, ser. Fiz.* **52** (1988) 2132.

[17] V. M. Dubovik and L. A. Tosunyan, *Particles and Nuclei* (Atomizdat, Moscow) **14** (1983) 1193.

[18] V. A. Khodel, E. E. Saperstein, *Phys. Rep.* **92** (1982) 185.

[19] J. P. Providencia, G. Holzwarth, *Nucl. Phys.* **A439** (1985) 477.

[20] S. F. Semenko, *Sov. J. of Nucl. Phys.* **34** (1981) 356;
Preprint FIAN USSR, Moscow, 1986, No.76.

[21] M. Buenerd, *J. de Phys.* **45** (1984) C4-115.

[22] G. Holzwarth, G. Eckart, *Nucl. Phys.* **A325** (1979) 1.

[23] B. Bonin et al., *Nucl. Phys.* **A430** (1984) 349.

[24] E. B. Balbutsev, I. V. Molodtsova, J. Piperova, *Sov. J. of Nucl. Phys.* **53** (1991) No.3.

[25] E. B. Balbutsev et al., *Nucl. Phys.* **A571** (1994) 413.

[26] E. B. Balbutsev et al., *Europhys. Lett.* **26** (1994) 499.

[27] T. D. Poelhekken et al., *Phys. Lett.* **B278** (1992) 423.

[28] S. N. Belyaev et al., *Sov. J. of Nucl. Phys.* **42** (1985) 662.

[29] E. B. Balbutsev et al., *Physics of Atomic Nuclei (Yadern. Fiz.)* **58** (1995) 1.

[30] P. Ring and P. Schuck, *The nuclear many-body problem* (Springer, Berlin, 1980).

SYMPLECTIC DYNAMICS OF THE NUCLEAR MEAN-FIELD

MARIUS GRIGORESCU
Department of Theoretical Physics, Institute of Atomic Physics, P.O. Box MG 6
Bucharest, R-76900, Romania

ABSTRACT

Collective and microscopic pictures of nuclear dynamics are related in the frame of time-dependent variational principle on symplectic trial manifolds. For symmetry breaking systems such manifolds are constructed by cranking, and applied to study the nuclear isovector collective excitations.

1. Introduction

The interplay between quantum and classical aspects in the nuclear collective dynamics is a long standing puzzle, similar to the one represented by the mesoscopic physics[1], and is not yet completely understood.

The phenomenological collective models are based essentially on the quantization of some simple classical systems (rigid body, liquid drop), with parameters obtained by fitting data[2]. Therefore, in this approach the nucleus is supposed to be almost frozen, because the model Hamiltonian depends on a small number of variables. Also, the Hilbert space constructed by quantization is rather artificial, because it does not account for all the observables of the many-nucleon system.

In the microscopical approach, the nuclear dynamics is represented in the full Hilbert space by the time-dependent Hartree-Fock (HF), or Hartree-Fock-Bogolyubov (HFB) equations[3]. These equations have static solutions corresponding to the ground state, while the excited states are obtained by the random phase approximation (RPA), or, more generally, using requantization methods[4,5]. A clear sign of collective behaviour, in the sense of the phenomenological models, appears when the ground state is non-invariant to a continuous symmetry group of the Hamiltonian (spontaneous symmetry breaking). This situation may appear for geometrical symmetries, like rotation, or dynamical, like particle-number, and the corresponding nuclei are known as deformed, respectively superfluid. For these nuclei, the inertial parameters of the collective motion may be calculated microscopically using the average energy of the ground state shifted to a moving frame by the symmetry generators (the cranking method). However, the cranking is not related strictly to the symmetry breaking and is applied, for instance, to obtain the effective mass at fission[6].

The choice of the cranking operators is not arbitrary, because they should be in one-to-one correspondence with the canonical collective variables, up to a unitary change in the Hilbert space representation. This problem of correspondence is not simple, but a natural solution can be given if the cranking is applied at a more fundamental level, by constructing both the collective phase space and the phenomenological Hamiltonian. The key object necessary for this purpose is represented by the

shifted ground states, which play only a secondary role in the standard cranking calculation. These states are parameterized by the "shift" variables, and may be joined in trial manifolds S, endowed with a classical phase space structure (symplectic form) induced from the many-body Hilbert space[7]. By construction, S should be considered both as collective phase space and as trial manifold for a time-dependent variational treatment of the microscopic Hamiltonian. Moreover, the Hamilton equations for the collective variables are related kinematically to the evolution of the trial functions produced by the variational calculation. Therefore, the "artificial" quantization of the collective motion becomes useless, and can be replaced by requantization, to obtain directly the microscopic states which correspond to a particular collective motion. It is interesting to remark that the standard RPA is included in this formalism as a limit case, reached when S is constructed without any correspondence to an intuitive model, but taking as generators all possible particle-hole (ph) or particle-particle (pp) operators in some finite basis. This nice example will be discussed in the next section. Sect. 3 presents the construction of the symplectic trial manifolds for deformed, or superfluid systems, and two applications to the treatment of the isovector "scissors-like" collective excitations.

2. Symplectic dynamics on trial manifolds and RPA

2.1. Symplectic Dynamics and Requantization

Let us assume that $\mathcal{H}$ is the many-body Hilbert space, H is the microscopic Hamiltonian, $S = \{| \psi > (X)\}$ is a $2N$-dimensional trial manifold of normed functions, parameterized by the variables $X = \{x^i\}$, $i = 1, 2N$, and the matrix $\omega^S = [\omega^S_{ij}(\psi)]$, $\omega^S_{ij}(\psi) = 2\hbar Im < \partial_i\psi \mid \partial_j\psi >$ is non-singular. Then, ω^S defines a symplectic form on S, and the functional $\mathcal{J}[X] = \int_a^b < \psi \mid i\hbar\partial_t - H \mid \psi > dt$ is stationary for the solution X_t of the Hamilton equations

$$\sum_{j=1}^{2N} \dot{x}^j \omega^S_{jk}(\psi) = \frac{\partial < \psi \mid H \mid \psi >}{\partial x^k} \tag{1}$$

Therefore, the solution of a time-dependent variational calculation within S has the form $| \psi > (X_t)$, where X_t is a trajectory given by Eq. (1). It is interesting to note that when the couple $\mathcal{H}$, H corresponds to the quantum harmonic oscillator and S is the manifold of the Glauber coherent states, then Eq. (1) represents the Hamilton equations for the classical oscillator.

The procedure of extracting information about the spectrum of H from the orbits $| \psi > (X_t)$ is called "requantization", and if the system of Eq. (1) is integrable, then the method GIPQ[4] (gauge-invariant periodic quantization) can be applied. According to this method, the periodic orbits $\gamma = \{X^\gamma_t\}$, $X^\gamma_t = X^\gamma_{t+T_\gamma}$ should be quantized by a Bohr-Wilson-Sommerfeld (BWS) condition

$$\int_0^{T_\gamma} dt < \psi \mid i\partial_t \mid \psi >= 2\pi n, \qquad n = 0, 1, 2, ... \tag{2}$$

This gives the energy spectrum, while the eigenstates corresponding to a quantized orbit γ^n should be approximated by the time-average

$$| \Omega_\gamma >= \frac{1}{T_{\gamma^n}} \int_0^{T_{\gamma^n}} dt e^{i\Theta_t} | \psi > (X_t^{\gamma^n}) \tag{3}$$

with $\Theta_t = \int_0^t dt' < \psi | i\partial_{t'} | \psi >$ (the "Berry's phase").

An extended version of GIPQ includes also the quantization of the invariant tori[8]. As it will be shown further, the physical applications strongly support the requantization by Eq. (3), though its geometrical meaning is not yet completely clear. The study of such integral representations ("quantization by membranes") represents an active field of research in mathematical physics[9].

2.2. The Random Phase Approximation

Suppose now that the output of a static mean-field calculation (HF or HFB) consists in the ground state $| g >$ and the set of $2N$ operators $E_{\pm\alpha}$, $\alpha = 1, N$, $E_{-\alpha} = E_\alpha^\dagger$, such that $E_{-\alpha} | g >= 0$. If the single-particle basis contains n states, then in the HF case $| g >= c_1^\dagger c_2^\dagger c_3^\dagger ... c_A^\dagger | 0 >$ is constructed by acting with A fermion creation operators $c_h^\dagger$, $h = 1, A$, on the particle vacuum $| 0 >$, and a possible choice is $E_\alpha = c_p^\dagger c_h$, with $1 \leq h \leq A$, $A < p \leq n$, and $N = A(n - A)$. If there are no "hole" states, and $| g >=| 0 >$ is the particle (or quasiparticle in HFB) vacuum, then we may have $E_\alpha = c_{p_i}^\dagger c_{p_j}^\dagger$, with $p_i < p_j = 1, n$, and $N = n(n-1)/2$.

The operators $E_{\pm\alpha}$ can be used to construct a trial manifold S^{RPA} represented by the set of functions

$$| \psi > (Z) = U(Z) | g > \tag{4}$$

where

$$U(Z) = e^{\sum_\alpha (z_\alpha E_\alpha - z_\alpha^* E_{-\alpha})} \tag{5}$$

is a unitary operator and z_α are N complex variables. Therefore S^{RPA} is parameterized by $2N$ real variables, denoted x^i, $i = 1, 2N$, such that for $i \leq N$, x^i are $Re(z_\alpha)$, and for $N < i \leq 2N$, x^i are $Im(z_\alpha)$.

The condition as $| g >$, $(x^i = 0)$, to be a fixed point for Eq. (1) gives the static "mean-field" equations $< g | [H, E_{-\alpha}] | g >= 0$, automatically fulfilled in the HF or HFB case.

Let us consider now a small amplitude vibrational periodic orbit γ around $| g >$ with the period T, such that all x^k perform harmonic oscillations. This means $z_\alpha = X_\alpha e^{-i\Omega t} + Y_\alpha e^{i\Omega t}$, with $\Omega = 2\pi/T$, and T, X_α, Y_α unknowns which should be determined from the equations of motion. For the orbit γ,

$$U(Z_t^\gamma) = exp(e^{-i\Omega t} B^\dagger - e^{i\Omega t} B) \tag{6}$$

with $B^\dagger = \sum_\alpha (X_\alpha E_\alpha - Y_\alpha^* E_{-\alpha})$ and in the linear approximation Eq. (1) reduces to the RPA-like equation

$$< g | [[H, B^\dagger] - \hbar\Omega B^\dagger, E_{\pm\alpha}] | g >= 0 \tag{7}$$

The standard particle-hole or particle-particle RPA are recovered when $\mid g >$ is the HF or HFB ground state and $E_\alpha = c_p^\dagger c_h$, or $E_\alpha = c_{p_i}^\dagger c_{p_j}^\dagger$, respectively. Eq. (7) gives the "normal mode frequency" Ω and a one-parameter family of periodic orbits having this frequency. As parameter we may consider for instance the energy $E =< g \mid U(Z)^{-1} H U(Z) \mid g >$. However, if E is too large, the amplitudes X, Y increase and Eq. (7) fails in approximating Eq. (1).

Until now the whole discussion was about the classical dynamics on S^{RPA}, and to establish the connection with the quantum many-body system is necessary to requantize the RPA periodic orbits according to Eq. (2). To perform this integral we will assume that exists a Hermitian operator W, such that $[W, B^\dagger] = B^\dagger$, although the explicit form of W is not necessary. If W exists, then $U^{-1} i\partial_t U = \Omega(U^{-1} W U - W) = \Omega(e^{-i\Omega t} B^\dagger + e^{i\Omega t} B + [B, B^\dagger] + ...)$. By integrating this sum over a period, the terms linear in $B, B^\dagger$ vanish, and the first non-vanishing term is $2\pi[B, B^\dagger]$. Thus, the BWS quantization gives $< g \mid [B, B^\dagger] \mid g >= n$, and for $n = 1$ (the first excited state), it coincides with the RPA "normalization" condition. This interesting result was proved before using path integrals[10].

After quantization, the state associated by Eq. (3) to γ can be easily obtained expanding U in powers of $B^\dagger, B$, and retaining only the linear terms. The result has the familiar form $\mid \Omega >= B^\dagger \mid g >$, but by contrast to the RPA assumption, the excitation operator $B^\dagger$ acts on the uncorrelated ground state. However, on particular examples it can be shown that if the whole expansion of U is considered, then $\mid \Omega >= B^\dagger P_{RPA} \mid g >$, with P_{RPA} a Hermitian operator which gives an approximate projection of $\mid g >$ on the vacuum $\mid RPA >$ of B, defined by $B \mid RPA >= 0$. Moreover, if $\mid g >$ is symmetry breaking and γ is a related rotational orbit, then Eq. (3) gives $P_s \mid g >$, with P_s a symmetry restoring projection operator[5].

3. Isovector excitations in symmetry breaking nuclei

3.1. The Two Rotor Model

The prediction of the isovector angular rotational oscillations[11] (scissors vibrations) in deformed nuclei has been particularly stimulating for the experimental research of the nuclear magnetism, leading to the discovery of low-lying M1 states. These states were observed in high resolution (e, e') scattering experiments on rare earths[12], in the fp shell nuclei[13], and in actinides[14]. The apparent weak excitation of these states in intermediate energy proton scattering[15] has supported the orbital character predicted by the two rotor model (TRM), but the highly fragmented structure has generated a long standing debate about their real origin. On one side were the phenomenological models supporting the TRM picture, like CSM[16], or IBA-II[17], while on the other were the microscopic RPA or QRPA calculations, indicating that the observed M1 excitations are produced by only few quasiparticle pairs. Not less important for this debate was the difficulty to decide if the states obtained by microscopic calculations correspond or not to angular vibrations. Therefore, the problem of finding the appropriate microscopic correspondent for the collective motion appears

to be rather important.

This problem can be solved by an RPA calculation based on special trial manifolds S^{rot}, generated by cranking, instead of S^{RPA} defined in Sec. 2.2. Let us denote by $\mathcal{G}_x$ the group of rotations around the X axis, L_x the orbital angular momentum operator, and by $\mid g >$ the axially-deformed ground state of the microscopic Hamiltonian H. Then, the intrinsic ground state of a system rotating around the X-axis with angular momentum J, is given by the solution $\mid Z >_\omega$ of the variational equation $\delta < Z \mid H - \omega L_x \mid Z >= 0$. The set of functions $\mid Z >_\omega$ represents a curve in $\mathcal{H}$ containining $\mid g >$ and parameterized by the Lagrange multiplier ω, or, implicitly, by the angular momentum $J =_\omega < Z \mid L_x \mid Z >_\omega$. $\mathcal{G}_x$ moves this curve over a surface in $\mathcal{H}$ which contains the states

$$\mid \psi > (\phi, \omega) = e^{-i\phi L_x/\hbar} \mid Z >_\omega \tag{8}$$

and defines the trial manifold S^{rot}. In arbitrary variables $\{q, p\}$, the symplectic structure of S^{rot} is given by the 2-form ω^{rot}, $\omega^{rot}_{qp} = 2\hbar Im < \partial_q \psi \mid \partial_p \psi >$. An obvious choice of these variables is $q = \phi$, and p a function of ω. When this function is the angular momentum, $(p = J)$, then $\omega^{rot}_{\phi J} = 2\hbar Im < \partial_\phi \psi(\phi, \omega) \mid \partial_J \psi(\phi, \omega) >= \partial_J (_\omega < Z \mid L_x \mid Z >_\omega) = 1$, proving that ϕ and J are canonical, and S^{rot} is the phase space of the classical rotor.

In the case of a deformed nucleus, S^{rot} can be constructed separately for protons and neutrons, and the trial wave function corresponding to the total phase space $S^{rot}_{pn} = S^{rot}_p \times S^{rot}_n$, is

$$\mid \psi > (\phi_p, \phi_n, \omega_p, \omega_n) = e^{-i(\phi_p L^p_x + \phi_n L^n_x)/\hbar} \mid Z^p >_{\omega_p} \mid Z^n >_{\omega_n} \tag{9}$$

Let us consider now a schematic nuclear Hamiltonian

$$H = \sum_{\mu,\nu} (h_0)_{\mu\nu} c^\dagger_\mu c_\nu - \frac{\chi_0}{2} (Q_{is} Q^\dagger_{is} + b Q_{iv} Q^\dagger_{iv}) \tag{10}$$

consisting in a spherical oscillator term (h_0 is the one-body spherical oscillator Hamiltonian with frequency $\omega_0 = 41 A^{-1/3}$ MeV$/\hbar$), and the quadrupole-quadrupole (QQ) interaction, with both isoscalar and isovector components ($b \approx -0.6$). Then, for S^{rot}_{pn} and H, Eq. (1) takes the form of the Hamilton system of equations for two rotors[18], having the cranking moments of inertia I_p, I_n, and interacting by a restoring elastic potential $C_\chi(\phi_p - \phi_n)^2/2$. Worth noting, $C_\chi = 3\chi_0(1-b) < Q^p_0 >_g < Q^n_0 >_g \approx 9\delta^2 A$ MeV appears related to the microscopic QQ interaction, $(Q^{p,n}_0 = \sqrt{5/16\pi}(2z^2 - x^2 - y^2)_{p,n})$, by contrast to the TRM estimate related to the symmetry energy, $C_{TRM} \approx 6\delta^2 A^{4/3}$ MeV (δ is the deformation parameter).

Eq. (2) is identical with the BWS condition for the two-rotor system, giving the quantized angular oscillation amplitudes $a_\tau = (2\hbar I_\tau/\Omega_\chi)^{1/2}/I_\tau$, $\tau = p, n$, while the excitation energy is $E_x = \hbar\Omega_\chi = \hbar\sqrt{C_\chi/I_\tau}$, $I_\tau = I_p I_n/(I_p + I_n)$.

To apply Eq. (3), $\mid Z >_\omega$ was approximated near $\mid g >$ using a first order perturbative treatment of the cranking term. The "scissors-like" state (not normalized)

obtained from Eq. (3) has the form

$$\mid \Omega_\chi >= \frac{1}{2\hbar}(\frac{\Omega_\chi}{D}+1)[a_p L_x^p - a_n L_x^n] \mid g > \tag{11}$$

with $D = \delta\omega_0$. This state gives the $B(M1)$ strength[18]

$$B(M1) = \frac{3}{4\pi\hbar}(g_p - g_n)^2 I_r D \mu_N^2 \tag{12}$$

The comparison with the experiment is complicated by the ambiguities of separating the orbital and the spin strengths, and defining a reasonable sum over fragments. Assuming the dominance of the orbital strength at low energy, under 6 MeV in rare earths, and 4 MeV in actinides, the data are well reproduced by Eq. (12) with the irrotational moments of inertia. The range of the energy E_x calculated by taking I_r at the rigid or irrotational limits is not very large (below 2 MeV) and include the data through all the mass regions investigated.

After normalization, the state $\mid \Omega_\chi >$ becomes the same as the term independent of spin and pairing from the state $\mid ROT >$, constructed before[20] to represent microscopically the scissors modes. However, this is not similar to an RPA state, because the "excitation operator" $a_p L_x^p - a_n L_x^n$ is Hermitian. A quasiboson operator may be obtained if the cranking wave functions $\mid Z >_\omega$ are related to $\mid g >$ by a unitary transformation. This problem is not easy, but was solved recently[7] in terms of an unitary operator U_ω which relates the cranked anisotropic oscillator eigenstates $\mid Z >_\omega$ to the eigenstates of a spherical harmonic oscillator $\mid g_s >$. Thus, if ω is not larger than $\omega_s\sqrt{3}/2$, $\omega_s = \sqrt{(\omega_y^2+\omega_z^2)/2}$, then we have

$$h_0 - \delta m\omega_0^2(2z^2 - x^2 - y^2)/3 - \omega l_x = U_\omega h_s U_\omega^{-1} \tag{13}$$

with

$$U_\omega = e^{(-i\lambda c_x)} e^{(-i\sum_{k=x,y,z}\theta_k s_{2,k})} \tag{14}$$

In the left-hand side of Eq. (13) the first two terms correspond to the anisotropic oscillator with frequencies $\omega_x = \omega_y = \omega_0\sqrt{1+2\delta/3}$, $\omega_z = \omega_0\sqrt{1-4\delta/3}$, while

$$h_0 = \sum_{k=x,y,z} \hbar\omega_0(b_k^\dagger b_k + 1/2), \qquad b_k^\dagger = \sqrt{m\omega_0/2\hbar}(x_k - ip_k/m\omega_0)$$

$$h_s = \sum_{k=x,y,z} \hbar\Omega_k(\tilde{b}_k^\dagger \tilde{b}_k + 1/2), \qquad \tilde{b}_k^\dagger = \sqrt{m\omega_s/2\hbar}(x_k - ip_k/m\omega_s)$$

$$l_x = i\hbar(b_y b_z^\dagger - b_z b_y^\dagger) \qquad c_x = \tilde{b}_y^\dagger \tilde{b}_z + \tilde{b}_z^\dagger \tilde{b}_y, \qquad s_{2,k} = i((\tilde{b}_k^\dagger)^2 - (\tilde{b}_k)^2)/4$$

and the parameters λ, θ_k of U_ω are given by

$$tan2\lambda = 2\omega/\omega_s\eta \qquad sinh\theta_k = \omega_s(1-\omega_k^2/\omega_s^2)/2\Omega_k \qquad \eta = (\omega_y^2 - \omega_z^2)/2\omega_s^2$$

$$\Omega_x = \omega_x \quad \Omega^2_{y,z} = (\omega_s + \epsilon_{y,z})^2 - (\omega_s \eta/2)^2$$

with $\epsilon_y = -\epsilon_z = \omega_s \eta / 2cos2\lambda$.

The operators $s_{2,k}$, k=x,y,z are the "squeezing" generators, and they produce the transition from a spherical to a deformed basis. This transition corresponds to the "cranking" of h_0 by the term $\delta m\omega_0^2(2z^2 - x^2 - y^2)/3$, proportional to Q_0. Therefore, the unitary operator U_0 with θ_k as variables may be used to generate trial manifolds for the treatment of the quadrupole vibrations ($E_x \sim 2\hbar\omega_0$). The commutation relations between $s_{2,k}$ and $b_k^\dagger b_k$ close to the su(1,1) ($\approx$sp(1,R)) algebra[19].

The operator c_x generates the shift from a static frame to a frame rotating with the angular velocity ω, and it appears as an "angle" operator conjugate to l_x. Analog operators, c_y, c_z are associated to l_y and l_z, and by commutation c_x, c_y, c_z and l_x, l_y, l_z generate an su(3) algebra. Similarly, $s_{2,x}, s_{2,y}, s_{2,z}$ and l_x, l_y, l_z generate by commutation a gl(3,R) algebra. This rather complicated set of algebras is included in the symplectic Lie algebra sp(3,R)[21].

In the many-fermion case the one-body operators $h, h_0, h_s, l_k, c_k, s_k$ become particle-hole operators, denoted $H, H_0, H_s, L_k, C_k, S_k$, and may be used to write $\mid Z >_\omega$ as $U_\omega \mid g_s >$. This form is especially suited to study large amplitude vibrations, but corrections to Eq. (11) appear already in the linear approximation. If the dependence of θ_k on ω is neglected, then during the scissors vibration $\mid Z >_\omega$ in Eq. (9) changes in time only due to the factor of C_x, and Eq. (3) gives $\mid \Omega_\chi >= B_\chi^\dagger \mid g >$, with

$$B_\chi^\dagger = \frac{1}{2\hbar}[a^p L_x^p - a^n L_x^n - \frac{i\hbar\Omega_\chi}{\omega_y - \omega_z}(a^p C_x^p - a^n C_x^n)] \tag{15}$$

Unexpectedly, though $a^{p,n}$ are the same angular amplitudes as in Eq. (11), $B_\chi^\dagger$ is normalized in the RPA sense, $< g \mid [B_\chi, B_\chi^\dagger] \mid g >= 1$. In fact, if the particle-hole excitations between different oscillator shells are neglected, then $sgn(\eta) i\hbar C_x \mid g > \approx -L_x \mid g >$, and $B_\chi^\dagger \mid g >$ reduces to Eq. (11).

The operator $B_\chi^\dagger$ was obtained recently also by the canonical quantization of the TRM in relative coordinates[22], and was proved to support the interpretation of all the low-lying orbital 1^+ excitations as a scissors mode.

It is interesting to note that if the dependence of θ_k on ω is taken into account, then $B_\chi^\dagger$ will contain operators from gl(3,R). Such terms are related to the excitation operator proposed long time ago by Hilton[23]. Instead of constructing $B_\chi^\dagger$ within the "angular momentum & shift" algebra, su(3), he proposed a combination within the "angular momentum & squeezing" algebra, gl(3,R), between l_y and the "shear" generator $zp_x + xp_z \sim i(b_z^\dagger b_x^\dagger - b_z b_x)$.

3.2. The Isovector Josephson Oscillations

The combined effect of the proton-neutron interaction and breaking of the translational or rotational symmetries is related to the giant dipole resonance[24] or to the "scissors modes", respectively. However, there is one more important symmetry breaking in nuclei for which such type of isovector collective motion was not studied, and this appears when the nuclei are "superfluid".

The ground state of a superfluid system accounts for the pp correlations produced

by the pairing interaction, and is well approximated by a BCS function. For a single j-shell, the pairing Hamiltonian and the BCS function are

$$H_0 = \epsilon N - \frac{G}{4} P^\dagger P \qquad | BCS > (\varphi, \rho) = e^{(zP^\dagger - z^* P)} \mid 0 > \tag{16}$$

where $z = \rho e^{-i\varphi}$, φ is the BCS "gauge" angle, $N = \sum_{-j,j} c_m^\dagger c_m$ is the particle-number operator, and $P^\dagger = \sum_{m=-j,j} c_m^\dagger c_{-m}^\dagger$ is the pair creation operator. The angle φ is not a constant, and a superfluid system in the ground state performs a free gauge rotation with the angular velocity $\dot{\varphi} = 2\epsilon_F$, twice the Fermi energy. In a nucleus, the proton and neutron systems are not isolated, but change particles until the Fermi energies ϵ_F^p, ϵ_F^n become equal. Thus, we may see this as an indication about the existence of a phenomenological "gauge restoring interaction", which tends to fix the relative gauge angle $\varphi_p - \varphi_n$ at a constant value. If this is true, and there is an interaction between *pairs* of protons and neutrons, then oscillations of the protons against neutrons in the BCS gauge space should appear.

A pairing-like proton-neutron interaction $H_{pn} = -\sigma(P_p^\dagger P_n + P_n^\dagger P_p)/4$ may be related to the isospin symmetry breaking mean-field for a four particle interaction. The problem of the mean-field created by the four particle interaction is not new, but previously[25] the main interest was for terms $\sim P_p^\dagger P_n^\dagger$, assumed to represent α clusters, while terms like $P_p^\dagger P_n$ were neglected. Because H_{pn} do not commute with the isospin $T_0 = (N_n - N_p)/2$, it produces an "isorotational" term $k_\sigma (N-Z)^2$ in the total energy. This means a term in the symmetry energy $k_W (N-Z)^2$, $k_W = 28/A$ MeV from the Weiszäcker mass formula with a "dynamical" origin, beside the "kinematic" one determined by the Pauli principle[26]. Thus, σ can be obtained by a fit of the symmetry energy produced by the Hamiltonian

$$H = H_0^p + H_0^n + H_{pn} \tag{17}$$

in a single j-shell. Considering the case of $1d_{3/2}$ nuclei, σ was estimated to be $\approx 2.7/A$ MeV[27]. However, the consideration of j-shells with high degeneracies suggests a value about ten times larger[28].

The interaction H_{pn} contributes to the symmetry energy in all nuclei, but in the superfluid nuclei produces also a restoring potential for the BCS angles, $C_\sigma(\varphi_p - \varphi_n)^2/2$. This potential can be related to H_{pn} by a treatment similar to the one applied to the QQ interaction responsible for the orbital scissors modes. Indeed, the BCS functions define symplectic manifolds S^{BCS} which can be parameterized by φ and ρ, or by the canonical variables φ and $p =< BCS \mid N \mid BCS > /2 = (j+1/2) sin^2(2\rho)$. In these variables $\omega_{\varphi p}^{BCS} = 2\hbar Im < \partial_\varphi BCS(\varphi,\rho) \mid \partial_p BCS(\varphi,\rho) >= \hbar \partial_p (< BCS \mid N/2 \mid BCS >) = \hbar$. For a proton-neutron system the trial manifold will be represented by the product $S_p^{BCS} \times S_n^{BCS}$, and the collective motion determined for H by Eq. (1) shows the occurence of the isovector gauge vibrations. For a half-filled shell, the fixed point in Eq. (1) corresponds to the ground state of H,

$$\mid g >= e^{\frac{\pi}{4}(P^\dagger + N^\dagger - P - N)} \mid 0 > \tag{18}$$

and the gap parameter $\Delta = G < g \mid P^\dagger \mid g > /2$ is the same both for protons and neutrons. The restoring potential has the constant $C_\sigma = 2\sigma(\Delta/G)^2$, and the excitation energy for the isovector oscillations is $E_\sigma = \hbar\Omega_\sigma = 4\sqrt{2k_W C_\sigma}$.

The excitation operator defined by Eq. (3) has the form

$$B^\dagger_\sigma = \frac{1}{2j+1}\sqrt{\frac{E_\sigma}{\sigma}}[T_0 - \frac{\sigma(2j+1)}{4E_\sigma}(P^\dagger - P - N^\dagger + N)] \tag{19}$$

and by accident, is the same as the one provided by the standard QRPA[29]. However, the RPA vacuum defined by $B_\sigma \mid RPA >= 0$ exists only if $j+1/2$ is an even integer[28].

The states generated by $B^\dagger$ are isovector monopoles, and correspond to Josephson oscillations between the proton and neutron superfluids. Such oscillations might be excited by the Coulomb interaction in electron scattering[28], or by the current of pairs between the two superfluids produced in pion double charge-exchange (DCX) reactions. The importance of Josephson-type correlations in DCX reactions was proved first by shell - model calculations[30], suggesting that the "scissors modes" in gauge space discussed here are worth of experimental investigation.

4. Summary

In this lecture I presented a microscopic approach to the collective motion, based essentially on the time-dependent variational principle and GIPQ requantization, (Sec. 2.1), but which is peculiar by the choice of the trial functions. The trial manifolds are supposed to have the phase-space (symplectic) structure of the collective model, and for the symmetry breaking nuclei are constructed using the cranking procedure[7]. The Hamilton equations of motion (Eq. (1)) appear by a constrained variational calculation in the Hilbert space, rather than by semiclassical approximations ($\hbar \to 0$). This formalism includes the standard RPA or QRPA (Sec. 2.2), and was applied with succes to the treatment of the collective isovector excitations (Sec. 3). It solves the problems of the inertial parameters, restoring force constants, and of the microscopic analog for a particular collective motion (here the scissors vibrations). Moreover, isovector vibrations in the BCS gauge space of the superfluid nuclei were predicted. The variational formulation is appropriate to account for the coupling between a quantum system and a thermal environment[31]. Therefore, the study of giant resonances using a Langevin form of Eq. (1), with noise and memory-friction terms in the right-hand side appears highly interesting.

5. Acknowledgements

I would like to express my grateful thanks to Roland Nojarov for his kind encouragements and for valuable discussions on the problem of M1 states.

Special thanks are due to the organizers of this summer school for their invitation and for their care to create a stimulating scientific atmosphere.

6. References

1. A. J. Leggett, in *Proc. 4th Int. Symp. Foundations of Quantum Mechanics*, Tokyo, 1992, (JJAP Series 9 1993).
2. A. Bohr, B. R. Mottelson, *Nuclear Structure*, vol. I,II (W. A. Benjamin, New York, 1969).
3. P. Ring, P. Schuck, *The Nuclear Many-Body Problem* (Springer-Verlag, New York, 1980).
4. K. K. Kan, J. J. Griffin, P. C. Lichtner, M. Dworzecka, *Nucl. Phys.* **A332** (1979) 109.
5. M. Grigorescu, *Rom. Journ. Phys.* **38** (1993) 859.
6. M. Brack, J. Damgaard, A. S. Jensen, H. C. Pauli, V. M. Strutinsky, C. Y. Wong, *Rev. Mod. Phys.* **44** (1972) 320.
7. M. Grigorescu, in *Frontier Topics in Nuclear Physics*, ed. W. Scheid and A. Sandulescu (Plenum Press, New York, 1994).
8. S. Drożdż, M. Ploszajczak, E. Caurier, *Ann. Phys.* **171** (1986) 108.
9. M. Karasev, *Cont. Math.* **179** (1994) 83.
10. S. Levit, J. W. Negele, Z. Paltiel, *Phys. Rev.* C **21** (1980) 1603.
11. N. Lo Iudice, F. Palumbo, *Phys. Rev. Lett* **41** (1978) 1532.
12. D. Bhole et. al. *Phys. Lett.* **137B** (1984) 59, *Phys. Lett* **148B** (1984) 260.
13. D. C. Zheng, L. Zamick, E. Moya de Guerra, A. Richter, *Phys. Rev. C* **42** (1990) 1408.
14. R. D. Heil et. al. *Nucl. Phys. A* **476** (1988) 39.
15. D. Frekers et. al. *Phys. Lett. B* **218** (1989) 439, **244** (1990) 178.
16. A. A. Raduta, A. Faessler, V. Ceausescu, *Phys. Rev. C* **36** (1987) 2111.
17. H. R. Walet, P. J. Brussard, A. E. L. Diperink, *Phys. Lett. B* **163** (1985) 4.
18. M. Grigorescu, *Rev. Roum. Phys.* **34** (1989) 1147.
19. M. M. Nieto, D. R. Truax, *Phys. Rev. Lett.* **71** (1993) 2843.
20. A. Faessler, R. Nojarov *Phys. Lett.* **B137** (1988) 1147.
21. D. J. Rowe, M. G. Vassanji, J. Carvalho, *Nucl. Phys.* **A504** (1989) 76.
22. R. Nojarov, *Nucl. Phys.* **A571** (1994) 93.
23. R. R. Hilton, *Ann. Phys. (NY)* **214** (1992) 258.
24. M. Goldhaber, E. Teller, *Phys. Rev.* **74** (1948) 1046.
25. V. G. Soloviev, *Nucl. Phys.* **18** (1960) 161.
26. A. de Shalit, H. Feshbach, *Theoretical Nuclear Physics* vol. I (John Willey & Sons Inc. 1974), p. 127.
27. M. Grigorescu, *J. Phys. G* **16** (1990) 417.
28. M. Grigorescu, *Rev. Roum. Phys.* **37** (1992) 107.
29. M. Grigorescu, E. Iancu, *Z. Phys. A* **337** (1990) 139.
30. N. Auerbach, in *Pion-Nucleus Double Charge Exchange*, ed. W. R. Gibbs, M. J. Leitch (World Scientific, Singapore 1990).
31. M. Grigorescu, N. Carjan, *Phys. Rev. E* **51** (1995) 1996.

2. CLUSTERING PHENOMENA AND LARGE AMPLITUDE MOTION

NONLINEAR EXCITATIONS OF THE NUCLEAR SURFACE. QUASIMOLECULAR RESONANCES AS SOLITONS AND BREATHERS

ANDREI LUDU,
Bucharest University, Department of Theoretical Physics
Bucharest-Magurele, P.O.Box MG-5211, Romania

AUREL SANDULESCU,
Department of Theoretical Physics, Institute of Atomic Physics,
Bucharest-Magurele, P.O.Box MG-6, Romania

and

WALTER GREINER
Institut für Theoretische Physik der Johann-Wolfgang-Goethe-Universität,
D-60054, Frankfurt am Main, Germany

ABSTRACT

We introduce a Lagrangean depending of a complex scalar field, which gives a quantum analogue of the classical large amplitude collective motion in nuclei as solitonic excitations of the nuclear surface. By using a non perturbative weak-coupling procedure we have quantized the normal modes of the soliton and breather solutions. The corresponding Hamiltonian becomes diagonal with a spectrum similar with a sum of nonlinear harmonic oscillator spectra. Additional degrees of freedom and new quantum numbers are introduced. This formulation, applied for the description of the quasimolecular spectra, explaines and predicts energy levels spins.

1. Introduction

One of the interesting aspects of heavy ion nuclear physics is the existence of quasimolecular structure. In such complex nuclear systems, there are groups of states with the structure polarized strongly into subunit nuclear clusters which can be defined as molecule-like structures [1]. Alpha-particle scattering has been known to be an important tool for studies of the general mechanism of reactions between complex nuclear particles and for exploring interesting nuclear structure properties. During the last decades, a big amount of data for elastic scattering of alpha particles on heavy or medium heavy nuclei has been published. These data showed rich resonant structure corresponding to many possible intermediate configurations. These intermediate states of α+nucleus could be considered as belonging to an α-molecular cluster structure. In the scattering from ^{40}Ca [2], ^{28}Si [3] and ^{20}Ne [4], for example, they occur as fragments of broad resonances forming groups with a common angular momentum in a mixed parity rotational band of excited states. There are many theoretical attempts (microscopical and phenomenological models) to explain such resonances or the intermediate structure [5-19], (for several excellent review articles see the references in

the Preface of [1]). The great number of states as well as their irregular appearance, and the relatively small moment of inertia of the α+nucleus-systems [3] call for other models. However, the shell model can not describe the cluster aspects of nuclei [20]. Microscopically one has to introduce in the shell model a cluster-like component [21] or the many-body correlations. We consider that a collective description, in which the outside nucleons of a rigid core join together to form a cluster, could also represent an appropriate frame for the evaluation of cluster preformation factors [22].

In this paper (and in two other recent ones, [23,24]) we shall address the problem of obtaining an expression for the energy spectra of such α+cluster resonances. We introduce here another possible mode of explanation of these spectra, in the frame of a certain Lagrangean model. We use a nonlinear Lagrangean for the description of the system in terms of the dynamics of the nuclear surface, in the background of the liquid drop model. This dynamical description of these states was first introduced [22,23] by considering that in the intermediate states the alpha particle interacts with the nucleus as a soliton or a breather. In this description we assume that the outside nucleons do not polarize the core and these nucleons join together due to the nonlinear effects, i.e. the stability of the solitonic shapes. Consequently in this collective description new shapes appear which are hardly described by a simple multipole expansion of the nuclear surface. Recently [22], we have shown that by considering the nonlinear terms in the classical hydrodynamic equations, stable solitons exist on a circle with the shape $r = R + \eta(\theta, t)$ respectively on a sphere if the perturbation has an axial symmetry. The soliton as a perturbation of the shape $\eta(\phi, t)$, is described by the Korteweg-de Vries (KdV) equation, and the breather (modulated soliton) is described by the Nonlinear Schrödinger equation (NLS) [25]. The conserved energy (the corresponding Hamiltonian of the nonlinear system), under the condition of constancy of the volume of the soliton-like alpha particle, and the phenomenological shell corrections for the core and the soliton, lead to a new minimum on the total energy surface as a function of the new collective coordinates, chosen to be degenerated with the ground state minimum. The penetrability between the two minima give the probability of the formation of the soliton on the nuclear surface. In this way we introduced a new coexistence model consisting of the usual shell model and a cluster-like model describing a soliton moving on the nuclear surface.

We introduce a quantum nonlinear analogue of the above classical hydrodynamic description of the soliton with the help of a Lagrangean depending of a complex scalar field. The corresponding Lagrange equation is a modified nonlinear Schrödinger (MNLS) equation. The resulting Hamilton equations lead to the same MNLS equation. We have shown that by assuming a traveling wave profile this equation becomes a MKdV equation which, by a nonlinear Miura transformation, yields finally in a KdV equation. Consequently, a full correspondence with the previous classical description is obtained [22]. The quantum fluctuations around the clasical solutions (i.e. solitons and breathers) are obtained by a non-perturbative weak-coupling procedure, which consists in a functional Taylor expansion of the potential up to third order around the static solutions. A parallel between the MNLS and KdV equations is shown to exist at the classical and quantum level. We diagonalize the Hamiltonian, and the obtained

spectra are similar with a sum of nonlinear harmonic oscillators spectra determined uniquely by the soliton geometry.

The above quantum approach of cluster formation on the nuclear surface was succesfully applied to the description of the resonances observed in the elastic scattering of alpha particles on ^{28}Si [28]. In the present approach we find a generalisation of this previous model and we apply also this description to the resonances observed in the elastic scattering of alpha particles on ^{20}Ne. We assume that the free alpha particle, in contact with the nucleus, looses its entity and becomes a breather state with the preformation factor 1. At present this model can reproduce and predict the energies and the spins of the resonances, but can not give widths, because the resonance states are treated as bound states.

We concluded that the quasimolecular spectra can be described in the present model by a rotational part $\frac{\hbar^2}{2I}I(I+1)$ and a solitonic part $\sum_k \hbar\omega_k\left(N_k+\frac{1}{2}\right)+\sum_k B_k\left(N_k+\frac{1}{2}\right)^2$ which contains a finite number of nonlinear harmonic oscillators with new quantum numbers N_k, energies $\hbar\omega_k$ and quadratic corrections B_k determined by the soliton geometry and no other free parameters are introduced.

2. Solitons and breathers on the nuclear surface

Solitons and breathers are special solutions (solitary waves) of nonlinear partial differential equations like Korteweg-de Vries (KdV), Modified Korteweg-de Vries (MKdV), Nonlinear Schrödinger (NLS) equations [25]. We apply such a formalism to the classical nonlinear large amplitude collective motion which was recently introduced [22] for the description of the formation of the clusters on the nuclear surface. We introduce a class of Lagrangeans with the property that the solutions of their Lagrange equations are reducible to the KdV or NLS equations.

The first step is to consider a model physical system described by a complex field $u(\phi,t)$ defined on a circle of radius R, $\phi\in[0,2\pi)$. This is an infinite-dimensional Hamiltonian system characterised by a Lagrangean depending on the field $u(\phi,t)$ and its complex conjugate, in the general form:

$$L[\phi,\phi^*]=\int_0^{2\pi}\mathcal{L}(u,u^*)d\phi=\int_0^{2\pi}\left[\frac{1}{\lambda}|u_t|^2-\frac{i\mu}{2}(uu_t^*-u^*u_t)+|u_\phi|^2-\frac{1}{4}|u|^4+4\beta^2|u|^2\right]d\phi \tag{1}$$

where ϕ represents the angular coordinate on the circle, $\lambda=c^2/R^2$, c is the velocity of light, β is a real parameter similar with the mass parameter in Φ^4 field theory [31,32] and μ another free parameter. The corresponding Lagrange density equation for the Lagrangean density $\mathcal{L}$ is

$$\frac{\partial}{\partial t}\left(\frac{\partial\mathcal{L}}{\partial u_t^*}\right)+\frac{\partial}{\partial\phi}\left(\frac{\partial\mathcal{L}}{\partial u_\phi^*}\right)-\frac{\partial\mathcal{L}}{\partial u^*}=0, \tag{2}$$

which leads to the following modified nonlinear Schrödinger equation (MNLS)

$$\frac{1}{\lambda}u_{tt} - i\mu u_t = -u_{\phi\phi} - \frac{1}{2}|u|^2 u + 4\beta^2 u. \tag{3}$$

This equation is a generalization of the NLS equation, at which we can reduce in the limit $\lambda \to \infty$, $\mu = -1$ and $\beta = 0$

$$iu_t = -u_{\phi\phi} - |u|^2 u. \tag{4}$$

In the limit $\mu = 0$ we obtain again a nonlinear wave equation. From the Lagrangean density equation (1) we obtain the corresponding energy density:

$$\mathcal{H}(u, u^*) = u_t \frac{\partial \mathcal{L}}{\partial u_t} + u_t^* \frac{\partial \mathcal{L}}{\partial u_t^*} - \mathcal{L} \tag{5}$$

$$= \frac{1}{\lambda}|u_t|^2 - |u_\phi|^2 + \frac{1}{4}|u|^4 - 4\beta^2|u|^2,$$

with the property that its integral, the Hamiltonian, is conserved as t varies, and gives the total energy functional E

$$E[u, u^*] = \int_0^{2\pi} \mathcal{H} d\phi = T + U. \tag{6}$$

Here we defined the total kinetic energy T and the total potential energy U from $L = T - U$ and eq.(5). The Lagrangean can now be written as a sum of three terms

$$L = T + \mu Q - U \tag{7}$$

with

$$T[u, u^*] = \frac{1}{\lambda}\int_0^{2\pi} |u_t|^2 d\phi, \tag{8}$$

$$U[u, u^*] = \int_0^{2\pi} \left(-|u_\phi|^2 + \frac{1}{4}|u|^4 - 4\beta^2|u|^2\right) d\phi. \tag{9}$$

The remaining term in eq.(7)

$$Q(u, u^*) = -\frac{i}{2}\int_0^{2\pi} (u u_t^* - u^* u_t) d\phi, \tag{10}$$

corresponds to another conserved quantity, the conserved topological charge Q [32]. The conservation of Q is evident from the $U(1)$ global symmetry of the Lagrangean (1). By introducing the conjugate momenta

$$u_t = \lambda\left(p^* + \frac{i\mu}{2}u\right) \quad ; \quad u_t^* = \lambda\left(p + \frac{i\mu}{2}u^*\right), \tag{11}$$

the kinetic energy becomes

$$T = \lambda \int \left(pp^* - \frac{i\mu}{2} p^* u + \frac{i\mu}{2} p u - \frac{1}{4} u u^* \right) d\phi. \tag{12}$$

Consequently the Hamilton equations

$$\begin{aligned} u_t = \frac{\partial \mathcal{H}}{\partial p} \quad ; \quad u_t^* = \frac{\partial \mathcal{H}}{\partial p^*} \\ p_t = -\frac{\partial \mathcal{H}}{\partial u} \quad ; \quad p_t^* = -\frac{\partial \mathcal{H}}{\partial u^*} \end{aligned} \tag{13}$$

give directly the same MNLS eq.(3)

$$\frac{1}{\lambda} u_{tt} - i\mu u_t = \frac{\partial \mathcal{U}}{\partial u^*}. \tag{14}$$

In the following we show how the solutions of the MNLS eq.(3) are connected with solitons and breathers. We find for eq.(3) quasi-static solutions:

$$u(\phi, t) = u_0(\phi) e^{i\alpha t}, \tag{15}$$

with α a parameter which labels these solutions. By introducing the solution (15) in eq.(3) we obtain the following differential equation for $u_0(\phi)$

$$u_{0\phi\phi} = \left(-\alpha\mu + 4\beta^2 + \frac{\alpha^2}{\lambda} \right) u_0 - u_0^3, \tag{16}$$

with the general solution in the form

$$u_0(\phi) = \pm \sqrt{2\left(-\alpha\mu + 4\beta^2 + \frac{\alpha^2}{\lambda} \right)} sech\left(\sqrt{-\alpha\mu + 4\beta^2 + \frac{\alpha^2}{\lambda}} \phi \right). \tag{17}$$

With the condition $\alpha\mu - 4\beta^2 - \frac{\alpha^2}{\lambda} > 0$ this solution yields a static soliton for $|u|^2$ and a breather-like solution for $Re(u)$ [29]

$$|u|^2 = 2\left(-\alpha\mu + 4\beta^2 + \frac{\alpha^2}{\lambda} \right) sech^2\left(\sqrt{-\alpha\mu + 4\beta^2 + \frac{\alpha^2}{\lambda}} \ \phi \right), \tag{18}$$

$$Re(u) = \sqrt{2\left(-\alpha\mu + 4\beta^2 + \frac{\alpha^2}{\lambda} \right)} sech\left(\sqrt{-\alpha\mu + 4\beta^2 + \frac{\alpha^2}{\lambda}} \ \phi \right) cos(\alpha t). \tag{19}$$

We note that LHS of eq.(3), i.e. the time depending part, cancels for $\alpha = \lambda\mu$. This case corresponds to the static solution of MNLS and will be used further in the

quantizing procedure. We can consider more general solutions of eq.(3), in the form of a traveling wave packet with half width L and the speed V

$$u(\phi,t) = r\left(\frac{\phi - Vt}{L}\right)e^{i(a\phi+bt)}, \tag{20}$$

where r is an analytical function and a and b are constants. In this case, by taking $\mu = 1$, and by introducing the explicite dependence of λ as a function of R, we obtain, from the real part of eq.(3), by differentiation with respect to ϕ, the MKdV equation for r:

$$\frac{4\beta^2 + a^2 + Rb/c - R^2b^2/c^2}{V}r_t + \frac{3}{2}r^2r_\phi + \left(1 - \frac{R^2V^2}{c^2}\right)r_{\phi\phi\phi} = 0, \tag{21}$$

with the solution

$$r = r_0 sech\left(\sqrt{\frac{4\beta^2 + a^2 + Rb/c - R^2b^2/c^2}{1 - R^2V^2/c^2}}(\phi - Vt)\right), \tag{22}$$

and its amplitude

$$r_0 = 2\sqrt{-R^2b^2/c^2 + a^2 + b + 4\beta^2}. \tag{23}$$

By introducing eqs.(22,23) in eq.(21) and by using now the imaginary part of eq.(3)

$$(1 - 2bR^2/c^2)r_t = -2ar_\phi,$$

we determine the parameters V, a and b as functions of r_0, L and β only:

$$V = c\sqrt{4 - L^2r_0^2}/2R,$$

$$a = \sqrt{(r_0^2 - 16\beta^2)(L^2r_0^2 - 4)}/2Lr_0,$$

$$b = c\sqrt{r_0^2 - 16\beta^2}/RLr_0.$$

By analysing these last expressions for the velocity of the shape V and the parameters a and b we find that all the traveling wave solutions of eq.(3) are classified into four types, depending on the values of the parameters $x = r_0/4\beta$ and $y = Lr_0/2$. The parameter x controls the stability of the solution against decaying to zero and y controls the modulation in time and space of these solutions. An example is presented in Fig.1, where typical solutions $u(\phi,t)$ given by eq.(21) are ploted at three different moments of time. For simplification the coordinate ϕ was drawn as a line, with the horizontal axis representing the time evolution. For $x > 1$ we have instable solutions which can decay into small normal modes of oscillation (linear waves), i.e. for $y < 1$ (Fig.1a) a soliton-like solution and for $y > 1$ (Fig.1b) a breather-like solution. For $x < 1$ we have stable solutions in the form of a traveling oscillating soliton $y > 1$ (Fig.1c) and breather solutions $y < 1$ (Fig.1d). Consequently, the range of physical interest

of the parameters is given by the stability condition for the solitary waves $r_0 \leq 4\beta$.

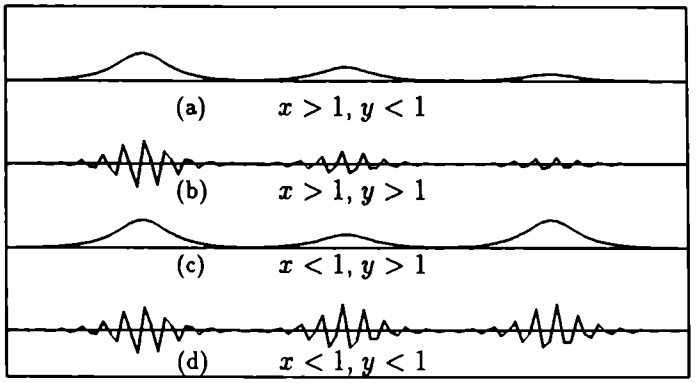

Fig. 1 The classification of the solutions of the Lagrangean eq.(3) according to their time behaviour: (a) instable soliton solution, (b) instable breather solution, (c) oscillating soliton solution and (d) breather solution. The corresponding examples are ploted against the ϕ coordinate for three different moments of time.

We stress that by the continuous variation of the parameter x we can describe in this model both nonlinear solutions of the dynamics of the surface and the linear dynamics of the traditional liquid drop model as an asymptotical limit of this model. In order to obtain this limit we have to reduce the amplitude r_0 of the solution such that the last two terms of the RHS of eq.(3) could be treated as small terms. Consequently, if we choose $\beta = 0$, $\mu = 0$ and $r_0 \to 0$ we obtain the conditions $L = 2$ and $a = \sqrt{r_0^2 - 1}/2$ and $b = c/2R$. In this case eq.(3) reduces to the wave equation on the circle with the corresponding normal modes as solutions.

In order to make the connection with the classical hydrodynamic approach [22,23] we apply the complex nonlinear Miura transformation [25] to the solution given by eq.(20)

$$\eta(\phi, t) = u(\phi, t)^2 \mp i u_\phi(\phi, t). \tag{24}$$

In this case it is known that η is a solution of the KdV equation which describes the classical soliton. The parameter r_0 can not be correlated with the soliton amplitude due to the fact that the amplitude of the field u can not be interpreted as the probability of localization as eq.(3) is not a Schrödinger equation (does not describe a Fermi field). We note only that in the time independent limit ($V = a = b = 0$) we obtain a simple connection between the amplitude of the soliton and the parameter β, $4\beta = r_0$. In this case the remaining parameters r_0 and L are determined only

by the geometry of the corresponding soliton which overlaps the alpha volume. No other free parameters are left in this approach. If we investigate the time dependent solutions the parameter β could be fixed by a similar condition, i.e., by comparing the shapes of such solutions with the geometry of the soliton overlaping an alpha particle. Finally we note the role of the topological charge invariant term Q in the Lagrangean. If we choose $\mu = 0$ in eq.(3) than the parameters a and b become zero and the oscillating behaviour of the solution desappears. The corresponding solutions are still time dependent and represent a soliton (a breather) moving on the nuclear surface and having a constant envelope.

3. Quantization of the soliton and breather solutions

In order to quantize the classical soliton and breather solutions of the nonlinear Lagrange equation we use the well known non perturbative weak-coupling procedure. We begin by quantizing the Lagrangean (1) in the condition $\mu = 0$. We impose this condition because when we finally express the Hamiltonian in terms of the normal modes the topological charge term introduces a strong coupling even in the second order. We write the potential energy in eq.(9) as a functional Taylor expansion about the solutions which are its extrema. These are given by the equation:

$$\frac{\delta \mathcal{U}(u,u^*)}{\delta u^*} = u_{\phi\phi} + \frac{1}{2}|u|^2 u - 4\beta^2 u = 0. \tag{25}$$

The above equation has two classes of solutions. Trivial static solutions

$$u_{0k}^{vac}(\phi) = \sqrt{2(k^2 + 4\beta^2)}e^{\pm i(k\phi+\phi_{0k})}, \tag{26}$$

depending on the integer label k and on an arbitrary phase factor ϕ_{0k}, and non trivial ones

$$u_0(\phi,t) = 4\beta sech(2\beta\phi). \tag{27}$$

connected with the solitons. The functional Taylor expansion $u(\phi,t) = u_0(\phi,t) + \xi(\phi,t)$ for the potential $\mathcal{U}(u,u^*)$ in second order in ξ gives

$$\mathcal{U}(u,u^*) = \mathcal{U}(u_0,u_0^*) + \mathcal{U}_2(\xi,\xi^*) + corrections. \tag{28}$$

Evidently, the first term $\mathcal{U}_1(\xi,\xi^*)$ is zero due to the extremum conditions for the potential. The second order term $\mathcal{U}_2(\xi,\xi^*)$ can be written in the integral form

$$U_2(\xi,\xi^*) = \int \xi^* \Omega \xi d\phi + c.c. \tag{29}$$

where Ω is a hermitian operator

$$\Omega = \frac{1}{2}\frac{\partial^2}{\partial\phi^2} + \frac{1}{2}|u_0|^2 + \frac{1}{4}u_0^2\mathcal{C} - 2\beta^2 \tag{30}$$

in which $\mathcal{C}$ denotes the complex conjugation (c.c.) operator, i.e. $\mathcal{C}\xi = \xi^*$. In order to find the fluctuations around the solutions u_0 and u_0^* we have to find the eigenvalues $\omega_k^2 > 0$ and eigenfunctions ξ_k of the operator Ω, $\Omega\xi_k = \omega_k^2\xi_k$. We consider only positive eigenvalues such that the static solution must be stable against the fluctuations. Due to the fact that Ω is hermitian, its eigenfunctions form a complet orthonormal set of "normal modes" of fluctuations around the static solution. The most general perturbation can be expressed then like

$$\xi(\phi,t) = \sum_k C_k(t)\xi_k(\phi,t). \tag{31}$$

where $C_k(t)$ are Hermitian quantum operators. With this choice for ξ, the Hamiltonian (6) assumes a simple form in the second order:

$$H(u_0+\xi,c.c.) = T(u_0+\xi,c.c.) + U(u_0+\xi,c.c.) \tag{32}$$

$$\simeq H^2(u_0,\xi) = U(u_0,u_0^*) + \sum_k\left(\left|\frac{dC_k}{dt}\right|^2 + \omega_k^2\frac{c^2}{R^2}|C_k|^2\right),$$

which reduces the problem to a set of independent harmonic oscillators with the energy spectrum given by:

$$E^{0,2} = U(u_0,u_0^*) + \sum_k \hbar\tilde{\omega}_k\left(N_k + \frac{1}{2}\right) \tag{33}$$

where $\tilde{\omega}_k = c\omega_k/R$ and the N_k's are new quantum numbers associated with the excited states of the vacuum of the system or of the soliton. The range of k is fixed by the condition $\omega_k^2 > 0$. If we take into account the higher orders, i.e. the third and the fourth order in ξ, ξ^*, we obtain, following the same algorithm of functional derivatives, the next higher order terms in the form

$$U^{3,4} = \frac{1}{2}\int_0^{2\pi}(u_0^*\xi^*\xi^2)d\phi + \frac{1}{8}\int_0^{2\pi}|\xi|^4 d\phi + c.c. \tag{34}$$

The contribution of these terms is no more diagonal and mixes the different states, with different k-values. Consequently, we can treat these higher orders only in the frame of stationary perturbation theory. We can write the final form of the Hamiltonian, up to the fourth order, from eqs.(32) and (34) as a sum between a non-perturbative diagonal term and a perturbation

$$H^4 \simeq H^2 + U^{3,4} \tag{35}$$

In the following we first investigate the eigenvalue problem for H^2. The trivial solutions (26) describe the vacuum associated with this theory and its excitations. However the vacuum sector of these energies and solutions is unconnected with the sector of nontrivial solutions because its states are orthogonal to the states of the soliton or breather solutions and, furthermore, not connected by any localised operator to them. In particular, the quantum soliton is stable against decay into mesons, except for the action of the instanton operator. The static solutions (27) form an infinite set of discrete functions and for each such solution we have an unique eigenvalue problem $\Omega\ \xi_k^{vac} = \omega_{0k} u_{0k}^{vac}$. The corresponding eigenvalues have the form $\omega_{0k}^2 = k^2 + 2\beta^2$. We can now construct a "tower" of approximate harmonic oscillator states arround each u_{0k}^{vac} with the spectrum given by

$$E_{vac} = \sum_k \hbar\tilde{\omega}_{0k}^2 \left(N_k + \frac{1}{2} \right), \tag{36}$$

We can interpret these quanta as the mesons of the vacuum of the system due to the fact that the excitation energy of the k^{th} mode is $\hbar\omega_{0k} = \hbar\sqrt{(k^2c^2/R^2 + 2c^2\beta^2/R^2)}$ which is similar with the kinetik energy of a meson with momentum $\hbar ck/R$ and the mass $\sqrt{2}\beta/R$. A possible interpretation for the parameter β is supported now by this last observation.

In the following we investigate the nontrivial solution u_0, eq.(27). In order to solve the eigenvalue problem we look for ξ_k in the form

$$\xi_k(\phi) = sech^{\gamma_k}(2\beta\phi) F(2\beta\phi), \tag{37}$$

where γ_k is a parameter and F an arbitrary function. This leads to the following eigenvalue equation for Ω

$$\frac{1}{2}\xi_k'' + \frac{3}{4}u_0^2\xi_k = (\omega_k^2 + 2\beta^2)\xi_k. \tag{38}$$

By using the substitution $v = \frac{1}{2}[1 + th(2\beta\phi)]$ we transform eq.(38) in a hypergeometric differential equation for F

$$v(v-1)F'' + \left[\left(2 + \frac{\gamma_k}{\beta} \right) v - \left(1 + \frac{\gamma_k}{2\beta} \right) \right] F' + \frac{\gamma_k(\gamma_k + 1) - 6}{4\beta^2} F = 0 \tag{39}$$

with the eigenvalues given by $\omega_k^2 = 2\beta^2(\gamma_k^2 - 1)$. In order to have localized solutions (rapidly decreasing functions for large v), the asymptotic behavior of the hypergeometric function F [30] asks for the condition:

$$\gamma_k = -\frac{1}{2} - 2k\beta \pm \sqrt{\frac{25}{4} - 4k\beta^2 + 2k\beta} \tag{40}$$

where $k = 0, 1, ..$ such that $\omega_k^2 > 0$. The remaining spectrum of Ω is continuous. The spectrum associated with the excitations of the soliton is given by the expression eq.(33), the value of the ω_k given above.

We stress that the eigenvalues ω_k are uniquely determined by β. The states of the theory, $\Psi^{sol}_{N_k,k}(\phi,t)$, are defined as eigenstates of the Hamiltonian associated with expression (5) and by the occupation numbers N_k of the different modes k. The wave functions associated with the excitations of the soliton have the form:

$$u_k(\phi) = u_0(\phi) + \sum_k sech^{\gamma_k}(2\beta\phi) F(a_k, b_k c_k v), \tag{41}$$

where F is the hypergeometric function in two arguments: $a_k = -k$, $b_k = (6 - \gamma_k(\gamma_k + 1))/4\beta^2 k$, $c_k = 1 + \gamma_k/2\beta$. By taking into account the quasi-periodicity condition for the solitonic solutions in eqs.(27,37), the halh-width L must lay in the range $(0, \pi)$ and consequently the parameter β is limited to the range $(1/2\pi, \infty)$. The stability condition for the perturbed solutions ($\omega_k^2 > 0$) drastically limits this domain to $\beta \in (0.15, 0.9)$. The solutions with the negative sign are eliminated from these reasons. For the different values of the occupation numbers k, the corresponding solitonic wave functions, eq.(41), is modulated in different ways. The solitonic solution (k=0) is modulated, for higher occupation numbers ($k = 1, 2$), into a breather solution keeping the same solitonic envelope. These breather solutions travel around the circle.

The calculation of the correction terms, given by the third and fourth orders follows from a perturbation technique applied to the Hamiltonian (32) with the perturbation given by eqs.(34), (35). We investigate here only a special case, i.e. of the geometry imposed by the α+^{20}Ne system. An example of such a calculation is given in the next section. In this case one can approximate eq.(34) with a third order term in $|\xi|$ and consequently we can apply in eq.(35) the usual perturbation technique for third order perturbations of an harmonic oscillator, [7,31].

4. Quasimolecular energy spectra for the α+^{20}Ne system

In the following we apply the above quantum nonlinear approach of clusters in nuclei for the description of quasimolecular spectra observed in elastic scattering of two colliding nuclei. Recently we have shown that such spectra are in very good agreement with experimental data for the scattering of alpha particles on ^{28}Si [24]. In that case we had to add to the solitonic spectrum two other terms, i.e. another harmonic oscillator term and a quadratic perturbation. These terms were believed to be obtained from the Lagrangean theory of the soliton.

In the present approach we can show that we obtain the complete structure of this spectrum by using only the energies obtained from the quantization of the soliton. In this respect we take here into account the higher corrections in the energy, up to the third order. Due to the fact that the absolute value of the coefficients γ_k increase with the increasing of k, eq.(40), and the support of the hypergeometric functions in eq.(41) decreases strongly with k eqs.(39,40), [30], we make an approximation in eq.(35): we use only the first term in the RHS of eq.(35), i.e. the third order correction, and we approximate this term with: $\sum_k const.|C_k|^3$. This approximation is reasonable because we take into account that the wave functions (41) strongly decrease in modulus with the increasing of k. This allows us to consider in the third

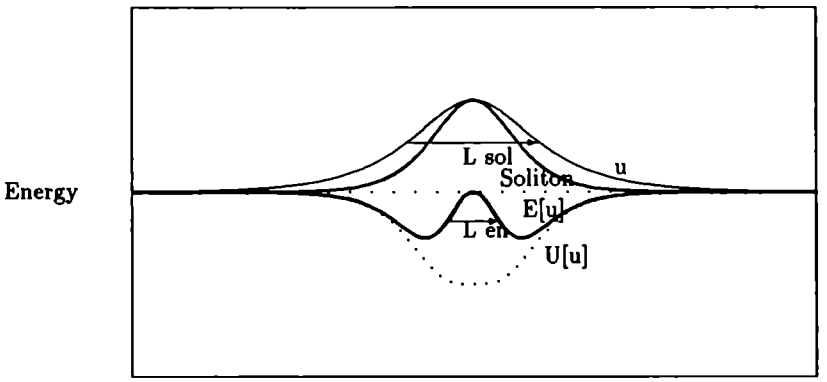

Fig. 2 The shape of the static solution given in eq.(28) ("u"), its corresponding hydrodynamical soliton solution ("Soliton") and the energy density ("E[u]") are ploted against the ϕ coordinate. The energy density shows a potential energy valley ("V[u]") in which is self-confined the soliton. The half-width L of the solution u and the corresponding half-width L_{en} of the energy density profile are drawn, for comparison.

and fourth order corrrections in eq.(35) only the highest terms, i.e. the diagonal ones. Consequently, we can write again, in this approximation, the Hamiltonian in the form:

$$H^3 \simeq U(u_0, u_0^*) + \sum_k \left(\left| \frac{dC_k}{dt} \right|^2 + \omega_k^2 \frac{c^2}{R^2} |C_k|^2 \right) + \frac{1}{2} \sum_k B_k \hbar \omega_k \left(|C_k|^3 \right). \quad (1)$$

This Hamiltonian represents a sum of independent anharmonic oscillators. Its corresponding spectrum is given, [31], in the first-order perturbation calculus, by

$$E^3 \simeq U(u_0, u_0^*) + \sum_k \hbar \tilde{\omega}_k \left(N_k + \frac{1}{2} \right) - \sum_k \left[\frac{15}{4} B_k^2 \hbar \omega_k \left(N_k + \frac{1}{2} \right)^2 + \frac{7}{16} \hbar \omega_k B_k^2 \right]. \quad (2)$$

For the elastic scattering of alpha particles on ^{20}Ne the total wave function for the $\alpha + ^{20} Ne$-system, taking into account the global rotation of the system, is

$$\Psi_{I,N_k}(\tilde{\theta}, \tilde{\phi}, \phi, r, t) = \Psi_{rot,I}(\tilde{\theta}, \tilde{\phi}, t) \Psi_{sol,N_k}(r, \phi, t) \quad (3)$$

The polar coordinates denoted with tilde are those associated with the global rotation.

Like in the previous work [24] the α-particle in its cluster states is a soliton with a height $r_0 R_{20_{Ne}}$ and an angular half-width L. According to the dynamics of the soliton the α-cluster moves on a shallow liquid layer arround a rigid spherical core, with a depth $h < R_{20_{Ne}}$. The parameters r_0 and L are fixed, for each geometry, by imposing the same two conditions as in the earlier work [24]: the mass of the soliton is equal with the mass of the α-particle ($A_{sol} = 4$) and we ask for the maximum overlap between the soliton shape and a sphere of radius $R_\alpha = 1.3 A_\alpha^{1/3}$ fm. Consequently, r_0 and L are not considered as free parameters. The reciprocal moment of inertia $C = \hbar^2/2\mathcal{I}(r_0, L, h)$ can also be extracted from the soliton geometry. The energy density profile of the α-cluster, considered as a quantum extended particle, characterized by the half-width associated with this energy density, L_{en}, is presented in Fig. 2 together with the corresponding solitonic solution. We remark that the potential energy, eq.(6), forms a valley which localises the soliton. The total energy density consists in a small maximum localised in this valley which characterises the associated quantum extended particle. The parameter β and the range of the quantum number k are fixed by the equation $L_{en} = L$. Under these restrictions we obtain the following values for the parameters: $r_0 = 0.62$, $L = 0.636$, $\beta = 0.345$ and $k = 0, 1$. The corresponding values for the soliton excitation energy are $\hbar\omega_k = 0.533$ and 1.0655 MeV for $k = 0, 1$, correspondingly. We note that for other cluster configurations (i.e. larger mass of the colliding particle or of the target) a larger number of solitonic bands (ω_k's), $k > 1$, is allowed. In this case we must take into account that only the $k = 0, 1$ solitonic modes are excited (the other two modes modes introduce negative ω^2). For the perturbation in the third order we take only its highest term, i.e. that one corresponding to the highest value of ω_k, $k = 0$. The total spectrum is limited to the following equation:

$$E_{I,N_0,N_1} = E_0 + \hbar\tilde{\omega}_0\left(N_0 + \frac{1}{2}\right) - B_0\left(N_0 + \frac{1}{2}\right)^2 + \hbar\tilde{\omega}_1\left(N_1 + \frac{1}{2}\right) + CI(I+1) \quad (4)$$

We stress that this equation for the energy levels, though looks similar with those obtained in different other theoretical models [5-13], it is obtained from an unitary collective nonlinear model and has no connection with the interpretation of the previous ones. More than this, though the third order correction is obtained by comparison with the experiment, we note that we obtain its negative sign from the theory only.

The solitonic model, based on this nuclear molecular behaviour, succeeds to reduce the number of the parameters to only four: L, E_0, h and B_0. The other parameters occuring in the theory (i.e. β, r_0 or equivalently C and ω_k) are obtained from the geometry of the system.

We compare our calculations with the experimental data given in [4], i.e. the excitation function for elastic scattering of alpha particles from ^{20}Ne. By fitting the theoretical spectrum (49) with the above mentioned experimental resonances, we obtain, for the above theoretically calculated values of $\tilde{\omega}_k$ and $E_0 = 9.465$ MeV, $h = 0.121 R_{20_{Ne}}$, $C = 0.13052$ and $B_0 = 0.07878$ MeV a good agreement, shown in Figs. 4. The theoretical spectrum is ploted in the right part together with the values

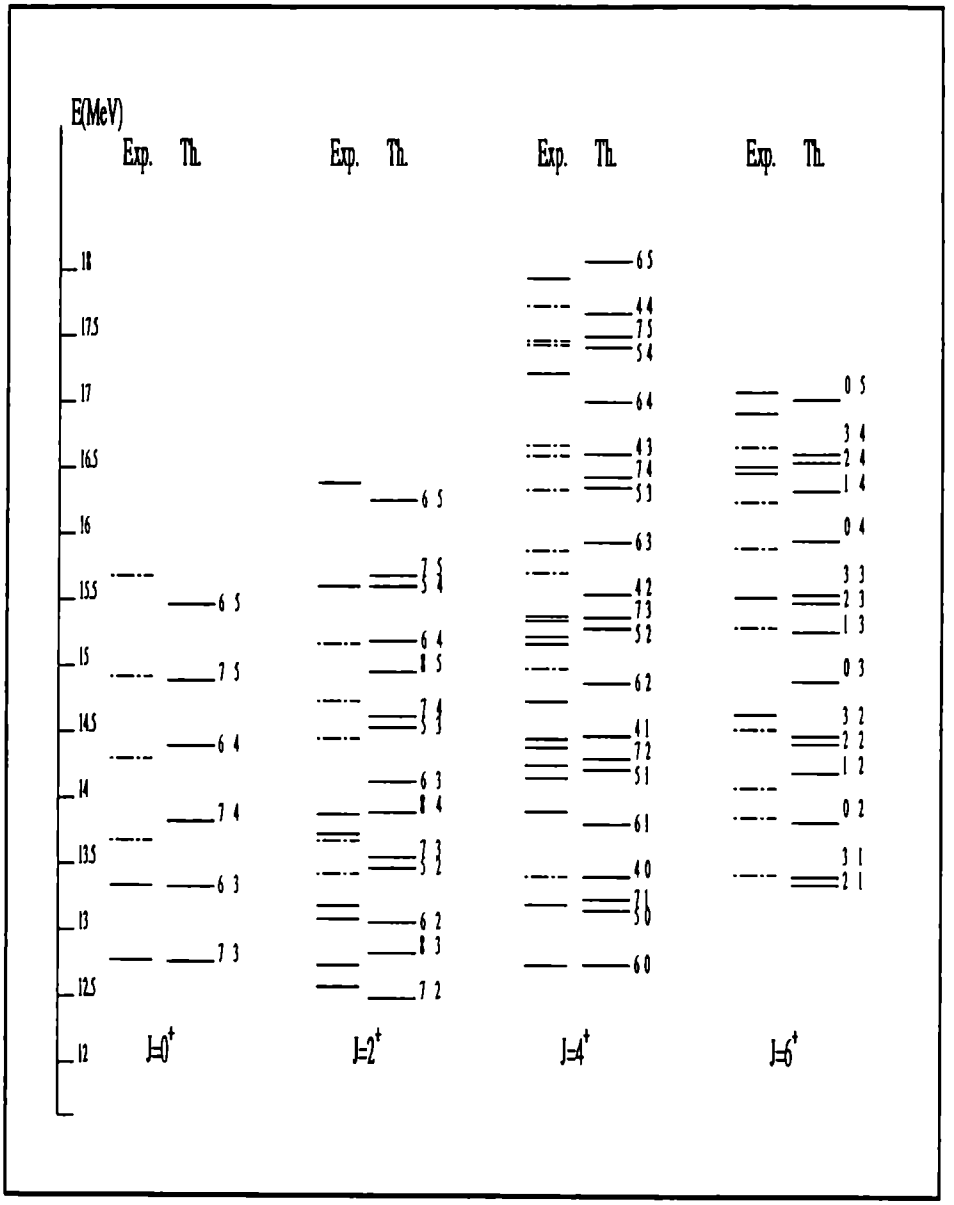

Fig.3a The experimental and theoretical spectra of the excitation energy fo $\alpha+^{20}$Ne elastic scattering, for even spins I. The experimental lines are divided i three categories: full lines, where the value of I is assigned with a good experimenta precision and the reduced widths of the resonances are semnificative, dotted lines where the experimental spin is not accurate obtained and dashed-dotted lines where the corresponding reduced widths of the resonances are smaller than 10, [4].

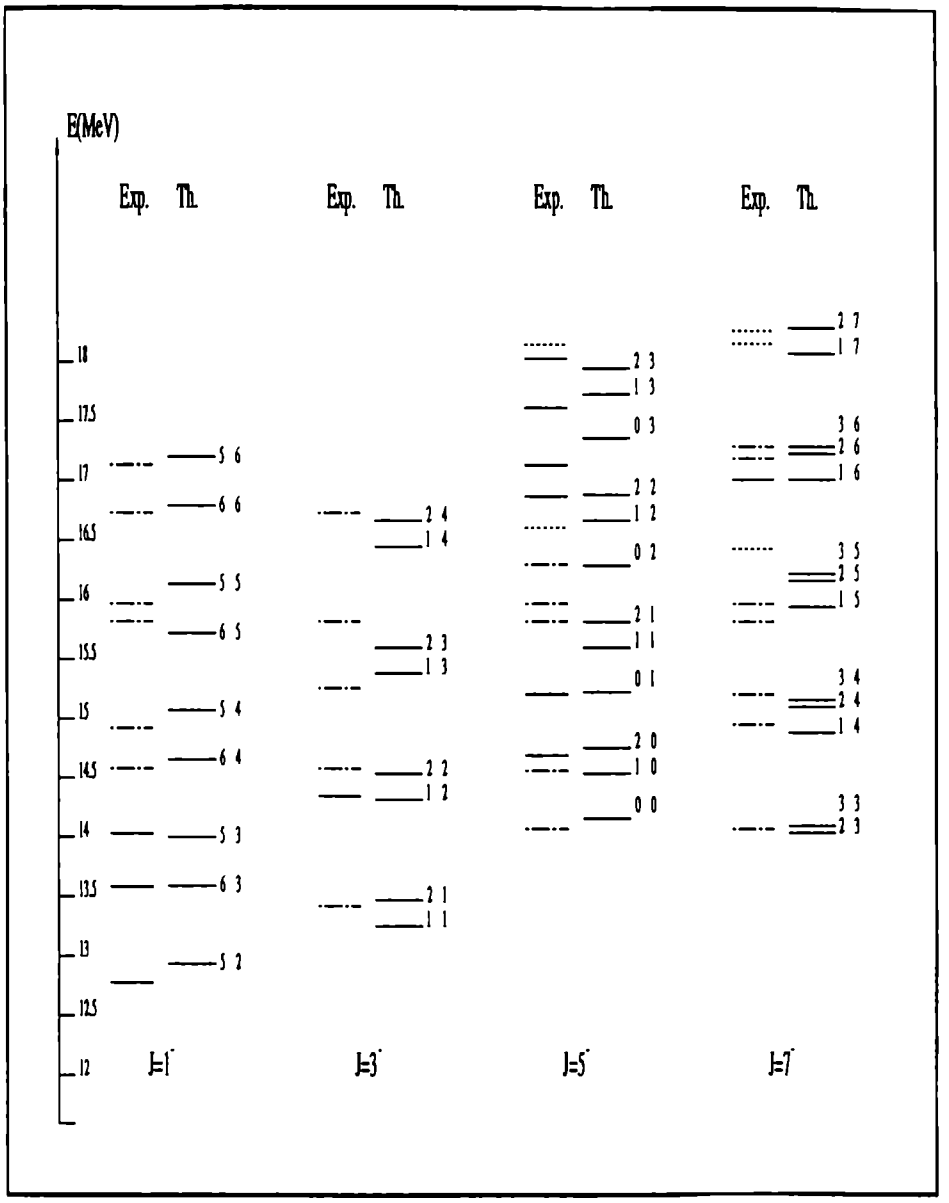

Fig.3b The experimental and theoretical spectra of the excitation energy for the ame elastic scattering system as in Fig.3a but for odd spins I. The experimental lines ave the same codification. We note that, different from the case of even spactra, the ensity of the levels is smaller.

of the quantum numbers (N_1, N_0), for even and odd values of I (Fig.3a and 3b). The nonlinear degree of freedom which is related to the soliton quantum number N_0 is essential to reproduce the appearance of irregulary spaced levels with the same spin I. Reasonable good agreement is obtained and the solitonic description can describe the observed experimental energies and spins of the intermediate states of $\alpha + {}^{20}$Ne system, like in the previously case for $\alpha+{}^{28}$Si system [28]. Both even and odd parities are fitted by using the same values for the parameters. The even and odd states form again mixed parity bands which can be interpreted like the rotating mass has an asymmetric shape as it is normal for the $\alpha+{}^{20}$Ne-system. The present theoretical description could imply that the alpha cluster as a soliton could be viewed as a new kind of nuclear deformation, with quasi-bound states which could be regarded as soliton and breather states.

5. References

1. W. Greiner, J. Y. Park and W. Scheid, *Nuclear Molecules* (World Scientific, Singapore, 1995).
2. D. Frekers, R. Santo and K. Langanke, *Nucl. Phys. A* **394** (1983) 189.
3. K. P. Artemov *et al.*, *Sov. J. Nucl. Phys.* **55** (1992) 492; P. Manngård, *Z.Physik A* **349** (1994) 335.
4. R. Abegg and C. A. Davis, *Phys. Rev.* **C 43** (1991) 2523.
5. F. Iachello, *Phys. Rev.* **C 23** (1981) 2778.
6. L. Satpathy, P. Sarangi and A. Faessler, *J. Phys. G: Nucl. Phys.* **6** (1986) 201.
7. N. Cindro and W. Greiner, *J. Phys. G: Nucl. Phys.* **9** (1983) L175.
8. K. Kato and Y. Abe, *Prog. Theor. Phys.* **80** (1988) 119.
9. H. J. Fink, W. Scheid and W. Greiner, *J. Phys. G* **1** (1975) L85.
10. P. Holzer, U. Mosel and W. Greiner, *Nucl. Phys.* **A 138** (1969) 241; D. Scharnweber, W. Greiner and U. Mosel, *Nucl. Phys.* **A 164** (1971) 257; J. A. Maruhn and W. Greiner, *Z. Phys.* **251** (1972) 431.
11. K. A. Erb and D. A. Bromley, *Phys. Rev.* **C 23** (1981) 2781.
12. H. Feshbach, *Theoretical Nuclear Physics: Nuclear Reactions*, (John Wiley, 1992).
13. T. Fliessbach and H. J. Mang, *Nucl.Phys.* **A 263** (1976) 75.
14. I. Tonozuka and A. Arima, *Nucl.Phys.* **A 323** (1979) 45.
15. F. A. Janouch and R. J. Liotta, *Phys.Rev.* **25** (1982) 2123.
16. A. Insolia, R. J. Liotta and E. Miglione, *Europhys.Lett.* **209** (1988) 7.
17. S. Okabe, *J.Phys.Soc.Jap.Suppl.* **58** (1989) 516.
18. A. Insolia, P. Curutchet, R. J. Liotta and D. S. Delion, *Phys.Rev.* **C 44** (1991) 545.
19. U. Abbondanno and N. Cindro, *J. Phys. G: Nucl. Part. Phys.* **19** (1993) 757; S. Romano and D. Vinciquerra, *J. Phys. G: Nucl. Part. Phys.* **20** (1994)

L57.
20. A. Sandulescu and W. Greiner, *Rep.Prog.Phys.* **55** (1992) 1423.
21. K. Varga, R. G. Lovas and R. J. Liotta, *Phys.Rev.Lett.* **69** (1992) 37.
22. A. Ludu, A. Sandulescu and W. Greiner, *Conf. on Nucl. and Atom. Clusters* (Turku, Finland, eds.M.Brenner, T.Lönnroth and F.B.Malik, Springer Verlag, Berlin) (1991) p.262; A. Ludu, A. Sandulescu and W. Greiner, *Int. J. Mod. Phys.* **E 1** (1992) 169 ; A. Ludu, W. Greiner and A. Sandulescu, *Int. J. Mod. Phys.* **E 2** (1993) 855.
23. A. Ludu, A. Sandulescu and W. Greiner, *Proc. 7th Inter. Conf. on Nucl. Reaction Mechanisms, June 6-11, Varenna* (ed. E. Gadioli) (1994) p.466.
24. A. Ludu, A. Sandulescu, W. Greiner, K. M. Källman, M. Brenner, T. Lönnroth and P. Manngård, *J. Phys. G: Nucl. Part. Phys.* **21** (1995) L41; A. Ludu, A. Sandulescu and W. Greiner, *J. Phys. G: Nucl. Part*, (1995), submitted.
25. G. L. Lamb jr., *Elements of Soliton Theory* (J. Wiley and Sons) (1980).
26. R. Könnecke, W. Greiner and W. Scheid, *Nuclear Molecular Phenomena* (ed. Cindro N, North Holland) (1978).
27. A. M. Polyakov, *JETP Lett.* **20** (1974) 194.
28. R. Rajaraman, *An Introduction to Solitons and Instantons in Quantum Field Theory* (North-Holland, Amsterdam) (1984).
29. R. Abraham and J. E. Marsden, *Foundation of Mechanics* (The Benjamin/Cummings P.C., Reading, Massachusetts) (1978).
30. P. Morse and H. Feshbach, *Methods in Mathematical Physics* (McGraw-Hill Book Co., New York) **1** (1953) p. 545-546.
31. J. P. Codaccioni and R. Caboz, *J. Math. Phys.* **25** (1984) 2436.

NUCLEAR QUASIMOLECULAR STATES

THORSTEN RITZ, WERNER SCHEID
Institut für Theoretische Physik der Justus-Liebig-Universität,
Giessen, Germany
and
JÜRGEN SCHMIDT
Mathematisches Institut der Justus-Liebig-Universität,
Giessen, Germany

ABSTRACT

Two aspects are reported: (a) Resonances in the scattering of ^{12}C on ^{12}C are interpreted within a phenomenological model of two oblately deformed ^{12}C nuclei. The corresponding quasibound states describe the nuclei rotating around the internuclear axis and carrying out butterfly and radial oscillations. (b) Angle-integrated cross sections of the scattering of ^{58}Ni on ^{58}Ni are calculated with the coupled channel method by taking the low energy spectrum of ^{58}Ni into account and compared with recent experimental data of Cindro et al. in the energy range between E_{cm}= 110 and 115 MeV.

1. Introduction

The field of "nuclear molecules" started with the $^{12}C + ^{12}C$ experiment of Bromley et al.[1] who found resonance structures in the low energy scattering of two ^{12}C nuclei. These structures were interpreted as signatures of the formation of a $^{12}C+^{12}C$ molecule[2]. Similar resonance structures were observed in various light heavy ion systems up to composite systems in the mass range of A=50 ($^{24}Mg + ^{24}Mg, ^{28}Si + ^{28}Si$)[3]. Guided by the prediction of the orbiting cluster model for possible resonance structures in the $^{58}Ni+^{58}Ni$ system[4], Cindro, Abbondanno et al.[5] recently found signatures for molecular resonances in the scattering of ^{58}Ni on ^{58}Ni, which is the first evidence for observable nuclear molecular states in medium heavy nuclei.

All nuclear reactions between two nuclei run through molecular configurations during the touching of the nuclei. When these configurations live longer than the scattering time, resonance structures appear in the cross sections and we speak of the excitation of nuclear molecular states[3]. These states are closely related to

superdeformed states of the composite nuclei and also appear in processes like fusion, fission and cluster radioactivity[6].

In this conference contribution we report on the description of gross and intermediate structures in the cross sections in terms of quasimolecular resonance states. In Section 2 we investigate quasibound states in the $^{12}C + ^{12}C$ system within a phenomenological model describing the ^{12}C nuclei with oblately deformed shapes. We give the spectrum and decay widths of states when the ^{12}C nuclei come into contact in the equator-equator relative orientation. Section 3 contains recent results of coupled channel calculations for the scattering of ^{58}Ni on ^{58}Ni. We show that the observed structures in the elastic and inelastic excitation functions can be qualitatively explained as caused by quasimolecular states.

2. Phenomenological description of molecular states with oblately deformed ^{12}C nuclei

After the study of molecular states in the system built up by two prolately deformed ^{24}Mg nuclei[7,8], we investigated the $^{12}C + ^{12}C$ system assuming the ^{12}C nuclei as oblately deformed. Similar calculations were carried out by Uegaki and Abe[9] for the $^{28}Si + ^{28}Si$ system. Here, we give a short review of the phenomenological treatment of Schmidt[10].

The nuclear molecular system is phenomenologically described in the molecular coordinate system defined with the z'-axis in the direction of the relative coordinate $\vec{r}$ between the nuclei. The intrinsic structure of the two nuclei is treated with the rotation-vibration model. The Hamiltonian can be written

$$\begin{aligned} H &= \frac{p_r^2}{2\mu} + \frac{(\vec{I}-\vec{J}_1-\vec{J}_2)_{x'}^2 + (\vec{I}-\vec{J}_1-\vec{J}_2)_{y'}^2}{2\mu r^2} + \sum_{i=1}^{2} T_{RVM}(\vec{J}_i, \beta_i, \gamma_i) \\ &+ U(r, \beta_1, \gamma_1, \Omega_1', \beta_2, \gamma_2, \Omega_2') + iW \\ &+ \sum_{i=1}^{2} \left(\frac{C_\beta}{2}(\beta_i \cos\gamma_i - \beta_o)^2 + \frac{C_\gamma}{2}(\beta_i \sin\gamma_i)^2\right). \end{aligned} \tag{1}$$

The primed coordinates are referred to the molecular coordinate system. $\vec{I}$ denotes the operator of the total angular momentum and $\vec{J}_1$ and $\vec{J}_2$ those of the spins of the nuclei. The Euler angles $\Omega_i' = (\varphi_i', \theta_i', \psi_i')$ describe the rotation of the nuclei with respect to the molecular frame. β_i and γ_i are the intrinsic quadrupole deformation coordinates of which γ_i will not be considered in the following. The Hamiltonian is commonly used in coupled channel calculations of elastic and inelastic cross sections. On the other hand, the same Hamiltonian encloses also molecular quasibound states which generate Breit-Wigner resonance terms in the S-matrix and, therefore, should be observable by finer structures in the cross sections. In Fig. 1 we show various modes of the $^{12}C + ^{12}C$ nuclear

molecule around the equator-equator orientation which are related to quasibound molecular states.

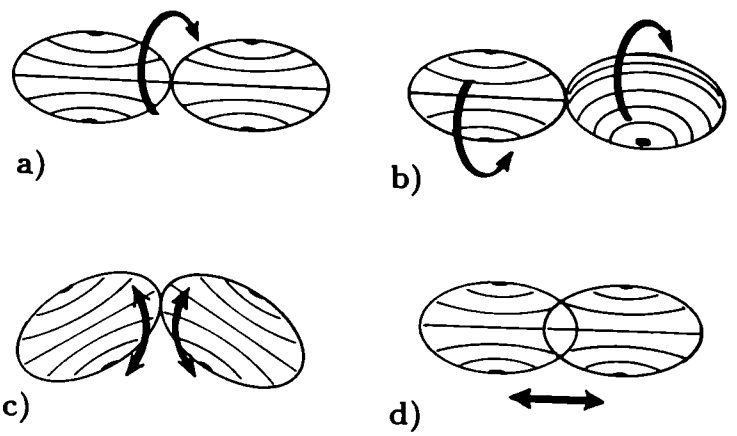

Fig.1: The various modes of the $^{12}C + ^{12}C$ nuclear molecule around the equator-equator orientation: (a) joint rotation about the internuclear axis (K-mode), (b) opposite rotation about the internuclear axis (κ-mode), (c) butterfly-mode, (d) radial oscillation-mode.

First the potential U is calculated within a double-folding model in sudden approximation by using the following effective nucleon-nucleon interaction

$$v(\vec{r},\rho) = \frac{1}{r}\left[V_a exp(-r/\mu_a) + V_r exp(-r/\mu_r)\right] exp(-\gamma\rho) + V_p\delta^{(3)}(\vec{r}) + V_{Coul}. \quad (2)$$

The ranges of the Yukawa forces are those of the M3Y interaction, i.e. μ_a=0.45 fm and μ_r=0.25 fm. The strength parameters were determined via an optical model calculation of the elastic 90^0 differential cross section of ^{12}C on ^{12}C with the result V_a=-780 MeVfm, V_r=1460 MeVfm and V_p=25 MeVfm^3(γ=5.4 fm^3). In these calculations the ^{12}C nuclei were assumed as spherical.

Next the potential U in H is calculated with oblately deformed ^{12}C nuclei (β_o=-0.60) in form of a multipole expansion (zero γ_i-deformations)

$$U = \sum_{\substack{\ell_1\ell_2 m \\ m\geq 0}} U^m_{\ell_1\ell_2}(r,\beta_1,\beta_2)cos(m(\varphi'_2 - \varphi'_1))P^m_{\ell_1}(cos\theta'_1)P^m_{\ell_2}(cos\theta'_2). \quad (3)$$

The expansion coefficients $U^m_{\ell_1\ell_2}$ depend on the interaction (2) in the double-folding model and on the density distributions of the ^{12}C nuclei. Only the terms with ℓ_1, ℓ_2=0 and 2 are taken into account in our calculations. The quasibound states are localized around the minima of a potential energy surface (PES) consisting of the potential and a rotation energy. The rotation energy is approximated by the energy of a stiff rotation of the whole molecule with frozen intrinsic degrees of freedom. The corresponding Hamiltonian is given by

$$H^I_{PES} = \frac{1}{2}\vec{I}\Theta^{-1}\vec{I} + U(r,\beta_1,\varphi'_1,\theta'_1,\beta_2,\varphi'_2,\theta'_2) + \sum_{i=1}^{2}\frac{C_\beta}{2}(\beta_i - \beta_o)^2 \qquad (4)$$

with fixed coordinates $r,\beta_1,\beta_2,\varphi'_1,\varphi'_2,\theta'_1,\theta'_2$ and Θ as the inertia tensor. For symmetric orientations of the intrinsic axes the inertia tensor is diagonal in the MO-system. For example, in the equator-equator (E-E) orientation we have $\varphi'_1 = \varphi'_2 = 0, \theta'_1 = \theta'_2 = \frac{\pi}{2}$ and $\Theta_{x'x'} = \mu r^2, \Theta_{y'y'} = \mu r^2 + 2\Theta_o, \Theta_{z'z'} = 2\Theta_o$, where $\Theta_o = 3B_o\beta_i^2$ is the moment of inertia of ^{12}C according to the rotation-vibration model. The constants B_o and C_β are set: $B_o = 0.626\hbar^2 MeV^{-1}$ and C_β=36.6 MeV with $\beta_o = -0.60$. The kinetic energy operator in (4) describes an asymmetric triaxial rotator which is diagonalized with basis functions of the symmetric rotator.

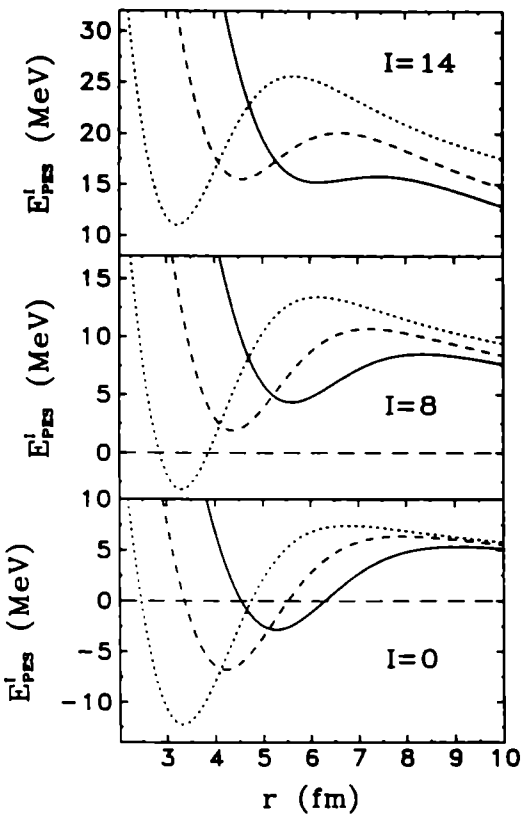

Fig.2: Radial intersections of the PES for angular momenta I=0,8,14 and the parallel equator-equator (—), pole-equator(- - -) and pole-pole (...) orientations. The used values of β_1 and β_2 are those at the corresponding minimum.

Fig.2 shows the resulting potential as a function of r for the total angular momenta I=0, 8 and 14 and three different orientations, namely for the parallel equator-equator (EE, solid curve), pole-equator (PE, dashed curve) and pole-pole

orientations (PP, dotted curve). Parallel (orthogonal) EE orientation means that the symmetry axes of the nuclei are parallel (orthogonal). The potentials in Fig.2 are only minimal in energy near the minima since we kept the β_i-values fixed at the values of the minima. The difference between the internuclear potentials of the orthogonal and parallel EE orientations is roughly 0.25 MeV and the rotational energies differ at most by 0.75 MeV without significantly different r- and β_i-coordinates of their minima.

The equator-equator orientation is important for the appearence of molecular resonances since the corresponding potential minimum is located at larger relative distances than the minima of other symmetric orientations of the intrinsic axes. Therefore, we restrict the further considerations to the calculation of quasibound states for the equator-equator orientation of the ^{12}C nuclei. We assume that the motion of the nucleus-nucleus system can be approximately described by independent degrees of freedom around the molecular minimum of the EE orientation. The Hamiltonian used is written with the abbreviations $\xi_\pm = 2^{-\frac{1}{2}}(\xi_1 \pm \xi_2), \xi_i = \beta_i - \tilde{\beta}_o, \tilde{\theta}'_i = \theta'_i - \frac{\pi}{2}$ (i=1,2) and by changing the volume elements $d\Omega'_i$ from $\sin\theta'_i d\theta'_i d\varphi'_i$ to $d\theta'_i d\varphi'_i$:

$$\begin{aligned} H_{EE} &= -\frac{\hbar^2}{2\mu}\frac{1}{r}\frac{\partial^2}{\partial r^2}r - \frac{\hbar^2}{2B_o}\left(\frac{\partial^2}{\partial\xi_+^2}+\frac{\partial^2}{\partial\xi_-^2}\right) + \frac{I^2 - I_{z'}^2}{2(\mu r_o^2 + \frac{4}{3}\Theta_o)} \\ &\quad -\frac{\hbar^2}{2\Theta_o}\sum_{i=1}^{2}\left[\frac{\partial^2}{\partial\tilde{\theta}_i'^2} + (1+\tilde{\theta}_i'^2)\frac{\partial^2}{\partial\varphi_i'^2}\right] + \frac{C_r}{2}(r-r_o)^2 \\ &+ \frac{\tilde{C}_\beta}{2}(\xi_+^2+\xi_-^2) + \frac{1}{2}(C_1 - \frac{\hbar^2}{4\Theta_o})(\tilde{\theta}_1'^2 + \tilde{\theta}_2'^2) + V_o - \frac{\hbar^2}{2\Theta_o}. \end{aligned} \tag{5}$$

The intrinsic angular momentum operators are expanded around $\tilde{\theta}'_i = 0$. The rotation energy with the effective moment of inertia $\mu r_o^2 + \frac{4}{3}\Theta_o(\Theta_o = 3B_o\tilde{\beta}_o^2)$ approximates the more complex rotation operator given in Eq.(1). The rotation of the nuclei in the relative angle $\varphi'_2 - \varphi'_1$ is governed by small potential terms which are neglected here; this means a free rotation in this degree of freedom. The constants are obtained by a quadratic approximation of the PES around the EE minimum. For example, for I=8 we obtained: r_o=5.60 fm, $\tilde{\beta}_o$ = -0.66, C_r=6.72 MeVfm^{-2}, $\tilde{C}_\beta$=36.7 MeV, C_1=3.96 MeV, V_o=-2.19 MeV.

The eigenfunctions of H_{EE} can be separated in the following form:

$$\Psi_\nu = N_\nu R_\nu(r) S\left[D^{I*}_{MK}(\Omega)\Xi_\alpha(\Omega'_1,\Omega'_2)v_{\mu_+}(\xi_+)v_{\mu_-}(\xi_-)\right]. \tag{6}$$

Here, S is an operator for symmetrization. The functions $rR_\nu(r) = g_\nu(r - r_o), v_{\mu+}(\xi_+)$ and $v_{\mu-}(\xi_-)$ are harmonic oscillator functions. The wave function Ξ_α for the intrinsic rotation-vibration motion can be written as

$$\Xi_\alpha(\Omega'_1,\Omega'_2) = exp(ik_1\varphi'_1)exp(ik_2\varphi'_2)\varphi_{n_1|k_1|}(\tilde{\theta}'_1)\varphi_{n_2|k_2|}(\tilde{\theta}'_2), \tag{7}$$

where $\varphi_{n_i|k_i|}$ are harmonic oscillator functions. Since these functions must be invariant with respect to an inversion of the intrinsic z_i''-axes ($\tilde{\theta}_i' \rightarrow -\tilde{\theta}_i'$ and $\varphi_i' \rightarrow \varphi_i' + \pi$), we find the condition: $k_i + n_i$ = even number. Further symmetry conditions result from the exchange of the nuclei and from the parity transformation ($\vec{r} \rightarrow -\vec{r}$). We restrict our considerations to states with an even angular momentum quantum number I and positive parity since only these states can be excited in the scattering of ^{12}C on ^{12}C. Setting $k_1 = (K+\kappa)/2$ and $k_2 = (K-\kappa)/2$ we have

$$K \pm \kappa : even, (K+\kappa)/2 + n_1 : even, (K-\kappa)/2 + n_2 : even, K \geq 0, n_1 \geq n_2,$$

$\kappa \geq 0$ if K=0 or $n_1 = n_2$, μ_-:even if $n_1 = n_2$ and K=0 or κ=0.

The eigenvalues of H_{EE} can then be obtained:

$$\begin{aligned} E_\nu &= V_o + \frac{I(I+1)\hbar^2}{2(\mu r_o^2 + \frac{4}{3}\Theta_o)} + D_K K^2 + D_\kappa(\kappa^2 - 2) + \hbar\omega_r(n_r + 1/2) \\ &+ \hbar\omega_{\theta_1}(n_1 + \frac{1}{2}) + \hbar\omega_{\theta_2}(n_2 + \frac{1}{2}) + \hbar\omega_\beta(\mu_+ + \mu_-), \end{aligned} \tag{8}$$

where the constants $D_K, D_\kappa, \hbar\omega_r, \hbar\omega_{\theta_i}$ and $\hbar\omega_\beta$ depend on the quantities given in H_{EE}. As example, for I=8 we calculated the values 0.216, 0.306, 2.115, 7.66 and 6.84 MeV for $D_K, D_\kappa, \hbar\omega_{\theta_i}(K = \kappa = 0), \hbar\omega_\beta$ and $\hbar\omega_r$, respectively. Fig.1 shows the main modes of motion. The quantum number K is connected with a rotation of the total system around the internuclear axis; the quantum number κ belongs to an opposite rotation of the nuclei; $\hbar\omega_{\theta_i}$ are the energies of the butterfly modes and $\hbar\omega_r$ and $\hbar\omega_\beta$ are those of the radial and β-vibrational energies. Since the excitation energies of the β-vibrational modes are nearly identical to the corresponding values of an isolated nucleus, we left their zero-point energy out.

On each ground state for a given I, bands of states are built up with the same angular momentum. The lowest states are generated by the rotational and butterfly modes. As shown in Fig.3 for I=8, they can be ordered in terms of (n_1, n_2)-bands with variable κ-values for fixed values of K. The lowest excited state is the (K, κ, n_1, n_2)=(2,2,0,0) state in our model. In the states with $K = \kappa$ and $n_1 = n_2 = 0$, one of the nuclei is fixed and the other one rotates around the z'-axis. Comparing the theoretical states with experimentally observed resonances we find that the theory reproduces the experimental level density only at higher energies. However, the absolute location of the theoretical spectrum on the energy scale is not too certain since the absolute energy values depend on the parameters of the double-folding potential (2) fitted to the elastic $^{12}C + ^{12}C$ cross section.

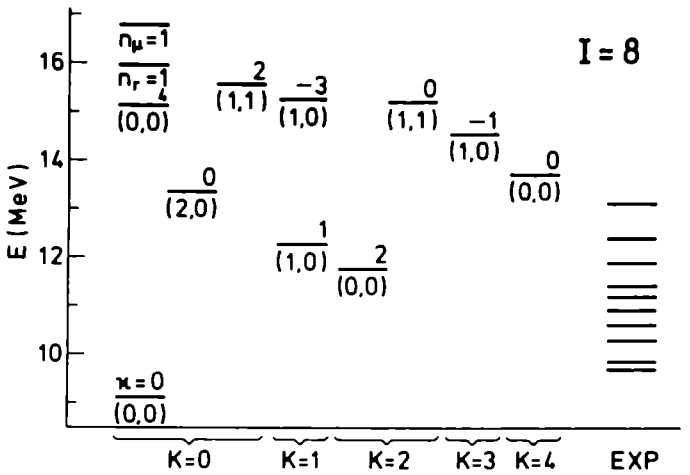

Fig.3: Calculated and experimental energies of nuclear molecular states for the $^{12}C + {}^{12}C$ system around the parallel equator-equator orientation for an angular momentum I=8. Only energies up to 16 MeV are given. For each state the quantum numbers K, κ (numbers above the lines), n_1 and n_2 ((n_1, n_2)=numbers below the lines) are shown, the other ones are set zero with exception of the first excited states with n_r=1 and n_μ=1 (μ_+ or μ_-). The calculated levels are ordered according to the scheme of Uegaki and Abe[9]. The experimental resonance energies are taken from Abbondanno.

In order to calculate the decay widths of resonance states ν into the channels $\mid c >$ of elastic and inelastic scattering we apply the R-matrix theory. The partial width is defined as

$$\Gamma_{\nu c} = 2P_c(k_c a)\gamma_{\nu c}^2 \tag{9}$$

with the Coulomb penetrability $P_c(k_c a) = k_c a/[G_{\ell c}(k_c a)^2 + F_{\ell c}(k_c a)^2]$ and the reduced partial width

$$\gamma_{\nu c}^2 = \frac{\hbar^2 a}{2\mu}(R_\nu(a))^2 \mid < c \mid \nu > \mid^2 . \tag{10}$$

Since we use harmonic oscillator potentials for the calculation of the radial functions $R_\nu(r)$ (see Eq.(5)), we choose I-dependent channel radii $a(I)$ between 6.7 fm for I=0 and 7.3 fm for I=14. The wave number k_c is determined by $(\hbar k_c)^2/(2\mu) = E_\nu - E_{exc}(c)$, where $E_{exc}(c)$ is the excitation energy of the final state c. The channel wave functions $\mid c >$ describe the ground state, 2^+ and 4^+ states of ^{12}C within the rotator model and enclose the $(gs, gs), (2^+, gs), (2^+, 2^+)$ and $(4^+, gs)$ channels. The elastic channel functions only overlap with resonance functions Ψ_ν having no intrinsic rotations, i.e. $K = \kappa = 0$. In Table 1 we present the summed partial widths for the decay of a molecular state ν into scattering states for the total angular momentum I=14, where the summation runs over all possible decay channels leading to the given final states.

Table 1: Summed partial widths (in keV) for the decay of molecular states into scattering states $(J_1^{\pi_1}, J_2^{\pi_2})$ for an angular momentum of I=14. The summation of widths runs over all possible decay channels c leading to the given final states. The brackets in the first column mean (K, κ, n_1, n_2). The energies E_ν are given in MeV.

		Widths			
State	E_ν	$(0^+,0^+)$	$(2^+,0^+)$	$(2^+,2^+)$	$(4^+,0^+)$
(0,0,0,0)	19.72	582.7	11.1	0.0	-
(2,2,0,0)	21.57	-	71.2	0.5	0.00
(4,0,0,0)	22.85	-	-	6.3	-
(1,1,1,0)	22.90	-	122.5	2.2	0.01
(0,4,0,0)	24.01	-	-	7.5	-
n_r=1	24.29	2476.2	81.9	0.5	0.01
(3,-1,1,0)	24.46	-	-	16.3	-
(0,0,2,0)	24.81	357.5	92.1	3.3	0.38
(1,-3,1,0)	25.04	-	-	17.9	-
(2,0,1,1)	25.93	-	-	20.5	-
(0,2,1,1)	26.22	-	-	20.6	-
(4,4,0,0)	26.91	-	-	-	7.58

The calculated decay widths of the molecular states into $^{12}C + ^{12}C$ channels show the experimental characteristics in average, but for a detailed comparison the Hamiltonian (1) should be completely diagonalized. Since the nuclei deviate much from the EE-orientation in certain cases, one can draw the conclusion that the butterfly modes are strongly coupled to the oscillations of the radial relative motion and have to be studied in more detail next.

3. Coupled channel results for the $^{58}Ni + ^{58}Ni$ system

Experiments of the scattering of ^{58}Ni on ^{58}Ni and ^{62}Ni have been performed at the Laboratori Nazionali di Legnaro XTU Tandem accelerator (Cindro, Abbondanno et al.[5]). The angle-summed ($76° \leq \theta_{cm} \leq 104°$) elastic and inelastic (single excited first 2^+-state) cross sections for the scattering of ^{58}Ni on ^{58}Ni show correlated peak structures as a function of energy in the measured range between E_{cm}=110 and 115 MeV. The elastic angular distributions taken at the peaks of the excitation function oscillate regularly with a periodicity of $\Delta\theta_{cm} = 3°$ observed between θ_{cm}=82 and 98° and can be almost perfectly fitted by squared single polynomial forms $\mid P_\ell(\cos\theta) \mid^2$ with ℓ around 60. These values of ℓ are in good agreement with those angular momentum predictions obtained with the orbiting cluster model ($\sim 64\hbar$).

The experimental results were interpreted by Cindro et al.[11] as effects of molecular resonances in medium heavy ion systems. In order to explain the

$^{58}Ni + ^{58}Ni$ data we carried out traditional coupled channel calculations for this system starting with the Hamiltonian[12]

$$H = T(\vec{r}) + V(r) + iW + H_1(1) + H_2(2) + \sum_{LM} Q_{LM}(r,1,2)Y^*_{LM}(\Omega). \qquad (11)$$

This Hamiltonian consists of the kinetic energy of relative motion, the radial optical potential, the Hamiltonians of the individual nuclei and the internuclear coupling potentials depending on the intrinsic structure of the nuclei. Expanding the wave function into products of radial and channel functions

$$\Psi = \sum_{\ell,J,I,\lambda} R_{\ell JI\lambda}(r)\left[i^\ell Y_\ell(\Omega) \otimes \xi_{J\lambda}(1,2)\right]^{[I]} \qquad (12)$$

we obtain coupled equations for the radial functions

$$(-\frac{\hbar^2}{2\mu r}\frac{d^2}{dr^2}r + V(r) + iW + \frac{\ell(\ell+1)\hbar^2}{2\mu r^2} + \epsilon_{\alpha_1} + \epsilon_{\alpha_2} - E)R_{\ell JI\lambda}(r)$$

$$= -\sum_{\ell',J',\lambda',L} i^{\ell'-\ell}(-1)^{I+J+\ell'}\begin{Bmatrix} IJ\ell \\ L\ell'J' \end{Bmatrix}(\ell \parallel Y_L \parallel \ell')(J\lambda \parallel Q_L \parallel J'\lambda')R_{\ell'J'I\lambda'}(r). \qquad (13)$$

Here, ϵ_{α_1} and ϵ_{α_2} are the excitation energies of the nuclei. Eq. (13) constitutes a system of differential equations which have to be solved in order to obtain the S-matrix and the differential cross sections. The potentials between the nuclei, V(r) and Q_{LM}(r,1,2), are calculated with the double-folding procedure in sudden approximation

$$\mathcal{V}(\vec{r},1,2) = \int\int \rho_1(\vec{r}_1)\rho_2(\vec{r}_2)v(\mid \vec{r} + \vec{r}_1 - \vec{r}_2 \mid)dV_1 dV_2, \qquad (14)$$

where the effective nucleon-nucleon interaction $v(r)$ contains an attractive and repulsive Yukawa term and the Coulomb part:

$$v(r) = V_a exp(-r/\mu_a)/r + V_r exp(-r/\mu_r)/r + (Z/A)^2 e^2/r. \qquad (15)$$

The densities $\rho_i(i = 1,2) = 3A/(4\pi R_o^3)$ are set constant over the nuclear volumes with radii (i=1,2)

$$R_i = R_o(1 + \sum_{\ell,m} \alpha_{\ell m}(i)Y^*_{\ell m}(\Omega_i)). \qquad (16)$$

Since the low-energy spectrum of ^{58}Ni shows a vibrator structure, we describe this nucleus with the model of quadrupole surface vibrations using the coordinates $\alpha_{2m}(i)$ for the intrinsic degrees of freedom and expanding the transition potentials Q_{LM}(r,1,2) up to quadratic terms in $\alpha_{2m}(i)$. The transition matrix elements of α_{2m} can be related to the B(E2)-values:

$$|< I_f n_f \parallel \alpha_2 \parallel I_i n_i >|^2 = (2I_i + 1)(\frac{4\pi}{3eZR_0^2})^2 B(E2, I_i \to I_f). \qquad (17)$$

We insert experimental B(E2)-values into the reduced matrix elements linear in α_{2m} and approximate the reduced matrix elements quadratic in α_{2m}. Also experimental values for the energies of the excited ^{58}Ni states $2_1^+, 0_2^+, 2_2^+, 4^+$ are used in the coupled channel calculations.

For the Yukawa potentials in Eq. (15) we choose the parameters μ_a=0.6 fm, V_a=-8300 MeVfm, μ_r=0.4 fm, V_r=21500 MeVfm. Then the effective potential $V(r) + \ell(\ell+1)\hbar^2/(2\mu r^2)$ has a barrier of 114.20 MeV at 11.05 fm for an angular momentum of $58\hbar$. Near this energy at E_{cm}=114.5 MeV both the measured elastic and inelastic excitation functions have a resonance-like maximum and the elastic angular distribution could be fitted by a squared Legendre polynomial with $\ell = 58 \pm 2.^5$. Fig. 4 shows the real effective potential for selected values of the angular momentum in the relevant range of the radial relative coordinate. The absorptive potential has been set to zero which needs some corrections in future calculations.

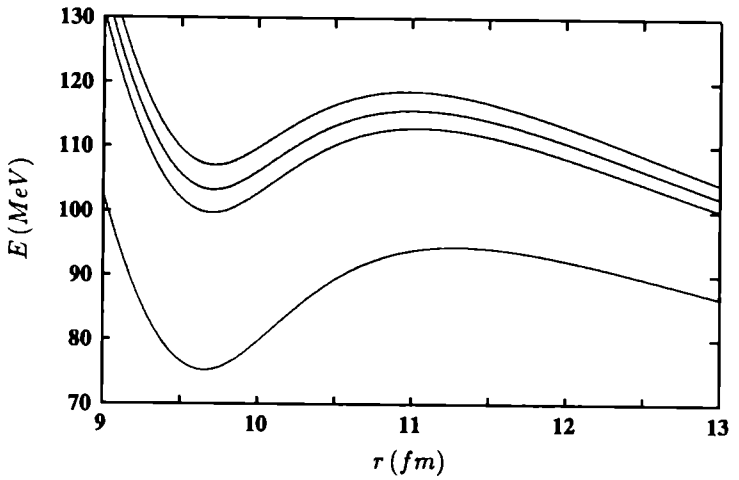

Fig.4: Effective potentials of the $^{58}Ni + ^{58}Ni$ system for ℓ=0, 56, 60 and 64.

First coupled channel calculations were done with the elastic channel and the channels describing the single excitation of the first 2^+-state of ^{58}Ni at 1.45 MeV. Fig. 5 shows the elastic angular distributions at selected energies which agree roughly with the experimental data. The excitation functions for the elastic and inelastic scattering are calculated by summing up the angular distributions in the range from 76° to 104°. In Fig. 6 we compare the experimental excitation functions of the elastic and inelastic 2^+-channels with the calculated ones. The regularly repeated structures in the calculated elastic excitation function are generated by partial waves with angular momenta of 54, 56 and 58 $\hbar$ near E_{cm}=111.2, 113.0 and 114.7 MeV. Whereas the calculated elastic excitation function lies above the experimental data with about 200 mb, the calculated inelastic excitation function has values which are smaller by about 30 mb than the experimental ones. This situation is not much changed if the channels with the

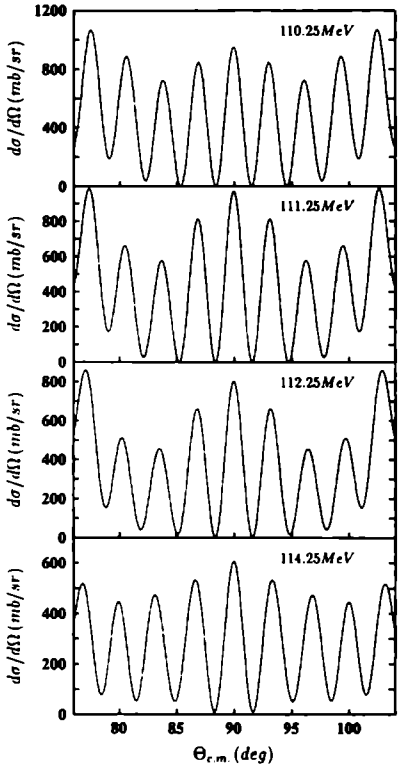

Fig.5: Calculated elastic angular distributions for the scattering of ^{58}Ni on ^{58}Ni with incident energies E_{cm}=110.25, 111.25, 112.25, 114.25 MeV.

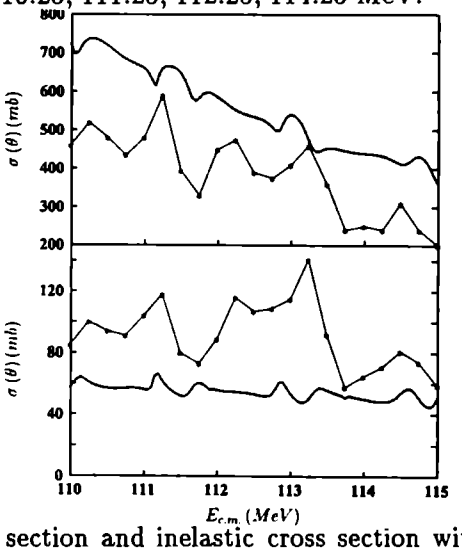

Fig.6: Elastic cross section and inelastic cross section with the excitation of the first 2^+-state for the scattering of ^{58}Ni on ^{58}Ni as a function of E_{cm}. The cross sections are integrated in the angular range from θ_{cm} = 76° to 104°. The experimental data of Abbondanno et al.[5] are shown by stars connected by straight lines. The theoretical results depicted by solid curves are obtained by a coupled channel calculation including the elastic and first 2^+ excitation channels.

mutual excitation of the first 2^+-state and the single excitation of the $0_2^+, 2_2^+$ and 4^+-states (E^*=2.94, 2.78, 2.46 MeV) are included into the coupled channel calculation. Fig. 7 shows the angle-integrated excitation functions for several additional channels. A more satisfying agreement between coupled channel calculations and experimental data could probably be obtained if imaginary potentials were taken into account which depend on the individual channels.

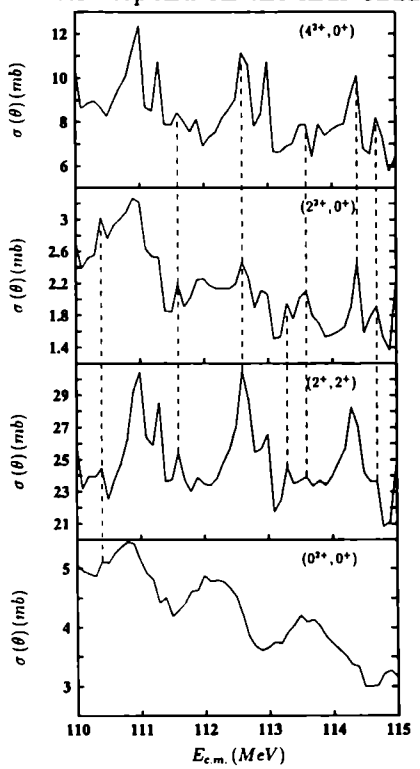

Fig.7: Angle integrated (θ_{cm}=76-104°) cross sections of ^{58}Ni on ^{58}Ni for the channels $(4^+, gs), (2_2^+, gs), (2_1^+, 2_1^+), (0_2^+, gs)$ as a function of E_{cm} obtained by coupled channel calculations.

The interpretation of the structures in the scattering of ^{58}Ni on ^{58}Ni near the Coulomb barrier by quasimolecular resonance states is qualitatively proved with the coupled channel calculations. Virtual and quasibound states of the radial relative motion in the potential shown in Fig. 4 have relative distances of about 1.5 MeV for angular momenta differing by $2\hbar$ around $56\hbar$ and E_{cm}=112 MeV. Similar energy differences are observed between the structures in the experimental excitation functions[5]. Therefore, we conclude that the structures can be explained by virtual and quasibound states in a properly chosen potential between the ^{58}Ni clusters. A quantitative proof is very complex for these medium heavy ions because of several reasons: The energies of the resonance states in the potential depend on the parameters of the Yukawa potentials (15). Since we calculate the

internuclear coupling potentials consistently with the same parameters as V(r), the heights and structures of the calculated elastic and inelastic excitation functions are sensitively correlated. Furthermore, the Coulomb excitation plays a major role in the $^{58}Ni + ^{58}Ni$ scattering at the considered incident energies and is destructive with respect to the nuclear excitation. If the Coulomb excitation is excluded from the coupled channel calculations and the same parameters for the Yukawa potentials as given above are used, we find an inelastic 2^+ excitation function in good agreement with the experimental data.

4. Conclusions

The advantage of using collective phenomenological models for the description of quasimolecular states is the visual clearness of the underlying dynamics. These models get complicated for larger state densities. In contrast semimicroscopic cluster models (e.g. for $^{12}C + ^{12}C$ see Cseh et al.[13]) can have a simple structure and allow easily to calculate the energies of resonances and electromagnetic transition probabilities between them. However, their relation to scattering states is complex and they were only applied in a few reaction calculations within the resonating group or generator coordinate methods. Further investigations are necessary.

In the case of the $^{58}Ni + ^{58}Ni$ scattering the results of the coupled channel calculations are sensitively dependent on the coupling potentials. Very recently we developed a solution of the inverse scattering problem based on the modified Newton-Sabatier method which in principle allows to extract coupling potentials from measured angular distributions at a fixed incident energy[14]. Applying this method to the experimental data of the scattering of ^{58}Ni on ^{58}Ni would be an interesting new way to determine the molecular resonance states in this system.

Molecular resonance states have similar properties as superdeformed states of composite nuclei and decaying states observed in fission and cluster radioactivity[6]. We would gain new insight into the nuclear structure and dynamics when these fields could be united into a single research field.

Acknowledgements

W.S. thanks the Romanian Academy for supporting his stay at the International Summer School on Collective Motion and Nuclear Dynamics in Predeal in September 1995.

References

1. D.A. Bromley, J.A. Kuehner and E. Almqvist,*Phys.Rev.Lett.* **4** (1960) 365

2. D.A. Bromley, in *Nuclear Molecular Phenomena*, ed. N. Cindro (North-Holland, 1978) p.3

3. W. Greiner, J.Y. Park and W. Scheid, *Nuclear Molecules* (World Scientific, Singapore, 1995)

4. N. Cindro and M. Božin, *Ann.Phys.(N.Y.)***192** (1989) 307

5. N. Cindro, U. Abbondanno, Z. Basrak, M. Bettiolo, M. Bruno, M. d'Agostino, P.M. Milazzo, R.A. Ricci, W. Scheid, J. Schmidt, G. Vannini and L. Vannucci, in *Frontier Topics in Nuclear Physics*, ed. W. Scheid and A. Sandulescu (Plenum Press, New York, 1994), p. 421;
U. Abbondanno, M. Bettiolo, M. Bruno, N. Cindro, M. d'Agostino, P.M. Milazzo, R.A. Ricci, T. Ritz, W. Scheid, G. Vannini and L. Vannucci, *Elastic and inelastic scattering of* $^{58}Ni + ^{58}Ni$ *and* $^{58}Ni + ^{62}Ni$ *at the Coulomb barrier and intermediate dinuclear states*, preprint (Zagreb, Croatia, 1995)

6. see e.g. in *Frontier Topics in Nuclear Physics*, ed. W. Scheid and A. Sandulescu (Plenum Press, New York, 1994)

7. E. Uegaki and Y. Abe, *Phys.Lett.B* **231** (1989) 28, *Prog.Theor.Phys.* **90** (1993) 615

8. R. Maass and W. Scheid, *J.Phys.G: Nucl.Part.Phys.* **18** (1992) 707

9. E. Uegaki and Y. Abe, *Phys.Lett.B* **340** (1994) 143

10. J. Schmidt, *Diploma-Thesis*, University of Giessen (1993) (unpublished)

11. N. Cindro et al., in *Nuclear Physics of Our Times*, ed. A. Ramayya (World Scientific, Singapore, 1993), p. 423

12. T. Ritz, *Diploma-Thesis*, University of Giessen (1995) (unpublished)

13. J. Cseh, *Phys.Lett.B* **281** (1992) 173; J. Cseh and G. Lévai, *Ann.Phys.(N.Y.)* **230** (1994) 165;
J. Cseh, G. Lévai and W. Scheid, *Phys.Rev.C* **48** (1993) 1724

14. M. Eberspächer, B. Apagyi and W. Scheid,*Solution of a coupled channel inverse scattering problem at fixed energy with a modified Newton-Sabatier method*, preprint (1995)

DEUTERON FORMATION IN EXPANDING NUCLEAR MATTER FROM A STRONG COUPLING BCS APPROACH

M.BALDO[1], J.DUKELSKY[2], F.GULMINELLI[3], U.LOMBARDO[1,4], P.SCHUCK[5]
[1] *INFN, 57 Corso Italia, I-95129 Catania, Italy*
[2] *IEM, Serrano 123, E-28006 Madrid, Spain*
[3] *LPC, Boulevard du Maréchal Juin, F-14050 Caen Cedex, France*
[4] *Università di Catania, 57 Corso Italia, I-95129 Catania, Italy*
[5] *ISN, 53 Avenue des Martyrs, F-38026 Grenoble Cedex, France*

Abstract

The process of deuteron formation in intermediate heavy ion reactions is approached within the strong coupling BCS theory assuming that the final stage of the reaction can be described as an adiabatic expansion of a piece of nuclear matter. Since the gap equation in the $^3S_1 - ^3D_1$ channel goes into the deuteron Schrödinger equation in the low density limit, a smooth transition from the superfluid Cooper pair phase to a Bose deuteron gas is found. For a fixed entropy the deuteron fraction as a function of density shows a steep uprise, up to one in the limit of vanishing density. The relevance of these results for heavy ion collisions and the shortcomings of the present approach are briefly discussed. The model is further generalised to the time dependent case. A semiclassical set of HFB equation is presented and the limiting situation of an adiabatic expansion is detailed. A schematic calculation suggests that the Fermi energy regime should be the best suited to observe the phenomenon of deuteron formation via BCS pairing. The inclusion of fluctuations is outlined by coupling the BCS equations with a self-consistent nonlinear quasi-particle RPA (SCqpRPA). This theory is tested in a schematic model.

1. Introduction

Central heavy ion collisions at E/A in the 50 to 200 MeV range can roughly be described by the initial build up of compressed and hot nuclear matter and by a sequential decompression. At low energies the system may pass through the spinodal instability region and may undergo a liquid-gas phase transition or, at higher energies, the temperature and the internal pressure involved may be so high that the piece of nuclear matter just vaporizes into the individual nucleons. In any case, however, the expanding gas cools down rather fast, allowing for deuterons, as well as other fragments, to form again in the final stage. Actually the yields of deuterons in high energy reactions always exhibit a surprisingly high production rate[1]. Typically, *e.g.* the ratio of deuterons to protons is of the order of unity. At higher bombarding energies ($E/A \geq 200$ MeV) such

abundances have been successfully explained from a transport model[2], where the deuteron pole in the n-p scattering matrix has been explicitly isolated. Though pure phase space considerations may account for a large fraction of the deuteron production rate[3] it still may be interesting to investigate the problem, for instance, of deuteron production from a slightly different point of view. We have in mind the very idealized situation of a piece of hot nuclear matter expanding quasi-stationarily with total entropy kept constant. The latter feature seems to be realized in heavy ion reactions[4]. When lowering the density, the temperature will then drop, and the combination of both effects will allow the appearance of deuterons (Mott transition). The phenomenological observation that the main components of the outgoing fragments, in this energy region, are nucleons and deuterons indicates that nuclear matter has not enough time, during the expanding phase, to get close to its lowest free energy state. In fact, at low enough densities and temperatures, nuclear matter is expected to form a gas of alpha particles. Therefore a mixture of nucleons and deuterons is a metastable system, which spontaneously decays in a gas of alpha particles. This metastable system, however, is worth to be studied, since it is likely to be the one which is more closely related to the final stage of heavy ion reactions. The characteristic time of the expanding phase is, therefore, assumed to be faster than the alpha formation rate, consistently with phenomenology, and slow enough, as already mentioned, to consider nuclear matter not too far from thermal equilibrium.

In this work we will be mainly concerned with the deuteron formation. An aspect we will partially develop is that nuclear matter at low density, below a certain critical temperature T_c, may show strong n-p pairing in the deuteron channel. This has been revealed in several recent studies[5,6,7] and, in fact, it can be anticipated since the NN force in the deuteron channel is more attractive than in the usual p-p or n-n pairing channels. At higher bombarding energies the entropy production is typically several units (see for instance ref. 8) and this is probably too high for the superfluid phase to occur but at lower energies ($E/A \leq 100$ MeV) the entropy per nucleon $S/A < 1$ and this may well allow the appearance of deuteron pair condensation. The reason why such a pair condensate may be relevant for the deuteron production can qualitatively be explained, at least, within the BCS approach to superfluidity. In this approach it has been shown[9] that in the low density limit the BCS equations for the pairing condensate goes over into the Schrödinger equation for the deuteron. In a first attempt we will try to get some insight into the physics of this process in adopting a mean field strong coupling BCS approach. We know about the weakness of this approach, which completely leaves aside the influence of fluctuations, that, in this type of situation, may be crucial, both with respect to the finiteness of the system and with respect to a possible crossover from BCS superconductivity to Bose-Einstein condensation of the deuterons. Indeed, in the limit of inter-particle distance much larger than the deuteron radius a_0, i.e. $k_F a_0 << 1$, the deuterons behave essentially as a gas of bosons, which can

undergo the usual condensation phenomenon. We may deal with this difficult problem in the future. Here we shall stay within the pure BCS approach. We shall first treat the equilibrium case[10], and at the end indicate how to generalise to the dynamic case. A schematic pilote calculation will be presented for a dynamically expanding blob of nuclear matter. Furthermore, we also outline how fluctuations can be taken care of within a self consistent version of the quasi particle RPA (SCqpRPA).

2. Strong coupling Brückner-BCS approach

Proton-neutron pairing in nuclear matter has only been investigated very recently[5,6,7]. Using realistic bare forces in the gap equation and a Brückner Hartree-Fock G-matrix approach for the normal mean field, surprising high values for the gap in the deuteron channel have been found in symmetric nuclear matter. Since the attraction in the deuteron channel,i.e. $S-D$ T=0 channel , is stronger than in the T = 1 neutron-neutron or proton-proton channels, this may actually be not a complete surprise. However, the in medium renormalization (screening) of the bare n-p force is certainly an unsolved problem, in spite of the fact that the use of a bare n-n and p-p forces yields quite reasonable values for the gap Δ in the scalar isovector channel T = 1. Bearing this difficulty in mind, we nonetheless go on using the bare Paris force as the n-p interaction in the $S-D$ pairing channel, which in the mostly interesting low density regime may eventually not be a quite unreasonable choice.

For the normal mean field we use, as in an early paper[11], the one from the Brückner HF approach. The intermediate two particle propagator g is given by

$$g = \frac{(1-f_k)(1-f_{k'})}{\omega - \epsilon_k - \epsilon_{k'} + i\eta} \tag{1}$$

where f_k is the Fermi function, calculated at the single particle energy ϵ_k, the latter being obtained from the Brückner HF self consistent potential.

The gap equation reads

$$\Delta_p = -\sum_k v_{pk} \frac{\Delta_k}{2E_k} \tanh(\frac{\beta E_k}{2}) \tag{2}$$

with $E_k = \sqrt{(\epsilon_k - \mu)^2 + \Delta_k^2}$. As usual the density is obtained from

$$\rho = \frac{\mathrm{N}}{\mathrm{V}} = \sum_{\vec{k},\sigma,\tau} n_k \tag{3}$$

$$n_k = \frac{1}{2}(1 - \frac{\epsilon_k - \mu}{E_k} \tanh \frac{\beta E_k}{2}) \tag{4}$$

and the anomalous density is given by

$$\kappa_k = \frac{\Delta_k}{2E_k} \tanh \frac{\beta E_k}{2} \tag{5}$$

The entropy reads

$$\frac{S}{V} = -\sum_{\vec{k},\sigma,\tau} f(E_k)\log f(E_k) - (1-f(E_k))\log(1-f(E_k)) \qquad (6)$$

The coupled set of non-linear equations (2),(4) is solved, for a given total density ρ, adopting a separable form of the Paris potential[12]. The same numerical method as in ref. 7 is used in solving the gap equation for Δ_k. In the present work, however, the chemical potential μ has been also determined from the set of equations (2),(4). Once the solution for the gap function Δ_k and the chemical potential μ are found, the quantities κ and S are calculated from eqs. (5),(6), respectively.

It is also interesting to combine equations (2),(4), (5) to obtain an expression equivalent to the gap equation:

$$\frac{p^2}{m}\kappa_p + (1-2n_p)\int \frac{d^3k}{(2\pi\hbar)^3} v_{pk}\kappa_k = 2\mu\kappa_p \qquad (7)$$

This equation looks very much like the deuteron Schroedinger equation into which it turns for a dilute system, *i.e.* in the limit $\rho \to 0$. The quantity in which we are mostly interested here is the ratio of the number of deuterons N_s to the number of unbound nucleons N, or equivalently the ratio between the abnormal and normal density. According to standard BCS theory we have

$$\frac{\rho_S}{\rho} = 1 - \frac{\hbar^2}{2m}\frac{1}{6\pi^2\rho}\beta\int dk k^4 \left[1 - \tanh^2\left(\frac{\beta E_k}{2}\right)\right]. \qquad (8)$$

which will be evaluated, as already mentioned, at constant entropy.

3. Results

The transition from the superfluid phase to the deuteron gas is best illustrated by considering the pairing anomalous density κ_k, or its Fourier transform in coordinate space $\phi(r)$, which should smoothly merge into the deuteron wave function in the low density limit. This is displayed in Fig. 1, where the two components of $\phi(r)$ are drawn at different densities. For the lowest density at $\rho = 0.0075$ fm^{-3} a comparison is made with the deuteron wave function. One can observe a large overlap between $\phi(r)$ and the deuteron wave function, which indicates that already at this density the BCS solution is hardly distinguishable from a gas of deuterons, despite the fact that the chemical potential is about $+1$ MeV, still away from the deuteron limit value $\mu = E_D/2 = -1.1$ MeV. At increasing densities the inner part of $\phi(r)$ is not so much affected, while the large r behaviour changes drastically.

From these results one can conclude that the BCS theory describes, in the low density limit, a smooth transition from the $S-D$ superfluid phase of symmetric nuclear matter, to the Bose condensate phase of an ideal deuteron

gas. In BCS language it corresponds to a transition from the weak to the strong coupling limit. The Cooper pairs, each one of which has zero momentum, merge naturally into the zero momentum condensate of deuterons.

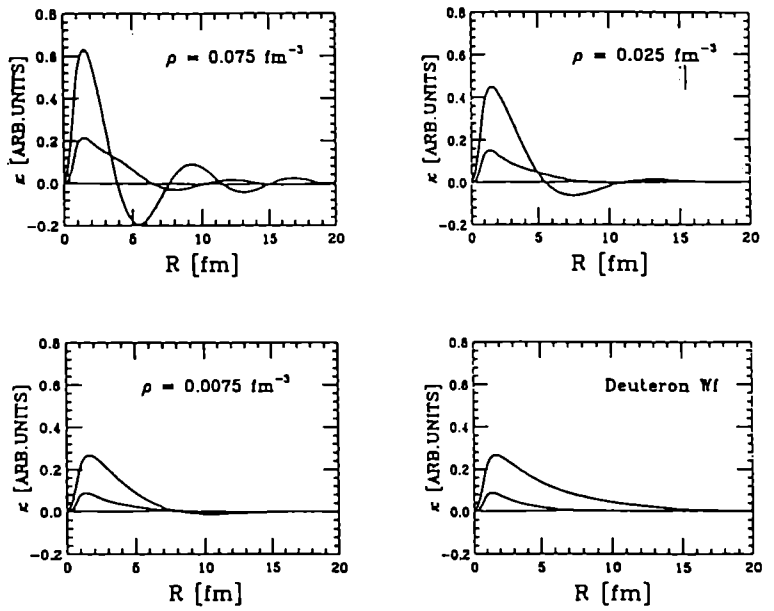

Fig. 1. The S and D components of the pairing correlation function in coordinate space for three different values of the baryonic density. The right lower figure displays for comparison the deuteron wave function.

According to the scenario mentioned in the introduction we assume a piece of hot and compressed nuclear matter formed by a HIC which expands isentropically. At some low density and temperature deuteron superfluidity pops up. When the gas expands further to lower and lower densities the chemical potential μ will turn negative (relative to the mean field value $U(k_F)$ at the Fermi momentum) from where on at a certain density the deuterons are being formed. This actually occurs at extremely low densities $\rho < \rho_o/30$ where the mean distance of the deuterons from one another is about 2-3 times their diameter ($\sim$ 3 fm). At low densities we shall calculate the ratio of the number of deuterons versus the total number of nucleons, given by equation (8). This ratio is shown in Fig. 2, for fixed values of the entropy per particle, as a function of the total density. As we can see, there is a steep increase of deuterons as a function of decreasing density. For a typical value of $S/A \approx 1$ there exists already an appreciable number of deuterons at $\rho = \rho_0/5$.

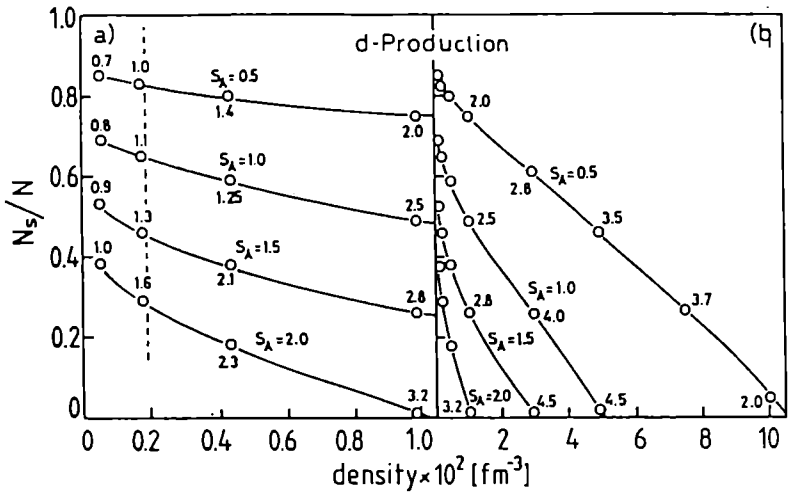

Fig. 2. (right) Deuterons to nucleons ratio N_S/N vs density for four values of the entropy.(left) The same ratio but in an enlarged scale at low densities. In some cases the corresponding temperatures are indicated. The dashed line connects the points corresponding to $\mu = 0$ MeV.

The strongly uprising branch of N_s/N in the final stage of the expansion is due to the fact that the final infinitely diluted stage is always at zero temperature where, within the pure BCS theory, everything is paired ($N_s/N = 1$). This behaviour can be seen more clearly in the blow up of Fig.2 for low densities. The ratio N_s/N tends to one as ρ tends to zero. On the other hand,since the entropy is kept constant also T tends to zero as $\rho \to 0$. In Fig.2 are indicated on the lines of constant entropy in addition to the temperatures at various values of the density also the corresponding values of the chemical potential. Since $\mu = 0$ marks the border from where on deuterons are bound, we connected the points $\mu = 0$ on the various curves S_A = const by the broken line. We should, however, like to point out that deuterons are formed already at higher densities. For example, the coalescence model gives[2] a freeze-out density of $\approx \rho_o/10$ similar to our calculation. On the other hand one sees on Fig.2 that the points $\mu = 0$ where the chemical potential turns negative all lie at a density of around $\rho = 0.002$ fm^{-3} for the various entropies.

It may seem surprising that the chemical potential turns negative only at such extremely low densities where the interparticle distance is of order of 8 fm. One should bear in mind, however, that the deuterons are only weakly bound

and that therefore the corresponding wave function reaches out appreciably to distances beyond 8 fm as can be seen on Fig.1. The Pauli principle therefore is still active. An inter-particle distance 2-3 times the deuteron diameter can therefore seem reasonable for the Mott transition. We must of course always be aware of the weakness of our present approach where we completely neglect thermal and quantal fluctuations which may be very important at such low densities. For instance, the fact that BCS theory even at finite temperature imposes that the deuterons are at rest seems to be a drastic assumption, which should be relaxed in a more realistic approach (see Section 5). Nevertheless our study may set qualitative indications. The fact seen on Fig.2 that the ratio deuteron to unpaired nucleons varies very strongly in the low density regime of expanding nuclear matter should probably remain. This mechanism of deuteron production can then coexist with other normally considered mechanisms where the deuterons are formed in final state interactions of an emitting source or by coalescence.

4. Dynamics of the Expansion

It is evident that the assumption of quasi-static expansion cannot be valid in practice. One therefore should generalise the present formalism to the time dependent case. With the generalised density matrix $\mathcal{R}$ and the HFB hamiltonian $\mathcal{H}$ we then have[13]

$$i\hbar\dot{\mathcal{R}} = \left[\mathcal{H}, \mathcal{R}\right] \tag{9}$$

with

$$\mathcal{R} = \begin{pmatrix} \rho & \kappa \\ -\kappa^* & 1-\rho^* \end{pmatrix} \ , \ \mathcal{H} = \begin{pmatrix} h & -\Delta \\ \Delta^* & -h^* \end{pmatrix} \tag{10}$$

The semiclassical limit of this equation can be found (see *e.g.* ref. 14) introducing a unitary transformation

$$\mathcal{R} = \mathcal{U}\mathcal{R}_0\mathcal{U}^\dagger \ , \ \mathcal{U} = exp(\frac{i}{\hbar}\Phi\tau_3) \tag{11}$$

As a matter of fact, the phase of the abnormal density is of order $1/\hbar$ and a semiclassical transport theory is possible only if we put ourselves in the frame where the gap is real, *i.e.* in the frame where the phase is gauged out. Supposing the phase to be a local operator $< \vec{r}|\Phi|\vec{r'} >= \Phi(\vec{r})\delta(\vec{r}-\vec{r'})$, we then obtain[15] in semiclassical (first order in $\hbar$) approximation

$$\dot{f_0} = \left\{h_0, f_0\right\} + \left\{\Delta_0, \kappa_0\right\} \tag{12}$$

$$\dot{\kappa_0} = \left\{\frac{\vec{p}}{m}\nabla\Phi, f_0\right\} + \frac{1}{2}\{\Delta_0, f_0 - \overline{f}_0\} \tag{13}$$

$$\frac{\vec{p}^2}{m}\kappa_0 + (2f_0 - 1)\int \frac{d^3k}{(2\pi\hbar)^3} v_{pk}\kappa_0(\vec{k}) = 2\lambda\kappa_0 \tag{14}$$

with

$$h_0 = h_\Phi + \frac{\vec{p}}{m}\nabla\Phi - \mu = \frac{(\vec{p}+\nabla\Phi)^2}{2m} + \dot{\Phi} + U^H - \mu \quad (15)$$

$$\lambda = \mu - U^H - \dot{\Phi} - \frac{(\nabla\Phi)^2}{2m} \quad (16)$$

and the shorthand notation $\overline{f}_0 = f_0(\vec{r}, -\vec{p}, t)$. Equations (12), (13), (14) represent three evolution equations for the three unknowns f_0, κ_0, Φ (the subscript "0" always denotes gauge transformed quantities). The self-consistent solution of these equations constitutes the semiclassical time dependent BCS approach (TDBCS). The modified gap equation eq.(14) has the form of a local Schroedinger equation for the deuteron wave function, with a local eigenvalue[10] represented by eq.(16). Therefore eq.(14) is formally the same as in the static case eq.(7) (up to the fact that f_0 is obtained from a dynamical equation), only the "eigenvalue" $2\lambda(\vec{r}, t)$ is now a field of the two parameters $\vec{r}, t$. One can verify that in the static limit equations (12), (13), (14) are equivalent to our previous equilibrium equations (2),(4),(5). To further clarify the physical meaning of the transport equations it may be instructive to calculate the first moments of the distributions. By introducing the usual notations for the densities and currents

$$\rho \equiv \int d^3p\, f_0(\vec{r}, \vec{p}, t) \ , \ \rho_s \equiv \int d^3p\, \kappa_0(\vec{r}, \vec{p}, t) \ , \ \vec{j}_0 \equiv \int d^3p\, \frac{\vec{p}}{m} f_0(\vec{r}, \vec{p}, t)$$

One straightforwardly gets

$$\dot{\rho} + \nabla_r \cdot \vec{j}_0 + \nabla_r \cdot \vec{j} = 0 \quad (17)$$

$$\dot{\rho}_s + \nabla_r \cdot \vec{j}_s = 0 \quad (18)$$

$$m\frac{d\vec{j}_s}{dt} = \rho_s \nabla_r \Big(\mu - \frac{(\nabla\Phi)^2}{2m} - G\rho - U^H\Big) + \nabla_r \Pi_0 \quad (19)$$

where

$$\vec{j} \equiv \frac{1}{m}\rho\nabla_r\Phi$$

$$\vec{j}_s \equiv \frac{1}{m}\rho_s\nabla_r\Phi$$

$$\Pi_0 \equiv \frac{1}{\rho_s}\int d^3p\, \frac{\vec{p}^2}{2m}\kappa_0$$

and for simplicity we have assumed a local gap, $\Delta = G\rho_s$. Equation (19) is equivalent to a London equation for the superfluid velocity, with an inhomogeneity represented by the coupling to the normal phase[16]. So we can see that in the limit of a local pairing gap the problem can be reduced to a closed set of hydrodynamical equations, that is a continuity equation for the supermatrix eq.(17),(18) and an Euler equation eq.(19) for the collective velocity, in perfect

analogy with the non superfluid case[13]. The physical meaning of the gauge transformation is now clear: among all the possible unitary transformations of the generalised density matrix, the physical gauge is defined by the constraint that a (2X2) continuity equation is fulfilled, *i.e.* by the requirement that the phase $\nabla\Phi$ actually represents the collective superfluid velocity[17]. The gauge transformation eq.(11) that we have employed up to now is in principle a simple change of the reference frame, with no loss of generality. Correspondingly the TDBCS equations exhibit all the complexity of a coupled set of integro-differential equations, and in general solutions cannot be given in an analytical form. However, the problem is drastically simplified in the special case where this transformation isolates all the time odd components of the generalised density matrix[15].

Let us suppose that with the transformation (11) the matrix $\mathcal{R}_0$ coincides with the time even part of $\mathcal{R}$. For the distribution functions in Wigner space this means[18] $f_0(\vec{r},\vec{p},t) = f_0(\vec{r},-\vec{p},t)$ and $\kappa_0(\vec{r},\vec{p},t)$ real (as before). Then the local velocity of both the normal and superfluid phase are represented by $\nabla_r\Phi$ and one can readily write down the solution of the transport equations

$$\kappa_0 = \frac{\Delta_0}{2E_\Phi} \;\; ; \;\; f_0 = \frac{1}{2}\Big(1 - \frac{h_\Phi}{E_\Phi}\Big) \tag{20}$$

with $E_\Phi^2 = \Delta_0^2 + h_\Phi^2$ and h_Φ defined in eq. (15). The structure of these solutions is the same as in the equilibrium case, but the dynamics of the phase is governed by the time odd components of the transport equations, namely

$$\dot{f}_0 \;\; - \;\; \Big\{\frac{\vec{p}}{m}\nabla_r\Phi, f_0\Big\} = 0 \tag{21}$$

$$\dot{\kappa_0} \;\; - \;\; \Big\{\frac{\vec{p}}{m}\nabla_r\Phi, \kappa_0\Big\} = 0 \tag{22}$$

Remark that in the case of a constant collective velocity eqs.(21), (22) represent a trivial streaming motion, and the equilibrium solution is recovered. Let us examine the structure of the modified gap equation in more detail. If we specify to a separable interaction in momentum space $v(\vec{p},\vec{p}') = V_0 v_p v_p'$ the gap equation can be rewritten as

$$1 = 4\pi V_0 \int_0^\infty dk \frac{k^2 v_k^2}{2\sqrt{\Big(\frac{k^2+(\nabla\Phi)^2}{2m} + \dot{\Phi} + U^H - \mu\Big)^2 + v_k^2 V_0^2 C^2(r)}} \tag{23}$$

that in spherical symmetry is a one dimensional implicit equation for the r-dependent part of the gap $C(r)$ (here, $\Delta(r,p) = V_0 v_p C(r)$). As a first application let us drop self-consistency and solve eq.(23) for the simple dynamical case of a spherical nucleus at zero temperature immersed into an external uniformely accelerated velocity field. For U^H we use a standard Wood Saxon, the pairing interaction is taken from ref.19, and the chemical potential μ is fixed to conserve the total number of particles. A result of this model calculation is

presented in Fig.3, where the momentum dependence of the gap in the center $\Delta(r = 0)$ is plotted for three different values of the (constant) acceleration.

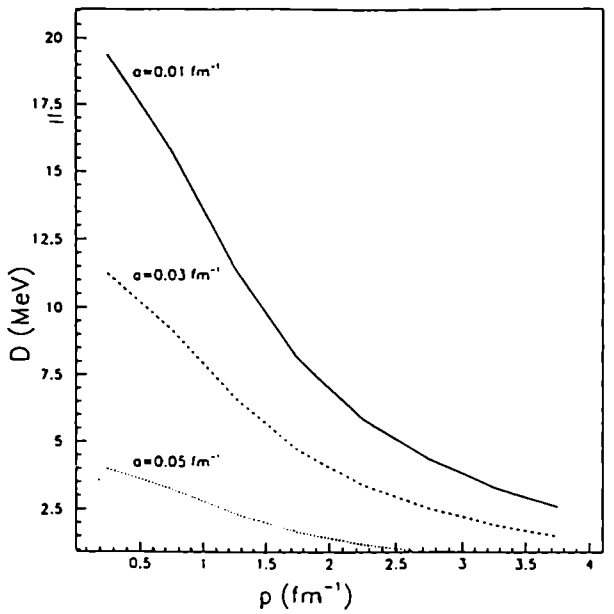

Fig. 3. Pairing gap as a function of momentum for a portion of uniformly accelerated nuclear matter at normal nuclear matter density, for three different values of the acceleration.

The acceleration is seen to systematically reduce the pairing gap, up to a critical value - specific to the chosen pairing interaction - where the gap completely vanishes. This pair breaking effect of an acceleration field is well known in the standard theory of superconductivity.

Let us now turn to deuteron production in expanding nuclear systems.

The solution of TDBCS for a spherically symmetric expanding nucleus at zero temperature is readily written (after an inverse gauge transformation) as

$$f(\vec{r},\vec{p},t) = \frac{1}{2}\Theta \quad (\quad R(t) - r) \cdot \qquad (24)$$
$$\left(\frac{(\vec{p} - m\vec{u})^2/2m + U^H - \mu(t)}{\left[\left((\vec{p} - m\vec{u})^2/2m + U^H - \mu(t)\right)^2 + \Delta^2(\vec{r},\vec{p},t)\right]^{1/2}}\right)$$

The simplest possibility for the velocity field is to take a time independent function $\vec{u}(\vec{r}) = c_0 \cdot \vec{r}$. In this case the time dependence of the macroscopic parameters is given by the continuity equation

$$\rho = \rho_0 e^{-3c_0 t} \ , \ R = R_0 e^{c_0 t} \ , \ \mu = \mu_0 e^{-2c_0 t} \qquad (25)$$

and the distribution functions (normal and abnormal) can be determined at any time by solving the gap equation (23). As an example we report in Fig.4 the distribution functions evaluated at the center of the nucleus, at different times up to vanishing density.

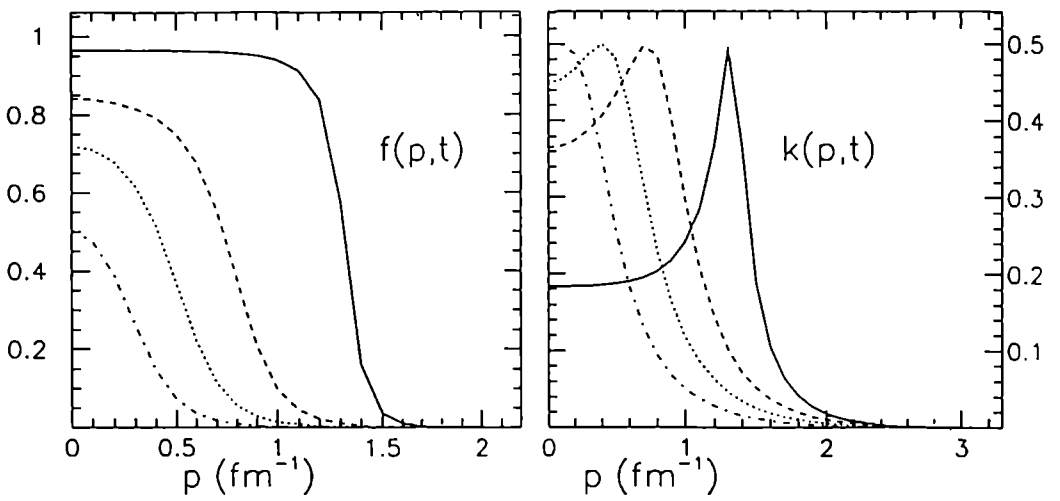

Fig. 4. Normal and abnormal distribution functions versus momentum for a spherical uniformly expanding nucleus with a radial collective velocity u=0.035 r/c Full line: normal nuclear matter density. Dashed line: after 50 fm/c. Dotted line: after 100 fm/c. Dash-dotted line: asymptotic time.

As the density gets lower, not only the average Fermi momentum diminishes as in the non pairing case, but also the average occupation of low momentum states is progressively reduced. Correspondingly the distribution of paired nucleons is shifted towards lower energies as a function of time. In the limit of asymptotic times the wave function of the deuteron is recovered, and all nucleons are paired.

However it is clear that this model is too schematic in many respects. Temperature effects are neglected, for any initial value of the collective velocity a state at zero density is asymptotically reached, and the acceleration is not taken into account. From the structure of eq.(23) and the results of Fig.3 we expect that these results will not necessarily be preserved for a more realistic dynamics of the expansion. However, the adiabatic dynamics will be recovered if the initial density and thermal pressure stored in the compound system is sufficiently low to make the term $\dot{\Phi}$ in eq. (23) negligeable. On the other side, from the preceding section we know that in order to have a transition to the

superfluid phase the initial pressure must be high enough to lead to a very dilute system in the final stage, and the balance between these two effects can be very delicate.

We shall therefore consider a more realistic model for the macroscopic parameters of the expansion entering the gap equation. For this purpose we shall use the hydrodynamical model of ref.20. Here the mean field U^H is neglected as before, but an homogeneous expansion of the nucleus is assured by a self-similar radial velocity field of the form

$$\frac{\nabla\Phi}{m} = u(r,t) = c_0(t)\cdot r = a_0\frac{R_0}{R(t)}\sqrt{\frac{t^2}{t^2+t_0^2}}\cdot r \qquad (26)$$

Here, R is the (sharp) radius of the expanding system, R_0 the radius at the time of formation of the composite system, and a_0,t_0 are parameters. With the constraints of mass and energy conservation, the parameter a_0 can be fixed to obtain a given initial excitation energy while t_0 measures the acceleration of the collective motion. The continuity equation is again solved with the ansatz (26) for the time evolution of the density ρ, chemical potential μ and nuclear radius R. If we neglect the time dependence of c and R with respect to the time dependence of ρ, eq.(25) is still valid. From the preceding section we know that the correction to the chemical potential due to the pairing gap is important only at very low densities. For this simplified analysis we shall therefore keep eqs.(25) as a qualitative representation of the time evolution of the normal phase. However now c_0 has the more complicated time dependent form of eq.(26), that simulates the effect of mean field and thermal pressure. The parameters E^* and t_0 are then fixed to approximately reproduce the expansion dynamics (initial excitation energy, time behaviour of the average density and radial velocity) calculated from a BUU simulation[8] of a heavy ion collision.

As an example in Fig.5 we report the quality of the fit for the density evolution in a central $Au + Au$ collision at two different bombarding energies. Only at the highest energy a complete vaporisation of the system is seen, while at 50 MeV/u the calculation has been stopped at the time when density inhomogeneities start to appear, leading to fragment formation. In the same figure we show the time evolution of the surface velocity from eq.(26) for the two cases. The acceleration is clearly much more important for the high energy collision. Finally temperature is calculated at any time from energy conservation, and the gap equation eq.(23) is correspondingly modified as in eq. (2).

For the highest excitation energy the acceleration of the expansion turns out to be higher than the limiting value: the gap vanishes. The upper limit of a complete pairing at zero temperature given by the BCS theory is not true any more, and deuteron production due to BCS coupling - if any - has to be calculated from the complete self consistent transport equations eqs.(12)(13)(14).

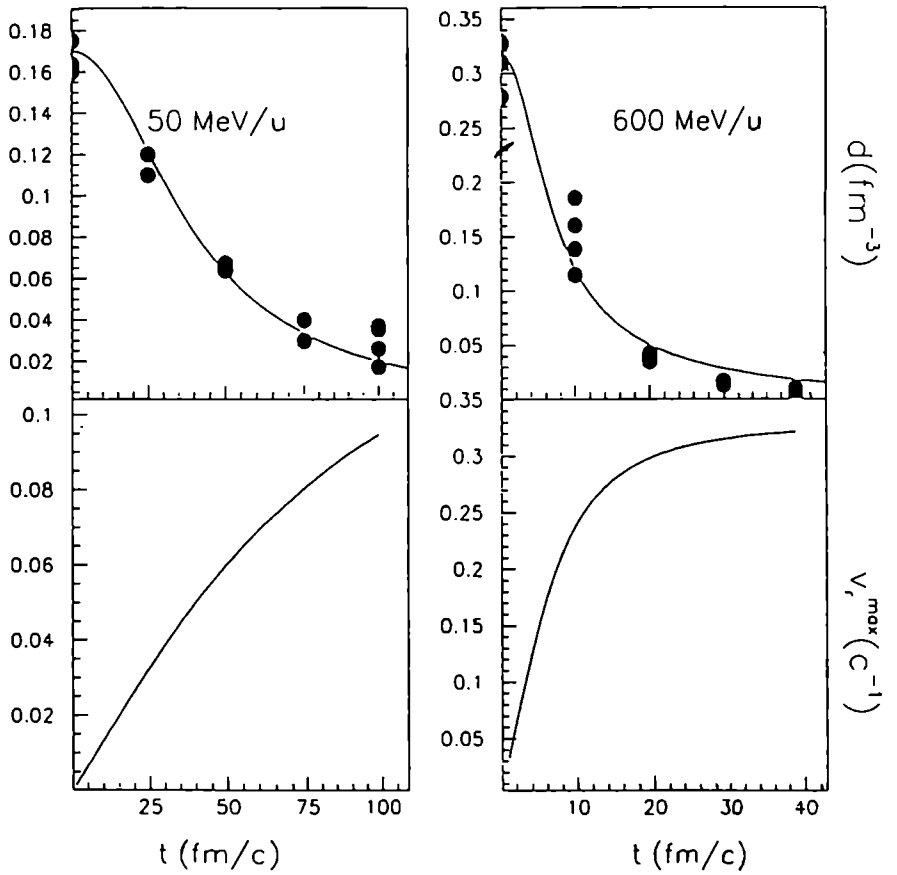

Fig. 5. (upper part) Average density as a function of time for a central Au+Au collision at 50 MeV/u(left) and 600 MeV/u(right) obtained in a BUU calculation. The dispersion of the points reflects the density inhomogeneities. The solid line is a calculation from an hydrodynamical model (see text). (lower part) Collective radial velocity at the surface of the expanding nucleus as a function of time, from the hydrodynamical model with the same parameters as in the upper part.

On the other hand at the lowest bombarding energy the gap is only slightly reduced with respect to the equilibrium case, and the dynamics is qualitatively like in Fig. 4. The corresponding number of deuterons as a function of time, calculated from eq.(8), is plotted in Fig.6. At longer times the average density does not evolve any more due to the showing up of fragments, therefore the ratio will be approximately frozen, if recombination effects are negligeable.

It is interesting to observe that an anomalous proportion of deuterons has been recently measured by the INDRA collaboration in vaporisation events at a

similar bombarding energy[21]. Our calculation suggests that a systematic study of deuteron yields and deuteron correlation functions in vaporisation events as a function of excitation energy will be very helpful in clarifying the possible observation of a Mott transition in deuteron production.

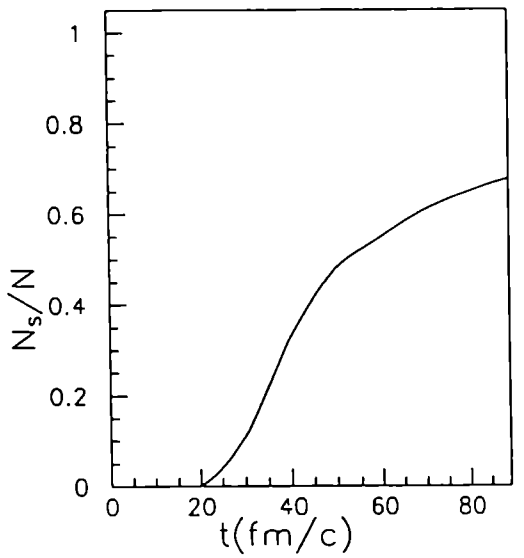

Fig. 6. Deuterons to nucleons ratio N_S/N versus time for a central Au+Au collision at a beam energy of 50 MeV/u, calculated with the macroscopic parameters from the hydrodynamical model.

A word of caution is however necessary: the result presented in Fig.6 must be considered only as a very qualitative indication of the effects of the expansion dynamics, and not as a real theoretical prediction of deuteron yield in a realistic reaction. The complete lack of self-consistency and the schematicity of the macroscopic model do not yet allow to attach a quantitative meaning to the numbers obtained. Further work in this direction is in progress[15].

5. Inclusion of Fluctuations within a Generalised RPA Formalism

Our formalism of static BCS in Section 2 has the great disadvantage that the deuterons stay immobile even at finite temperature. The time dependent description remedies this to some extent (it gives the usual quasi-particle RPA in the small amplitude limit, see below) but even this has some shortcomings. We therefore want to present here the so called self-consistent quasi-particle RPA (SCqpRPA) which, as we shall see, has many rather appealing features[22].

Let us define the qp RPA excitation operator

$$Q_K^\dagger = \frac{1}{2}\sum_{pp'} X_{pp'}^K \alpha_p^\dagger \alpha_{p'}^\dagger - Y_{pp'}^K \alpha_p \alpha_{p'} \tag{27}$$

Here K,p are general quantum numbers. In infinite matter they represent momenta and spins. It is clear that eq.(27) can create a "deuteron" pair with total momentum $\vec{K}$. The excited state is then

$$|K>= Q_K^\dagger |0> \tag{28}$$

where the ground state is defined by

$$Q_K|0>= 0 \tag{29}$$

The standard equation of motion method leads to the following RPA type of equations[13]

$$\sum_{ll'} \begin{pmatrix} A & B \\ B^* & A^* \end{pmatrix}_{kk'll'} \begin{pmatrix} X^K \\ Y^K \end{pmatrix}_{ll'} = \Omega_K \sum_{ll'} \begin{pmatrix} N & 0 \\ 0 & -N \end{pmatrix}_{kk'll'} \begin{pmatrix} X^K \\ Y^K \end{pmatrix}_{ll'} \tag{30}$$

where

$$A_{kk'll'} = <0|\left[\alpha_{k'}\alpha_k, \left[H, \alpha_l^\dagger \alpha_{l'}^\dagger\right]\right]|0> \tag{31}$$

$$B_{kk'll'} = -<0|\left[\alpha_{k'}\alpha_k, \left[H, \alpha_l \alpha_{l'}\right]\right]|0> \tag{32}$$

$$N_{kk'll'} = <0|\left[\alpha_{k'}\alpha_k, \alpha_l^\dagger \alpha_{l'}^\dagger\right]|0> \tag{33}$$

Replacing in these equations the ground state $|0>$ defined by (29), by the BCS ground state, linearizes eq.(30) and we arrive to the usual qpRPA, equivalent to the linearised version of the time dependent BCS equation (9). Here we want to avoid this "quasi-boson" approximation. We therefore must find a way to fully express the matrix elements in eqs. (31), (32), (33) by the X, Y amplitudes. This can be achieved in the following way. Employing the usual normalisation of the RPA amplitudes $\frac{1}{2}\sum |X|^2 - |Y|^2 = 1$ we can invert eq.(27)

$$\alpha_p^\dagger \alpha_{p'}^\dagger = \sum_K X_{pp'}^K Q_K^\dagger + Y_{pp'}^K Q_K \tag{34}$$

For a two-body Hamiltonian H, the matrix elements in eqs. (31),(32),(33) will involve the following densities (schematically)

$$\begin{aligned} &< \alpha^\dagger\alpha >\ , < \alpha^\dagger\alpha^\dagger >\ , < \alpha^\dagger\alpha^\dagger\alpha^\dagger\alpha^\dagger >\ , \\ &< \alpha^\dagger\alpha^\dagger\alpha\alpha >\ , < \alpha^\dagger\alpha^\dagger\alpha^\dagger\alpha >\ + c.c. \end{aligned} \tag{35}$$

Let us first discuss the third and fourth element. Inserting eq.(34) and commuting Q_K to the right we can use (29). Then $< \alpha^\dagger\alpha^\dagger\alpha^\dagger\alpha^\dagger >$ and $< \alpha^\dagger\alpha^\dagger\alpha\alpha >$ are expressed by X, Y and the density $< \alpha^\dagger\alpha >$. The element $< \alpha^\dagger\alpha^\dagger >= 0$, using eqs.(29) and (34). For the density $< \alpha^\dagger\alpha^\dagger\alpha^\dagger\alpha >$ we insert (34) for the left pair operator, commute Q_K to the right, and are left with an expression directly containing $< \alpha^\dagger\alpha^\dagger >$. So the last density is also zero. Of course analogous considerations hold for the complex conjugate quantities (*c.c.*). We now have reduced everything to the single unknown $< \alpha^\dagger\alpha >$. This quantity is not so easily expressed in a consistent way through the RPA amplitudes and in the past mostly perturbative methods have been applied[23]. It turns, however, out that a fully consistent expression can be found via the single particle Green's function

$$\mathcal{G}^{t-t'}_{kk'} \equiv -i < 0|T \begin{pmatrix} \alpha_k(t)\alpha^\dagger_{k'}(t') & \alpha_k(t)\alpha_{k'}(t') \\ \alpha^\dagger_k(t)\alpha^\dagger_{k'}(t') & \alpha^\dagger_k(t)\alpha_{k'}(t') \end{pmatrix} |0 > \tag{36}$$

This Green's function obeys Dyson's equation: $\mathcal{G} = \mathcal{G}^0 + \mathcal{G}^0\mathcal{M}\mathcal{G}$, which we shall treat in perturbation theory *i.e.* $\mathcal{G} = \mathcal{G}^0 + \mathcal{G}^0\mathcal{M}\mathcal{G}^0$. The mass operator $\mathcal{M}$ is known to have the following exact representation which we show graphically

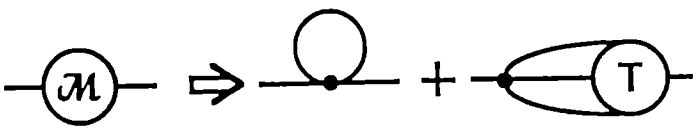

where the dot represents the bare interaction and the other vertex contains the exact 4 point T-matrix. We replace it by the expression that corresponds to our RPA eq.(30).

Graphically this can be achieved in the following way

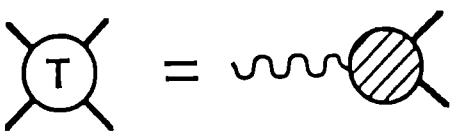

where on the r.h.s the wiggly line stands for the solution of (30), *i.e.* the corresponding RPA propagator, and the shaded cercle stands for the $\begin{pmatrix} A & B \\ B & A \end{pmatrix}$ matrix in (30). We now have a well defined expression for $\mathcal{G}$ in terms of X, Y from which we can calculate $< \alpha^\dagger\alpha >$ in the usual way. This method implies a strong consistency check. It is well known (see *e.g.* ref. 13) that the ground

state energy E_0 can be obtained directly from the single particle Green's function (36) and it will contain the RPA amplitudes. On the other hand from our RPA formalism we can express at least the potential energy part of E_0 which contains the two-body amplitudes of (35) directly by the RPA amplitudes, as this was explained above. It turns out that both ways to calculate E_0 lead to the same functional $E_0[X,Y]$ which represents our above mentioned consistency relation.

Still one ingredient is missing. This concerns the u,v amplitudes of the Bogoliubov transformation to quasi-particles. As usual we determine them from the minimisation of the ground state energy where we can show the following interesting equality[22]

$$\frac{\partial E_0}{\partial u_k} =< 0|[H,Q_K^\dagger]|0 >= 0 \tag{37}$$

where again $|0>$ is the RPA ground state of eq.(29). Equation (37) is a very natural relation, since it is completely consistent with the equation of motion method. The expectation value in (37) again only contains the densities of (35) and thus our set of equations is completely closed. It is interesting to write (37) and (30) somewhat differently

$$< 0|[H,\alpha_k^\dagger\alpha_{k'}^\dagger]|0 > \;=\; F[u,v,X,Y] = 0 \tag{38}$$

$$< 0|[H,Q_k^\dagger Q_{k'}^\dagger]|0 > \;=\; G[u,v,X,Y] = 0 \tag{39}$$

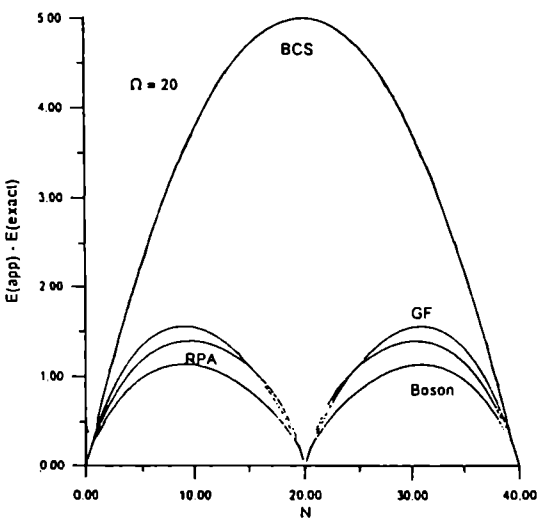

Fig. 7. Ground state energy with respect to the exact one in the BCS and SCqpRPA theories for the seniority model as a function of particle number.

We recognize in eq.(38) the usual fermion gap equation, if we replace the ground state by its BCS approximation[13]. Loosely speaking we then can say that eq.(39) represents a "boson" BCS equation, if we identify the $Q^\dagger$ operator roughly as bosons.

We therefore have the very gratifying situation that we have in (38),(39) two coupled BCS equations, one fermionic (the nucleons) and one bosonic (the "deuterons"). Of course here now the bosons (deuterons) are in motion, and we can describe the real physical situation because it is well known how to generalise qp RPA to finite temperatures[24]. An interesting aspect of eq.(39) is that, since it is a bosonic gap equation, it should describe Cooper pairs of bosons. Indeed it does. It is not difficult to show that (39), in the limit of vanishing density, goes over into the Schroedinger equation of an α- particle in the same way as (38) goes over into the Schroedinger equation of the deuteron eq.(7).

Other interesting properties of our formalism are

- the f- sum rule is automatically fulfilled[22]
- an approximate form of (38),(39) is the Brueckner Hartree Fock equation[25]. It thus seems that one can use hard core potentials in our theory.
- it yields ground state and excitation energies simultaneously
- it sums *ph* and *pp* correlations democratically.

Applications of this theory are only in their infancy. Apart from rather simple models like the Lipkin model[22] the formalism has recently been applied to spin waves in an Heisenberg antiferromagnet[22]. The SCRPA reproduces in 1D the exact one magnon dispersion $\omega_k = \frac{\pi}{2}|sink|$ known from the Bethe ansatz, and in two dimension the dispersion is in agreement with the most recent Monte Carlo calculations. Concerning our present subject of SCqpRPA the theory was only applied to the standard seniority model of nuclear physics[26]. We show in Fig.7 the difference of the exact ground state energy and *i*) the BCS energy *ii*) the SCqpRPA energy. We can notice the strong improvement over BCS. The same improvement occurs for the number fluctuation $\Delta N/N$.

6. Conclusions

In the last section we have seen that the coexistence of (bound) neutron-proton pairs with a nucleon gas contains a variety of interesting and challenging physical and theoretical aspects. We have demonstrated that already usual equilibrium BCS theory is capable to describe important aspects of the problem. A major deficiency there, however, is the fact that the bound pairs (deuterons) are kept immobile. At finite temperature and very low densities where we then essentially have a dilute gas of bosons this is clearly an unphysical feature. A first remedy to this deficiency is given by the time dependent generalisation of BCS (TDBCS). This can also describe the time evolution of the decompression

phase in a head on heavy ion collision, allowing - at least in principle - to give quantitative predictions for the physical observables. TDBCS also puts the Cooper pairs into motion, which for instance can break the pairs. Such an effect has been demonstrated within pilote calculations.

However even TDBCS has deficiencies. We therefore discussed a self-consistent generalisation of RPA theory which ressembles very much BCS theory for bosons, however, we never really introduce the concept of bosons and always work with fermion pairs. It turns out that this SCqpRPA has very nice properties. The essence is that we arrive at two coupled Hartree Fock Bogoliubov equations: one for fermions and one for fermion pairs (deuterons or "bosons").

The possible extension to finite temperature is then ideally suited for the description of our problem: how does an expanding piece of hot nuclear matter first turn into a $n-p$ pairing phase and then, at very low densities, into a gas of dilute deuterons and eventually α- particles.

Acknowledgements: We thank T. Alm, A. Bonasera, P.Danielewicz and G. Röpke for stimulating discussions.

7. References

1. K. G. R. Doss, et al. *Phys. Rev.* **32C** (1985) 116 and *Phys. Rev.* **C37** (1988) 163.
2. P. Danielewicz and G.F. Bertsch, *Nucl. Phys.* **533A** (1991) 712.
3. J. Pluta, private communication. S. Mrowczynski, *Phys. Lett.* **277B**(1992) 43.
4. G.F. Bertsch and S. Das Gupta, *Phys. Reports* **160**(1988) 189.
5. T. Alm, G. Röpke and M. Schmidt, *Z. Phys.* **337A** (1990) 355.
6. B.E. Vondefecht, C.C. Gearhart, W.H. Dickhoff, A. Polls, A. Ramos, *Phys. Lett.* **253B** (1991) 1.
7. M. Baldo, I. Bombaci and U. Lombardo, *Phys. Lett.* **283B** (1992) 8.
   M. Baldo, I. Bombaci and U. Lombardo, P. Schuck, Proceeding of the Conference on 'Realistic Nuclear Structure', Stony Brook, 1992 , *Phys. Reports* **242** (1994) 159.
8. A. Bonasera, F. Gulminelli andf J.J. Molitoris *Phys.Reports* **243** (1994) 1.
9. L.V. Kjeldysh and A.N. Kozlov, *Sov.Phys. JETP* **27** (1968) 521.
   P. Nozieres and S. Schmitt-Rink, *J. Low Temp. Phys.* **59** (1985) 195.
10. M. Baldo, U. Lombardo, P. Schuck, to appear in *Phys. Rev.* **C**.
11. M. Baldo, J. Cugnon, A. Lejeune and U. Lombardo, *Nucl. Phys.* **536A** (1992) 349.
12. J. Haidenbauer and W. Plessas, *Phys. Rev.* **30C** (1984) 1822.
13. P. Ring, P. Schuck, *The Nuclear Many Body Problem*, Springer-Verlag (1980)
14. D. Vollhardt, P. Wolfle, *the Superfluid Phases of Helium 3*, Taylor and

Francis (1982)
15. F. Gulminelli, P. Schuck, in preparation.
16. M. Di Toro, V.M. Kolomietz, *Zeit.Phys.* **328A** (1987) 285
17. O. Betbeder-Matibet, P. Nozieres, *Ann.Phys.* **51** (1969) 392
18. M. Baranger, M. Véneroni, *Ann. Phys.* **114** (1978) 123
19. Y. Yamaguchi, *Phys. Rev.* **95** (1954) 1628
20. J.P. Bondorf, S.I.A. Garpman, J. Zimany, *Nucl. Phys* **296A** (1978) 320.
21. Indra Collaboration, *Phys. Lett.* **353B** (1995) 27.
22. J. Dukelsky, P. Schuck, *Nucl. Phys.* **512A** (1990) 466 and *Mod. Phys. Lett.* **26A** (1991) 2429.
    P. Krüger, P.Schuck, *Europhys. Lett.* 27 (1994) 395.
23. D.J. Rowe, *Rev. Mod. Phys.* 40 (1968) 153.
24. H.M. Sommermann, *Ann. Phys.* 151 (1983) 163.
25. D. Janssen, P. Schuck, *Zeit. Phys.* **339A** (1991) 43.
26. J. Dukelsky, P. Schuck, to be published.

NEW ASPECTS IN MICROSCOPIC DESCRIPTION OF CLUSTER DECAY PROCESSES

D. S. DELION
Institute of Atomic Physics
POB MG-6, Bucharest, Romania

and

A. INSOLIA
Department of Physics, University of Catania and INFN
Corso Italia 57, I-95129 Catania, Italy

and

R.J. LIOTTA
KTH, Physics at Frescati
Frescativägen 24, S-10405 Stockholm, Sweden

ABSTRACT

A single particle basis, consisting of two different harmonic oscillator representations, is introduced with the aim of studying microscopically cluster decay processes. A correct description of the wave functions at large distances is obtained within a minimal single particle basis. Experimental data corresponding to a large number of alpha and ^{14}C decay transitions from even-even nuclei are well reproduced.

1. Introduction

The discovery of the heavy-cluster decay [1] triggered a febril theoretical activity. Many models, both phenomenological and microscopical, were proposed trying to understand the mechanisms that induce the clustering of the nucleons, as well as to predict new candidates for experimental searches. Phenomenological models were rather successful in this respect (for review see [2,3]).

The microscopic approaches were much hindered by the great difficulties that appear when one wants to describe the motion of the nucleons that constitute the cluster in the field generated by the other nucleons, including the effects of the Pauli principle. A microscopic approach consistent with nuclear spectroscopic properties, but with the Pauli principle included only partially, was presented in ref. [4]. The role of the Pauli principle would be diminished if one would be able to evaluate the formation amplitude of the cluster at large distances. But this requires the inclusion of the continuum in the single-particle basis because bound states do not extend far outside the nuclear radius [5,6].

For instance, in ref. [5] it was found that the inclusion of 13 major harmonic oscillator shells was not enough to explain the ground-state to ground-state α-decay width of ^{212}Po. In deformed nuclei it was possible to reproduce the total α-decay width

within a factor of three, only including up to 18 major shells [6]. In heavy cluster decay the use of very large number of shells in the basis improves the calculation but still the calculated absolute decay widths are too small by 1−2 orders of magnitude with respect to the corresponding experimental data [7,8].

The aim of this talk is to present a single-particle representation which is rather small, but at the same time is adequate to simulate the continuum as quasi-continuum bound states. The basis consists of the eigenstates of two different sets of harmonic oscillators (h.o.) states. One is suited to describe the discrete part of the spectrum and the other one, with a smaller h.o. parameter, the quasi-continuum.

The formalism is described in Section 2, applications concerning alpha and ^{14}C decay processes from even-even nuclei are performed in Section 3. Finally the conclusions are drawn in the last Section.

2. Formalism

The many-body problem in nuclear physics can conveniently be treated using the harmonic oscillator representations. The stationary Schrödinger equation describing the single-particle motion of a particle of mass M_0 in a spherical mean field $V(r)$

$$H\psi(\xi) \equiv [-\frac{\hbar\omega}{2\lambda_0}\vec{\nabla}^2 + V(r)]\psi(\xi) = E\psi(\xi) \tag{2.1}$$

where $\xi = (\vec{r}, s)$ is the set of spatial and spin coordinates, and

$$\lambda_0 = \frac{M_0\omega}{\hbar} \tag{2.2}$$

has solutions in a separable form

$$\psi_{Elj\Omega}(\xi) = u_{Elj}(r)[i^l Y_l(\hat{r})\chi_{\frac{1}{2}}(s)]_{j\Omega} \tag{2.3}$$

Here l is the angular momentum of the particle, j its total spin and Ω the corresponding projection on the z-axis.

It is known that in order to have a proper asymptotic behaviour of the wave functions at large distances it is necessary to include up to $N = 18$ major shells in heavy nuclei [7]. But this can also be achieved by using a mixed non-orthogonal h.o. basis in the diagonalisation procedure, thus reducing the number of shells needed in the expansion and, at the same time, obtaining a better description of the decay process

$$u_\alpha(r) = \sum_{2n_1+l=N_1\leq N_0} c^{(1)}_{\alpha n_1} R^{(\lambda_1)}_{n_1 l}(r) + \sum_{2n_2+l=N_2>N_0} c^{(2)}_{\alpha n_2} R^{(\lambda_2)}_{n_2 l}(r); \quad \alpha = (E, l, j) \tag{2.4}$$

where λ_1 is the h.o. parameter coresponding to the h.o. potential which fits the Woods-Saxon interaction in the region of the discrete spectrum with $2n_1 + l \leq N_0$,

while $\lambda_2 < \lambda_1$ corresponds to an h. o. potential that describes better the continuum part of the spectrum, with $2n_2 + l > N_0$.

The diagonalization of the potential V in terms of the two h.o. representations can be performed by inserting in eq. (2.1) the expanded wave function (2.4). One then obtains the following set of equations for the amplitudes c

$$\begin{pmatrix} \mathcal{H}^{(11)}_{n_1 n_1'} & \mathcal{H}^{(12)}_{n_1 n_2'} \\ \mathcal{H}^{(21)}_{n_2 n_1'} & \mathcal{H}^{(22)}_{n_2 n_2'} \end{pmatrix} \begin{pmatrix} c^{(1)}_{\alpha n_1'} \\ c^{(2)}_{\alpha n_2'} \end{pmatrix} = E \begin{pmatrix} \mathcal{I}^{(11)}_{n_1 n_1'} & \mathcal{I}^{(12)}_{n_1 n_2'} \\ \mathcal{I}^{(21)}_{n_2 n_1'} & \mathcal{I}^{(22)}_{n_2 n_2'} \end{pmatrix} \begin{pmatrix} c^{(1)}_{\alpha n_1'} \\ c^{(2)}_{\alpha n_2'} \end{pmatrix} \tag{2.5}$$

where $\mathcal{I}^{(ik)}_{n_i n_k'}$ are the overlap integrals, $\mathcal{H}^{(ik)}_{n_i n_k'}$ the Hamiltonian kernels and

$$f_k = \frac{\lambda_k}{\lambda_0}; \qquad k = 1, 2 \tag{2.6}$$

Let us first consider the ground state to ground state α-decay process for an even-even nucleus

$$B \rightarrow A + \alpha \tag{2.7}$$

We will assume that the mother nucleus (B) as well as the daugther nucleus (A) are spherically symmetric. Within the R-matrix approach [9,10] the total α-decay width can be written as

$$\Gamma(R) = \sum_{L_\alpha=0}^{\infty} \gamma^2_{L_\alpha}(R) P_{L_\alpha}(R); \quad \gamma^2_{L_\alpha}(R) = \frac{\hbar^2}{2M_\alpha} R |F_{L_\alpha}(R)|^2 \tag{2.8}$$

where $F_{L_\alpha}(R)$ is called formation amplitude. The L_α component of the formation amplitude is the overlap integral between the entrance and exit α-decay channels, i. e.

$$F_{L_\alpha}(R) = \int d\hat{R} d\xi_\alpha d\xi_A d\xi_B [Y_{L_\alpha}(\hat{R}) \Psi_\alpha(\xi_\alpha) \Psi_A(\xi_A)]^* \Psi_B(\xi_B) \tag{2.9}$$

where $\hat{R} = (\theta, \phi)$ are the angular center of mass coordinates and $\Psi_X(\xi_X)$ is the internal wave function of the nucleus $X = A, B$ with internal coordinates ξ_X.

We will describe the internal α-particle wave function as a product of $n = l = 0$ h. o. states, and the mother and daughter nuclei within the BCS formalism [10].

One can perform all integrals over the coordinates in eq. (2.9) analitically by transforming to relative coordinates. Using the generalized Talmi-Moshinsky transformation with different masses [11] (i. e. with the different size parameters λ_1 and λ_2 in our case) one obtains for $L_\alpha = 0$ [6]

$$F_0(R) = \sum_{Niki'k'} \Phi^{(\Lambda^{i'k'}_{ik})}_{N0}(R) \sum_{nN_\pi N_\nu} < n0N0; 0 | N_\pi 0 N_\nu 0; 0 >_{D^{i'k'}_{ik}} \mathcal{I}^{(\lambda^{i'k'}_{ik}, \lambda_\alpha)}_{n0} G^{(ik)}_{N_\pi} G^{(i'k')}_{N_\nu} \tag{2.10}$$

where $G^{(ik)}_\pi (G^{(i'k')}_\nu)$ are geometrical coefficients depending on the proton (neutron) single particle parameters [12] and brackets denote Talmi-Moshinsky transformation.

The radial c.m. wave function $\Phi^{(\Lambda_{ik}^{i'k'})}_{N_a L_a=0}(R)$ corresponds to an h.o. potential with the c.m. and relative parameters given respectively by

$$\Lambda_{ik}^{i'k'} = \frac{1}{2}(\Lambda_{ik} + \Lambda_{i'k'}), \qquad \lambda_{ik}^{i'k'} = \frac{\Lambda_{ik}\Lambda_{i'k'}}{\Lambda_{ik}^{i'k'}} \tag{2.11}$$

where

$$\Lambda_{ik} = \frac{1}{2}(\lambda_i + \lambda_k), \qquad \lambda_{ik} = \frac{\lambda_i \lambda_k}{\Lambda_{ik}} \tag{2.12}$$

The Talmi-Moshinsky brackets in eq. (2.10) depend on the mass ratio

$$D_{ik}^{i'k'} = \Lambda_{i'k'}/\Lambda_{ik} \tag{2.13}$$

Since in the applications it may be interesting to know in which potential a given particle is moving, we will clearly specify all the possible combinations in the summation (2.10). There are five terms

1) $i = k = 1, \quad i' = k' = 1;$ 2) $i = k = 2, \quad i' = k' = 2;$
3) $i = k = 1, \quad i' = k' = 2; \quad i = k = 2, \quad i' = k' = 1; \quad i \neq k, \quad i' \neq k';$
4) $i = k = 1, \quad i' \neq k'; \quad i \neq k, \quad i' = k' = 1;$
5) $i = k = 2, \quad i' \neq k'; \quad i \neq k, \quad i' = k' = 2;$

The formation amplitude can then be written as

$$F_0(R) = \sum_{k=1}^{5} F_0^{(k)}(R) \tag{2.14}$$

In order to estimate the formation amplitude for more general cluster decay processes

$$B \rightarrow A + C \tag{2.15}$$

we will use the multistep shell-model method [13]. In this method one calculates a many-body system in several steps. In each step one includes all the interactions and Pauli effects properly.

Within this approximation and including the pairing correlations through the BCS formalism we calculated the first step as in the case of α-decay [6]. For the second step, i. e. daughter nucleus plus two alpha-like excitations, we proceeded in the same fashion. Finally, we repeated this procedure for the third step thus reaching the mother nucleus corresponding to the decay of ^{12}C. For the case of the decay of ^{14}C we added a neutron pair.

The internal wave functions of the $^{12,14}C$ clusters were given in ref. [7].

With standard transformations to center of mass and relative motion and performing the integrals analytically one gets for the formation amplitude [14]

$$F_{^{14}C}(\vec{R}) = \sum_{Nik} \Phi_{N0}^{(\lambda_{ik})}(\vec{R}) F_N(i,k) \tag{2.16}$$

where

$$F_N(i,k) = \sum_{nn_{12}n_3N_{\alpha_1}N_{\alpha_2}N_{\alpha_3}N_{\nu_4}} < n0N0;0|N_{12}0N_30;0 > \mathcal{I}_{n2}^{(\lambda_{ik},\lambda_{14C})}$$
$$\times < n_{12}0N_{12}0;0|N_{\alpha_1}0N_{\alpha_2}0;0 > \mathcal{I}_{n_{12},2}^{(\lambda_{ik},\lambda_{14C})} < n_30N_30;0|N_{\alpha_3}0N_{\nu_4}0;0 > \mathcal{I}_{n_3,1}^{(\lambda_{ik},\lambda_{14C})}$$
$$\times F_{N_{\alpha_1}}(i,k,i,k)F_{N_{\alpha_2}}(i,k,i,k)F_{N_{\alpha_3}}(i,k,i,k)G_{N_{\nu_4}}^{(ik)} \qquad (2.17)$$

In this equation all angular momenta are zero because the different MSM steps proceed through ground states.

Since the basis is not an orthogonal basis different components of the basis elements may overlap which each other. This overlap is expressed by the quantities $\mathcal{I}$. The coefficients $F_{N_{\alpha_i}}$ and $G_{N_\nu}^{(ik)}$ are the same as in eq. (2.10).

3. Numerical results

The width (2.8) consists of two very distinct parts, namely the formation probability and the penetration through the Coulomb barrier. Deformations are very important regarding the penetration through the Coulomb barrier, but much less important for the formation probability [7]. We therefore will calculate in this section the formation amplitude neglecting deformations. The effects of deformations on the penetration will be shown at the end.

The idea of this calculation was to find a minimal basis that describes well the calculated width. The parameter f_1 was fixed to have the value f_1=1.2 [15] and, therefore, the possible different bases are determined by the parameter f_2. But let us stress once more that the results do not (and cannot) depend on the value that one chooses for f_2. If f_2 is big then one needs many shells to reach the final values of the calculated quantities, as expected [7]. We found that the minimal basis is given by the choice $f_2 = 0.7$. The basis consists then of the h. o. shells $N_1 = 0 - 6$ corresponding to the parameter $f_1 = 1.2$ and the shells $N_2 = 7 - 11$ corresponding to $f_2 = 0.7$. Considering that the basis provided by only one h. o. potential requires at least 18 major shells to reproduce the experimental results [6] one can say that our basis is very small.

First we analyzed the alpha decay from ^{220}Ra within the minimal basis, around the touching radius, which is defined by

$$R_c = 1.2\ (A_{^{216}Rn}^{1/3} + A_{^4He}^{1/3}) = 9.15\ fm \qquad (3.1)$$

In figure 1.a we present different terms entering the formation amplitude (2.14) as a function of the c.m. radius R. One sees that the contribution corresponding to the discrete part of the spectrum (k=1, drawn by dashes) is peaked on the nuclear radius while the mixed contribution between discrete and quasicontinuum parts (k=3, plotted by dots) is centered on the touching radius. The total amplitude is drawn by a solid line.

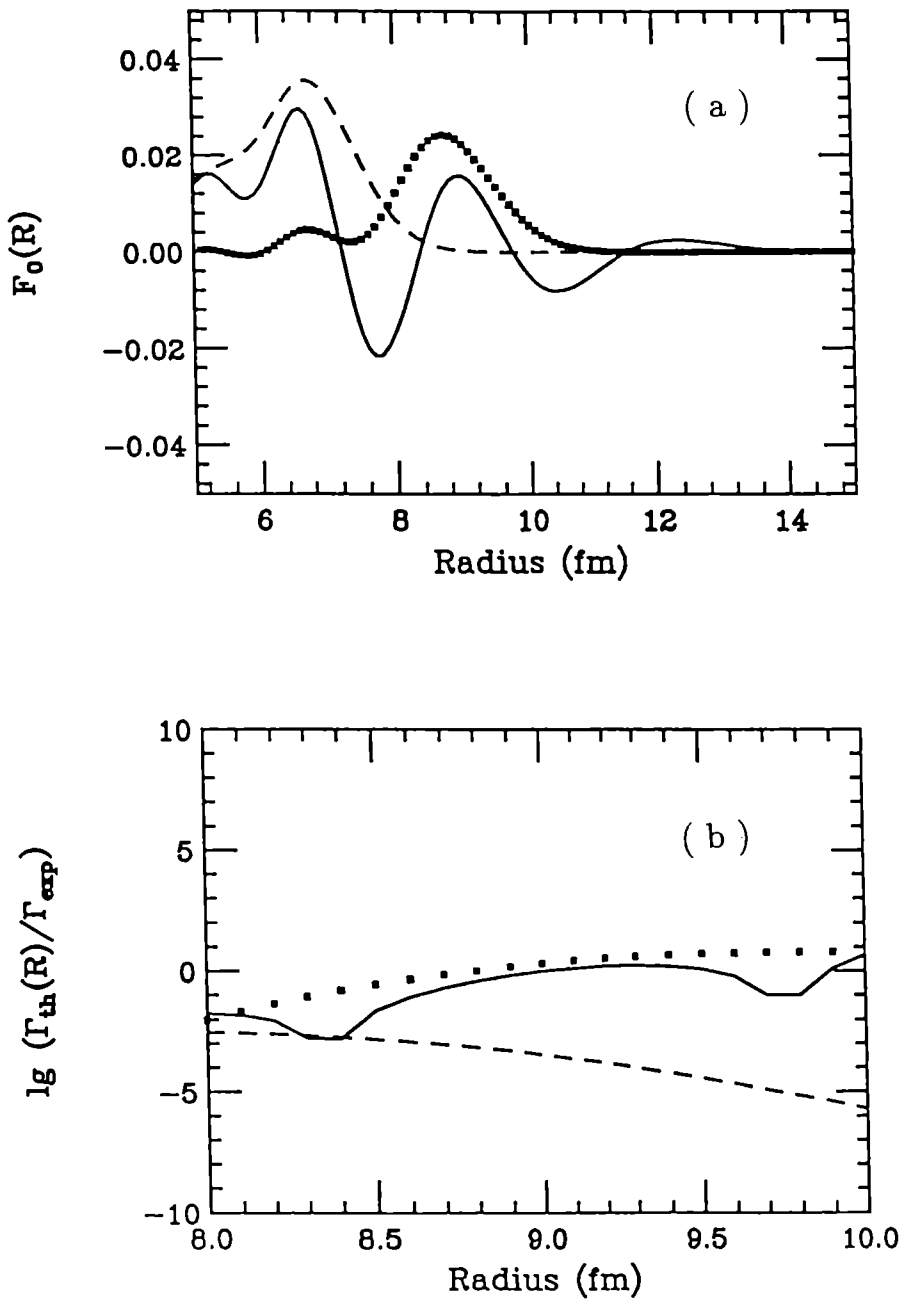

Fig. 1. Formation amplitude (a) and ratio between the theoretical and experimental width (b) corresponding to the ground state to ground state transition of ^{220}Ra as a function of the distance between the α-particle and the daughter nucleus ^{216}Rn. The dashed line is the contribution from $F_0^{(k=1)}$ in the expansion (2.14) while the dotted line is the contribution from $F_0^{(k=3)}$. The final values are represented by the full lines.

An important test for the calculation is that the total decay width should be independent upon the distance R outside the nuclear surface. This dependence is shown in figure 1.b for the three cases of figure 1.a. One can notice that the main contribution to the total width is provided by the term in eq. (2.14) that contributes most to the formation amplitude around the touching radius, i. e. the term $k = 3$. The contribution from the inner part of the nucleus (k=1) is very small. The total contribution (full line) is indeed practically independent upon the distance for $R \geq 9fm$, i.e. beyond the touching radius, and reproduces well the experimental value. For smaller radius the width is very small. This is because we have neglected antisymmetrisation effects between the daughter nucleus and the α-cluster [4,16,17] but this does not affect our results because we are able to compute the formation amplitude well beyond the touching point, where those effects are negligible [18]. This is the main reason why it is important to have a reliable theory capable of describing the decay process at large distances.

It is important to mention that by increasing the basis dimension one gets saturation for the total decay width.

Another quantity that can be calculated with our formalism is the spectroscopic factor

$$S = \int_0^\infty |R_0(R)|^2 R^2 dR \tag{3.2}$$

The result of the calculation for this decay is $S = 7.0\ 10^{-2}$, which is in agreement with a calculation where the Pauli principle acting among the particles in the core and in the α-particle was taken into account properly [4].

We will analyse ground state to ground state alpha decays from several even-even nuclei by using the minimal basis discussed in the previous section. For the Woods-Saxon potential we adopted the universal set of values [15]. The BCS gap parameters were calculated according to the third order mass formula [19]. Even if the dependence of the width upon the distance around the touching point is weak, we will present the calculated values averaged on the interval $R = 8 - 10fm$, i.e. around the touching point.

We have calculated the total α-decay width corresponding to 26 cases of even-even heavy nuclei, i. e. above the ^{208}Pb in the periodic table. We computed the total width by using a spherical as well as a deformed Coulomb barrier for the penetration problem. In both cases we applied the semiclassical (WKB) approximation, which is known to be very good in alpha decay [6,20]. The deformation parameters were taken from ref. [21] and the experimental values of the widths from ref. [22].

In table 1 are given the results of the calculation. Considering that this is a complete microscopic calculation without any free parameter, one can say that the agreement between theory and experiment is excellent.

One important feature that can be seen in this table is the contributions of deformations to the decay widths. As expected, when the deformation increases the difference between the calculated spherical and deformed widths also increases, but the contribution of deformations always improves the calculation, sometimes by large factors, as for instance in the decay of ^{244}Pu.

Table 1. Absolute alpha decay widths calculated assuming a spherical barrier (Γ_{sph}) and deformed barrier (Γ_{exp}).

No	Nucleus	β_2	$\Gamma_{exp}(MeV)$	$\Gamma_{sph}(MeV)$	$\Gamma_{def}(MeV)$	$\Gamma_{sph}/\Gamma_{exp}$	$\Gamma_{def}/\Gamma_{exp}$
1	^{212}Po	0.00	1.5(-15)	1.7(-15)	1.7(-15)	1.14	1.14
2	^{214}Po	0.00	2.9(-18)	1.5(-18)	1.5(-18)	0.53	0.53
3	^{216}Po	0.00	3.0(-21)	2.0(-21)	2.0(-21)	0.68	0.68
4	^{218}Po	0.00	2.4(-24)	1.3(-24)	1.3(-24)	0.56	0.56
5	^{216}Rn	0.07	1.0(-17)	4.8(-18)	5.0(-18)	0.47	0.50
6	^{218}Rn	0.09	1.3(-20)	6.7(-21)	7.3(-21)	0.51	0.56
7	^{220}Rn	0.13	8.1(-24)	4.5(-24)	5.6(-24)	0.55	0.69
8	^{222}Rn	0.14	1.4(-27)	6.1(-28)	8.3(-28)	0.44	0.60
9	^{220}Ra	0.11	2.0(-20)	1.5(-20)	1.8(-20)	0.79	0.91
10	^{222}Ra	0.19	1.2(-23)	5.4(-24)	9.1(-24)	0.46	0.77
11	^{224}Ra	0.18	1.4(-27)	5.2(-28)	8.4(-28)	0.37	0.61
12	^{226}Ra	0.20	8.6(-33)	2.6(-33)	5.0(-33)	0.30	0.58
13	^{224}Th	0.21	3.5(-22)	1.4(-22)	2.5(-22)	0.39	0.71
14	^{226}Th	0.23	1.8(-25)	4.7(-26)	1.0(-25)	0.26	0.56
15	^{228}Th	0.23	5.5(-30)	1.7(-30)	3.9(-30)	0.30	0.71
16	^{230}Th	0.24	1.5(-34)	5.0(-35)	1.4(-34)	0.34	0.94
17	^{232}Th	0.26	8.0(-40)	2.2(-40)	7.6(-40)	0.27	0.94
18	^{230}U	0.26	1.7(-28)	7.1(-29)	2.1(-28)	0.42	1.24
19	^{232}U	0.26	1.4(-31)	4.6(-32)	1.5(-31)	0.32	1.04
20	^{234}U	0.27	4.2(-35)	1.1(-35)	4.0(-35)	0.26	0.96
21	^{236}U	0.28	4.6(-37)	9.8(-38)	4.1(-37)	0.22	0.89
22	^{238}U	0.28	2.5(-39)	3.7(-40)	1.6(-39)	0.14	0.65
23	^{238}Pu	0.28	1.2(-31)	3.5(-32)	1.4(-31)	0.30	1.21
24	^{240}Pu	0.29	1.6(-33)	3.1(-34)	1.3(-33)	0.19	0.82
25	^{242}Pu	0.29	3.0(-35)	5.4(-36)	2.5(-35)	0.18	0.82
26	^{244}Pu	0.29	1.4(-37)	2.9(-38)	1.4(-37)	0.20	0.97

The numerical results for ^{14}C decay process are given in table 2. We found in all cases that the widths are only weakly dependent upon distance in the range $R = 10fm - 13fm$, i. e. beyond the touching point, confirming the soundness of this approach. One sees in table 2 that the influence of deformations can be very important.

Except ^{222}Ra for which the daughter nucleus is the double magic nucleus ^{208}Pb, the theoretical and experimental absolute decay widths agree within a factor of five. The corresponding values relative to α-decay are also reasonable.

The spectroscopic factors, given in the last column of table 2, are within the accepted order of magnitude [4]. It is worthwhile to mention that the main contribution

to this spectroscopic factor is provided by the first N_0 major shells, i.e. from the bound states of the minimal representation ($i = 1$ in eq. (2.16)), while in the absolute decay width the main contribution is provided by shells with $N > N_0$ ($i = 2$), i. e. from high lying configurations in the representation. Although expected, this is an important feature.

Table 2. Absolute decay widths for ^{14}C-decay and the corresponding values relative to α-decay.

Nucleus	β_2	Γ_{exp} (MeV)	Γ_{sph} (MeV)	Γ_{def} (MeV)	$(\frac{\Gamma_{^{14}C}}{\Gamma_\alpha})_{exp}$	$(\frac{\Gamma_{^{14}C}}{\Gamma_\alpha})_{th}$	$\frac{S_{^{14}C}}{S_\alpha}$
^{222}Ra	0.19	4.1(-33)	1.9(-35)	2.1(-34)	3.4(-10)	2.3(-11)	1.0(-7)
^{224}Ra	0.18	6.3(-38)	1.2(-39)	1.4(-38)	4.5(-11)	1.7(-11)	8.1(-8)
^{226}Ra	0.20	2.9(-43)	3.8(-44)	1.1(-42)	3.3(-11)	2.2(-10)	1.0(-7)

4. Conclusions

The calculation of absolute cluster decay widths is a very difficult undertaking because either one calculates it at a short distance, as for spectroscopic quantities, where the Pauli principle acting among the particles in the core and in the α-particle is important, or one calculates it at large distances, where standard shell model representations are inadequate to describe the decay process. In this talk we have attacked this problem by choosing as representation a basis provided by two different harmonic oscillator potentials. The lowest shells of the representation are taken from an h.o. potential that describes well spectroscopic properties, i. e. distances up to around the nuclear surface. The highest shells are taken from an h.o. potential that is rather shallow, thus with a greater density of states in the quasicontinuum, i. e. suited to describe distances outside the nuclear surface.

Within this representation one is able to calculate the formation amplitude of the cluster at large distances, thus avoiding the formidable task of considering exactly the Pauli principle among the core and the cluster. Besides, one achieves this with a rather small basis.

In our calculations we have used for the mean field standard Woods-Saxon potentials with parameters that we have taken from independent spectroscopic calculations. We included the pairing correlations among the particles as prescribed by standard BCS calculations and, therefore, there is not any free parameter in the calculated absolute decay widths.

With these prescriptions we calculated a rather large number of α and cluster decay widths in heavy nuclei. To probe the validity of the calculations, we have checked in all cases that the widths are only weakly dependent upon the distances

between the cores and the cluster outside the nuclear surfaces. The calculated values of the widths agree well with the corresponding experimental values.

We also calculated spectroscopic factors, which are in good agreement with other calculations, where the Pauli principle was taking into account properly.

5. References

1. H.J. Rose and G.A. Jones, Nature **307** (1984) 245,
   D.V. Aleksandrov. et. al., JETP Lett. **40** (1984) 909
2. P.B. Price, Nucl. Phys. **A502** (1989) 41c
3. A. Sandulescu and W. Greiner,
4. R. Blendowske, T. Fliessbach and H. Walliser, Nucl. Phys. **A464** (1987) 75
   Rep. Prog. Phys. **55** (1992) 1423
5. A. Arima and I. Tonozuka, Nucl. Phys. **A323** (1979) 45
6. D. S. Delion, A. Insolia and R. J. Liotta, Phys. Rev **C46** (1992) 884;
   Phys. Rev **C46** (1992) 1346
7. D.S. Delion, A. Insolia and R. J. Liotta, J. Phys. **G19** (1993) L189;
   J. Phys. **G20** (1994) 1483
8. A. Florescu and A. Insolia, Phys. Rev. C (1995) in press
9. R. G. Thomas, Prog. Theor. Phys. **12** (1954) 253
10. H. J. Mang, Ann. Rev. Nucl. Sci. **14** (1964) 1;
    Phys. Rev. **181** (1969) 1697
11. M. Sotona and M. Gmitro, Comp. Phys. Comm. **3** (1972) 53
12. A. Insolia, P. Curutchet, R. J. Liotta and D. S. Delion, Phys. Rev. **C44**
    (1991) 545
13. R. J. Liotta and C. Pomar, Nucl. Phys. **A382** (1982) 1
14. D.S. Delion, A. Insolia and R.J. Liotta, Phys. Rev. C (submitted)
15. S. Cwiok, J. Dudek, W. Nazarewicz, J. Skalski and T. Werner, Comp. Phys.
    Comm. **46** (1987) 379
16. T. Fliessbach, H. J. Mang and J. O. Rasmussen, Phys. Rev. **C13** (1976)
    1318
17. D. F. Jackson and M. Rhoades-Brown, J. Phys. **G4** (1978) 1441
18. K. Varga, R. G. Lovas and R. J. Liotta, Nucl. Phys. **A550** (1992) 421
19. A.Bohr and Mottelson, Nuclear structure, vol. 1 (Benjamin, New York, 1975)
20. P. O. Fröman, Mat. Fys. Skr. Dan. Vid. Selsk. 1 (1957) no. 3.
21. S. Raman, C. H. Malarkey, W. T. Milner, C. W. Nestor,JR and P. H. Stelton,
    Atomic Data and Nuclear Data Tables **36** (1987) 1
22. B. Buck, A. C. Merchand and S. M. Perez, Atomic Data and Nuclear Data
    Tables **54** (1993) 53

FINE STRUCTURE IN CLUSTER DECAYS (^{4}He, ^{14}C, ^{20}O and ^{34}Si)

Ovidiu Dumitrescu
International Centre for Theoretical Physics, Trieste, Italy
and
Department of Theoretical Physics,
Institute of Atomic Physics,
Măgurele, Bucharest,P.O. Box MG-6, R - 76900, Romania

ABSTRACT

Within the one level R-matrix approach several hindrance factors for the radioactive decays in which are emitted ^{4}He, ^{14}C, ^{20}O and ^{34}Si atomic nuclei are calculated. The interior wave functions are supposed to be given by the recently proposed enlarged superfluid model, an extension of the JINR - Dubna's quasiparticle phonon nuclear model. The spectroscopic factors are expanded in terms of products of cluster overlaps and intrinsic overlap integrals. The cluster overlaps are equivalents of the generalized coefficients of fractional parentage, while for the intrinsic overlap integrals we construct a model, which is an extension of the usual models for simple particle decay such as deuteron, triton and alpha decay. The exterior wave functions are calculated from a cluster - nucleus double - folding model potential obtained with the M3Y interaction. As examples of the cluster decay fine structure we analyzed the particular cases of α - decay of ^{241}Am, ^{243}Cm and ^{255}Fm, ^{14}C - decay of ^{223}Ra , ^{20}O - decay of ^{229}Th and ^{255}Fm and ^{34}Si - decay of ^{243}Cm. A relatively good agreement with the experimental data is obtained especially in the case of α - decay fine structure.

1. Introduction

The spontaneous emission of nuclear fragments heavier than alpha particles and lighter than the most probable fission fragments, termed as exotic or cluster decays, has now become an experimentally confirmed reality (see Refs. [1-8] and references therein). Moreover, Hourani and his co - workers [4] experimentally discovered the fine structure in the ^{14}C radioactivity, opening in this way a new area of research (see Refs. [5-8]). All nuclei with $Z > 40$ are unstable with respect to radioactive decay into two nuclear fragments (A_1, Z_1 and A_2, Z_2 with $A = A_1 + A_2$ and $Z = Z_1 + Z_2$), i.e. the energy release $Q = M(A,Z) - M_1(A_1,Z_1) - M_2(A_2,Z_2)$ is positive, however, only for certain combinations - (A_1, Z_1) plus (A_2, Z_2), the high value of potential barrier (proportional to $Z_1 Z_2$) is almost compensated by a high value of Q, and these decay modes may be detectable. By using a triple gamma coincidence technique in the spontaneous fission of ^{252}Cf recently [3] neutronless fragmentations, such like ^{104}Mo +

^{148}Ba, ^{106}Mo + ^{146}Ba and ^{104}Zr + ^{148}Ce, have been experimentally observed for the first time. In this way it was experimentally proved that the spontaneous decay with emission of light fragments, such as α -, ^{14}C, ^{20}O, ^{23}F, ^{24}Ne, ^{28}Mg and ^{32,34}Si (cluster radioactivity) and the neutronless spontaneous fission defined as a process where all the available energy goes into the total kinetic energy of the fragments (cold fission) may have an analogous decay mechanism. Also, for the first time [4], a double fine structure, i.e. decay to the excited states of both fragments of the final channel were experimentally observed in analogy with the usual fine structure, i.e. decays only to the excited states of the daughter nuclei already known in alpha decay [9] and ^{14}C - decay [4], [6].

The interest in studying these new decay modes lies in the quantitative estimations of the life times and branching ratios on one hand and, in the construction of models regarding nuclear clustering, nucleus - nucleus potentials, the nature of spontaneous fission process etc., on the other hand.

In the present paper we touch both the above aims of study concerning the fine structure of cluster decay. First, we construct a mechanism of clustering by using the enlarged superfluid model (ESM) [13] for the nuclear states, which is an extension of the JINR - Dubna's quasiparticle phonon nuclear model (QPNM) [14]. The spectroscopic factors are expanded [12] in terms of products of cluster overlaps and intrinsic overlap integrals. The cluster overlaps are equivalents of the generalized coefficients of fractional parentage while for the intrinsic overlap integrals we construct a model, which is an extension of the usual models for light particle decay such as deuteron, triton and alpha decay [5]. Secondly we calculate several hindrance factors for the ^{4}He -, ^{14}C -, ^{20}O -, and ^{34}Si - radioactivity of some translead nuclei and compare with the experimental data and some previous calculations. In the case of alpha decay a relatively good agreement with the experiment is obtained.

2. Hindrance Factors and Relative Intensities

The hindrance factor (HF) is defined [15] as a ratio of the actual half life for a given cluster transition characterized by the energy release Q to the half life obtained from the Geiger - Nuttal [5] law at the same energy Q. Such a definition of the hindrance factor determines a quantity, which is almost independent on energy Q. This quantity measures the attenuation of the decay probability due to the mechanism of the cluster formation and not to the barrier penetration. The microscopic description of preformation has a key role in the understanding of the decay process and requires a precise knowledge of the initial and final quantum states. The HF plays the same role as the lgft plays in the β - decay.

When we are dealing with a cluster transition from the initial state $(I_iK_i\pi_i)$ of a heavy deformed nucleus with axial symmetry to the ground or excited states $(I_1K_1\pi_1)$ and $(I_2K_2\pi_2)$ of the residual axial deformed nuclei the corresponding theoretical hindrance factor has the following expression [6], [16]:

$$HF^{(I_iK_i\pi_i\to I_1K_1\pi_1;I_2K_2\pi_2)} = \left[\sum_l F_l \mid d_{l\,K=|K_1+K_2-K_i|}^{(I_iK_i\pi_i\to I_1K_1\pi_1;I_2K_2\pi_2)} \mid^2\right]^{-1} \quad (1)$$

When any of the residual nuclei is a spherical nucleus, the K quantum number disappears from the sets $IK\pi$ of quantum numbers that identify the nuclear state (see e.g. the case of the α - decay). Using for the channel quantum numbers $I_1K_1\pi_1; I_2K_2\pi_2;\ l\ K = |K_1 + K_2 - K_i|$ the abbreviation c the quantities d are defined as follows

$$d^{(I_iK_i\pi_i\to c)} = \frac{\sum_{c'} \mathbf{K}_{[c|c']}\gamma^{(I_iK_i\pi_i)\to c'}}{\sum_{c'} \mathbf{K}_{[(00+(g.s.);00+(g.s.);\ l=0\ K=0)|c']}\gamma^{(00+(g.s.)\to c'}} \quad (2)$$

The quantity γ_l^2 is the reduced width [9] while $F_l = \frac{P_l(Q)}{P_{l=0}(Q)}$ where $P_l(Q)$ stands for the penetrability. $Q = Q_c = Q_0 - E^*_{I_1K_1\pi_1} - E^*_{I_2K_2\pi_2}$.

For deformed nuclei there is a matrix part of the penetrability (see Refs. [9], [10], [11] and Refs. [26,27] cited in [5]), - ($\mathbf{K}_{cc'}$) - the Fröman - Nosov matrix,

$$\mathbf{K}_{[c|c']} = < \Phi_{c'} \mid \exp(\frac{i}{\hbar} S_c^1(\mathbf{R})) \mid \Phi_c > \quad (3)$$

responsible for the channel coupling. Here $\mid \Phi_c >$ is the channel spin function [6], [5] including the angular momentum part in the relative motion of the decay products. The function $S_c^1(\mathbf{R})$) is the JWKB expression (see Ref.[24] cited in Ref. [5]) of the noncentral part of the action

$$\frac{i}{\hbar} S_c^1(\mathbf{R})) = -\frac{1}{\hbar}\int_{R_c}^{R_o} dR \cdot (\sqrt{2m_0 A_{red}(V(\mathbf{R},\theta_i^1,\theta_i^2) - \mathbf{Q_c})} - \sqrt{2m_0 A_{red}(V(R) - Q_c)}) \quad (4)$$

The noncentral part of the action is generated by the noncentral part - $V_1(\mathbf{R},\theta_i^{(1)},\theta_i^{(2)})$ of the double folded M3Y interaction potential [5] (see also Refs.[29-32] from Ref. [5]) in which the nucleon - nucleon potential has the following form

$$v(r) = v_{00}(r) + \mathcal{J}_{00}\delta(r) + v_{01}(r)\tau_1 \cdot \tau_2 + V_{Coul} \quad (5)$$

where the central term of the M3Y force is $v_{00}(r) = \left[7999\frac{\exp(-4r)}{4r} - 2134\frac{\exp(-2.5r)}{2.5r}\right]$ MeV, while the isospin part is $v_{01}(r) = \left[-4885.5\frac{\exp(-4r)}{4r} + 1175.5\frac{\exp(-2.5r)}{2.5r}\right]$ MeV. The δ - force term approximate the single nucleon exchange through the zero range pseudopotential ($\mathcal{J}_{00}$ = -262 MeV fm^2). The spin - spin and spin - isospin terms are neglected here. The nuclear densities are given by the following formula: $\rho(\mathbf{r}) = \rho_0\left[1 + \exp\frac{1}{a}\left(r - \frac{R_0}{c}(1 + \beta_2\mathcal{Y}_{20}(cos\theta))\right]^{-1}$ with the constant ρ_0 fixed by normalizing the proton and neutron densities to the Z proton and N neutron numbers respectively, the diffusivity a = 0.63 fm and $R_0 = r_0A^{1/3}$ with r_0 = 1.19 fm if otherwise not stated. Here β_2 is the quadrupole deformation and c is the usual constant which ensures

the volume conservation condition $\int_V d^3r = \frac{4\pi}{3}R_0^3$, from which it results $c(\beta_2) = \left[1 + \frac{3}{4\pi}\beta_2^2 + \frac{1}{14\pi}\beta_2^3\right]^{1/3}$

The general expression for the relative intensities in cluster decay or cold fission leading to a definite channel quantum state $(I_1K_1\pi_1;I_2K_2\pi_2)$ is defined as a ratio of two quantities. The numerator represents the partial decay width that define a given channel of the cluster radioactivity $(A,Z) \rightarrow (A_1,Z_1) + (A_2,Z_2)$. The denominator is the sum of all partial decay widths.

Thus

$$\mathcal{I}_{rel}^{(I_1K_1\pi_1;I_2K_2\pi_2)} = \frac{\Gamma^{(I_iK_i\pi_i\rightarrow I_1K_1\pi_1;I_2K_2\pi_2)}(Q_c)}{\sum_{I_1K_1\pi_1;I_2K_2\pi_2}\Gamma^{(I_iK_i\pi_i\rightarrow I_1K_1\pi_1;I_2K_2\pi_2)}(Q_c)} = \frac{\left(HF^{(I_iK_i\pi_i\rightarrow I_1K_1\pi_1;I_2K_2\pi_2)}\right)^{-1}R(Q_c,Q_0)}{\sum_{I_1K_1\pi_1I_2K_2\pi_2}\left(HF^{(I_iK_i\pi_i\rightarrow I_1K_1\pi_1;I_2K_2\pi_2)}\right)^{-1}R(Q_c,Q_0)} \quad (6)$$

where $Q_0 = M(A,Z) - M_1(A_1,Z_1) - M_2(A_2,Z_2)$,
$Q_c = Q_0 - E^*_{I_1K_1\pi_1} - E^*_{I_2K_2\pi_2}$. The quantity $R(Q,Q_0)$ is defined as follows $R(Q,Q_0) = \frac{P_{l=0}(Q)}{P_{l=0}(Q_0)}$

3. Alpha Decay

By using the enlarged superfluid model (ESM) [13], we calculated the quasiparticle - phonon structure of the ground state of the ^{223}Ra, ^{229}Th, ^{241}Am, ^{243}Am, ^{243}Cm and ^{255}Fm nuclei and of several specific excited states of some daughter nuclei populated by α -, ^{14}C -, ^{20}O - and ^{34}Si decays [5], [6], [7]. The results are reproduced in Tables 1 and 6 of Ref. [5], Tables 1 and 2 of Ref. [6] and Table 1 of Ref. [7]. The structures of these states are very close to the structures given within the quasiparticle - phonon nuclear model (see Ref.[5] and Refs. [13,36,37] cited therein).

In calculating the ^{255}Fm - and ^{251}Cf - excited states structure the ESM parameters used are: $G_p = 0.14$ MeV, $G_n = 0.12$ MeV, $G_4 = 0.25$ keV. The parameters of the average field are taken from Ref. [5]. The deformation parameters used are: $\beta_{20} = 0.26$ and $\beta_{40} = 0.035$. They are taken from the calculations of ^{251}Cf static deformations (see Ref.[5]). The particle - hole quadrupole and octupole parameters used (see eq. 26 from the Ref. [5]) are: $\kappa_{n\tau}^{\lambda\mu} = \kappa_{0\tau}^{2\mu} = 0.664$ keV fm^{-4}; $\kappa_{n\tau}^{\lambda\mu} = \kappa_{1\tau}^{2\mu} = 62.4$ eV fm^{-4}; $\kappa_{n\tau}^{\lambda\mu} = \kappa_{0\tau}^{3\mu} = 8.6$ eV fm^{-6} $\kappa_{n\tau}^{\lambda\mu} = \kappa_{1\tau}^{3\mu} = 1.2$ eV fm^{-6}. The particle - particle quadrupole parameters used (see eq. 26 from the Ref. [5]) are: $G_{n\tau}^{L\lambda\mu} = G_{0\tau}^{L2\mu} = 12$ eV fm^{-4}. All the other coupling constants entering eq. (26 from the Ref. [5]) and not mentioned here have been taken equal to zero. For ^{235}U the above parameters are the same except the deformation parameters ($\beta_{20} = 0.23$ and $\beta_{40} = 0.08$), which are taken from experiment [18], [19]. These values are close to the values obtained in the calculations of ^{235}U static deformations (see Ref.[37] cited in [5]).

In the calculated structures we restricted the valence single particle space to 52 proton levels and 52 neutron levels centered around the Fermi levels and the number of the quadrupole and octupole phonons with $\lambda\mu$ = 20,22,30,31,32 and i=1,2 (see Ref. [13]), following the recipe used within the quasiparticle - phonon model developed in Refs. [14,36] cited in Ref. [5].

Within the R-matrix approximation [6] we calculated the HF's for the favored and some unfavored α - decays. The expressions of the reduced widths within the superfluid model are given in Ref. [16]. The results have been compared with the calculations of Ref. [11] and the experimental data [17] (see Table 3a from Ref. [5], Tables 4-9 from Ref. [6] and Table 2 from Ref. [7]). They are not far from our previous calculations [9]. A relatively good agreement with the experimental data is obtained. The data denoted by HF_{MPR} have been obtained by using the reduced widths from Ref. [11], however, the penetrability ratios and the Fröman - Nosov matrices have been calculated with the M3Y double folding potential (see section 2.A from Ref. [5]). The calculations reported in the mentioned tables lead to the conclusion that the α - decays: ^{255}Fm (g.s.) $\rightarrow \alpha +$ ^{251}Cf($\frac{7}{2}^+$ 106.33 keV), ^{241}Am (g.s.) $\rightarrow \alpha +$ ^{237}Np($\frac{5}{2}^-$ 60 keV), ^{243}Am (g.s.) $\rightarrow \alpha +$ ^{239}Np($\frac{5}{2}^-$ 75 keV) and ^{243}Cm (g.s.) $\rightarrow \alpha +$ ^{239}Pu($\frac{5}{2}^+$ 286 keV) can be considered as favored α - transitions, while ^{241}Am (g.s.) $\rightarrow \alpha +$ ^{237}Np($\frac{5}{2}^-$ 721 keV) and ^{243}Am (g.s.) $\rightarrow \alpha +$ ^{239}Np($\frac{5}{2}^-$ 666 keV) can be considered as weak unfavored α - transitions. The explanation of small (close to unity) HF's in this case is based on the picture according to which, the cluster (in this case an α - particle) is built from the fermions just situated at the Fermi surface, where strong pairing correlations occur and, in addition, one may neglect the differences in structure of the parent and daughter states. The difference between the favored and weak unfavored is that the mentioned weak unfavored α - transitions populate the so - called β - vibrational states with the structure very close to the structure of the ground state of the mother nucleus [14].

On the other hand, for the other α - transitions to the intrinsic states the hindrance factors are large, and this is explained by the fact that during the formation process of the α - cluster, at least one Cooper pair is destroyed and one nucleon from this Cooper pair is coupled to the uncoupled nucleon of the mother nucleus in order to participate in the formation of the α - cluster. The theoretical HF's for unfavored alpha transitions are, as a rule, larger than the experimental ones, except those corresponding to the alpha transitions to the members of the ^{251}Cf ground state rotational band. Within the ESM picture the small spins of the final states are more favored than the large ones.

The channel radial regular and irregular wave functions have been calculated by using the Coulomb potential plus the realistic M3Y double folding potential [5]. There is well known that the barrier penetrabilities are very sensitive to assumptions about nuclear potential (radius, slope, etc.) and channel radius. The nuclear densities used in our folding procedure are described by the above mentioned Fermi functions with $r_0^{(\alpha)} = 1.2$ fm, $a^{(\alpha)} = 0.5$ fm. We used different sets of density parameters and concluded (see e.g. Table 3b from Ref. [5]) that the penetrability ratios (F_l) are

relatively stable, i.e. they do not depend very much on the parameters entering the partners densities and they are close to the values given by the Rasmussen's formula (see Refs. [5], [15]). Since in the expressions of the hindrance factors we need the penetrability ratios (F_l) only, we believe, the predictions we give are more credible.

4. Cluster Decay

We also calculated several favored and unfavored cluster - transitions (^{255}Fm (g.s.) $\rightarrow$ ^{20}O + ^{235}U, ^{243}Cm (g.s.) $\rightarrow$ ^{34}Si + ^{209}Pb, ^{229}Th (g.s.) $\rightarrow$ ^{20}O + ^{209}Pb and ^{223}Ra (g.s.) $\rightarrow$ ^{14}C + ^{209}Pb) using the approach presented in [5], [6], [7]. Studying the decay ^{255}Fm (g.s.) $\rightarrow$ ^{20}O + ^{235}U, we see that a relatively large number of nucleons (8 protons and 12 neutrons), occupying the levels around the Fermi proton and neutron levels , the single - particle level [613] $\frac{7}{2}^+$, which has the main contribution in the structure of the ground state of ^{255}Fm nucleus can be found at a relatively high excitation energy of ^{235}U nucleus.

From the Table 1 from the Ref. [5] we learn that within the ESM - model [13] the structure of the ^{255}Fm ground state contains contributions from two single quasiparticle states namely, 97.9 % - [613] $\frac{7}{2}^+$ and 2.1 % - [624] $\frac{7}{2}^+$ emerging from $1i_{\frac{13}{2}}$ and $2g_{\frac{9}{2}}$, respectively. These states occur also in the structure of ^{235}U excited states lying at 446 keV and 1236 keV excitation energy, respectively (see Table 1 from Ref. [5] and Ref.[37] cited in the Ref. [5]). By using the ESM structure for the above initial and final odd-mass nuclei, the expression for the hindrance factor becomes:

$$HF\left[^{255}Fm(I_i^{\pi_i}K_i) \rightarrow ^{20}O + ^{235}U(I_f^{\pi_f} = I_i^{\pi_i}K_f = K_i)\right] \approx \tag{7}$$
$$\left\{\sum_l F_l \left| C^{I_i\ l\ I_i}_{K_iKK_i} C_{\rho_i}(K_i\pi_i) C_{\rho_f=\rho_i}(K_i\pi_i)(RSA)^{(i\rightarrow f)}_{lK}\right|^2\right\}^{-1}$$

where

$$(RSA)_{LK}(K_i\pi_i \rightarrow K_f\pi_f) = \tag{8}$$
$$\frac{\sum^{odd}_{\nu_1\ldots\nu_4}\sum^{odd}_{\omega_1\ldots\omega_6} {}_{odd}A^{LM}_{fav}(\nu_1\ldots\nu_4 \mid \omega_1\ldots\omega_6)\prod^4_{s=1} u^f_{\nu_s}v^i_{\nu_s}\prod^6_{j=1} u^f_{\omega_j}v^i_{\omega_j}}{\sum^{ee}_{\nu_1\ldots\nu_4}\sum^{ee}_{\omega_1\ldots\omega_6} {}_{ee}A^{LM}_{fav}(\nu_1\ldots\nu_4 \mid \omega_1\ldots\omega_6)\prod^4_{s=1} u^f_{\nu_s}v^i_{\nu_s}\prod^6_{j=1} u^f_{\omega_j}v^i_{\omega_j}}$$

in which ${}_{ee}A^{LM}_{fav}$ and ${}_{odd}A^{LM}_{fav}$ are the intrinsic overlap integrals [5], $C_{\rho_{i(f)}}$ are the weights of the single - quasiparticle state in the structure of the $i(f)$ - state. The only difference (see also Ref. [16]) between the cases corresponding to the odd- mass and doubly - even nuclei is that in the first case the sum in the above equation excludes the common quasiparticle state of both the mother and daughter nuclear states (e.g. $[613]\frac{7}{2}^+$ for the ^{255}Fm$\rightarrow$^{20}O+^{235}U case). The predicted HF's are given in the Table 1a. Table 1b contains several intermediate quantities, such as penetrabilities, penetrability ratios, inner and outer turning points calculated with different parameters entering the densities of the fragments.

Table 1a :

favored band			*weak unfavored band*		
E_f (keV) [23]	$I_f^{\pi f}$	HF_{ESM}	E_f (keV) [23]	$I_f^{\pi f}$	HF_{ESM}
1236.	$\frac{7}{2}^+$	≈ 5	445.716	$\frac{7}{2}^+$	≈ 185
	$\frac{9}{2}^+$	≈ 11	509.92	$\frac{9}{2}^+$	≈ 428
	$\frac{11}{2}^+$	≈ 18	587.82	$\frac{11}{2}^+$	≈ 729
	$\frac{13}{2}^+$	≈ 31	682.57	$\frac{13}{2}^+$	≈ 1224

Table 1b :

l	P_l, F_l, r_i, r_o	Rasm.	$r_0 = 1.2$, $a = 0.5$	$r_0 = 1.3$, $a = 0.7$
0	P_0 (r_i)	-	$0.117 \cdot 10^{-90}$	$0.149 \cdot 10^{-90}$
0	P_0 (10.41 fm)	-	$0.125 \cdot 10^{-57}$	$0.124 \cdot 10^{-57}$
2	F_2	0.809	0.859	0.861
4	F_4	0.494	0.605	0.610
6	F_6	0.227	0.350	0.357
-	r_i	-	5.7	6.3
-	r_o	-	27.1	27.1

In the calculations presented in the Table 1 we neglected the collective - state contributions in the structure of the initial and final states, which may affect a little the presented predictions.

Unfortunately, the above discussed ^{20}O radioactivity cases have half - lives greater than the maximum half - life ($10^{25.75}$ sec.) among the experimentally measured [2] cluster decay half - lives and, hence, would be hard to measure.

The ^{223}Ra and ^{229}Th nuclei belong [6] to the well known region of soft nuclei with $Z \approx 88$ and $N \approx 134$, with strong octupole correlations in the ground and low lying excited states, where the $1j_{\frac{15}{2}}$ intruder orbital interacts strongly with the $2g_{\frac{9}{2}}$ natural - parity orbital. The HF's for both the α - and ^{14}C - decays of the ground state of ^{223}Ra are very difficult to be calculated at present, due to the lack of accurate structure informations of the mother and daughter nuclei. Studying the experimental HF for α - decays to ^{219}Rn ground and low lying excited states [20] we learn that $\approx$ fifteen [20] transitions have small (< 100) HF's and from these transitions five have HF's < 10. The corresponding excited states (158.64 keV; $(\frac{3}{2}, \frac{5}{2})^+$; HF = 7.9; 269.48 keV; $(\frac{3}{2}^+, \frac{5}{2}^+)$; HF = 4.5; 338.27 keV; $(\frac{3}{2})^+$; HF = 5.6; 446.83 keV; $(\frac{3}{2})^-$; HF = 7.9 and 515.1 keV; HF = 4.5) have very different structure, and this fact tells us that the structure of the ground state of ^{223}Ra is not as simple as e.g. the ^{255}Fm case. It may contain many more or less equal components of single quasi - particle or quasi - particle - phonon states. Unfortunately, not all the spins and parities of the ^{219}Rn - excited states, populated by α - decay, are known. Thus, it is a difficult problem to describe the quantum states involved in the α - and ^{14}C

- decay of ^{223}Ra. In our opinion, it is not sufficient to have a description of these states within an independent particle model only (see Refs.[24-28] from [6]). Residual interactions could play an important role [9]. The restrictions concerning the valence single particle space (52 proton levels and 52 neutron levels centered around the Fermi levels) and the number of quasiparticles and phonons (as e.g. in the case of ^{255}Fm$\rightarrow\alpha+^{251}$Cf - decay, where only $\lambda\mu$ = 20,22,30,31,32 and i=1,2 - phonons have been used), may lead to inaccurate structure of the ^{223}Ra - nucleus. First, the valence single particle space should be extended and secondly, at the next step, when incorporating the quasiparticle - phonon interaction, the number of quasiparticles and phonons should be increased. Such a task is as hard to perform as the calculations within the OXBASH shell model code with realistic residual interactions [6].

Nevertheless we calculated the hindrance factors for ^{223}Ra (g.s) $\rightarrow$ ^{14}C + ^{209}Pb - and ^{229}Th (g.s) $\rightarrow$ ^{20}O + ^{209}Pb - cluster transitions in a restricted basis analogous to that used for ^{255}Fm (g.s.) $\rightarrow$ ^{20}O + ^{235}U decay [5]. In these calculations only the decays that populate the ground and the 779 keV excited state of ^{209}Pb have been considered. The calculated HF's are 668 and 28 for the Ra case and 1070 and 20 for the Th case [5].

A few more comments may be in order here. First of all, our ESM model is not to be taken too seriously for very complex structures, which should be the case of ^{223}Ra. This should be not true even for structures close to single quasiparticle states, because the assumption of ^{223}Ra as an axial symmetric deformed nucleus seems to be not realistic [6], [5]. On the other hand, in order to have realistic structures for both the initial and final nuclear states, calculations within shell model codes like OXBASH or ESM are practically impossible for present computers. Therefore simple schematic models like presented above would be useful.

5. Conclusions

In this work we reported the results of several calculations performed within the enlarged superfluid model [13]. The alpha decay mechanism used is derived [10], [9], [16] directly from the R - matrix approach to nuclear reactions, i.e. it is assumed that the alpha cluster can be found with some probability in the structure of the decaying nucleus. The external wave functions are calculated from a cluster - nucleus double - folding model potential obtained with the M3Y interaction. A relatively good agreement with the experimental data has been obtained. An analogous mechanism has been applied for ^{223}Ra (g.s) $\rightarrow$ ^{14}C + ^{209}Pb; ^{255}Fm (g.s) $\rightarrow$ ^{20}O + ^{235}U, ^{229}Th (g.s) $\rightarrow$ ^{20}O + ^{209}Pb and ^{243}Cm (g.s) $\rightarrow$ ^{34}Si + ^{209}Pb processes. For these four processes the spectroscopic factors are expanded in terms of products of cluster overlaps and intrinsic overlap integrals. Explicit expressions for the cluster overlaps have been derived. For the intrinsic overlap integrals we construct a model, which is an extension of the usual models for simple particle decay such as deuteron, triton and alpha decay. In these cases difficulties arise with increasing the complexity in the structure of the involved nuclear states and due to lack of realistic structure of ^{223}Ra and ^{229}Th ground states.

Within ESM we overestimate the experimental HF corresponding to the ^{223}Ra (g.s) $\rightarrow$ ^{14}C + ^{209}Pb process leading to the ground state of ^{209}Pb and to the first excited state of ^{209}Pb. We cannot explain the experimental HF corresponding to the $\frac{15}{2}^-$ (1423 keV) state, but our approach does not use a very large basis of both single particle and phonon states.

Predictions have been done for the hindrance factors corresponding to the following cluster transitions: ^{255}Fm (ground state) $\rightarrow$ ^{20}O + ^{235}U (445.716 keV, 1236 keV and their rotational bands) and ^{229}Th (ground state) $\rightarrow$ ^{20}O + ^{209}Pb (ground state and $\frac{11}{2}^+$, 779 keV excited state).

6. Acknowledgements

The author would like to express his gratitude to Professor Luciano Fonda from the ICTP - Trieste for his permanent encouragement and fruitful discussions.

7. References

1. H.J. Rose and G.A. Jones, Nature, **307** (1984) 245
2. A. Sandulescu and W. Greiner, Rep. Progr. Phys. **55** (1992) 1423
3. J.H. Hamilton, J. Kormicki, Q. Lu, D. Shi, K. Butler - Moore, A.V. Ramaya, W.C. Ma, B.R.S. Babu, G.M. Ter - Akopian, Yu. Ts. Oganesian, G.S. Popeko, A.V. Daniel, S. Zhu, M.G. Wang, J. Kliman, V. Pohorsky, M. Morhac, J.D. Cole, R. Aryaeinejad, R.C. Greenwood, N.R. Johnson, I.Y. Lee and F.K. McGovan, *"Neutron Multiplicities in Spontaneous Fission and Nuclear Structure Studies"*, Lecture at the International NATO Advanced Study Institute, Predeal (Sept. 1993), Romania, *"Frontier Topics in Nuclear Physics"*, Eds. W. Scheid and A. Sandulescu, in press; see also R. Aryaeinejad *et al* Phys. Rev., **C 48** (1993) 566.
4. E. Hourani *et al* Phys. Rev., **C 44** (1991) 1424; L. Brillard *et al* C.R. Acad. Sci. Paris, **309** (1989) 1105
5. O. Dumitrescu and C. Cioacă, Phys. Rev. C 51 (1995) 3264; Preprint ICTP Trieste IC/94/122 (1994);
6. O. Dumitrescu, Phys. Rev. C 49 (1994) 1466; Preprint ICTP Trieste IC/93/164 (1993);
7. O. Dumitrescu, *"Fine Structure in Cluster Decays"* Proc. International NATO Advanced Study Institute, Predeal (Sept. 1993), Romania, *"Frontier Topics in Nuclear Physics"*, Eds. W. Scheid and A. Sandulescu, NATO - ASI Series B: **334** (1994) 73.
8. O. Dumitrescu *et al*, *"Double Fine Structure in the Cluster Radioactivity of ^{252}Cf"* Preprint ICTP Trieste IC/95/175 (1995);
9. O. Dumitrescu, Fiz. Elem. Chastits At.Yadra **10** (1979) 377 (Sov.J.Part.Nucl., **10** (1979) 147) O. Dumitrescu and A. Sandulescu, Nucl. Phys., **A 100** (1967) 456; Phys. Lett., **B 19** (1965) 404; Phys. Lett., **B 24** (1967) 212; Annales

Acad. Sci. Fennicae, Series A, VI.Physica **265** (1968); M.I. Cristu, O. Dumitrescu, N.Y. Pyatov and A. Sandulescu, Nucl. Phys., **A 130** (1969) 31; O. Dumitrescu and D.G. Popescu, Revue Roumaine de Physique **18** (1973) 1065 and **21** (1976) 323; O. Dumitrescu, M. Petrascu, D.G. Popescu and A. Sandulescu, Revue Roumaine de Physique **18** (1973) 1231;

10. H.J. Mang, Ann. Rev. Nucl. Sci., **14** (1964) 1, Z. Phys., **148** (1957) 572, Phys.Rev., **119** (1960) 1069, Proc. Second International Conf. Clust. Phen. Nucl. College Park, Maryland (1975);
11. H.J. Mang, J.K. Poggenburg and J.O. Rasmussen, Phys. Rev.,**181** (1969) 1697; J.K. Poggenburg UCRL - 16187 (1965)
12. M. Grigorescu, B.A. Brown and O. Dumitrescu, Phys. Rev., **C 47** (1992) 2666
13. O. Dumitrescu, Fiz. Elem. Chastits At. Yadra 23 (1992) 430 (Sov.J. Part. Nucl., **23** (1992) 187); Nuovo Cimento **A 104** (1991) 1057 Preprint ICTP - Trieste **IC/91/72** (1991); O. Dumitrescu and M. Horoi, Nuovo Cimento, **A 103** (1990) 653; M. Apostol, I. Bulboaca, F. Carstoiu, O. Dumitrescu and M. Horoi, Nucl. Phys., **A 470** (1987) 64; M. Apostol, I. Bulboaca, F. Carstoiu, O. Dumitrescu and M. Horoi, Europhys. Letters, **4** (1987) 197;
14. V.G.Soloviev, *Theory of Complex Nuclei*, (Nauka, Moscow,1971; Pergamon Press, New York,1976)
15. I.K. Hyde, I. Perlman and G.T. Seaborg, *The Nuclear Properties of the Heavy Elements*, Prentince - Hall,Inc., Englewood Cliffs, New Jersey (1964); S. Bjornholm, *Radiochemical and Spectroscopic Studies of Nuclear Excitations in Even Isotopes of the Heaviest Elements*, Munksgaard, Copenhagen, (1965); S. Bjornholm, M. Lederer, F. Asaro and I. Perlman, Phys. Rev., **130** (1963) 2000.
16. O. Dumitrescu and A. Sandulescu, Nucl. Phys., **A 100** (1967) 456; Annales Acad. Sci. Fennicae **Series A VI**, Physica (1968) Nr. 265
17. Y. A. Ellis and M. R. Schmorak, Nuclear Data Sheets, **B 8** (1972) 345
18. C.M. Lederer, V.S. Shirley, E. Browne, J.M. Daikiri, R.E. Doebler, A.A. Shihab - Eldin, L.J. Jardine, J.K. Tulli, A.B. Buisin, *"Tables of Isotopes"* 7^{th} Ed. John Wiley and Sons, N.Y. (1978)
19. G. Haouat, J. Lackhkar, Ch. Lagrange, J. Jary, J. Sigaud and Y. Patin, Nucl. Sci. Eng. **81** (1982) 491
20. C. Maples, Nuclear Data Sheets, **22** (1977) 223
21. M.R. Schmorak, Nuclear Data Sheets **40** (1983) 67
22. M.R. Schmorak, Nuclear Data Sheets **59** (1990) 507
23. M.R. Schmorak, Nuclear Data Sheets **69** (1993) 375
24. M.J. Martin, Nuclear Data Sheets **63** (1991) 723
25. I. Ahmad, F. T. Porter, M.S. Freedman, R.F. Barnes, R.K. Sjoblon, F. Wagner Jr, J. Miested and P.R. Fields, Phys. Rev., Ç 3 (1971) 390; I. Ahmad and J. Milsed, Nucl. Phys. **A 239** (1975) 1

3. NUCLEAR REACTIONS: EXOTIC NUCLEI, FUSION, FISSION

FUSION OF HALO NUCLEI WITH LIGHT NUCLEAR TARGETS

M. Petrascu
Institute of Physics and Nuclear Engineering
P.O.B MG-6, Bucharest, Romania.

Abstract

A specific mechanism for the ^{11}Li fusion with light nuclear targets, has been emphasized. Due to the very large dimension of ^{11}Li, one may expect that the valence neutrons will not be absorbed in the fusion process together with ^{9}Li core, but will be emitted in the early stage of the reaction, with practically non altered beam velocity energy

The fusion of ^{9}Li and ^{11}Li with Si targets has been experimentally investigated, in a global approach. The neutrons resulting from Si(^{9,11}Li,fus.) were measured by the aid of the RIKEN "long neutron wall". While for the energy range 0.4-5 MeV the neutrons show the same behaviour as concerns their number and position spectra, for the range 5-22 MeV there is a dramatic difference between the two kind of beams, for both mentioned parameters. Thus in the case of ^{11}Li, an important fraction of the neutrons are concentrated in a very narrow region, according to the results of position measurement by the central 7, 8, 9, detectors of the wall. The radius of the spot on the "wall"for these neutrons is of the order of 10 cm. For the rest of detectors, the position spectra appear to be broader but essentially narrower than in the case of ^{9}Li beam. From a correlation analysis, it follows as a preliminary conclusion, that in the central spot, the neutrons are emitted in pairs, presumably after a smooth breakup from the colliding cores. Outside this zone they are emitted as single neutrons or in pairs with a much larger correlation lengths, following a 1 step interaction with the colliding cores. This observation of "focused" neutrons, confirms the recent prediction of the mechanism consisting in the pre-emission of one or two halo neutrons in the early stage of the fusion process. From the width of the central neutron spot, an estimate of the internal momentum p_i of the halo neutrons could be obtained. This value of p_i turns out to be 11.4±0.6 MeV/c

1. Introduction

The neutron halo nuclei were discovered by I. Tanihata, T.Kobayashi and coworkers[1]. These nuclei are characterized by the very large matter radii, by the small separation energy and the small internal momentum of the valence neutrons. Until now the halo nuclei were investigated, mostly by elastic , inelastic scattering and breakup processes. Recently it was predicted[2], that due to the very large dimension of ^{11}Li, one may expect that in a fusion process on a light target, the valence neutrons will not be absorbed together with the ^{9}Li core, but will be emitted in the early stage of the reaction, with practically non altered beam velocity energy.

An experiment aiming to check this expectation, was

recently performed at the RIKEN-RIPS facility. The experimental results are confirming the emphasized mechanism of valence neutron pre-emission in the fusion process. The following topics will be considered bellow:

- A sharp cut-off estimation of the halo neutron pre-emission probabilities, at the fusion of ^{11}Li with light targets.
-Experimental investigation of the fusion of 13 MeV/n ^{11}Li projectiles with Si targets
-Conclusions

2. Sharp cut-off estimation of the halo neutron pre-emission probabilities at the fusion of ^{11}Li with light nuclear targets.

Due to the very large dimension[1)] of ^{11}Li, one may expect in a fusion process on light target, that the valence neutrons will not be absorbed together with ^{9}Li core, but will be emitted in the early stage of the reaction, with practically non altered beam velocity energy. A simple sharp cut-off approach was considered for the fusion of ^{11}Li with the light ^{12}C and ^{27}Al targets. In this approach, a straight forward derivation of the valence neutron pre-emission probability can be obtained, as it is illustrated in Fig. 1 and Fig. 2. These probabilities are provided in Table 1 and Table 2.

TABLE 1
Probabilities for uncorrelated valence neutron pre-emission

Reaction	Emission prob.	Absorb-tion prob.	Prob. for 2 neutron pre-emi-ssion	Prob. for 1 neutron pre-emi-ssion	Prob. for 2 neutron absorb-tion
^{11}Li+^{12}C	85.2%	14.8%	72.5%	25.2%	2.19%
^{11}Li+^{27}Al	71.3%	28.4%	51.3%	40.6%	8.0%

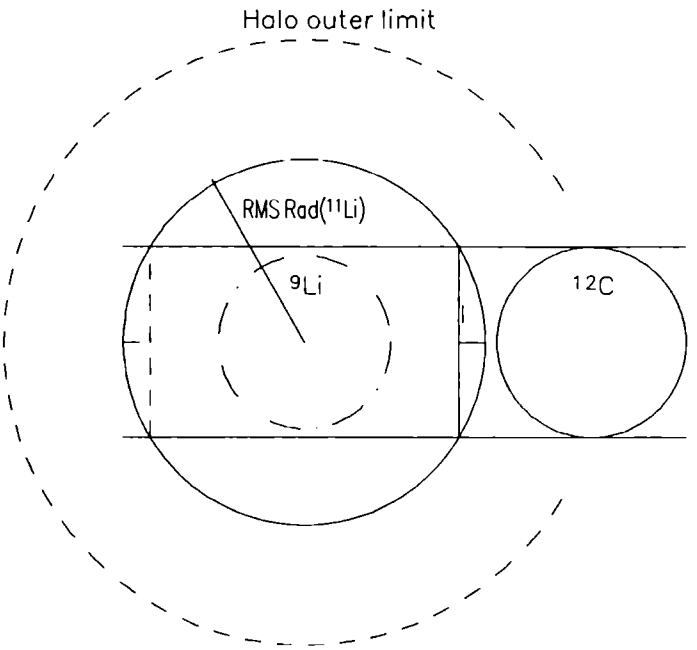

Fig. 1

Scaled image for the ^{11}Li + ^{12}C fusion

$S = 4\pi\ (\text{RMS-Rad}(^{11}\text{Li}))^2$

$S_1 = 2(\pi*(R(^{12}\text{C}))^2 + \pi*L^2)$

$S_2 = S - S_1$

Prob. for uncorr. neutron capture = S_1/S

Prob. for uncorr. neutron pre-emission = S_2/S

$S_1/S = 14.8\%$

$S_2/S = 85.2\%$

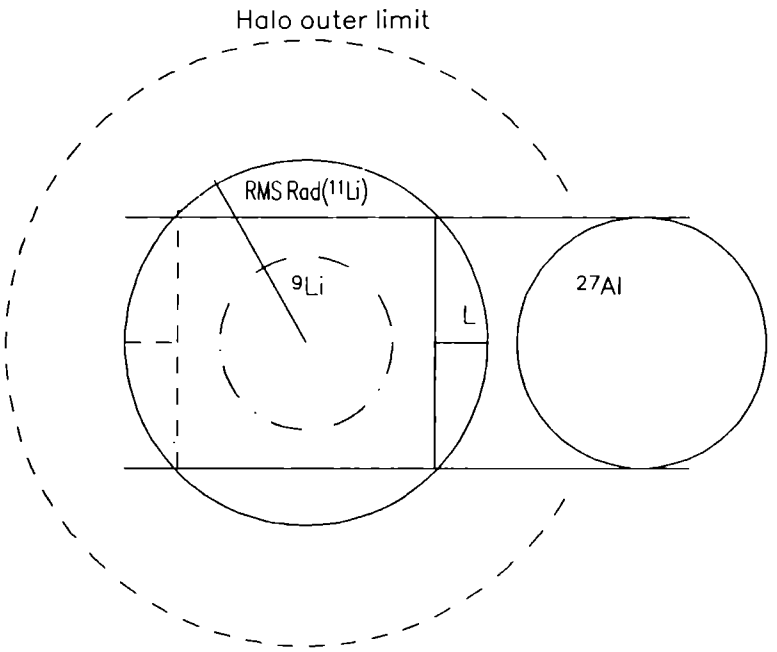

Fig. 2

Scaled image for the ^{11}Li + ^{27}Al fusion

$S = 4\pi\ (\text{RMS-Rad}(^{11}\text{Li}))^2$

$S_1 = 2(\pi*(R(^{27}\text{Al}))^2 + \pi*L^2)$

$S_2 = S - S_1$

Prob. for uncorr. neutron capture = S_1/S

Prob. for uncorr. neutron pre-emission = S_2/S

$S_1/S = 28.3\%$

$S_2/S = 71.6\%$

TABLE 2

Probabilities for correlated valence neutron pre-emission

Reaction	Emission prob.	Absorbtion prob.	Prob. for 2 neutron pre-emission	Prob. 2 neutron absorbtion
$^{11}Li+^{12}C$	85.2%	14.8%	85.2%	14.8%
$^{11}Li+^{27}Al$	71.6%	28.4%	71.6%	28.4%

*) Observation: The values provided in this table are actually limits. In fact one may expect, whatever values between the uncorrelated ones, and the values in Table 3, depending on the degree of correlation.

One can see that the pre-emission probabilities, calculated in a sharp cut-off approach could be quite high. This could be tested experimentally by comparing the fusion product yields obtained with ^{11}Li and ^{9}Li beams. An alternative way to test experimentally this prediction, is to measure directly the energy spectra and position distribution of the neutrons coming out from the fusion of ^{11}Li with a light nuclear target. An experiment aiming to measure the neutrons from the fusion will be presented in the following.

3. Experimental investigation of the fusion of 13 MeV/n ^{11}Li projectiles with Si targets.

The experimental arrangement is shown in fig 3. In this arrangement, a thin scintillator at F2, two position-sensitive Plane Parallel Avalanche Counters (PPAC-1, PPAC-2), two removable detectors (3mm-Si, 0.5mm-Scintillator),a Veto1 scintillator detector,having a 2X2 cm^2 hole, a Multiple Sampling Ionization Chamber (MUSIC) with a Microstrip Silicon detector and a Veto2 silicon detector mounted inside, and a 2-wall neutron detector, each consisting of 15 plastic scintillators 2X0.1 m^2 viewed by photomultipliers at both ends, can be seen. The MUSIC chamber consisting of 11 anode pads, was filled with Argon at a pressure of 350 torr. The window of the chamber was

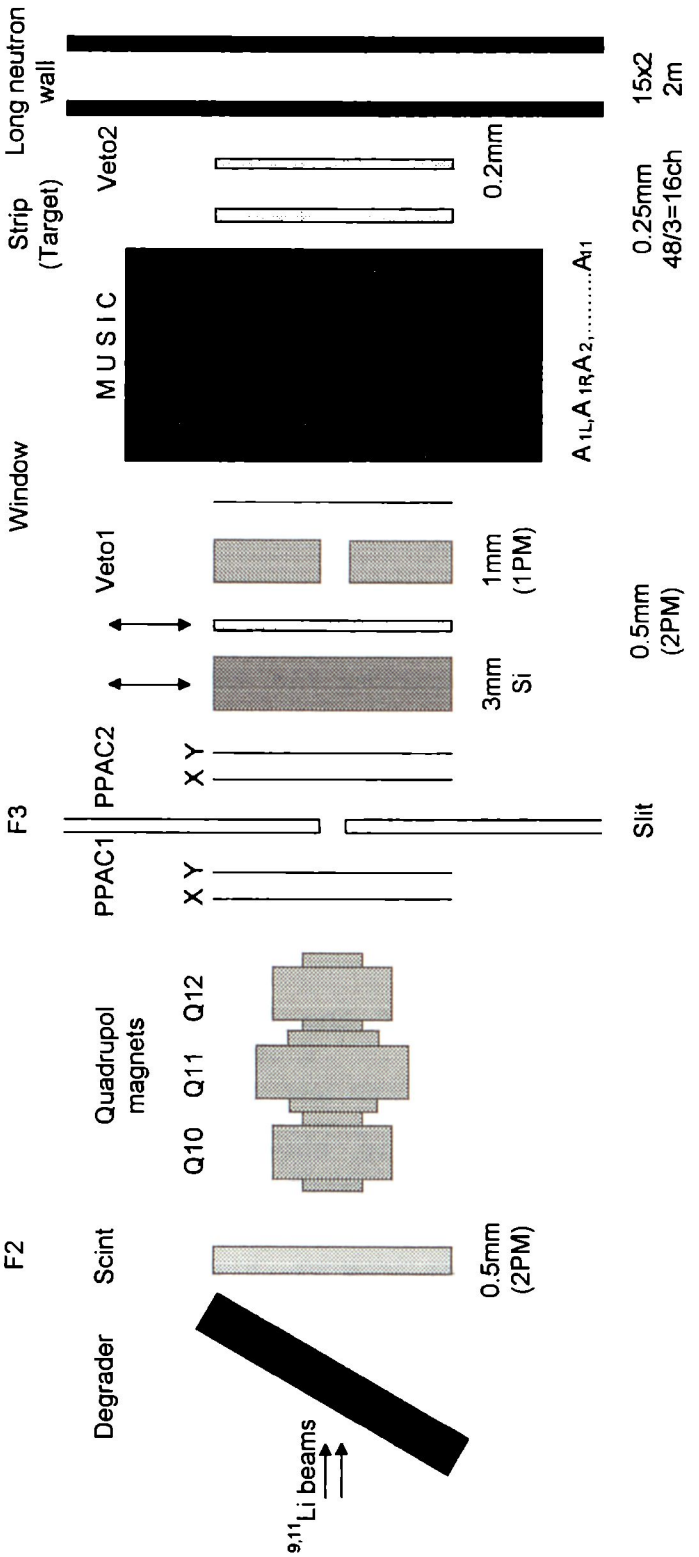

Fig.3 General layout of the experiment

made of thin aluminum or polypropylene. As trigger, the coincidences F2*PPAC*AntiVeto1*SiMS*AntiVeto2 were chosen. With this condition, by choosing the proper gates in processing of the data, one could either do the study of particular fusion channels, taking place in the thin MUSIC-chamber entrance window, or to investigate globally the ^{9,11}Li+Si fusion, by considering the events produced by the incoming beam inside the 250 μ microstrip silicon detector . In this paper, the results processed for this global approach will be presented.

The energy of ^{9,11}Li beams was chosen ~ 13 MeV/n. At this energy, the excitation in the compound nucleus (~ 3,3 MeV), is much lower than the value 4.98 MeV/n, at which the near ^{14}N+^{12}C system studied earlier[4], showed still a large fusion cross-section (>700 mb).

The large 5X5 cm^2 silicon veto detector placed behind the microstip detector eliminated the elastic, inelastic, and breakup processes at forward angles. The contribution of elastic and inelastic scattering at backward angles, is expected to be very low. In Fig 4a, the energy spectrum given by the microstrip Si detector, gated by the ionization loss of ^{9}Li- beam in the MUSIC-chamber, is shown. The data in fig 4a correspond to the cumulated runs 015 and 018 with ^{9}Li beam. The dashed line represents the global fusion energy spectrum obtained by the aid of the Monte Carlo program[5] "PACE", by taking into account the following pedestals:

1. The pedestal due to the ^{9}Li energy loss in the Si detector. This was taken 7.5 MeV, as corresponding to the middle position at 125 μ, in the Si detector. The width was taken also 7.5 MeV.

2. The pedestal corresponding to the alpha particles emitted in the fusion process. This pedestal was calculated by the aid of the α spectra given by the Code "Pace" for various angles in the lab system. The deposited energy/fusion =13.32 MeV, the width=16.88 MeV.

3. The pedestal corresponding to protons emitted in the fusion process. This pedestal was calculated as mentioned upper The value for the energy deposited in the Si detector by

Fig. 4a

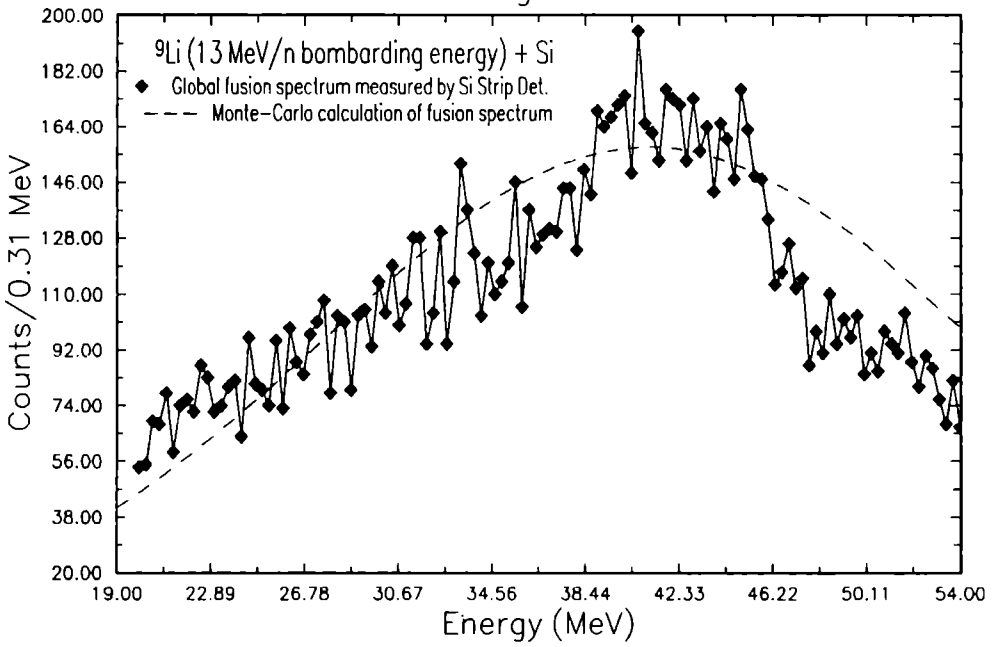
^{9}Li (13 MeV/n bombarding energy) + Si
Global fusion spectrum measured by Si Strip Det.
Monte-Carlo calculation of fusion spectrum
Counts/0.31 MeV
Energy (MeV)
200.00
182.00
164.00
146.00
128.00
110.00
92.00
74.00
56.00
38.00
20.00
19.00
22.89
26.78
30.67
34.56
38.44
42.33
46.22
50.11
54.00

Fig. 4b

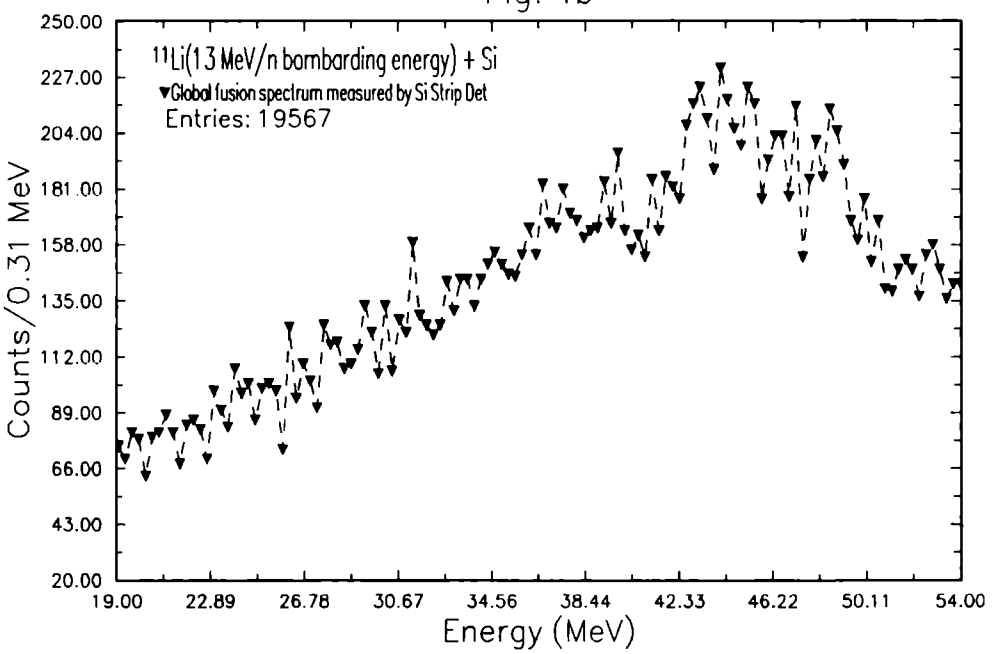
^{11}Li(13 MeV/n bombarding energy) + Si
Global fusion spectrum measured by Si Strip Det
Entries: 19567
Counts/0.31 MeV
Energy (MeV)
250.00
227.00
204.00
181.00
158.00
135.00
112.00
89.00
66.00
43.00
20.00
19.00
22.89
26.78
30.67
34.56
38.44
42.33
46.22
50.11
54.00

protons was found, rather low, being only 1.2 MeV. No width was assigned to this value.

The global energy spectrum for the ^{9}Li+Si fusion, calculated by the "Pace" code, for the incident energy 109.5 MeV (corresponding to the middle of the detector) is shown in fig 5 (the solid line) This spectrum was then approximated by a gaussian as it is shown by the dotted line in fig 5. To this gaussian were added then the upper mentioned pedestals and widths to obtain the dashed curve in fig 4a. A fairly good overall agreement can be noticed in fig 4a between the experimental spectrum an the calculated one, indicating that what is measured in the present arrangement, are really fusion processes.In fig. 4b, the cumulated energy spectrum of runs 025, 027, 028, 029, 031 and 032 with ^{11}Li, are presented. This energy spectrum is similar to that in fig 4a.

In fig 6a one of the time of flight neutron spectra measured with ^{11}Li, by the detector #7 of the long neutron wall is illustrated. The small peak at channel ~750 is due to gamma rays and it is used for the neutron energy calibration. More than 90% of the statistics of this spectrum could be reproduced by using a gate related also to the ionization loss of Li beam in MUSIC as it is shown in fig 6b. A small statistics of the order of 4% obtained by the complementary gating with the MUSIC, up to the channel 4000, presumably related to the events produced in the thin entrance window of the chamber, is shown in fig 6c. The remaining 5% difference could be considered as a background, although part of this, may be related to the threshold cut produced by the encoder.

The cumulated neutron spectra with ^{9}Li and ^{11}Li beams were processed in order to get the contributions of two energy groups to the position spectra, namely the energy group 0.4-5 MeV and 5-22 MeV. In this second group are expected to be present, the ^{11}Li valence neutrons (energy about 13 MeV), pre-emitted in the early stage of the fusion process. The energy range was taken somewhat larger, by considering the energy resolution of the detecting system (width of the gamma ray peak). This aspect will be discussed at the end of the paper.

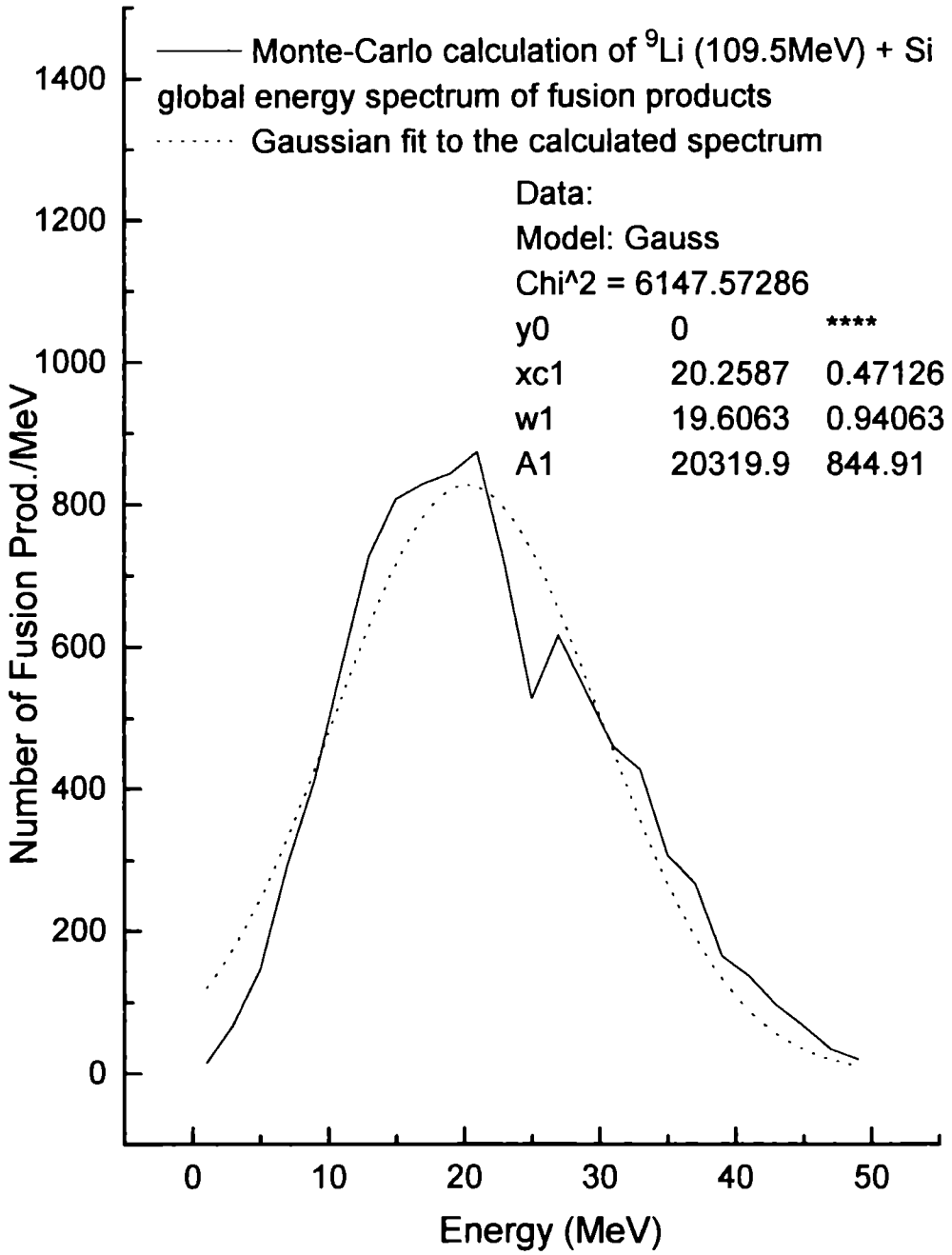

Fig. 5. Monte-Carlo calculation of global energy spectrum for ^{9}Li +Si fusion

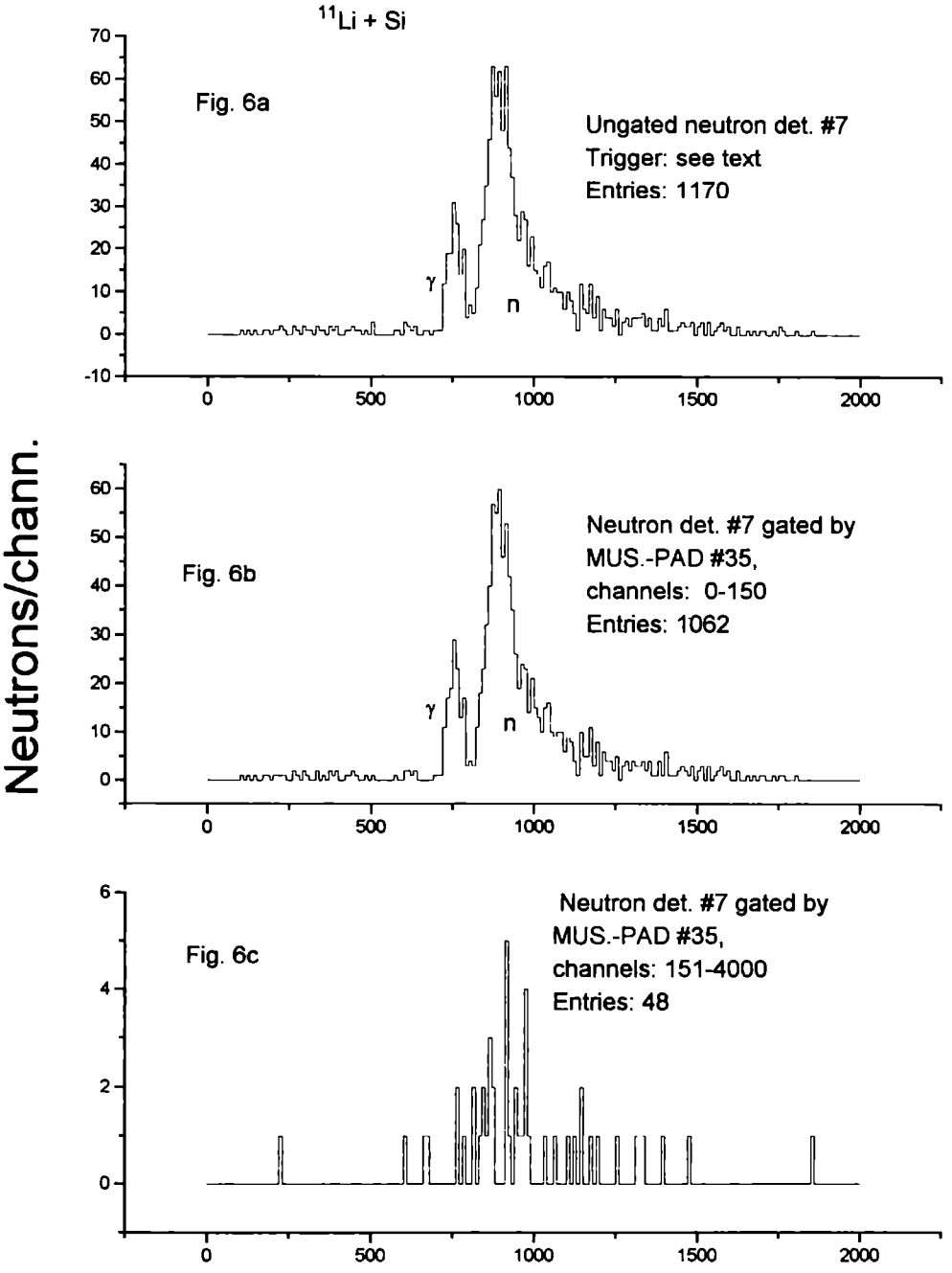

Fig. 6. Neutron time of flight spectra, obtained for different gating conditions

In fig. 7, neutron position spectra for the energy range 0.4-5 MeV, measured by the detectors 6-10, of the front neutron wall, are illustrated. The spectra with ^{9}Li were normalized to the same number of entries as in the case of ^{11}Li. As can be seen the intensity and the widths of the spectra are quite similar for ^{9}Li and ^{11}Li, as it should be for similar fusion processes. This is further underlined in fig.9a, in which the widths obtained for the position spectra with ^{9}Li and ^{11}Li beams, are represented A dramatic difference between the neutron position distributions corresponding to the ^{9}Li and ^{11}Li beams,appears for the energy range 5-22 MeV, as can be seen in fig. 8. Especially striking are the position spectra for detectors 7-9, being much narrower in the case of ^{11}Li beam. This difference is further stressed in Fig 9b, in which, the widths for all 15 neutron position spectra,measured by the first neutron wall, both for the ^{9}Li and ^{11}Li beams , are presented. The solid triangles and the solid circles are representing the widths obtained by applying a single gaussian model for the spectra.But for detectors 7-9 one could easily notice from fig.8, that 2 distinct gaussians, are contributing to the position spectra. Indeed, in an automatic search with 2 gaussians the width of both gaussians are displayed with very small errors, as can be seen in fig 10a-10c, or in fig 9b,(the open boxes). The widths of the narrow gaussians for detectors 7-9 are about 20 channels or 22 cm by taking into account the calibration of the detectors (see also table 1) For detectors 6 and 10 a 2 gaussian approach is less successful since the error bars are sensibly increased. However these two detectors are marking a transition from the very narrow width to a larger one, but definitely smaller then the width corresponding to the evaporation neutrons. This latter one is in the range of 90-100 channels, as can be seen in fig 9b for ^{9}Li. Therefore in the case of ^{11}Li beam one has to distinguish between the following three types of position spectra:

1. A broad type, characterized by widths near 90-100 chann. (Detectors 13-15 and possible 1-2). This type should correspond to evaporation neutrons.

2. An intermediate type characterized by widths near 50-60

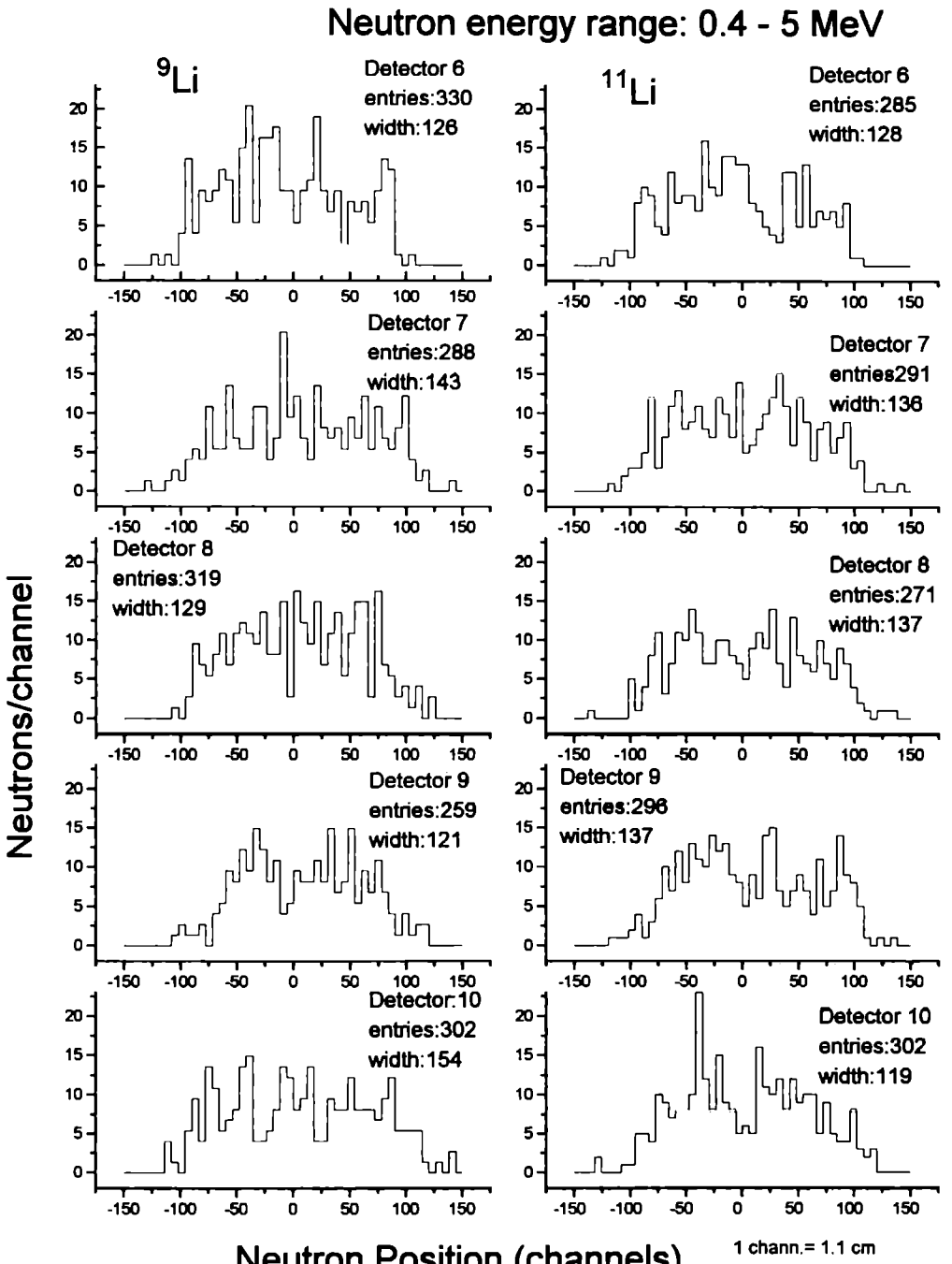

Fig. 7: Comparison between neutron position spectra for ^{9}Li and ^{11}Li beams; Neutron energy range:0.4-5 MeV; Neutron detectors: 6-10

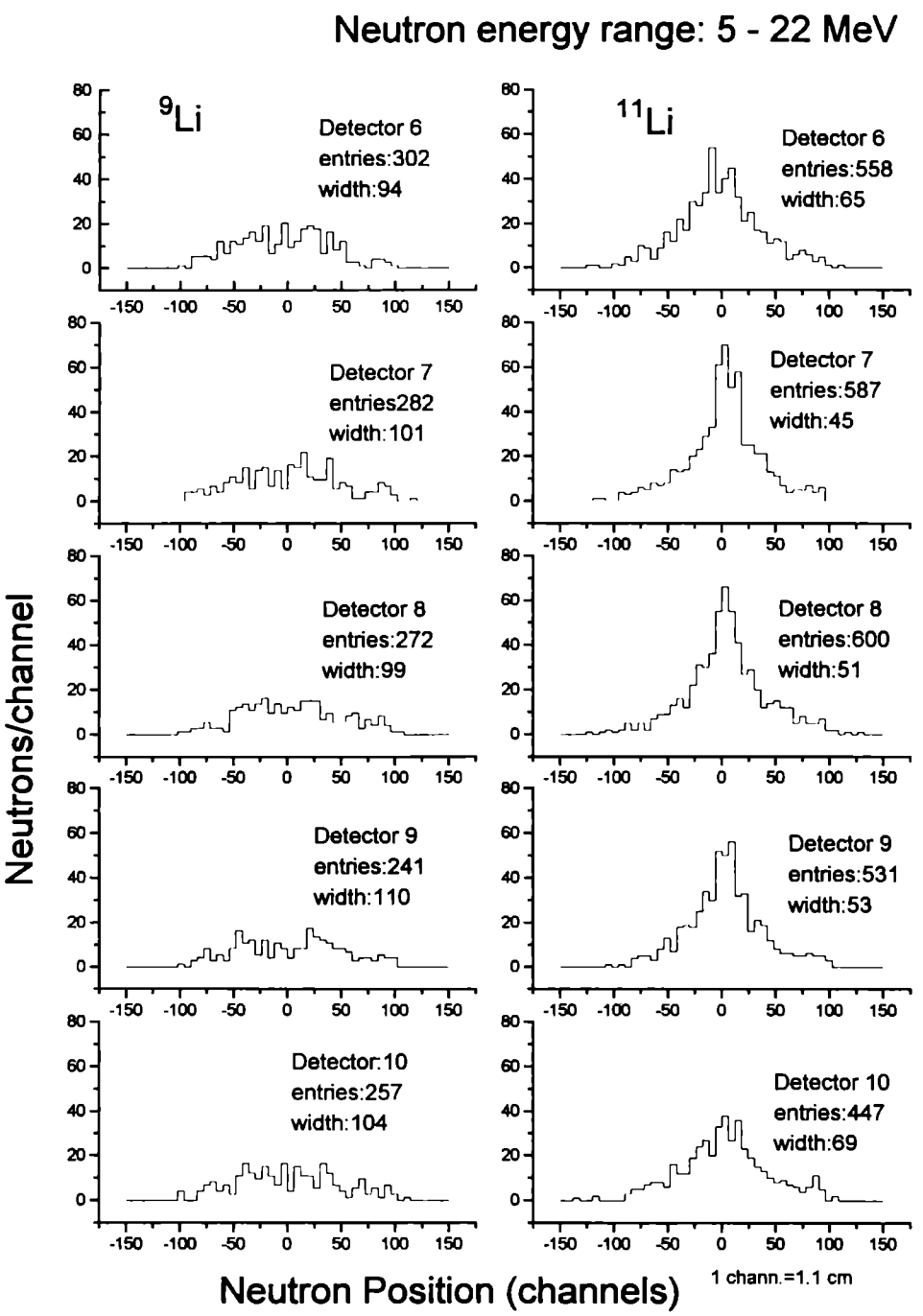

Fig. 8. Comparison between neutron position spectra for ^{9}Li and ^{11}Li beams; Neutron energy range: 5-22 MeV; Detectors: 6-10

Fig. 9. Comparison between widths of neutron pos. distributions

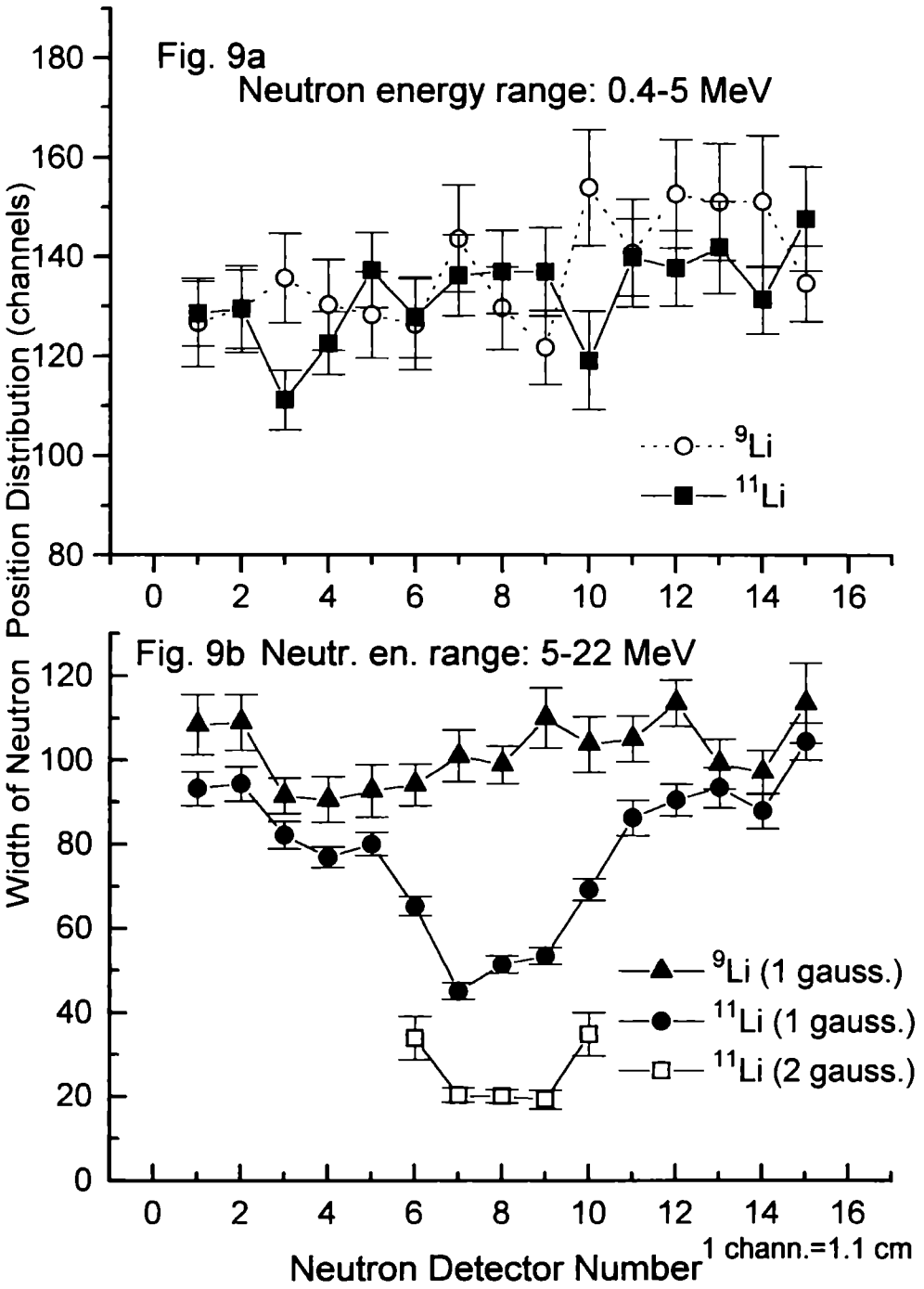

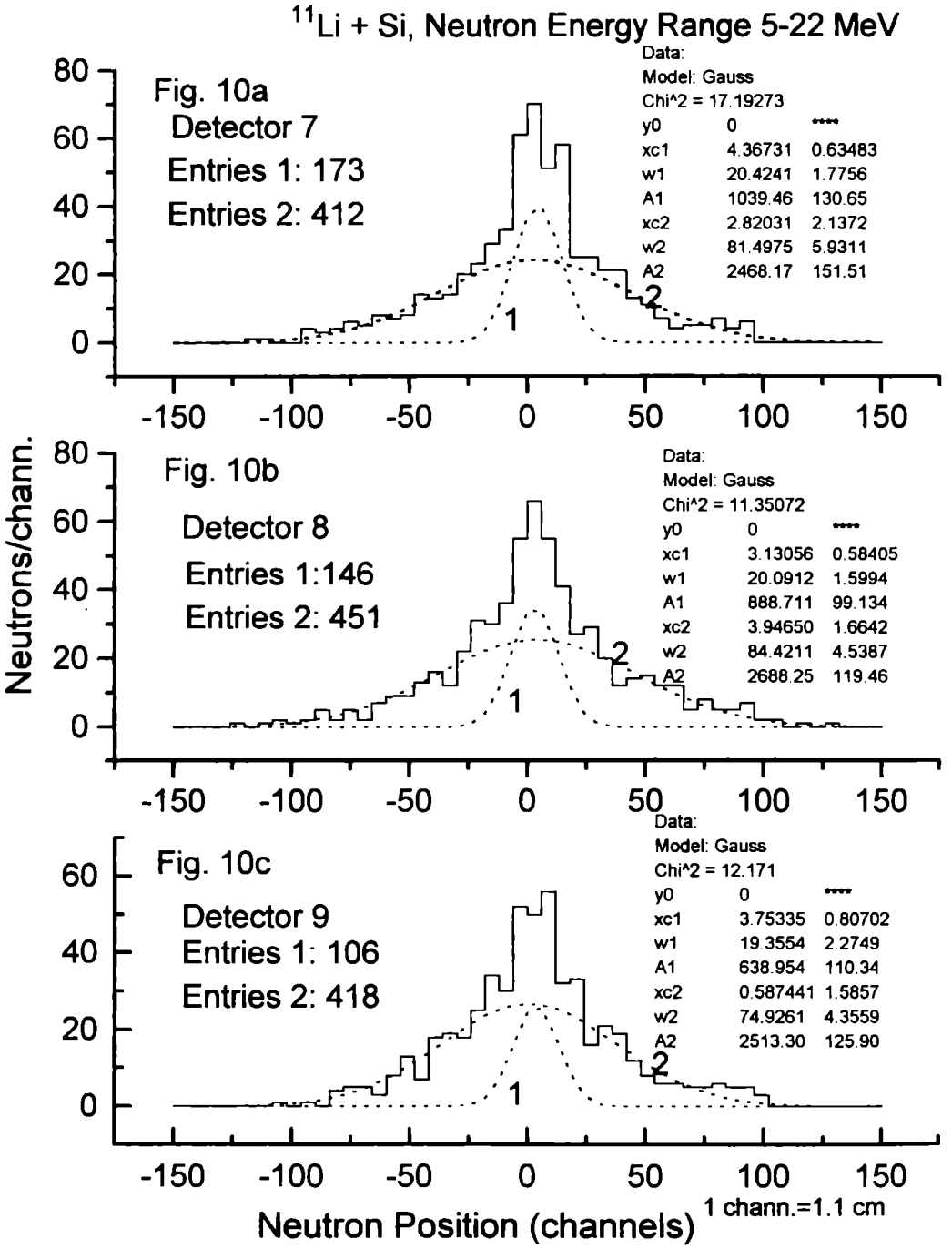

Fig. 10. Two-gaussian fit for detectors 7, 8 and 9

channels, so that by combining with the widths of evaporation neutrons distribution should result in a near 80 channels width as can be seen for detectors 3-5 and 11,12.

3. A very narrow type characterized by widths near 20 channels, superimposed on the background due to the groups 1 and 2. In figure 12b it is shown that this background is strongly reduced by choosing a neutron range between 10 and 20 MeV.

A hypothesis concerning this last type could be the assumption that the less perturbed valence neutrons in the pre-emission process, even without the breaking the correlation existing between these two neutrons, are detected by detectors 7-9. This narrow distribution should belong to somewhat correlated neutrons. If this is so, one should see in processing the data, a definite number of correlations between the adjacent, say 7 and 8 detectors, or between the non adjacent 7 and 9. But in attempting this procedure,it was found that there is a cross-talk between the adjacent detectors as can be seen in fig 11 , (^{9}Li data). An 11% (31/282) cross talk, can be seen for detectors 7-8 with ^{9}Li. Therefore it is much safer to consider the correlations between detectors 7-9 for which the cross-talk is negligible, as can be seen from fig 11 (^{9}Li data)

By assuming a correlation length between the neutrons of the order of 20 cm one should see then coincidences between the detectors 7 and 9 separated by detector 8, whose width is 6 cm.

In this case one should expect a number C of coincidences between detectors 7-9 equal to:

$$C \approx 1/6\ N_o/k.k^2 = 1/6\ N_o.k$$

in which k represents the neutron detection efficiency. By taking N_o = 425 (see Figs 8) and k~0.25, one should expect a number of about 18 coincidences. From fig. 11, the number of counts (det7-9, ^{11}Li) in the central zone, is about 25. This is in a good agreement with the expected number of coincidences. However further investigations of the found effect are needed. First of all, a more suitable to this purpose neutron detector is needed. As was mentioned above a somewhat large energy range 5-22 MeV (150 TOF channels) was considered in order to avoid looses, because the width of the γ ray peak is equal to $\approx$50 TOF

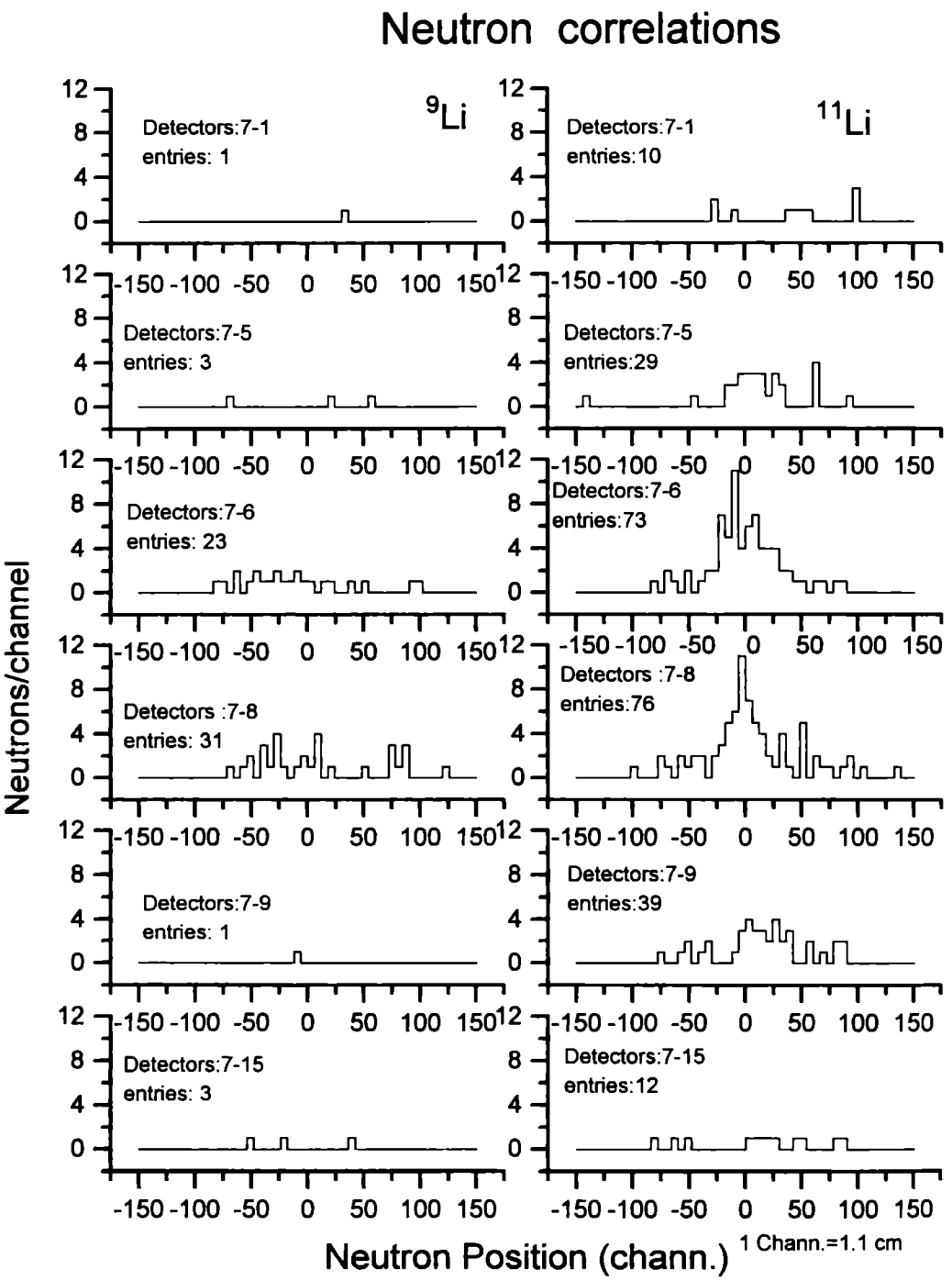

Fig. 11. Comparison between neutron correlation Det 7-Det i for ^{9}Li and ^{11}Li beams

channels. One can see from Fig. 12b that a reduction of the number of TOF channels to 60, causes a drastic reduction of the background by a factor of 2.3, together with a relatively small reduction, by about 15% of the effect. A further reduction of TOF range to 34 channels, (Fig 12c) reduces more drastically, by about 50%,the effect. In follows that for further studies of the neutron focusing effect, much shorter neutron detectors are needed, in order to obtain better energy resolution.

As for the intermediate type of position spectra, this could be related to the pre-emission of one or two valence neutrons, after some interaction with the core took place.

From the data presented above, one could determine a maximum value of the valence neutron internal momentum p_i. Preliminary values are given in table 3.

Table 3

	w(chann.)	w_1(cm) w_1=1.1w	tan(θ)= tan(w_1/2/140)	$p_i=p_L.\tan(\theta)$ p_L(13MeV)=160MeV/c
Det 7	20.4	22.4	0.073*	11.7±1.0 MeV/c
Det 8	20.1	22.1	0.071	11.5±0.9 MeV/c
Det 9	19.35	21.3	0.068	11.0±1.1 MeV/c
			Mean Value=	11.4±0.6 MeV/c

*)Observation: In calculating tan(θ), the half width of the target (1 cm), was subtracted from $w_{1/2}$

The mean value p_i = 11.4±0.6 MeV/c, should be considered a maximum transversal internal momentum of the valence neutrons. In fact this value is safe, since due to the incident momenta spread, a lower value should be taken instead 160 MeV/c, producing the same width at the neutron wall position. The dispersion (emmitance) of the beam at the target position was considered negligible, due to the relatively large dimension of the spot.

An estimation of the number of fusions leading to the neutron focusing effect, by taking the total numbers of detected neutrons within the narrow gaussians (Det. 7,8,9) and by taking an intrinsic detection efficiency of 25%, was made. This number of fusion events appears to be about 10% of the total.

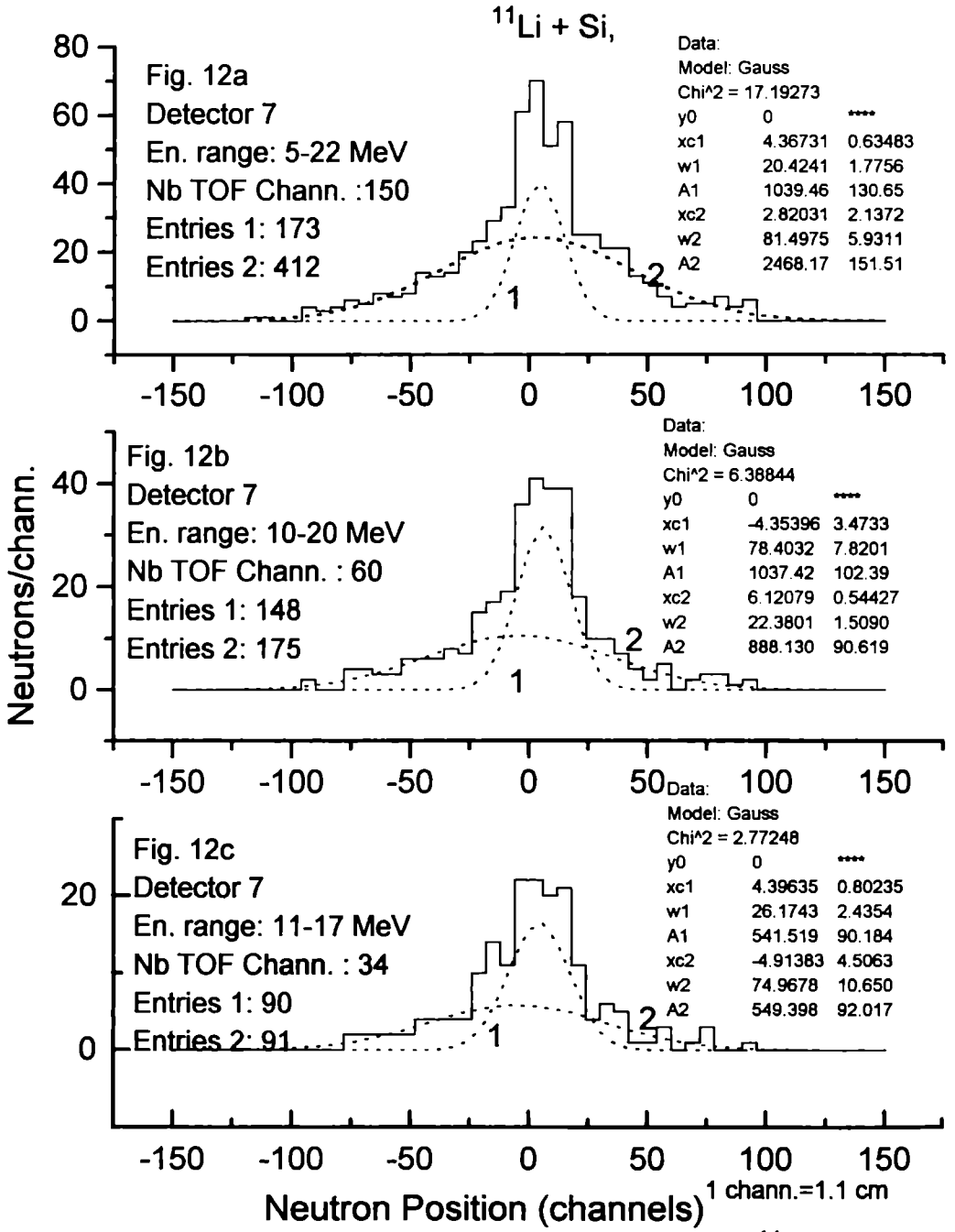

Fig 12. Neutron position spectrum, det. 7, ^{11}Li beam, for different neutron energy ranges

4. Conclusions

In conclusion:

1. A focused neutron group in the energy range 5-22 MeV was observed, in the experimental investigation of ^{11}+Si fusion. This group is only slightly reduced when the energy interval is taken 10-20MeV and is still surviving by further reducing the energy interval to 11-17 MeV. Thus it follows that this group consists of the ^{11}Li valence neurons emitted in a smooth breakup in the early stage of the fusion process.

2. The focused neutron group appears to consist of neutron pairs, as it is indicated by a preliminary neutron correlation analysis of the data.

3. Neutron pairs are estimated to be emitted in about 10% of the fusion processes.

4. A maximum value of the valence neutrons internal momentum, has been preliminarily derived from the width of the focused neutron spot.

5. A wider group of neutrons are also present in the measurement with ^{11}Li. This group consists presumably of valence neutrons that had a 1 step interaction with the colliding cores.

6. The experimental approach described here could be a way for obtaining ternary beams of coherent neutron pairs.

Acknowledgements. The results presented here are based on a common work with: I.Tanihata, T.Kobayashi, A.Korsheninnikov, K.Fukuda, H.Kumagai, T.Momoto, A.Ozawa, K.Yoshida, (RIKEN), A.Isbasescu, H.Petrascu, I.Lazar, I.Mihai, G.Vaman, A.David (Bucharest), E.Nikolski (Moskow).

The author wishes to express his gratitude to Prof. A.Arima, President of the RIKEN Institute, for the hospitality, and support during the measurements performed at RIKEN Ring Cyclotron, and to Prof. H. Morinaga, for the many valuable discussions on problems related to this work.

References

[1] I. Tanihata, T. Kobayashi et al. Phys. Rev. Lett. 55 (1985) 2676
[2] M. Petrascu et al., Contribution to the Balkan Phys.Soc. Meeting, Izmir, Turkey, Sept. 1994, To be printed in Balkan Phys.Lett. 1995
[3] M.Petrascu, I.Tanihata, T.Kobayashi, A.Isbasescu, H. Petrascu, A.Korsheninnikov, E.Nikolski, K.Fukuda, H.Kumagai, T.Momoto, A.Ozawa, K.Yoshida, I.Lazar, I.Mihai, G.Vaman, A.David, to be published.
[4] J.Gomez del Campo et al., Phys.Rev. C19 (1979) 2170
[5] see A. Gavron, Phys. Rev. C20 (1980) 230

The momentum Distribution of Projectile Fragments from the Breakup of Light Exotic Nuclei and The Wave Function of Weakly-bound Valence Nucleons

T. Kobayashi

The Institute of Physical and Chemical Research (RIKEN)
2-1 Hirosawa, Wako, Saitama 351-01, Japan

[1] Introduction

In a p-shell region, there are several nuclei in which valence nucleons are very weakly bound to the rest of the system (core). Two-neutron-separation energies in ^{6,8}He and ^{11}Li are 1.0, 2.1, and 0.3 MeV respectively. They are very small compared with the average binding energy of nucleons in the nucleus (about 8 MeV). The nucleus ^{11}Be also has a weakly-bound valence neutron in a $\nu 2s_{1/2}$ orbit with S_n=0.51 MeV. In these neutron-rich nuclei, the valence neutron(s) extends further outside the core, and this phenomenon is called a neutron halo or a neutron skin [1,2]. Several proton-dripline nuclei, such as ^{8}B, ^{9}C, and ^{13}O, have also small one-proton-separation energies, 0.14 MeV, 1.3 MeV, and 1.5 MeV, respectively. These nuclei are also good candidates with a possible proton halo.

The halo nucleus is believed to have a long tail in the density distribution, and it is usually difficult to determine the real shape of the density distribution. The momentum distribution of the projectile fragment can be used to extract the information on such density distributions, since the momentum distribution is considered to be related to the single-particle wave function of the valence nucleon through the Fourier transform. In this talk, I would like to summarize our efforts to understand the wave function of weakly-bound valence nucleons from the momentum distribution of projectile fragments produced from the breakup of light exotic nuclei, ^{6,8}He, ^{9,11}Li, ^{11}Be, ^{8}B, ^{9}C, and ^{13}O, at the incident energies between 0.8 GeV/nucleon and 2.0 GeV/nucleon.

[2] Projectile fragmentation of stable nuclei

Projectile fragmentation of stable beams, such as ^{12}C and ^{16}O, was studied almost 20 years ago at the Bevatron [3]. The momentum distributions of various projectile fragments were measured, and the widths of the momentum distribution could be empirically fitted by a parabolic shape

$$\sigma = \sigma_0 \sqrt{\frac{F(B-F)}{B-1}}$$

with a constant σ_0 at about 90 MeV/c.

Shortly after those measurements, A. Goldhaber proposed a simple model based on the momentum conservation, and σ_0 was shown to be related to the root mean square momentum of nucleons in the nucleus [4]. Since this simple relation explained the general tendency of the data, it was recognized that the momentum distribution of the projectile fragment reflects the momentum distribution of removed nucleons inside the projectile.

More detailed calculation on the momentum distribution of projectile fragments for the one-nucleon-removal process was performed using a Glauber model [5]. The important conclusion is that the momentum distribution comes from three processes. The 1st process is called a "elastic fragmentation", where the fragment and the nucleon are both scattered elastically from the target. The cross section of this process at high energy is estimated to be less than 10% of the cross section. The 2nd process is called a "spectator", where the nucleon is scattered from the target while the fragment behaves as a spectator. The 3rd process is called a "hard scattering", where the fragment is scattered from the target while the nucleon behaves as a spectator. Due to the 3rd process, the transverse momentum distribution has an additional broad component.

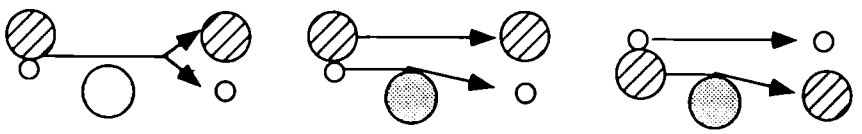

Fig.1 : Three processes for the breakup of the projectile, elastic fragmentation, spectator, and hard collision (from left to right).

The momentum distribution of the "spectator" process is expressed by the Fourier transform of the single-particle wave function of the removed nucleon, modified slightly by an additional term due to the impact parameter cut-off. Due to this effect, the momentum distribution of the projectile fragment is sensitive to the wave function on the nuclear surface.

In the following sections, momentum distributions of projectile fragments and projectile-rapidity neutrons from the breakup of various β-unstable nuclei on a light target such as C will be discussed.

[3] Two-neutron-removal process from neutron-rich nuclei (projectile fragment)

The transverse momentum distribution of ^{9}Li fragments from the breakup of ^{11}Li was measured soon after the secondary nuclear beam became available at 800 MeV/nucleon [6]. This nucleus has been known to have two interesting properties : (1) the two-neutron-separation energy S_{2n} is extremely small (0.3 MeV), (2) the interaction cross section is much larger than ^{9}Li. The transverse momentum distribution was measured and analyzed using two Gaussian components. The rms width of the "narrow" component turned out to be about 20 MeV/c. In terms of the reduced width σ_0, it was about 15 MeV/c. This value is much smaller than the nominal value of 90 MeV/c from the fragmentation of stable nuclei. Since the small momentum fluctuation corresponds to the extended object in space coordinate, this observation supported the idea of the neutron halo in ^{11}Li, i.e. the two valence neutrons are extended further outside the core. The longitudinal momentum distribution

of the same process was measured, and essentially gave the same result [7].

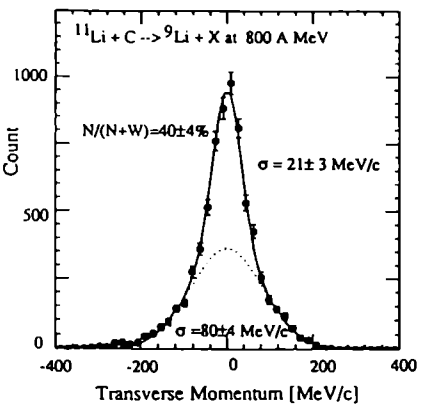

Fig.2 :Transverse momentum distribution of ^{9}Li fragment from ^{11}Li+C reaction at 800 MeV/nucleon.

It is worth while to mention the origin of the "wide" component in the transverse momentum distribution. We think that the "wide" component corresponds to the "hard scattering" term, in which the fragment is scattered from the target. The width of the transverse momentum distribution from this process is inversely proportional to the radius of the target or sum radii of the target and the fragment. The value is about 100 MeV/c for a carbon target, and actually the observed width of the "wide" component is between 60 and 100 MeV/c, slightly depending on the projectile.

A simple cluster model was used to explain the narrow momentum distribution. If the nucleus is composed of a core and a valence nucleon(s) with a separation energy ε, the wave function outside the potential, i.e. on the nuclear surface, is expressed by the Yukawa-type wave function,

$$\psi(r) \propto \frac{e^{-kr}}{r} \quad \text{with} \quad k = \sqrt{2\mu\varepsilon}$$

where μ is the reduced mass of the system. The wave function in a momentum space is given by the Fourier transform of the spatial wave function, and has a Lorentzian shape. The momentum distribution observed in the experiment is obtained by integrating the square of the momentum wave function in two momentum directions. The final momentum distribution also has a Lorentzian shape. If the central part of the Lorentzian distribution is approximated by the Gaussian distribution, the width of the momentum distribution can be written in a same way as the Goldhaber model, but with the reduced width σ_0 as

$$\sigma_0 = \sqrt{2\frac{B-1}{B}M_p\varepsilon}$$

where M_p and B is the mass of the nucleon and mass number of the projectile, respectively.

Measurements of the momentum distribution of the projectile fragment was extended to other neutron-rich projectiles such as ^{6,8}He, ^{9,11}Li, and ^{11}Be. The reduced width σ_0 of the momentum distribution is summarized in Fig.3 together with the estimate based on the cluster model (dashed

line). The simple cluster model can reproduce quite well the overall tendency of the momentum distribution of projectile fragment from the breakup of neutron-rich nuclei.

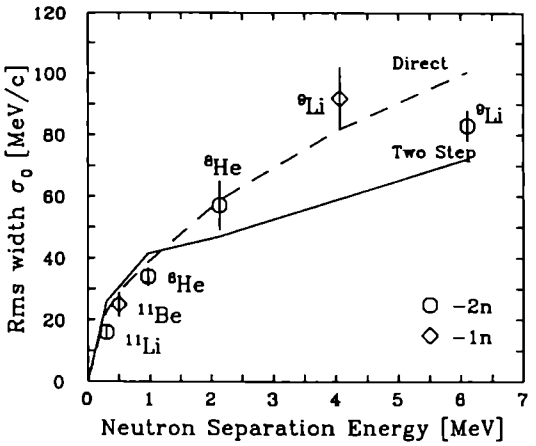

Fig.3 : The reduced width of the projectile fragment from various neutron-rich projectiles.

[4] Two-neutron-removal process from neutron-rich nuclei (forward neutron)

The angular distribution of forward neutrons in coincidence with ^{9}Li from the breakup of ^{11}Li was measured at 30 MeV/nucleon [8]. If the measured angular distribution is converted into the transverse momentum width, it is about 10 MeV/c. This value is much smaller than the momentum width of ^{9}Li fragment (about 20 MeV/c). This observation might suggest the correlation between two valence neutrons in ^{11}Li, since the momentum fluctuation of the valence neutron should be $1/\sqrt{2}$ times the momentum fluctuation of the ^{9}Li fragment without the correlation between two valence neutrons [9].

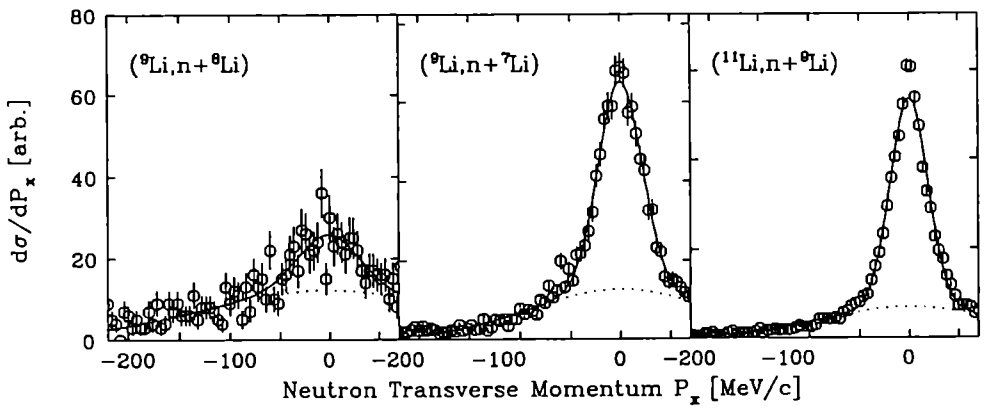

Fig.4 : Transverse momentum distribution of projectile-rapidity neutrons in coincidence with projectile fragments.

The transverse momentum distributions of neutrons were measured in coincidence with projectile fragments at 800 MeV/nucleon from the breakup of ^{6,8}He and ^{9,11}Li. As shown in Fig.4,

all the distributions have one common broad component of about 100 MeV/c. This component can be interpreted as the process in which one of the valence neutrons is removed from the projectile by the scattering with the target nucleus. The Glauber model shows that the transverse width of this process is 100 MeV/c (inversely proportional to $R_{rms}(^{12}C)$), and agrees well with the observed broad width.

After understanding the broad component, the narrow components are studied as shown in Fig.5.

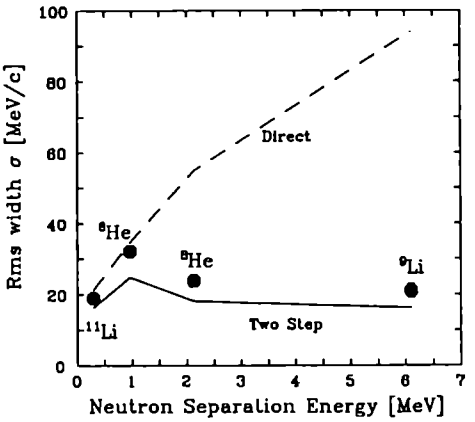

Fig.5 : Transverse momentum width of neutrons

One surprise was that the neutron momentum distribution from the two-neutron-removal process from ^{9}Li is as narrow as that from ^{11}Li. Under the assumption that there is no correlation between two valence neutrons in the projectile, the neutron momentum width, σ(n), can be estimated from the momentum width of the fragment, σ(F), as

$$\sigma(n) = \frac{\sigma(F)}{\sqrt{2}} = \sqrt{2\frac{F(B-F)}{B}M_p\varepsilon}$$

The dashed curve in Fig.5 is much larger than the experimental data.

We therefore considered the possibility of the two-step process. It is already shown that we have observed the broad component in the momentum distribution of neutrons, which corresponds to the removal of one of the valence neutrons by the scattering with the target. After the one nucleon removal process from ^{6,8}He,and ^{11}Li projectiles, particle-unstable resonances, ^{5,7}He, and ^{10}Li, are formed, and decay by neutron emissions. For the one-neutron removal from ^{9}Li, ^{8}Li* has a p-wave resonance just 0.22 MeV above the threshold. In such cases, the transverse momentum distribution of the 2nd neutron can be expressed as,

$$\sigma(n) = \sqrt{\frac{2}{B(B-1)}M_pS_n + \frac{2(B-2)}{3(B-1)}M_pQ}$$

while the momentum distribution of the final (heavy) fragment can be expressed as

$$\sigma(F) = \sqrt{\frac{B-2}{B-1}M_pS_n + \frac{B}{B-1}M_p\frac{Q}{3}}$$

where S_n and Q is the one-neutron-separation energy from the projectile and the decay Q value of the resonance, respectively. In a case of the neutron, the 2nd term from the 2nd process (the decay of the resonance) is about 10 times larger than the 1st term. Therefore the momentum distribution of the neutron is dominated by the decay energy of the resonance. In a case of the fragment, on the other hand, the 1st term (the removal of one neutron from the projectile) is larger than the 2nd term. Therefore the momentum width of the fragment is relatively insensitive to the decay of the resonance. Experimental values are compared with the two-step model in Fig.5 by the solid line. The agreement is quite good.

This model may be too crude to see clearly the differences in a case of ^{11}Li. But we have already observed the broad component corresponding to the removal of one of the valence neutrons by the scattering with the target. Therefore the momentum distribution of neutrons from ^{11}Li must be also influenced by the decay of ^{10}Li. How about the structure of ^{10}Li. Since ^{10}Li has 7 neutrons, we naively expect that the ground state of ^{10}Li has $\nu 1p_{1/2}$ configuration. The systematics of N=7 isotone show, however, that the relative position between $\nu 2s_{1/2}$ and $\nu p_{1/2}$ is becomes closer from ^{15}O to ^{12}B, and the $\nu 2s_{1/2}$ orbit becomes the ground state in ^{11}Be. Since ^{10}Li is one proton less than ^{11}Be, we might also expect that ^{10}Li has $\nu 2s_{1/2}$ neutron orbit as its ground state. The structure of ^{10}Li has been studied by various reactions, and data does not seem to be consistent with each other. Those data, more or less, suggests that there is one or two p-wave resonances between 0.5 MeV and 1.0 MeV above the threshold, and possibly one s-wave resonance very (less than 0.2 MeV) close to the threshold. The momentum width of the neutron based on the two-step model is about 20 MeV/c for the p-resonance and about 10 MeV/c for the s-resonance. The observed width is somewhat in between these two values. This problem is also related to the important question on the amount of the possible $(\nu 2s_{1/2})^2$ component in ^{11}Li.

Therefore the systematic study of the momentum distribution of the projectile fragments and the neutrons in the two-neutron-removal process from various neutron-rich projectile showed that the two-step process via the resonance is the dominant process. In such cases, the momentum distribution of the neutron is dominated by the decay property of the resonance rather than the information of the initial nuclei which we want to study.

[5] One-neutron-removal process from ^{11}Be

In order to understand the relation between the single-particle wave function and the experimentally observed momentum distribution of the projectile fragment, we studied the case in which one valence neutron is removed from the projectile. As an example, we selected ^{11}Be because this nucleus is also a good candidate of one neutron halo due to its orbit ($\nu 2s_{1/2}$) and a small one-neutron separation energy of 0.51 MeV.

The single-particle wave function of the valence neutron is obtained in a Woods Saxon potential with standard parameters (radius=$2.65 \times A^{1/3}$ fm, diffuseness=0.65 fm) by adjusting the potential depth to get the correct separation energy. The wave function in the momentum space is given by

the Fourier transform.

$$R_{nl}(p) = \int j_l(pr) R_{nl}(r) r^2 dr$$

The momentum distribution in one direction (longitudinal or transverse) is calculated after integrating the momentum density over two directions.

$$\frac{d\sigma}{dp_x} = \int |R_{nl}(p)|^2 dp_y dp_z$$

Finally the experimental resolution is folded, and the calculated distribution is compared with the narrow component of the transverse momentum distribution as shown in Fig.6.

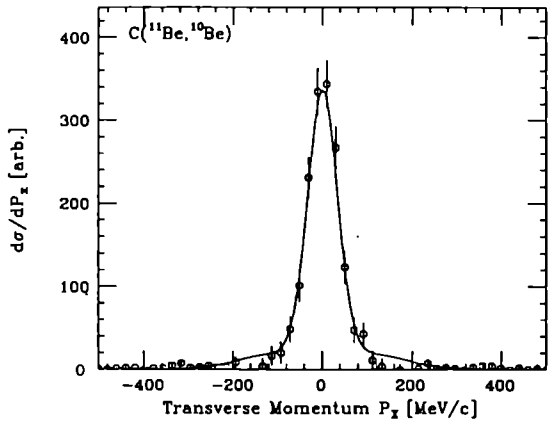

Fig.6 : Narrow component of the ^{10}Be momentum distribution from ^{11}Be, compared with the calculation.

The agreement is very good, showing that the single-particle wave function can reproduce well the observed momentum distribution. Actually this method provides a good experimental tool to study the halo nuclei with a single valence neutron. Recent measurement on the momentum distribution from the breakup of ^{19}C showed a very narrow distribution, and this nucleus is a very good candidate for the heaviest halo nucleus [10].

[6] One-proton-removal process from ^{8}B, ^{9}C, and ^{13}O

After understanding the one-neutron-removal process from neutron-rich nuclei, we further studied the one-proton-removal process from proton-dripline nuclei, such as ^{8}B (S_p=0.14MeV) , ^{9}C (S_p=1.3 MeV), and ^{13}O (S_p=1.5 MeV). Due to their small proton separation energies, these nuclei are also good candidates for halo nuclei. It may be, however, less probable that the halo is formed due to the centrifugal and the Coulomb barriers.

Using the same procedure as in section 5, the momentum distribution of the fragment is calculated using the single-particle wave function in Woods Saxon potential, and compared with the narrow component of the transverse momentum distribution. As shown in Fig.7, the agreement is good for ^{13}O, but the experimental distributions are narrower than the calculations for ^{8}B and ^{9}C.

The longitudinal momentum distribution of ^{7}Be from the breakup of ^{8}B was also measured [11], and both distributions are roughly the same.

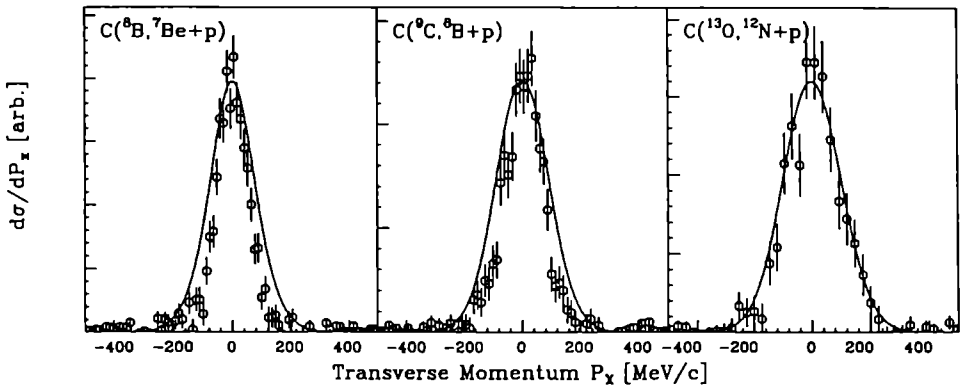

Fig.7 : Narrow component of the transverse momentum distribution of fragments in the one-proton-removal process from proton-rich projectiles, compared with the calculation.

There are several possible reasons which may modify the momentum distribution. The existence of particle-stable excited states in ^{7}Be from the breakup of ^{8}B might produce wider distributions. Since number of protons in ^{9}C and ^{13}O are even, the momentum distribution may be narrower if the pairing energy (estimated to be about 0.5 MeV compared with an average proton-separation energy of 1.5 MeV) is taken into account. Simple estimate gives that the distribution will be narrower by about 5-7 MeV/c. The third possibility is that the single-particle wave function of the valence proton has a long tail as calculated by the QRPA method [11]. This calculation might be checked experimentally by comparing the one-proton-removal cross section with the difference of the interaction cross sections. If the wave function Ψ_A can be written as $\Psi_{A-1}\Psi_p$, then the relation

$$\sigma_{-p}(B+T) = \sigma_I(B+T) - \sigma_I(\text{"}B-1\text{"}+T)$$

holds from the Glauber model. This relation provides an experimental method to study the "modified core" in the nucleus. The comparison shows that the core may be smaller than the core in a free space, but the difference is much smaller than what is estimated by the QRPA calculation. Therefore, it is not clear at the moment why the momentum distribution is narrower than what is calculated from the simple single-particle wave function in a Woods Saxon potential. There might be other reasons such as the possible deformation.

[7] Summary

The momentum distribution of projectile fragments produced from the breakup of β-unstable nuclei were studied, and we have tried to extract the information on the single-particle wave function of valence nucleon(s) from the momentum distribution.

For the two-neutron-removal process from ^{6,8}He and ^{9,11}Li, the momentum distribution of the projectile-rapidity neutron showed that the main reaction mechanism is the two-step process via the

intermediate resonance. In such cases, the momentum distribution is determined by the properties of the resonance rather than the initial nuclei. For understanding the single-particle wave function of valence neutrons in such halo nuclei, it is necessary to develop other type of experimental technique.

For the one-neutron-removal process from ^{11}Be, the single-particle wave function in a Woods Saxon potential reproduced well the observed momentum distribution, if the separation energy is treated properly. This method provides a nice experimental tool to study the nucleus with a single halo neutron.

For the one-proton-removal process from ^{8}B, ^{9}C, and ^{13}O, the calculated momentum distribution for ^{8}B and ^{9}C were wide than the experimental distribution. The reason for this is not clear at the moment.

All the experimental results were obtained in collaboration with I. Tanihata, K. Yoshida, A. Ozawa (RIKEN), K. Matsuta, S. Fukuda, K. Sugimoto (Osaka), B. Christie, H. Wieman, D. Olson, and T.J.M. Symons (LBL), performed at the Bevalac facility (LBL)

[8] References

1) P.G. Hansen & B. Johnson, Europhys. Lett. **4** (1987) 409.
2) I. Tanihata et al., Phys. Lett. **B289** (1992) 261.
3) D.E. Greiner et al., Phys. Rev. Lett. **35** (1975) 152.
4) A.S. Goldhaber, Phys. Lett. **53B** (1974) 306.
5) T. Fujita & J. Hüfner, Nucl. Phys. **A343** (1980) 493.
6) T. Kobayashi et al., Phys. Rev. Lett. **60** (1988) 2599.
7) N.A. Orr et al., Phys. Rev. Lett. **69** (1992) 2050.
8) R. Ann et al., Phys. Lett. **B304** (1993) 55.
9) I. Tanihata et al., Phys. Lett. **B287** (1992) 307.
10) D. Bazin et al., Phys. Rev. Lett. **74** (1995) 3569.
11) W. Schwab et al., Z. Phys. **A350** (1995) 283.

DYNAMICS OF COLD FISSION PROCESSES

D. N. POENARU, R. A. GHERGHESCU and W. GREINER
Institute of Atomic Physics, P. O. Box MG-6, RO-76900 Bucharest, Romania

and

Institut für Theoretische Physik der Universität, Pf. 111932, D-60054 Frankfurt am Main, Germany

ABSTRACT

The neutron-rich ^{264}Fm should be the best cold-fissioning nucleus, owing to the strong shell effect of the doubly magic fragments ^{132}Sn. The optimum cold fission path in the plane of two independent shape coordinates, the separation distance R and of the radius of the light fragment R_2, is determined. Werner-Wheeler inertia tensor and Yukawa-plus-exponential deformation energy are used to calculate the action integral. Microscopic shell and pairing corrections are based on the asymmetric two-center single-particle model. Different variation laws $R_2 = R_2(R)$, for the fission trajectory were tested: polynomials of 2nd, 3rd, and 4th degree and an exponential function. The partial half-life for cold fission is estimated to be several orders of magnitude shorter than that of α-decay.

1. Introduction

A rich variety of nuclear decay modes have been recently discovered and intensively studied. [1-7] Fission models, extended to very large mass asymmetry, have been applied since 1980 to predict *cluster radioactivities* (see the above cited review papers and references therein). In the usual mechanism of fission, a significant part (about 25-35 MeV) of the released energy Q is used to deform and excite the fragments (which subsequently cool down by neutron and γ-ray emissions); hence the total kinetic energy of the fragments, TKE, is always smaller than Q. Since 1980 a new mechanism has been experimentally observed – *cold fission*[8,9,3] characterized by a very high TKE, practically exhausting the Q-value, and a compact scission configuration. Cold fission with compact shapes can be considered to be the inverse of a fusion process. Experimental data have been collected in two regions of nuclei: (a) thermal neutron induced fission on some targets like ^{233,235}U, ^{238}Np, ^{239,241}Pu, ^{245}Cm, and the spontaneous fission of ^{252}Cf; (b) the *bimodal* spontaneous mass-symmetrical fission of ^{258}Fm, ^{259,260}Md, ^{258,262}No, and ^{260}104. The yield of the cold fission mechanism is comparable to that of the usual fission events in the latter region, but it is much lower (about five–six orders of magnitude) in the former.

Since 1986 we have systematically studied the cold fission process viewed as cluster radioactivity within our ASAF model.[10,11,3] According to our calculations, performed within the analytical superasymmetric fission (ASAF) model, the cold fission mechanism could be the main decay mode of the neutron-rich nucleus ^{264}Fm, which has

not been produced until now. It also should give the most pronounced symmetrical distribution of fission fragments, owing to the doubly magic character of ^{132}Sn fragments. The half-life of 5.7 μs for a "new fission path" with compact shapes calculated by Möller and Nix,[12] is not very far from our[10] $log_{10}\, T(s) = -5.6$.

A very powerful technique has been used[13] to measure the spontaneous cold-fission of ^{252}Cf. Also, new experimental methods to produce nuclei far from stability have been developed. It would be very interesting to synthesize the neutron-rich ^{264}Fm in the near future.

In the parametrization of two intersected spheres assumed by ASAF model, the radius of the emitted fragment, R_2, was kept constant. In this work we would like to present a two-dimensional dynamics of the cold fission process, where both the separation distance R and the radius R_2 are independent variables. The analytical relationships, derived for the components of the nuclear inertia tensor, are published elsewhere.[14]

2. Werner–Wheeler inertia tensor

The potential energy surface in a multi-dimensional hyperspace of deformation parameters $q_1, q_2, ..., q_n$ gives the generalized forces acting on the nucleus. Information concerning how the system reacts to these forces is contained in a tensor of inertial coefficients, or the effective mass parameters $\{B_{ij}\}$. The contribution of a shape change to the kinetic energy is expressed by

$$E_k = \frac{1}{2} \sum_{i,j=1}^{n} B_{ij}(q) \frac{dq_i}{dt} \frac{dq_j}{dt} \tag{1}$$

As an approximation to the incompressible irrotational flow, one can use the Werner-Wheeler assumption.

The kinetic energy of a non-viscous fluid due to a shape change is written as

$$E_k = \frac{\sigma}{2} \left[\int_V \mathbf{v}^2 d^3r - \left(\int_V \dot{z} d^3r \right)^2 \Big/ \int_V d^3r \right] \tag{2}$$

if the system possesses a cylindrical symmetry relative to the z-axis. V is the volume assumed to be conserved, $\sigma = 3m/(4\pi r_o^3)$ is the mass density, $\mathbf{v}$ is the velocity; the nuclear radius constant $r_o = 1.16$ fm within Y+EM.

By assuming irrotational motion, the velocity field may be derived from a scalar velocity potential φ, i.e. $\mathbf{v} = \nabla\varphi$. From the continuity equation of an incompressible fluid it follows that the Laplace equation, $\nabla^2\varphi = \Delta\varphi = 0$, should be satisfied with kinematical boundary conditions

$$\frac{DF}{\partial t} = \mathbf{v}\nabla F + \frac{\partial F}{\partial t} = 0 \tag{3}$$

where the surface equation for axially symmetric shapes in cylindrical coordinates $(\rho,\ \varphi,\ z)$ is written as $F(r,t,q) = \rho - \rho_s(z,t,q) = 0$ in which ρ_s is the value of ρ on

the surface. The velocity components, $\dot{z} = \partial\varphi/\partial z$ and $\dot{\rho} = \partial\varphi/\partial\rho$, are both functions of z and ρ.

In the Werner–Wheeler approximation the flow is considered to be a motion of circular layers of fluid, $\dot{z}$ is independent of ρ, and $\dot{\rho}$ is linear in ρ:

$$\dot{z} = \sum_i X_i(z,q)\dot{q}_i; \quad \dot{\rho} = (\rho/\rho_s)\sum_i Y_i(z,q)\dot{q}_i \tag{4}$$

A vanishing total (convective) time derivative of the fluid volume to the right (or left) side of an arbitrary plane normal to the z-axis leads to

$$X_{il} = -\rho_s^{-2}\frac{\partial}{\partial q_i}\int_{z_{min}}^{z}\rho_s^2 dz, \qquad X_{ir} = \rho_s^{-2}\frac{\partial}{\partial q_i}\int_{z}^{z_{max}}\rho_s^2 dz \tag{5}$$

By requiring a vanishing normal component of the velocity at the surface, one has

$$Y_{ir(l)} = -\frac{\rho_s}{2}\frac{\partial}{\partial z}X_{ir(l)} \tag{6}$$

from which the functions X_i and Y_i are found as a sum of two terms for the left (l) and right (r) side of the shape.

After substitution in the relationship for the kinetic energy and comparison with the initial equation for E_k we find:

$$B_{ij} = \pi\sigma\int_{z_{min}}^{z_{max}}\rho_s^2\left(X_iX_j + \frac{1}{2}Y_iY_j\right)dz + B_{ij}^c \tag{7}$$

$$B_{ij}^c = -(\pi^2\sigma/V)\int_{z_{min}}^{z_{max}}\rho_s^2 X_i dz\int_{z_{min}}^{z_{max}}\rho_s^2 X_j dz \tag{8}$$

where $\rho_s = \rho_s(z)$ is the nuclear surface equation in cylindrical coordinates, with z_{min}, z_{max} intercepts on the z-axis. The correction term for the center of mass motion B_{ij}^c is different from zero if the origin of z is not placed in the center of mass.

3. Two-dimensional dynamics

The cold fission character of the fission process under investigation justify a nondissipative approach. We consider a parent nucleus AZ decaying into two fragments A_dZ_d and A_eZ_e. A given exit channel corresponds to a certain final value of the mass asymmetry parameter $\eta_t = (A_d - A_e)/A$. In an intermediate stage of the deformation from one nucleus up to two fragments at the touching point, the mass asymmetry can be expressed as $\eta = (V_1 - V_2)/V$, where V_1, V_2, and V are the volumes of the two fragments and of the parent, respectively. At the touching point $V_1 = V_d$ and

$V_2 = V_e$. By assuming the incompressibility of nuclear matter, the total volume of the fragments, $V = V_1 + V_2$, is conserved during the deformation.

The measurable partial half-life

$$T = \frac{h \ln 2}{2E_v S P_s} \tag{9}$$

is determined[15,16] by a product of three (model-dependent) quantities: a zero-point vibration energy, $E_v = h\nu/2$ (ν is the frequency of assaults on the barrier, and h is the Planck constant), a preformation probability of the emitted cluster into the parent nucleus, S, and the external barrier penetrability, P_s, given by

$$S = \exp(-K_{ov}) \; ; \quad P = \exp(-K_s) \tag{10}$$

They are calculated within the Wentzel-Kramers-Brillouin (WKB) approximation, where the action integrals, K_{ov} (for overlapping fragments) and K_s (for separated fragments), are expresed as

$$K_{ov,s} = \frac{2}{\hbar} \int_{R_i,R_t}^{R_t,R_b} [2B(R)E(R)]^{(1/2)} dR \tag{11}$$

The least action trajectory in the plane R, R_2 is a curve $R_2 = R_2(R)$ along which the minimum value of K is obtained. By chosing a trajectory in the plane of the two independent shape coordinates, given in a parametric form: $R_2 = R_2(s)$; $R = R(s)$, and by taking $s = R$, an inertia scalar, $B(R)$, used to calculate the tunneling penetrability along this path is derived

$$\begin{aligned} B(R) = \quad & B_{RR}(R, R_2) + 2B_{RR_2}(R, R_2)\left(\frac{dR_2}{dR}\right) \\ & + B_{R_2R_2}(R, R_2)\left(\frac{dR_2}{dR}\right)^2 \end{aligned} \tag{12}$$

from the components of the inertia tensor, and the two-dimensional problem is reduced to a single dimensional one. At the touching point and for separated fragments, $B(R)$ is equal to the reduced mass $\mu = mA_eA_d/A$, where m is the nucleon mass. $E(R)$ is the interaction energy of the two fragments from which the Q-value has been subtracted. R_i and R_b are the turning points of the WKB integral, $E(R_i) = E(R_b) = 0$. The zero-point vibration energy can be estimated from the stiffness of the potential barrier and the reduced mass.

3.1. Nuclear shape

The parametrization of two intersected spheres with radii R_1 and R_2 has been adopted. By placing the origin in the center of the large sphere, the surface equation

can be written as:

$$\rho_s^2 = \begin{cases} \rho_{sl}^2 = & R_1^2 - z^2 & , \ -R_1 \le z \le z_s \\ \rho_{sr}^2 = & R_2^2 - (z-R)^2 & , \ z_s \le z \le R + R_2 \end{cases} \tag{13}$$

in which $z_s = D_1$ is the position of the separation plane, where the matching condition, $R_1^2 - D_1^2 = R_2^2 - D_2^2$, should be fulfilled, and $R = D_1 + D_2$ is the distance between the two centers. The fragment radii, R_1 and R_2, take the constant values R_d and R_e beginning with the touching point separation distance $R_t = R_d + R_e$.

Since the final nuclei are assumed to posses spherical shapes, we shall be mainly concerned with the dynamics of the overlapping fragments, from $R = R_i = R_0 - R_2$ up to R_t. Here $R_0 = r_0 A^{1/3}$, with $r_0 = 1.16$ fm. The radius of the heavy fragment is obtained as a function of these variables, $R_1 = R_1(R, R_2)$. One can find solutions of R_1 and D_1, fulfilling the volume conservation and matching conditions with a constraint of a given η_t in a limited area of the plane of independent variables R and R_2.

3.2. Inertia Tensor

The tensor of inertia for two independent variables

$$\begin{pmatrix} B_{RR}(R,R_2) & B_{RR_2}(R,R_2) \\ B_{R_2R}(R,R_2) & B_{R_2R_2}(R,R_2) \end{pmatrix} \tag{14}$$

has the non-diagonal components equal to each other, $B_{R_2R} = B_{RR_2}$, due to the symmetry property. It depends on the arbitrarily chosen set of shape coordinates. We have obtained[14] analytical relationships for the three components of the inertia tensor.

3.3. Deformation Energy

In the numerical superasymmetric fission (NuSAF) model, the nuclear energy, replacing the Myers-Swiatecki's liquid drop model surface energy, is given by the double folded Yukawa-plus-exponential (Y+E) potential[17] extended[18] to binary systems with different charge densities.

3.3.1. Yukawa-plus-exponential potential

The general relationship of the Y+E potential is given by a double volume integral

$$E_Y = -\frac{c_s}{8\pi^2 r_0^2 a^4} \int_{V_n} \int \left(\frac{r_{12}}{a} - 2\right) \frac{\exp(-r_{12}/a)}{r_{12}/a} d^3r_1 d^3r_2 \tag{15}$$

where $r_{12} = |\mathbf{r}_1 - \mathbf{r}_2|$, $a = 0.68$ fm is the diffusivity parameter, and $c_s = a_s(1 - \kappa I^2)$, $a_s = 21.13$ MeV is the surface energy constant, $\kappa = 2.3$ is the surface asymmetry

constant, and $I = (N - Z)/A$. By taking into account the difference between the charge densities of the two fragments, this energy can be expressed[18] as a sum of two self-energies and one interaction energy between them. For overlapping fragments with axial symmetry, the six-fold integrals can be reduced to three-dimensional ones which are calculated numerically by Gauss-Legendre quadrature. The relative energy is

$$B_Y = \frac{E_Y}{E_Y^0} = \frac{a_{21}}{a_{20}} B_{Y1} + \frac{\sqrt{a_{21}a_{22}}}{a_{20}} B_{Y12} + \frac{a_{22}}{a_{20}} B_{Y2} \tag{16}$$

where E_Y^0 corresponds to a spherical compound nucleus, B_{Y1} and the similar terms depend on the nuclear shape. The corresponding threedimensional integrals are computed numerically by Gauss-Legendre quadratures.

3.3.2. Coulomb potential

Similar to the (Y+E) term, one has a Coulomb energy

$$\begin{aligned} E_C &= \frac{\rho_{1e}^2}{2} \int_{V_1} d^3r_1 \int_{V_1} \frac{d^3r_2}{r_{12}} + \frac{\rho_{2e}^2}{2} \int_{V2} d^3r_1 \int_{V2} \frac{d^3r_2}{r_{12}} + \\ &\quad \rho_{1e}\rho_{2e} \int_{V1} d^3r_1 \int_{V2} \frac{d^3r_2}{r_{12}} \end{aligned} \tag{17}$$

where the first two terms belong to individual fragments and the third one represents their interaction. The charge densities of the compound nucleus and of the two fragments are denoted by ρ_{0e}, ρ_{1e} and ρ_{2e} respectively.

A typical shape-dependent term for axially-symmetric shapes[19] is of the form

$$B_{c12} = b_c \int_{-1}^{x_c} dx \int_{x_c}^{1} dx' F(x, x') \tag{18}$$

where $b_c = 5d^5/8\pi$, $d = (z'' - z')/2R_0$, and x_c is the position of separation plane between fragments with -1, +1 intercepts on the symmetry axis (surface equation $y = y(x)$ or $y_1 = y(x')$).

When the fragments are separated, i.e. the distance, R, between the centers of the two fragments is larger than the touching-point configuration value R_t, analytical relationships are available. Owing to the exponential term the contribution of the Yukawa-plus-exponential potential becomes negligibly small as soon as the separation distance is larger by few fm than the touching point value.

3.3.3. Shell and pairing corrections. Total energy

To the total macroscopic deformation energy, $E_{def} = E_Y + E_C$ (plus the volume term E_V for different charge densities), one has to add the microscopic shell and pairing corrections, δE, calculated with the Strutinsky method.[20] Strutinsky gave a microscopic definition of shell corrections and the method of calculation based on the

levels of a single particle shell model. The single-particle levels used in the present paper are obtained from a recently developed variant[21] of the asymmetric two-center shell model.[22] The diagonalization of the involved large matrix is a time-consuming procedure. Once the levels are known, one has to find separately for protons and neutrons, the smoothed-level density, the Fermi energy of a uniform-level distribution, and the shell correction energy for a given number of protons and neutrons.

The gap parameter Δ and the Fermi energy with pairing corellations λ, are then obtained as solutions of a nonlinear system of two Bardeen-Cooper-Schriefer (BCS) equations. They are used to find the pairing corrections, added to the shell corrections.

4. Results

In the following we report our results concerning a two-dimensional dynamics for the symmetrical cold fission of ^{264}Fm. As a starting point we consider the region of the plane in which the geometry of two intersected spheres allows physically acceptable pairs of independent variables R, R_2. It is reasonable to assume that a physical solution of R_2 should be found in the range (R_e, R_0), while the corresponding R_1 can take values from R_d to R_0. Then, from the volume conservation and matching conditions, for every R, a certain range of R_2 values are permitted.

The left hand side straight line gives the minimum value of $R = R_i = R_0 - R_{2i}$, where the light fragment sphere is still inside the parent nucleus. Any possible solution beyond the right hand side limit would violate the usually adopted convention $R_1 \geq R_2$. Some possible fission paths will be presented bellow.

4.1. Mass parameters and deformation energy

The maximum value of $B_{RR}(R, R_2)$ is reached at the touching point configuration where the reduced mass is obtained, $B_{RR}(R_t, R_e) = \mu$. For R =constant, B_{RR} decreases when the value of R_2 is increased up to the allowed limit. The mountain ridge corresponds to small separation distances R at a constant $R_2 > R_e$. The mixing component $B_{RR_2}(R, R_2)$ behaves similarly, except for the highest values of R, where a maximum of $107m$ is reached at $R < R_t$ (not shown in the figure). On the other hand, the diagonal component $B_{R_2R_2}(R, R_2)$ increases continuously toward infinity when the touching point configuration is approached, (in the limit of vanishing H_1 and H_2).

In the absence of a microscopical shell and pairing correction, the macroscopic deformation energy $E_{def}(R, R_2)$ monotonously increases with R and exhibits a very slow variation with R_2 at a constant R. E_{def} slightly increases at small R, and remains almost constant in the vicinity of the touching point configuration.

4.2. Fission paths

It is convenient to choose different laws of variation $R_2 = R_2(R)$ describing a possible sequence of shapes during the fission process from one parent nucleus to

two final fragments at the touching point, in order to study the fission dymamics. Two conditions should be fulfilled: cofinement within the allowed region and vanishing derivative $R_2'(R_t)$ =0 faster than H_1 and H_2, at the touching point. The first condition allows to get a finite inertia scalar despite the trend toward infinity of $B_{R_2R_2}(R_t, R_2(R_t))$. Moreover, in this way $B(R_t)$=$B_{RR}(R_t, R_2(R_t))$ equals the reduced mass, which is a general law to be fulfilled by inertia of separated fragments, when the deformation coordinate is the distance between geometrical centers or mass centers of the fragments.

From several tested variation laws $R_2 = R_2(R)$ the following four have been choosen to illustrate the least action principle.

1. second order polynomial

$$R_2(R) = \frac{R_{2i} - R_e}{(R_0 - R_{2i} - R_t)^2}(R - R_t)^2 + R_e \tag{19}$$

2. third order polynomial

$$R_2(R) = \frac{R_{2i} - R_e}{(R_0 - R_{2i} - R_t)^3}(R - R_t)^3 + R_e \tag{20}$$

3. fourth order polynomial

$$R_2(R) = \frac{R_{2i} - R_e}{(R_0 - R_{2i} - R_t)^4}(R - R_t)^4 + R_e \tag{21}$$

4. exponential function

$$R_2(R) = \begin{cases} R_{2i} \exp\left(-\frac{R-(R_0-R_{2i})}{a}\right) & , \; R \leq 0.8R_t \\ R_2 = R_e & , \; R \geq 0.8R_t \end{cases} \tag{22}$$

The initial value of R_2 is $R_{2i} = R_0$ or in the last Eq. R_{2i}=$0.6R_0 + 0.31$ and a=3.298. These choices lead to a minimum value of the action integral. The best result ($K_{ov}^{min} = K_0$) was found with the second order polynomial law; the three others are less convenient, yielding higher K_{ov} values by 3.1% (third order polynom), 3.6% (exponential function), and 5.7% (fourth order polynom).

By adding a correction energy, allowing to reproduce the Q-value estimated from a mass table,[23] the fission barrier is reduced. We get $K = K_{ov} + K_s = 34.597$ and E_v=0.141 MeV, hence $\log_{10} T(s) \simeq$ -5, very close to the preceding values mentioned in the introduction.

4.3. Mass asymmetry

Up to now we have been only concerned with the symmetrical cold fission process, which intuitivelly seems to yield the highest rate, due to the strong shell effects of the doubly magic fragments $^{132}_{50}$Sn. It is possible to represent in a two dimensional plot

(R,η) the inertia components $B_{RR}(R,\eta)$, $B_{RR_2}(R,\eta)$, and $B_{R_2R_2}(R,\eta)$ as well as the corresponding scalar $B(R)$ along a fission path given by the 2nd order polynomial law identical for every value of the mass asymmetry parameter η. Again we observe that $B(R_t,\eta) = B_{RR}(R_t,\eta) = \mu$ at the touching point configuration, and the trend toward infinity of $B_{R_2R_2}$.

The potential energy surface with shell and pairing corrections included, $E+\delta E$, shows the typical two minima (ground state and shape isomeric state) at symmetrical split, where the lowest potential barriers lead to the highest yield at symmetry in this case.

For alpha-decay, we estimate the following half-lives: $log_{10}\ T(s) = 10.77$, 11.00, 12.49, 12.67, 12.86, 13.75, and 14.32, which correspond to $Q_\alpha = 5.905$, 5.865, 5.615, 5.585, 5.555, 5.415, and 5.330 MeV, obtained by taking the masses of the parent ^{264}Fm and of the daughter ^{260}Cf, from the mass tables calculated by: Pearson *et al.*;[24] Liran and Zeldes;[25] Möller *et al.* [26] — FRLDM (finite range liquid drop model); Myers and Swiatecki;[27] Möller and Nix;[28] Möller *et al.*[26] — FRDM (finite range droplet model), and Möller *et al.*[23] In conclusion the cold fission process should be several orders of magnitude stronger than the α-decay.

5. Acknowledgments

This work was supported by the Bundesministerium für Forschung und Technologie, Bonn, and the Institute of Atomic Physics, Bucharest. D.N.P. received a donation of computer and copying equipment from the Soros Foundation for an Open Society. R. A. G. is grateful to the Konferenz der Deutschen Akademien der Wissenschaften, Mainz, for a grant of a Volkswagenstfiftung fellowship.

6. References

1. W. Greiner, M. Ivaşcu, D. N. Poenaru, and A. Săndulescu, in *Treatise on Heavy Ion Science, Vol. 8*, ed. D. A. Bromley (Plenum Press, New York, 1989), p. 641.
2. A. Săndulescu, D. N. Poenaru, and W. Greiner, *Sov. J. Part. Nucl.* **11** (1980) 528.
3. D. N. Poenaru, M. Ivaşcu, and W. Greiner, in *Particle Emission from Nuclei, Vol. III*, eds. D. N. Poenaru and M. Ivaşcu (CRC Press, Boca Raton, Florida, 1989), Chap. 7, p. 203.
4. D. N. Poenaru and W. Greiner, in *Handbook of Nuclear Properties*, ed. D. N. Poenaru and W. Greiner (Oxford University Press, Oxford, 1995), in press.
5. E. Hourany, I. H. Plonski, and D. N. Poenaru, in *Experimental Techniques in Nuclear Physics*, eds. D. N. Poenaru and W. Greiner (Walter de Gruyter, Berlin, 1995), in press.
6. D. N. Poenaru and W. Greiner, in *Nuclear Decay Modes*, ed. D. N. Poenaru (Institute of Physics Publishing, Bristol, 1995), in press.

7. D. N. Poenaru, W. Greiner, and E. Hourany, *Phys. Rev.* **C51** (1995) 594.
8. F. Gönnenwein, in *The Nuclear Fission Process*, ed. C. Wagemans (CRC Press, Boca Raton, Florida, 1991).
9. E. K. Hulet, in *Proc. R. A. Welch Foundation Conference on Chemical Research: Fifty years with transuranium elements, Houston, 1990*, 279–310, (1990).
10. D. N. Poenaru *et al.*, Report NP-54, Central Institute of Physics, Bucharest (unpublished).
11. D. N. Poenaru *et al., Z. Phys.*, **A 328** (1987) 309.
12. P. Möller and J. R. Nix, *J. Phys. G* **20** (1994) 1681.
13. G. M. Ter-Akopian *et al. Phys. Rev. Lett.* **73** (1994) 1477.
14. R. A. Gherghescu, W. Greiner, and D. N. Poenaru, *Phys. Rev.* **C** in press.
15. M. Brack *et al. Rev. Mod. Phys.* **44** (1972) 320.
16. D. N. Poenaru and W. Greiner, *Phys. Scripta* **44** (1991) 427.
17. W. Scheid and W. Greiner, *Z. Phys.* **A 226** (1969) 364. H. J. Krappe, J. R. Nix, and A. J. Sierk, *Phys. Rev.* **C 20**, (1979) 992.
18. D. N. Poenaru, M. Ivaşcu, and D. Mazilu, *Comp. Phys. Communic.* **19** (1980) 205.
19. K. T. R. Davies and A. J. Sierk, *J. Comput. Phys.* **18** (1975) 311.
20. V. M. Strutinsky, em Nucl. Phys. **A 95** (1967) 420.
21. M. Mirea, D. N. Poenaru, and D. Mirea, *Rom. J. Phys.* **38** (1993) 71.
22. J. A. Maruhn and W. Greiner, *Z. Phys.* **251** (1972) 431.
23. P. Möller, W. D. Myers, W. J. Swiatecki, and J. Treiner, em Atomic Data Nucl. Data Tables **39** (1988) 225.
24. Y. Aboussir, J. M. Pearson, A. K. Dutta, and F. Tondeur, *Nucl. Phys.* **A 549** (1992) 155.
25. S. Liran and N. Zeldes, em Atomic Data Nucl. Data Tables **17** (1976) 431.
26. P. Möller, J. R. Nix, W. D. Myers, and W. J. Swiatecki, em Atomic Data Nucl. Data Tables, to be published.
27. W. D. Myers and W. J. Swiatecki, Report LBL-36803, Lawrence Berkeley Laboratory (unpublished).
28. P. Möller and J. R. Nix, em Atomic Data Nucl. Data Tables **39** (1988) 213.

New Data for Nucleosynthesis Processes

L. Trache* R.E. Tribble
A. Mukhamedzhanov
Cyclotron Institute, Texas A&M University, College Station, TX

Abstract

The question of obtaining data needed in nuclear astrophysics using alternative methods to the direct measurement of the cross sections for the reactions and energies involved in stellar nuclear reactions is discussed for a few specific examples. The stellar reaction rate for the radiative proton capture on ^{56}Ni, important in the rp-process is obtained from the study of excited states in ^{57}Cu with MARS. Use of Coulomb dissociation and alpha transfer reactions to extract data for the radiative alpha capture on ^{12}C and ^{14}C and finally the use of the Asymptotic Normalization Coefficient method and a few proposed experiments, including one with a ^{7}Be radioactive beam at the K500 superconducting cyclotron at TAMU are briefly discussed.

1. Introduction

Nuclear physics in general deals with the study of the structure of nuclei, their interactions and the interactions of their constituents. The simple fact that nuclei make up roughly 99 percent of the mass of the Universe, or at least that which is presently known, is probably enough of a reason to justify the scientific efforts of the nuclear physics community! Naturally a question arose very early: how were these nuclei formed? The answer was given with a newly invented word: nucleosynthesis! And nuclear astrophysics, the branch of nuclear physics that tries to understand and provide data for the nuclear reactions that occur in the Universe is almost the age of nuclear physics itself!

The cross sections for a wide range of nuclear processes are the key ingredients in model calculations of the nucleosynthesis taking place in the Universe, either in the primordial explosion, or in latter stages of stellar evolution. These cross sections must be determined in the nuclear physics laboratory.

The need for better data for the cross sections of the nuclear reactions relevant in various nucleosynthesis scenarios is an undisputable fact. This need grows with

*Permanent address: Institute of Atomic Physics Bucharest, Romania

the advent of new cosmological models like the Inhomogeneous Big Bang Model [1] and the rp-process [2] taking place in hot cosmological environments. Not only do we need more reliable reaction rates to work out the details of the nucleosynthesis in the standard cosmological model, but also to understand other fundamental aspects of the Universe and its evolution, such as the missing mass. The experimental problems one encounters arise for two main reasons: the very low energies and, in most of the cases, the exotic nature of the reacting partners. There are sometimes enormous difficulties in connection with these experiments and we need to use a variety of methods to overcome them.

We want to present here a few ways of obtaining data on the cross sections for the nuclear reactions taking place in stellar media by using alternative methods to that of the measurement of the real reaction at the energies involved. We shall do it only in connection with experiments or studies we conducted or planned at the K500 superconducting cyclotron of the Texas A&M University. Given the unicity, in subject, of this lecture at this School, I shall start with a short glossary of terms like primordial and stellar nucleosynthesis, Gamow peak (the energy region that contributes most to the reaction rate in stellar conditions) , astrophysical S-factor, H and He burning processes, rp-process, etc. which we skip from the text of the Proceedings. Then, in Sect. 2 we present how we found the resonant contribution of the reaction rate for the radiative proton capture on ^{56}Ni by studying the excited states of ^{57}Cu in a gamma-ray spectroscopy experiment using the Momentum Achromat Recoil Separator (MARS) [3] as a mass filter. In Section 3 we discuss reactions relevant for He-burning and in Section 4 we present schematically the Asymptotic Normalization Coefficient (ANC) method and its planned use in a few experiments.

2. The stellar reaction rate for the ^{56}Ni(p,γ) ^{57}Cu reaction

Wallace and Woosley [2] introduced the rp-process as a sequence of nuclear reactions in explosive hydrogen burning and showed that at high temperatures T_9=0.1–2.0 this nucleosynthetic process can lead within seconds to the production of heavy elements up to and beyond the iron gap. It proceeds through fast proton capture reactions to nuclei close to the proton drip line where β -decay is fast enough to equilibrate the radiative capture. The main path of the rp-process passes through ^{56}Ni which due to its doubly magic structure is more bound than any of its neighbours and has a longer lifetime. These properties make it a waiting point in the reaction network. The production of all heavier nuclei is therefore dominated by the rate of the radiative proton capture ^{56}Ni$(p,\gamma)^{57}$Cu. The binding energy of the last proton in ^{57}Cu is very low: S_p = 695(20) keV [4]. This makes all the excited states in ^{57}Cu (Figure 2) proton unbound, and consequently they are resonances in the proton capture reaction leading to this nucleus.

The reaction rate in stellar conditions,

$$\lambda = N_A < \sigma v >= N_A(\frac{8}{\pi\mu})^{1/2}(kT)^{-3/2}\int \sigma(E)Eexp(-E/kT)dE \quad (1)$$

will be dominated by the contribution of the resonances that lie in the region of the Gamow peak. For separate narrow resonances as the ones we are facing in this case the temperature averaged resonant reaction rate can be written as:

$$\lambda = N_A(\frac{2\pi}{\mu kT})^{3/2}\sum_{res}\omega\frac{\Gamma_p\Gamma_\gamma}{\Gamma_p+\Gamma_\gamma}exp(-\frac{E_R}{kT}) = T_9^{-3/2}\sum_i A_i exp(-\frac{B_i}{T_9}) \quad (2)$$

where ω is a statistical weight factor, $\Gamma_p(\Gamma_\gamma)$ are the proton (gamma) decay width of the $i-$th resonance of energy E_R, and T_9 is the temperature in units of 10^9 K.

We caried out a gamma-ray spectroscopy experiment [5] using the inverse kinematic reaction $H(^{58}Ni,^{57}Cu)2n$ at an incident energy E(^{58}Ni)=1.8 GeV to determine the excited states of ^{57}Cu. Prompt gamma-rays were measured at the target position by an array of seven Ge detectors positioned in two rings at 120° and 155° respectively, in coincidence with recoiling nuclei separated in the focal plane of MARS . The use of the inverse reaction made possible the efficient use of MARS as a mass separator and enabled us to unambigously separate $^{57}Cu^{+29}$ as at these energies most recoiling reaction products leave the polyethylene target fully stripped, but create enormous problems with the large Doppler shift and broadening of the in-flight emitted gamma-rays. Special, rectangular (16 x 8 and 16 x 4 mm^2) rather than cyllindrically symmetric collimators were prepared for the Ge detectors in this experiment where very large velocities of the emitting sources are encountered (β = 0.24) in order to balance between the need to minimize the Doppler broadening arrising from the finite angular acceptance of the detectors and the need to maximize the detection efficiency. By positioning these rectangular collimators with the long side perpendicular to the reaction plane, a factor 2 to 4 was gained in efficiency as compared with cyllindrically symmetric collimators which would give the same Doppler broadening. A resolution of about 10 keV (FWHM) at E_γ =1 MeV was obtained.

In Figure 1 we show a gamma-ray spectrum taken in coincidence with the $^{57}Cu^{+29}$ peak in the energy vs. position matrix measured with a position sensitive silicon strip detector in the focal plane of MARS. Three gamma-rays are clearly identified as being emmitted from ^{57}Cu: 1028, 1106 and 2398 keV (after Doppler shift correction). They are from the decay of the first three excited states of ^{57}Cu to the g.s. and therefore give their excitation energy.

To have a good estimate of the reaction rate from Eq. (2) we need both reliable resonance energies, $E_R = E_{exc} - S_p$, from the knowledge of the position of the excited states in ^{57}Cu and of its mass, and good knowledge of the decay widths Γ_p, Γ_γ. We use in what follows the newest value for the proton separation energy S_p =695(20) keV [4] and the excitation energies from the present experiment to locate the resonance energies, and a description of the structure of the lowest lying excited states in

^{57}Cu using a particle-core coupling model to obtain the nuclear structure information needed in order to calculate the decay widths.

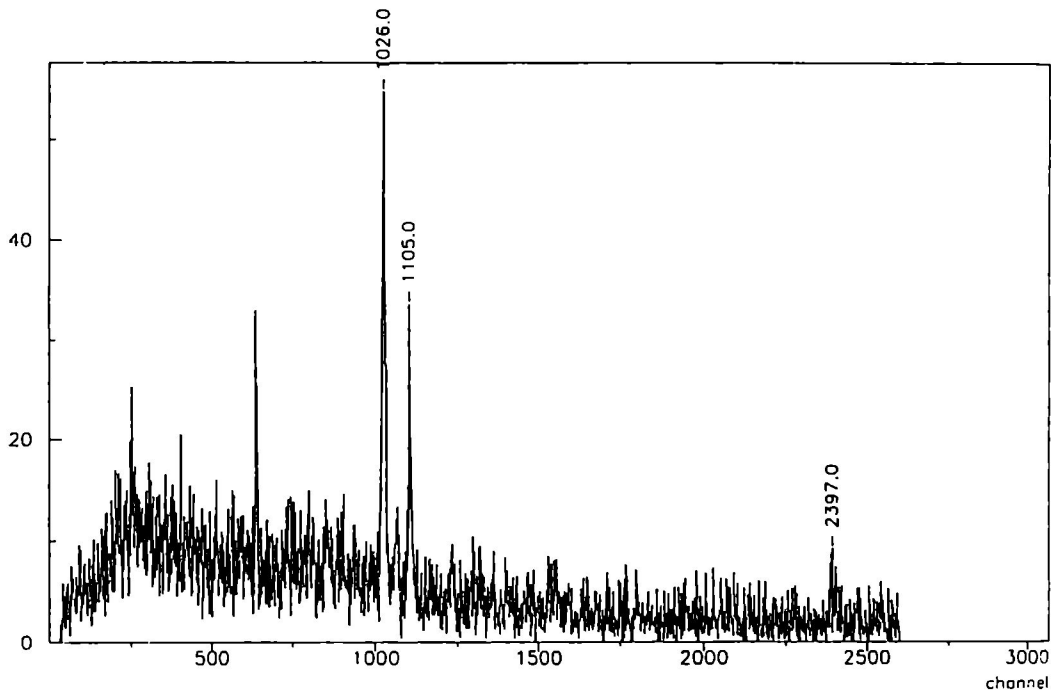

Fig. 1. gamma-ray spectrum measured at 155° in coincidence with recoiling ^{57}Cu nuclei detected in the focal plane of MARS.

This description is based on the fact that the mirror nuclei ^{57}Ni and ^{57}Cu are one neutron and one proton respectively, outside the doubly closed shell core ^{56}Ni. Their lowest excited states are in lowest order approximation obtained by promoting the odd nucleon in the available orbitals above N=Z=28: $2p_{3/2}$, $2p_{1/2}$, $1f_{5/2}$ and $1g_{9/2}$ or from collective excitations of the even-even core. In particular the first excited state of ^{56}Ni, the 2^+ level at E_x = 2701 keV, has the features of a quadrupole vibration and is at an energy comparable with the single particle excitations. Consequently the residual particle-core interaction leads to configuration mixing between the single-particle and the core-coupled configurations which affects the purity of the expected single-particle states.

The Extended Unified Model [6] used takes into account the coupling between the odd nucleon and the excitations of the core via a particle-vibration coupling

hamiltonian [7]. The excitations of the spherical core ^{56}Ni were considered harmonic vibrations of quadrupole and octupole type. Essentially we have undertaken a detailed study of ^{57}Ni for which much experimental data exist [8]. Its lowest excited states arise from the mixing of the single particle neutron orbitals $2p_{3/2}$, $2p_{1/2}$, $1f_{5/2}$ with the quadrupole multiplet of the ground state orbital $(2^+ \otimes 2p_{3/2})1/2^-, 3/2^-, 5/2^-, 7/2^-$. In the calculations we took the energy of the quadrupole phonon as the energy of the 2_1^+ state in ^{56}Ni (2701 keV) and extracted the quadrupole coupling strength from the recently measured reduced transition probability for the same state: $B(E2; 0^+ \rightarrow 2^+) = 600 \pm 120e^2\ fm^4$ [9]. The splitting of the 3 states ($5/2^-$, $7/2^-$ and $3/2^-$) known experimentally around E_x =2701 keV is given by the interaction between the quadrupole moment of the core state and that of the single particle [10]. To reproduce the observed spin order and the energy splitting for the quadrupole multiplet, a value $Q_m(2_1^+) = 10\ fm^2$ for the isoscalar (mass) quadrupole moment of the core state has been used. This is in fact the only free parameter used in the calculations. With the calculated wave functions and using in the transition operator the collective E2 contribution taken from the core nucleus, and the rather usual choice of the effective charge, $e_{eff} = 0.6e$, and the gyromagnetic factor $g_s^{eff} = 0.6g_s^{bare}$ for the single-particle part, we obtain decay patterns and lifetimes for ^{57}Ni which compare very well with those measured.

Using exactly the same procedure, coupling constants, Q(2^+)- core state quadrupole moment and the experimental energies for the first excited states in the single proton nucleus ^{57}Cu, we can extract the equivalent proton single-particle energies (different from those for the neutrons due to the Coulomb displacement) and the wave functions for the lowest lying states in ^{57}Cu.

We mention that the results from the calculations predict that in both nuclei the first three states are far from being pure single-particle, but have spectroscopic factors $S(2p_{3/2}) = 0.92$ and 0.92, $S(1f_{5/2}) = 0.89$ and 0.87 and $S(2p_{1/2}) = 0.75$ and 0.76 respectively for ^{57}Ni and ^{57}Cu.

With the wave functions we calculate the proton decay width as

$$\Gamma_p(E, l) = (\frac{2E}{\mu})^{1/2} P_l(E_r, R_n) C_{sp}^2 \chi_{nlj}^2(R_n) \qquad (3)$$

where C_{sp}^2 is the square of the coefficient of the single particle component in the wave function (the spectroscopic factor), $\chi_{nlj}(R_n)$ is the single-particle radial wave function of the (nlj) orbital at the nuclear radius R_n and $P_l(E_r, R_n)$ is the barrier penetration factor. The same EUM wave functions and an electromagnetic transition operator with the E2 collective part from the core nucleus the proton single particle effective charge $e_{eff} = 1.3e$ was used for the calculation of the $\gamma-$ray decay widths.

The results obtained are sumarized in Table 1 in the form of the coefficients A_i and B_i defined in Eq. (e2) where they are compared with those of Refs. 1 and 2. In addition to the first three resonances which correspond to the first three excited states in ^{57}Cu with the main configurations $1f_{5/2}$, $2p_{1/2}$ and $(2^+ \otimes 2p_{3/2})5/2^-$ respectively,

we include the next calculated level, the $7/2^-$ member of the quadrupole multiplet. In principle it should not contribute because it does not contain a pure single-particle component ($\pi 1f_{7/2}$ is filled up at Z=28). In the calculation we considered, rather arbitrarily, a small spectroscopic factor C^2_{sp}=0.01 for this state to account for the missing contributions the model does not consider. The contribution of this resonance never becomes important compared with the nearby $5/2^-$ resonance.

In Figure 3 the stellar reaction rate versus temperature is plotted in the range up to T_9 =2.0. For temperatures bellow T_9 = 0.08 the first resonance dominates due to its closests location to the reaction threshold, but its absolute value is very small due to the barrier penetrability for this l = 3 resonance. The second resonance with a larger penetrability due to a lower orbital momentum l = 1 becomes dominant for T_9 =0.08 to T_9 =1.2 where the third resonance becomes more important due to the penetrability factor in spite its rather low spectroscopic factor S_{sp} = 0.028. Our present results are very different from those recently obtained in [11] exactly in the relevant temperature range, but are close to those originally considered in [2].

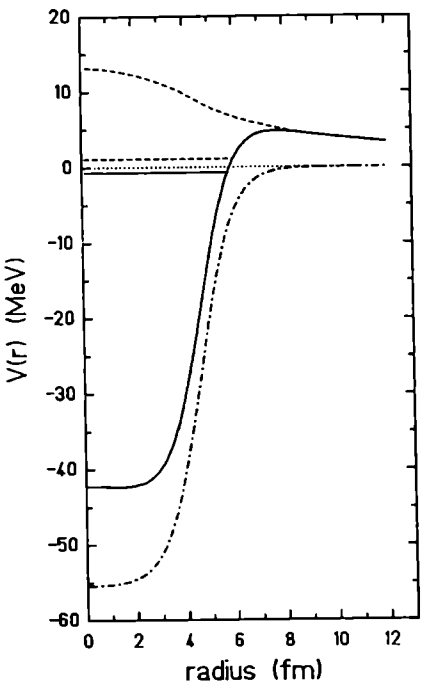

Fig.2. The potential well for the ^{56}Ni + p system (full line = total; dot-dashed = nuclear; dot line = Coulomb) showing the position of the g.s. (bound) and first excited state (proton unbound) of ^{57}Cu.

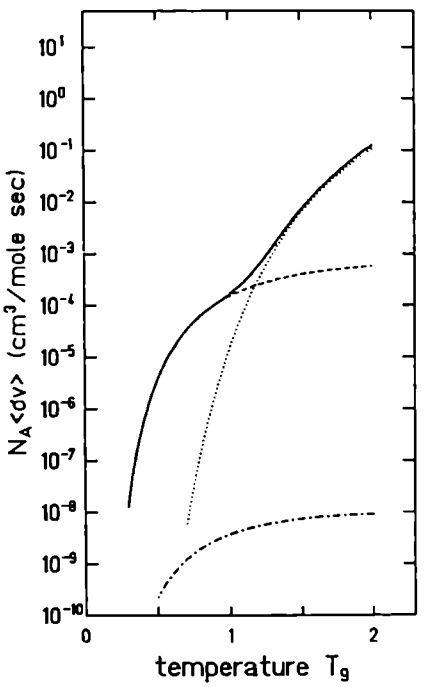

Fig. 3. The resonant contribution to the reaction rate for the proton radiative capture on ^{56}Ni vs. stellar temperature (full line). The contributions of the first 3 resonances are individually shown (dash-dot, dash and dot lines respectively).

3. Experimental studies relevant for He-burning

Another method to determine reaction rates would be to measure instead of the 'direct' reaction $a + b \rightarrow c + d$, the 'inverse' one $c + d \rightarrow a + b$ and to use the detailed balance theorem to extract the cross-section for the first. In the case of a *radiative capture reaction* $a + b \rightarrow c + \gamma$, its inverse is the *photodissociation* $c + \gamma \rightarrow a + b$. Experimentally this is not a very good trade because obtaining intense gamma-ray sources of high energy is not easy and the resulting fragments a, b have very low energies and are stopped in the targets. In the second half of the last decade, *Coulomb dissociation* was proposed [12] as a way to investigate radiative capture processes at very low relative energies, and has become a powerful tool in nuclear astrophysics (see the recent review of Baur and Rebel, 1993 [13]). Coulomb dissociation is the process in which a fast nuclear projectile breaks-up into two fragments when it passes peripherically by the Coulomb field of a heavy target nucleus. The photon source of the photodissociation is replaced by the virtual photons represented by the fast varying Coulomb field seen by the moving projectile. It provides information on electromagnetically induced interactions of the projectile constituents, which are subsequently used to extract the astrophysical S-factor for reactions of radiative capture. This is a nice example of how one can use fast projectiles from new accelerators to study processes at very low energies which cannot be accessed directly. The feasability of the Coulomb dissociation measurements was shown by the pioneering work done at Karlsruhe and Heidelberg for ^6Li [14,15] and at Texas A&M University for ^7Li [16]. Several measurements were completed recently or were proposed [17] but more work is still needed in order to understand it completely, and to extract the astrophysical S-factors from the measured data. Better data are needed in order to understand the mechanism itself, for example to establish the effect of multiple excitations, of the post-Coulomb acceleration and of the nuclear-Coulomb competition, before establishing reliable procedures to extract the data necessary in nuclear astrophysics. All these studies must be done with stable projectiles before extending to cases where radioactive beams are involved. We plan some of them at the K500 cyclotron and at the future AGOR superconducting cyclotron of KVI Groningen.

3.1. Coulomb dissociation of ^{16}O and ^{18}O projectiles

Dissociation of $^{16}O \rightarrow ^{12}C + \alpha$. The radiative capture reaction $^{12}C(\alpha,\gamma)^{16}O$ is part of the helium burning reaction chain:

$$3\alpha \rightarrow ^{12}C(\alpha,\gamma)^{16}O(\alpha,\gamma)^{20}Ne(\alpha,\gamma)^{24}Mg(\alpha,\gamma)^{28}Si$$

Because the α-capture on ^{16}O is very slow, it stops the reaction chain, and He is mainly converted into ^{12}C and ^{16}O, in proportions that depend on the rates of the 3α process and of that of the radiative α capture on ^{12}C. These reactions determine the existence of C and O in the Universe, which has consequences that we know very

well, including the existence of life itself and the possibility of this very interesting nuclear physics school.

Helium burning in Red Giants takes place at temperatures T= 2–8 10^8 K. Accordingly, the position of the Gamow peak varies from about 300 keV to 800 keV and its width from 170 keV to 540.keV. It follows that the cross section (or equivalently the astrophysical S-factor) must be determined for relative energies down to 300 keV. It is sometimes considered as "the most important unknown single quantity in nuclear astrophysics" because the values currently used for the S-factor do not explain the observed C/O abundance in the Universe and constitue a longstanding puzzle of the nuclear astrophysics.

Existing data: It is believed from the present data that the capture cross section at low energies ($E_0 \simeq 300$ keV) is determined by the dipole and quadrupole components. They have unknown contributions from the continuum, from 2 subthreshold resonances in the compound nucleus ^{16}O: 2^+ at E_x=6.917 MeV ($\rightarrow E_{\alpha C} = -245$ keV), 1^- at E_x=7.117 MeV ($\rightarrow E_{\alpha C} = -45$ keV) and from two resonances $E_{\alpha-C}$ =2.390 (1^-) and 2.683 MeV (2^+). Currently used S-values are extrapolated from data measured above $E_{\alpha-C} = 1$ MeV.

Competing measurements. The measurement of a *direct reaction* at such low energies is hindered by the very low (expected) cross-section in the *fb* region. The *β-delayed α decay of ^{16}N (gs 2^-)* gives data on the E1 component of the astrophysical S-factor, but not on E2. Recent measurements extended the analysed region down to E_α=0.63 MeV ($E_{\alpha-C}$=0.84 MeV) [18].

Experiment. One can show that despite the fact that the probability for the Coulomb break-up increases with increasing the projectile energy, practical considerations about the angular cone where measurements can be done impose restrictions. Calculations lead us to the conclusion that an energy around E/A=100 MeV/nucleon is optimum, considering the virtual photon spectrum and practical requirements (avoid $\theta = 0°$, finite angular openings, lower background, etc).

Baur and Weber [19] have shown that measurements of the angular correlations are necessary in order to disentangle the E1 and E2 contributions to the process. This is done by measuring at different angles of the spectrometer (different $\theta_{^{16}O}$), using the fact that the E1 and E2 photon yields varry differently, and by measuring the dependence on $\theta_{\alpha-^{12}C}$. We calculated that the c.m. angular range accessible and the angular resolution (1 mrad in the lab. angle, after raytracing) available at the Multipole Dipole Multipole (MDM) spectrometer at Texas A&M University and and the Big Bite Spectrometer (BBS) at KVI Groningen should allow us to do so. It is the only experiment in which these crucial angular correlations can be determined in Coulomb dissociation. Calculations by the French group [20] that attempted the GANIL experiments have shown that the nuclear contribution is very large and the nuclear-Coulomb interference must be used to extract the useful data. However the uncertainties in the calculation of the nuclear contribution are large (compare results in Refs. [20] and [21]) and can only be fixed by experiments at several bombarding

energies. This lead to the necessity of measurements at lower energies where the Coulomb part is small. The Cyclotron Institute at Texas A&M University was a pioneer in this field by measuring the dissociation of ^{16}O at 30 MeV/nucleon [22] a few years ago but with no results in the astrophysically relevant E_{cm} due to the low bombarding energy. The new MDM spectrometer provides opportunities to attempt the measurement at higher incident energies. We intend to join forces with a group from KVI Groningen, The Netherlands and a French group from Orsay who proposed a similar experiment to be done at the AGOR cyclotron at KVI, presently in final stage of construction. At E/A=95 MeV/nucleon (maximum energy for AGOR) the Coulomb contribution should increase versus the nuclear one and comparison of the results with those at the K500 energy will provide a way to disentangle them and solve the above mentioned puzzle appearing in the calculations of the nuclear part.

Dissociation of $^{18}O \rightarrow^{14} C + \alpha$. Another experiment in the same category of projectile dissociation, but presenting different experimental peculiarities, is the dissociation of the heavier oxygen isotope $^{18}O \rightarrow^{14} C + \alpha$.

Astrophysical motivation. There are two strong motivations for the importance of this reaction, pointing to two different relative energy regions of interest.

1) *Inhomogeneous Big Bang Nucleosynthesis.* After Witten recognized in 1984 that a QCD phase transition may lead to important cosmological consequences (e.g. that the hypothesis of a closed Universe $\Omega_b = 1$ is not excluded), Applegate, Hogan and Scherrer [1] proposed that a first order phase transition quark-gluon plasma to hadron matter would lead to inhomogeneous nucleon densities, which consequently would affect very much the primordial nucleosynthesis. Regions with increased densities of neutrons are possible, which would lead to the synthesis of neutron-rich light nuclei, the first of which is ^{14}C. This nucleus is the seed of a process that leads to ^{22}Ne for which the key-rate is that of the capture reaction $^{14}C(\alpha,\gamma)^{18}O$. The resulting ^{22}Ne is the seed for the development of an r-process leading to nuclei in the iron region and beyond, to the heaviest elements. (see e.g. Ref. [23] and refs. therein for further discussion).

The above process is suggested to occur in the primordial explosion, at temperatures ranging from T=1 MeV to T=0.1 MeV and at times between t=1 sec. and t=200 sec. and could lead to the nucleosynthesis of heavy elements in the primordial explosion. In the Standard Big Bang model the primordial nucleosynthesis only reaches ^4He and small quantities of ^7Li. The test of the model requires a good knowledge for the α-capture reaction on ^{14}C at energies around 1 MeV and beyond.

2) *Helium burning in accreting White Dwarfs.* To understand this, one needs reaction rates around 300 keV. **Experiment.** We investigated the possibility of measuring the Coulomb dissociation of ^{18}O on a ^{208}Pb target at the bombarding energy of E/A=60 MeV/nucleon. Because the fragments resulting from the dissociation have mass to charge ratios m/q=2.33 ($^{14}C^{+6}$) and m/q=2 ($^4He^{+2}$), respectively, the momentum (equivalent magnetic rigidity) acceptance must be larger than 17%. This condition is met by few existing spectrometers, including the MDM. RAYTRACE

calculations have shown a complete separation of the ^{14}C, beam (^{18}O) and ^{4}He spots in the focal plane. The two fragments can be detected in coincidence in two separate detectors, while the elastically and inelastically scattered projectiles are let through, and stopped beyond.

At very low relative energies (300 keV) one expects a dominant contribution from the E1 multipole component of the radiation, due to a subthreshold 1^- resonance, and a possible contribution of the E3 component, due to the influence of the narrow resonance 3_2^- at $E_{cm} = 178$ keV. At higher energies a broad 1^- resonance is suggested at E_{cm} =2.78 MeV [24] which may significantly contribute to the thermonuclear reaction rate in the region of interest for IHBB. This suggestion can be checked in the proposed measurement and the parameters of the resonance can be determined. The expected cross sections for the dissociation of ^{18}O are about two orders of magnitude larger than those for the ^{16}O case so the experiment would be simpler to carry out. However, the larger number of excited states in ^{18}O below and around the $\alpha-$C dissociation threshold implies that several excitation pathes are possible and the coupled channel calculations become unreliable due to the large number of intervening parameters. Nevertheless, simpler conclusions, as for example the existence of the above mentioned resonance can be checked. It will also provide a useful case for the study of the reaction mechanism itself which is far from being completely understood. In particular we will seek data about the post-breakup Coulomb acceleration [25], which is present in this case due to the fact that the resulting fragments have different mass-to-charge ratios.

3.2. The measurement of the reactions alpha transfer reactions $^{12}C(^{16}O,^{12}C)^{16}O$ and $^{14}C(^{18}O,^{14}C)^{18}O$

We also have plans to use transfer reactions in order to extract quantities that are latter used to determine cross-sections at very low energies. They are based on the Asymptotic Normalization Coefficient method which is schematically explained in the next section. In essence we intend to measure the elastic and inelastic alpha transfer reactions ^{12}C(^{16}O,^{12}C)^{16}O and ^{14}C(^{18}O,^{14}C)^{18}O using the MDM spectrometer. The interference due to the $\alpha-$exchange elastic scattering at large angles will allow a reliable determination of the ANC for the processes $^{16}O \rightarrow ^{12}C+\alpha$ and $^{18}O \rightarrow ^{14}C+\alpha$.

Measuring the elastic transfer of an alpha particle from ^{18}O will alow us to determine the ANC for the process ^{18}O(g.s)$\rightarrow ^{14}C + \alpha$ and the optical potential for the elastic scattering of ^{18}O on ^{12}C. From the measurement of the inelastic transfer of alpha particles to excited states of ^{18}O we can extract the ANC for different bound states of ^{18}O. The most important quantity is the ANC for the 1^- state at $E^* = 6.198$ MeV. From the shape of the spectrum in its continuum region we will identify the contribution of the resonant states and, in particular, will attempt to locate a broad dipole resonance which is suspected to exist at about $E_{cm} \simeq 2.78$ MeV [24]. If it exists it would make a major contribution in the thermonuclear reaction rate for the radiative capture in the primordial nucleosynthesis.

Moreover, these experiments will add data about the use of the Asymptotic Normalization Coefficient in the determination of reaction cross sections at very low energies. The same quantities are sought after by the alternative method of the Coulomb breakup studies. The comparison of the results of the two methods in the case of ^{18}O, together with those from the envisaged studies of ^{16}O and ^{6}Li, will add to the very few existing ones and will help establish the ANC method as a reliable way to extract data needed for nuclear astrophysics.

4. Asymptotic Normalization Coefficient Method

The concept of the asymptotic normalization coefficient (ANC) turns out to be a useful and alternative approach to other methods to derive the information about important astrophysical radiative capture processes. Consider the radiative capture reaction

$$a + b \rightarrow c + \gamma. \tag{4}$$

The matrix element for that reaction is given by

$$M = \langle \varphi_c(\zeta_a, \zeta_b, \mathbf{r}) \mid O(\mathbf{r}) \mid \varphi_a(\zeta_a)\varphi_b(\zeta_b)\psi_i^+(\mathbf{r}) \rangle, \tag{5}$$

where φ_j is the bound state wave function of particle j, ζ_j is the set of the internal coordinates of nucleus j, ψ_i^+ is the scattering wave function describing the relative motion of the colliding particles in the initial channel, $O(\mathbf{r})$ is the electromagnetic transition operator, $\mathbf{r}$ is the relative coordinate between particles a and b. For simplicity we neglect the spins of particles and took into account the dependence of the electromagnetic transition operator only on $\mathbf{r}$ disregarding its dependence on nucleon degrees of freedom. This assumption is justified for peripheral radiative capture reactions. Integrating over the internal coordinates ζ_a and ζ_b we derive from (5)

$$M = \langle I_{ab}^c(\mathbf{r}) \mid O(\mathbf{r}) \mid \psi_i^+(\mathbf{r}) \rangle. \tag{6}$$

Here $I_{ab}^c(\mathbf{r})$ is the overlap function (reduced width amplitude). Since the overlap function is not an eigenfunction of a Hermitian Hamiltonian, it is usually approximated by

$$I_{ab}^c(\mathbf{r}) = S^{1/2}\varphi_c(\mathbf{r}), \tag{7}$$

where

$$S = \langle I_{ab}^c \mid I_{ab}^c \rangle \tag{8}$$

is the spectroscopic factor of the configuration $a + b$ in c, $\varphi_c(\mathbf{r})$ is the single-particle bound state wave function decribing the relative motion of particles a and b in c. Assume for simplicity that the relative angular orbital momentum of particles a and b in c is 0. Taking into account the behavior of the radial parts of I_{ab}^c and φ_c at large $r > R_N$, where R_N is the nuclear interaction radius,

$$I_{ab}^c(r) \overset{r>R_n}{\approx} C_{ab}\frac{W_{-\eta_c,l+1/2}(r)}{r}, \tag{9}$$

$$\varphi_c(r) \overset{r>R_n}{\approx} c_{ab}\frac{W_{-\eta_c,l+1/2}(r)}{r}, \tag{10}$$

we derive the relation between the ANC C_{ab} of the overlap function, single-particle ANC c_{ab} and spectroscopic factor S:

$$C_{ab} = S^{1/2}c. \tag{11}$$

In Eq. (10) $W_{-\eta_c,l+1/2}(r)$ is the Whittaker function, η_c is the Coulomb parameter for the bound state $a+b$. Many of important astrophysical radiative capture processes with small binding energy of the final nucleus c in the channel $a+b$ due to the strong Coulomb repulsion at very low relative kinetic energies of the colliding particles in the initial channel are peripheral ones. For such reactions the dominant contribution comes from $r > R_N$, that is why we can approximate the overlap function in (6) by its asymptotic expression (10) what leads to

$$M = C_{ab}\langle\frac{W_{-\eta_c,1/2}(r)}{r} \mid O(\mathbf{r}) \mid \psi_i^+(\mathbf{r})\rangle. \tag{12}$$

Here we assumed for simplicity that the $l = 0$. It follows from (12) that the only unknown quantity we need to know to calculate the cross section of direct peripheral astrophysical processes is the ANC C_{ab}. It means that it is not necessarily always try to measure the cross sections at very low energies what is often impossible to do in the lab. Instead sometimes it is enough to measure the corresponding ANC. The ANC can be found experimentally from analysis of different nuclear reactions. One of possible nominees to extract the ANC are the cluster transfer reactions induced by heavy ions. Consider, for example, the reaction

$$c + A \rightarrow a + B, \tag{13}$$

where $c = a + b$, $B = A + b$. Typically the transfer reactions induced by heavy ions at energies $\sim 100MeV$ are peripheral ones due to the strong absorption in the initial and final channels. That is why the DWBA cross section for such reactions can be parametrized in terms of the ANC's for $c \rightarrow a + b$ and $B \rightarrow A + b$ rather than in terms of spectroscopic factors [26,27]:

$$\frac{d\sigma}{d\Omega} = C_{ab}^2 C_{Ab}^2 \tilde{\sigma}. \tag{14}$$

Here $\tilde{\sigma}$ is the reduced DWBA cross section which does not depend on the structure of interacting ions. Normalizing the DWBA cross section to the experimental one in the main stripping peak in the angular distribution we can extract the product $C_{ab}^2 C_{Ab}^2$ and then the ANC C_{ab} if the ANC has been known.

As an example we want to indicate the reactions $^{14}N(^7Be,^8B)^{13}C$, $^{12}C(^{16}O,^{12}C)^{16}O$ and $^{14}C(^{18}O,^{14}C)^{18}O$. Analysis of these reactions shows that they are peripheral at

Table 1. Constants for the resonant reaction rate for the proton radiative capture on ^{56}Ni. The constants are defined in Eq. (2).

E	Present	exp.	Ref. ([2])		Ref. ([11])	
keV	A_i	B_i	A_i	B_i	A_i	B_i
1028	1.81(-7)	3.86	-	-	9.5(-7)	3.482
1106	1.78(-2)	4.77	1.29(-2)	4.90	4.59(-5)	3.482
2398	6.9(+3)	19.76	7.06(+3)	20.33	9.97(+3)	19.75
2520	2.0(+3)	21.18	-	-	8.87(+3)	21.38

incident ions energies $\sim 100MeV$. Hence, for example, from the first reaction the ANC for $^8B \rightarrow {}^7Be + p$ (a key reaction in the ppIII chain and for the understanding of the solar neutrino puzzle) can be defined if the ANC for $^{14}N \rightarrow {}^{13}C + p$ is known. Similarly from analysis of the second and third reactions we can extract the ANC's for $^{16}O \rightarrow {}^{12}C + \alpha$ and $^{18}O \rightarrow {}^{14}C + \alpha$, correspondingly. The experiment using the radioactive beam ^{7}Be is under way at the K500 cyclotron. The ^{7}Be beam was obtained with a ^{7}Li beam on a H target and using MARS for the separation of the secondary beam. The first scattering data with this beam were already obtained.

ACKNOWLEDGMENTS. The results presented were obtained together with our colleagues at the Cyclotron Institute, Texas A&M University. We kindly acknowledge theyr contributions and the many fruitfull discussions with C.A. Gagliardi, H. Dejbakhsh, R.P. Schmitt, J. Jiang, X.G. Zhou, D. Youngblood and Y.-W. Lui.

1. Applegate, Hogan and Scherrer, Phys. Rev. D 35(1987)1151, Astroph. J. 329(1988)572
2. R.K. Wallace and S. E. Woosley, Astrophys. J. Suppl. 45, 389 (1981).
3. R.E. Tribble, R. H. Burch, and C. A Gagliardi, Nucl. Instr. Meth. A285, 441 (1989).
4. C.A. Gagliardi, D. R. Semon, R. E. Tribble, and L. A. Van Ausdeln, Phys. Rev. C 34, 1663 (1986)
5. X.G. Zhou, H. Dejbakhsh, C.A. Gagliardi, J. Jiang, L. Trache and R.E. Tribble, submitted to Phys. Rev. C, 1995
6. L. Trache, K. Heyde and P. von Brentano, Nucl. Phys. A554(1993)118
7. A. Bohr and B. Mottelson, *Nuclear Structure*, vol. 2, 1975, W.A. Benjamin Inc., Reading, MS
8. M.R. Bhat, Nucl. Data Sheets 67(1992)195
9. G. Kraus et al., Phys. Rev. Lett. 73(1994)1773
10. L. Trache, A. Clauberg, C. Wesselborg, P. von Brentano, J. Wrzesinski, R. Broda, A. Berinde and V.E. Iacob Phys. Rev. C 40(1989)1006
11. L. van Wormer, J. Gorres, C. Iliadis, M. Wiesher and F.-K. Thielemann, Astroph. J. 432(1994)326
12. G. Baur, C. A. Bertulani and H. Rebel, Nucl. Phys. A458(1986)188: G. Baur Phys. lett. B178(1986)135

13. G. Baur and H. Rebel, J. Phys. G (1994)
14. Jelitto H. et al., Z. f. Phys. A332(1989)317; Kiener J. et al., Phys. Rev. C 44(1991)2195
15. Hasselbarth et al., Z. f. Phys. A331(1988)365
16. Utsunomiya et al., Phys. Lett. B211(1988)24
17. "Coulomb Dissociation as a tool of Nuclear Astrophysics", Proc. Symp. Oct. 1993, Strasbourg and Aug.-Sept. 1994, Tours (France), unpublished
18. L. Buchmann et al., Phys. Rev. Lett. 70(1993)726
19. G. Baur and M. Weber, Nucl. Phys. A504(1989)352
20. V. Tatischeff et al., Phys. Rev. C 51(1995)2789
21. C. Bertulani, Phys. Rev. C49(1994)2688
22. D. O'Kelly et al., in *Research in Progress*, Annual Report, Cyclotron Institute, Texas A&M University (1993), p.36 and to be published
23. Thompson W. et al. (eds), Workshop on Primordial Nucleosynthesis, Chapel Hill, 1989, World Sci. Publ. Co., Singapore, 1990
24. M. Gai, Phys. Rev. C 45(1992)R2548
25. E.O. Alt, B.F. Irgaziev, A.T. Muminov and A. Mukhamedjanov, Russ. J. Nucl. Phys., 1995, in press
26. Sh. S. Kayumov, A. M. Mukhamedzhanov and R. Yarmukhamedov, Z. Phys. A331, 315 (1988).
27. Sh. S. Kayumov, A. M. Mukhamedzhanov, R. Yarmukhamedov and I. Borbely, Z. Phys. A336, 297 (1990).

NARROW "BARRIER-RESONANCE" STATES IN ELASTIC α-PARTICLE SCATTERING

TOM LÖNNROTH
Department of Physics, Åbo Akademi
Porthansgatan 3, FIN-20500 Turku, Finland

ABSTRACT

Groups of narrow states with a rotational-like structure are observed from the Coulomb barrier up to an excitation energy of about 35 MeV in ^{28}Si. The properties of these states, observed in α-particle elastic scattering, will be described. There are few, if any, models on the market that are able to explain the experimental findings in a consistent way.

1. Introduction

This lecture will present the results of an experimental investigation of α-particle elastic scattering on a number of nuclides. The most comprehensive data in from scattering on ^{28}Si, but also some other cases will be discussed. Narrow states, which seem to form a rotational structure excited in the elastic scattering process, are observed from the Coulomb barrier up to an excitation energy of about 35 MeV.

We discuss properties of highly-excited states, i.e. states in the continuum region above the effective Coulomb barrier. The elastic alpha scattering is a powerful tool (at least on even-even nuclei) to study states with presumed alpha-cluster structure at high excitation. For lower excitations, and for quasi-bound states the (^{6}Li,αd) break-up reaction is quite well suited, see e.g. the works on ^{28}Si(^{6}Li,αd) and ^{40}Ca(^{6}Li,αd), cf. refs.[5,46] and references therein. The interpretation of the observed structures are not easy, and it will be shown that the models on the market have serious problems to explain the experimental findings in a consistent way.

The theoretical analysis has progressed along two main lines:

1. Classical potential scattering along the lines of e.g.[40] using an optical potential with slowly energy-dependent real and imaginary potentials has been attempted. This results in a smooth energy-angle surface $\sigma(E,\theta)$ for the cross section, as shown in figure 1, which is adapted from the very instructive figure 2 of ref.[41].

2. Cluster models have been applied to light nuclides, i.e. for $A \leq 40$, see e.g.[18,24] for good reviews. In these approaches one uses descriptions within several model frameworks: the oldest one is the Resonating Group Method (RGM) due to Wheeler as early as 1937[44]. In order to avoid calculational difficulties in the RGM, the Generator Coordinate Method by Hill, Wheeler and Griffin, see[22,19], were brought into the RGM by Brink[10], thereafter called the Bloch-Brink approach. The third model, the Orthogonality Condition Model (OCM), which approximates the RGM non-local potential by an effective local one for which the forbidden states are removed by projection, was worked out by Saito[43].

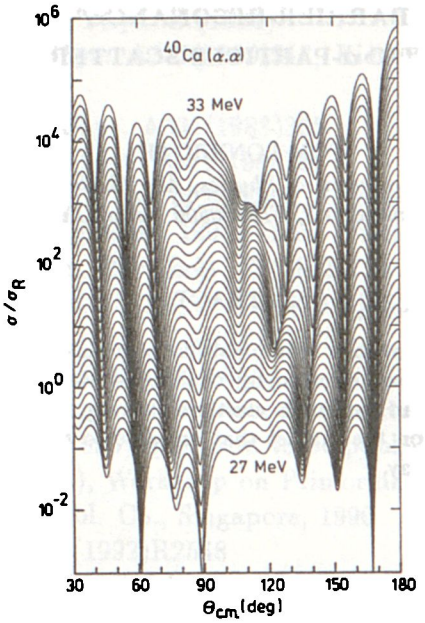

Figure 1. Theoretical energy-angle surface $\sigma(E,\theta)$ for the cross section of elastic scattering of the α+^{40}Ca system. From ref.[41].

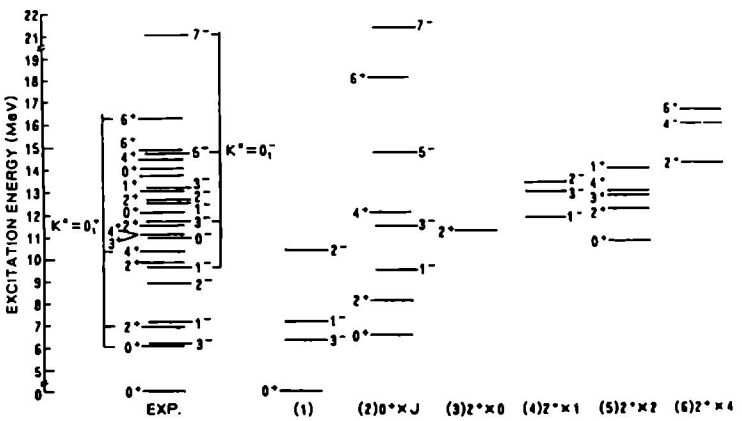

Figure 2. Theoretical and experimental states in ^{16}O calculated as α+^{12}C in the OCM[17] for states that are interpreted to have large fractional parentage of an α-cluster structure. Note the fairly good correspondance.

An example of the correspondance of theoretical structures within the OCM with selected experimental states is shown figure 2, which is adapted from ref.[17]. In the discussion we will show that some of the reported features are quite well discribed

within existing models, especially near the doubly magic ^{16}O. However, we will also show that these approaches rather fail to describe the wealth of structures we observed around A~30-36.

2. Experimental

The experimental data of elastic α-particle scattering were obtained at Åbo Akademi (ÅA), at the Tandem van de Graaff Accelerator of the The Svedberg Laboratory in Uppsala University, and at the cyclotron of Oslo University. The main part of the experiments (and the methodical development) presented here was performed with the MGC-20 (K=20) cyclotron of the ÅA Accelerator Laboratory. The accelerator has been designed and constructed by SRIEA (the D. Efremov Scientific Research Institute of Electrophysical Apparatus, Leningrad), see figure 3. The accelerator was first reported in ref.[21] and subsequent reports of the Accelerator Laboratory have appeared since.

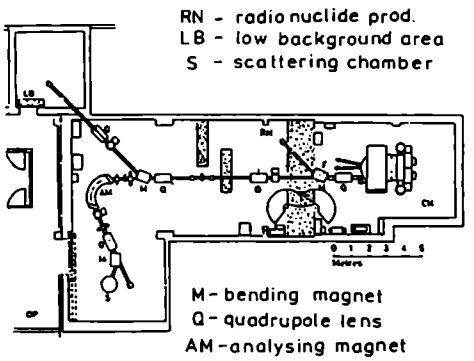

Figure 3. Schematic presentation of the Accelerator Laboratory of Åbo Akademi. The vital instrument for the present purposes is the analyzing magnet AM, the trimming of which allows a use of the cyclotron which resembles that of an electrostatic accelerator — i.e. fast trimming af narrow (~20 keV) well-defined energy steps.

The ÅA cyclotron was originally designed for the production of medical isotopes, which use implies high beam intensities. Since the acceleration is done during a fairly large angular acceptance phase, the outcome is a high beam intensity at a nominal energy E_0, although with a substantial beam energy spread ΔE_0 of the order of several hundred keV. Using narrow slits on the entrance and exit of the analyzing magnet AM, working on NMR basis, one is able to physically "cut" the energy, but retaining a sufficient fraction of the initial total beam intensity in order to be able to obtain on-target intensities at the scattering chamber SC of about 20 enA. The beam resolution is then obtained to be $\leq$15 keV and a typical room-temperature Si(Li) detector resolution is similar. If the target thickness is kept below some 10 keV (*thin-target* measurements, see below) we thus obtain an all-over resolution of ~20

keV. This very feature has been used in our studies, which first results were reported in[37].

Below we will report results of two methods, which will be referred to as the 'stepping method', and a novel method, called the 'thick-target method', which was developed in order to save time – one can convince oneself that even if energy change is done in about 5 minutes, an experiment covering an excitation energy of some 30 MeV will be tedious if done in 20 keV steps, and usually in three angle settings (see below).

2.1. Thin target technique. Stepping procedure

Strongly varying cross sections, as a function of energy, in elastic α-particle scattering were observed some two decades ago on ^{28}Si[11,45] and also on ^{24}Mg[6] and ^{40}Ca[16,23,39] targets. The large cross section can be explained as a resonance phenomenon, see e.g. the discussion of Hodgson's[23].

The existing data have, generally speaking, been much too scant to allow for a detailed analysis of the distribution, strengths, widths and angular momenta of the wealth of states inferred. For this reason we have started a program which aims at completing the data over a large energy region – from the Coulomb barrier as high up as possible, for example up to $E^* \sim 30$ MeV in ^{32}S, where the data shown in ref.[11] looks like having an experimental problem, but which seems to be a physical effect, though! The requirement is that the energy covered must be almost 'continuous', implying short energy-step lengths, and the recording of angular distributions at as many energies as possible. The cross section can be obtained when the target thickness (in our work determined by Rutherford scattering) and beam intensity are measured.

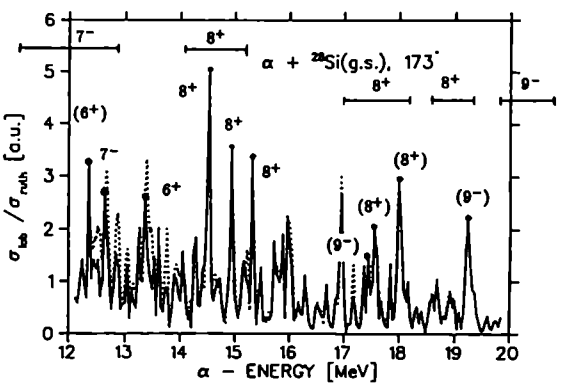

Figure 4. Excitation function of ^{28}Si(α, α_0). Angular momenta are determined from experimental angular distributions. The upper values are from the ^{28}Si(^{6}Li,αd) transfer reaction, reported in[5].

The first examples of such data were shown in[37], and subsequently also in[5], see figure 4. The latter report also shows a comparison to transfer data from the ^{28}Si(^{6}Li,αd)

reaction. The angular distributions are fitted to the Breit-Wigner expression on peak

$$\frac{d\sigma}{d\Omega} = \frac{1}{k^2}(2\ell+1)^2 \left(\frac{\Gamma_\alpha}{\Gamma}\right)^2 P_\ell^2(\cos\theta),$$

which is valid for resonance scattering when the process is dominated by one particular ℓ-value (also σ_{Coul} is neglected). In this well-known expression it is worth noting that $d\sigma/d\Omega$ is the measured cross section in a specific angle, $1/k^2$ is the beam energy, ℓ gives the angular momentum value of the peak, $\Gamma_\alpha$is the measured α-width, and Γ is a total width of a region, which experimentally is often not unambiguous to determine.

2.2. Thick target technique. Continuous energy[28]

The measurements of subsection 2.1 are, despite some ingenious technical methods, fairly tedious and time consuming. In order to improve on this a more effective method has been developed. It is, in fact, a straightforward extension on the principle of the inverse-geometry scattering of heavy particles on alpha-particle gas[4].

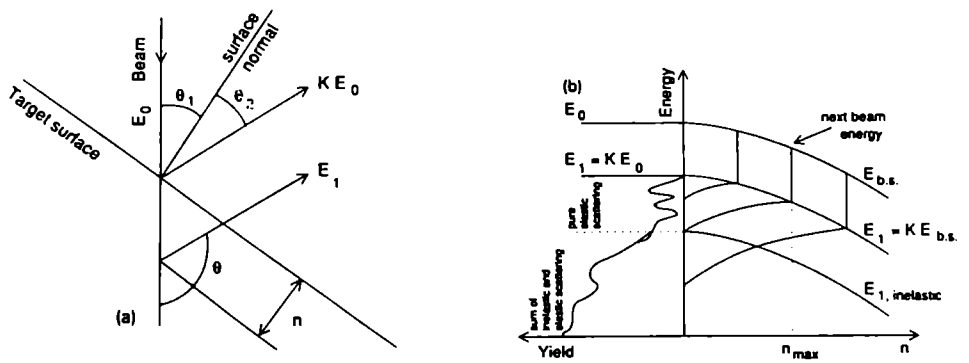

Figure 5. Illustrating the 'thick-target' method for continuous energy degrading in elastic backward-angle scattering. Further details can be found in the original publication[28].

In that set-up the scattered α-particle is detected at 0° (with respect to the incoming beam) in the laboratory, and the beam energy itself is continuously degraded down to zero. The path length of the heavy-ion beam is only some few cm, and thus not endangering the detector. If this principle is translated to running α-particles on a material thick target it means that the target material again acts as a continuous energy degrader, the α-particles (beam) are scattered, but in this case by 180°, which, however, is completely analogous to a scattering in 0° seen from the c.m. frame! The principle is illustrated in figure 5, for details see[28]. It turns out that the method, which mainly is restricted by the energy of the 2_1^+ state in the target nucleus (at 1.778 keV in ^{28}Si, which allows more than 500 keV long energy steps), indeed gives *better* resolution than the stepping method, for the simple reason that the energy is continuous, and no minor dips/peaks are 'missed'. The use of this method has recently also been reported elsewhere[12].

Figure 6 shows two spectra recorded with an energy interval of 600 keV, and the cross section is reported on a linear scale. Note the very minor differences in intensity. Note further that the peak broadening due to straggling in the material becomes important only at a depth of more than 500 keV. The detailed discussion of the beam energy resolution, as stated in the beginning of this section, is now seen to be of major importance – the spectral details need an overall resolution of some 20 keV or better!

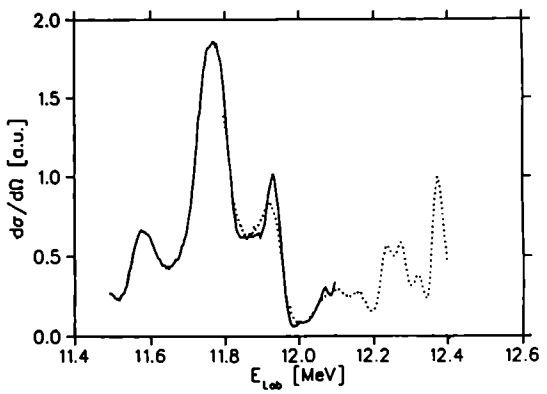

Figure 6. 'Glueing' consecutive parts of the excitation functions. Note that only at a depth of more than 500 keV the straggling starts to affect the resolution.

3. Results

The following experiments have been performed: The most comprehensive data is for ^{28}Si, which was first studied using the stepping method, but subsequently run over the "entire energy region" (by which is meant from the Coulomb barrier to where the effect "ends" – at about 35 MeV). Further, we also have data on ^{18}O (thick-target) over a region additional to previous experiments[42], ^{27}Al over E_{lab}=12-19 MeV (thick target), and ^{29,30}Si and ^{32,34,36}S all using the stepping method. Some tests have also been performed on evaporated KCl, which provides the four isotopes ^{35,37}Cl and ^{39,41}K with comparable intensities.

The angular distributions were recorded in 14 or 21 angles, which for the case of ^{28}Si means that the data is continuous in energy, and after splining the angle data, quasi-continuous in angle. When the energy pieces are 'glued' together, and likewise the angular parts (taking into account the differential stopping power, which amounts to non-linear angular pieces, see[28]), one obtains an energy-angle cross section *matrix* which can be analyzed subsequently. This is, in fact, a unique kind of data. An example of such a matrix is shown in figure 7. Note that the energy interval of the figure covers only about 1 MeV, but despite this there is a substantial 'fine structure' in the data, again calling for the energy resolution.

The analysis is performed by slicing the angular distribution in the chosen energy

intervals/bins. In doing so one can obtain angular distributions for chosen energies, $\sigma_E = \sigma_E(\theta)$, and the strength of the data is, that one is *not* restricted to a given set of angular distributions, but one can rechose the "gates" at will. Especially, since the 'peaks' seen are not well defined, one can analyze the evolution of the angular distribution when gating/scanning over one specific 'peak', and thus obtain information as to the compositeness of the peak in question. The fits of the intensities of accepted energy slices are then done to the squared Lagrange polynomial $P_\ell^2(\cos\theta)$ of the above-mentioned Breit-Wigner expression. Some examples of the quality are given in figure 8.

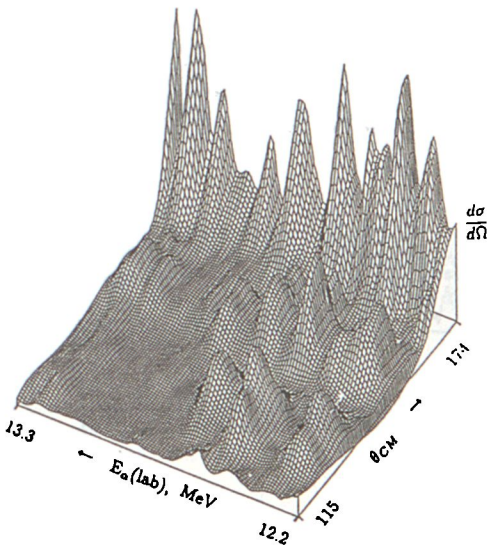

Figure 7. Dependence of the cross section σ on total energy and angular information, i.e. a $\sigma(E,\theta)$ matrix, which is seen to be a continuous data set. The angular analysis can be performed in the same way as the "gating procedure", which is familiar from $\gamma - \gamma$ spectroscopy.

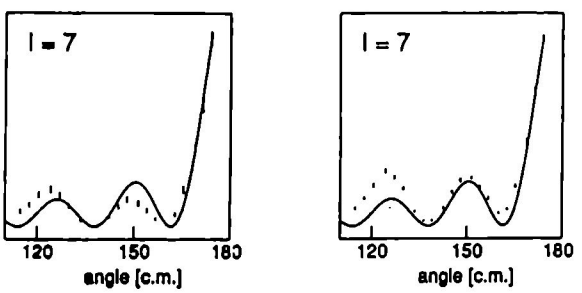

Figure 8. Examples of angular distributions for two gates centered around E=12.67 MeV, the left panel from a 25 keV wide slice, and the right one from a 188 keV wide one. Note the energy accuracy!

The total information of the cross section experiments and the subsequent angular-distribution analysis is given in figure 9. In addition we have data down to the Coulomb barrier, see[29], and from experiments in Oslo up to E_{lab}=34 MeV, where the fluctuating pattern "vanishes", by which is meant that the cross section goes down by two orders of magnitude (see the Summary).

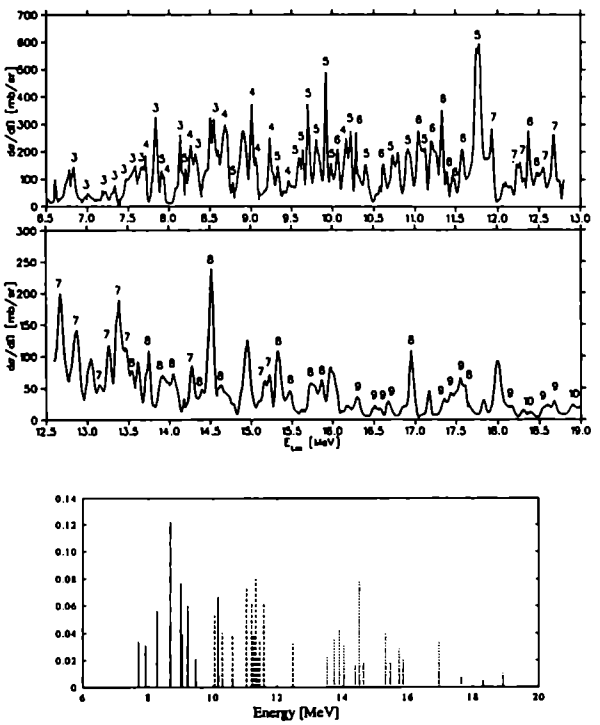

Figure 9. Upper panel. Excitation function of the elastic scattering of alpha particles on silicon, ^{28}Si(α, α_0). Additonal data goes down to $\sim$ 3.0 MeV, see[29], and up to a laboratory energy of 34 MeV (Oslo experiment). The total excitation energy range covered is thus E*=9.6-35.0 MeV continuously! The numbers are angular momentum values where they are found to be uniquely defined (some 'peaks' still seem composite!). Lower panel. Exctracted "strengths" for groups of peaks with well-defined angular momenta. Note that the groups are 2-3 MeV wide, and that the widths are slowly increasing with energy.

In addition to the data on ^{28}Si there is data on ^{29,30}Si. The structures of the excitation functions are virtually identical, with strongly fluctuating strengths as a function of energy. However, there are large differences in the cross section mean values. For the three silicon isotopes ^{28,29,30}Si they vary roughly as 8:1:3 (i.e. for N=14,15,16), see figure 10. A similar behaviour is seen for ^{32,34,36}S, where on the contrary the ratios are 5:4:1 (for N=16,18,20), cf. ref.[3].

In the experiments on ^{28}Si using the stepping method, there is, in addition to ^{28}Si

the isotopes ^{29,30}Si which are present in sufficient amounts on a target of natural silicon (4.7 and 3.1%, respectively) to allow extraction of excitation functions of various inelastic peaks, mainly the 2_1^+, 4_1^+ and 0_2^+ states. These inelastic data have been presented in[9]. We note that the inelastic and elastic peaks seem *not* to occur at the same excitation energies, even if the effect of shifting the *observed* resonance position due to penetrability effets[27] is included. We calculate the shifts to be not more than about 10 keV. This effect has also been discussed[32] in the α+^{16}O(0_2^+) scattering leading to ^{20}Ne.

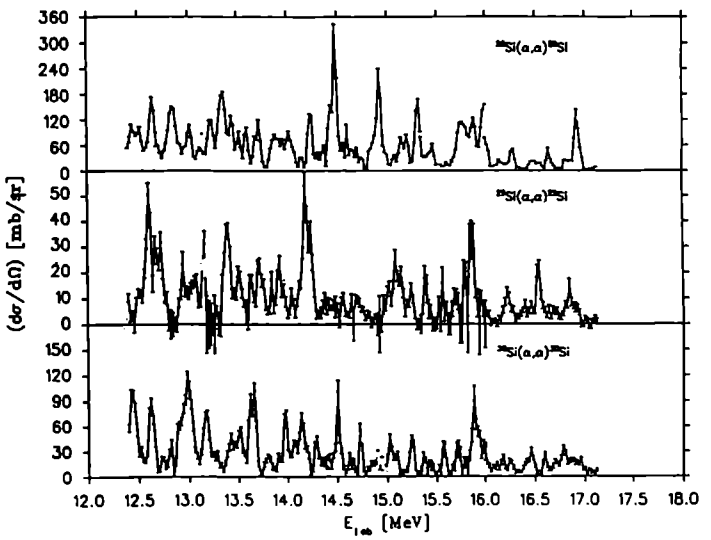

Figure 10. Excitation function of the elastic scattering of alpha particles on three silicon isotopes: ^{28,29,30}Si(α, α_0). Note the similarity of the excitation functions irrespective if the system is odd or even, but the difference in absolute cross section values.

4. Discussion and interpretation

When the centroids of the angular momenta reported in figure 9 (lower panel) are plotted against $\ell(\ell+1)$ one obtains a straight line, as shown in figure 11. There are two major facts to be noted from this figure:

1. The linear behaviour vs. $\ell(\ell+1)$ indicates a rotational behaviour in the α+^{28}Si system. The moment of inertia can be obtained as $J = 4.85\,\hbar^2\mathrm{MeV}^{-1}$, which indicates that the states constitute an object that is slightly more extended[38] than the "ground-state band" configuration.
2. As is well seen, there is no splitting in energy between positive- and negative-parity states, i.e. the experimental so-called parity splitting is absent. This will be shown to be in serious conflict with most model predictions.

Below will be mentioned a number of theoretical approaches, but it will be shown that none of the following models is able to explain the experimentally observed

features:

-classical potential descriptions with e.g. a Dunham-type[14] shape seem not to be able to produce a sufficient number of vibrational states without being unphysical as too shallow, which feature also is connected to inconsistency in the rotational-vibrational description[30],

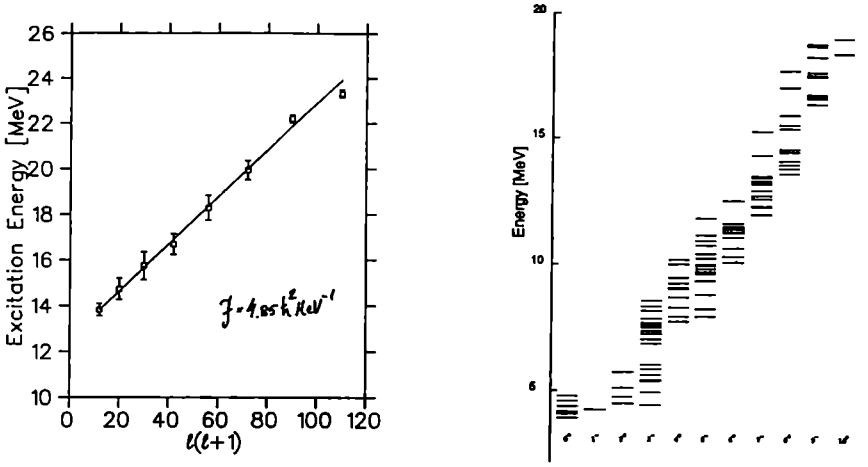

Figure 11. Left. Plot of $E_{exc}=E_{exc}(\ell)$ for a quadratic angular-momentum dependence. A straight line indicates a rotational behaviour and defines the effective moment of inertia. Right. Phase space plot (or yrast plot) of all the states in figure 9 that have an exprimentally determined angular momentum.

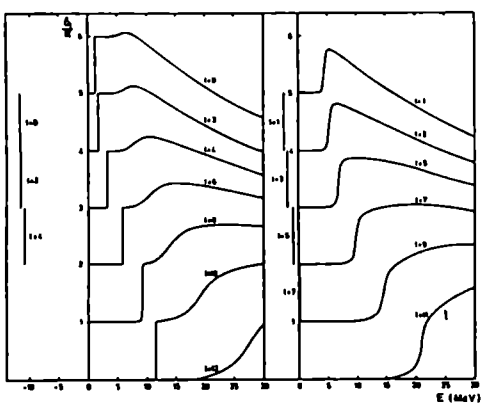

Figure 12. A typical phase-shift behaviour, in this case for the GCM[31], giving one narrow quasi-bound state, and one broad state at an excitation energy some few MeV above the effective barrier. *No large number of states* can be obtained! Similar calculations done for ^{20}Ne in ref.[40] give the same kind of results — here it is interesting to notice that a large number of states with relatively large α-widths can be found[2]. Corresponding features are also found in all heavier nuclides[15].

-cluster models fail in that they cannot produce the required large number of

states in ℓ-value bunches, see e.g. the results shown in figure 12,

- scattering using various potentials[36,8] run into discrepancies regarding the Wildermuth condition vs. fitted potential-well depths and especially sizes,

- semimicroscopic descriptions (e.g. figure 13), like the Cranked Shell Model (CSM) approach[33,47] are not either able to produce a sufficient number of single-particle "bands", the rotating structures of which would represent the bands (if the states are so interpreted, see figure 11) observed experimentally. Further, they require too large deformations, see figure 14, and they describe the shapes in the quadrupole-deformation approach,

- the soliton approach [34,35] is, indeed, the only description so far that can give a suffiently large number of states, see figure 15! It has, however, problems with a physical interpretation – because of the non-linear approach,

- microscopic shell model calculations[20] can, in principle, give *all* the states that can be constructed of the nucleonic orbitals, but it is not evident that the residual interaction is able to create the correct alpha-cluster correlations. These calculations would also need very large bases, and this is a well-known problem,

- IBA[25] approaches do not give the correct state structures. We have tried to do calculations in the SU(5) and O(6) limits with the number of alpha particles as bosons, but these calculations fail to give the correct structures, and finally

- the rotation-vibration approaches[1,13] seem to run into unphysical potentials[30].

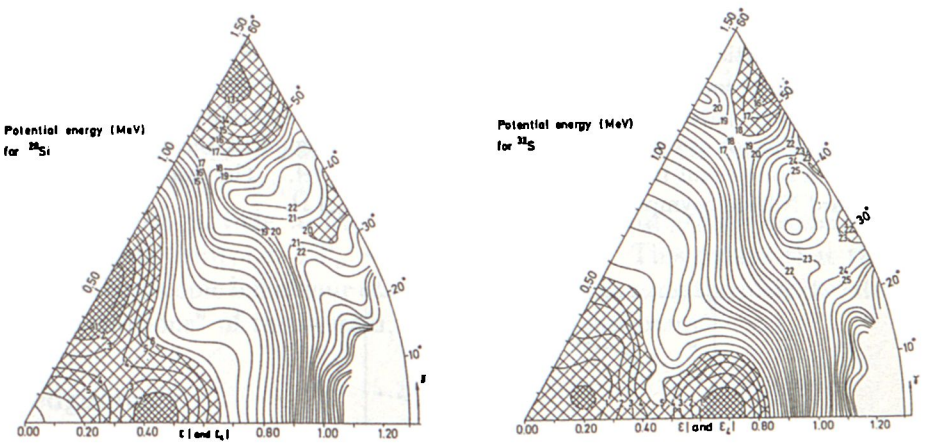

Figure 13. CSM diagrams for ^{28}Si and ^{32}S as calculated in[33]. It is seen that local energy minima at large deformations do occur, but they seem to be too deformed for the states we have observed.

5. Summary and outlook

In order to clarify the situation, including the isotope effects in the cross sections (also for odd-A isotopes), more experiments must be done. Doing experiments on other nuclides runs into problems (see figure 1) since, counting from ^{16}O, the next

nuclides are ^{20,22}Ne which mean gaseous targets. For these, however, experiments at JYFL (Accelerator Laboratory at University of Jyväskylä) are being planned. The next heavier elements is magnesium with its isotopes ^{24,25,26}Mg, which unfortunately tend to evaporate at the heating of the beam due to low vapour pressure already at room temperature. Above Si we have sulphur (with three isotopes ^{32,34,36}S) which behaves much like Mg, and the next is again a gaseous specimen, Ar, until we hit calcium. As is seen, each experiment has its own difficulties.

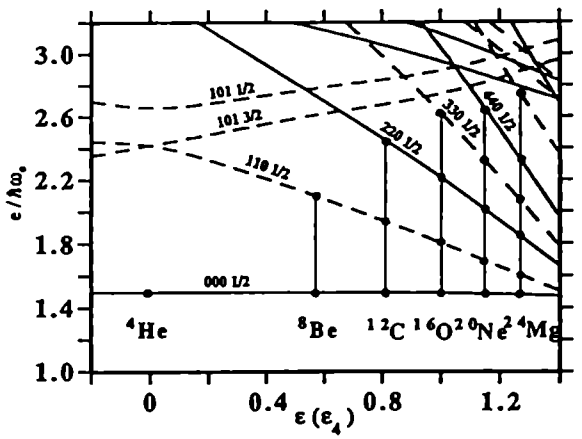

Figure 14. Single-particle Routhians (extended Nilsson diagram) for neutrons and protons at large prolate deformations corresponding to α "strings", from ref.[47]. At deformations $\epsilon \sim 1.1$ one observes many single-particle orbitals at similar energies ($e \sim 3.0\hbar\omega_0$) which may give rise to several rotational bands at similar energies. However, like for figure 13, the deformations seem to be too large. For a state count in a sense of alpha particles, see ref.[7]. The displayed states are labeled in the standard Nilsson asymptotic quantum numbers $Nn_z\Lambda\Omega$.

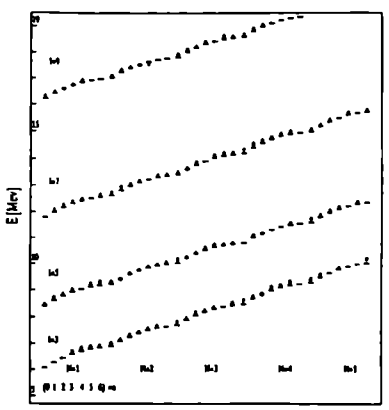

Figure 15. Soliton-energy fit to the ^{28}Si data. For more details, see [34].

On the theoretical side a serious attempt should be made to improve the microscopic descriptions, probably the shell model[20] has to be applied starting from ^{16}O and working up into more complex cases, with larger number of nucleons.

For example, can the "cut-off" in the excitation function of ^{32}S at ~32 MeV be explained as running out of valence-particle spin? The sd-space configuration $d^2_{3/2}d^3_{5/2}s_{1/2}$ has a maximum spin of 14 $\hbar$, whereas $d^2_{3/2}d^4_{5/2}$ has 12 $\hbar$. This set has a big drawback, though, since the sd space has no negative-parity states, and an inclusion of the $f_{7/2}$ orbital implies a shift of negative-parity states to higher energies, i.e. parity splitting, which is contrary to the experimental findings!

As a future outlook one can conclude, that the forthcoming theory/theories must be able to explain at least the following experimentally observed features:
- there are a large number of states with the same ℓ-value which seem to be grouped in energy regions of some few MeV,
- the moment of inertia of $J = 4.85\hbar^2\text{MeV}^{-1}$ is that of a slightly extended object, and this value corresponds to a center-of-mass separation of 5.5-6.0 fm for an α+^{28}Si system, but the object cannot probably be described by a quadrupole deformation,
- the observed states have narrow widths, ranging from some 20-50 keV at $\ell \sim 4\hbar$ and increasing to about 100 keV at the highest spins. This implies that the lifetimes of the observed states are ~100 times larger than what is anticipated from transit-time arguments, or calculations of resonance widths. So this quasiboundedness has to be explained by some attractive interaction,
- there is a marked isotope effect in the measured cross sections which may or may not be related to the N=20 shell-model closure,
- there seems to be a cross section cut-off at $E^* \sim 35$ MeV, i.e. at an angular momentum of about $12\hbar$, "the effect disappears".
- the excitation functions of odd and even systems seem to be fairly indentical, at least as judged from state density, and
- the summed alpha-particle widths of angular-momentum groups seems to nearly exhaust the Wigner limit, i.e. $\Sigma\Gamma_\alpha \sim 60 - 100\%$ of Γ_W. This means that the effect *may have* the microscopic behaviour of alpha particles retaining the identity/structure for "50-100 revolutions" of the system, i.e. they are quasi-bound.

Acknowledgements

The present lecture is an account of a collaborative work with several persons and institutions: M. Brenner, K.-M. Källman and P. Manngård (Åbo Akademi), A. Ludu and A. Săndulescu (Bucureşti), W. Greiner (Frankfurt-am-Main), V.Z. Goldberg, A.E. Pakhomov and V.V. Pankratov (Moscow) and A.E. Antropov (St. Petersburg). For support in the experiments performed in Oslo I am indebted to M. Guttormsen, G. Løvhøiden, E. Olsen and J. Rekstad, and correspondingly in Uppsala to J. Nyberg and G. Possnert.

References

1. U. Abbondanno, K. Bethge, N. Cindro and W. Greiner, *Phys. Lett.* **B249** (1990) 396.
2. F. Ajzenberg-Selove, *Ncul. Phys.* **A475** (1990) 1.
3. A.E. Antropov, M. Brenner, K-M. Källman, T. Lönnroth and P.Manngård, *Z. Physik* **A347** (1994) 291.
4. K.P. Artemov, O. Belanin, A.L. Vetoshkin, R. Wolski, M.S. Golovkov, V.Z. Goldberg, M. Maddeja, V.V. Pankratov, I.N. Serikov, V.A. Timofeev, V.N. Shadrin, Y. Szmider and A.E. Pakhomov, *Sov J. Nucl. Phys.* **52** (1990) 634.
5. K.P. Artemov, M. Brenner, M.S. Golovkov, V.Z. Goldberg, K-M. Källman, T. Lönnroth, P.Manngård, V.V. Pankratov and V.P. Rudakov, *Sov J. Nucl. Phys.* **55** (1992) 492.
6. F. Auger, B. Berthier, P. Charles, B. Fernandez, J. Gasebois and E. Plagnol, *Compt. Rend. Activité Dept. Phys. Nucl. 1974-95, Report CEA-N-1861, Saclay* (1975) 38.
7. T. Berggren, private communication (Lund university).
8. Å. Bredbacka, M. Brenner, K-M. Källman, P. Mannård, Z. Máté, S. Szilágyi and L. Solnai, *Nucl. Phys.* **A574** (1994) 397.
9. M. Brenner, *Z. Physik* **A349** (1994) 233.
10. D. Brink, in *Proc. Int. School Physics* "Enrico Fermi", course 36 1965, ed. C.Bloch (Academic Press, New york, London, 1966), p.247
11. A. Budzanowski, L. Jarczyk, B. Kamys and A. Kapuścik, *Nucl. Phys.* **A265** (1976) 461.
12. H-S. Cheng, H. Shen, F. Yang and J-Y. Tang, *Nulc. Instr. Meth.* **B85** (1994) 47.
13. N. Cindro and W. Greiner, *J. Phys. G: Nucl. Phys.* **9** (1983) L175.
14. J.L.Dunham, *Phys. Rev.* **41** (1932) 713, 721.
15. P.M.Endt, *Nucl. Phys.* **A521** (1990) 1.
16. D. Frekers, R. Santo and K. Langanke, *Z. Physik* **Z394** (1983) 189.
17. H. Furutani, H. Kanada, T. Kaneko, S. Nagata, H. Nishioka, S. Okabe, S. Saito, T. Sakuda and M. Seya, *Prog. Theor. Phys. Suppl.* **68** (1980), ch. 3
18. W. Greiner, J.Y. Park and W. Scheid, Nuclear Molecules (World Scientific, Singapore, 1995).
19. J.J. Griffin and J.A. Wheeler, *Phys. Rev.* **108** (1957) 311.
20. M. Grigureşcu, B.A. Brown and O. Dumitreşcu, *Phys. Rev.* **C** (1995) in press.
21. J. Heikell, in *The Accelerator of Åbo Akademi Annual Report 1975*, ed. M. Brenner (Åbo Akademi, 1976), p. 4.
22. D.L. Hill and J.A. Wheeler, *Phys. Rev.* **89** (1953) 1102.
23. P.E.Hodgson, in *Clustering Phenomena in Atoms and Nuclei*, eds. M. Brenner, T. Lönnroth and F.B. Malik (Springer Series in Nuclear and Particle Physics, Springer-Verlag, Berlin Heidelberg, 1992), p. 350.
24. H. Horiuchi and K. Ikeda, in *Cluster Models and Other Topics*, International Review of Nuclear Physics **4** (World Scientific, Singapore, 1986), p. 2.

25. F. Iachello, *Phys. Rev.* **C23** (1981) 2778.
26. K. Ikeda, N. Takigawa and H. Horiuchi, *J. Phys. Soc. Jap. Suppl. Extra number* (1969) 464.
27. D.F. Jackson, *Nuclear Reactions* (Science Paperbacks, Chapman and Hall, London, 1970), p. 109.
28. K-M. Källman, V.Z. Goldberg, T. Lönnroth, P. Manngård, A.E. Pakhomov and V.V. Pankratov, *Nucl. Instr. Meth. Phys. Res.* **A338** (1994) 413.
29. K-M. Källman, to be published.
30. K. Kato and Y .Abe *Prog. Theor. Phys.* **80** (1988) 119.
31. K. Langanke, R. Stademann and D. Frekers, *Phys. Rev.* **C29** (1984) 40.
32. C.M. Laymon, K.D. Brown and D.P.Balamuth, *Phys. Rev.* **C45** (1992) 576.
33. G. Leander and S.E. Larsson, *Nucl. Phys.* **A239** (1975) 93.
34. A. Ludu, A. Săndulescu, W. Greiner, K-M. Källman, M. Brenner, T. Lönnroth and P. Manngård, *J. Phys. G: Nucl. Part. Phys.* **21** (1995) L41.
35. A. Ludu, A. Săndulescu and W. Greiner, *these proceedings.*
36. P.Manngård, M. Brenner, M.M. Alm. I. Reichstein and F.B. Malik, *Nucl. Phys.* **A504** (1989) 130.
37. P.Manngård, M. Brenner, K-M. Källman, T. Lönnroth, M. Nygård, V.Z. Goldberg, M.S. Golovkov, V.V. Pankratov and V.P. Rudakov, in *Clustering Phenomena in Atoms and Nuclei*, eds. M. Brenner, T. Lönnroth and F.B. Malik (Springer Series in Nuclear and Particle Physics, Springer-Verlag, Berlin Heidelberg, 1992), p. 377.
38. P. Manngård, *Z. Physik* **A349** (1994) 335.
39. A.C. Merchant, K.F.Pál and P.E.Hodgson, *J. Phys G: Nucl. Part. Phys.* **15** (1989) 601.
40. F. Michel, J. Albinski, P. Belery, Th. Delbar, Gh. Grégoire, B. Tasiaux and G. Reidemeister, *Phys. Rev.* **C28** (1983) 1904.
41. F. Michel and G. Reidemeister, *Phys. Rev.* **C29** (1984) 1928.
42. G.L. Morgan, D.R. Tilley, G.E. Mitchell, R.A. Hilko and N.R. Robertson, *Nucl. Phys.* **A148** (1970) 480.
43. S. Saito, *Prog. Theor. Phys.* **40** (1968) 893; **41** (1969) 705.
44. J.A. Wheeler *Phys. Rev.* **51** (1937) 1083, 1107.
45. W. Wühr, A. Hoffmann and G.Philipp, *Z. Physik* **A269** (1974) 365.
46. T. Yamaya, M. Saitoh, M. Fujiwara, T. Itahashi, K. Katori, T. Suehiro, S. Kato, S. Hatori and S. Ohkubo, *Nucl. Phys.* **A573** (1994) 154.
47. S. Åberg and L-O. Jönsson, *Z. Physik* **A349** (1994) 205.

4. NUCLEAR DYNAMICS: NONLINEAR EFFECTS AND FINITE TEMPERATURE

NUCLEAR DYNAMICS AND NONLINEAR SCHROEDINGER EQUATION

K.A. GRIDNEV
Institute of Physics, St. Petersburg State University
Sanct Petersburg, 198904, Russia

ABSTRACT

Analogies to hydrodynamics led to the derivation of a nonlinear Schroedinger equation for the elastic scattering of heavy ions. The problem of dynamical instability and clustering in a breakup of excited nuclear systems are considered from the points of view of the soliton concept.

1. Nonlinear approach for nuclei

The aim of the present lecture is to apply Nonlinear Schroedinger Equation (NoSE) and Korteveg de Vries Equation (KdVE) to an interpretation of some effects in nuclei. Earlier we applied the NoSE for the explanation such phenomena as the ALAS (Anomalous Large Angular Scattering) in interactions of α-particles with light nuclei[1]. Also we used the NoSE for the description of α-particle spectra in ^{20}Ne [2].

The general philosophy giving birth to the NoSE is a rather simple one. Previous studies into the anomalous large angle scattering (ALAS) of α-particles by light and intermediate (α-cluster) nuclei that the rise in $d\sigma/d\Omega$ (elastic) for backward angles – together with the measured resonances, E_x, and decay widths, Γ_x, of the dinuclear (α-cluster) system – may be described by (the same parameter of) a crude effective surface potential (ESP) arrived at by supplementing the optical model interaction, V_{OM}, by a repulsive (hard or soft) core, V_r:

$$V_{ESP} = V_{OM} + V_r$$

V_{OM} facilitates the correct evaluation of $d\sigma/d\Omega$ for forward angles while V_r gives the additional potential contribution allowing for an appropriate description of the measured E_x, Γ_x and of the backward rise in $d\sigma/d\Omega$ as observed for $\theta_{cm} > 90°$.

Similar quasi–molecular features as in these α-scattering experiments have also been measured in elastic collisions between heavy ions. Knowing that semi–classical and in particular hydrodynamical approaches work nicely when applied to heavy ion physics, it appears very suggestive to try to model the elastic scattering of two heavy ions in terms of colliding liquid drops with diffuse surfaces.

Assuming that the "membranes"/surfaces of the two drops remain impenetrable, one thus obtain automatically a compression of the densities in the surface regions of the two touching drops. The physically motivated boundary condition is then

that this compession — giving rise to a repulsive spring–force proportional to V_r — vanishes for separations

$$r > r_0 = R_1 + R_2 + (a_1 + a_2)/2$$

between the two ions/drops, i.e. $V_r \stackrel{r \geq r_0}{\rightarrow} 0$. R_i and a_i denote radius and diffuseness of the i-th ion; $i = 1, 2$. Thus the dynamical interaction between the two nuclei is for $r > r_0$ characterized by their unperturbed/uncompressed asymptotic densities $\rho_{0i}(R_i, a_i)$ — corresponding to the measured (charge) densities — and for $r < r_0$ by the perturbed/compressed densities $\rho_i(r; R_i, a_i)$.

The central equation emerging from such considerations together with the use of the Euler equation and some algebra in liaison with the neglect of higher order derivatives is the nonlinear Schroedinger equation (NoSE)[1]

$$-\frac{\hbar^2}{2m}\nabla^2\Psi + \nabla\Psi - C(1 - \frac{\rho}{\rho_0})\Psi = E\Psi, \qquad \rho = \mid \Psi \mid^2, \qquad \rho_0 = \rho_{01} + \rho_{02} \quad (1)$$

where we use the conventional notation with $C = K/9$ for the nuclear compressibility, ρ and ρ_0 denote the perturbated and unperturbated densities respectively. (Usually K is taken to apply to the bulk of nuclear matter while we consider only compressions in the surface regions.)

It turned out that Eq. (1) is a particular solution of a general equation suggested by Bialynsky-Birula and Mysielsky[3]. Using instead of cubic term $\epsilon \log(a \mid \psi \mid^2)\psi$ they formulated the nonlinear quantum mechanics without any contradiction in classical quantum mechanics. By the way, Gaehler, Klein and Zeilinger[4] attempted to find the constant ϵ according to the predictions made in the work[3]. But it was made without any success. Our approach supposes the constant $C = K/9$ or ϵ (here both constants are the same) to be the compressibility constant. It was confirmed from the values of the constant K, obtained from different experiments with the help of this approach ($K \approx 270MeV$) and also by the recent work of J.Braecher[5]. J.Braecher considered the nonlinear term in the NoSE from the point of view of the information theory. According to the work of Shannon and Weaver [6] the information I acquired upon measurements of the state $\mid \psi >$ is proportional to the logarithm of the probability $I = -\log_2(a \mid \kappa \mid^2)$ bits, where $a = \mid \psi_0 \mid^{-2}$.

The certain amount ϵ of energy per bit is expended, transferred, stored, associated with the information encoded. That's why it is necessary to add the term ϵI to the standard Hamiltonian:

$$H = H_0 + \epsilon I = \sum_{j=1}^{N} \frac{1}{2m}\nabla_j^2 + U - \epsilon \log_2(a \mid \psi \mid^2) \quad (2)$$

Now it is possible to show that this constant ϵ is very close to our compressibility constant. The total energy as the expectation value of the Hamiltonian (2) is:

$$E = < \psi \mid H > = < \psi \mid H_0 \mid \psi > + \epsilon < \psi \mid H_0 \mid \psi > =$$

$$= E_0\epsilon < \psi \mid \log_2(a \mid \psi \mid^2) \mid \psi > \tag{3}$$

Defining the entropy for the subsystem:

$$S = K < \psi \mid \ln(a \mid \psi \mid^2) \mid \psi > \tag{4}$$

Where K - the Boltzmann constant. Now we obtain the free energy E_0, the temperature T and constant ϵ :

$$E_0 = E - TS, \quad T = \left(\frac{\partial E}{\partial S}\right)_V, \quad \epsilon = KT\ln(2) \tag{5}$$

The value ϵ is very close to the constant C. If we suppose the value KT for the average kinetic energy of nucleons $\approx 30MeV$ we obtain the reasonable value of compressibility constant.

Besides NoSE there is another interesting equation, which was applied many times for the prediction of new forms of the motion in nuclei[7]. This is the KdV equation. KdV equation, was applied many times in nuclear physics[7,8,9,10,11,12].

In the work[7] the connection was established between the solution of the KdVE and the nuclear potential in Schroedinger equation. At the certain circumstances we can see the evolution of the nuclear potential with time.

G.N.Fowler, S.Raha and R.M.Weiner[10] attempted to predict the localized stable surface excitations in peripheral heavy ion collisions like in Rossby waves.

In the work[11] A.Sandulesky and W.Greiner obtained a new coexistence model consisting of the usual shell model and a cluster model, describing a soliton moving on the nuclear surface. They got the excellent description of experimental spectroscopic factors for cluster decays.

In its turn we considered the perturbation of the nuclear surface as a quadrupole deformation of the nuclear potential:

$$U = U_0 \operatorname{sech}^2((r-R)/a) = 2aU_0\frac{df(2(r-R)/a)}{dr} \tag{6}$$

The evolution of this perturbation having the soliton form with time is given by the KdV equation[13]:

$$U_t - 6UU_x + \beta U_{\mathrm{xxx}} = 0, \tag{7}$$

where the function U is the potential of Schroedinger equation

$$\beta\psi_{xx} - U\psi = 0, \qquad \beta = \hbar^2/2m \tag{8}$$

On the other hand this perturbation in the form of soliton can decay on the certain quantity of solitons with the small amplitude[14,15]. If we fix the KdVE in the form

$$U_t + UU_x + \beta U_{\mathrm{xxx}} = 0, \tag{9}$$

its solution will be in the form:

$$U(x) = U_0 \operatorname{sch}^2(U_0/12\beta)^{1/2}X) \tag{10}$$

Now we apply the similarity principle. The initial condition we take in the form:

$$U(x,0) = U_0\phi(x,l). \tag{11}$$

With new variables

$$\eta = U/U_0, \quad x = X/l, \quad \tau = U_0 t/l, \tag{12}$$

we obtain the new KdVE:

$$\eta_t + \eta\eta_x + \sigma^{-2}\eta_{xxx} = 0, \tag{13}$$

where $\sigma = l(U_0/\beta)^{1/2}$.

In the work[14] the critical value $\sigma = \sqrt{12}$ was obtained. With increasing number σ the corresponding perturbation breaks up into a larger number of solitons. The number of this solitons was determined by Karpman[15]

$$N = 2a\sqrt{\frac{U_0}{6\beta}}. \tag{14}$$

For the scattering of α-particles with kinetic energies in the range 4 and 12 MeV we can get for the nucleus ^{12}C the value $N{\sim}5$. It corresponds to the number of existing states generated by the surface potential well: $K^+ = 0, 2, 4, 6, 8$. Gardner et al.[16] showed, that the amplitude of solitons determined by eigenvalues: $A = 2E_n$.

The potential having the soliton shape gives the following spectrum[17]:

$$E_n = -\frac{\hbar^2}{8m\Delta}\left(-(1-2n) + (1 + 8m\Delta U_0\hbar^{-2})^{1/2}\right). \tag{15}$$

For our example ($n = 0, 2, 4, 6, 8$) we can get the following values (MeV): -15.57, -8.65, -1.75, 5.19, 12.11 respectively. The smaller eigen value the lager soliton amplitude. Knowing the eigen values one can construct the total potential [18].

This expression (6) provides the key to the understanding of the behaviour of the deformation length for different targets and for different projectiles. In a recent paper by Koster et. al.[19] the empirical formula

$$(\beta_2 r_0)_{nucleons} = \frac{Z}{A_T}(\beta_2 r_0)_{protons} + \frac{N}{A_T}(\beta_2 r_0)_{neutrons} \tag{16}$$

is given to explain the different values of the deformation length for even isotopes of Pd[20].

In terms of the soliton approach the compatibility condition for solitons in different media can be written[21]

$$A\delta = A'\delta' = const \tag{17}$$

where A and A' correspond to the formula (17) and

$$\delta = \frac{\hbar^2}{2\mu} \qquad \delta' = \frac{\hbar^2}{2\mu'}$$

and

$$\mu = \frac{A_{p,n} \cdot A_T}{A_{p,n} + A_T} \qquad \mu' = \frac{A_{p,n} \cdot A'_T}{A_{p,n} + A'_T}$$

The product $A\delta$ should be the same for different isotopes of the target nucleus. The resulting prediction is that the deformation length in the case of inelastic scattering of α-particles on different Pd isotopes is should be largest for the heavest one for the 2^+ state.

Thus we interpreted two equations NoSE and KdVE respectively to the problem of clustering. This work is only the first approximation to this problem because we used only one dimension. To our mind the nextstep should be the application of Kadomtsev-Petviashvily equation to this problem.

The most promising thing is the application of the Similarity principle to the linear alpha-chain states in nuclei[22].

2. Solitons as the clusters

What are clusters? Clusters are spatially correlated nucleons. What kind of forces are between clusters and clusters and nuclei? Japanes theoreticians showed[23], that there are four typical "di-molecules" in nature (moleculas consisting from atoms, nuclei, nuclei plus hyperon, nucleons) with the same kind of potential. We consider the typical potential interaction between ^4He atoms.

In the approximation one can consider He atoms as hard spheres with the radius $2.7A$. Minimum says that atoms have a tendency to develop into crystall. But the warm energy does not permit it.

In the different energy scales the situations is very similar.

The origination of the attractive part of the potential is due to the exchange of nucleons in the case of nuclear potential[24] .

We shall consider the repulsive core. The best understanding can be obtained in the micro and macro approaches. The existence of a repulsive core in the potential interaction of two complex nuclei follows from Pauli principle which forbidds their mutual interpenetration. Let us give one example - the interaction of two alpha-particles. In this interaction the repulsive core is manifested as a result of which quasimolecular state the nucleus formes. The $\alpha + \alpha$ phase shifts were obtained from the different experiments. The phase shift δ_2 begins to increase rapidly from an energy about 1 MeV and δ_4 from an energy about 6 MeV. This indicates an extension with a fairly abrupt boundary in the exterrior region with $r \leq 4fm$ (the impact parameter $b = \lambda l$ is approximately 4 fm at $E_{cm} = 1$ MeV and 3 fm at $E_{cm} = 6$ MeV). This character of the scattering can be well described by a phenomenological potential with the repulsive core.

In terms of the NoSE we can estimate the value of a hard core. For this purpose it is necessary to rewrite the NoSE.

$$-\frac{\hbar^2}{2m}\frac{d^2}{dx^2}U + (E - V)U + \beta U^3 = 0. \tag{18}$$

After the factorization at the wave funtion U

$$U = \psi_0 f,$$
$$f = 0, \ at \ x = 0,$$
$$f = 1, \ at \ x \to \infty$$

we obtain the NoSE

$$\frac{\hbar^2}{2m}\frac{d^2}{dx^2}\psi + \alpha\psi + \beta\psi^3 = 0. \tag{19}$$

Then using such approaches $\alpha \to \infty, U = \psi_0, \psi_0^2 = -\alpha/\beta$ we have

$$\frac{\hbar^2}{2m\alpha}\frac{d^2}{dx^2}\psi + \frac{\beta}{\alpha}\psi^3 = 0. \tag{20}$$

In the compact form this equation can be transformed into another equation

$$-\xi^2\frac{d^2}{dx^2}f - f + f^3 = 0. \tag{21}$$

Multiplaying this equatin on the derivative df/dx we can obtaind a solution

$$f = th[x/\sqrt{2}\xi]. \tag{22}$$

The solution is very similar on the correlation function of Boze gas with hard spheres:

$$f = 0, \ for \ r < \delta,$$
$$f = th[r/\delta - 1].$$

Where δ – is the radius of a hard sphere. In terms of this approach the radius of the hard core is:

$$R_0 = \sqrt{2}\xi = \sqrt{2}\frac{\hbar^2}{\sqrt{2m(E-V)}}\frac{\hbar^2}{\sqrt{m(E-V)}}. \tag{23}$$

The microscopic estimates of the value of the hard core were made in the work of V.N.Bragin and R.Donangelo[25] and in the work of A.Tohsaki-Suzuki and K.Naito[26] . The last athors used RGM. In this case it is very evident to expect the appearance of the hard core. In the first work the athors used the Brukner theory according to whitch the total energy of a system of interacting fermions can be written as a functional of the local single-particle energy density. They have computed the heavy ion potential in the sudden approximation as

$$V(r) = \int[\xi(\rho_1 + \rho_2) - \xi(\rho_1) - \xi(\rho_2)]d\tau. \tag{24}$$

The potential which was obtained in this approuch is highly repulsive in the nuclear interior quite an opposite behavior to that of the folding model calculations. Summing up, it is necessary to say, that the momentum and energy dependent hard or soft core appears in the microseoptic calculations of two interacting nuclei due to Pauli prinsiple. On this base this core can be taken in account also in the macroscopic approaches.

Keeping in mind the structure of the potential for nucleous–nucleous collision (the repulsive and attractive parts) we applied the inverse field method, which will be described in the next section. Within the inverse mean field method solitons are taken to model of elastic $\alpha + \alpha$ collisions in a TDHF–like fasion. Attention is drawn to common points of this approach with TDHF. The analytical formula for the phase-shift within this approach yields a nice correspondence to experiment[27].

3. Nuclear instability and soliton theory

An existence of solitary waves is determined by two essential factors, namely, nonlinearity and dispersion. Both the factors, which are responsible for the stability of a wave, are connected in their turn with two different types of instability. A localized pulse will tend to spread out due to dispersion terms of the equations of motion. The nonlinearity which is responsible for the formation of solitary waves, on the other hand, automatically leads to their destruction, if it is alone. Both instabitities may compensate each other and lead to stable solutions (solitons).

Let us look from these points of view at multifragmentation phenomena. The formation and breakup of a highly excited and compressed nuclear system is the most striking process observed in intermediate-energy heavy ion reactions. How does such a system expand and finally disassemble when passing through a regime of dynamical instabilities? What is the mechanism of the clustering (stable light and intermediate mass fragment production)? Quite a variety of models have been developed to discuss this question (see, for instance, the recent review[29] and Proceedings[30]). The dynamical clusterization in the presence of instabilities is the focus of attention of the intermediate energy heavy ions physics[31,32]. Ten years ago multifragmentation has been associated with the onset of the spinodal instability[33]. This instability is associated with the transit of a homogeneous fluid across a domain of negative pressure, which leads to its breaking up into droplets of denser liquid embedded in a lower density vapor. Since the spinodal instability can occur in an infinite system, it can be called the bulk or volume instability. On the other hand, it physically means that pressure depends on density, that is just a nonlinearity in terms of density [34].

Recently[35], it has been pointed out that a new kind of instability (sheet instability) may play an important role in multifragmentation. This new instability can be assigned to the class of surface instabilities of the Rayleigh-Taylor kind[36]. System escapes from the high surface energy of the intermediate complex by breaking up into a number of spherical fragments with less overall surface. At the same time, it physically means the existence of the gradient terms of the equations of motion, i.e the dispersion[34].

The spinodal instability and the Rayleigh-Taylor instability may compensate each other and lead to stable quasi-soliton type objects. In the next Sec. we present this physical picture using a simple analytical model proposed to describe the time evolution of compressed nuclear systems.

An analysis of stability of nonlinear dynamical systems and an analysis of nonlinear evolution of initial complex states is a traditional goal of Soliton Theory. The inverse methods to integrate nonlinear evolution equations are often more effective than a direct numerical integration. Let us demonstrate this statement for a very simple case[39].

The type of systems under our consideration are uncharged slabs of nuclear matter. The slabs are finite in the z coordinate and infinite and homogeneous in two transverse directions.

The basic equations for the static mean-field description of the slabs are the following

$$\psi_{\mathbf{k}_\perp n}(\mathbf{x}) = \frac{1}{\sqrt{\Omega}}\psi_n(z)\exp(i\mathbf{k}_\perp\mathbf{r}), \qquad \epsilon_{\mathbf{k}_\perp n} = \frac{\hbar^2 k_\perp^2}{2m} + e_n,$$

$$-\frac{\hbar^2}{2m}\frac{d^2}{dz^2}\psi_n(z) + U(z)\psi_n(z) = e_n\psi_n(z),$$

$$\rho(\mathbf{x}) \Longrightarrow \rho(z) = \sum_{n=1}^{N_0} a_n\psi_n^2(z), \tag{25}$$

$$A \Longrightarrow \mathcal{A} = (6A\rho_N^2/\pi)^{1/3} = \sum_{n=1}^{N_0} a_n, \qquad a_n = \frac{2m}{\pi\hbar^2}(e_F - e_n),$$

$$\frac{E}{A} \Longrightarrow \frac{\hbar^2}{2m\mathcal{A}}\Big(\sum_{n=1}^{N_0} a_n\int_{-\infty}^{\infty}\big(\frac{d\psi_n}{dz}\big)^2 dz + \frac{\pi}{2}\sum_{n=1}^{N_0} a_n^2\Big) + \frac{1}{\mathcal{A}}\int_{-\infty}^{\infty}\mathcal{E}[\rho(z)]dz,$$

where $\mathbf{r} \equiv (x, y), \mathbf{k}_\perp \equiv (k_x, k_y)$, and Ω is the transverse normalization area. N_0 is the number of occupied bound orbitals.

The dynamical description will be done in the framework of the inverse mean field method. One can found the details of this approach in[40],[41]. We concentrate here only on essentials.

The evolution of a system is given by the famous hydrodynamical Korteweg-de Vries equation (KdV) for the mean-field potential $U(z,t)$

$$\sum_{n=1}^{N}\frac{\partial U}{\partial(S_n t)} = 6U\frac{\partial U}{\partial z} - \frac{\hbar^2}{2m}\frac{\partial^3 U}{\partial z^3}, \tag{26}$$

where S_n are constants which are determined by the initial conditions.

General solution of KdV Eq. (26) can be derived in principle via direct methods numerically. This way is to assign a functional of interaction $\mathcal{E}$ (as usual an effective density dependent Skyrme force), a total number of particles (or a thickness of a slab

$\mathcal{A}$) and to solve Hartree-Fock equations to derive a spectrum of the single particle states e_n and wave functions $\psi_n(z,0)$, the density profile $\rho(z,0)$ and the one-body potential $U(z,0)$ for the initial compressed nucleus. Then, one calculate an evolution of the one-body potential with the help of Eq. (26).

However, there is an inverse method to solve KdV Eq. (26). The main advantage of this way is to reduce the solution of the nonlinear KdV Eq. (26) to the solution of the linear Schroedinger - type equation

$$-\frac{\hbar^2}{2m}\frac{d^2}{dz^2}\psi_n(z,t) + U(z,t)\psi_n(z,t) = e_n\psi_n(z,t), \tag{27}$$

and linear integral Gelfand - Levitan - Marchenko equation to derive the function $K(x,y)$

$$K(x,y) + B(x+y) + \int_x^\infty B(y+z)K(x,z)dz = 0. \tag{28}$$

The kernel B is determined by the reflection coefficients $R(k)(e_k = \hbar^2k^2/2m)$. and by the N bound state eigenvalues $e_n = -\hbar^2\kappa_n^2/2m$. N is the total number of the bound orbitals.

$$B(z) = \sum_{n=1}^{N} C_n^2(\kappa_n) + \frac{1}{\pi}\int_{-\infty}^{\infty} R(k)exp(ikz)dk.$$

The coefficients C_n are uniquely specified by the boundary conditions

$$C_n(\kappa_n) = \lim_{z\to\infty} \psi_n(z)\exp(\kappa_n z),$$

and the wanted single particle potential is given by

$$U(z,t) = -\frac{\hbar^2}{m}\frac{\partial}{\partial z}K(z,z).$$

The time t is included in Eqs. (27,28) only as a parameter, so it has been omitted in the above formulas.

The general solution, $U(z,t)$, should naturally contain both, contributions due to the continuum of the spectrum and to its discrete part. There is no way to obtain the general solution $U(z,t)$ in a closed form. Eqs. (27,28) have to be solved only numerically.

However in the case of reflectless ($R(k) = 0$) symmetrical ($U(-z,0) = U(z,0)$) potentials one can derive the following basic relations

$$U(z,t) = -\frac{\hbar^2}{m}\frac{\partial^2}{\partial z^2}\ln(\det\|M\|) = -\frac{2\hbar^2}{m}\sum_{n=1}^{N}\kappa_n\psi_n^2(z,t),$$

$$\psi_n(z,t) = \sum_{n=1}^{N}(M^{-1})_{nl}\lambda_l(z,t),$$

$$\lambda_n(z,t) = C_n(\kappa_n)\exp(-\kappa_n z + 2\hbar^2\kappa_n^3 S_n t/m)), \tag{29}$$

$$M_{nl}(z,t) = \delta_{nl} + \frac{\lambda_n(z,t)\lambda_l(z,t)}{\kappa_n + \kappa_l},$$

$$C_n(\kappa_n) = \Big(2\kappa_n \prod_{l\neq n}^{N} \frac{\kappa_n + \kappa_l}{\kappa_n - \kappa_l}\Big)^{1/2}.$$

So, the wave functions, potential and the density profile are completely defined by the bound state eigenvalues. The first step is to solve the Schroedinger Eq. (27) for the initial potential $U(z,0)$, which is suitable to simulate compressed nuclear system or to simulate this state with the help of spectrum. Then one calculates the evolution of $\rho(z,t)$ and $U(z,t)$ with the help of Eqs. (29).

Although there is definitely some progress in the application of the inverse methods to nuclear physics they are not yet too popular. As illustration of these methods, we consider a one-dimensional three-level system in details[42].

A three-level system may be useful for modelling the evolution of light nuclei, for instance, of oxygen[43].

Let us present the main formulas to calculate wave functions of a three-level system $\kappa_3 > \kappa_2 > \kappa_1$

$$\psi_1(z,t) = \Big(2\kappa_1\big(\frac{\kappa_2+\kappa_1}{\kappa_2-\kappa_1}\big)\big(\frac{\kappa_3+\kappa_1}{\kappa_3-\kappa_1}\big)\Big)^{1/2} D^{-1}(z,t)\big(ch(\xi_2+\xi_3) - \big(\frac{\kappa_3+\kappa_2}{\kappa_3-\kappa_2}\big)ch(\xi_3-\xi_2)\big),$$

$$\psi_2(z,t) = \Big(2\kappa_2\big(\frac{\kappa_2+\kappa_1}{\kappa_2-\kappa_1}\big)\big(\frac{\kappa_3+\kappa_2}{\kappa_3-\kappa_2}\big)\Big)^{1/2} D^{-1}(z,t)\big(sh(\xi_3+\xi_1) - \big(\frac{\kappa_3+\kappa_1}{\kappa_3-\kappa_1}\big)ch(\xi_3-\xi_1)\big),$$

$$\psi_3(z,t) = \Big(2\kappa_3\big(\frac{\kappa_3+\kappa_2}{\kappa_3-\kappa_2}\big)\big(\frac{\kappa_3+\kappa_1}{\kappa_3-\kappa_1}\big)\Big)^{1/2} D^{-1}(z,t)\big(ch(\xi_1+\xi_2) - \big(\frac{\kappa_2+\kappa_1}{\kappa_2-\kappa_1}\big)ch(\xi_2-\xi_1)\big),$$

$$\begin{aligned} D(z,t) &= ch(\xi_1+\xi_2+\xi_3) + \big(\frac{\kappa_2+\kappa_1}{\kappa_2-\kappa_1}\big)\big(\frac{\kappa_3+\kappa_1}{\kappa_3-\kappa_1}\big)ch(\xi_3+\xi_2-\xi_1) \\ &+ \big(\frac{\kappa_2+\kappa_1}{\kappa_2-\kappa_1}\big)\big(\frac{\kappa_3+\kappa_2}{\kappa_3-\kappa_2}\big)ch(\xi_3+\xi_1-\xi_2) + \big(\frac{\kappa_3+\kappa_1}{\kappa_3-\kappa_1}\big)\big(\frac{\kappa_3+\kappa_2}{\kappa_3-\kappa_2}\big)ch(\xi_2+\xi_1-\xi_3), \end{aligned}$$

$$\xi_n(z,t) \equiv \kappa_n z - 2\hbar^2\kappa_n^3 S_n t/m \qquad n = 1,2,3. \tag{30}$$

The asymptotic behavior of the wave functions and the mean - field potential have the following form (ξ_n is fixed)

$$\lim_{t\to\infty} \psi_k = \delta_{kn}\sqrt{\kappa_n}\,sech(\xi_n - \xi_n^0),$$

$$\lim_{t\to\infty} U(z,t) = -\frac{\hbar^2\kappa_n^2}{m} sech^2(\xi_n - \xi_n^0),$$

$$\xi_n^0 = \frac{1}{2}\ln\Big(\prod_{k=1}^{n-1}\Big(\frac{\kappa_n - \kappa_k}{\kappa_n + \kappa_k}\Big)^2 \prod_{m\neq n}^{n} \Big|\frac{\kappa_n + \kappa_m}{\kappa_n - \kappa_m}\Big|\Big).$$

So, for large z and t the time - dependent one - body potential and the corresponding density distributions are represented by a set of stable solitary waves. The energy spectrum of an initially compressed system completely determines widths, velocities and the phase shifts of the solitons.

The number of waves is equal to the number of occupied bound orbitals. Thickness ('number' of particles) of an n - wave is equal to a_n.

Reflecting terms ($R(k) \neq 0$) of $U(z,t)$ cause ripples (oscillating waves of a small amplitude) in addition to the solitons in the final state.

The initially compressed system expands so that for large times one can observe separate density solitons and ripples ('emissions'). This picture is in accordance with the TDHF simulation of the time evolution of a compressed O^{16} nucleus[43]. The disassembly shows collective flow and clusterization. It is important to note that the clusterization was not observed in the absence of the self-consistent mean-field potential, i.e this confirmes our supposition that the nonlinearity is very important for the clustering.

It is necessary to note that the present model is too primitive in order to describe a real breakup process. However this model can be used to illustrate an inverse mean-field method scheme, a nonlinear principle of superposition and the idea that nonlinearity and dispersion terms of the evolution equation can lead to clusterization in the final channel.

Certainly there are a lot of open questions relative to the presented approach. The most crucial concerns the generalization to 3+1 dimensional model with a finite temperature. One possible way to do it keeping symplicity of the approach would be to use an information theory[44]. Such investigations are in progress.

The problem of dynamical instability and clusterization (stable fragments formation) in a breakup of excited nuclear systems are considered from the points of view of the soliton concept. It is noted that the volume (spinodal) instability can be associated with nonlinear terms, and the surface (Rayleigh-Taylor type) instability, with the dispersion terms in the evolution equations. The both instabilities above may compensate each other and lead to stable solutions (solitons).

The simple analytical model is presented to describe the time evolution of the cold compressed nuclear systems in the framework of the inverse mean-field method. It is demonstrated that the nonlinearity and dispersion terms of the evolution equations can lead to clusterization in the final channel.

4. Conclusion

The NoSE has been shown to be a very useful tool for the analysis of experimental data involving the elastic interaction of light and heavy ions. Its novel future is that it determines fairly accurately the compressibility modulus of nuclear matter. The problem of dynamical instability and clustering are considered from the points of

view of the soliton conception. Due to the soliton conception it is understandable the behavior of the quadrupole deformation parameters for different isotopes of one nucleus.

5. Acknowledgments

The author is very appreciate Dr. D.Delion who took part in the work, connecting with the NoSE, Dr. E.Hefter who created the inverse mean field scheme for nuclei, Dr. V.Kartavenko who applied nonlinear equations for the study of such process as fragmentation.

6. References

1. Gridnev K.A., Hefter E.F., Mikulas K., Semjonov V.M., Subbotin V.B.,*Aust. J. Phys.* **36**, 155 (1983); *Nuovo Cimento* **93**, 135 (1986)
2. Gridnev K.A., Darwish N., Ivanov A.G., Subbotin V.B., Fadeev S.N., Heffer E.F.: *The notes of Ac.Sci of USSR (physics)* **50**, 1980 (1986)
3. Bialynicki-Birula I., Mycielski J., *Annals of Physics* **100**, 62 (1976)
4. Gaehler R., Klein A.G., Zeilinger A., *Phys. Rev.* **A23** 1611 (1981)
5. Bracher J.D., *Int. Journal of Theor. Physics* **30**, 979 (1991)
6. Shannon C.E., Weaver W., *The Mathematical Theory of Communication* (University of Illinois Press, Urbana, Illinois 1979).
7. Gridnev K.A., Hefter E.F., *Phys. Lett.* **A77**, 490 (1980)
8. Hefter E.F., Mitropolsky I.A., *J. Moscow Phys. Soe*, **99** (1991)
9. Hefter E.F., Gridnev K.A., *Prog. Theor. Phys.* **77**, 549 (1984)
10. Fowler G.N., Raha S., Weiner R.M., *Phys. Rev.* **C31**, 1515 (1985)
11. Sandulesku A., Greiner, *Rep. Prog. Phys.* **55**, 1423 (199 2)
12. Kartavenko V.G., *Sov. J. of Nucl. Phys.* **40**, 337 (1984)
13. Miura R.M., *SIAM Review* **18**, 412 (1976)
14. Berezin Ju.A., Karpman V.I., *Soviet Physics JETP* **24**, 1045 (1967)
15. Karpman V.I., *Phys. Lett.* **A25** 708 (1967)
16. Gardner C.S., Green J.M., Kruskal M.D., Miura R., *Phys. Rev. Lett.* **19**, 1095 (1967)
17. Landau L.D., Lifshiz I.M., *Quantum Mechanics*, 97 (1974)
18. Gridnev K.A., Semtchenkov A.G., *The Theory of the Quantum Systems With the Strong Interaction*, Tver 45 1992
19. J.E. Koster, et. al., *Phys.Rev.* **C49** (1994), 710
20. V.Riech, R.Scherwinski, G.Lindstroem, E.Fretwurst, K.Gridnev, P.P.Zarubin, R.Kolalis, *Nucl.Phys.* **A542** (1992), 61
21. K.A.Gridnev, E.F.Hefter, *Phys.Lett.* **177A** (1980), 490
22. Ikeda R., Takigawa N., Hariuchi H, *Suppl. Prog. Theor. Phys.* **Extra Number**, 464 (1968)
23. K.Ikeda, R.Tamagaki, *in Proc.of the Fifth Int. Conf. on Clustering Aspects*

in Nuclear and Subnuclear Systems (Kyoto, 1988).
24. K.Langanke et al., *Z.Physik* **A291**, 267 (1979).
25. V.N.Bragin, R.Donangello, *Phys.Rev.* **32C**, 2176 (1985).
26. A.Tohsaki-Suzuki, K.Naito, *Prog.Theor.Phys.* **58**, 721(1977).
27. E.F.Hefter, K.A.Gridnev, *Prog.Theor.Phys.* **72**, 549 (1984).
28. V. G. Kartavenko, *Phys. Part. Nucl.* **24**, 619 (1993).
29. L. G. Moretto and G. J. Wozniak, *Ann. Rev. Nucl. Part. Sci.* **43**, 379 (1993).
30. *Proc. Hischegg'94, Int. Workshop on Multifragmentation*, ed. H. Feldmeier and W. Noerenberg, GSI Darmstadt, 1994.
31. J. Knoll and B. Strack, *Phys. Lett.* **112B**, 45 (1984).
32. G. F. Burgio, Ph. Chomaz and J. Randrup, *Phys. Rev. Lett.* **69**, 885 (1992).
33. P. J. Siemens, *Nature*, **305**, 410 (1983).
34. V. G. Kartavenko, *Clusters'93, 2nd Int. Conf.*, Santorini, Greece, 1993, p.63.
35. L. G. Moretto, K. Tso, N. Colonna and G. J. Wozniak, *Phys. Rev. Lett.* **69**, 1184 (1992).
36. Lord Rayleigh, *Scientific Papers*, Article 58, (New York, Dover 1964), p.361.
37. H. Stoecker, J. Hofmann, J. Maruhn and W. Greiner, *Prog. Part. Nucl. Phys.* **4**, 113 (1980).
38. H. Stoecker and W. Greiner, *Phys. Rep.* **137**, 277 (1986).
39. V. G. Kartavenko, *Proc. III Int. Conf. on Nucl.-Nucl. Collis.*, San-Malo, France, June, 1988, p.142.
40. E. F.Hefter, *Journ. de Phys.* **45**, C6:67 (1984).
41. E. F. Hefter and V. G. Kartavenko, *JINR Rapid. Comm.*, 29 **3** (1987).
42. V. G. Kartavenko, W. Greiner and K. A. Gridnev, *JINR preprint E4-94-175, Dubna* (1994)
43. A. Dhar and S. Das Gupta, *Phys. Rev.* **C30**, 1545 (1984).
44. K. A. Gridnev, *Clusters'93, 2nd Int. Conf.*, Santorini, Greece, 1993, p.51.

PRE-EQUILIBRIUM GIANT RESONANCES IN FUSION REACTIONS *

V.BARAN[1,2], M.COLONNA[1,3], M.DI TORO[1], A.GUARNERA[1,3],
T.I.MIKHAILOVA[4],and A.SMERZI[1,5]

[1])*Laboratorio Nazionale del Sud, INFN*
44, Via S.Sofia, 95125 Catania, Italy
and
Dipartimento di Fisica dell' Universitá di Catania,

[2])*IFA Bucharest, Romania*

[3])*GANIL, Caen, France*

[4])*Laboratory of Nuclear Problems, JINR, Dubna, Russia*

[5])*Physics. Dept., University of Illinois, Urbana, USA*

ABSTRACT

In this report we focus on specific features associated with the Giant Dipole (GDR) γ-ray emission from deformed long-living nuclear systems. Solving numerically the Vlasov equation, we follow the fusion path for entrance channels with different mass-asymmetry in low energy heavy ion collisions, just above the fusion threshold. We observe the formation of long-living deformed compound nuclei in the more symmetric cases. We show that very important features, such as the energy and the angular correlation of the emitted γ's are characteristic effects of the emission from such deformed systems. For charge-asymmetric channels we reveal the presence of a new "direct" dipole mode, related to the charge equilibration dynamics. The relative observation in medium energy dissipative collisions can bring some new independent information on the temperature dependence of the GDR spreading width.

* *Presented by M.Di Toro.* This work is supported in part by the Commission of the European Community, under Contract No. ERBCHBI-CT-930619, by the US National Science Foundation under Grant PHY-94-21309, and by the INFN-IFA Bucharest and the INFN-JINR Dubna exchange agreements.

1. Introduction

Nuclear Giant Resonances and, in particular, the Giant Dipole Resonance (GDR), represent universal collective excitation modes involving all the nucleons,

very well established in all nuclei.

Its specific characteristics, such as the dependence of the strength function and of the angular distribution of the emitted gamma rays on the shape of nuclei and the fast coupling to the compound nucleus, make it a very good instrument to learn about the nuclear properties in situations in which other probes, like neutrons, fail to give reliable informations. Thus, it is possible to follow the dependence of some nuclear characteristics on various quantities, like the angular momentum or the excitation energy [1].

Moreover, comparing gamma yields from similar systems, but formed in different dynamical conditions, one can learn about non-statistical processes which can eventually appear. In such situations, together with the complementary information obtained from other emitted particles, we can hope to understand the involved reaction mechanisms. In this way it is possible to observe when a nucleus is trapped in a superdeformed state, as well as some effects due to detailed nuclear structure or to the dissipation in the entrance or decay channel [2].

So the possibility of observing some GDR photon emission from intermediate di-nuclear states in fusion, fusion-fission and deep-inelastic collisions looks extremely stimulating in order to gain a direct insight into the dynamics of the process. The most evident feature of a Giant Dipole γ-emission from a very deformed system will be a clear splitting of the resonance: i.e. for a quadrupole leading shape we expect to see two main peaks in the γ-yield with a separation proportional to the amount of deformation [1]. There are some first experimental evidences of this effect in fusion reactions [3,4]. In ref.[3] such two-bump γ-emission is needed to account for the measured spectrum when the fused system, ^{164}Yb at $E_x \simeq 50MeV$ is formed in the more mass-symmetric entrance channel, where one expects longer times for the fusion dynamics [5]. In ref. [4] coincidences with α-particles are used as a clock for the emission time. When the γ-spectrum is measured, in the $^{nat}Sn + ^{20}Ne$ reaction at $164MeV$ of beam energy, in coincidence with forward emitted α's (short-living source), the two bumps are neatly seen. They disappear in spectra with α-backward coincidences.

Evidences of GDR-photon emission from very deformed systems have been observed also in fission channels, either in fusion-fission reactions [6] or in spontaneous fission decay [7]. A quite complete recent review can be found in [8]. Similar effects in most dissipative deep-inelastic collisions have been recently seen [9].

In this article we will focus on the fusion path, solving numerically the Vlasov equation for the evolution of the one-body distribution function. At low beam energies the times involved in the fusion dynamics are, in some cases, long enough to allow the formation of long-living very deformed compound nuclei, close to di-nuclear systems. The effect seems to be ruled by the entrance channel mass-symmetry and the compound nucleus fissility. This is discussed in Sect.2.

In Sect.3 we evaluate the very characteristic features of a GDR γ-decay from such exotic systems. We show also that in cases of similar fusion paths we can have a GDR pre-equilibrium source during the charge equilibration process for charge asymmetric entrance channels.

This new "dynamical" dipole decay is studied in Sect.4 for incomplete fusion reactions at medium energies. We show how it would be possible to extract some independent information on the excitation energy dependence of the GDR spreading width.

Finally some conclusions and perspectives are presented in section 5.

2. Entrance channel effect in the fusion dynamics.

Our aim is to follow a microscopic description of the fusion dynamics to clearly show the presence of long-living intermediate states and the properties of their giant dipole decay. We have followed a fully mean field picture of the dynamics based on the solution of the Vlasov kinetic equation [10,11]. Since we are considering fusion processes above the Coulomb barrier we are confident that our semi-classical approach retains a good validity. We have solved the Vlasov equation using the test particle method introduced by Ch.Gregoire et al.[12], where the time evolution of gaussian phase space wave packets is considered. Fifty test particles per nucleon are used, which represents a reasonably good phase space mapping in order to have a fermionic dynamics. The mean field is built from simplified Skyrme forces corresponding to a soft equation of state [13]. Surface effects are accounted for through the gaussian widths. However, we cannot take into account effects from ground state deformations.

We have considered the systems studied in ref.[3], i.e. the formation of a compound nucleus ^{164}Yb at $E_x \simeq 55MeV$ in two different entrance channels: the mass-asymmetric $^{16}O + ^{148}Sm$ at $83MeV$ of beam energy, and the mass-symmetric $^{64}Ni + ^{100}Mo$ at $237MeV$ of beam energy.

In order to have roughly the same angular momentum in the compound system we will compare the dynamics of the impact parameter $b = 5fm$ for the $O - Sm$ reaction to the $b = 3fm$ collision for the $Ni - Mo$ case. We have selected a large impact parameter, near to the fusion limit in each case, because at larger angular momentum a slower evolution of the shape is expected. However, the main aspects are not changed when passing to lower impact parameters.

In fig.1 we show the density plots on the reaction plane for the two reactions, at time steps of $100fm/c$ up to $1000fm/c$. The time evolution of the shape of the two systems is clearly different. In the mass symmetric case the system has still an elongated shape at $1000fm/c$. The effect is quite evident from the analysis of the mass quadrupole moment shown in fig.2.

The asymmetric case shows a shape equilibration already at about $400-500fm/c$. We obtain interesting oscillations in the symmetric case. For numerical reasons we cannot follow the evolution up to very large times. However, in a crude approximation, extrapolating the decreasing behaviour of the quadrupole momentum, we can estimate a time of the order of $2000 - 2500fm/c$ for the equilibration of the shape degree of freedom.

It is worth comparing these times with the results obtained by using the nucleon exchange HICOL code, which is based on Swiatecki's model of macroscopic

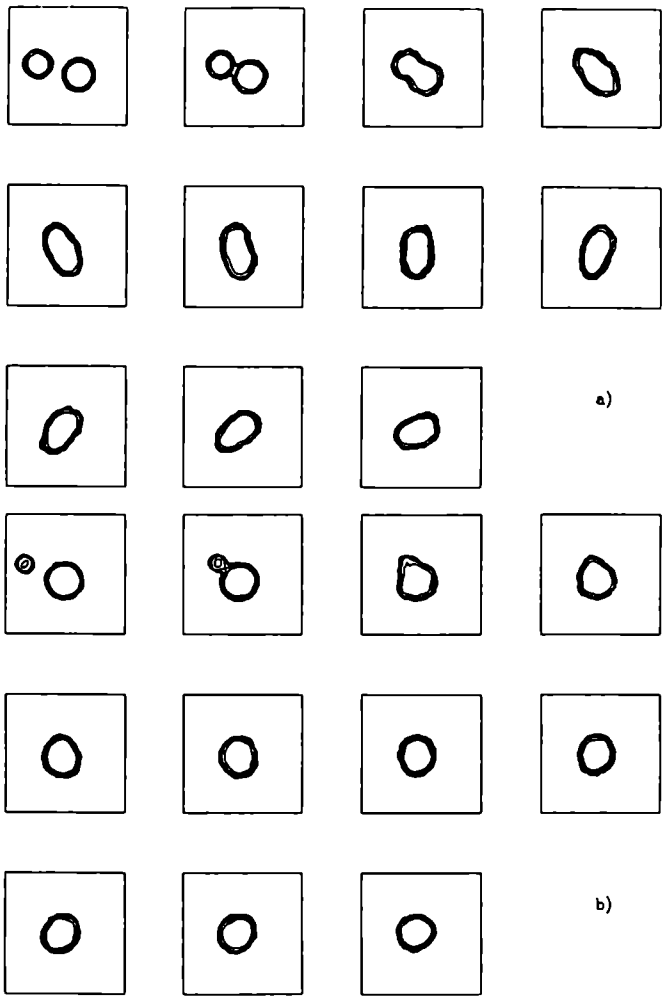

Fig.1: *Time evolution of the density contour plot in the reaction plane for the collision: (a) $Ni - Mo$ at $237MeV$, $b = 3fm$; (b) $O - Sm$ at $83MeV$ of beam energy, $b = 5fm$.*

dissipative dynamics [5]. In this framework, the Ni induced reaction is in the extra push region , while the asymmetric reaction is not. So, a much larger time is expected in the former case, around $3000fm/c$ while in the latter case it is $600fm/c$, both being calculated at smaller angular momentum [3, 17]. For the same reason it is also predicted that in symmetric reactions an important contribution to the reaction cross section will come from deep-inelastic collisions, even at energies near to the Coulomb barrier. Since the largest angular momentum for which fusion occurs is around $30\hbar$, HICOL underestimates the total fusion cross section. Experimentally, the angular momenta corresponding to fusion are found larger than $40\hbar$, while the fusion excitation function is $235mb$, this being obtained summing only the evaporation residue cross section [14] .

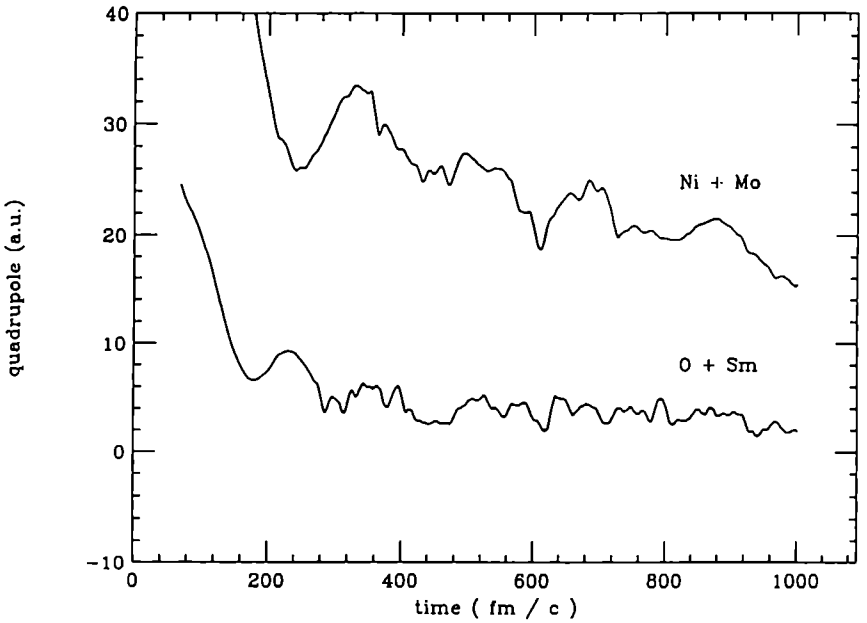

Fig.2 : *Time evolution of the mass quadrupole moment for the collisions: $Ni-Mo$ at $237MeV$, $b=3fm$ and $O-Sm$ at $89MeV$ of beam energy, $b=5fm$.*

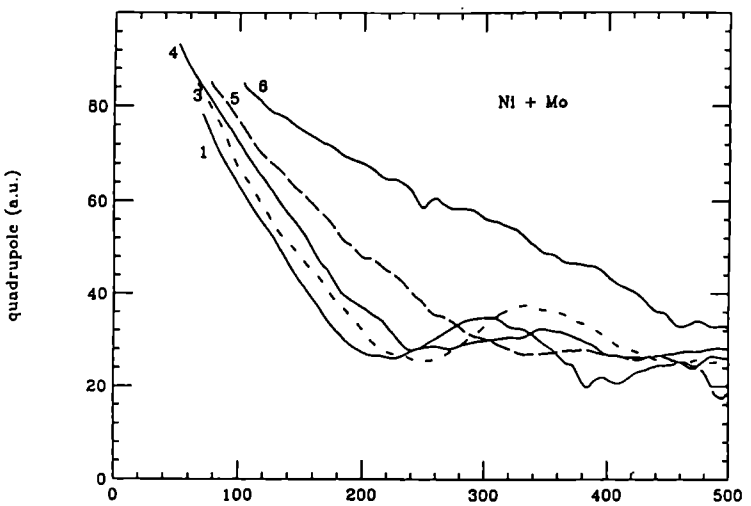

Fig.3 : *Time evolution of the mass quadrupole moment for the collision $Ni-Mo$ at different impact parameters; the numbers on each curve represent the corresponding value of the impact parameter (in fm).*

In our calculations we have an enhancement of the total fusion cross section since we can still see fusion events at larger angular momentum. However, we want to stress that our transport equation evolution follows the most probable path and an overestimation of the fusion cross section is not surprising. Dynamical fluctuations can lead the system to a different outcome than that predicted by the mean trajectory. Therefore we have tried to find a criterium which can indicate

when the reaction mechanism is changing. To do this, we plot the time evolution of the quadrupole momentum in coordinate space for different impact parameters, fig.3.

We notice a clear difference between the curves corresponding to $b = 5fm$ and $b = 6fm$ (the last impact parameter for which we observe a compound system up to $1000fm/c$) and those obtained for $b = 1, 3$, and $4fm$, where we see clear quadrupole oscillations. We can interpret this behaviour assuming that, starting from $b = 4fm$, we have a transition from fusion to deep-inelastic mechanisms, through a fast fission process. We conclude that fusion can exist up to an angular momentum of the order of $80 - 90\hbar$, but we cannot apply the sharp cut-off approximation to calculate the total cross section or to plot the angular momentum distribution. However, these quantities can be estimated by approximating the entrance channel transmission coefficients by a Fermi function with a smooth cut-off [1], [15], [16]:

$$\sigma_{fus} = \Sigma_l \sigma_l = \Sigma_l \pi \bar{\lambda}^2 (2l+1)[1 + exp\frac{(l - l_0)}{\Delta}]^{-1} \qquad (2.1)$$

with $\bar{\lambda}$ the asymptotic wavelength.

We plot in fig.4 the results obtained using eq.(2.1) and matching the conditions to have a non-zero partial fusion cross section up to the angular momentum value observed in our calculations and a total cross section in agreement with the experimental one. In the Ni induced reaction the parameters which fulfill both requirements are $l_0 = 40\hbar$ and $\Delta = 11\hbar$ and the first two moments obtained in this way are $< l >= 35\hbar$ and $< l^2 >= 1680\hbar^2$. We see that the unitarity limit is not fulfilled at low partial wave in the Ni induced reaction. The quite large diffuseness parameter is a signature of the presence of effects like neck formation or surface excitation of the partners above the barrier, which cooperate in order to have fusion at higher spins. It indicates also that fluctuations are an important ingredient for a proper description of the data. Indeed, using a treatment based on the Langevin equation, in ref.s [18,19] it was possible to account simultaneously for the total cross section and for the angular momentum distribution.

On the other side, in the asymmetric channel, the two parameters are $\Delta = 2\hbar$ and $l_0 = 36.5\hbar$, which are quite consistent with the sharp cut-off approximation. In this case $< l >= 24\hbar$, $< l^2 >= 692\hbar^2$ and, as expected, dynamical fluctuations seem to be less important.

We extend our discussion to other two reactions, which form the same compound nucleus, ^{137}Sm, at the same excitation energy, $E_x \simeq 66MeV$, namely the mass-asymmetric $^{32}S + ^{105}Pd$ at $150MeV$ of beam energy, and the mass-symmetric $^{60}Ni + ^{77}Se$ at $249MeV$ of beam energy. Considering, in each reaction, the impact parameter which forms the compound system at around $l = 30\hbar$, we plot again the time dependence of the quadrupole moment, fig.5.

We do not find a noticeable difference in the time needed for the shape equilibration, which is around $800 - 1000fm/c$, in the two cases.

The density contour plots obtained at larger angular momentum, $l = 45\hbar$, confirm this result, fig.6, although it seems that in the very early stage the symmetric

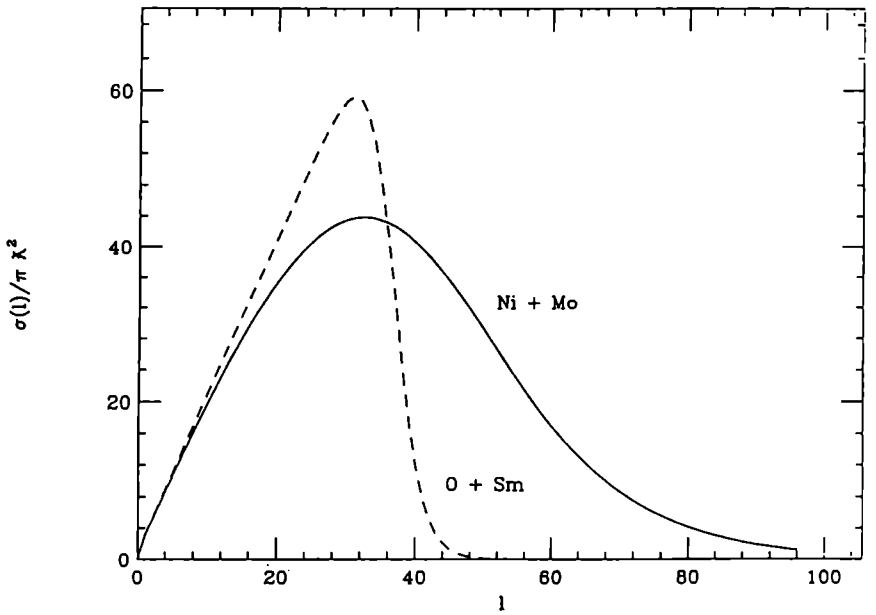

Fig.4: *Reduced angular momentum distribution (see text)*

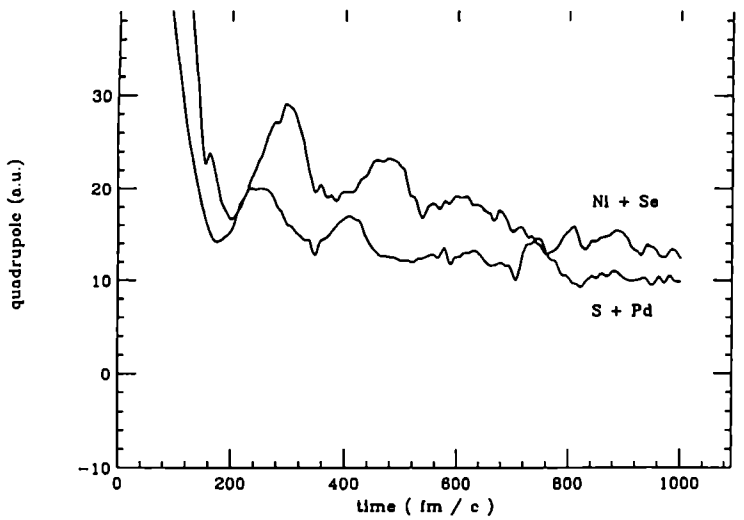

Fig.5 : *Time evolution of the mass quadrupole moment for the collisions:* $Ni - Se$ *at* $249MeV$ *of beam energy,* $b = 2fm$*, and* $S - Pd$ *at* $150MeV$*,* $b = 3fm$*.*

system is more deformed. This result is in agreement with the macroscopic HICOL predictions [20], which suggest that since both systems are located above the critical curve [21] in the fissility-mass asymmetry plane, the dynamical effects on the compound nucleus formation should be small. Also, plotting the time evolution of the quadrupole momentum at several impact parameters in the mass-symmetric case, we are able again to distinguish a different evolution starting from $b = 5fm$. Deep-inelastic mechanisms in the mean path are dominant at b=7fm, see Fig.7.

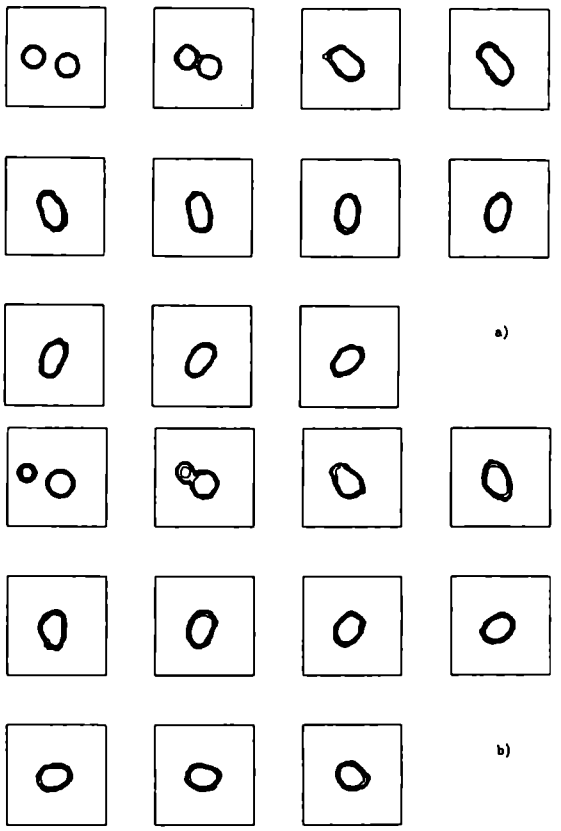

Fig.6: *Time evolution of the density contour plot on the reaction plane for the collision: (a) $Ni-Se$ at $249MeV$ of beam energy, $b = 3fm$; (b) $S-Pd$ at $150MeV$, $b = 4fm$.*

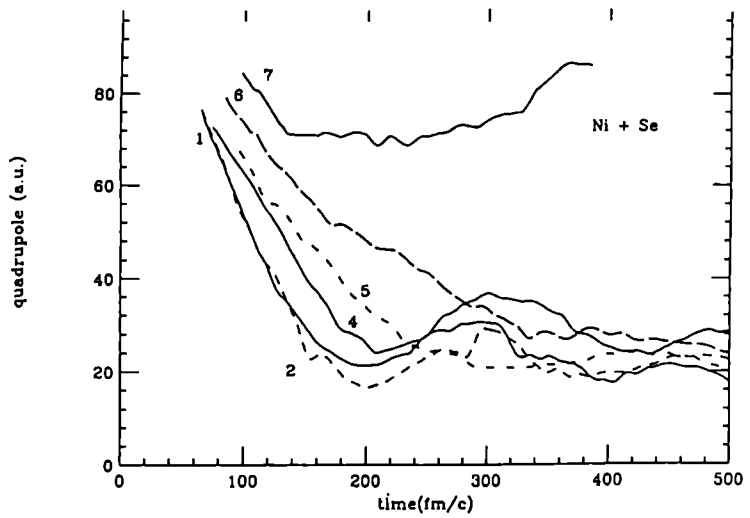

Fig.7: *Time evolution of the mass quadrupole moment for the collision $Ni-Se$ at different impact parameters; the numbers on each curve represent the corresponding value of the impact parameter.*

The main conclusion of this section is that it is possible to describe the dynamics of the compound nucleus formation, within the Landau-Vlasov formalism. In fact the effects which, in a macroscopic approach, are connected with dissipation through the effective fissility are well accounted for. On the other hand this means that typical dynamical features of the mean field dissipation, surface modes or neck formation, clearly observed in our simulations, can play an important role.

3. Pre-equilibrium GDR emission

Another process present in the first stage of a reaction is the charge equilibration, which can be seen as an isospin transfer [22]. This is obviously more pronounced when the N/Z difference between the two partners increases and it is an important mechanism in triggering the dipole collective modes [23]. In order to follow the dipole dynamics of the whole interacting system, we have evaluated the isovector dipole moment in coordinate space at each time step, choosing the $z-$direction along the rotating maximum elongation axis and the $x-$direction on the reaction plane:

$$D_z(t) = \frac{N\ Z}{A}\ [< z >_{proton}\ -\ < z >_{neutron}] \tag{3.1}$$

where

$$< z >_{proton} = \Sigma_{i=p} z_i/Z\ \ ,\ \ < z >_{neutron} = \Sigma_{i=n} z_i/N \tag{3.2}$$

and the same for the $x-$ and $y-$ components. We plot the time evolution starting from the moment when the nuclei touch, for $O - Sm$ and $Ni - Mo$, at the impact parameters considered in the previous section, fig.8.

The dipole moment along the $z-$axis becomes zero in less then $200 fm/c$ and this can be considered as the time needed for charge equilibration. After that we observe the onset of periodic oscillations, the giant dipole mode. A time delay seems to exist between the normal mode along the $z-$axis and the other two modes. In the Ni induced reaction we clearly distinguish two different frequencies, with the smallest one for the parallel component, as expected for a deformed system.

This effect is particularly evident from the Fourier transforms, defined as

$$S_i(\omega) = |F_i(\omega)|$$

with

$$F_i(\omega) = \int_{t_{min}}^{t_{max}} dt\ e^{i\omega t} D_i(t) \tag{3.3}$$

and plotted in fig.9.

In all our calculations we have chosen the interval $200 - 1000 fm/c$ for the $t_{min} - t_{max}$ interval, following the interpretation of fig.3. and the above discussion about charge equilibration.

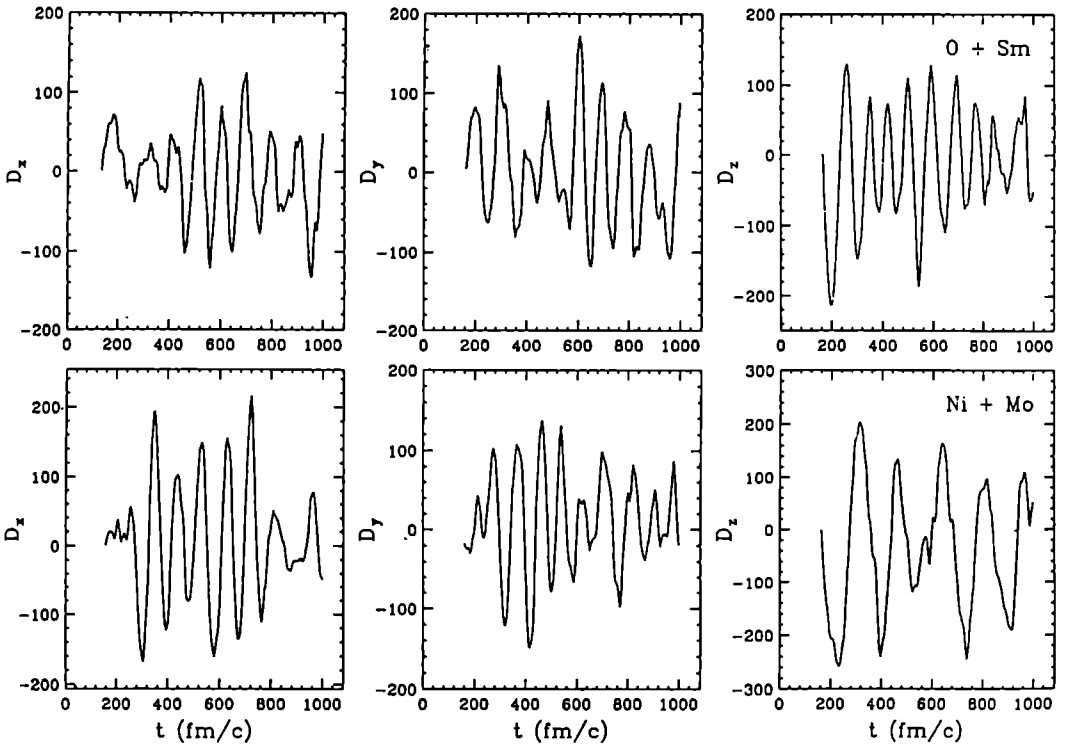

Fig.8: *Time evolution of the dipole moment components for the collision $O - Sm$ at $83MeV$, $b = 5fm$ (upper) and for the collision $Ni - Mo$ at $237MeV$, $b = 3fm$ (lower). Arbitrary units, same normalization.*

Due to the use of simplified Skyrme forces, we expect the values for the GDR energy centroids obtained in this way to be underestimated. However our task is not to reproduce the experimental values, but to put in evidence a difference between the two systems under study in the pre-equilibrium stage of the reaction. In the more symmetric case the GDR energies associated with the oscillations along the short axes are shifted to larger values, around $14MeV$, for the $x-$component and the $y-$component, while the $z-$component is moved to $7 - 8MeV$. In the asymmetric case all the components are in the same energy region, $12 - 13MeV$. So, we can conclude that the system formed in the Ni induced reaction is elongated during a long time. This is consistent with the results found from the quadrupole analysis. On the other side, since all the three components are more or less at the same value in the O induced reaction, it means that the shape becomes spherical or in any case very small deformed in a short time interval.

Using the results of our calculations, it is instructive to calculate the energy weighted strength function of the dipole operator, which is proportional to the absorption cross section::

$$\sigma(\omega) = \sum_n \omega_n |\langle n|\vec{D}|0\rangle|^2 \delta(\omega_n - \omega) \tag{3.4}$$

To to this, we consider a linear response theory treatment and we express the e.w.-

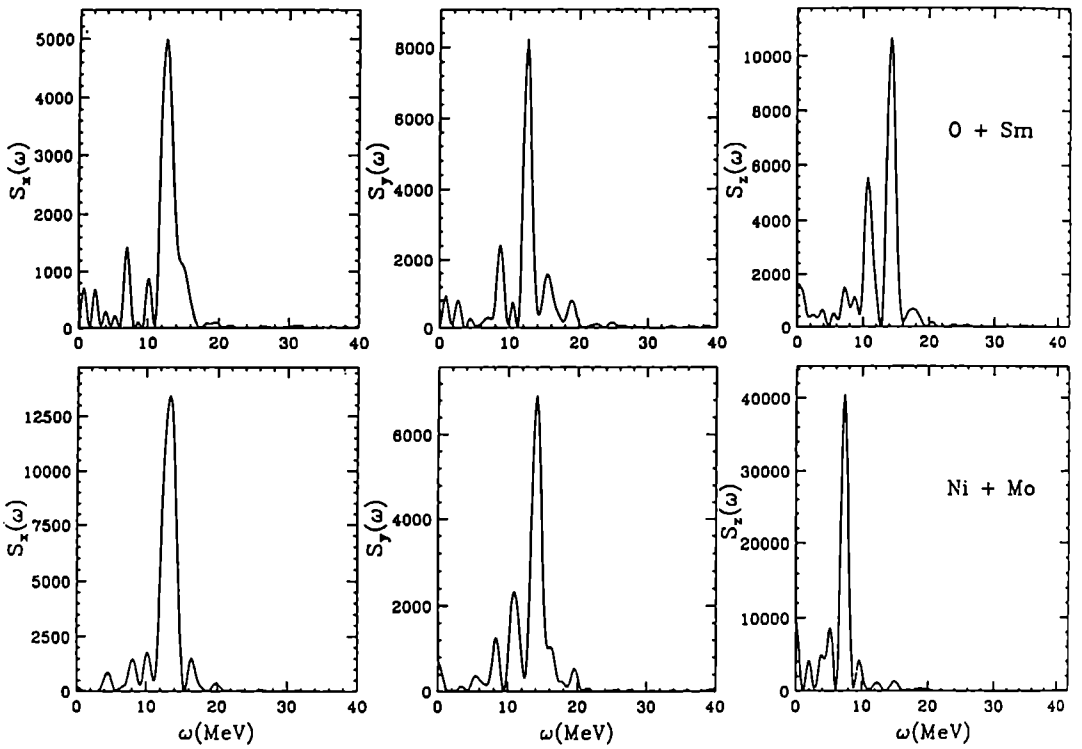

Fig.9: *Fourier transform of the dipole moment components for the collision $O-Sm$ at $83MeV$, $b = 5fm$ (upper) and for the collision $Ni-Mo$ at $237MeV$, $b = 3fm$ (lower). Arbitrary units, same normalization.*

strength function through the Fourier transform of the response function [24], [25]:

$$\sigma_i(\omega) = \sigma_0 \omega \left| \int_{t_{min}}^{t_{max}} dt \; e^{i\omega t} D_i(t) \right| = \sigma_0 \omega |F_i(\omega)| \tag{3.5}$$

where i stands for x, y and z.

Although the main source of damping, the one-body dissipation, is present in our dynamical approach, it is clear that resonance widths cannot be easily extracted from the Fourier transforms. We can overcome this difficulty just taking a realistic value, $\Gamma = 6MeV$, for the GDR spreading width in this region mass and at excitation energies around $50 - 60MeV$ [3, 17, 29]. In any case in the following we will show also the dependence on this parameter of our main results. Supposing now a Lorentzian shape for the strength function of each component, centered at the energies determined through the Fourier analysis, we obtain the total cross section shown in fig.10, for both cases.

So, differences in the shape evolution are clearly reflected in the gamma ray spectra from the pre-equilibrium GDR. Of course, in a statistical calculation, the contribution from the later stage of the reaction will be superimposed on the pre-equilibrium spectrum, and this contribution can attenuate the differences between the two gamma ray spectra. We can evaluate the relative strength of each compo-

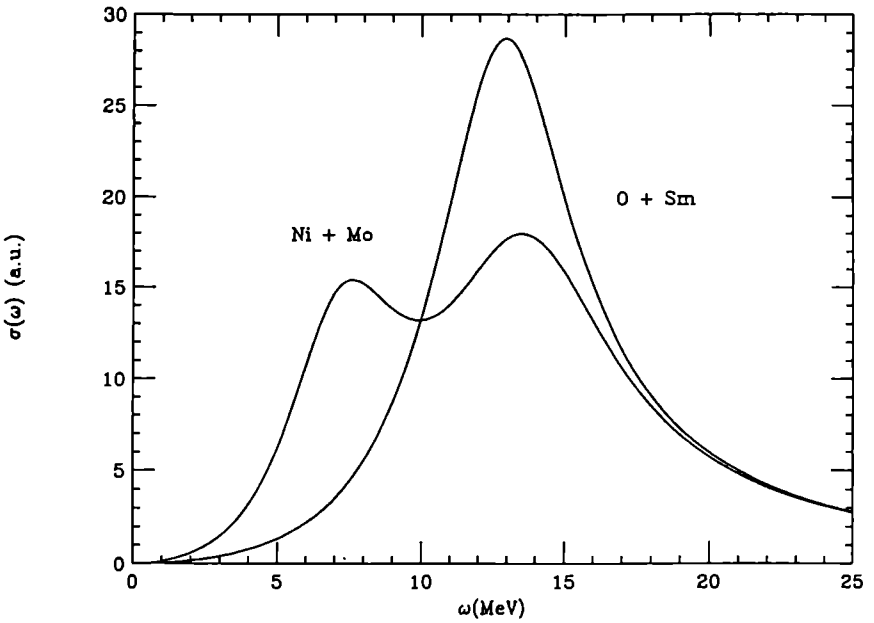

Fig.10: *GDR strength function for the systems formed in the reactions $Ni - Mo$ and $O - Sm$, obtained using a width equal to $6MeV$ for each component.*

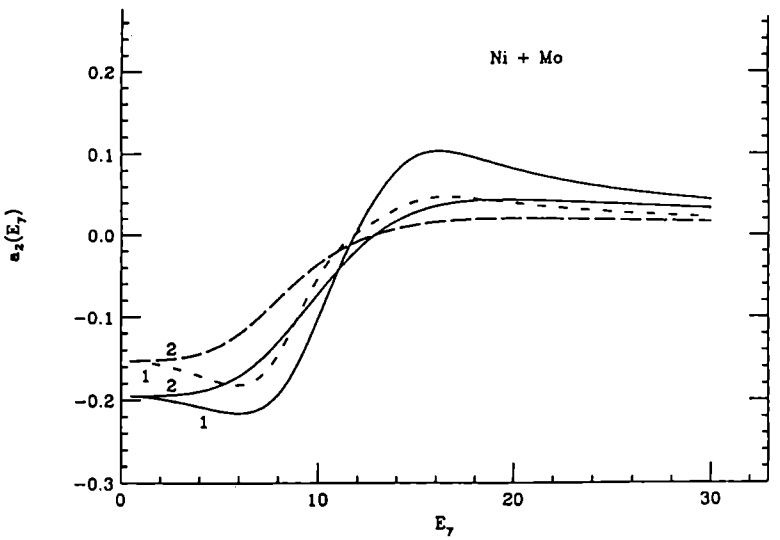

Fig.11: *Angular anisotropy parameter a_2 for the reaction $Ni - Mo$; contribution from preequilibrium ((1), solid line), contribution from equilibrium and preequilibrium, using a width equal to $6MeV$ for each component ((1), dashed line); the same calculation, but with a width equal to $12MeV$, for each component is represented in (2) (solid and dashed lines).*

nent in the pre-equilibrium stage:

$$W_i = \frac{\int_0^{30} \omega |F_i(\omega)| d\omega}{\Sigma_i \int_0^{30} \omega |F_i(\omega)| d\omega} \tag{3.6}$$

We find $W_x = 0.31$, $W_y = 0.31$, $W_z = 0.38$ in the Ni case, and $W_x = 0.25$, $W_y = 0.33$, $W_z = 0.41$ in the O case. The slightly larger value on the $z-$ direction is also a direct effect of the entrance channel dynamics.

At this point we can also try to see the differences between the angular distributions of gamma rays coming from the compound systems formed in the two entrance channels [6]:

$$W(\theta, E_\gamma) = \frac{W_z L_z(1 - 1/4P_2(\theta)) + W_x L_x(1 - 1/4P_2(\theta)) + W_y L_y(1 + 1/2P_2(\theta))}{W_z L_z + W_y L_y + W_x L_x}$$

$$= W_0(1 + a_2(E_\gamma)P_2(\theta)) \tag{3.7}$$

where L_i is the Lorentzian function corresponding to the $i - GDR$ component:

$$L_i = \frac{\Gamma_i E_\gamma^2}{(E_\gamma^2 - E_i^2)^2 + \Gamma_i^2 E_\gamma^2} \tag{3.8}$$

W_i, the preequilibrium strengths, are calculated as above and $P_2(\theta)$ is a Legendre Polynomial in the polar angle θ between the direction of the gamma ray emission and the beam axis. We take again all the widths equal to $6MeV$ but the results are not very much changed if we consider a little difference in the widths corresponding to the short and the long axis. We can directly deduce the expression for the angular anisotropy parameter:

$$a_2 = \frac{\sigma_y/2 - (\sigma_z + \sigma_x)/4}{\sigma_x + \sigma_y + \sigma_z} \tag{3.9}$$

with

$$\sigma_i = W_i L_i$$

In fig.11 a_2 is plotted for the more symmetric case. The presence of the deformation has, as a result, a non-zero value of this coefficient. Moreover deviations of the relative strengths from the equilibrium value, 1/3, change the shape of the curve comparing with what is expected in the equilibrium case. Of course, the final measured anisotropy coefficient will result from a superposition of pre-equilibrium and equilibrium contributions, so we may suppose that:

$$\sigma_i^{tot} = c_{pre}\sigma_i^{pre} + c_{eq}\sigma_i^{eq} \tag{3.10}$$

with

$$c_{pre} + c_{eq} = 1$$

The relative results are also shown in fig.11, choosing an equal weight of the two contributions $c_{pre} = c_{eq} = 1/2$. We remark that this choice likely overestimates the equilibrium GDR emission since we should actually expect a reduced high energy photon decay from a cooler compound system. Since the the system is spherical at the equilibrium the total outcome will be a decrease of the absolute value of the

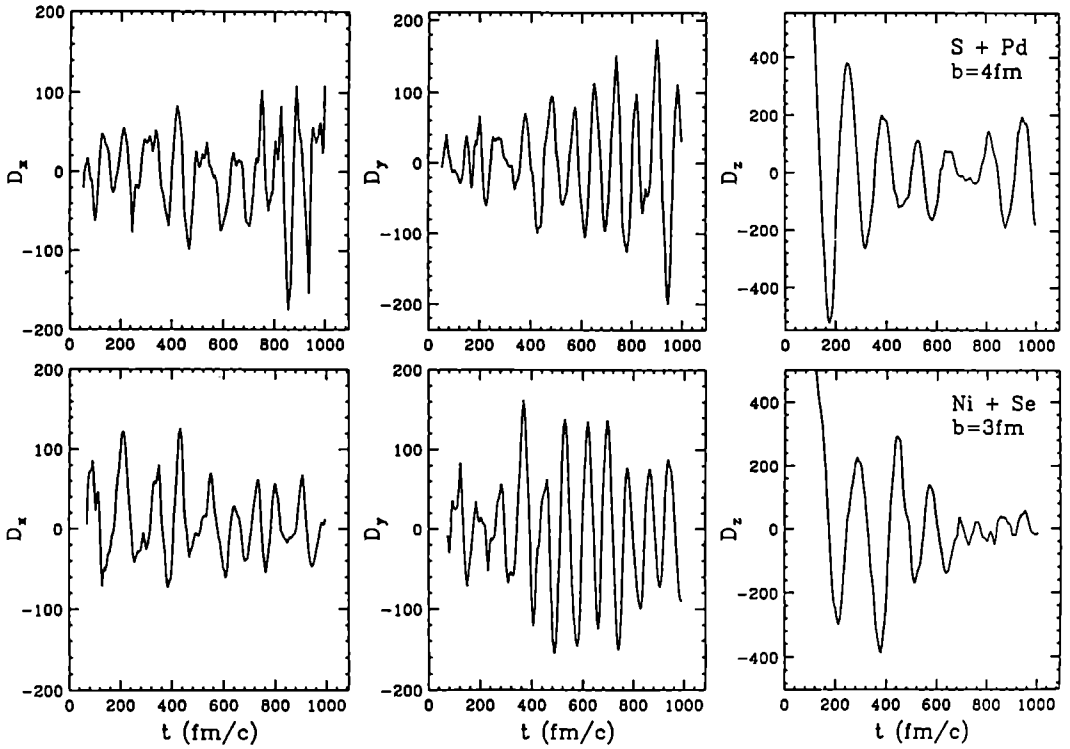

Fig.12: *Time evolution of the dipole moment components for the collision $S - Pd$ at $150MeV$, $b = 4fm$ (upper) and for the collision $Ni - Se$ at $249MeV$, $b = 3fm$ (lower). Arbitrary units, same normalization.*

angular anisotropy coefficient , but the effect is still present. In the same figure we plot the pre-equilibrium and total angular anisotropy coefficient considering a doubled value for the GDR widths.

For the asymmetric case, in the pre-equilibrium stage we have again deviations of the strengths from the equilibrium value, and generally it is possible to have a non-zero contribution to the anisotropy coefficient, even if the system becomes very quickly spherical, if the $y-$ relative strength S_y is different from 1/3. However, in our situation this is equal to 0.333, so the pre-equilibrium and equilibrium contributions to a_2 are both zero.

Finally, we have performed a similar analysis for the systems formed in $Ni + Se$ and $S + Pd$ reactions at $b = 3fm$ and $b = 4fm$ respectively (fig.12, fig.13 and fig.14).

The main observation is that now the positions of the energy centroids are more or less the same in the two cases, in full agreement with the similarity of the fusion path. However just because the fusion dynamics is nearly equal we can have now the chance of observing the presence of a "direct" dipole oscillation in the charge-equilibration process, for charge-asymmetric entrance channels. Indeed in correspondence to the more charge asymmetric case, $^{32}S(N/Z = 1.0) + ^{105}Pd(N/Z = 1.28)$, we get a larger value of the dipole strength along the $z-$direction (see fig.13) and as a consequence an enhanced a_2 coefficient (see fig.14).

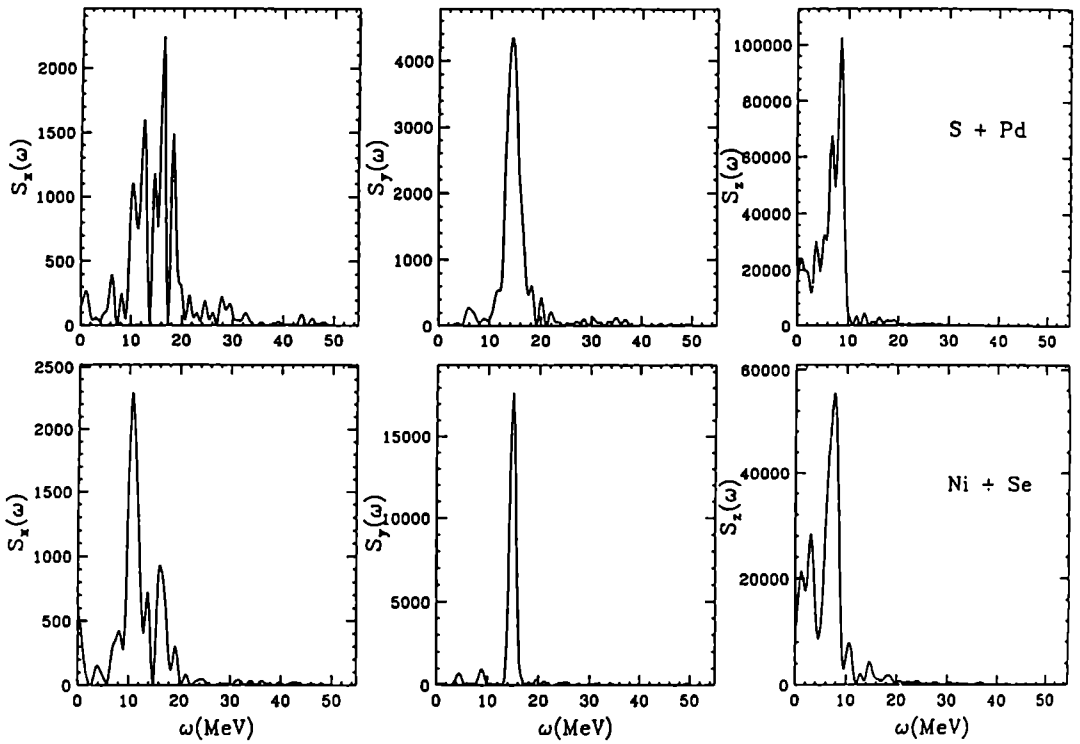

Fig.13: *Fourier transform of the dipole moment components for the collision $S-Pd$ at $150MeV$, $b = 4fm$ (upper) and for the collision $Ni - Se$ at $249MeV$, $b = 3fm$ (lower). Arbitrary units, same normalization.*

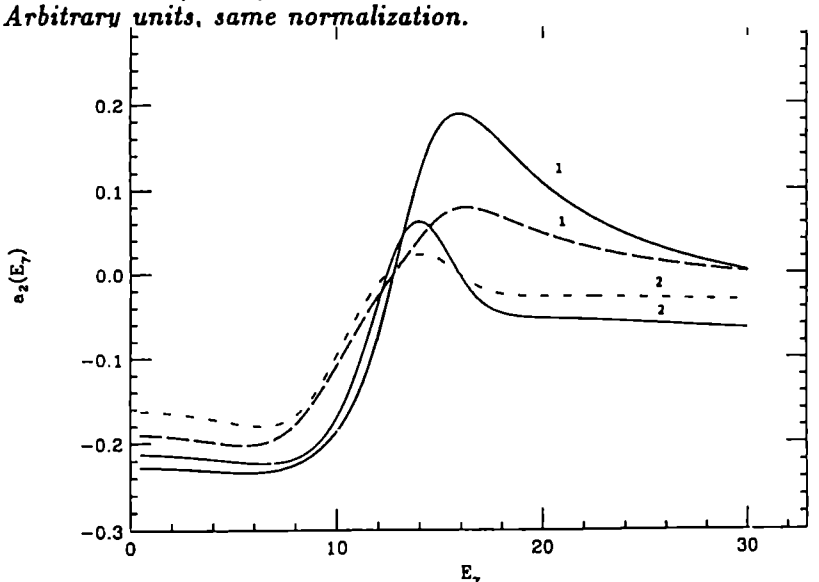

Fig.14: *Angular anisotropy parameter a_2 for the reactions: $S - Pd$; contribution from preequilibrium ((1), solid line), contribution from equilibrium and preequilibrium ((1), dashed line), calculated using a width equal to $6MeV$ for each component; (2) $Ni - Se$; solid and dashed lines as in (1).*

This new dipole mode in charge asymmetric entreance channels will be the subject of the next section, where we will discuss its relevance in incomplete fusion processes at higher energy.

4. Stretching the "iso-spring": the dynamical dipole

In medium energy fusion events energy and angular momentum are quickly distributed among all single particle degrees of freedom due to the combined action of mean field and collisional dissipation. Charge equilibration takes place on longer time scales and for charge-asymmetric entrance channels we can easily have some pre-equilibrium GDR strength due to dipole oscillations in this isospin transfer dynamics [27]. Such direct *dynamical* dipole will be also damped through the coupling to the hot compound system given by the spreading width. Therefore a direct observation of this "entrance channel" dipole emission could bring independent information on properties of the GDR-$\Gamma^{\downarrow}$ at high excitation energies [27]. We claim that the detection of this new giant photon decay is possible since there are two main features that can trigger an experimental observation:

i) The emitting system is still highly deformed in shape, so we expect a neat splitting of the GDR with an important contribution at lower $\gamma-$energies due to oscillations along the maximum elongation axis ($z-$axis in our definition);

ii) The direct oscillation is preferentially on the reaction plane. This means that the strength along the $z-$axis is much larger than the statistical value and the associated photon emission will show a clear angular anisotropy with respect to the beam axis.

In order to to show quantitatively such expected properties we have performed a whole microscopic simulation of an incomplete fusion collision, following the dynamics with the BNV transport theory [12,13], including the collision term and studying the time evolution of dipole oscillations of the compound system.

We have considered the collision $^{36}Ar(N/Z = 1.0) + ^{90}Zr(N/Z = 1.25)$, charge asymmetric entrance channel, at $27AMeV$ beam energy for impact parameter $b = 3fm$ where we have incomplete fusion events. This system has been recently studied by the $MEDEA$ collaboration [30]. Fig.15 shows the main features of the incomplete fusion dynamics: Excitation energy (E^*, MeV), Mass (A), Charge (Z), Mass-Quadrupole moment (Q, fm^2) and Angular Momentum ($J, \hbar$) of the formed bound system at each time step are reported. We see a noticeable pre-equilibrium particle emission which implies a fast dissipation of about fifty percent of the available c.m. energy, typical of this medium energy region [13]. We can assume an equilibration time around $300 - 400fm/c$ to a compound nucleus almost spherical in shape, with a relatively low angular momentum and excitation energy about $250MeV$.

To follow the dipole dynamics of the whole interacting system, we have evaluated the isovector dipole moment in coordinate space at each time step, using the same procedure presented in Sect.3.

In fig.16 we plot the Fourier transforms of the oscillations along different axes.

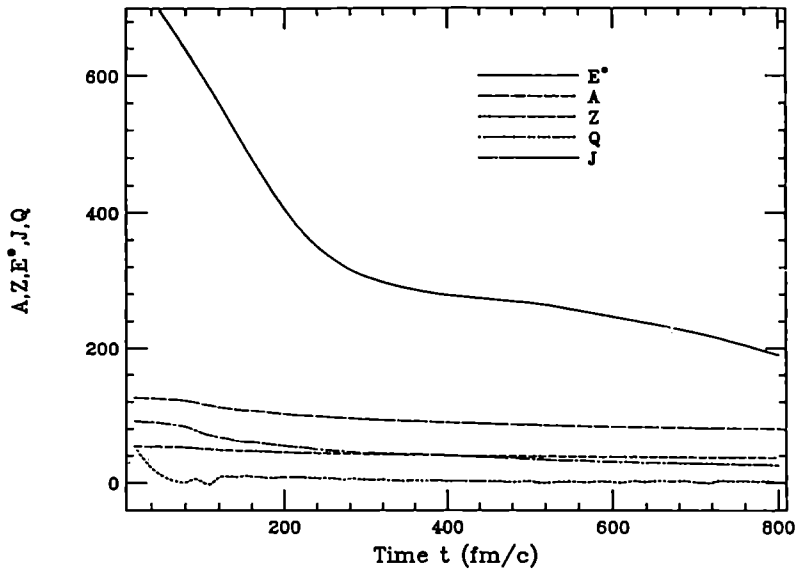

Fig.15: *Time evolution of the compound system for the reaction* $^{36}Ar +^{90} Zr$ *at* $27AMeV$ *for* $b = 3fm$. *Symbols are explained in the text.*

We have chosen the $t_{min} - t_{max}$ interval as: $20 - 1000fm/c$ for the total strength distribution (a), $20 - 400fm/c$ for the pre-equilibrium part (b) and $400 - 1000fm/c$ for the equilibrium one (c). We clearly see the difference in frequencies and strengths of the two contributions. Particularly noticeable the pre-equilibrium $z-$component.

We can evaluate the relative weight of each (x, y, z)-component in the various stages. We find $W_x = 0.15$, $W_y = 0.15$, $W_z = 0.70$ in pre-eq. and almost equal weights $1/3$ in equilibrium, as expected. We remark that the difference in the weights is also strongly related to the GDR spreading width at high excitation energy. Indeed in presence of a very strong coupling the effect should quickly disappear [27].

For the centroid energies we can extract $E_z \simeq 8MeV$, $E_x \simeq E_y \simeq 15MeV$ from pre-eq. and $E_z \simeq E_x \simeq E_y \simeq 11MeV$ for the equilibrium contribution.

At this point we can compute the giant photon decay rate [31]

$$\frac{dN_\gamma}{dE} = 1/\hbar \int_{t_{min}}^{t_{max}} dt \frac{E_\gamma^2}{(\pi\hbar c)^2} \sigma_{\gamma-abs}(E_\gamma, t)\, e^{-E_\gamma/T(t)} \tag{4.1}$$

with a $\gamma-$absorption cross section, normalized to the classical TKR sum rule,

$$\sigma_{\gamma-abs} = \Sigma_{i=1,3} W_i L_i \tag{4.2}$$

where the sum is over the different axes of oscillation, with relative weights W_i and Lorentzian functions L_i. The dependence on time evolution is given by the excitation energy at each time step, after a subtraction of the collective part, which means different temperatures and total widths.

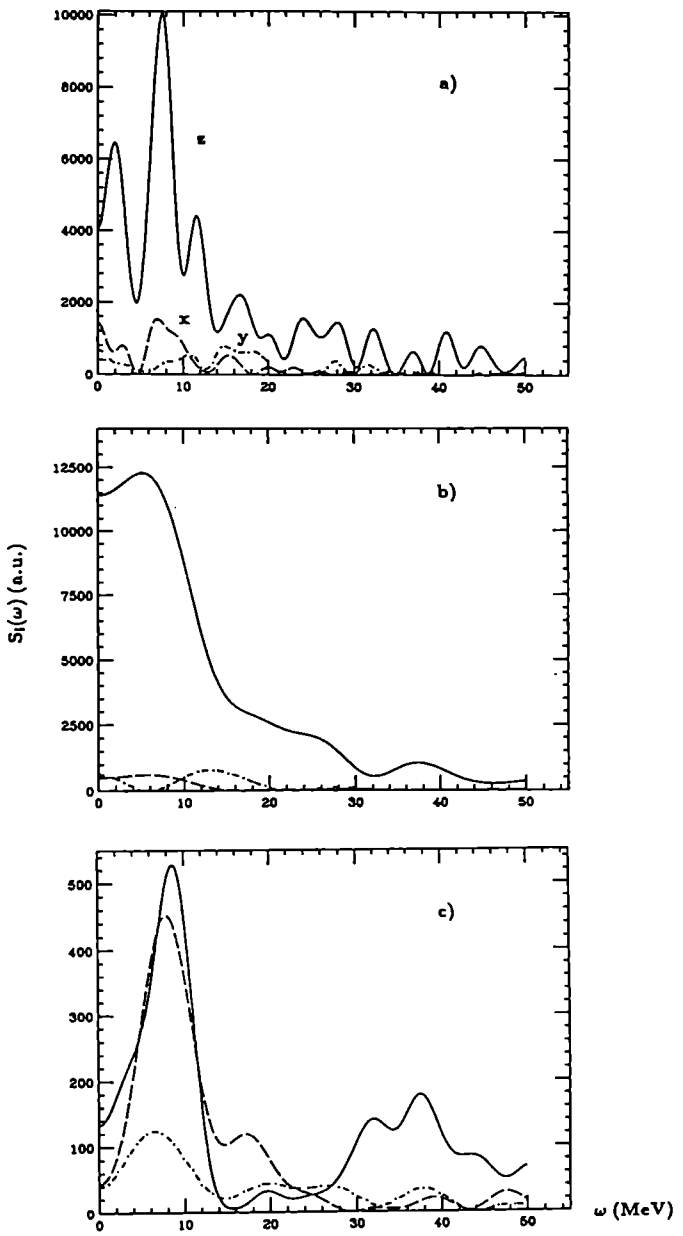

Fig.16 : *Fourier transforms of dipole oscillations of the compound system for the reaction* $^{36}Ar +^{90} Zr$ *at* $27AMeV$ *for* $b = 3fm$. *a) total; b) pre-equilibrium; c) equilibrium. Solid line: z-axis; long-dashed: z; dot-dashed: y*

In fig.17 we plot the GDR $\gamma-$rate dN_γ/dE as a function of E_γ in the case *a*) of a Γ_{TOT} saturation and *b*) of an E^*-increasing. Dashed lines: pre-equilibrium contributions; long-dashed: equilibrium; solid: sum of eq. and pre-eq.; dot-dashed:

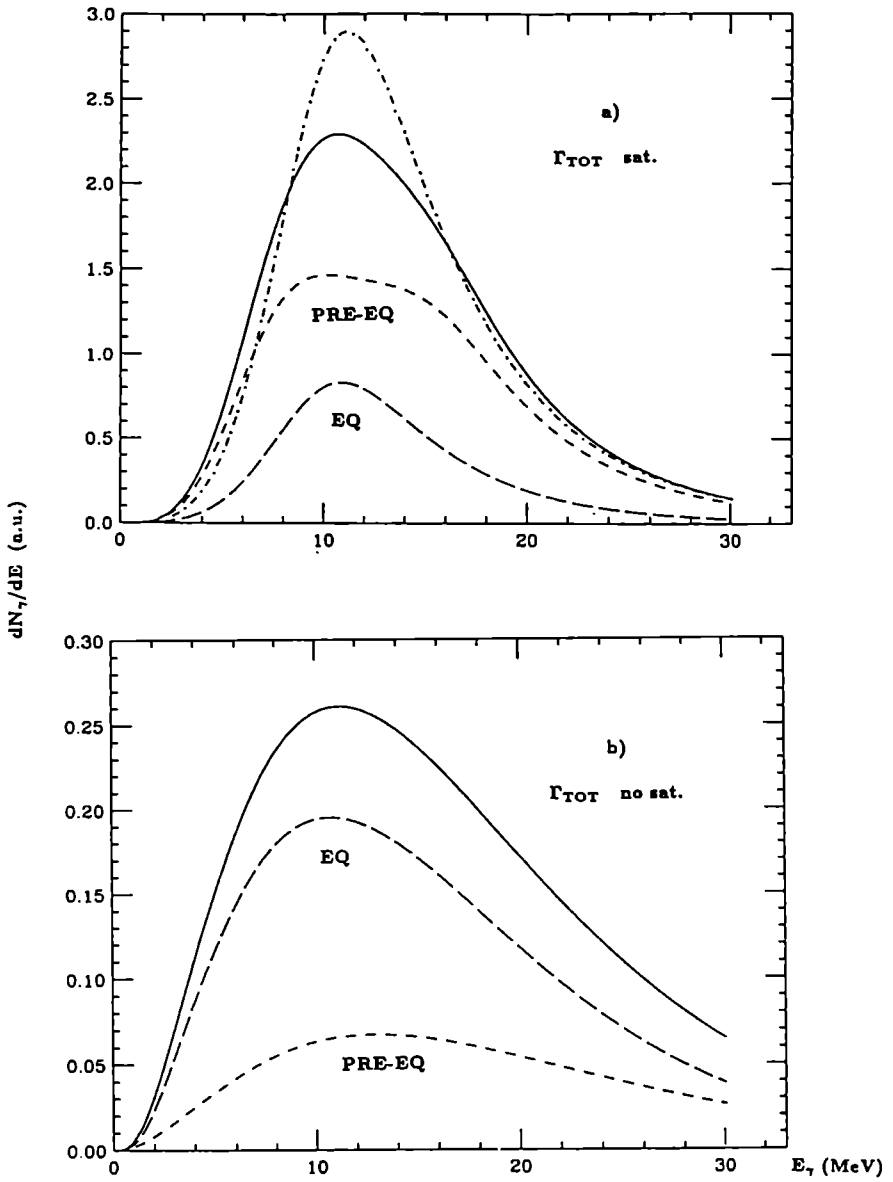

Fig.17 : *GDR $\gamma-$decay rate of the compound system for the reaction $^{36}Ar +^{90} Zr$ at $27AMeV$ for $b = 3fm$. a) saturating Γ_{TOT}; b) no saturation. Different curves explained in the text.*

no pre-eq. contribution, only equilibrium parameters at each time step.

We remark that in the case of an increasing total width (17*b*) the overall rate is quite small and in particular the pre-equilibrium contribution is negligible. The effect seems to be important for a saturating Γ_{TOT} (17*a*) also with a possible shift to lower energies of the $\gamma-$yield, as observed in the *MEDEA* data [30].

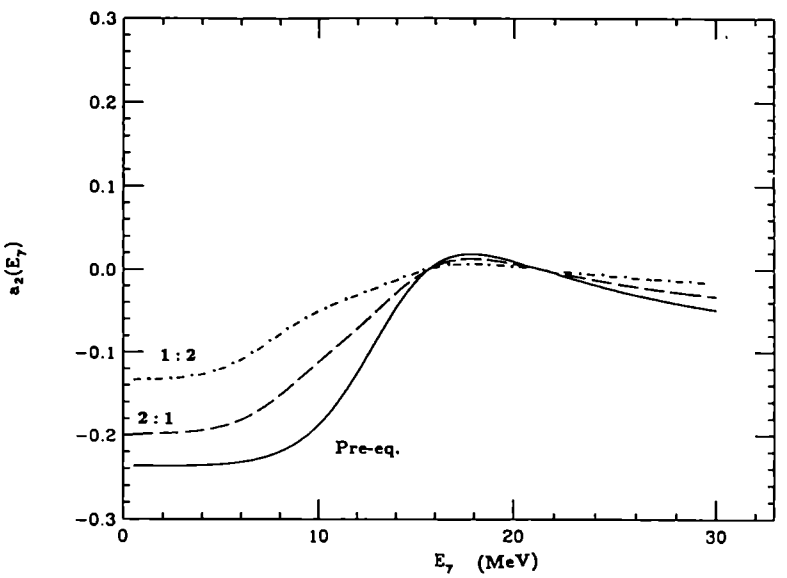

Fig.18 : *Anisotropy coefficient of the giant photon emission by the compound system for the reaction* $^{36}Ar + ^{90}Zr$ *at* $27AMeV$ *for* $b = 3fm$. *Solid line: pre-eq. only; long-dashed:* 2 : 1 *mixing; dot-dashed:* 1 : 2

A nice way to see the effect of the pre-equilibrium component is to look at the angular distributions of the emitted giant photons, the $a_2(E_\gamma)$, eq.(3.9). In fig.18 a_2 is plotted for the pre-equilibrium emission (solid line) in the case of a saturating Γ_{TOT}. The presence of a deformation and of different weights lead to a non zero value of this coefficient in the lower E_γ region.

As already stressed in the previous section, the final measured anisotropy coefficient will result from a superposition of pre-equilibrium and equilibrium contributions, see eq.(3.10). The relative results are also shown in fig.18, choosing a 2 : 1 ratio the two contributions $c_{pre} = 2/3, c_{eq} = 1/3$ (long dashed) and a 1 : 2 ratio $c_{pre} = 1/3, c_{eq} = 2/3$ (dot-dashed). We remark that the latter choice likely overestimates the equilibrium GDR emission since we should have a reduced high energy photon decay from a cooler compound system. Since the the system is spherical at the equilibrium the total outcome will be a decrease of the absolute value of the angular anisotropy coefficient, but the effect is still present. Of course for low energy photons we have a dominant isotropic statistical contribution, not related to GDR states, which brings back to zero the $a_2(E_\gamma)$ parameter. A definite minimum around $8 - 10MeV$ γ−energy in this mass region should be observed.

We have similar results for various impact parameters, so we predict a relatively large cross section. However with increasing b we start to see a transition to a different reaction mechanism, of binary type, since fluctuations are included in our dynamics [32]. We can have deep inelastic events but still a direct dipole emission with the above characteristics from an intermediate compound system, before separation, should be detected.

This can be clearly seen from fig.19, showing dipole strengths for a more pe-

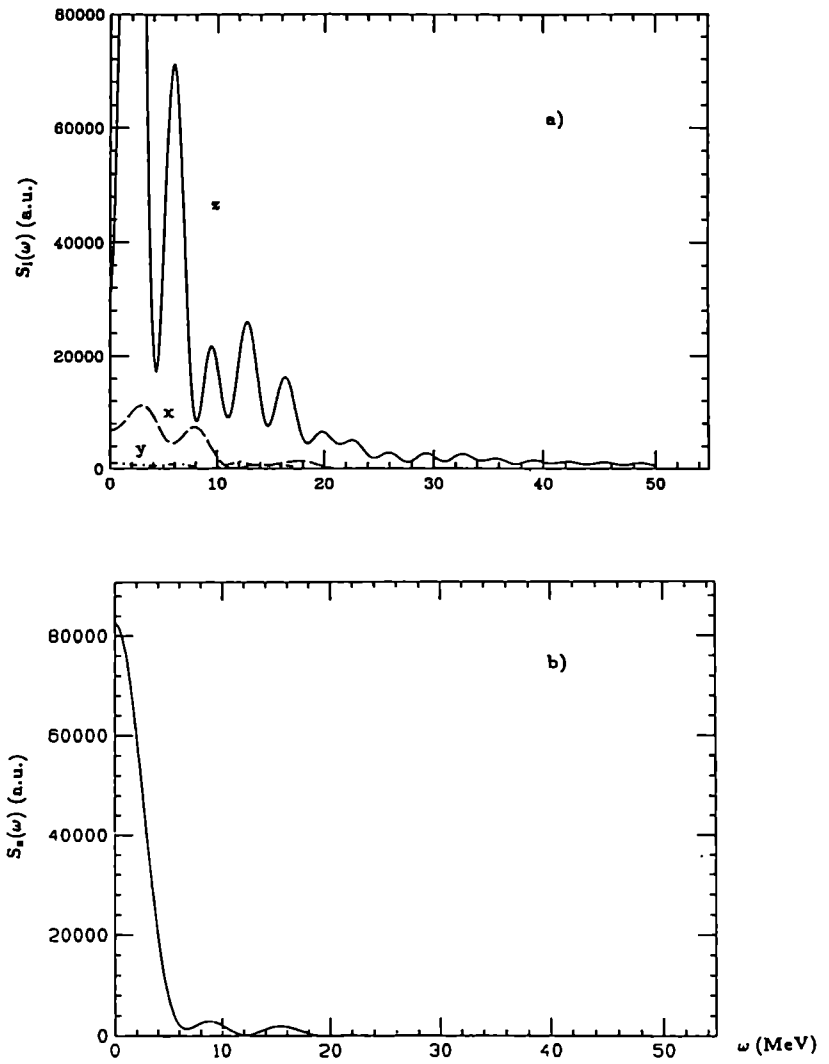

Fig.19 : *Fourier transforms of dipole oscillations of the compound system for the reaction* $^{36}Ar + ^{90}Zr$ *at* $27AMeV$ *for* $b = 5fm$. *a) before two fragment separation; b) separation time interval (z−component only). Curves like in fig.16*

ripheral impact parameter $b = 5fm$, where the binary mechanism is dominant. In (19*a*) we have strengths computed in the time interval before separation, in (19*b*) the $S_z(\omega)$ from the separation times, where no nucleon exchanges and consequent dipole oscillations are expected. Such collective analysis represents also a nice method to separate different reaction mechanisms, as shown in Sect.2.

We finally remark that in binary dissipative reactions, like fast fission events, we would have also a clean way to determine the reaction plane: then the dynamical dipole emission should be essentially orthogonal to it.

5. Conclusions

We have shown the possibility of detecting GDR γ-decays from long-living intermediate and very deformed nuclear systems, in fusion reactions just above the Coulomb barrier. The strength and the angular distribution of such exotic photon emission will present very peculiar features which should favour a direct observation, particularly focussing on the angular distribution as a good trigger. In any case this can represent an important pre-equilibrium cooling mechanism before the compound nucleus is formed. Similar results have been shown in a preliminary way for deep-inelastic collisions in ref.[26].

We have discussed pre-equilibrium GDR emissions in connection with different fusion paths ruled by the mass asymmetry in the entrance channel. Consistently with previous expectations by Swiatecki we have shown that these effects disappear for lighter compound nuclei, below a critical fissility point. However in such cases we have revealed another interesting source of pre-equilibrium GDR emissions, a direct dipole oscillation due to the charge equilibration dynamics for charge asymmetric entrance channels. This oscillation is also on the reaction plane implying again a characteristic angular anisotropy in the photon emission. It would be quite interesting to study the interplay between charge and mass asymmetry in regions around the critical fissility point, possibly with a selection of different angular momentum intervals for the fused nucleus. We expect indeed angular momentum effects to be more important in that fissility range [29]. In this way we can get a very clean picture of the fusion path.

Similar results can be obtained in a more analytic way, with some imposed symmetries, starting from the *Dubna* phase space model for nuclear dynamics [33].

Radioactive beams appear to be quite ideal tools to study the isospin effect. A "dynamical" dipole emission is expected to be very important with increasing beam energy, in presence of shorter fusion times [27]. It could also bring new independent information on the GDR damping at high excitation energy [27, 28]. A shift to lower energies of the GDR strength and a clear angular anisotropy are the main signatures of this new collective mode. The effect should be seen also for dissipative binary processes, that represent the dominant reactions mechanisms in this region of medium energy heavy ion collisions.

A saturation of Γ_{TOT} can shift the disappearence of the GDR emissions to higher excitation energies. This is possible if the Giant Dipole spreading width $\Gamma^{\downarrow}$ will actually decrease. Such behaviour has a fascinating link with the zero- to first-sound transitions already observed in other Fermi liquids [28].

Finally we remark that the analysis presented in this paper could give valuable information on the best entrance channel choices for the population of very deformed bands in highly rotating compound nuclei. Moreover the "direct" dipole emission could be an interesting cooling mechanism to favour the fusion of very heavy nuclear systems.

6. References

1) K.A.Snover, Ann.Rev.Nucl.Part.Sci. 36 (1986) 545.
2) M.Thoennessen et al., "Nuclear Structure and Heavy-ion Reaction Dynamics 1990", Ed.s R.R. Betts and J.J. Kolata, Inst. Phys. Conf. Ser. No 109, IOP Publish. 1991, p.135., R.Butsch et al., Phys.Rev. C44 (1991) 1515
3) M.Thoennessen et al., Phys.Rev.Lett. 70 (1993) 4055.
4) V.V.Kamanin et al., Z.f.Physik A337 (1990) 111.
5) H.Feldmeier, Rep.Progr.Phys. 50 (1987) 915, and ref.s therein.
6) J.J.Gaardhoje, Ann.Rev.Nucl.Part.Sci. 42 (1992) 483 and ref.s therein.
7) H.Van der Ploeg et al., Phys.Rev.Lett. 68(1992) 3145 and 69 (1992) 1148 (errata).
8) P.Paul and M.Thoennessen, "Fission time scales from Giant Dipole Resonances", Ann.Rev.Part.Nucl.Sci. 44 (1994) 65
9) L.Campajola et al., Nucl.Phys. A583 (1995) 119, J.Ps. van Schagen et al., ibidem p.123
10) G.F. Bertsch, Z.f.Physik A289 (1978) 103.
11) M.DiToro, "Winter College on Fundamental Nuclear Physics", Ed.s K.Dietrich, M.Di Toro and H.J.Mang, World Sci. 1984, Vol I p.451.
12) Ch.Gregoire et al., Nucl.Phys. A465 (1987) 315, A.Bonasera et al. Phys.Lett. B221 (1989) 233 and Phys.Lett. B259 (1991) 399.
13) M.Colonna, N.Colonna, A.Bonasera and M.Di Toro, Nucl.Phys. A541 (1992) 295
14) J.L. Barreto at al. Phys. Rev. C48 (1993) 2881.
15) F. Puhlhofer, Nucl.Phys. A267 (1977) 267.
16) J.R. Birkelund, J.R. Huzeinga, Ann.Rev.Part.Nucl.Sci. 33 (1983) 265.
17) M.Thoennessen et al., "Dynamical effects in fusion reactions forming ^{110}Sm", Preprint MSUCL-967, March 1995
18) P. Fröbrich and J. Richert, Phys. Lett. B237 (1990) 328.
19) N.G. Nicolis and D.G. Sarantites, Phys. Rev. C48 (1993) 2895.
20) G. Viesti et al., Nucl. Phys. A579 (1994) 225.
21) W.J. Swiatecki, Nucl. Phys. A391, 471 (1982).
22) Ch.Gregoire, see ref.[11], Vol.I, p.501.
23) E. Suraud , M. Pi and P. Schuck, Nucl. Phys. A492 (1989) 294.
24) S. Stringari and D. Vautherin, Phys. Lett. B88 (1979) 1.
25) Y. Alhassid and B. Bush, Nucl. Phys. A509 (1990) 461.
26) Cai Yanhuang, M.DiToro, M.Papa, A.Smerzi and Zhong Jiquan, "Nuclear Giant Resonances: a never ending story", Proc. "Dynamical Features of Nuclei and Finite Fermi Systems", Ed.s X.Vinas et al., World Sci. 1994, pp.393-413
27) Ph.Chomaz, M.Di Toro and A.Smerzi, Nucl.Phys. A563 (1993) 509
28) V.Baran, M.Colonna, M.Di Toro, A.Guarnera, V.Kondratyev and A.Smerzi, "The many facets of Giant Resonances at high excitation energy", Proc. Int.Conf. on Giant Resonances, Groningen 1995, Ed.M.Harakeh to appear on Nucl.Phys.A
29) M.Cinausero et al., "Giant Dipole Resonances studied with GASP", Proc. Int.Conf. on Giant Resonaces, see before, and private communication

30) J.H.Le Faou et al., Phys.Rev.Lett. 72 (1994) 3321
T.Suomiijarvi et al., Nucl.Phys. A583 (1995) 105c,
P.Piattelli et al, Proc.Int.Conf.on Giant Resonances, see ref.28)
31) D.M.Brink, Nucl.Phys. A519(1990) 3c
32) M.Colonna, M.DiToro, A.Guarnera, Nucl.Phys. A589 (1995) 160
33) I.N.Mikhailov, T.I.Mikhailova, M.DiToro, V.Baran and Ch.Briancon
"Collective Dynamics of Nuclear Fusion: deformation changes and heating during the fusion", Orsay Preprint Sept.1995, sub.to Nucl.Phys.A

Rotation and Giant Dipole Vibration in Hot Nuclei

A. Bracco, F. Camera, M. Mattiuzzi
Dipartimento di Fisica, Universitá di Milano and INFN sez. Milano
via Celoria,16 20133 Milano, Italy

ABSTRACT

A study of the spectral and angular distributions of the high energy γ rays emitted by the giant dipole resonance (GDR) in the compound nuclei ^{166,165}Er at $E^* =$ 51 and 45 MeV and ^{176}W at $E^* = 70$ MeV formed with with heavy ion reactions is presented. A comparison of the data with model predictions at the equilibrium deformation and with thermal fluctuations in the adiabatic limit is discussed. This comparison indicates that at these moderate temperatures (T= 1.3-1.4 MeV) the collisional damping width is independent of temperature and rotational frequency and that thermal shape and orientation fluctuations are responsible for the measured widths and angular anisotropies.

1. Introduction

The properties of hot rotating nuclei can be explored making use of the most basic of the nuclear collective modes, namely the giant dipole resonance (GDR). The development of this field, started more than a decade ago, has been rapid and many experimental and theoretical studies are now available.

Many of the overall features of excited giant resonances have been obtained and substantial amount of data is available. However, the characteristic parameters of the GDR such as the centroid, width and fraction of the energy weighted sum rule were so far deduced by analysis of the high energy γ ray spectra measured with rather inclusive experiments. With "inclusive" it is meant that the detected γ rays mostly originate from the entire space spanned by the variables E^* and I_{rot} available to the decaying compound nucleus.

Recently, the experimental techniques have progressed to be able to select with quite good precision the angular momentum of the emitting nucleus and and to measure the strength function and the angular distribution of the high energy γ rays in the GDR region associated to rather narrow intervals of angular momentum. In this conditions, the sensitivity to the changes of nuclear properties and GDR damping mechanisms is enhanced.

The improvement of the experimental selectivity was motivated by the need of a better understanding of the width of the GDR at finite temperature that requires the determination of the role played by both the collisional damping and thermal fluctuations. Studies in the two mass regions A= 110 [1] and A =165-175 [2] at temperatures T = 1.5 - 2 MeV were made with the HECTOR detector array [3]. This interval of temperatures is of particular interest to study the transition between the region (close to the yrast line) dominated by quantal effects to the region where

nuclei can be described by models based on classical and macroscopic concepts as in the case of the liquid drop model. Since nuclei at finite temperatures are described by an ensemble of shapes, thermal fluctuations are expected to play an important role in the the response of the giant dipole resonance (see section 2).

In this paper we discuss in particular the study of the spectra and angular distribution of the high energy gamma rays emitted by the GDR in the hot ^{176}W (section 4) and ^{166}Er (see section 5). It will be shown that both studies suggest that at these moderate temperatures and rotational frequencies the collisional damping width is equal to the zero temperature value and that thermal shape and orientation fluctuations are responsible for the measured widths and angular anisotropies.

2. Fluctuation models for hot nuclei

The thermal fluctuation models, extensively discussed in references 4 and 5, make use, among their basic ingredients, of the Boltzmann factor P describing the probability for a nuclear shape in terms of the deformation and orientation parameters (β, γ, Ω),

$$P(\beta,\gamma,\Omega,\omega,T) = Z(T,\omega)^{-1} \ exp[-F(\beta,\gamma,\Omega,\omega,T)/T] \qquad (1)$$

In the above expression F is the free energy, T the nuclear temperature, ω the rotational frequency and Z(T,ω) the partition function.

In the limiting case of adiabatic coupling the stretched components, $f_{\pm1}(E_\gamma)$, (associated to dipole vibrations orthogonal to the spin axis) and the unstretched component, $f_0(E_\gamma)$, (associated to dipole vibration parallel to the spin axis) of the giant dipole resonance are calculated as follows (see eq. 2). For each value of the deformation (β,γ) and orientation (Ω) parameters one constructs the Lorentzian functions $L_k(E_\gamma,\beta,\gamma,\Omega)$ (k=-1,0,1), describing a dipole vibration along the k axis, with centroid E_{GDR}, determined with the Hill-Wheeler parameterization, and width given by $\Gamma_{GDR} = \Gamma_0^{\downarrow}(E_{GDR}/E_0)^{\delta}$. E_0 and $\Gamma_0^{\downarrow}$ are the GDR centroid energy and the GDR width before the thermal coupling to the shape and δ= 1.9 . The width $\Gamma_0^{\downarrow}$ represents the damping due to the coupling of the correlated 1p-1h state, describing microscopically the GDR state, to more complicated np-nh states, the doorway states being the 2p-2h states. In the calculations, $\Gamma_0^{\downarrow}$ was kept constant at the different spins. The averaging in the adiabatic limit is made integrating over the whole shape and orientation distributions:

$$f_k(E_\gamma) = \int L_k(E_\gamma,\beta,\gamma,\Omega)\ P(\beta,\gamma,\Omega,\omega,T)\ d\tau \qquad k=-1,0,1 \qquad (2)$$

where $d\tau$ is $\beta^4|sin(3\gamma)|d\gamma d\beta d\Omega$.

From these components the total strength function ($\Sigma f_k(E_\gamma)$), is constructed together with the quadrupole coefficient a_2 in terms of the unstretched (f_0) and stretched ($f_{\pm1}$) cross sections:

$$a_2(E_\gamma) = \frac{1}{2}\frac{f_0(E_\gamma) - 0.5(f_1(E_\gamma) + f_{-1}(E_\gamma))}{f_0(E_\gamma) + f_1(E_\gamma) + f_{-1}(E_\gamma)} \qquad (3)$$

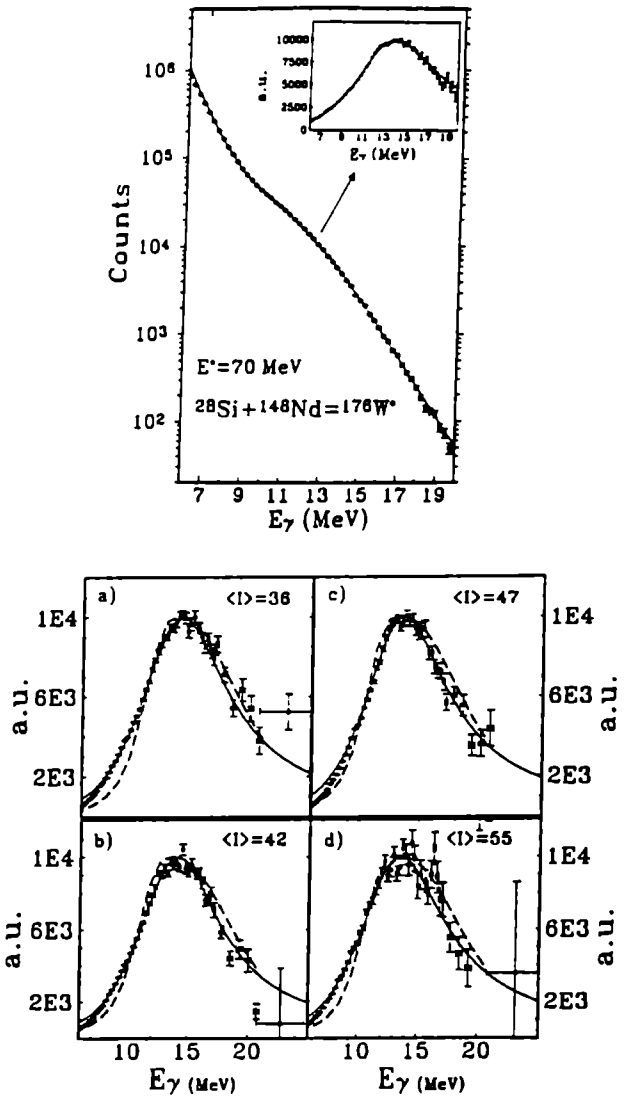

Figure 1 *Top: measured γ spectrum associated to fold $F \geq 9$ (circles). The full drawn line shows the best fitting statistical model calculation using E_{GDR} = 14.0 MeV and Γ_{GDR} = 8.8 MeV. Inset: the same spectrum displayed in linearized form as explained in the text. Bottom: the measured and calculated strenght function for ^{176}W in four spin windows. (a) corresponds to $< I >$ = 36, E_{GDR} = 14.2 MeV, Γ_{GDR} = 8.9 MeV; (b) corresponds to $< I >$ = 42, E_{GDR} = 14.1 MeV, Γ_{GDR} = 8.4 MeV; (c) corresponds to $< I >$ = 47, E_{GDR} = 13.6 MeV, Γ_{GDR} = 8.6 MeV; (d) corresponds to $< I >$ = 55, E_{GDR} = 13.5 MeV, Γ_{GDR} = 8.9 MeV. Also shown are the Lorentzian obtained from the best fitting statistical model calculations (full drawn lines). Adiabatical calculations as described in the text are also shown (dashed lines).*

Contrary to the strength function the $a_2(E_\gamma)$ depends on orientation fluctuations which produce an attenuation of the angular anisotropy that is particularly large at low spins.

3. The experiments

The γ rays emitted by the selected heavy ion reactions were measured by the detection system HECTOR [3]. It consists of 8 large volume BaF_2 detectors (14.5 cm in diameter x 17.5 cm in length) measuring the energy and the time of the high energy gamma rays at 4 different angle pairs ($\pm 160^0$, $\pm 120^0$, $\pm 90^0$, and $\pm 60^0$) and 38 small BaF_2 (5.54cm x 7.54 cm covering altogether a fraction larger than 80% of the full solid angle) placed around the target used as a multiplicity filter for low-energy γ transitions. Gain drifts of the large volume BaF_2 were corrected to better that 0.2% using the light pulses of an LED system.

The quadrupole coefficient a_2 was extracted as a function of the γ energy E_γ by fitting the measured spectra of the high energy γ rays with the function $N(E_\gamma, \theta) = N_0(E_\gamma)[1 + a_2(E_\gamma)P_2(cos\theta)]$, where $P_2(cos\theta)$ is the Legendre Polynomial.

4. The strength function and angular distribution of GDR photon from $^{176}W^*$

Fig. 1 (top part) shows the measured high energy γ-ray spectrum associated to coincidence fold of low energy γ rays $F_\gamma \geq 9$. The reaction ^{28}Si (E_{beam} = 147 MeV) + ^{148}Nd was used, leading to the ^{176}W compound at excitation energy E^* = 70 MeV and average angular momentum $\approx$ 40 $\hbar$. It is apparent that this "inclusive" spectrum is well fitted by the shown statistical model calculations (full drawn lines) using the GDR parameters E_{GDR}=14.0 MeV and Γ_{GDR} =8.8 MeV. For the statistical model calculations the code CASCADE was employed. The dipole strength was assumed to exhaust 100% of the energy weighted sum rule (EWSR). The level density parameter a was $\frac{A}{8}$ in accord with most previous analysis in this excitation energy region.

The high energy γ-ray data have been also sorted gating on different F_γ intervals to select different angular momentum I regions.

The data corresponding to the selected restricted regions of I are shown together with the statistical model calculations in figure 1 (bottom part). In this figure and in the inset, the quantity $F(E_\gamma) * Y_\gamma^{exp}(E_\gamma)/Y_\gamma^{cal}(E_\gamma)$ was plotted in order to display spectra on a linear scale to emphasize the GDR region. The espression $Y_\gamma^{exp}(E_\gamma)$ represents the experimental spectrum and $Y_\gamma^{cal}(E_\gamma)$ the best fit calculated spectrum, corresponding to the single Lorentzian function $F(E_\gamma)$. Calculations with two Lorentzians gave poorer fits to the data.

The measured GDR width is found to be constant within the error bars when the angular momentum varies in the considered interval. This result is in contrast with the result of the study of $^{109,110}Sn$ at T= 1.8 MeV and angular momentum in the same interval. In that case an increase of the width of the order of 20% was found,

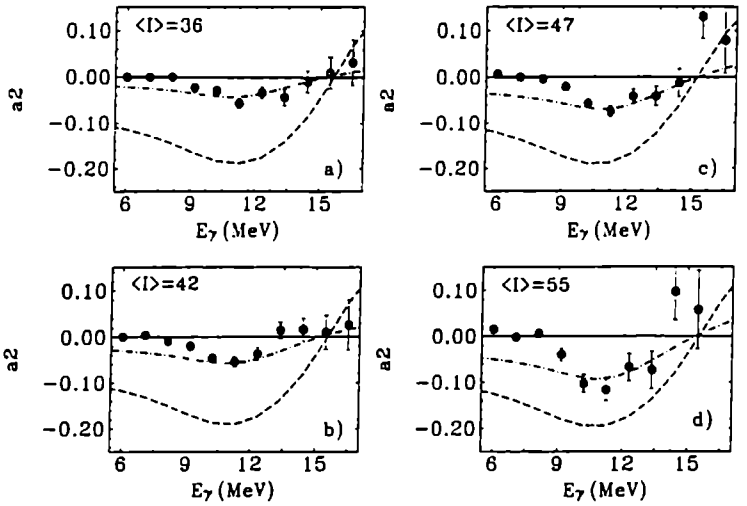

Figure 2 *The measured $a_2(E_\gamma)$ coefficients as a function of E_γ. The four plots correspond to different spin windows centered at the average value (in $\hbar$ units) shown in each panel. The experimental points (full circles) are compared with adiabatic calculations including only thermal shape fluctuations (dashed line) and including both thermal shape and orientation fluctuations (dot-dashed line).*

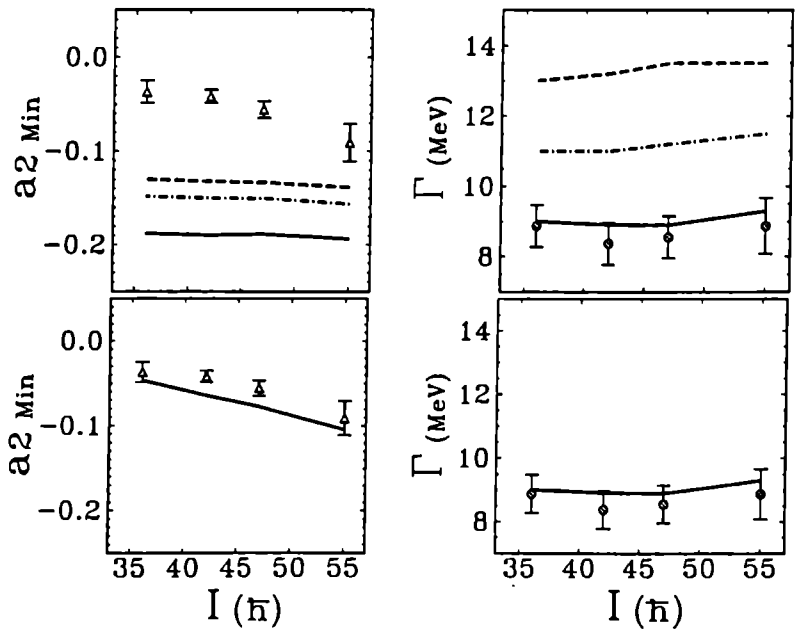

Figure 3 *The measured values of the minimum of $a_2(E_\gamma)$ (left column) and of the Γ_{GDR} (right column) as a function of spin of compound nucleus ^{176}W are compared with calculations. In the top row the data are compared with the predictions of an adiabatical model including only shape fluctuations with intrinsic width $\Gamma_0^{\downarrow} = 4.7$ MeV (full drawn lines), $\Gamma_0^{\downarrow} = 9.0$ MeV (dot-dashed lines) and $\Gamma_0^{\downarrow} = 12.0$ MeV (dashed lines). In the bottom row calculation including thermal fluctuations of shape and orientation and using $\Gamma_0^{\downarrow} = 4.7$ MeV are shown (full drawn lines).*

attributed to shape changes driven by angular momentum (centrifugal stretching of the oblate shape). Consequently, the present data of the GDR width suggest that the effective shape distributions to which the giant dipole vibration couples do not change substantially when the angular momentum is increased at this temperature. In addition, since the rotational frequencies, in the case of ^{176}W, are almost a factor of two smaller than in ^{110}Sn in the same angular momentum interval, the smaller measured widths for ^{176}W are consistent with smaller deformations due to slower rotation.

The calculated GDR strength functions including only shape fluctuations are shown with the dashed lines in figure 1 in comparison with the data. The associated FWHM are displayed in figure 3 together with the measured GDR width. Note the very good agreement between the data and the model predictions. The calculated shape distributions have equilibrium deformations that are oblate and whose size is changing from the value β=0.06 at I= 35 $\hbar$ (ω = 0.4 MeV) to β = 0.14 at I = 55 $\hbar$ (ω = 0.6 MeV)). In spite of this, the calculated GDR widths do not change appreciably. This is a consequence of the small equilibrium deformations and of the shape averaging that give rise to a GDR response reflecting more similar effective shapes.

The measured $a_2(E_\gamma)$ for the different angular momentum windows are shown in figure 2. In contrast to the near constancy of the GDR width the angular anisotropy (around E_γ = 10-12 MeV) increases by more than a factor of two when the angular momentum increases.

In order to summarize the present findings for the GDR width and $a_2(E_\gamma)$ as a function of angular momentum and to discuss the role of both thermal fluctuations and collisional damping we show in figure 3 the minimum value of the $a_2(E_\gamma)$ distribution (left columns) and the GDR width resulting from the statistical model analysis of the measured spectra (right column) in comparison with different theoretical predictions. The calculated GDR widths were taken from the line shapes shown with the dashed lines in the rigth part of figure 1. Similarly calculated $a_2(E_\gamma)$ values have been taken as the minimum value of the distributions shown in figure 2. In the top row of figure 3 the data are compared with calculations including only shape fluctuations and using $\Gamma_0^\downarrow$ = 4.7 MeV for the collisional damping width, as deduced from the T= 0 MeV systematics. These calculations are displayed with the full drawn lines. While the calculations account well for the measured systematics of the GDR widths, the $a_2(E_\gamma)$ systematics are severely overestimated indicating that shape fluctuations alone cannot give a consistent description of the two observables. From (3) one sees that the magnitude of the angular anisotropy is decreased when the overlap of the stretched and unstrected components increases. A way to increase this overlap and thus decrease the calculated a_2 value is to increase the collisional damping width $\Gamma_0^\downarrow$ (as shown in the top part of figure 3). Nevertheless, even for a very large $\Gamma_0^\downarrow$ = 12 MeV (dashed lines) the calculated anisotropy is still larger than the measured values but in addition the width is grossly overestimated. Instead, by considering in the calculations shape and orientation fluctuations but keeping $\Gamma_0^\downarrow$ =4.7 MeV equal to the T = 0 MeV value the two measured observables are con-

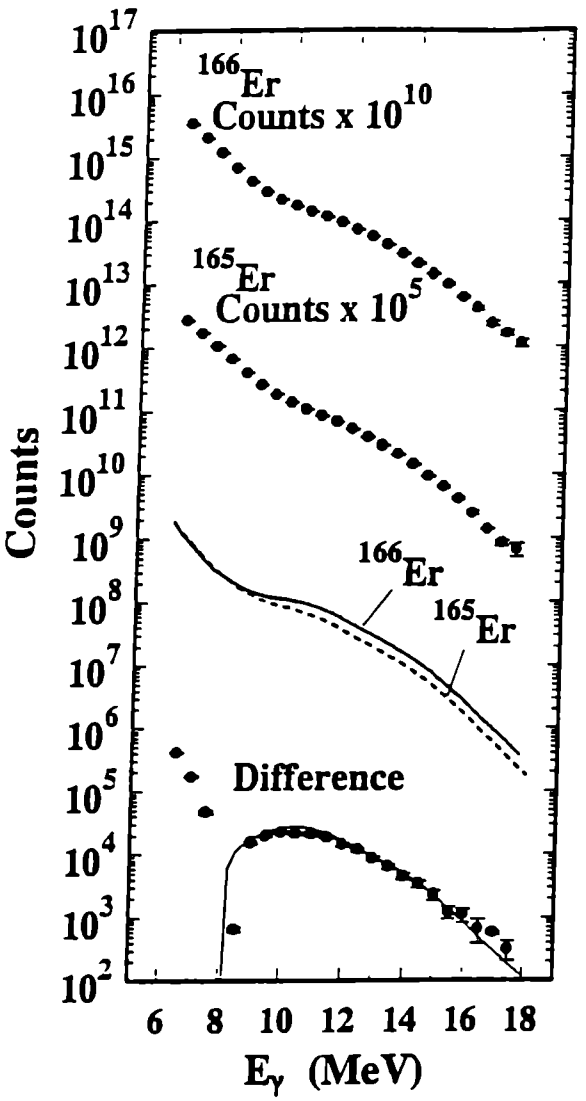

Figure 4. *The measured high energy γ-ray spectra for ^{166}Er and ^{165}Er are shown with filled circles together with their difference. The associated statistical model calculations, with GDR parameters given in the text, are shown with the lines and their difference is compared to the experimental data.*

sistently reproduced by the calculations, (bottom row of figure 3 and see also the dot-dashed lines in figure 2). We also note that the increase of the absolute value of the a_{2min} with angular momentum (while Γ_{GDR} stays constant) independently indicates that orientation fluctuations decrease with increased rotation.

The present study of ^{176}W at fixed temperature, but varying angular momentum, shows that both shape and orientation fluctuations play a significant role in explaining the measured the GDR width and $a_2(E_\gamma)$. The collisional damping does not change with angular momentum and remains equal to the T = 0 MeV value, supporting the predictions of reference 6. In addition this result agrees with that obtained with the experimental study of excited ^{109,110}Sn nuclei that have very different shape distributions [1].

5. The GDR in hot ^{166}Er studied with the difference technique

A limitation of most of the existing comparisons between measured and calculated GDR strength functions, is that they are based on spectra reflecting the γ emission from the entire ensamble of nuclei that are populated by the deexcitation cascades of the compound nucleus. Although the hottest part of the deexcitation cascade gives the largest contribution to the total yield at γ-energies larger than the neutron binding energy, the selection of the decay restricted to a narrow interval of excitation energy results in an improved experimental sensitivity over the inclusive measurements which sample the entire phase space available for the decay.

A study of the GDR decay associated to a narrow interval of excitation energy for the nucleus ^{166}Er has been made making use of the reactions $^{18}O(E_{beam} = 78MeV) + ^{148}Nd \rightarrow ^{165}Er(E^* = 51MeV)$, and $^{17}O(E_{beam} = 70MeV) + ^{148}Nd \rightarrow ^{166}Er(E^* = 45MeV)$. The detector array HECTOR in the configuration described in [3] has been employed. The method to isolate the high energy γ-rays from the decay of the GDR from the hottest compound is based on energy difference technique [3,7]. The two measured spectra (see figure 4) were normalized in the region E_γ = 8 MeV to the values calculated with the statistical model assuming the same total fusion cross sections for the two reactions. The statistical model calculations were made with the code CASCADE and a two Lorentzian GDR strength function was used. In accordance with the results of refs. 7 and 8, the employed parameters were $E_1^{gdr} = 12.5MeV, \Gamma_1^{gdr} = 4.6MeV, E_2^{gdr} = 15.2MeV, \Gamma_2^{gdr} = 4.2MeV, S_1 = 60\%, S_2 = 40\%$, for ^{166}Er and $E_1^{gdr} = 12.5MeV, \Gamma_1^{gdr} = 4.3MeV, E_2^{gdr} = 15.2MeV, \Gamma_2^{gdr} = 4.0MeV, S_1 = 60\%, S_2 = 40\%$, for ^{165}Er. The two statistical model calculations, displayed in figure 3, show a rather small increase of the γ-yield above 10 MeV because of the small difference in excitation energy (ΔE^* = 6 MeV). The difference of these two calculations contains 13% of the total ^{166}Er spectrum in the region E_γ= 10-17 MeV. The measured difference spectrum is remarkably well reproduced by the calculated difference both in shape and in yield. It is worth noticing that the present measurements represent an accurate test of the statistical model.

In the case of identical spin distributions for the two reactions the difference spectrum coincides with the first step decay of the compound nucleus. In the present

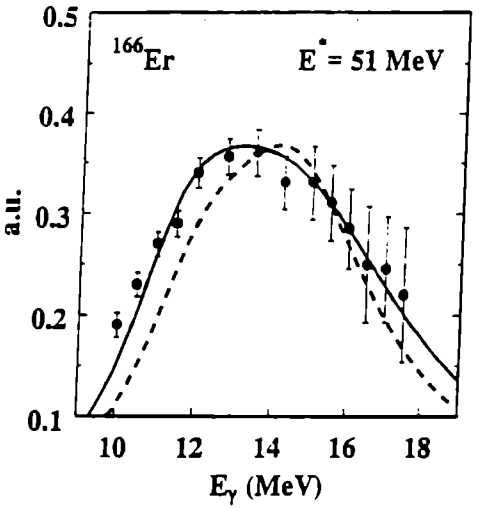

Figure 5. *The dipole strength function for ^{166}Er, obtained from the difference spectrum as described in the text. The full drawn line is a calculation of thermal shape and orientation fluctuation at T= 1.3 MeV and I = 23 ħ with collisional damping equal to the T=0 value ($\Gamma_0^{\downarrow}$ = 4.7 MeV). The dashed line is the predicted line shape at the equilibrium deformation at T = 1.3 MeV.*

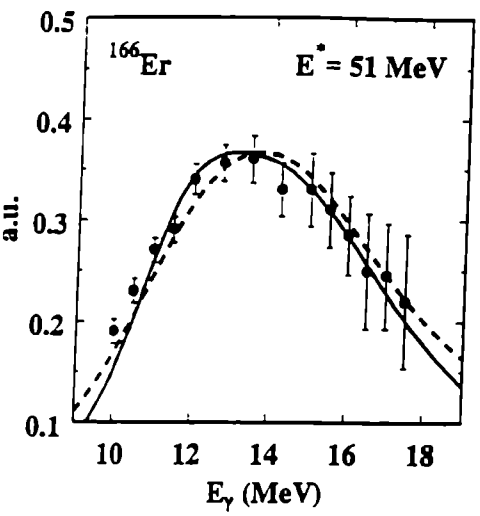

Figure 6. *The dipole strength function for ^{166}Er, obtained from the difference spectrum as described in the text. The full drawn line is the same calculation of figure 4 while the the dashed line is the predicted GDR shape for the equilibrium deformation at T = 1.3 and with collisional damping width $\Gamma_0^{\downarrow}$ = 7 MeV.*

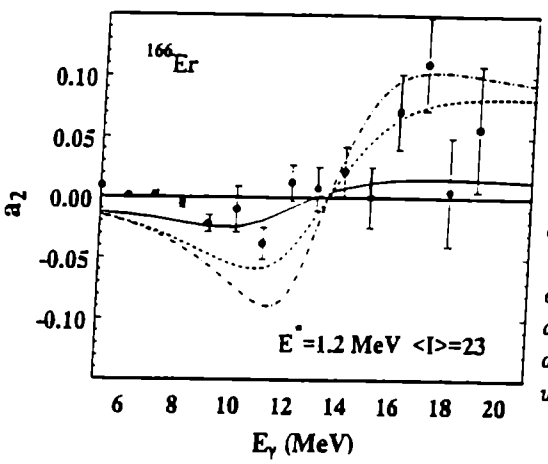

Figure 7. *The $a_2(E_\gamma)$ deduced from the angular distribution measurements is plotted as a function of the energy of the γ-rays and compared with the predictions. The full drawn line is a calculation of thermal shape and orientation fluctuation at T= 1.3 MeV and I = 23 ħ with $\Gamma_0^{\downarrow}$ =4.7 MeV (as at T=0). The dotted-dashed line is the predicted line shape at the equilibrium deformation at T = 1.3 with $\Gamma_0^{\downarrow}$ = 4.7 MeV while the dashed line is a calculation at the equilibrium deformation with $\Gamma_0^{\downarrow}$ = 7 MeV.*

case there is some mismatch in the spin distribution because the average spin is 23 $\hbar$ for ^{166}Er and 16 $\hbar$ for ^{165}Er. However, due to the fact that at temperature T = 1.3 MeV (cf. ref. 10) the shape distributions of Er are not sensitively changing when the angular momentum varies in the interval 0-35 $\hbar$, the difference spectrum, containing to a large extent the first step decay (up to $\approx$ 80 %), should reflect mainly temperature effects.

In order to emphasize the details of the measured GDR strength function, the experimental spectrum of figure 3 has been divided by the statistical model calculation of the first step decay of the compound nucleus with a constant B(E1) strength. The resulting spectral shape is shown in figure 5 together with spectral shape calculated within the model of thermal shape and orientation fluctuations. The full drawn line curve uses a collisional damping width equal to the zero temperature value as in references 4 and 5. The GDR line shape calculated at the equilibrium deformation (dashed line of figure 5) does not account equally well for the experimental data.

However, in the case one wants to disregard thermal fluctuations, it is still possible by using an intrinsic collisional damping width of 7 MeV and the nuclear deformation of the equilibrium shape to obtain a rather satisfactory description of the measured GDR line shape. This calculation is shown in figure 6 with the dashed line. The present comparisons, although the most direct and precise so far made, do not allow to infer unambiguosly that collisional damping is equal to the zero temperature value and that thermal fluctuations are responsible for the observed line shape.

For the ^{166}Er nucleus we have also measured the angular distribution of the total gamma yield. In figure 7, the measured $a_2(E_\gamma)$ is compared to the theoretical predictions corresponding to the ones of figures 5 and 6. It is clear from the comparison of the measured and predicted $a_2(E_\gamma)$ that the adiabatic calculation with collisional damping equal to the zero temperature value gives a better description of the data while the calculation associated to the equilibrium deformation and with collisional damping equal to 7 MeV does not reproduce equally the experimental results.

6. Conclusion

The studies the γ-rays from the GDR in excited nuclei based on rather exclusive experiments sampling restricted intervals of excitation energy or of angular momentum, have allowed a more detailed investigation of shape effects and of the damping mechanisms of collective states at finite temperature.

The combined analyses of the GDR strength function and of angular distribution in ^{166}Er and ^{176}W show unambiguosly the important role of thermal shape fluctuations and suggest that at moderate temperatures the collisional damping width is equal to the zero temperature value. This results is in agreement with other experimental studies made in the mass regions A =110 [1] for nuclei characterized by different sizes and types of deformations.

7. References

1. A. Bracco et al. *Phys. Rev. Lett.*74,(1995)3748.
2. M. Mattiuzzi et al.,to be published in *Phys. Lett.* **B** (1995).
3. A. Maj et al. *Nucl. Phys.* **A571** (1994)185
4. E. W. Ormand et al *Phys. Rev. Lett.* **64**(1990) 2254; and E. W. Ormand et al. *Phys. Rev. Lett.* **69**(1992) 2905.
5. Y. Alhassid, B. Bush *Phys. Rev. Lett.* **65**(1990)2527
6. F. V. De Blasio et al., *Phys. Rev. Lett.* **68**, 1663 (1992).; and P.F. Bortignon et al.,*Nucl. Phys.* **A460** (1986)149.
7. Van Schagen *Phys. Lett.***B** 1995
8. C. Gossett et al. *Phys. Rev. Lett.* **54** (1985)1496
9. J.J. Gaardhøje et al. *Phys. Rev. Lett.* **53**,(1984)148.
10. F. Camera *Nucl. Phys.* **A572**(1994)401.

Temperature dependence of the response function of hot nuclear matter

Abdellatif Abada[1] and Dominique Vautherin[2]
[1] *Theoretical Physics Group, Department of Physics and Astronomy, University of Manchester, Manchester M13 9PL, UK*
[2] *Division de Physique Théorique *, Institut de Physique Nucléaire Orsay Cedex, F-91406, France*

ABSTRACT

The description of collective motion in nuclei at finite temperature using the framework of the random phase approximation is discussed. We focus on the special case of the isovector response function of hot nuclear matter using various effective Skyrme interactions.

1. Introduction

The purpose of the present notes is to investigate the response function of hot nuclear matter. We use the framework of time dependent mean field theory with the standard Skyrme type effective interactions which have provided in the past good descriptions of average nuclear properties. For such interactions analytic expressions for the response function are derived. From these analytic formulae we show that one can gain an understanding of the temperature dependance of the giant dipole resonance in finite nuclei. Although effects which are beyond the framework of linear response theory are important to account for the full width of the giant dipole state (e.g. two particle two hole configurations) many features of these resonances are known to be readily understood at this level already [1,2,3,4,5]. In the following we show that zero sound type modes become less collective as temperature rises and sometimes disappear at temperatures of a few MeV. We also show that for effective interactions with an effective mass close to unity collective effects are small already at zero temperature and depend weakly on temperature. We will thus argue that the temperature dependance of the giant dipole resonance provides valuable information on the effective interaction.

2. Linear response theory in hot nuclear matter

When an external field of the form

$$V_{\rm ext} = \epsilon \tau_3 e^{i(\mathbf{q}.\mathbf{r}-(\omega+i\eta)t}, \qquad (1)$$

*Unité de Recherche des Universités Paris XI et Paris VI associée au CNRS

is applied to nuclear matter, it induces a density change between neutron and proton densities which is of the form

$$\delta\rho(\mathbf{r},t) = \rho_n(\mathbf{r},t) - \rho(\mathbf{r},t) = \eta e^{i(\mathbf{q}.\mathbf{r}-(\omega+i\eta)t}. \tag{2}$$

The ratio of the amplitude α of the density oscillations to the external field strength is the response function (also called dynamic polarizability)

$$\Pi(\omega,q) = \frac{\alpha}{\epsilon} \tag{3}$$

In the case of Skyrme type forces it is possible to find analytic expressions for the response function of nuclear matter at finite temperature [6,7].

Calculations are particularly simple in the case of a simplified Skyrme interaction

$$v = t_0(1 + x_0P_\sigma)\delta(\mathbf{r}_1 - \mathbf{r}_2) + t_3\delta(\mathbf{r}_1 - \mathbf{r}_2)\delta(\mathbf{r}_2 - \mathbf{r}_3). \tag{4}$$

In this particular case one has the simple formula

$$\Pi(\omega,\mathbf{q}) = \frac{\Pi_0(\omega,\mathbf{q})}{1 - V_0\Pi_0(\omega,\mathbf{q})}, \tag{5}$$

where Π_0 is the unperturbed polarization propagator [8], also called Lindhard function

$$\Pi_0(\omega,\mathbf{q}) = \frac{2}{(2\pi)^3}\int d\mathbf{k}\frac{f(\mathbf{k}+\mathbf{q}) - f(\mathbf{k})}{\omega + i\eta - \epsilon(\mathbf{k}) + \epsilon(\mathbf{k}+\mathbf{q})}. \tag{6}$$

and where

$$V_0 = -t_0(x_0 + 1/2)/2 - t_3\rho_0/8. \tag{7}$$

For a given momentum $\mathbf{q}$ we thus see that there is a resonant response when the frequency ω of the external field corresponds to a zero in the denominator i.e. when

$$1 = V_0\Pi_0(\omega,\mathbf{q}). \tag{8}$$

The real part of ω determines the energy of the collective mode and its imaginary part the lifetime [8].

The previous formulae correspond to the special case of a simplified Skyrme force. They can however be generalized to the case of a full Skyrme force. Such an interaction contains a density independent part v_{12} and a density dependent part v_{123}. The density independent part is parametrized in momentum space as

$$< \mathbf{k}|v_{12}|\mathbf{k}' >= t_0(1 + x_0P_\sigma) + \frac{t_1}{2}(1 + x_1P_\sigma)(k^2 + k'^2) + t_2(1 + x_2P_\sigma)\mathbf{k}.\mathbf{k}'. \tag{9}$$

The density dependent part in ordinary space is

$$v_{123} = \frac{t_3}{6}(1 + x_3P_\sigma)\delta(\mathbf{r}_1 - \mathbf{r}_2)\rho^\sigma(\frac{\mathbf{r}_1 + \mathbf{r}_2}{2}). \tag{10}$$

For such an interaction the response function is given by

$$\Pi(\omega,\mathbf{q}) = \frac{\Pi_0(\omega,\mathbf{q})}{1-\bar{V}_0\Pi_0(\omega,\mathbf{q}) - 2V_1\Pi_2(\omega,\mathbf{q}) - V_1^2\Pi_2^2(\omega,\mathbf{q}) - V_1^2\Pi_4\Pi_0}. \tag{11}$$

In this equation Π_2 and Π_4 are generalized Lindhard functions defined by

$$\Pi_{2N}(\omega,\mathbf{q}) = \frac{4}{(2\pi)^3}\int \mathrm{d}^3k \frac{f(\mathbf{k}+\mathbf{q}) - f(\mathbf{k})}{\omega + i\eta - \epsilon(\mathbf{k}) + \epsilon(\mathbf{k}+\mathbf{q})} (\mathbf{k}.(\mathbf{k}+\mathbf{q}))^N \ , \tag{12}$$

while V_0 and V_2 are linear combinations of the parameters of the Skyrme interaction. Explicitely one has

$$\begin{aligned} V_0 = \ & -\frac{t_0}{2}\left(x_0+\frac{1}{2}\right) - \frac{t_3}{12}\left(x_3+\frac{1}{2}\right)\rho_0^\alpha \\ & -\frac{q^2}{16}(3t_1(1+2x_1)+t_2(1+2x_2)) \\ & -\left(\frac{m^*\omega}{q}\right)^2 \frac{2V_1}{1-2V_1m^*\rho_0}, \end{aligned} \tag{13}$$

where m^* is the effective mass and ρ_0 the saturation density of nuclear matter, while V_1 is:

$$V_1 = \frac{1}{16}(t_2(1+2x_2) - t_1(1+2x_1)) \tag{14}$$

In reference [10] a discussion of the properties of the response function in the case of a simplified Skyrme interaction was provided. It was found that for a momentum transfer q=0.23 fm^{-1} (a value which corresponds to the giant dipole resonance in lead- 208 in the Steinwedel- Jenssen model) the response function exhibits a sharp zero sound type peak at zero temperature. In contrast when temperature rises the smearing of the Lindhard function was found to make the peak much weaker and in fact nearly disappear for temperatures of a few MeV. Whether this conclusion holds for the more realistic Skyrme forces is a question which was investigated in reference [6]. Some results of this study are shown in Figure 1.

Fig.1a (left side) gives the strength

$$S(\omega) = -\frac{1}{\pi}\Im m\Pi(\omega,q). \tag{15}$$

as a function of the frequency ω for a momentum transfer q= 0.23 fm^{-1} in the case of the Skyrme force SIII while Fig.1b (right side) corresponds to interaction SV. It can be seen that for interaction SIII collective effects disappear as soon as temperature reaches a few MeV while for SV only a weak temperature dependance is observed. In reference [6] the difference between these two cases was attributed to a difference between the effective mass values for the two interactions. This difference shows that the temperature dependance of the response function provides information on the effective particle hole interaction. In this context it is worthwhile noting

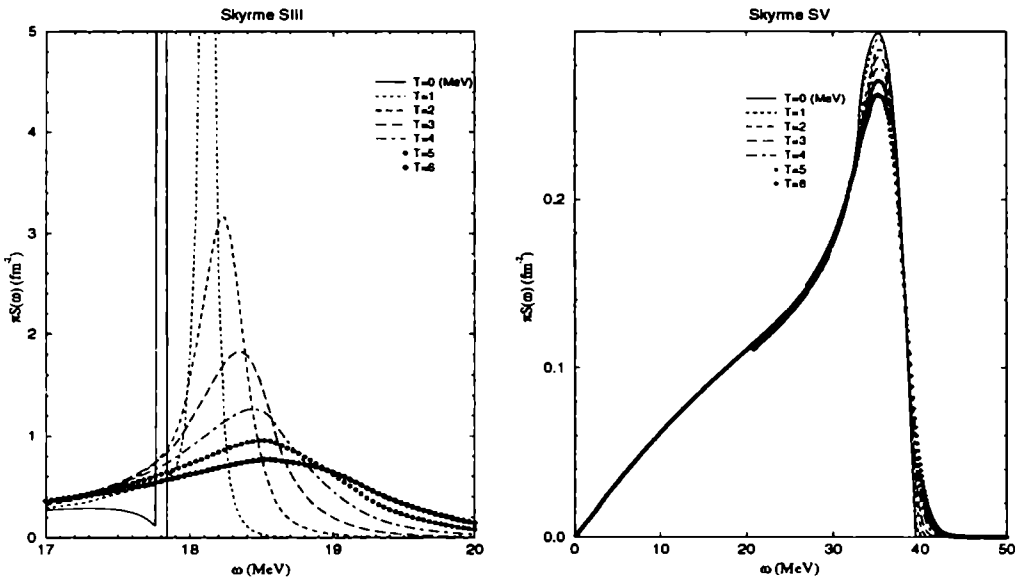

Fig. 1. Distribution of strength as a function of the frequency ω for a momentum transfer q=0.23 fm^{-1} in the case of interactions SIII and SV

that recent experimental studies of the giant dipole resonance found a saturation of photon multiplicities at high excitation energy [11]. This may be a signature of the loss of collectivity found at high temperature in the present calculation.

Acknowledgements One of us (D.V.) wishes to thank Prof. Apolodor Raduta for his invitation to present this lecture at the 1995 Predeal School on Nuclear Structure.

1. M. E. Faber, J. L. Egido and P. Ring, Phys. Leett. **127B** (1983) 5
2. M. Sommerman, Ann. of Phys. **151** (1983) 163
3. H. Sagawa and G. F. Bertsch, Phys. Lett. **333B** (1994) 289
4. D. Vautherin and N. Vinh Mau, Nucl. Phys. **A422** (1984) 140
5. N. Vinh Mau, Nucl. Phys. **A548** (1992) 381
6. F. Braghin, D. Vautherin and A. Abada, Phys. Rev. C (1995), in press
7. E.S.Hernandez, J. Navarro, A. Polls and J. Ventura, Finite Temperature RPA in Symmetric Nuclear Matter with Skyrme Interactions, University of Valencia preprint, July 27th, 1995
8. A.L. Fetter and J.D. Walecka, Quantum Theory of Many Particle Systems (Mc Graw-Hill, New York, 1971)
9. C. Garcia- Recio, J. Navarro, Nguyen van Giai and L.L Salcedo Ann. Phys. **214** (1992) 293
10. F. Braghin and D. Vautherin, Phys. Lett. **333B** (1994) 289
11. J. H. Le Faou *et al.*, Phys. Rev. Lett. **72** (1994) 3321

5. RELATIVISTIC COLLISIONS

RELATIVISTIC NUCLEAR COLLISIONS FROM THE EOS EXPERIMENT AT THE BEVALAC: COLLECTIVE OBSERVABLES AND MULTIFRAGMENTATION

A. Insolia for the EOS Collaboration:
S. Albergo[7], F. Bieser[1], F. P. Brady[4], Z. Caccia[7] , D. A. Cebra[4], A. D. Chacon[5], J. L. Chance[4], Y. Choi[3]† , S. Costa[7], J. B. Elliott[3], M. Gilkes[3], J. A. Hauger[3], A. Hirsch[3], E. L. Hjort[3], A. Insolia[7], M. Justice[2], D. Keane[2], V. Lindenstruth[6], M. Lisa[1], H. S. Matis[1], M. McMahan[1], C. McParland[1], W. F. J. Müller[6], D. L. Olson[1], M. D. Partlan[4], N. Porile[3], R. Potenza[7], G. Rai[1], J. Rasmussen[1], H. G. Ritter[1], J. Romanski[7]⋆ , J. L. Romero[4], G. V. Russo[7], H. Sann[6], R. Scharenberg[3], A. Scott[2], Y. Shao[2], B. Srivastava[3], T. J. M. Symons[1], M. Tincknell[3], C. Tuvè[7], S. Wang[2]‡ , P. Warren[3], H. H. Wieman[1], K. L. Wolf[5]

[1] *Nuclear Science Division, Lawrence Berkeley Laboratory, Berkeley, California, 94720*
[2] *Kent State University, Kent, Ohio, 44242*
[3] *Purdue University, West Lafayette, Indiana, 47907-1396*
[4] *University of California, Davis, California, 95616*
[5] *Texas A&M University, College Station, Texas, 77843*
[6] *Gesellschaft für Schwerionenforschung, D-64220 Darmstadt, Germany*
[7] *Università di Catania & INFN-Sezione di Catania, 95129 Catania, Italy*

ABSTRACT

The EOS Collaboration has completed an exclusive study of relativistic heavy ion collisions at the Bevalac using a variety of projectile, target and beam energy combinations. We report here results on directed sideward flow in Au + Au between $0.25A$ and $1.2A$ GeV, using a standard in-plane transverse momentum analysis.We also report on projectile fragmentation of Au in C at $1A$ GeV. An analysis of fluctuations and critical exponents for small systems seems to support the idea that the multifragmentation regime is associated with a liquid-gas phase transition in nuclear matter.

1. Introduction

Experiments at the Bevalac using the Plastic Ball and streamer chamber initiated the study of nucleus-nucleus collisions with close to 4π acceptance for charged particles [1]. Much was learned as a result of those experiments, and by the mid 1980s, there

† Current address: Sung Kwun Kwan University, Suwon 440-746, Republic of Korea
⋆ Current address: The Svedberg Laboratory, University of Uppsala, S751-21 Uppsala, Sweden
‡ Current address: Harbin Institute of Technology, Harbin 150001, People's Republic of China

was a widespread belief that it would soon be possible to constrain unambiguously the Equation Of State (EOS) of the compressed hadron gas that exists for a few fm/c during the early stage of the collision. During the years since then, we have come to a better understanding of the difficulties involved in inferring properties of the nuclear EOS, and while these difficulties are surmountable, there are some indications that experimental observables are less strongly influenced by the state variables of interest than it was initially assumed [2,3]. This is in part due to uncertainties in the theoretical description of the collision dynamics, like the influence of in-medium effects and momentum-dependent interactions on the EOS. We now hope ambiguities may be resolved by requiring models to simultaneously describe a comprehensive set of observables that are sensitive to the underlying EOS. This motivates new measurements with good statistics and the smallest possible observational biases, in order to experimentally establish the values and behavior of as many observables as possible.

2. The EOS Experiment

The EOS experiment was conducted at the Lawrence Berkeley Laboratory's Bevalac facility. The experimental setup consisted of four complementary detector systems to provide nearly complete phase space coverage: the new 4π continuous-tracking time projection chamber (TPC), called "EOS", a multiple sampling ionization chamber (MUSIC II) [4] positioned to intercept projectile spectator fragments, an array of scintillator slats to provide time-of-flight information (the TOF Wall), and a high efficiency neutron detector (MUFFINS) [5] centered on zero degrees with respect to neutrons emitted from the target. Details about the EOS TPC chamber, the electronics and the data acquisition have been reported previously [6,7,9].

The current status of results on collective observables as flow and multifragmentation will be reported here, in Sect. 3 and Sect. 4, respectively. Comparison with some theoretical calculations will be discussed. A more detailed account of the EOS data, can also be found in [8].

3. Collective Flow

One of the many interesting aspects of heavy ion collisions is the presence of collective motion that is the result of the expansion of the highly compressed nuclear matter created during the collision. This effect, known as directed collective flow, has been demonstrated in previous experiments[10,11]. Collective flow is evidence of a pressure build up during the collision process. The pressure can be related through models to the amount of compression achieved. For a recent review see A. Bonasera et al. [13]

One of the goals of the EOS collaboration was to complete a new measurement of collective flow in Au+Au collisions at the highest available energies to complement the study done earlier by the Plastic Ball group at the Bevalac.

In this proceedings, we report the results on directed sideward flow in collisions of Au + Au at beam energies of 0.25, 0.4, 0.60, 0.80, 1.00, 1.2A GeV [12].

3.1. In-Plane Transverse Momentum

To facilitate comparisons with previous work, our investigation of collective effects in Au + Au collisions starts with the same in-plane transverse momentum analysis with essentially the same data selection criteria as used by the Plastic Ball group [14,1]. In particular, all nuclear fragment species up to ^{4}He are included, and we select an interval of multiplicity centered about the value where the flow has its maximum. The in-plane transverse momentum method[15] involves estimating the orientation of the reaction plane for each event using the vector $\mathbf{Q} = \sum_{\nu=1}^{M} w(y_\nu)\mathbf{p}_\nu^\perp$, where $\mathbf{p}_\nu^\perp$ is the transverse momentum for the νth baryon track, $w(y_\nu)$ is a rapidity-dependent weighting factor, and M is the observed multiplicity.

A measure of directed flow is the amount of momentum per nucleon transferred to the participant region, $\langle p^x/A \rangle$. The quantity $\langle p^{x'}(y')/A \rangle$ is the mean component of transverse momentum per nucleon in the estimated reaction plane, where

$$p_\nu^{x'} = \mathbf{p}_\nu \cdot \hat{\mathbf{Q}}_\nu \,, \qquad \mathbf{Q}_\nu = \sum_{\mu \neq \nu} w(y_\mu)\mathbf{p}_\mu^\perp \,, \tag{1}$$

and $\hat{\mathbf{Q}}$ denotes a unit vector. Auto-correlations of the i^{th} fragment with the determined reaction plane are removed by determining the reaction plane for the i^{th} fragment by excluding the i^{th} fragment from the sum in eq. 1. We use the subevent method [15,14] to correct for this dispersion effect.

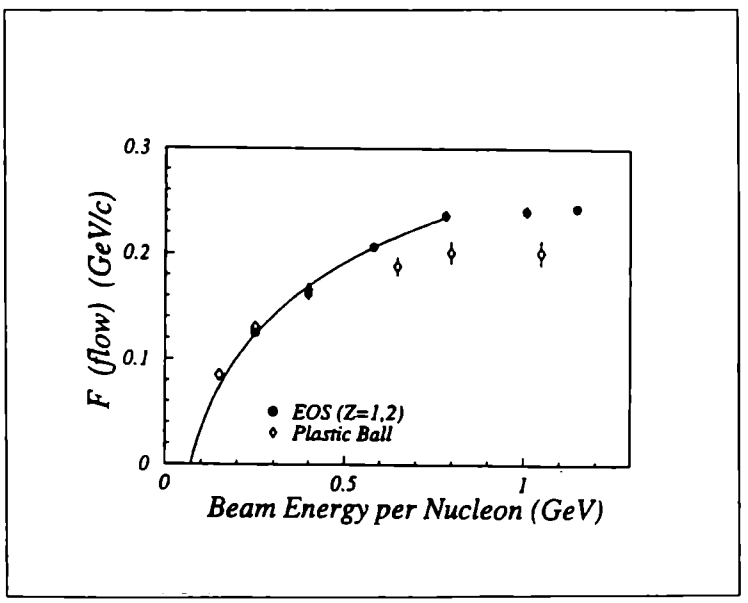

Figure 1: Flow excitation function for Au + Au collisions for Au + Au events measured by EOS and by the Plastic Ball.

We have studied the dependence of flow on fragment mass. For all the measured beam energies, we obtain the fragment-specific flow excitation functions shown in Fig. 2. This is the first measurement of this kind for light fragments over a range of intermediate incident energies, and shows both a consistent trend of increasing flow with increasing energy for each fragment species separately, and a consistent pattern of increasing flow per nucleon with increasing fragment mass A, over the whole measured energy range. Such an increase was previously reported by the Plastic Ball Group at a single energy, $0.2A$ GeV [16].

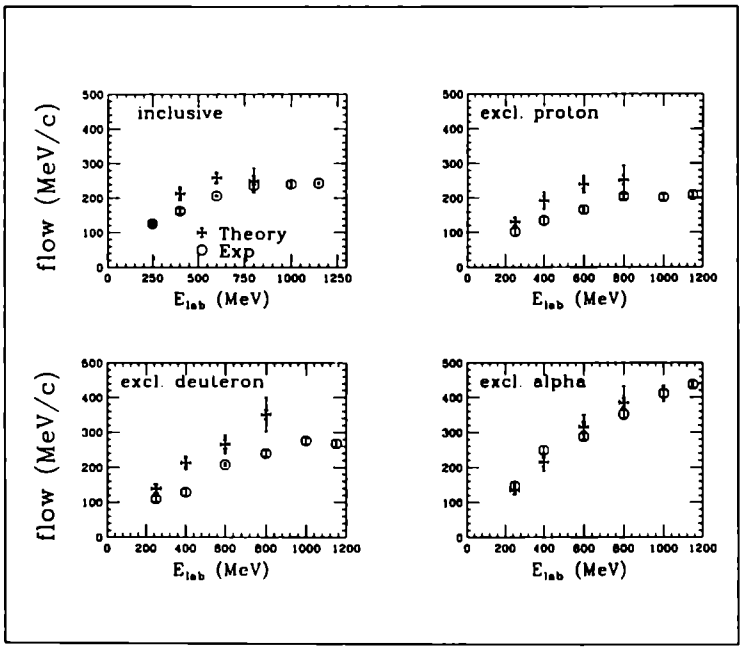

Figure 2: Inclusive (p + d + t + alpha) and exclusive (for proton and alpha) flow excitation functions.

3.2. BNV calculations with a momentum dependent mean field

In a transport model description, particles located at the very center of the collision region at the time of maximum density are likely to experience a smaller integrated potential gradient and a smaller sideward deflection. However, coalescence alone produces an increase in $\langle p^x(y')/A \rangle$ with fragment mass A and so offers a possible alternative explanation.

The idea of expressing flow magnitudes in scale-invariant form originated with Balazs *et al.* [21] and Bonasera and Csernai[22]. The simplest class of hydrodynamic models ("ideal" hydrodynamics) has a gaseous equation of state, and dissipative effects such as viscosity are neglected. Such a model predicts that scale-invariant flow

parameters at constant y' should be independent of beam energy and independent of the mass of the colliding system. It is clearly not applicable at beam energies of a few tens of A MeV, where the nuclear mean field changes from attractive to repulsive and sideward flow is observed to drop to zero. [23,24,25] However, the nuclear mean field is predominantly repulsive at and above $250A$ MeV, and a simple gaseous equation of state becomes more realistic. The EOS data are presented in Figs. 1. In addition we found a remarkable adherence to ideal hydrodynamic scaling for Au + Au collisions over the investigated range of y' and bombarding energy.

In Fig. 2 we present some realistic BNV calculations derived from s uch a microscopic momentum dependent (MD) mean field. More precisely our microscopic derivation is based on the non relativistic BBG approach, with the Paris potential as input for the NN interaction.

The calculation of the mean field has been reported in ref. [27]. The momentum profile of the BBG potential is flat at low momenta thus giving a vanishing momentum gradient in the BNV equation. The main effect is expected in the intermediate energy region where the slope is steepest. To calculate the exclusive fragment flow we have combined our BNV code with a phase-space coalescence model [19]. In this method we construct "events" by a random sampling of the one-body distribution at the freeze-out time. The fragments are then defined imposing proximity constraints in space and momentum. The calculated exclusive flow for p, d, t and α and the exclusive flows for protons and alphas are shown in fig. 2 to be compared with the EOS data. More precisely, the maximum value of the calculated flow, as a function of impact parameter, is compared to the maximum experimental flow, as a function of multiplicity bin. The flow for protons and deuterons is overestimated. For alpha particles the agreement is quite good even quantitatively. This could be an indication that the mean field plays the essential role in the dynamics of alpha particle formation.

The reported calculations show that the exclusive flow excitation function could be a strong test for the momentum dependent part of the interaction. From the calculations we have presented, it appears that a microscopic MD mean field could explain the increase of the exclusive flow with energy. This calls for further investigation. For instance, since QMD offers a more transparent way to deal with fragments, a comparison with the results coming from QMD, based on this microscopic mean field, would be very useful in settling down on a definitive conclusion. Another important step is to investigate the effect on flow and fragment formation due to the in-medium corrections of NN cross section, which should be calculated self-consistently from the same G-matrix used for mean field.

4. Multifragmentation

The EOS Collaboration interest in multifragmentation dates back over ten years ago. The Purdue High Energy Nuclear Physics Group studies of proton-nucleus collisions using an internal gas jet target of heavy noble gases allowed us to accurately measure target fragments yields over a wide range of fragment mass, charge and

incident energies [30]. A high statistics study of the fragment yield in the limiting fragmentation regime provided evidence that heavy fragments come from the simultaneous disassembly of a system somewhat lighter than the original target nucleus and nearly at rest in the laboratory [31]. Complementary studies indicated that the missing nucleons were knocked out in a prompt first stage, leaving the excited target remnant to decay [32]. In the second part of my talk, I will report results on a reverse–kinematics study of projectile fragmentation of 1.0A GeV Au nuclei incident on a C target. For the present analysis we have used fragments reconstructed in one detector only, in exclusive ranges: TPC for charges 1 to 6; TOF, 7 to 10; MUSIC II, 11 to Z_{beam}.

4.1. The Multifragmentation Regime

The mode of disintegration of a nucleus depends on the amount of excitation energy put into the system. As the event multiplicity is proportional to the energy deposited, we can illustrate these modes in the data by looking at the fragment yield vs. fragment size in three different multiplicity regions.

Fig. 3 shows the fragment yield for our Au + C at 1.0A GeV data, separately for three exclusive ranges of multiplicity. (Charges 1-3 have been omitted so that the yield of the heavier fragments is visible). At low multiplicities, corresponding to an excitation energy small compared with the total nuclear binding energy, the excited projectile remnant decays via evaporation of a few nucleons or light clusters, leaving a large residual fragment behind. At high multiplicities, the excitation energy is much greater than the binding energy, and the remnant is totally vaporized into nucleons and a few small fragments. But in the intermediate multiplicity range a spectrum of fragments of intermediate mass are produced. This is the regime of multifragmentation.

From the point of view of the liquid drop model of the nucleus, we might describe the three regimes as follows. At low excitation energies, we observe evaporation. At the highest excitation energies, the nucleus is vaporized into a gas of nucleons and light clusters. It is natural to imagine that at intermediate excitation energies, the nucleus is torn between the liquid and gas phases.

4.2. BNV + phase space calculations of fragment production

The observation of a power-law yield in earlier inclusive studies of the mass distribution of fragments produced in proton-nucleus reactions at the Fermilab [33,34], coupled to the particular value of the power-law exponent, 2.64, led us to speculate that perhaps nuclear multifragmentation was a critical phenomenon occurring in a small system. From this point of view, fragments would result from the density fluctuations that are characteristic of second order phase transitions. For example, in a fluid system whose phase diagram is described by the Van der Waals equation, at the critical temperature the compressibility diverges. This divergence makes it possible for large density fluctuations to occur near the critical point. Analogously, in the

context of the liquid drop model of the nucleus, we can view multifragmentation as the direct result of density fluctuations in a nucleus heated to its critical density and temperature in the collision. The calculated dependence [35] of mass yield distribution on impact parameter is shown in fig. 4 For semi-central collisions we get an almost linear dependence (in log scale), while approaching the semi-peripheral domain a power law starts to develop. This is in qualitative agreement with calculations by M. Baldo et al. [28] and V. Latora et al. [29].

The observation alone of a power law in the mass yield, with an exponent in the range of 2-3 is suggestive but not conclusive of a critical behavior. Besides, the Fermilab experiments where inclusive in that data could not be sorted according to multiplicity. As the excitation energy is the only proper measure of the approach to a critical region, an exclusive experiment must be performed in order to investigate further. The EOS experiment has provided this opportunity.

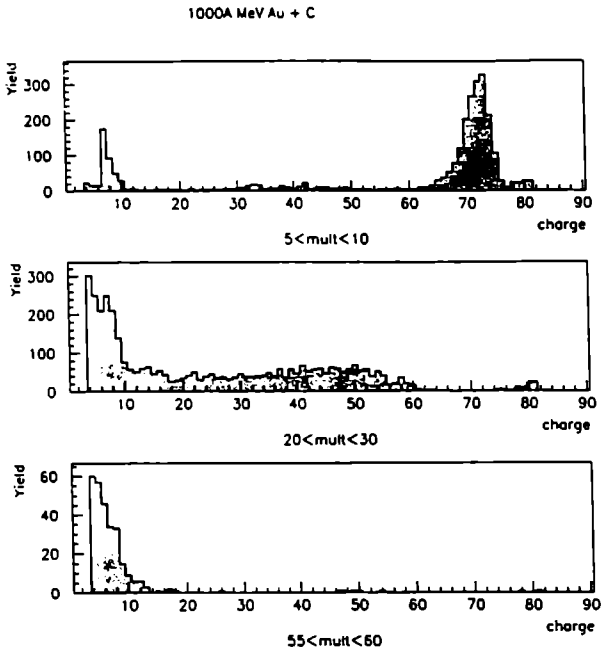

Figure 3: Fragment yields for different multiplicity intervals. Charges 1-3 have been omitted.

4.3. Signatures of Critical Behavior

It is well known from the theory of phase transitions [36], that critical behavior is characterized by fluctuations in the neighborhood of the critical point. These may be fluctuations of density in a fluid system, of magnetization in a magnetic system, or of cluster size in a percolation lattice. It is the fluctuations that we must study to

see whether a system is exhibiting critical behavior. These fluctuation are largest in the critical region and persist even with infinite statistics.

Another signature of second order phase transitions is the existence of a finite number of critical exponents, which govern the power–law behavior of several quantities of interest, appropriate to describe each particular system. Only two of these critical exponents are independent and are related to the others by a sum rule. This rule is obeyed by all known second order phase transitions.

To look for nonstatistical fluctuations of experimental observables as a function of multiplicity in multifragmentation data, we must first solve the problem of how to deal with the finite size of the nucleus. In order to develop suitable analysis tools we will use a prototypical system, a cubic percolation lattice of linear dimension L. We use percolation as a testing ground for our techniques. We will then apply these techniques to our preliminary multifragmentation data [37].

Let us address the question of what a second order phase transition looks like in a finite system, let say a system with about 200 constituents. This issue has been addressed by Campi in a series of papers [38,39]. As Campi shows, quantities that diverge at the critical point in infinite systems, show a peak in finite systems. The peak becomes broader as the system size gets smaller. The location of the peak in also somewhat shifted from the location of the divergence in the infinite system. As an example we examine the percolation quantity M_2, the second moment of cluster distribution (analogous to isothermal compressibility in a liquid) [40]:

$$M_2 = \sum_s s^2 n_s(p) \tag{2}$$

where n_s is the number of clusters containing s sites and p is the probability that a bond is formed between neighboring sites. In the infinite system, percolation does have a critical 'point': the particular value of p, p_c, necessary to form the infinite cluster, i.e. the cluster spanning the entire lattice. The behavior of $ln(M_2)$ vs. reduced multiplicity n, i.e. the numer of clusters formed per lattice site, is such that a peak, i.e. a 'critical' region, remains visible even at small lattice sizes.

Making an analogy with a fluid system in order to have a more physical picture, we will label the percolation probability region $p > p_c$ as the 'liquid' side (with those probabilities one would always form the cluster spanning the entire lattice, i.e. all sites would bond to each other) and below p_c as the 'gas' region. In the summation of eq. 2 the largest cluster must be omitted whenever we are on the 'liquid' side, since it represents what would be the infinite cluster if $L \rightarrow \infty$. Percolation theory shows that near the critical point the moments have power-law behavior [40]:

$$M_k \simeq \mid p - p_c \mid^{\frac{-1+k-\tau}{\sigma}} \tag{3}$$

where τ and σ are critical exponents.

Of course fragmentation is not percolation on a lattice. However, we wish to perform a cluster size analysis of our fragmentation data in an effort to evidence possible fluctuations and determine the exponents γ, β, and τ. Then we must find

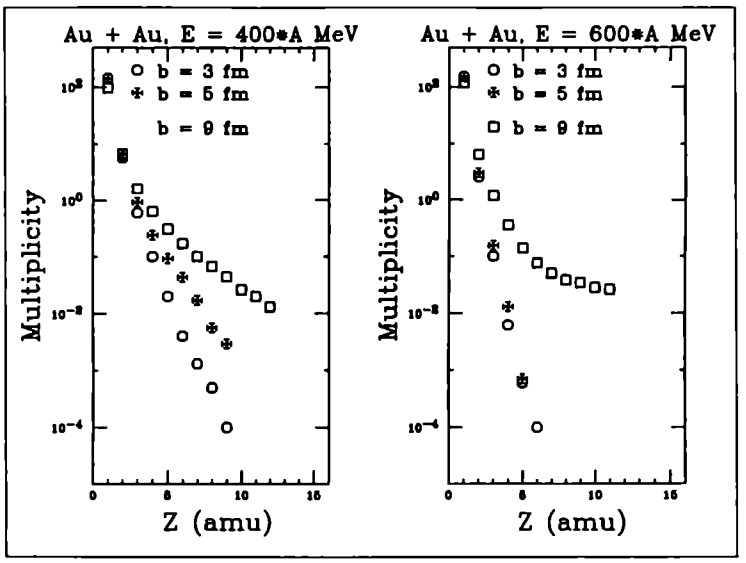

Figure 4: Mass yield distribution for two different impact parameters, $b = 3fm$ and $b = 9fm$. The results show a transition from a linear behavior (in log scale) to a power low.

a suitable substitute for the percolation probability p. Ideally we would like to use temperature, but since this is difficult to measure directly on an event by event basis, we follow Campi's suggestion [38,39] and use charged particle multiplicity, or better the reduced multiplicity $n = m/79$, 79 being the charge of the Au projectile.

We indeed do find fluctuations in the EOS Au + C data in a particular interval of multiplicity. We find them in the deviation of the size of the largest fragment produced, when plotted as a function of multiplicity, as shown in Fig. 5. This peak is the indication that our system is approaching criticality at a certain multiplicity. It is significant that these deviations follow closely those for a percolation lattice of comparable size. Remarkably, the peak occurs at the multiplicities for which we observed the multifragmentation regime.

4.4. Determination of Critical Exponents

Having some evidence of critical behavior in multifragmentation we want to pursue the investigation further calculating some critical exponents for nuclear fragmentation and verifying whether they obey the sum rule.

To develop a method to extract critical exponents for small systems, we use again small percolation lattices and then we apply the method to multifragmentation.

As eq. 3, with $k = 2$, represents the behavior of the second moment of cluster size distribution near the critical point, the key to determining critical exponents for

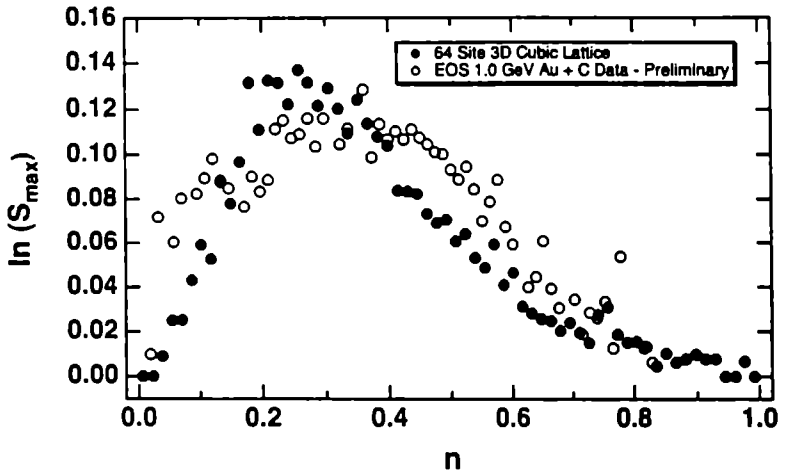

Figure 5: Fluctuations in the average size of the largest cluster versus multiplicity.

small systems is finding, for those system, a region in probability p where eq. 3 holds. This means that one cannot expect power–law behavior too close to the peak because finite size effects dominate. On the other hand one cannot go too far from the peak because fluctuations there, small compared to the mean, are only indicative of mean field regime.

Following the procedure of [37] the critical exponents γ, β and τ were determined from the EOS data in Au + C reaction at 1000 A MeV.

First of all we have to find a quantity to suitably replace the percolation probability p. We use multiplicity m. Next we have to determine the 'critical' multiplicity m_c. The location of the peak in Fig. 5 gives us a good starting guess. After some trial and error, following the above method to determine γ, we find that $m_c = 27$ gives a good fit on both the 'liquid' and 'gas' sides. The fits yield γ=1.40 . We then use the above value of m_c in our determination of β. Then we determine τ according to well known sum rules. The found values of the 4 critical exponents for Au multifragmentation are listed in Table 1 along with the canonical values that the same exponents have in other systems: a 3D percolation lattice, a real fluid, and the mean field theory. Also the value of the parameter σ is reported in the table. The value of β versus γ is finally reported in the Fig. 6 for the Au multifragmentation data and for the other systems in Table I. It useful to remark that the fragmentation pointy is close to the point for the liquid-gas system and is significantly distant from either the percolation or liquid-gas mean field results.

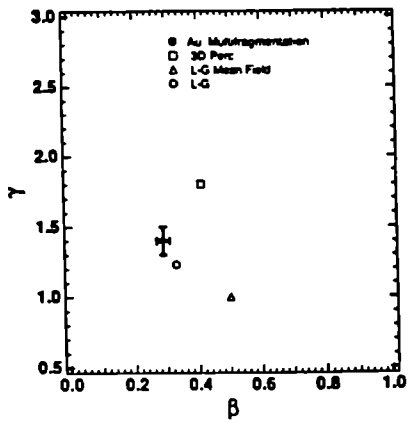

Figure 6: γ versus β for the systems considered in the Table 2.

System	γ	β	τ	σ
3D Percolation	1.80	0.41	2.18	0.45
Fluid	1.24	0.33	2.21	0.64
Mean Field Theory	1.0	0.5	2.33	2/3
Au+C fragmentation	1.4	0.31	2.14	0.67

Table 1: Critical Exponents for Various Systems

4.5. Discussion

The uncertainties in the exponents for the Au+C fragmentation data are 10-15%. These are due to different values one can obtain by varying m_c and the amplitude of the fitting regions. The significant point is that we are unable to find a set of the three exponents that is consistent with either the percolation or the mean field theory. On the contrary the similarity of the values with those for a fluid system is striking. Most remarkable is that the sum rule is obeyed by the nuclear matter exponents. If this analysis is correct, we have probed the nuclear EOS as it approaches the critical point using small samples of nuclear matter (finite nuclei).

We have now a stronger evidence that the multifragmentation regime, occurring when multiplicity is in a particular range of values, can be associated with critical behavior of the nuclear matter, and we have a significant indication that this critical behavior is a liquid-gas phase transition.

If this analysis is correct, the implication is that the fragmenting system has had

sufficient time to approximate thermal equilibrium. In a small system, the approach occurs over a considerable range of excitation energy, temperature and density. It remains to determine these quantities from the data.

5. References

1. Recent experimental reviews include: K.-H. Kampert, Nucl. Part. Phys. **15**, 691 (1989); H. H. Gutbrod, A. M. Poskanzer, and H. G. Ritter, Rep. Prog. Phys. **52**, 1267 (1989).
2. For reviews, see H. Stöcker and W. Greiner, Phys. Rep. **137**, 277 (1986); G. F. Bertsch and S. Das Gupta, Phys. Rep. 160, 189 (1988); *The Nuclear Equation of State*, Vol. 216 of *NATO Advanced Study Institute, Series B: Physics*, edited by W. Greiner and H. Stöcker, (Plenum, New York, 1989), Part A.
3. J. Jänicke and J. Aichelin, Nucl. Phys. **A547**, 542 (1992).
4. W. Christie *et al.*, Nucl. Inst. Meth. **A255**, 466 (1987).
5. S. Albergo *et al.*, Nucl. Inst. Meth. **A311**, 280 (1992).
6. J. Engelage *et al.*, Nucl. Inst. Meth. **A277**, 431 (1988).
7. G. Rai *et al.*, in *The Nuclear Equation of State*, ed. W. Greiner and H. Stöcker, NATO-ASI Vol. B216 part A (Plenum, NY 1989), p. 187.
8. S. Costa et al. (The EOS Collaboration), Proc. 32^{nd} Int. Winter Meeting on Nuclear Physics, Bormio, Italy, (1994); pag. 126, Ed. I. Iori.
9. G. Rai *et al.*, IEEE Trans. Nucl. Sci. **37**, 56 (1990).
10. H. A. Gustafsson *et al.*, Modern Phys. Lett. **A3**, 1323 (1988).
11. H. H. Gutbrod, A. M. Poskanzer, and H. G. Ritter, Rep. Prog. Phys. **52**, 1267 (1989).
12. M. D. Partlan et al., (The EOS Collaboration), Phys. Rev. Lett. (1995), in press.
13. A. Bonasera, F. Gulminelli, and J. Molitoris, Phys. Rep. **243** (1994) 1.
14. K. G. R. Doss, H.-Å. Gustafsson, H. H. Gutbrod, K. H. Kampert, B. Kolb, H. Löhner, B. Ludewigt, A. M. Poskanzer, H. G. Ritter, H. R. Schmidt, and H. Wieman, Phys. Rev. Lett. **57**, 302 (1986).
15. P. Danielewicz and G. Odyniec, Phys. Lett. **157B**, 146 (1985).
16. K. G. R. Doss *et al.*, Phys. Rev. Lett. **59**, 2720 (1987).
17. S. Wang et al, (The EOS Collaboration), Phys. Rev. Lett. **74**, 2646 (1995).
18. D.Keane and the EOS Collaboration, *Proceedings of the* 9^{th} *High-Energy Heavy Ion Study*, Berkeley, California, October 1993.
19. A. Bonasera, M. Colonna, M. Di Toro, F. Gulminelli and H.H. Wolter, Phys. Lett. **244** (1990) 169
20. S. Wang, Y. Z. Jiang, Y. M. Liu, D. Keane, D. Beavis, S. Y. Chu, S. Y. Fung, M. Vient, C. Hartnack, and H. Stöcker, Phys. Rev. C **44**, 1091 (1991).
21. N. Balazs, B. Schürmann, K. Dietrich, and L. P. Csernai, Nucl. Phys. **A424**, 605 (1984).
22. A. Bonasera and L. P. Csernai, Phys. Rev. Lett. **59**, 630 (1987); A.

Bonasera, L. P. Csernai, and B. Schürmann, Nucl. Phys. **A476**, 159 (1988).
23. D. Krofcheck, W. Bauer, B. M. Crawley, C. Djalali, S. Howden, C. A. Ogilvie, A. VanderMolen, G. D. Westfall, W. K. Wilson, R. S. Tickle, and C. Gale, Phys. Rev. Lett. **63**, 2028 (1989).
24. C. A. Ogilvie, W. Bauer, D. A. Cebra, S. Howden, J. Karn, A. Nadasen, A. VanderMolen, G. D. Westfall, W. K. Wilson, and J. S. Winfield, Phys. Rev. C **42**, R10 (1990).
25. W. M. Zhang, R. Madey, M. Elaasar, J. Schambach, D. Keane, B. D. Anderson, A. R. Baldwin, J. Cogar, J. W. Watson, G. D. Westfall, G. Krebs, and H. Wieman, Phys. Rev. C **42**, R491 (1990).
26. Y. Shao, Ph.D. Thesis, Kent State University (1994).
27. A. Insolia et al., Phys. Lett. **334**, 12 (1994).
28. M. Baldo, G.F. Burgio and A. Rapisarda, Phys. Rev. C **51** (1995) 198
29. V. Latora, M. Belkacem and A. Bonasera, Phys. Rev. Lett. **73** (1994) 1765
30. B. C. Stringfellow *et al.*, Nucl. Inst. Meth. **A251**, 242 (1986).
31. J. A. Gaidos *et al.*, Phys. Rev. Lett. **42**, 82 (1979).
32. K. Nakai *et al.*, Phys. Lett. **B121**, 373 (1983).
33. J. E. Finn *et al.*, Phys. Rev. Lett. **49B**, 1321 (1982).
34. R. W. Minich *et al.*, Phys. Lett. **B118**, 458 (1982).
35. A. Insolia et al., (The EOS Collaboration), in preparation
36. See for example: H. E. Stanley, *Introduction to Phase Transitions and Critical Phenomena*, Oxford University Press, New York, 1971
37. J.B.Elliott et al., Phys. Rev. bf 49, 3189 (1994); M.L. Gilkes et al., (The Eos Collaboration), Phys. Rev. Lett. **73**, 1590 (1994); J.B.Elliott et al., (The Eos Collaboration), to be published.
38. X. Campi, J. Phys. **A19**, L917 (1986).
39. X. Campi, Phys. Lett. **B208**, 351 (1988).
40. See for example: D. Stauffer, *Introduction to Percolation Theory*, Taylor & Francis, London, 1985

6. SINGLE AND DOUBLE BETA DECAY

SYSTEMATIC STUDY OF DOUBLE BETA DECAY TO EXCITED FINAL STATES

J. SUHONEN
Dept. of Physics, University of Jyväskylä, P.O. Box 35
FIN-40351 Jyväskylä, Finland

and

M. AUNOLA
Dept. of Physics, University of Jyväskylä, P.O. Box 35
FIN-40351 Jyväskylä, Finland

ABSTRACT

A systematic study of the two-neutrino double beta ($2\nu\beta\beta$) decay to the final ground state and excited states is performed within a microscopic quasiparticle random-phase approximation (QRPA) model. The excited states are assumed to have the structure of one or two QRPA phonons. The study of the $2\nu\beta\beta$-decay rates is complemented with the study of single-beta-decay feeding of the relevant nuclei taking part in the double beta process. The Woods–Saxon single-particle energies have been corrected near the fermi surface by comparing the BCS quasiparticle energies with spectroscopic data of the relevant odd-mass nuclei. Pairing gaps, energy systematics of the Gamow–Teller states and the available beta-decay data have been used to obtain effective, model-space adapted, two-body matrix elements starting from the G-matrix elements of the Bonn one-boson-exchange potential. This enables a parameter-free calculation of the double Gamow–Teller matrix elements and theoretical prediction of double-beta half lives. The harmonic two-phonon approximation has been used in the beta-decay analysis and the subsequent $2\nu\beta\beta$ calculation.

1. Introduction

During the past decade there has been an increasing experimental [1,2] and theoretical [3–7] interest in studying the double beta decay of atomic nuclei, both in its two-neutrino mode ($2\nu\beta\beta$) and in its neutrinoless ($0\nu\beta\beta$) mode. This growing experimental and theoretical effort has been stimulated by the emerging vast possibilities for testing various theoretical nuclear-structure approaches ($2\nu\beta\beta$ calculations) and by the unique chances in detecting and predicting something which goes beyond the so-called standard model (SM) towards the grand unification (GUT theories) of all fundamental forces.

The tritium beta decay and the neutrinoless double beta decay are to-date the only feasible means of extracting information about the mass and character of the neutrino. The tritium decay provides a more direct test of the mass of the neutrino since the $0\nu\beta\beta$ decay is more dependent on the nuclear-structure calculation of the participant nuclear matrix elements. On the other hand, the $0\nu\beta\beta$ decay, if detected, provides a more powerful tool for the exploration of the fundamental character of the neutrino and implications of various GUT theories of different unification structure.

The existence of $0\nu\beta\beta$ decay connects with the following fundamental aspects of particle physics [3–7]:

- lepton-number non-conservation,
- the existence and nature of neutrino mass,
- the existence of right-handed currents in the electroweak interaction,
- the existence of a massless Goldstone boson, the majoron,
- the structure of Higgs' sector,
- supersymmetry.

In the study of the above items the atomic nucleus provides at present by far the best available testing laboratory. By now, measured values of the lower limits of the $0\nu\beta\beta$ half-lives exist so that these fundamental observables are already exposed to study via the more or less direct relation between experiment and theory.

In the standard model of electroweak interactions the neutrinos are regarded as massless Dirac particles with only left-handed weak coupling. In addition, the lepton number is a conserved quantity. The GUT open up a possibility of lepton-number violation and birth of massive Majorana neutrinos through spontaneous breaking of a global symmetry associated to the lepton-number conservation. The generation of Majorana masses makes the neutrinoless double beta decay possible and enables also the right-handed leptonic and hadronic currents to contribute to this decay mode. However, the masses and the mass hierarchy of the neutrinos are poorly constrained by the phenomenological GUTs [5,7]. As an additional test of the GUT-predicted neutrino-mass scenarios one can use the stringent constraints coming from beta decay, neutrinoless double beta decay, neutrino oscillations (atmospheric and solar neutrinos), the Z^0-decay width data, and studies on nucleosynthesis.

Assuming the neutrinos to be massive and mixed, the theoretical information related to the $0\nu\beta\beta$ decay allows for a direct handle of the magnitude of the mixing parameter of the left- and right-handed intermediate bosons without resorting to any specific model of neutrino mixing. The analysis [8] indicates that the nuclear-structure calculations can give estimates for the mixing which complement the muon-decay and supernova data. Furthermore, it is possible to study the effects of a finite Majorana mass to right-handed weak currents. These effects arise when neutrino-mass corrections to the neutrino propagator are taken into account in the $0\nu\beta\beta$ decay. Due to these corrections the right-handed currents become effective even if all neutrinos have light masses (below 10 MeV) [9]. In addition, the experimental $0\nu\beta\beta$ half lives can be used [9] to obtain information about new kinds of effective right-handed coupling within various neutrino-mass scenarios.

Violation of lepton-number symmetry in the context of weak interactions makes neutrino-Majoron coupling possible. The Majoron, i.e. the massless Goldstone boson associated with the spontaneous symmetry breaking of the baryon minus lepton number conservation $(B - L)$, has been described in terms of weak-isospin-triplet and -doublet representations [10]. These models have been ruled out by the Z^0 width data of LEP. It has been suggested [11] that the singlet-Majoron model could contribute to the neutrinoless double beta decay. One can set limits to the corresponding neutrino-Majoron coupling strength by using calculated values of the nuclear matrix elements in the context of the $0\nu\beta\beta$ decay. The results [12] support the conclusion that Majoron emission not only constitutes an important component of the $0\nu\beta\beta$ background but, in addition, it can shift the end point of the electron sum-energy spectrum.

A source of uncertainty in the above analysis is the evaluation of the nuclear matrix elements entering the theoretical expressions for the fundamental observ-

ables. A task of utmost importance is to improve the accuracy of the double-beta matrix element calculation by developing new theoretical schemes and by improving the quality of the present ones. Another goal is to clarify the relation between the measured and the calculated quantities in the context of the $0\nu\beta\beta$ decay.

In the recent past a lot of theoretical effort in nuclear-structure calculation has been put to explaining the data on single beta decay and the two-neutrino double beta decay [2,6,13–23]. The nuclear shell model (for light nuclei) and the quasiparticle random-phase approximation (QRPA) model (for medium-heavy and heavy nuclei) have been the most promising microscopic nuclear-structure theories in this field. One particular problem concerning the nuclear-structure calculations has been the explanation of the quenching phenomenon, i.e. the experimentally observed suppression, when compared with the single-particle shell-model predictions, of the decay strength in the allowed beta decay of many heavy and medium-heavy nuclei, and also in the $2\nu\beta\beta$ decay to the final ground state. One has tried to account for this quenching either on the basis of conventional nuclear-structure effects or more exotic phenomena, like isobar excitations, tensor-type correlations or mesonic renormalization. This quenching is very pronounced in the allowed β^+/EC decay of some neutron-deficient even-even nuclei, where even an order of magnitude suppression of the Gamow–Teller decay strength has been measured.

Recently, in the context of the $2\nu\beta\beta$ decay, it was found [13] that the quenching can be nicely accounted for in the framework of the proton-neutron QRPA (pnQRPA) where the quenching can be studied as a function of the increasing strength of the particle-particle correlations emerging in the quasiparticle formalism of open-shell nuclei. Later this mechanism of suppression of the $2\nu\beta\beta$-decay rate was verified by the Tübingen group [14] and the Heidelberg group [15]. In the case of the neutron-deficient, β^+/EC-decaying nuclei the quenching can be, indeed, reproduced by the pnQRPA theory [16]. On the other hand, for the neutron-rich Pd isotopes the quenching was harder and even impossible to reproduce [17]. One possibility of improving the description in this case could be the higher-RPA approach of ref. [18]. A less drastic dependence of the participant nuclear matrix elements on the particle-particle interaction strength has been reported for the $0\nu\beta\beta$ decay [19–21].

A subject of great interest at the present is the measurement and calculation of $0\nu\beta\beta$ decay rates to excited 2^+ states of the final nucleus. This decay mode is particularly interesting since it is very sensitive to the right-handed content of the weak interaction lagrangian whereas the sensitivity to neutrino mass is minimal [6]. Some experimental results concerning the decay of ^{76}Ge to 2^+ states of ^{76}Se already exist [24]. A further motivation for the study of this decay mode comes from the very recent experimental and theoretical work done on the $2\nu\beta\beta$ decay to excited final states which provides a test of the nuclear wave functions participating in the $0\nu\beta\beta$ decay to excited states. These $2\nu\beta\beta$ studies are the subject of the present article and will be discussed below.

Theoretical study of the $2\nu\beta\beta$ decay to excited states is very much morivated by the first reported experimental evidences [2,25–34] of such a decay mode. The main aim is to obtain complementary information on the nuclear-structure matrix elements, i.e. to probe the involved nuclei via their excitations, a method of great sensitivity with respect to underlying theoretical assumptions. This aspect has been discussed by Griffiths and Vogel [35] (excited 0^+ final states) and Suhonen and Civitarese [36,37] (excited 0^+ and 2^+ final states) in the framework of the pnQRPA theory combined with the charge-conserving QRPA theory for like nucleons (hereafter simply denoted by the QRPA). The method of [36], namely the Multiple Commutator Method

(MCM), is briefly outlined in section 2 of this article, and it has been used [31,37–40] to calculate double-beta-decay rates of ^{76}Ge, ^{100}Mo, ^{116}Cd and ^{136}Xe to excited states of ^{76}Se, ^{100}Ru, ^{116}Sn and ^{136}Ba, respectively. It has also been applied for systematic beta-decay studies in the cadmium and tin regions [41]. In the present article it is used for a systematic study of $2\nu\beta\beta$ decay to excited final states.

Other approaches, worth of mentioning in the context of beta decay and $2\nu\beta\beta$ decay to excited states, are the higher-RPA approach of Raduta et al. [18] and its later applications [42]. A further development of the previous methods can be introduced by perturbing the participant final states by a boson expansion method [43]. In this method one introduces higher-RPA corrections, not only to the transition operator, as in the MCM of [36], but also to the initial and final states involved in the transition. All these corrections form a boson-expansion hierarchy which can be truncated in a consistent fashion. The emerging corrections are particularly important for the energies and beta-decay feeding of final states of two-phonon character [43]. Finally, for the deformed nuclei, the pseudo SU(3) scheme of the Mexico group [23] has been extended recently [44] to include transitions to excited 0^+ and 2^+ final states.

In this article we compare, in a systematic way, beta-decay and $2\nu\beta\beta$ observables on the same footing trying to extract information from the ordinary beta decay to complement the information coming from the $2\nu\beta\beta$ analysis of the ground-state and excited-state transitions. Excitation spectra and available beta-decay data are used to adjust the model parameters, like the single-particle energies and the scale of the nuclear two-body matrix elements, to yield parameter-free predictions of the $2\nu\beta\beta$ observables. In the present scheme the excited states of the final nucleus, which can be reached both by the beta decay and the double beta decay, are described as one- and two-quadrupole-phonon states. The harmonic approximation is used for the two-phonon excitations.

2. Formalism of the β and $\beta\beta$ decay

The parent and daughter nuclei involved in the double-beta-decay process are the initial (N,Z) and final $(N \pm 2, Z \mp 2)$ even-even nuclei with a 0^+ ground state $(0^+_{g.s.})$. For the double β^- $(2\nu\beta^-\beta^-)$ decay the final nucleus is $(N\text{-}2,Z\text{+}2)$ and for the double β^+/EC decay (we consider here only the double K-electron capture, 2ν2K) the final nucleus is $(N\text{+}2,Z\text{-}2)$. The odd-odd nucleus between the $2\nu\beta\beta$ parent and daughter provides the virtual excited 1^+ states (the intermediate states) through which the double beta decay can proceed.

To be able to describe the beta-decay transitions from the odd-odd nucleus to the ground state and various excited states of the even-even daughter nucleus one has to generate the nuclear wave functions for all the states involved in this process. This unified description of the parent and daughter states, called the Multiple Commutator Method (MCM) [36], is accomplished by the use of the QRPA framework in its charge-conserving formalism together with its charge-nonconserving formalism. In the MCM the leading component of the correlated ground states of the QRPA and the *pn*QRPA is the BCS vacuum, and in the commutator treatment of the β^- and the β^+/EC decay transitions one can assume the QRPA and the *pn*QRPA vacua to coinside.

In the language of the boson-expansion theory the MCM corresponds to perturbation of the beta-decay operator by higher-order terms containing also the charge-conserving QRPA phonons in addition to the *pn*QRPA phonons [43]. In the MCM the higher-RPA corrections to the participating nuclear states have been omitted,

Table 1. List of the beta-decay operators taken into account in the MCM calculations.

Operator	Type	$\|\Delta J\|$	Magnitude	Order
$\mathbf{1}$	F	0	1	Allowed
$\boldsymbol{\sigma}$	GT	0,1		$(\Delta\pi = \text{no})$
Y_1	F	0,1	$\mathbf{r}\cdot\mathbf{p}_{\text{lept}}$	1^{st}
$[\sigma Y_1]_0$	GT	0	$\sim RQ_\beta$	forb.
$[\sigma Y_1]_1$	GT	0,1	$= \frac{1}{20}$	$(\Delta\pi = \text{yes})$
$[\sigma Y_1]_2$	GT	0,1,2		
γ^5	relat.	0	$\sim \frac{p_N}{M_N}$	1^{st}
$\boldsymbol{\alpha}$	relat	0,1	$= \frac{1}{20}$	forb.

but they can be accounted for by a consistent use of the boson-expansion method [43].

In the MCM the states of the odd-odd parent nucleus are calculated by defining the *pn*QRPA phonons as linear combinations of quasiproton-quasineutron excitations [13,16]

$$|J^\pi M;m\rangle = \sum_{pn}[X_{pn}(J^\pi,m)A^\dagger(pn,JM) - Y_{pn}(J^\pi,m)\tilde{A}(pn,JM)]|\text{QRPA}\rangle \quad , \quad (1)$$

and the I^π excited states of the even-even nucleus by using the QRPA procedure built upon *pp* and *nn* two-quasiparticle excitations [45] . The associated QRPA phonons are given by

$$|I^\pi M;k\rangle = \sum_{a,a'}[Z_{aa'}(I^\pi,k)A^\dagger(aa',IM) - W_{aa'}(I^\pi,k)\tilde{A}(aa',IM)]|\text{QRPA}\rangle \quad . \quad (2)$$

Here m and k number the states with the same angular momentum (J,I) and parity π. The quasiparticle pair creation and annihilation operators $A^\dagger$ and $\tilde{A}$ for proton-proton and neutron-neutron quasiparticle pairs are given by

$$A^\dagger(aa',IM) = \frac{1}{\sqrt{1+\delta_{aa'}}}[\alpha_a^\dagger\alpha_a^\dagger]_{IM} \quad , \quad \tilde{A}(aa',IM) = (-1)^{I+M}A(aa',I,-M) \quad , \quad (3)$$

where a denotes all quantum numbers needed to specify a single-quasiparticle harmonic-oscillator state for protons $(a=p)$ or neutrons $(a=n)$.

The β^--decay transitions between the parent nucleus and the one-phonon and two-phonon states of the daughter nucleus are mediated by the various beta-decay operators $\hat{\beta}_L^-$ given in Table 1. The transitions can be divided to allowed and first-forbidden and, at the same time, to Fermi-type (F) and Gamow–Teller -type (GT, contains the Pauli operator $\boldsymbol{\sigma}$) transitions. The operators γ^5 and $\boldsymbol{\alpha}$ emerge from the small components of the nucleon wave functions and thus represent the relativistic corrections to the weak nucleonic current. They are suppressed by the large nucleon mass M_N. The other first-forbidden operators emerge from the large components

of the nucleon wave functions, but are suppressed by the small Q value of the β decay. The quantity ΔJ in Table 1 signifies the possible values of the difference between the initial and final total angular momentum J. In the case of decay to a one-phonon state the relevant reduced matrix element are given by

$$\begin{aligned}
\beta^-_{ILJ}(u,v) &\equiv (I^{\pi'}_k \| \hat{\beta}^-_L \| J^\pi_m) \\
&= 2\sqrt{(2I+1)(2J+1)}(-1)^{I+L+J} \sum_{pn}(p\|\hat{\beta}^-_L\|n)\Big\{\sum_{p'} W(JIj_nj_p;Lj_{p'}) \\
&\times [u_nu_pX_{p'n}(J^\pi,m)Z_{pp'}(I^{\pi'},k) - v_nv_pY_{p'n}(J^\pi,m)W_{pp'}(I^{\pi'},k)] \\
&+ \sum_{n'}(-1)^{n+n'+I}W(JIj_pj_n;Lj_{n'})[v_nv_pX_{pn'}(J^\pi,m)Z_{nn'}(I^{\pi'},k) \\
&- u_nu_pY_{pn'}(J^\pi,m)W_{nn'}(I^{\pi'},k)]\Big\} \quad , \qquad (4)
\end{aligned}$$

where the factors u and v are the usual BCS occupation factors obtained from the BCS calculation of the even-even daughter nucleus. The reduced transition probabilities to the $\frac{1}{\sqrt{2}}[2^+_1 \otimes 2^+_1]_{J_f}$ two-quadrupole-phonon states, in turn, read

$$\begin{aligned}
\beta^-_{J_fLJ}(u,v) &\equiv (J^+_f\|\hat{\beta}^-_L\|J^\pi_m) = \frac{40}{\sqrt{2}}\sqrt{(2J_f+1)(2J+1)}(-1)^{J+L+1} \\
&\times \sum_{pnp'n'}(p\|\hat{\beta}^-_L\|n)\Big[u_pv_nZ_{pp'}(2^+,1)Z_{nn'}(2^+,1)X_{p'n'}(J^\pi,m) \\
&+ v_pu_nW_{pp'}(2^+,1)W_{nn'}(2^+,1)Y_{p'n'}(J^\pi,m)\Big]\begin{Bmatrix} j_p & j_{p'} & 2 \\ j_n & j_{n'} & 2 \\ L & J & J_f \end{Bmatrix} \quad . \qquad (5)
\end{aligned}$$

The corresponding one- and two-phonon expressions for the β^+/EC decay can be obtained from the relation

$$(I^{\pi'}_k\|\hat{\beta}^+_L\|J^\pi_m) = (-1)^{I+r}\beta^-_{ILJ}(v,u) \quad , \qquad (6)$$

where $r = 0$ for the vector operators (V) and $r = 1$ for the axial-vector operators (A).

The logft values of both the β^- and β^+/EC transitions are defined as

$$\log ft_\pm = \log\Big[\frac{6147\text{s}}{S^\pm/S^\pm_0}\Big] \quad , \qquad (7)$$

where the integrated shape factors $S^\pm$ and $S^\pm_0$, for the allowed and first-forbidden transitions, are given in [36].

In the present scheme we have assumed that the final nucleus is spherical (permanent deformations and or intruder states are not included in the formalism) and that the one- and two-phonon states are described by the QRPA formalism. The one-phonon QRPA excitations range in character from collective phonons to pure two-quasiparticle or particle-hole (in the case of proton excitations of the tin isotopes) structures. The lowest quadrupole excitation (2^+_1) is usually rather collective. This can be seen from the large B(E2) values of the $2^+_1 \rightarrow$ g.s. transition. In the present higher-RPA approximation the two-phonon states are degenerate at twice the energy of the one-quadrupole-phonon state.

Table 2. Changes in the neutron and proton s.p. energies [MeV] for ^{106}Pd and ^{106}Cd

	^{106}Pd		^{106}Cd	
Orbital	$E^{n}_{sp,WS}$	$E^{n}_{sp,adj}$	$E^{n}_{sp,WS}$	$E^{n}_{sp,adj}$
$0g_{7/2}$	−7.78	−9.53	−8.68	−8.55
$1d_{3/2}$	−6.35	−6.49	−7.15	−8.49
$1d_{5/2}$	−8.83	−7.81	−9.71	−9.47
$2s_{1/2}$	−7.00	−7.55	−7.79	−7.93
$0h_{11/2}$	−5.28	−7.35	−6.20	−7.67
Orbital	$E^{p}_{sp,WS}$	$E^{p}_{sp,adj}$	$E^{p}_{sp,WS}$	$E^{p}_{sp,adj}$
$0f_{5/2}$	−10.92	−9.97	−9.34	−8.74
$1p_{1/2}$	−8.81	−8.47	−7.18	−6.38
$1p_{3/2}$	−10.39	−9.80	−8.75	−6.91
$0g_{9/2}$	−7.68	−9.39	−6.13	−5.75
$0h_{11/2}$	0.15	−1.05	1.74	1.74

Now that the matrix elements for the various beta-decay transitions (both β^- and β^+/EC) and the virtual $2\nu\beta\beta$ transitions (to the intermediate odd-odd nucleus) are defined, one can compute the matrix elements for the double Gamow–Teller operator, i.e:

$$M^{(2\nu)}_{GT}(J^+_f) = \sum_m \frac{\beta^{(f)}_m(J^+_f)\beta^{(i)}_m}{[(\frac{1}{2}Q_{\beta\beta} + E_m - M_i)m_e + 1]^s} \quad , \tag{8}$$

where $s = 1$ for $J = 0$ and $s = 3$ for $J = 2$, and the sum extends over all 1^+ states of the intermediate nucleus. The denominator of (14) consists of the energy E_m of the m:th intermediate 1^+ state and the mass energy M_i of the parent nucleus, as well as of the double-beta-decay Q value, $Q_{\beta\beta}$. The different matrix elements of the half-life expression (8) are defined as ($-$ for $2\nu\beta^-\beta^-$ and $+$ for 2ν2K decay)

$$\begin{aligned} \beta^{(i)}_m &\equiv (1^+_m \| \hat{\beta}^{\mp} \| 0^+_i) \quad , \\ \beta^{(f)}_m(0^+) &\equiv \sum_{m'} (0^+_f \| \hat{\beta}^{\mp} \| 1^+_{m'}) \langle 1^+_{m'} | 1^+_m \rangle \quad , \\ \beta^{(f)}_m(2^+) &\equiv \sqrt{\tfrac{1}{3}} \sum_{m'} (2^+_f \| \hat{\beta}^{\mp} \| 1^+_{m'}) \langle 1^+_{m'} | 1^+_m \rangle \quad . \end{aligned} \tag{9}$$

The overlap $\langle 1^+_{m'} | 1^+_m \rangle$ of the two 1^+ states of the intermediate nucleus coming from the two different pnQRPA calculations (one for the initial nucleus and the other for the final one) has been added to account for the matching of the intermediate 1^+ states [14].

The double-beta-decay half-life $t^{(2\nu)}_{12}$ can be obtained from the expression

$$[t^{(2\nu)}_{12}(0^+_{g.s.} \rightarrow J^+_f)]^{-1} = |M^{(2\nu)}_{GT}(J^+_f)|^2 F^{(2\nu)}_{GT}(J^+_f) \quad , \tag{10}$$

Table 3. Quasi-particle energies [MeV] in odd $A = 107$ nuclei obtained from a BCS calculation in ^{106}Pd and ^{106}Cd

		^{107}Pd			^{107}Cd		
Orbital	J^π	E_1^{exp}	$E^n_{qp,WS}$	$E^n_{qp,adj}$	E_1^{exp}	$E^n_{qp,WS}$	$E^n_{qp,adj}$
$2s_{1/2}$	$1/2^+$	0.12	0.21	0.13	–	0.43	0.43
$1d_{3/2}$	$3/2^+$	0.38	0.68	1.02	0.37	1.02	0.22
$1d_{5/2}$	$5/2^+$	0.00	0.33	0.00	0.00	0.10	0.00
$0g_{7/2}$	$7/2^+$	0.31	0.00	0.33	0.21	0.00	0.12
$0h_{11/2}$	$11/2^-$	0.22	1.25	1.03	–	1.78	0.60
		^{107}Ag			^{107}In		
Orbital	J^π	E_1^{exp}	$E^p_{qp,WS}$	$E^p_{qp,adj}$	E_1^{exp}	$E^p_{qp,WS}$	$E^p_{qp,adj}$
$1p_{1/2}$	$1/2^-$	0.00	0.88	0.00	0.68	0.96	0.67
$1p_{3/2}$	$3/2^-$	0.32	2.14	0.59	1.11	2.35	1.08
$0f_{5/2}$	$5/2^-$	0.42	2.77	0.74	–	2.95	2.78
$0g_{9/2}$	$9/2^+$	0.20	0.00	0.12	0.00	0.00	0.00

Experimental data from ref. [50]

where J_f^+ can either be the ground state ($0^+_{g.s.}$) or an excited state J_f^+ of the double-beta-decay daughter, and the integrated kinematical factors $F_{GT}^{(2\nu)}(J_f^+)$ can be calculated as described in refs. [4,46].

3. Results

Within the present framework, the calculations are performed combining the following four steps:
(i) The ground state and the excitation spectrum of the double-even nuclei are created using the QRPA method.
(ii) The states of the double-odd nuclei are generated using the *pn*QRPA approach.
(iii) Available experimental data on energy and β-decay observables are used to adjust the nucleon-nucleon interaction and the single-particle energies for each $2\nu\beta\beta$ mass chain.
(iv) The reduced matrix elements of the beta and double-beta transitions are treated using eqs. (4)-(10) assuming pure one- and two-phonon final states.

The active single-particle basis was confined, both for protons and neutrons, within the oscillator major shells $3\hbar\omega$ - $5\hbar\omega$, supplemented by the $i_{13/2}$ intruder orbital from the next higher major shell. For each mass region a reasonable subset of these single-particle orbitals was considered with the restriction that both protons and neutrons occupied the same orbitals. To first approximation, the single-particle energies were obtained from a Coulomb-corrected Woods–Saxon potential with the parametrization of ref. [47]. However, to better reproduce the observed low-energy spectrum of the neighbouring odd-mass nuclei in a BCS calculation, some neutron/proton single-particle energies were adjusted in the vicinity of the Fermi surface. This adjusted basis is used for most calculations (i.e. when there is enough

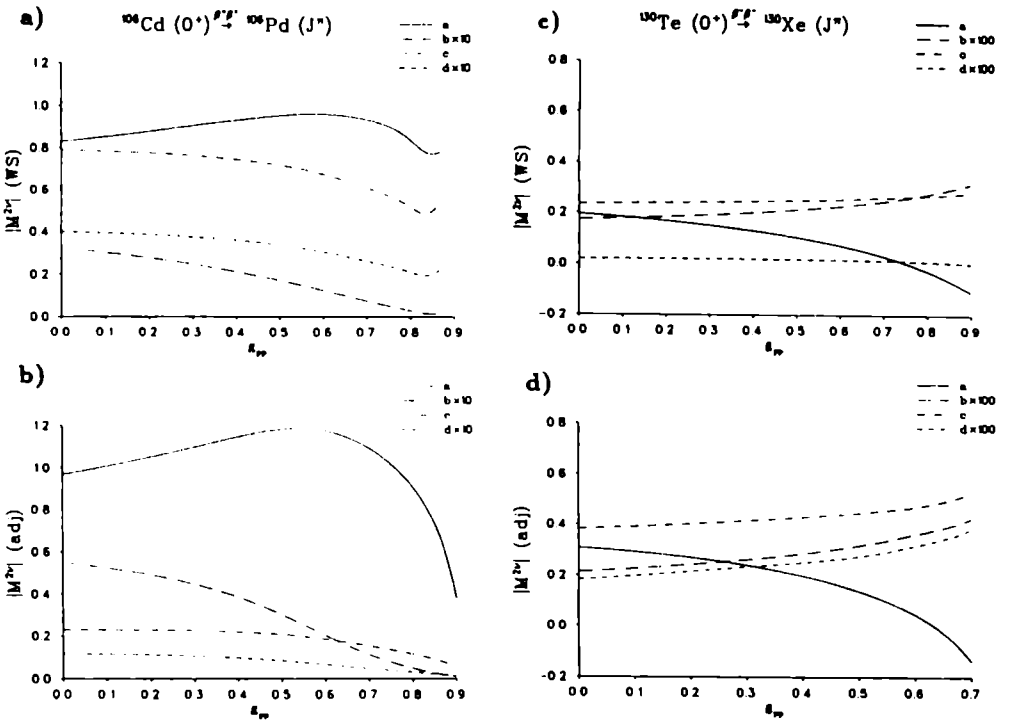

Fig. 1. Dependence of the double-beta matrix elements on g_{pp} for the decay ^{106}Cd $\rightarrow$ ^{106}Pd in a) WS basis, b) adjusted basis, and for the decay ^{130}Te $\rightarrow$ ^{130}Xe in c) WS basis, d) adjusted basis. Case a denotes the g.s. $\rightarrow$ g.s. transition, case b the g.s. $\rightarrow$ 2_1^+ transition, case c the g.s. $\rightarrow$ $0^+_{2-\text{phonon}}$ transition, and case d the g.s. $\rightarrow$ $2^+_{2-\text{phonon}}$ transition.

experimental data to make the adjustment).

A realistic nucleon-nucleon interaction, based on the G matrix derived from the Bonn one-boson-exchange potential [48], was used to calculate the two-body interaction matrix elements. The bare G matrix is renormalized to take into account the finite size of the nucleus [14] and the limited model space used in the calculations. The short-range part of the nuclear correlations is renormalized by introducing an overall scale of the monopole part of the interaction, separately for protons and neutrons. Technically this is achieved by performing a BCS calculation and comparing the thus-obtained pairing gap with the one extracted from the empirical separation energies [49]. In addition, to study the underlying mean field, the resulting quasiparticle energies are compared with the afore mentioned low-energy spectrum of the neighbouring nuclei with one extra nucleon.

To give a better quantitative idea of the adjustment process we show in the Table 2 the changes in s.p. energies in the vicinity of the Fermi surface for ^{106}Pd and ^{106}Cd. Subsequently, Table 3 shows the experimental low-energy spectrum of four $A = 107$ nuclei (Pd,Ag,Cd,In) and the corresponding theoretical quasi-particle energies with

and without adjustment in the s.p. basis. The corresponding values of the BCS proton and neutron pairing strengths can be found by fitting the pairing gap with the method described above. The changes in the s.p. energies have the effect of improving the QRPA energies both for ^{106}Pd and ^{106}Cd and the corresponding $\log ft$ values in β^- decays ^{106}Rh $\rightarrow$ ^{106}Pd and ^{106}Ag $\rightarrow$ ^{106}Cd and β^+/EC decays ^{106}Ag $\rightarrow$ ^{106}Pd and ^{106}In $\rightarrow$ ^{106}Cd. These changes are at most of the order of one unit in $\log ft$. Only the β^+/EC transition to the g.s. of ^{106}Cd is not affected.

The rest of the model parameters are defined as follows. The overall particle-hole strength, $G_{\rm ph}$, of the I^π $(= 0^+, 2^+, 3^-, 4^+)$ channel of the proton-proton and the neutron-neutron two-body matrix elements, used in the QRPA calculation, has been fixed by the energy of the lowest nuclear state of multipolarity I^π. In this energy fitting the experimental state has to be assumed to be dominated by seniority $v = 2$ components in order to correspond to two-quasiparticle excitations of the QRPA wave function. Thus, special care is needed in cases where two-phonon-type excitations (dominated by seniority $v = 4$ components) of $I^\pi = 0^+, 4^+$ enter the energy region of the $v = 2$ states in the experimental spectrum. In some cases one might expect mixing between $v = 2$ and $v = 4$ wave functions which renders a reliable fitting even more difficult. In these cases the QRPA energy can be roughly fixed to correspond to the energy region where the two mixing I^π states coexist.

The 0^+ states are a special case among the other multipolarities within the spherical QRPA framework. In the QRPA the lowest 0^+ two-quasiparticle state is spurious and arises from the non-conservation of the particle number in the BCS ground state [45]. A pleasant feature of this spuriosity is that there are no spurious components which would mix into the other two-quasiparticle 0^+ states than the lowest one, which leads to complete spuriosity of the lowest 0^+ QRPA phonon [45]. By bringing the first QRPA root to zero energy one can then easily get rid of this spuriosity and fix the interaction matrix elements by fitting the energy of the second QRPA root using the experimental energy of the lowest $v = 2$ 0^+ state.

The resulting deviations from the pure G matrix value $G_{\rm ph} = 1.0$ are at most of the order of 30 per cent for the Woods–Saxon basis and 40 per cent for the adjusted one. The adopted value of the particle-hole strength of the proton-neutron channel, $g_{\rm ph}$, reproduces the semiempirical location [51] of the Gamow–Teller giant 1^+ resonance (GTGR) for reasonable values of the particle-particle strength (see below) in a *pn*QRPA calculation. For other *pn*QRPA multipolarities J^π the pure G matrix value of $g_{\rm ph} = 1.0$ is chosen unless ordinary β decays are strongly dependent on this parameter.

The particle-particle strength, $g_{\rm pp}$, scaling the *pn* channel matrix elements, has traditionally been a free parameter of the *pn*QRPA theory with which one reproduces either experimental β-decay strengths [16] or $2\nu\beta\beta$-decay half-lives [14,15]. This adjustment has been done in a hope to create a systematics of the values of $g_{\rm pp}$ to be better able to predict the orders of magnitude of the $0\nu\beta\beta$-decay observables. This method is, however, not a very accurate one since in some cases, for the physically reasonable values (i.e. near $g_{\rm pp} = 1.0$) of $g_{\rm pp}$, the $2\nu\beta\beta$ half lives depend strongly on $g_{\rm pp}$ and a value of $g_{\rm pp}$, determined by systematics, might be too inaccurate. In addition, in some cases the break-down of the *pn*QRPA (imaginary first root of the *pn*QRPA equations) occurs well before the extrapolated value of $g_{\rm pp}$ and no systematics will produce a physically acceptable result.

The above-described behaviour is, of course, dependent on the single-particle

Table 4. The values of integrated kinematical factors $F_{GT}^{(2\nu)}$ for $2\nu\beta^-\beta^-$ decays for several parent nuclei and 0^+ and 2^+ final angular momenta.

	$F_{GT}^{(2\nu)}(J_f)$ [1/y]				
J_f	^{76}Ge	^{82}Se	^{96}Zr	^{100}Mo	^{116}Cd
$0^+_{g.s.}$	$1.3 \cdot 10^{-19}$	$4.2 \cdot 10^{-18}$	$1.8 \cdot 10^{-17}$	$8.9 \cdot 10^{-18}$	$7.4 \cdot 10^{-18}$
2^+_1	$1.1 \cdot 10^{-21}$	$2.0 \cdot 10^{-19}$	$2.1 \cdot 10^{-18}$	$1.7 \cdot 10^{-18}$	$5.8 \cdot 10^{-21}$
0^+_{2-ph}	$1.9 \cdot 10^{-22}$	$1.2 \cdot 10^{-20}$	$8.4 \cdot 10^{-20}$	$8.7 \cdot 10^{-20}$	$2.2 \cdot 10^{-22}$
2^+_{2-ph}	$3.7 \cdot 10^{-24}$	$2.4 \cdot 10^{-20}$	$2.4 \cdot 10^{-20}$	$1.0 \cdot 10^{-20}$	$6.6 \cdot 10^{-26}$
	^{124}Sn	^{128}Te	^{130}Te	^{136}Xe	
$0^+_{g.s.}$	$1.5 \cdot 10^{-18}$	$7.8 \cdot 10^{-22}$	$4.4 \cdot 10^{-18}$	$1.1 \cdot 10^{-18}$	
2^+_1	$2.5 \cdot 10^{-20}$	$3.0 \cdot 10^{-27}$	$2.6 \cdot 10^{-19}$	$3.2 \cdot 10^{-20}$	
0^+_{2-ph}	$3.3 \cdot 10^{-21}$	0	$4.6 \cdot 10^{-20}$	$1.2 \cdot 10^{-21}$	
2^+_{2-ph}	$1.2 \cdot 10^{-22}$	0	$5.7 \cdot 10^{-21}$	$3.0 \cdot 10^{-23}$	

Table 5. The values of integrated kinematical factors $F_{GT}^{(2\nu)}$ of 2νECEC decays fordecays for several parent nuclei and 0^+ and 2^+ final angular momenta.

	$F_{GT}^{(2\nu)}(J_f)$ [1/y]					
J_f	^{78}Kr	^{92}Mo	^{96}Ru	^{106}Cd	^{124}Xe	^{130}Ba
$0^+_{g.s.}$	$2.0 \cdot 10^{-21}$	$3.7 \cdot 10^{-22}$	$6.9 \cdot 10^{-21}$	$1.6 \cdot 10^{-20}$	$5.1 \cdot 10^{-20}$	$4.1 \cdot 10^{-20}$
0^+_{2-ph}	$1.2 \cdot 10^{-22}$	$1.9 \cdot 10^{-26}$	$4.7 \cdot 10^{-22}$	$1.5 \cdot 10^{-21}$	$3.0 \cdot 10^{-21}$	$2.5 \cdot 10^{-21}$

energies of the model space chosen: for some choices of the single-particle energies, typically for some adjusted bases in which orbitals are brought nearer to each other, the ground state correlations grow very rapidly with increasing g_{pp} and the violation of the Pauli exclusion principle by the excessive correlations eventually destroys the *pn*QRPA ground state. One possible method to avoid this anomaly is to resort to the renormalized *pn*QRPA theory [52] or to adjust g_{pp} by using β-decay data of the odd-odd nuclei near the $2\nu\beta\beta$ parent and daughter, a method used in this work. Here the β^- branch is preferred since the *pn*QRPA is flexible enough to reproduce almost any allowed $\log ft_-$ value of a $1^+ \rightarrow 0^+_{g.s.}$ transition. The β^+/EC branch is more problematic and usually the pnQRPA overestimates the associated $1^+ \rightarrow 0^+_{g.s.}$ decay strength. For the presently-discussed cases the obtained values of g_{pp} are systematically (10 to 30 per cent) less than 1.0 for the 1^+ pnQRPA channel. For other multipolarities than 1^+ the bare value of $g_{pp} = 1.0$ is, again, chosen unless ordinary β decays show considerable dependence on g_{pp}.

In all cases, discussed in the following, one notices the typical strong dependence of the g.s. $\rightarrow$ g.s. $2\nu\beta\beta$ transition matrix element on g_{pp} near $g_{pp} = 1.0$. Two typical examples are shown in Fig. 1 where the g_{pp} dependence of the transitions

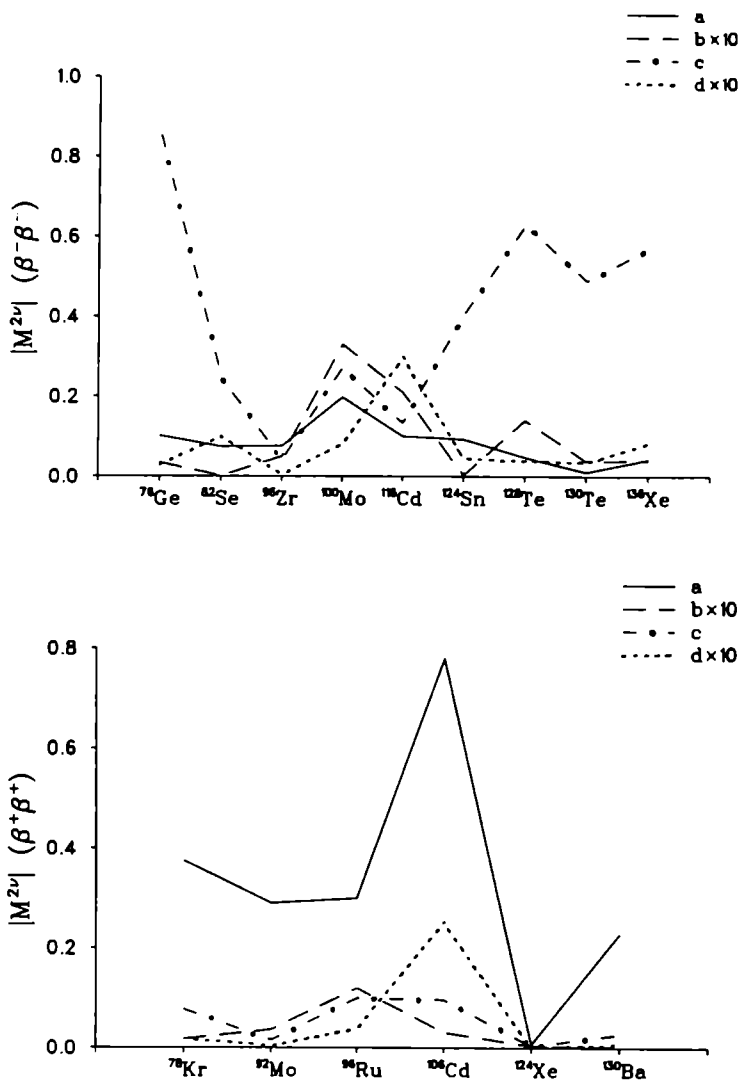

Fig. 2. Dependence of the double-beta matrix elements on parent nucleus for a) $2\nu\beta^-\beta^-$ transitions, and b) 2νECEC transitions. Case a denotes the g.s. $\rightarrow$ g.s. transition, case b the g.s. $\rightarrow 2_1^+$ transition, case c the g.s. $\rightarrow 0^+_{2-\text{phonon}}$ transition, and case d the g.s. $\rightarrow 2^+_{2-\text{phonon}}$ transition.

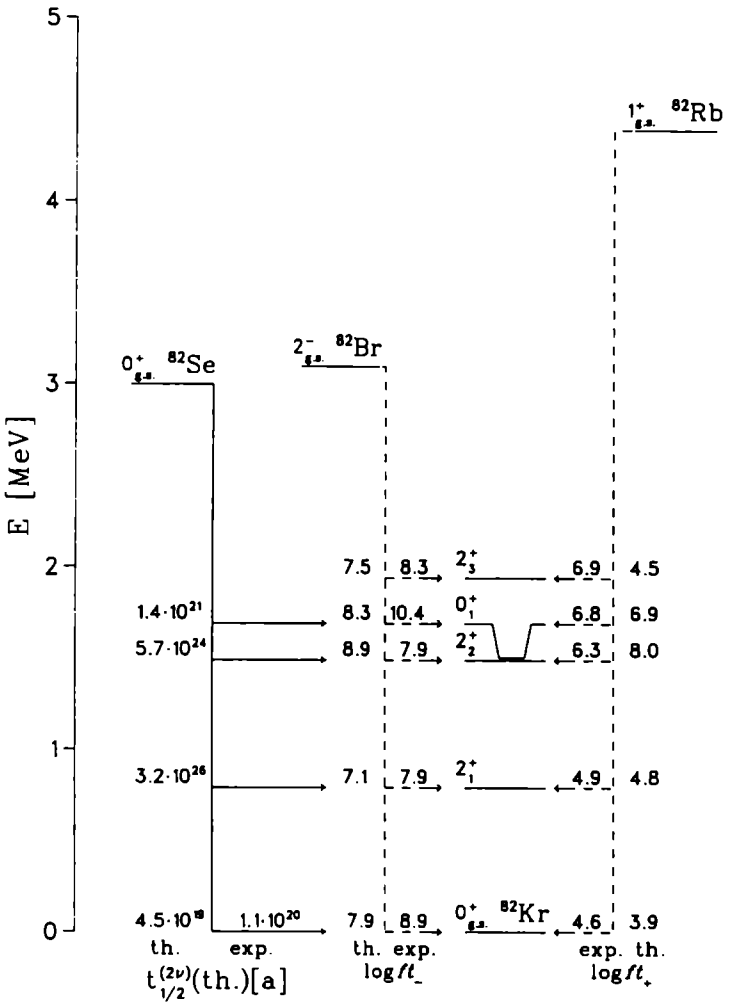

Fig. 3. Single and double beta decays for the $A = 82$ isobars in the Woods–Saxon single-particle basis. Experimental data is from ref. [34,55].

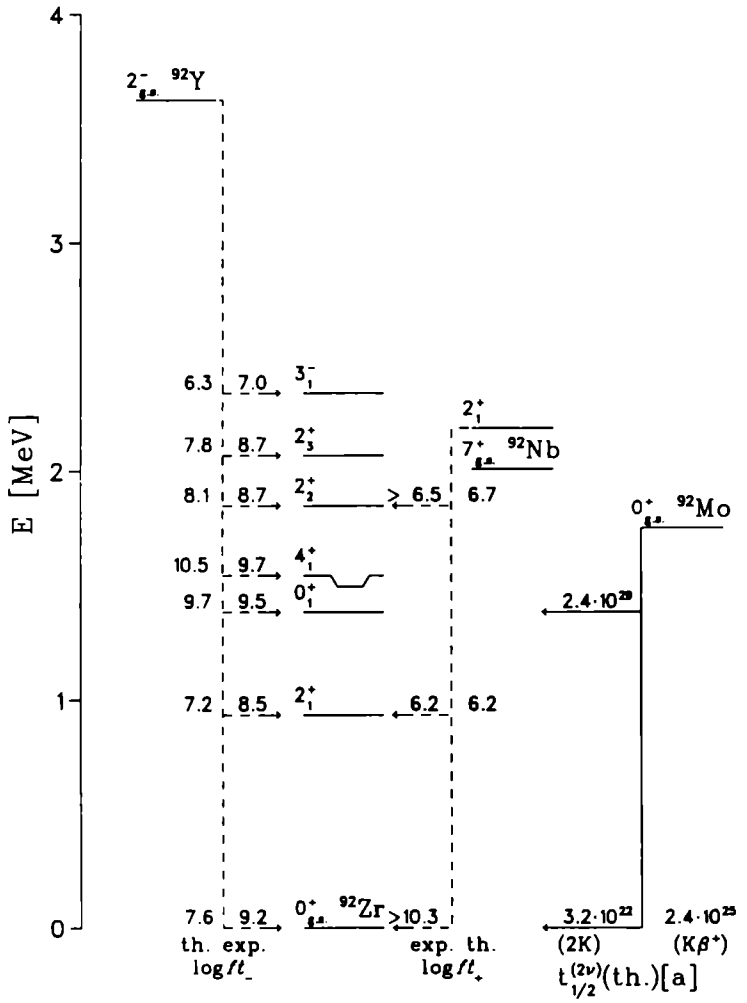

Fig. 4. Single and double beta decays for the $A = 92$ isobars in the Woods–Saxon single-particle basis. Experimental data is from ref. [56].

g.s. $\rightarrow$ g.s., g.s. $\rightarrow 2^+_1$, and g.s. $\rightarrow [2^+_1 \otimes 2^+_1]_{J_f}$, $J_f = 0^+, 2^+$ has been studied for the $2\nu\beta^-\beta^-$ transition ^{130}Te $\rightarrow$ ^{130}Te (Figs. 1a, 1b) and 2ν2K transition ^{106}Cd $\rightarrow$ ^{106} Pd (Figs. 1c, 1d). Both the Woods–Saxon and the adjusted basis have been used. "Negative" absolute value of a matrix element signifies a change in the sign of the matrix element. This strong variation of the $2\nu\beta\beta$ matrix element makes it necessary to fix the value of $g_{\rm pp}$ independently of the $2\nu\beta\beta$ decay.

In Fig. 1 one further notices that the rest of the transitions (to 2^+_1 and the two-phonon states) are not very sensitive to the variation in the value of $g_{\rm pp}$, especially for the $2\nu\beta^-\beta^-$ branch. This is a rather general feature and follows from the special structure of the one-phonon (4) and two-phonon (5) transition amplitudes where there are two or three small backward-going amplitudes ($Y_{\rm pn}$ and $W_{aa'}$) multiplied by each other thus yielding small numbers in comparison with a similar contribution coming from the forward-going amplitudes ($X_{\rm pn}$ and $Z_{aa'}$) which, in general, are

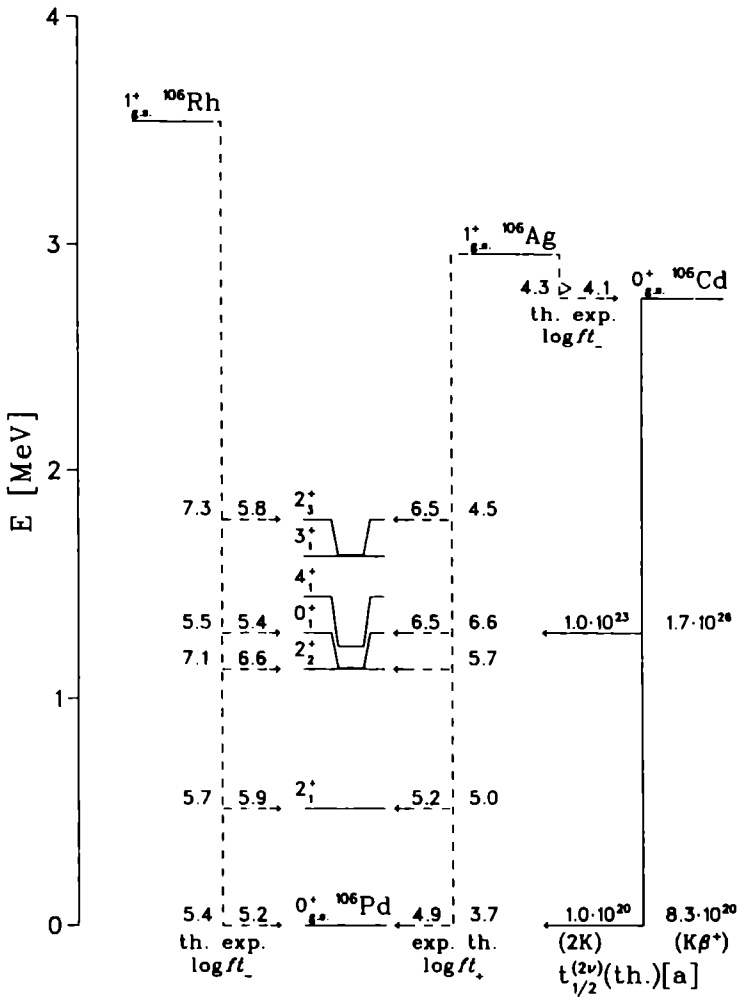

Fig. 5. Single and double beta decays for the $A = 106$ isobars in the adjusted single-particle basis. Experimental data is from ref. [57].

much bigger than the corresponding backward-going ones. Only in cases where the forward-going amplitudes are small and/or the BCS occupation factor u and v are extremely favourable (eg. when $v_p v_n$ or $u_p u_n$ are near unity in eq. (4), or $u_p v_n$ is much smaller than $v_p u_n$ in eq. (5)) the backward contribution can become important.

From figure 1c) one can see that for the Woods–Saxon basis the g.s. $\rightarrow$ g.s. matrix element behaves in a strange way near $g_{\rm pp} = 1.0$, as already seen in the case of the ^{96}Ru and ^{106}Cd decays in ref. [53]. This non-smooth behaviour of the WS matrix element may be associated with the single-particle energies and can be cured by resorting to the adjusted basis as seen in the figures. It has to be stressed that, contrary to the (rather arbitrary) method in [54], the present adjustment has been based strictly on odd-mass energy spectra, independently of the $2\nu\beta\beta$-decay observables.

In the case of ^{130}Te one can observe that the matrix elements to the excited states are almost independent of $g_{\rm pp}$, both for the Woods–Saxon and the adjusted basis. Another clear characteristic of Fig. 1 is the fact that the transition matrix elements to states with $J = 0$ are larger by a factor of at least 10 when compared to matrix elements describing $2\nu\beta\beta$ transitions to states with $J_{\rm f} = 2$. This is due to the energy denominator in Eq. (8) where the larger exponent for $J_{\rm f} = 2$ strongly suppresses the intermediate 1^+ contributions to the total matrix element.

In figure 2 we show the systematics obtained by our calculations for 9 $2\nu\beta^-\beta^-$ decays and 6 2νECEC decays. Matrix elements for transitions g.s. $\rightarrow$ g.s., g.s. $\rightarrow 2_1^+$, and g.s. $\rightarrow [2_1^+ \otimes 2_1^+]_{J_{\rm f}}$, $J_{\rm f} = 0^+, 2^+$ are depicted as functions of the parent nucleus. Tables 4 and 5 give the corresponding integrated kinematical factors for the $2\nu\beta^-\beta^-$ and 2νECEC decays, respectively. If the transition is forbidden by the Q value, the corresponding integrated kinematical factor has the value 0. For these cases no double beta transition is possible but the corresponding matrix element is calculated to complete the systematics. For the $2\nu\beta^-\beta^-$ decays the phase space factors are given for all final angular momenta but for the 2νECEC only the values for $J_{\rm f} = 0^+_{\rm g.s.}$ and $J_{\rm f} = 0^+_{\rm 2-ph}$ are available. The values given are those used for the half-life estimates.

We can easily see that the matrix elements for transitions to final states with $J_{\rm f} = 2$ are smaller than the $J_{\rm f} = 0$ matrix elements by at least an order of magnitude. Matrix elements for the ground state transition are of the order of 0.1 for the $2\nu\beta^-\beta^-$ decays and of the order of 0.3 for the 2νECEC decays with the major exceptions of ^{108}Cd for which the matrix element is enhanced and ^{124}Xe for which the matrix element is heavily suppressed. On the $2\nu\beta^-\beta^-$ side the matrix element for ^{130}Te is obtained by fitting the half-life estimate.

In the case of the excited states we can see that the transition to the $0^+_{\rm 2-ph}$ state has a quite large matrix element in the case of several $2\nu\beta^-\beta^-$ parent nuclei but for the 2νECEC transitions the matrix element is around 0.05. The transitions to 2_1^+ and $2^+_{\rm 2-ph}$ states have quite small matrix elements in general, the value lying between 10^{-4} and 10^{-2} and the largest matrix elements being -0.033 (^{100}Mo) and 0.021 (^{116}Cd) for $J_{\rm f} = 2_1^+$ and -0.030 (^{116}Cd) and -0.025 (^{106}Cd) for $J_{\rm f} = 2^+_{\rm 2-ph}$.

The main results of the calculations have been summarized in Figs. 3 - 7. In Fig. 3 the $2\nu\beta^-\beta^-$ decay ^{82}Se $\rightarrow$ ^{82}Kr is depicted. The β^- decay ^{82}Br $\rightarrow$ ^{82}Kr and β^+/EC decay ^{82}Rb $\rightarrow$ ^{82}Kr are also included. Here both decays give results of similar quality. In both cases the ground state transition is too strong. Transitions

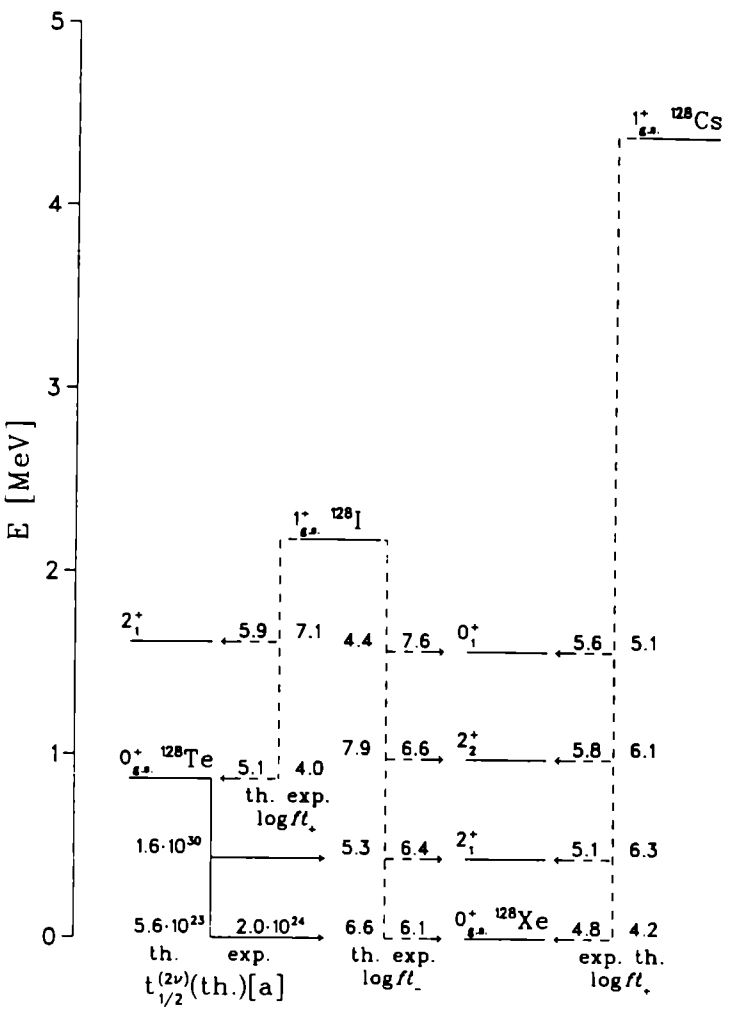

Fig. 6. Single and double beta decays for the $A = 128$ isobars in the adjusted single-particle basis. Experimental data is from ref. [34,59].

to the 2_1^+ state give the best results for this isobaric chain. The double beta decay g.s. $\rightarrow$ g.s. transition shows too short a half-life by a factor of 2.

In Fig. 4 the $2\nu 2K$ decay of ^{92}Mo is considered. Lack of available experimental data leaves us just with the β^- decay ^{92}Y $\rightarrow$ ^{92}Zr and β^+/EC decay ^{92}Nb $\rightarrow$ ^{92}Zr. All results are for the Woods–Saxon basis as there is not enough data to adjust the single-particle energies. The theoretical $\log ft$ values are not good on the average for either the β^- decay or the β^+/EC decay, but the comparison is slightly more favourable for the latter. As seen from table 5 the phase-space integrals for the double beta decay are quite small due to small Q value. Experimental limits for the half-lives are not yet very stringent, but the NEMO collaboration will conduct an experiment which should yield an improvement of the limits to around 10^{20} years.

Fig. 5 shows the 2νECEC decay of ^{106}Cd $\rightarrow$ ^{106} Pd. Also the ordinary β decays to ^{106}Pd are included. The behaviour of the 2νECEC matrix elements has been already shown as functions of g_{pp} in Fig. 1. The results in Fig. 5 are for the

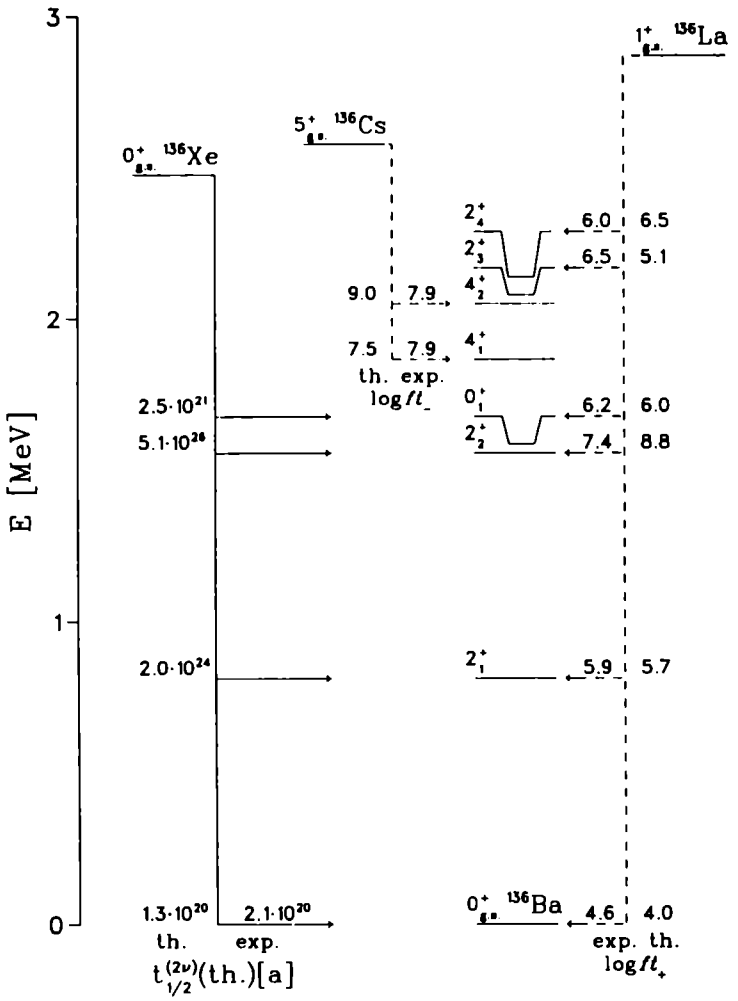

Fig. 7. Single and double beta decays for the $A = 136$ isobars in the adjusted single-particle basis. Experimental data is from ref. [35,55].

adjusted basis. The log ft values for β^- decay are, once again, nicely reproduced, but the results for the β^+/EC branch are not as good. Especially the ground-state transition is predicted too strong. For 2ν2K decay the predicted half-lives are very much larger than the experimental lower limits for half-lives, which are in the range of 10^{18} to 10^{19} years [58]. Other theoretical estimates can be found from [54].

In Fig. 6 another $2\nu\beta^-\beta^-$ decay is shown. It has quite small Q window so that the decay ^{128}Te $\rightarrow$ ^{128}Xe is only possible to the ground state and the 2_1^+ state. The β^- decay ^{128}I $\rightarrow$ ^{128}Xe is described reasonably, except in the case of the 0_1^+ transition which becomes much too strong in theoretical calculations. The β^+/EC decay ^{128}Cs $\rightarrow$ ^{128}Xe shows consistently too strong g.s. transition rate but otherwise the log ft values are predicted reasonably well. The obtained $2\nu\beta\beta$ half-life for the ground-state decay is too small by a factor of 4.

Lastly, we have the $2\nu\beta^-\beta^-$ decay ^{136}Xe $\rightarrow$ ^{136}Ba in Fig. 7. Here the β^- decaying ^{136}Cs has a ground state 5^+ which does not give much information on $g_{\rm pp}$ but ^{136}La has a 1^+ ground state which is suited for extracting an estimate for $g_{\rm pp}$. Here both β^- and β^+/EC decays give quite nice results and the overestimation of the allowed g.s. transition is not so bad. For the $2\nu\beta^-\beta^-$ decay one gets slightly too short theoretical half-life for the g.s. transition.

References

1. S. R. Elliott, A. A. Hahn and M. K. Moe, Phys. Rev. Lett. **59** (1987) 2020 ; S. R. Elliott, A. A. Hahn, M. K. Moe, M. A. Nelson and M. A. Vient, Phys. Rev. **C46** (1992) 1535 ; F. T. Avignone III *et al.*, Phys. Lett. **B256** (1991) 559 ; J. T. Lee, O. K. Manuel and R. I. Thorpe, Nucl. Phys. **A529** (1991) 29
2. M. K. Moe, Int. J. Mod. Phys. **E2** (1993) 507 ; M. Moe and P. Vogel, Annu. Rev. Nucl. Part. Sci. **44** (1994) 247
3. A. Faessler, Prog. Part. Nucl. Phys. **21** (1988) 183
4. M. Doi, T. Kotani and E. Takasugi, Prog. Theor. Phys. Suppl. **83** (1985) 1
5. J. D. Vergados, Phys. Reports **133** (1986) 1
6. T. Tomoda, Rep. Prog. Phys. **54** (1991) 1
7. R. N. Mohapatra, Prog. Part. Nucl. Phys. **26** (1991) 1
8. J. Suhonen and O. Civitarese, Phys. Lett. **B312** (1993) 367
9. J. Suhonen and E. Hammarèn Phys. Rev. **C47** (1993) 757
10. G. Gelmini and M. Roncadelli, Phys. Lett. **B99** (1981) 411 ; A. Santamaria and J. W. F. Valle, Phys. Rev. Lett. **60** (1988) 397 ; C. Aulakh and R. Mohapatra, Phys. Lett. **B119** (1982) 136
11. Z. G. Berezhiani, A. Yu. Smirnov and J. W. F. Valle, Phys. Lett. **B291** (1992) 99
12. J. Suhonen and O. Civitarese, J. Phys. **G20** (1994) 347
13. P. Vogel and M. Zirnbauer, Phys. Rev. Lett. **57** (1986) 3148
14. O. Civitarese, A. Faessler and T. Tomoda, Phys. Lett. **B194** (1987) 11
15. K. Muto, E. Bender and H. V. Klapdor, Z. Phys. **A334** (1989) 177
16. J. Suhonen, A. Faessler, T. Taigel and T. Tomoda, Phys. Lett. **B202** (1988) 174 ; J. Suhonen, T. Taigel and A. Faessler, Nucl. Phys. **A486** (1988) 91
17. J. Suhonen and O. Civitarese, Phys. Lett. **B280** (1992) 191
18. A. A. Raduta, A. Faessler and S. Stoica, Nucl. Phys. **A534** (1991) 149 ; A. A. Raduta, A. Faessler, S. Stoica and W. A. Kaminski, Phys. Lett. **B254** (1991) 7
19. T. Tomoda and A. Faessler, Phys. Lett. **B199** (1987) 475
20. K. Muto, E. Bender and H. V. Klapdor, Z. Phys. **A334** (1989) 187

21. J. Suhonen, S. B. Khadkikar and A. Faessler, Phys. Lett. **B237** (1990) 8 ; Nucl. Phys. **A529** (1991) 727 ; Nucl. Phys. **A535** (1991) 509
22. F. Krmpotić, Phys. Rev. **C48** (1993) 1452 ; F. Krmpotić and S. Shelly Sharma, Nucl. Phys. **A572** (1994) 329
23. O. Castaños, J. G. Hirsch, O. Civitarese and P. O. Hess, Nucl. Phys. **A571** (1994) 276
24. M. Beck *et al.*, Phys. Lett. **B283** (1992) 32
25. A. S. Barabash, A. V. Kopylov and V. I. Cherehovsky, Phys. Lett. **B249** (1990) 186
26. H. Ejiri *et al.*, Phys. Lett. **B258** (1991) 17
27. A. Balysh *et al.*, Phys. Lett. **B283** (1992) 32
28. N. Kudomi *et al.*, Phys. Rev. **C46** (1992) R2132
29. M. Beck *et al.*, Z. Phys. **A343** (1992) 397
30. A. S. Barabash *et al.*, Nucl. Phys. B (Proc. Suppl.) **28A** (1992) 236
31. A. Piepke *et al.*, Nucl. Phys. **A577** (1994) 493
32. C. Arpesella *et al.*, Europhys. Lett. **27** (1994) 29
33. A. S. Barabash *et al.*, Phys. Lett. **B345** (1995) 408
34. V. I. Tretyak and Yu. G. Zdesenko, to appear in At. Data Nucl. Data Tables
35. A. Griffiths and P. Vogel, Phys. Rev. **C46** (1992) 181
36. J. Suhonen, Nucl. Phys. **A563** (1993) 91
37. J. Suhonen and O. Civitarese, Phys. Lett. **B308** (1993) 212
38. O. Civitarese and J. Suhonen, Nucl. Phys. **A575** (1994) 251
39. O. Civitarese and J. Suhonen, J. Phys. **G20** (1994) 1441 ; ibid. Nucl. Phys. **A578** (1994) 62
40. J. Suhonen and O. Civitarese, Phys. Rev. **C49** (1994) 3055
41. J. Suhonen and O. Civitarese, Nucl. Phys. **A584** (1995) 449
42. S. Stoica, Phys. Rev. **C49** (1994) 2240 ; ibid. Phys. Lett. **B350** (1995) 152
43. A. A. Raduta and J. Suhonen, submitted for publication
44. J. G. Hirsch, O. Castaños, P. O. Hess and O. Civitarese, Nucl. Phys. **A589** (1995) 445
45. M. Baranger, Phys. Rev. **120** (1960) 957
46. M. Doi and T. Kotani, Prog. Theor. Phys. **87** (1992) 1207
47. A. Bohr and B.R. Mottelson, Nuclear structure, vol. I (Benjamin, New York, 1969)
48. K.Holinde, Phys. Reports **68** (1981) 121
49. G. Audi and A. H. Wapstra, Nucl. Phys. **A565** (1993) 1
50. J. Blachot, Nucl. Data Sheets **62** (1991) 709
51. D. J. Horen *et al.*, Phys. Lett. **B99** (1981) 383
52. J. Toivanen and J. Suhonen, Phys. Rev. Lett. **75** (1995) 410
53. J. Suhonen, Phys. Rev. **C48** (1993) 574
54. M. Hirsch, K. Muto, T. Oda and H. V. Klapdor-Kleingrothaus, Z. Phys. **A347** (1994) 151
55. T.W. Barrows Nucl. Data Sheets **52** (1987) 273
56. C.M. Baglin, Nucl. Data Sheets **70** (1993) 1
57. D. De Frenne et al., Nucl Data Sheets **53** (1988) 73
58. E.B. Norman and M.A. De Faccio, Phys. Lett. **B148** (1984) 31
59. K. Kitao, NDS **38** (1983) 191

7. INVESTIGATION OF NUCLEAR SYSTEMS BY ELECTRON SCATTERING

SPIN DEPENDENT OBSERVABLES IN ELECTRON SCATTERING

J. A. CABALLERO, E. GARRIDO, E. MOYA DE GUERRA, P. SARRIGUREN and J. M. UDIAS
Instituto de Estructura de la Materia, CSIC, Serrano 119
28006 Madrid, SPAIN

ABSTRACT

We study the properties of the spin–dependent one–body density for odd–A polarized deformed nuclei within the mean field approximation. We find analytic expressions connecting intrinsic and laboratory momentum distributions. The latter are related to observable transition densities that can be proved in $\overrightarrow{A}(\vec{e},e'N)R$ reactions. We also show that the complex structure of the deformed orbitals can be proved by coincidence measurements with polarized beam and targets. Illustrative results are presented for the reactions $^{21}\overrightarrow{Ne}(\vec{e},e'n)^{20}Ne$ and $^{37}\overrightarrow{K}(\vec{e},e'p)^{36}Ar$.

1. Introduction

Electron scattering is one of the most powerful tools to investigate nuclear structure and dynamics. For high incoming electron energy and transfer energy $\omega \sim q^2/2M$, the dominant process is quasi–elastic scattering. This roughly corresponds to interacting with a nucleon in the nucleus that is at rest and ejecting it with momentum q. Coincidence reactions of the type A(e,e'N)R provide very detailed information on the single–particle structure of the nucleus. The simplest approximation to analyze this type of processes is the Plane Wave Impulse Approximation (PWIA). Here, in addition to the one–photon exchange, one makes the assumption that the virtual photon is absorbed by a single–nucleon in the target nucleus that is ejected and detected, without any further interaction with the residual nucleus. Although PWIA is an oversimplification in the description of the reaction mechanism, it gives a very clear picture of the physics contained in the problem and has proven to be very useful in studying the nuclear structure under appropriate kinematic conditions.

In the case of unpolarized beam and target, and within PWIA, the differential cross section for coincidence reactions of the type (e,e'N), factorizes as

$$\frac{d\sigma}{d\Omega_e d\Omega_N d\epsilon' dE_N} = \frac{p_N M M_R}{E_R}\sigma^{eN} S(p,E) \ , \tag{1}$$

where σ^{eN} is the electron–nucleon cross section and $S(p,E)$ the spectral function. The kinematic variables p_N, M, M_R and E_R are the outgoing nucleon momentum, the nucleon mass, and the mass and total energy of the residual nucleus, respectively. The electron–nucleon cross section (σ^{eN}) deals directly with the interaction between the incident electrons and the bound nucleons inside the nucleus [1,2]. The spectral

function $S(p,E)$ provides the probability to find a nucleon in the target with certain energy (E) and momentum (p). It is given by

$$S(p,E) = \overline{\sum_A} \sum_R \delta(E - M_A^0 + E_R) |\langle \Psi_R | a_{p\sigma} | \Psi_A \rangle|^2 \ , \tag{2}$$

where $a_{p\sigma}$ is the annihilation operator for a nucleon with momentum p and spin projection σ, and M_A^0 represents the mass of the target nucleus in its ground state. The sum (average) over R (A) involves all possible nuclear states. Restricting to transitions to discrete states of the residual nucleus, the spectral function is most conveniently written in the form

$$S(p,E) = \frac{1}{2J_A+1} \sum_{\Psi_R J_R} \delta(E - M_A^0 + E_R) \sum_{\ell j} |\langle \Psi_R J_R | a_{\ell j}(p) | \Psi_A J_A \rangle|^2 \ , \tag{3}$$

where $\Psi_A J_A$ represents the wave function of the target nucleus in its ground state, $\Psi_R J_R$ is the wave function of the residual nuclear system in a bound state with angular momentum J_R, and $a_{\ell j}(p)$ is the annihilation operator for a nucleon with momentum p and quantum numbers ℓj. In the independent particle shell model where spherical orbitals $\alpha \equiv n\ell j$ with degeneracy $2j+1$ and binding energies E_α are occupied, the spectral function takes the simple form

$$S(p,E) = \sum_\alpha \delta(E_m - E_\alpha) N_\alpha n_\alpha(p) \ , \tag{4}$$

where N_α and $n_\alpha(p)$ are the occupation number and momentum distribution of the α orbital, respectively, and E_m is the missing energy [3]. Hence one can obtain clear information on the single–nucleon momentum distributions. However, as it was pointed out in Ref. [4] the interpretation of this information is not free from ambiguities because, at present, neither experimental data nor theoretical considerations are sufficiently comprehensive. Moreover, in principle, many corrections to PWIA can be important such as final–state nucleon–nucleus interactions (FSI), Coulomb distortions of the electron waves, two body nuclear currents, exchange terms,... In this case, although the differential cross section does not factorize in the form of Eq. (1), one can define modified spectral functions dividing the calculated and experimental cross sections by the single–nucleon cross section (σ^{eN}). Comparison of these calculated and experimental modified spectral functions allows to interpret the data within the independent particle (or quasi–particle) model framework and to identify individual bound orbitals in the target nucleus from their characteristic momentum distributions.

Most of the work in past years has been devoted to spherical nuclei. In this case each single–particle momentum distribution $n^{\{n\ell j\}}(p)$ is characteristic of the spherical orbital $\{n\ell j\}$ occupied by the nucleon. Very precise coincidence (e,e'N) measurements have made possible to map out the momentum distributions of various spherical bound orbitals [3,5]. In the case of deformed nuclei the momentum distribution of a given deformed orbital i is in general a linear combination of spherical orbitals ($n^i(p) = \sum_{\ell j} C^i_{\ell j} n_{\ell j}(p)$). Thus, for each orbital i and mean field deformation

there is a characteristic momentum distribution that can in principle be identified by these reactions. We studied in detail this issue for unpolarized even–even deformed nuclei [6-8]. We proved that the main effects of deformation in (e,e'N) are related to the higher level density of low–lying states in the residual nucleus and to the fragmentation of strength of spherical orbitals. It is important to remark that with even–even targets it is not possible to measure the total momentum distribution of the deformed orbital in a single transition, since for transitions to a well resolved discrete state of the residual nucleus only a given component ℓj of the deformed state i enters. This makes a difference with the case of odd–A deformed targets that can be polarized where, as we show in this work, one can gain the most direct evidence for the existence of deformed orbitals.

The inclusion of polarization degrees of freedom in exclusive electron scattering processes may be used as a powerful tool in extracting additional information on nuclear structure and dynamics from experiment. From general studies on this subject [9], it has been observed that polarization responses are generally comparable to the unpolarized ones and may be sensitive to specific details of the nuclear physics underlying the reaction, hence polarization experiments provide an effective mean of studying nuclear dynamics in greater detail than is available in the absence of any polarization measurement. In recent works [2,10] we have studied in detail this issue for deformed targets. We prove that, within PWIA, the differential cross section for polarized incoming electron and polarized target still factorizes in a spin–dependent electron–nucleon cross section times a polarized spectral function. How these new spin–dependent observables connect to intrinsic properties of nuclei that can not be revealed in the unpolarized case, is the other main issue we discuss in this work.

2. Brief Summary of Theory for $\vec{A}(\vec{e},e'N)R$ Reactions

The general formalism of quasi–elastic electron scattering from complex nuclei with polarized beam and target has been presented in detail in Refs. [2,9]. Here we follow the conventions of Donnelly and collaborators [2,9,10] and summarize briefly the equations of interest to describe processes of the type $\vec{A}(\vec{e},e'N)R$. We also use the same notation as in Ref. [2] for the different kinematic variables in the laboratory frame. The five–differential cross section for the $\vec{A}(\vec{e},e'N)R$ process, can be written in the form

$$\frac{d\sigma}{d\epsilon' d\Omega_e d\Omega_N} \equiv \Sigma + h\Delta = \Sigma_0(1 + \mathcal{P}_\Sigma + \mathcal{P}_\Delta) \,, \tag{5}$$

where h is the helicity of longitudinally polarized electron, and Σ_0 is the differential cross section for unpolarized beam and target. The terms $\mathcal{P}_\Sigma$ and $\mathcal{P}_\Delta$ are the polarization ratios. Using current conservation to separate transverse and longitudinal components of the electron and nuclear currents, the following standard expressions are obtained for the helicity sum (Σ) and the helicity difference (Δ) cross sections

$$\Sigma \;=\; \mathcal{K} \sum_X v_X R^X \qquad X = L, T, TL, TT \tag{6}$$

$$\Delta = \mathcal{K} \sum_{X'} v_{X'} R^{X'} \qquad X' = T', TL' \tag{7}$$

where v_X, $v_{X'}$ are the usual kinematical factors as given in Ref. [9]. The term $\mathcal{K}$ is a kinematical factor given by $\mathcal{K} = \sigma_M \frac{p_N M M_R}{M_A^0 f_{rec}}$ with σ_M and f_{rec} the standard Mott cross section and recoil factor, respectively [9].

In PWIA, the differential cross section and the different response functions can in turn be factored into a part that depends on the nuclear structure and a part that depends on the half–off–shell single–nucleon current

$$\frac{d\sigma}{d\epsilon' d\Omega_e d\Omega_N} = \frac{\mathcal{K}}{\sigma_M} \sum_{\sigma\sigma'} \sigma^{eN}_{\sigma\sigma'} M_{\sigma\sigma'}(\boldsymbol{p}, \boldsymbol{P}^*) \tag{8}$$

$$R^{X,X'} = \sum_{\sigma\sigma'} \mathcal{R}^{X,X'}_{\sigma\sigma'} M_{\sigma\sigma'}(\boldsymbol{p}, \boldsymbol{P}^*) \,, \tag{9}$$

where $\sigma^{eN}_{\sigma\sigma'}$ is the "off–shell polarized electron–nucleon cross section" and $\mathcal{R}^{X,X'}_{\sigma\sigma'}$ are the various single–nucleon response functions obtained by imposing current conservation for the single–nucleon current (see Ref. [2] for details). The function $M_{\sigma\sigma'}(\boldsymbol{p}, \boldsymbol{P}^*)$ is the "spin–dependent momentum distribution" in the laboratory frame. It is given explicitly by

$$M_{\sigma\sigma'}(\boldsymbol{p}, \boldsymbol{P}^*) = \sum_A p(A) \sum_R \langle R | a_{\boldsymbol{p}\sigma'} | A \rangle^* \langle R | a_{\boldsymbol{p}\sigma} | A \rangle \,, \tag{10}$$

where the sum over R involves all possible nuclear states including a sum over magnetic substates, since no final polarizations are measured. The initial state is assumed to be polarized, and hence the sum over A includes the weighting factor $p(A)$ that gives the probability that specific projections of the ground–state angular momentum occur; here $\boldsymbol{P}^* \equiv (\theta^*, \phi^*)$ defines the target polarization direction in the laboratory frame.

Although this paper focuses on the polarized spectral function, let us make some general comments on the half–off–shell single–nucleon current. Its study in the case of polarized target and beam was presented in detail in Ref. [2]. In that work we calculated the single–nucleon cross section $\sigma^{eN}_{\sigma\sigma'}$ and single–nucleon responses $\mathcal{R}^{K,K'}_{\sigma\sigma'}$ for two different choices of the half–off–shell nucleon current operator, as well as for different prescriptions concerning current conservation. In this sense, it is important to remark that the total many–body current (nuclear current) must be conserved; however the impulse approximation (IA) involves only one–body contributions. Consequently, there is no *a priori* reason to expect the IA to lead to a conserved current. In fact, we found that matrix elements of the two choices of the nucleon current violate conservation of the one–body current according to the amount of off–shellness. Therefore, one may impose current conservation and eliminate the third component of the single–nucleon current in favour of the zero component. One may also eliminate the zero component in favour of the third, or one may simply calculate independently the four components without imposing current conservation. Final analytic expressions for the single–nucleon responses as

well as a general study of their properties and symmetries, and the uncertainty in the results due to the off-shellness character of the bound nucleon are presented in Ref. [2].

2.1. Polarized Spectral Function and Deformed Nuclei

In this section we discuss the spectral function/momentum distribution that enters in the analysis (within PWIA) of the reaction $\overrightarrow{A}(\vec{e},e'N)R$ for odd-A deformed targets and transitions to discrete states J_R^π in the residual nucleus. In this case the spin-dependent momentum distribution in the laboratory frame is given by

$$M_{\sigma\sigma'}^{(J_A\to J_R)}(\boldsymbol{p},\boldsymbol{P}^*)=\sum_{M_A}p(M_A)\sum_{M_R}\langle J_RM_R|a_{\boldsymbol{p}\sigma'}|J_AM_A(\Omega^*)\rangle^*\langle J_RM_R|a_{\boldsymbol{p}\sigma}|J_AM_A(\Omega^*)\rangle\ . \tag{11}$$

It is important to note that the matrix $M_{\sigma\sigma'}^{(J_A\to J_R)}(\boldsymbol{p},\boldsymbol{P}^*)$ is related to the polarized spectral function by

$$S_{\sigma\sigma'}(\boldsymbol{p},E,\boldsymbol{P}^*)=\sum_{J_R}\delta\left(E-M_A^0+E_{J_R}\right)M_{\sigma\sigma'}^{(J_A\to J_R)}(\boldsymbol{p},\boldsymbol{P}^*)\ . \tag{12}$$

In these equations all the spin projections are referred to the laboratory z-axis (along $\boldsymbol{q}$) except for M_A. The polarized target nucleus is prepared with magnetic substates $|J_AM_A\rangle$ in the direction $\boldsymbol{P}^*$ populated in a non-uniform manner with probabilities $p(M_A)$.

After some algebra, the spin-dependent matrix $M_{\sigma\sigma'}^{(J_A\to J_R)}(\boldsymbol{p},\boldsymbol{P}^*)$ can be written as follows

$$M_{\sigma\sigma'}^{(J_A\to J_R)}(\boldsymbol{p},\boldsymbol{P}^*)=\sum_J f_J^{J_A}\sum_{\ell j}\sum_{\ell' j'}\mathcal{A}_{\ell j}^{J_AJ_R}(p)\left(\mathcal{A}_{\ell' j'}^{J_AJ_R}(p)\right)^*\sum_M\chi_{\ell j\sigma,\ell' j'\sigma'}^{JM}(\hat{\boldsymbol{p}})Y_J^{-M}(\Omega^*) \tag{13}$$

with*

$$\chi_{\ell j\sigma,\ell' j'\sigma'}^{JM}(\hat{\boldsymbol{p}})=(-1)^{J_A+J_R+j+\ell'+\sigma-1/2}\hat{\ell}\hat{j}\hat{\ell}'\hat{j}'\begin{Bmatrix}J_A & J_A & J\\ j & j' & J_R\end{Bmatrix}\sum_{L=\text{even}}\sum_{K=0,\pm1}\hat{L}\hat{K}^2$$
$$\times\begin{pmatrix}\ell & \ell' & L\\ 0 & 0 & 0\end{pmatrix}\begin{pmatrix}L & J & K\\ M_L & M & M_K\end{pmatrix}\begin{pmatrix}K & 1/2 & 1/2\\ M_K & \sigma & -\sigma'\end{pmatrix}\begin{Bmatrix}L & J & K\\ \ell & j & 1/2\\ \ell' & j' & 1/2\end{Bmatrix}Y_L^{-M_L}(\hat{\boldsymbol{p}}) \tag{14}$$

and $\mathcal{A}_{\ell j}^{J_AJ_R}(p)$ $\left(\mathcal{A}_{\ell' j'}^{J_AJ_R}(p)\right)$ are the reduced nuclear matrix elements. The terms $f_J^{J_A}$ are the spherical Fano statistical tensors [9].

What it is important to remark is that for tensor components $J>0$ (which only occurs with an oriented target) and $J_R>0$ (the residual nucleus in an excited state), $M_{\sigma\sigma'}^{(J_A\to J_R)}(\boldsymbol{p},\boldsymbol{P}^*)$ contains interference terms between different ℓj components of the bound nucleon wave function. In an independent particle model, contributions from $\mathcal{A}_{\ell j}^{J_AJ_R}(p),\mathcal{A}_{\ell' j'}^{J_AJ_R}(p)$ with $\ell j\neq\ell' j'$ can only occur when the bound nucleon is in a deformed k-orbital, *i.e.*, when the target nucleus is deformed. Note that for

*We use the notation $\hat{j}=\sqrt{2j+1}$

unpolarized targets, where only the tensor rank component $J = 0$ enters, most of this information is lost.

Summarizing, our main aim in this work is to set clearly the new information that can be gained by using polarized odd–A deformed nuclei in $\vec{A}(\vec{e},e'N)R$ reactions, compared to the case of even–even deformed nuclei. In this sense, our attention is centered in two main points. First, the connection between the polarized spectral function (or spin–dependent momentum distribution in the laboratory frame) and the "**intrinsic**" momentum distribution for odd–A deformed nuclei. We show that both are intimately related and thus, measuring the former gives information on the latter. Second, we prove that the existence of ℓ, j interference terms in the polarized case is one of the most direct evidence for the existence of deformed orbitals. These two issues are discussed in detail in Sections 3 and 4, respectively. To make easier the analysis that follows, one should note that the spin–dependent matrix $M_{\sigma\sigma'}^{(J_A \to J_R)}(\boldsymbol{p}, \boldsymbol{P}^*)$ can be decomposed into a scalar ($\overline{M}$) and a vector ($\widehat{\boldsymbol{M}}$) components

$$\overline{M}^{(J_A \to J_R)}(\boldsymbol{p}, \boldsymbol{P}^*) = \mathrm{Tr}\left[M^{(J_A \to J_R)}(\boldsymbol{p}, \boldsymbol{P}^*)\right] \tag{15}$$

$$\widehat{\boldsymbol{M}}^{(J_A \to J_R)}(\boldsymbol{p}, \boldsymbol{P}^*) = \mathrm{Tr}\left[\boldsymbol{\sigma} M^{(J_A \to J_R)}(\boldsymbol{p}, \boldsymbol{P}^*)\right] , \tag{16}$$

where traces are taken in spin space.

It is easy to see that the scalar component ($\overline{M}$) only has contributions from even–J values, whereas the vector part ($\widehat{\boldsymbol{M}}$) only has contributions from odd–J values. Moreover, combining these properties with the ones shown by the different single–nucleon responses [2], one gets that the scalar component $\overline{M}$ is the only one that contributes in the electron–unpolarized response functions R^X, $X = L, T, TL, TT$. The vector term $\widehat{\boldsymbol{M}}$ enters only in the electron–polarized response functions $R^{X'}$, $X' = T', TL'$.

3. Spin Dependent Momentum Distributions

In general the one–body density is a two by two matrix in spin space. For closed shell nuclei, the momentum distribution is independent of spin. The same is true, in the mean field approximation, for even–even axially symmetric deformed nuclei due to time reversal invariance of the intrinsic ground state. However, for an odd–A deformed nucleus the intrinsic ground state is no longer time reversal invariant and the one–body density matrix is in general non diagonal in spin space. Hence, similarly to Eqs. (15) and (16), **scalar** and **vector** momentum distributions can be defined in the intrinsic frame, that contain all the information on the intrinsic spin dependent momentum distribution. It is important to realize that in order to access to this new information one needs to relate the observable spin dependent momentum distributions of the polarized nucleus in the laboratory frame (section 2.1) with the intrinsic scalar and vector momentum distributions.

3.1. Intrinsic Momentum Distributions

We represent by Ψ_k the intrinsic ground state of an odd–A nucleus with odd nucleon in state k. $\tilde{\Phi}_k$ is the wave function in momentum space for the state k,

and π_k, $\Omega_k = K$ are its quantum numbers. The intrinsic one–body spin dependent momentum distribution is then given by

$$\begin{aligned} M_{\Sigma\Sigma'}(\boldsymbol{p}) &= \langle\Psi_k|a^+_{\boldsymbol{p}\Sigma}a_{\boldsymbol{p}\Sigma'}|\Psi_k\rangle \\ &= \sum_{i\neq k} v_i^2 \left[\langle\chi_{\Sigma'}|\tilde{\Phi}_i(\boldsymbol{p},s)\rangle\langle\tilde{\Phi}_i(\boldsymbol{p},s)|\chi_\Sigma\rangle + \langle\chi_{\Sigma'}|\tilde{\Phi}_{\bar{i}}(\boldsymbol{p},s)\rangle\langle\tilde{\Phi}_{\bar{i}}(\boldsymbol{p},s)|\chi_\Sigma\rangle\right] \\ &+ \langle\chi_{\Sigma'}|\tilde{\Phi}_k(\boldsymbol{p},s)\rangle\langle\tilde{\Phi}_k(\boldsymbol{p},s)|\chi_\Sigma\rangle \end{aligned} \tag{17}$$

with v_i^2 occupation probabilities. The last term gives the contribution from the odd nucleon, while the first one gives the contribution from the nucleons in the even–even core. Introducing a **scalar** ($\overline{M}$) and a **vector** ($\widehat{M}$) components (Eqs. (15,16)), it is easy to show that the even–even core contributes only to $\overline{M}$, while the vector momentum distribution $\widehat{M}(\boldsymbol{p}) = \left(\cos\varphi_p \widehat{M}_\perp(\boldsymbol{p}), \sin\varphi_p \widehat{M}_\perp(\boldsymbol{p}), \widehat{M}_z(\boldsymbol{p})\right)$ is made up entirely by the odd nucleon. Therefore, for spin–saturated even–even nuclei the vector momentum distribution is zero in the intrinsic ground state and only the scalar momentum distribution remains. This can be written in the form

$$\overline{M}(\boldsymbol{p}) = n(\boldsymbol{p}) + n^{\text{odd}}(\boldsymbol{p}) = \sum_{\lambda=\text{even}} P_\lambda(\cos\theta_p)\left[n_\lambda(p) + n^{\text{odd}}_\lambda(p)\right] \equiv \sum_{\lambda=\text{even}} P_\lambda(\cos\theta_p)\overline{M}_\lambda(p)\ , \tag{18}$$

where $n(\boldsymbol{p})$ and $n^{\text{odd}}(\boldsymbol{p})$ denote the contribution from the even–even core and from the odd–nucleon, respectively, and $n_\lambda(p)$ represent the multipoles.

To understand better the discussion that follows it is convenient to express the densities in momentum space in terms of the spherical components of the single–particle wave functions. After some algebra we finally get,

$$\overline{M}_\lambda(p) = \sum_i \frac{2}{4\pi}\left[v_i^2 + \delta_{i,k}\left(\frac{1}{2} - v_i^2\right)\right] \sum_{\ell j \ell' j'} \Theta^{\ell j,\ell' j'}_{i,\lambda}(p) \begin{Bmatrix} j & j' & \lambda \\ \ell' & \ell & 1/2 \end{Bmatrix} (-1)^{\Omega_i+1/2}\langle j\Omega_i j' - \Omega_i|\lambda 0\rangle \tag{19}$$

$$\widehat{M}_z(\boldsymbol{p}) = \frac{\sqrt{6}}{4\pi} \sum_{L=\text{even}} \sum_{\lambda=\text{odd}} \hat{\lambda}\hat{L} P_L(\cos\theta_p) \begin{pmatrix} 1 & L & \lambda \\ 0 & 0 & 0 \end{pmatrix} \Pi^0_{L,\lambda}(p) \tag{20}$$

$$\widehat{M}_\perp(\boldsymbol{p}) = -\frac{2\sqrt{3}}{4\pi} \sum_{L=\text{even}} \sum_{\lambda=\text{odd}} \frac{\hat{\lambda}\hat{L}}{\sqrt{(L+1)L}} P^1_L(\cos\theta_p) \begin{pmatrix} 1 & L & \lambda \\ 1 & -1 & 0 \end{pmatrix} \Pi^0_{L,\lambda}(p)\ , \tag{21}$$

where we have introduced the momentum dependent density

$$\Pi^0_{L,\lambda}(p) = \sum_{\ell j \ell' j'} \Theta^{\ell j,\ell' j'}_{k,L}(p) \begin{Bmatrix} j' & \lambda & j \\ \ell' & L & \ell \\ 1/2 & 1 & 1/2 \end{Bmatrix} (-1)^{\ell'+j'+K}\langle j\ K\ j'\ -K|\lambda\ 0\rangle \tag{22}$$

with

$$\Theta^{\ell j,\ell' j'}_{k,L}(p) = \tilde{\phi}^{\ell j}_k(p)\tilde{\phi}^{\ell' j'}_k(p)\hat{\ell}\hat{\ell}'\hat{L}\hat{j}\hat{j}' \begin{pmatrix} \ell & \ell' & L \\ 0 & 0 & 0 \end{pmatrix} \tag{23}$$

and $\tilde{\phi}^{\ell j}_k(p)$ ($\tilde{\phi}^{\ell j}_i(p)$) the spherical components of the odd nucleon (core nucleons) wave function.

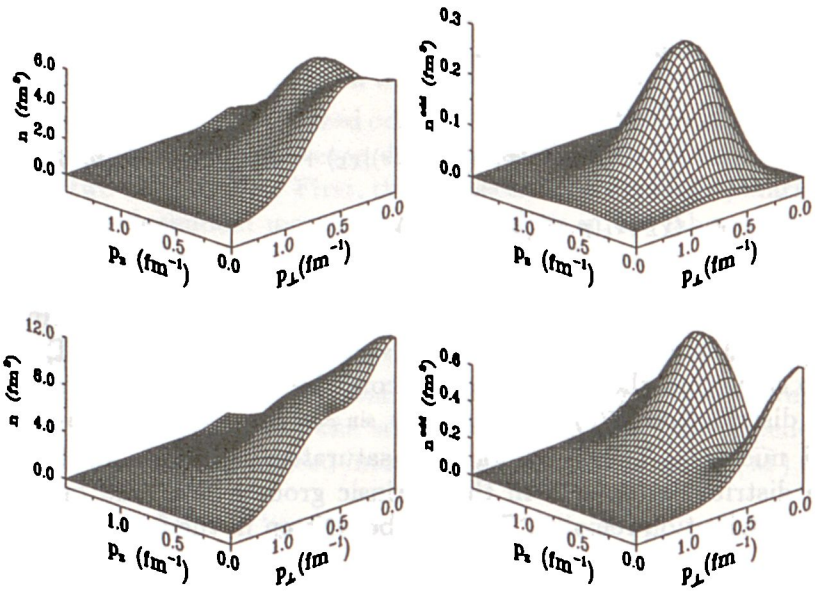

Figure 1: Contributions from the even–even core (left) and from the odd nucleon (right) to the scalar momentum distribution in ^{21}Ne (top) and ^{37}Ar (bottom).

The fact that each individual single–particle wave function contains in general more than one ℓj component, makes it possible to have contributions to Eqs. (19)-(22) coming from several ℓj–components, as well as contributions from interferences between different ℓj waves. This is an important feature that would not be possible in the spherical limit. The lower the K value is, the lower ℓj–values are allowed, producing a richer structure in the momentum distributions. This is clearly seen in figures 1 and 2 where we show scalar and vector intrinsic momentum distributions of ^{21}Ne and ^{37}Ar. In Fig. 1 we show the contributions to the scalar momentum distribution in ^{21}Ne (top) and ^{37}Ar (bottom) from the core (left) and from the odd nucleon (right). The clear difference between the odd nucleon contributions in ^{21}Ne and in ^{37}Ar is due to the different K values and mean field deformations. Note that the odd nucleons in ^{21}Ne and ^{37}Ar have $\Omega_k = 3/2$ and $1/2$, respectively. It is also interesting to remark the difference between core nucleons and odd nucleon contributions. In the first case the monopole term is dominant while in the second the $\lambda = 2$ and higher multipoles are comparable to the monopole term. The vector momentum distribution components $\widehat{M}_z(p)$ and $\widehat{M}_\perp(p)$ are shown in Fig. 2, where the results on the top correspond to ^{21}Ne and the results underneath to ^{37}Ar. As seen in this figure, the momentum distributions in ^{37}Ar have a richer structure than those in ^{21}Ne. This is clearly explained by taking into account that for these sd-shell nuclei the dominant ℓj components of the outermost nucleons are $\ell = 0$ and $\ell = 2$. However, the $\ell = 0$ wave is allowed for the $K = 1/2$ wave function but not for

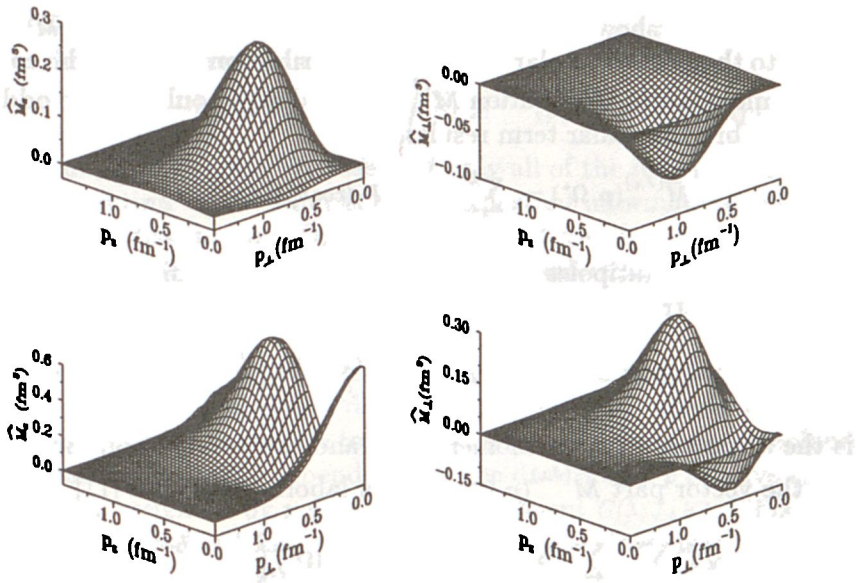

Figure 2: Components of the vector momentum distribution parallel and perpendicular to the symmetry axis for ^{21}Ne (top) and ^{37}Ar (bottom).

$K = 3/2, 5/2, ...$

3.2. Laboratory Frame. Polarization Considerations

We consider a nucleus in its ground state with angular momentum J_A completely polarized in a given direction $\boldsymbol{P}^*$ defined in the laboratory frame. The two by two matrix

$$M^{(J_A)}_{\sigma\sigma'}(\boldsymbol{p}, \Omega^*) = \langle J_A J_A(\Omega^*)|a^+_{\boldsymbol{p}\sigma} a_{\boldsymbol{p}\sigma'}|J_A J_A(\Omega^*)\rangle \tag{24}$$

measures the probability to find a nucleon with momentum $\boldsymbol{p}$ and spin projections σ, σ' in the laboratory frame. By selecting transitions to discrete states in the residual system, which is the case we are considering in (e, e'N) reactions, one can measure partial momentum distributions of the form (see section 2.1)

$$M^{(J_A \to J_R)}_{\sigma\sigma'}(\boldsymbol{p}, \Omega^*) = \sum_{M_R} \langle J_A J_A(\Omega^*)|a^+_{\boldsymbol{p}\sigma}|J_R M_R\rangle\langle J_R M_R|a_{\boldsymbol{p}\sigma'}|J_A J_A(\Omega^*)\rangle\,. \tag{25}$$

Our aim here is to relate momentum distributions that may be observed in the laboratory to the intrinsic momentum distributions studied in the previous section. To this end it is important to distinguish between the total and partial contributions as given in Eq. (24) and (25), respectively.

3.2.1. Total Momentum Distributions

Introducing a scalar and vector components for the matrix $M^{(J_A)}_{\sigma\sigma'}(\boldsymbol{p}, \Omega^*)$, it

is a simple matter to show† that the scalar momentum distribution $\overline{M}^{(J_A)}(\boldsymbol{p},\Omega^*)$ is proportional to the intrinsic scalar momentum distribution and that the components of the vector momentum distribution $\widehat{M}^{(J_A)}(\boldsymbol{p},\Omega^*)$ depend only on the odd nucleon. After some algebra the scalar term results,

$$\overline{M}^{(J_A)}(\boldsymbol{p},\Omega^*) = \sum_{\lambda=\text{even}} \overline{M}_\lambda(p) P_\lambda(\cos\theta_p^*) G(\lambda; J_A K) \,, \tag{26}$$

where $\overline{M}_\lambda(p)$ are the multipoles of the intrinsic momentum distribution (Eq. (19)), $G(\lambda; J_A K)$ is a geometrical coefficient

$$G(\lambda; J_A K) = (-1)^{J_A - K} \hat{j}_A^2 \begin{pmatrix} J_A & J_A & \lambda \\ J_A & -J_A & 0 \end{pmatrix} \begin{pmatrix} J_A & J_A & \lambda \\ K & -K & 0 \end{pmatrix} \tag{27}$$

and θ_p^* is the angle between the momentum $\boldsymbol{p}$ and the polarization direction $\boldsymbol{P}^*$.

For the vector part $\widehat{M}^{(J_A)}(\boldsymbol{p},\Omega^*)$, after a laborious algebra [11], we get

$$\widehat{M}_\alpha^{(J_A)}(\boldsymbol{p},\Omega^*) = \sqrt{6} \sum_{L=\text{even}} \sum_{\lambda=\text{odd}} \sum_{\mu} (-1)^\alpha Y_\mu^\lambda(\Omega^*) Y_{\alpha-\mu}^L(\Omega_p) \begin{pmatrix} 1 & L & \lambda \\ \alpha & \mu-\alpha & -\mu \end{pmatrix} \mathcal{L}_{L,\lambda}^{J_A K}(p) \tag{28}$$

with

$$\mathcal{L}_{L,\lambda}^{J_A K}(p) = G(\lambda; J_A K) \left\{ \Pi_{L,\lambda}^0(p) + (-1)^{J_A+K} \frac{\langle J_A\ K\ J_A\ K | \lambda\ 2K\rangle}{\langle J_A\ K\ J_A\ -K | \lambda\ 0\rangle} \Pi_{L,\lambda}^{2K}(p) \right\} \tag{29}$$

and $\alpha = 0, \pm 1$. The momentum dependent densities are given by

$$\Pi_{L,\lambda}^{2K}(p) = \sum_{lj} \sum_{l'j'} \Theta_{k,L}^{lj,l'j'}(p) \begin{Bmatrix} j' & \lambda & j \\ \ell' & L & \ell \\ 1/2 & 1 & 1/2 \end{Bmatrix} (-1)^{\ell'} \langle j\ K\ j'\ K | \lambda\ 2K\rangle \tag{30}$$

and $\Pi_{L,\lambda}^0(p)$ as given in Eq. (22). Note that the term $\Pi_{L,\lambda}^{2K}(p)$ only contributes for λ–values satisfying $2K \le \lambda \le 2J_A$, i.e., $\lambda = 2J_A$ when $K = J_A$.

Let us define $\widehat{M}_l^{(J_A)}$ and $\widehat{M}_t^{(J_A)}$ as the longitudinal and transverse components of the vector momentum distribution referred to the polarization axis. If we fix the polarization direction as the z–axis in laboratory frame, the longitudinal and transverse‡ components reduce to the simple expressions,

$$\widehat{M}_l^{(J_A)}(\boldsymbol{p},\Omega^*=0) = \frac{\sqrt{6}}{4\pi} \sum_{L=\text{even}} \sum_{\lambda=\text{odd}} \hat{\lambda}\hat{L} P_L(\cos\theta_p^*) \begin{pmatrix} 1 & L & \lambda \\ 0 & 0 & 0 \end{pmatrix} \mathcal{L}_{L,\lambda}^{J_A K}(p) \tag{31}$$

$$\widehat{M}_t^{(J_A)}(\boldsymbol{p},\Omega^*=0) = -\frac{2\sqrt{3}}{4\pi} \sum_{L=\text{even}} \sum_{\lambda=\text{odd}} \frac{\hat{\lambda}\hat{L}}{\sqrt{(L+1)L}} P_L^1(\cos\theta_p^*) \begin{pmatrix} 1 & L & \lambda \\ 1 & -1 & 0 \end{pmatrix} \mathcal{L}_{L,\lambda}^{J_A K}(p) \,. \tag{32}$$

The momentum distribution in the laboratory frame for the unpolarized nucleus can be easily obtained by integrating Eqs. (26) and (28) over the polarization

†We use the Bohr–Mottelson factorization approximation and take the quantization axis to be the z axis of the laboratory fixed frame.

‡Note that the two components of the vector momentum distribution in the transverse directions, sideways (s) and normal (n), are $\widehat{M}_s^{(J_A)}(p,\Omega^*=0) = \cos\varphi_p^* \widehat{M}_t^{(J_A)}(p,\Omega^*=0)$ and $\widehat{M}_n^{(J_A)}(p,\Omega^*=0) = \sin\varphi_p^* \widehat{M}_t^{(J_A)}(p,\Omega^*=0)$

direction. Clearly for an **unpolarized** nucleus only the $\lambda = 0$ multipole of the scalar momentum distribution remains:

$$\int d\Omega^* \widehat{M}_\alpha^{(J_A)}(\boldsymbol{p}, \Omega^*) = 0 \ , \qquad \int d\Omega^* \overline{M}^{(J_A)}(\boldsymbol{p}, \Omega^*) = 4\pi \overline{M}_{\lambda=0}(p) \ . \tag{33}$$

Hence in the **unpolarized** case one loses not only all of the information contained in the vector momentum distribution but also important information contained in the scalar momentum distribution. One misses the $\lambda \geq 2$ multipoles of the core and odd nucleon momentum densities that carry important information on shell admixtures and on details of the internal dynamics which are crucial to attain equilibrium in open shell nuclei.

Now we can easily compare the scalar momentum distribution in laboratory and intrinsic frames. Comparison of Eq. (18) to Eq. (26) shows that the dependence on the direction of $\boldsymbol{p}$ relative to the intrinsic symmetry axis, is replaced in the laboratory frame by a similar dependence on the direction of $\boldsymbol{p}$ relative to the polarization direction, weighted by a geometrical coefficient $G(\lambda; J_A K)$. This geometrical coefficient takes the value 1 for $\lambda = 0$ and decreases as λ increases.

For the vector momentum distribution we also see that the expressions for longitudinal and transverse components in the laboratory frame involve the intrinsic multipoles $\Pi^0_{L,\lambda}(p)$. These expressions are similar to the ones in the intrinsic frame, replacing the direction of $\boldsymbol{p}$ relative to the internal symmetry axis by the direction of $\boldsymbol{p}$ relative to the polarization direction, and weighting the intrinsic λ multipoles with the geometrical factor $G(\lambda; J_A K)$. However in the case of the vector components one has additional contributions for the $\lambda \geq 2K$ multipoles (see Eqs. (29) and (30)).

3.2.2. Partial Momentum Distributions

The partial contributions, as defined in Eq. (25), play a central role in coincidence $\vec{\mathrm{A}}(\vec{e}, e'\mathrm{N})\mathrm{R}$ experiments where transitions to discrete states J_R of the residual nucleus are selected (see section 2.1). In particular, our attention is focused on transitions in which the knock–out nucleon is the unpaired one, and the intrinsic structure of the residual nucleus is basically given by that of the even–even core of the parent nucleus. This is the case for transitions to the low lying states in the residual nucleus which are populated when the odd nucleon is knocked out.

We consider a transition from a 100% polarized nucleus in the direction $\boldsymbol{P}^* = (\Omega^*)$ to a discrete state J_R in the residual nucleus of unobserved polarization. In addition here we specialize to states J_R in the ground state rotational band ($K^\pi = 0^+$) of the residual nucleus. In this case we prove that the scalar and vector transition densities, $(\overline{M}^{(J_A \to J_R)}(\boldsymbol{p}, \Omega^*), \widehat{M}_\alpha^{(J_A \to J_R)}(\boldsymbol{p}, \Omega^*))$ (see Ref. [11] for explicit expressions and details), are made up of the same building blocks as the intrinsic and laboratory scalar and vector momentum distributions, respectively. The only difference is that for each λ multipole the sums over $\ell j, \ell' j'$ are now restricted to angular momentum values satisfying $|J_A - J_R| \leq j,\ j' \leq J_A + J_R;\ |j - J_R| \leq j' \leq j + J_R$, while in previous cases the sums over $\ell j, \ell' j'$ do not have these restrictions. Furthermore, we also show that

$$\sum_{J_R} \overline{M}^{(J_A \to J_R)}(\boldsymbol{p}, \Omega^*) = \sum_{\lambda=\text{even}} P_\lambda(\cos\theta_p^*) n_\lambda^{\text{odd}}(p) G(\lambda; J_A K) \ , \tag{34}$$

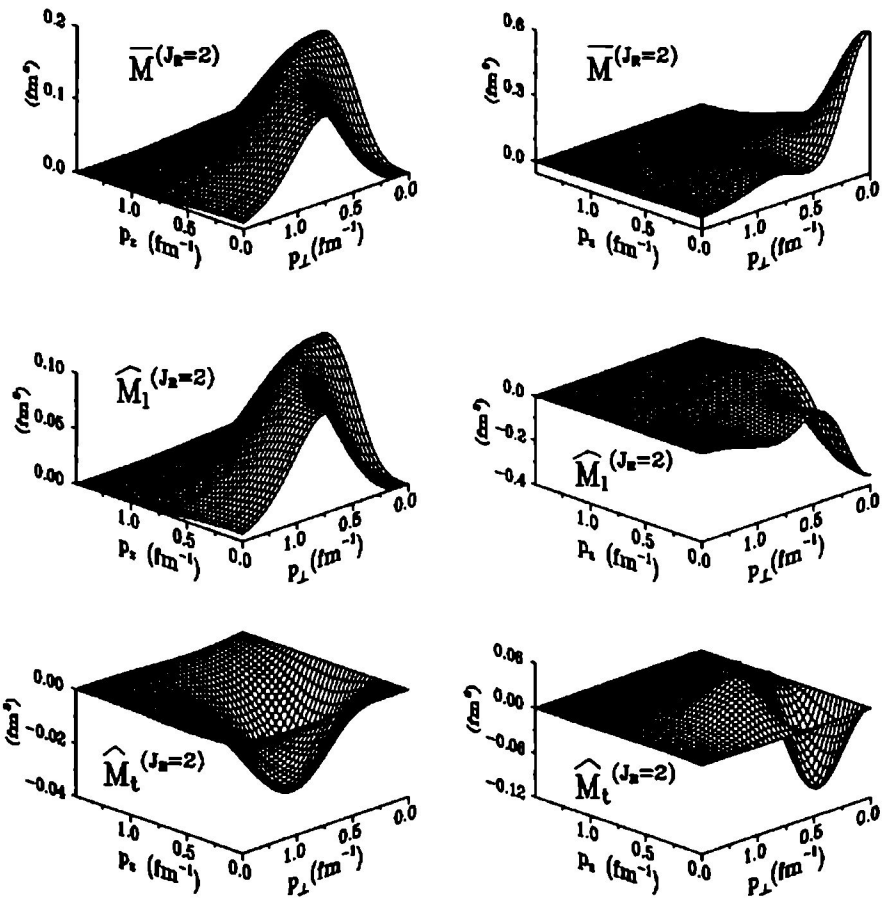

Figure 3: Scalar and vector components of the transition densities in momentum space (in fm^3) for $J_A \to J_R = 2$ in ^{21}Ne (left) and in ^{37}Ar (right).

which is the odd nucleon contribution to the total scalar momentum distribution $\overline{M}^{(J_A)}(\boldsymbol{p}, \Omega^*)$ (Eq. (26)), and that

$$\sum_{J_R} \widehat{M}_\alpha^{(J_A \to J_R)}(\boldsymbol{p}, \Omega^*) = \widehat{M}_\alpha^{(J_A)}(\boldsymbol{p}, \Omega^*) \,. \tag{35}$$

It is important to remark that in Eqs. (34) and (35) the sum over J_R runs over states belonging to the ground state band in the residual nucleus. Therefore, these equations show that measuring the transition densities to each state in the ground state band one can map out entirely the intrinsic momentum distribution spin matrix of the odd nucleon. In addition, Eq. (35) tells us that all possible information contained in the vector momentum distribution of the polarized target nucleus can be obtained by measuring the transition densities to the ground state band in the

residual nucleus. The same is true for the odd nucleon contribution to the scalar momentum distribution (Eq. (34)).

The restriction imposed by the J_R value may cause the transition densities to have quite different structures than the total momentum distributions in laboratory frame. As an example, in figure 3 we represent $\overline{M}^{(J_A\to 2)}(p,\Omega^*)$, $\widehat{M}_l^{(J_A\to 2)}(p,\Omega^*=0)$, and $\widehat{M}_t^{(J_A\to 2)}(p,\Omega^*=0)$ (defined by analogy to $\widehat{M}_l^{(J_A)}$ and $\widehat{M}_t^{(J_A)}$). The plots on the left correspond to $\overrightarrow{^{21}\mathrm{Ne}}$ $(3/2^+)\to{}^{20}\mathrm{Ne}(2^+)$ and the plots on the right correspond to $\overrightarrow{^{37}\mathrm{Ar}}$ $(3/2^+)\to{}^{36}\mathrm{Ar}(2^+)$. As shown, the momentum dependence changes much in going from $\overrightarrow{^{21}\mathrm{Ne}}$ to $\overrightarrow{^{37}\mathrm{Ar}}$. As discussed in section 3.1, in the case of ^{37}Ar the odd nucleon wave function contains mainly a mixture of s and d waves, whereas for ^{21}Ne it contains mainly d wave. Hence, for the transitions $J_A\to J_R=2$ all positive parity waves with $j=\frac{1}{2},\frac{3}{2},\frac{5}{2},\frac{7}{2}$ may contribute, but the $j=\frac{1}{2}$ is only present in the odd nucleon of ^{37}Ar, not in ^{21}Ne. This, together with the fact that also the $\frac{3}{2},\frac{5}{2},\frac{7}{2}$ components enter with different amplitudes in each case, explains why the momentum dependences in Fig. 3 are different for $\overrightarrow{^{21}\mathrm{Ne}}$ and $\overrightarrow{^{37}\mathrm{Ar}}$.

3.3. Comparison with Spherical Case

Finally, it is interesting to compare the results in previous sections with the ones corresponding to spherical nuclei. In this case the single particle wave functions are eigenstates of angular momentum and the system does not have a preferred direction unless the nucleus is polarized by an external field. Hence the main two differences with the deformed case are that now, i) each single particle wave function has a single ℓj–wave component ($\tilde{\phi}^i_{\ell j}(p)=\delta_{\ell,\ell_i}\delta_{j,j_i}\tilde{R}_{n_i\ell_i j_i}(p)$), and ii) there is no distinction between intrinsic and laboratory frames. We denote by $\{i\}\equiv\{n_i\ell_i j_i\}$ the set of orbitals filled by the nucleons of the even–even core and by $\{k\}\equiv\{n_k\ell_k j_k\}$ the odd nucleon orbital, which has $j_k=J_A$ and ℓ_k fixed by the parity and J_A values.

The scalar momentum distribution for the fully polarized nucleus is then given by

$$\overline{M}^{(J_A)\mathrm{sph.}}(p,\Omega^*)=\sum_{\lambda=\mathrm{even}}P_\lambda(\cos\theta^*_p)(\delta_{\lambda,0}\,n^{\mathrm{sph.}}(p)+n^{\mathrm{odd,\,sph.}}_\lambda(p))\,, \tag{36}$$

where "sph." stands for spherical limit; the odd nucleon multipoles are given by

$$n^{\mathrm{odd,sph.}}_\lambda(p)=\frac{\hat{\ell}_k^2\hat{\lambda}^2\hat{j}_k^2}{4\pi}|\tilde{R}_{n_k\ell_k j_k}(p)|^2\begin{pmatrix}\ell_k & \ell_k & \lambda\\ 0 & 0 & 0\end{pmatrix}(-1)^{j_k+\frac{1}{2}}\begin{pmatrix}j_k & j_k & \lambda\\ j_k & -j_k & 0\end{pmatrix}\begin{Bmatrix}j_k & j_k & \lambda\\ \ell_k & \ell_k & \frac{1}{2}\end{Bmatrix}\delta_{j_k,J_A} \tag{37}$$

and $n^{\mathrm{sph.}}(p)$ is the spherically symmetric momentum distribution of the core

$$n^{\mathrm{sph.}}(p)=n_0(p)=\frac{1}{4\pi}\sum_i v_i^2(2j_i+1)|\tilde{R}_{n_i\ell_i j_i}(p)|^2\,. \tag{38}$$

The differences between scalar momentum distributions in the spherical and deformed case are now made explicit by comparing Eqs. (36)–(38) with Eq. (26) (see also Eq. (19)). The core has now only a monopole contribution, while in the deformed case it has also small multipoles $n_\lambda(p)$ with $\lambda>0$. For the odd nucleon contribution the sum over ℓj, $\ell' j'$ in Eq. (22) is now reduced to a single term $\ell j=$

$\ell' j' = \ell_k j_k$, with $\ell_k j_k$ the values corresponding to the spin and parity of the nucleus, and with $\Omega_k = K = j_k = J_A$. Therefore, in the spherical case all the λ–multipoles have the same p dependence, whereas in the deformed case for each λ value we may have a different dependence on p. The geometrical coefficient $G(\lambda; J_A K)$, which appears in the deformed case, is not present in the spherical case. This reflects the fact that now, "a priori", there is no internal preferred direction. Analogously, we also prove that for the longitudinal (l) and transverse (t) components of the vector momentum distribution, the differences with the deformed case are also the absence of the geometrical factor $G(\lambda; J_A K)$ and the restriction of the sum over ℓj, $\ell' j'$ to a single term with $\ell_k j_k$ dictated by the spin and parity of the nucleus, and with $\Omega_k = j_k = J_A$ (see Ref. [11] for explicit expressions and details). It is also interesting to remark that if one restricts in the deformed case to a single term with $\ell j = \ell' j' = \ell_k j_k$, and takes $\Omega_k = j_k = J_A$, the expressions for the vector momentum distributions of spherical nuclei with respect to the polarization direction [11] are identical to the expressions for the intrinsic vector momentum distributions of the deformed nucleus along the symmetry axis (see section 3.1). This reflects the fact that for spherical nuclei polarizing the nucleus is the only way to define an internal preferred direction for the system.

4. Polarization Observables in $\overrightarrow{\mathrm{A}}(\vec{\mathrm{e}}, \mathrm{e'N})\mathrm{R}$ Reactions

In this section we present some representative results for the spin–dependent observables in $\overrightarrow{\mathrm{A}}(\vec{\mathrm{e}}, \mathrm{e'N})\mathrm{R}$ reactions. The kinematics selected corresponds to a value of the momentum transfer fixed to $q = 500$ MeV/c, and the transfer energy is set to the value corresponding to the quasi–elastic peak.

Figure 4 corresponds to the analysis of the process $^{21}\overrightarrow{\mathrm{Ne}}(\vec{\mathrm{e}}, \mathrm{e'n})^{20}\mathrm{Ne}$. Here we show the differential cross section for polarized beam and target at $p = 0.75$ fm^{-1} (*i.e.*, at the peak of the unpolarized cross section) as a function of the polarization angle θ^*. The results correspond to the inclusion of the 0^+ and 2^+ transitions. It is interesting to see that for each choice of ϕ_N–value, the cross section reaches its maximum when $\phi^* = \phi_N$, *i.e.*, when the neutron is detected in the plane of the target polarization, and that for the selected p–value the highest value of the cross section corresponds to $\phi_N = \phi^* = 90°$ and $\theta^* \approx 130°$. Actually, for unpolarized electron beam the maximum of the cross section for the case of 0^+ and 2^+ transitions is at $\phi^* = \phi_N = 90°$ and $\theta^* = \theta$, *i.e.*, when the struck neutron momentum $\mathbf{p}$ is parallel to the target polarization direction. This behaviour is dictated by the 2^+ transition. In the case of transitions to the 0^+ state the differential cross section at $\theta^* = \theta$ is zero and the maximum value of the cross section at $p = 0.75$ fm^{-1} is obtained for $\phi^* = \phi_N = 90°$ and $\theta^* = \theta - 90° \approx \theta_N$. These results can be also clearly observed by analyzing the polarization ratios $\mathcal{P}_\Sigma$ and $\mathcal{P}_\Delta$ [10]. We prove in general that the largest values of $|\mathcal{P}_\Sigma|$ and $|\mathcal{P}_\Delta|$ are obtained when the outgoing nucleon is detected in the polarization plane (preferably for $\mathbf{P}^*$ nearly parallel or antiparallel either to $\mathbf{p}$ or to $\mathbf{p}_N$), at moderate struck momenta $p \leq 1.5$ fm^{-1} and when a single J^π_R state in the residual nucleus is selected. The poorer the energy resolution the less is the

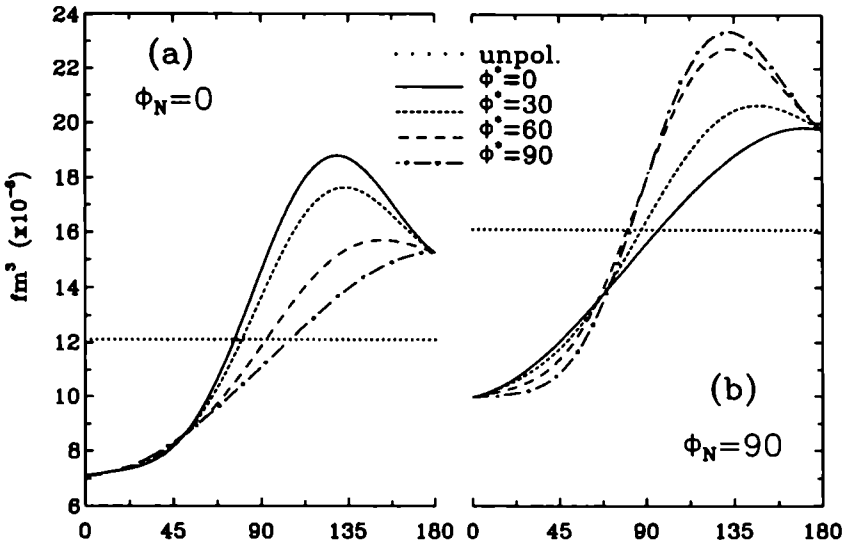

Figure 4: Differential cross section versus the target polarization angle θ^* at $p = 0.75$ fm^{-1}. DDHF single–nucleon wave functions have been used and contributions from the ground and first excited state in the residual nucleus ^{20}Ne are included. For comparison the results for the totally unpolarized cross section (Σ_0) are shown by the dotted line.

effect of the target polarization.

In some of the previous sections we mentioned that $\vec{A}(\vec{e},e'N)R$ reactions for specific transitions in deformed nuclei can give a very clear information on the ℓ–wave mixing in deformed orbitals. We discuss this issue in the figures that follow, where we show the response functions and asymmetries corresponding to the process $^{37}\vec{K}(\vec{e},e'p)^{36}$Ar with the residual nucleus in its first excited state (see Ref. [12] for specific details on the calculations).

In figure 5 we present the scalar ($\overline{M}$) and vector components ($\widehat{M}_l$, $\widehat{M}_t$) of the spin dependent momentum distributions for the transition from the ground state in ^{37}K to the 2^+ state in the ground state band of ^{36}Ar. In plot (c) we also show for comparison the $\lambda = 0$ multipole of the scalar momentum distribution $\overline{M}_{\lambda=0}$, which is the only one contributing when the target is unpolarized. Only the diagonal terms $\ell j = \ell' j'$ contribute to $\overline{M}_{\lambda=0}$, while $\overline{M}_{\lambda=2}$ and the vector momentum distribution components $\widehat{M}_l$, $\widehat{M}_t$ contain also important off–diagonal contributions. As seen in Fig. 5(a) the scalar momentum distribution has a maximum at $p = 0$ due to the ss contribution that dominates in the low p region, and a second maximum at $p \approx .8$ fm^{-1} that is made up not only from the dd contribution but also from the contributions of sd and ss terms. Though the scalar momentum distribution in the polarized case has a more pronounced second maximum than in the unpolarized case (compare plots (a) and (c)), the profiles are not very different in the two cases.

On the contrary the vector momentum distribution components l, t have quite different profiles. Particularly, $\widehat{M}_t$ is dominated by the sd interference term, and therefore contains basically the information missing in the unpolarized momentum distribution. The shape of $\widehat{M}_t$ is characteristic of the sd interference term and its observation would provide the most direct evidence for the ℓ–wave mixing in deformed orbitals.

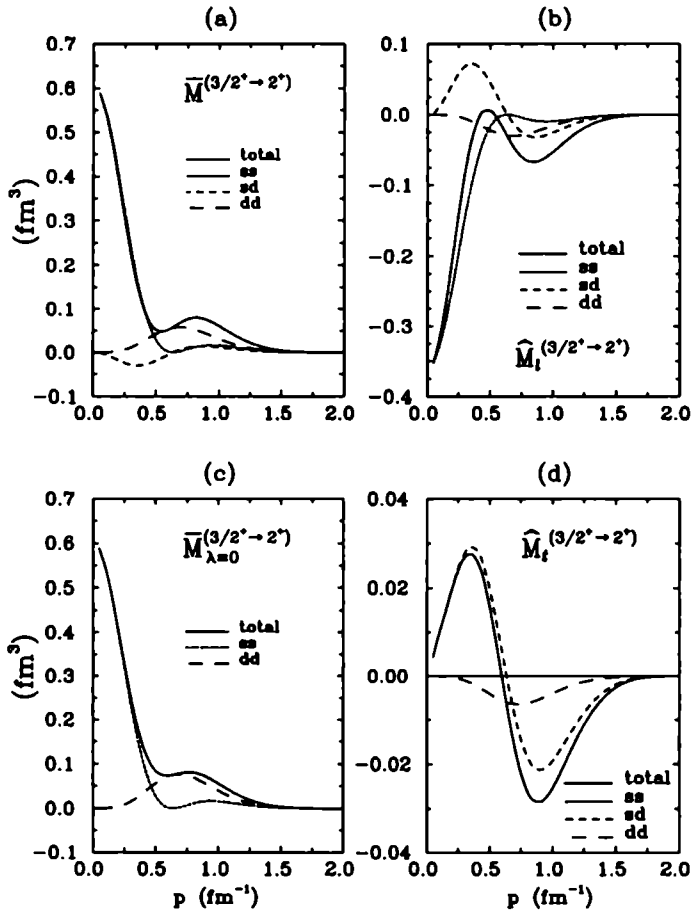

Figure 5: Scalar (a), and vector longitudinal (b) and transverse (d) momentum distributions for the transition to the first 2^+ state in the residual nucleus ^{36}Ar with polarized ^{37}K target. Results in (c) refer to the unpolarized target case. The dominant $\ell\ell'$ contributions are shown by short–dashed ($\ell = \ell' = 0$), dashed ($\ell = 0, \ell' = 2$), and long–dashed ($\ell = \ell' = 2$) lines.

In figure 6 we show the response functions for the reaction $^{37}\overrightarrow{\mathrm{K}}(\vec{\mathrm{e}},\mathrm{e'p})^{36}\mathrm{Ar}$. Also shown for comparison by dashed lines, are the response functions for unpolarized target. As seen in the figure the profiles of the response functions reflect quite nicely the features of the momentum distributions shown in Fig. 5, and de-

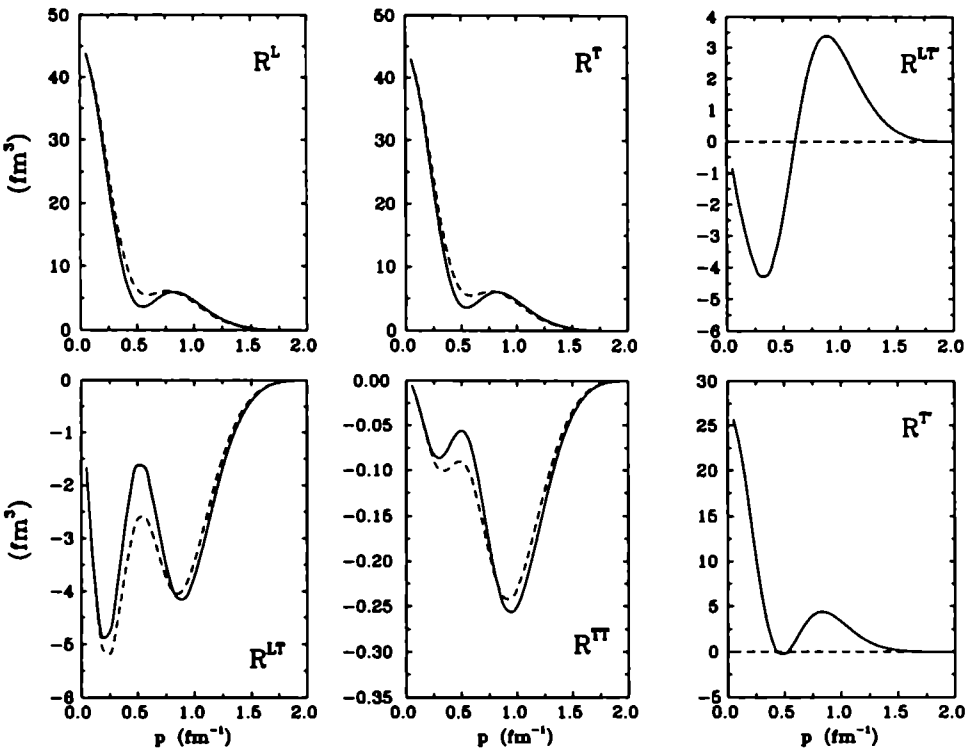

Figure 6: Response functions for the reaction $^{37}\overrightarrow{\mathrm{K}}(\vec{e},e'p)^{36}\mathrm{Ar}_{[2^+]}$ with polarized target (solid lines) and with unpolarized target (dashed lines). Polarization direction parallel to q and coplanar kinematics have been chosen.

pend strongly on the ℓ–mixing. The response functions R^X, $X = L,T,TL,TT$ depend on the scalar momentum distribution and follow closely the profiles in Figs. 5(a) and 5(c) for the polarized and unpolarized cases, respectively. As seen from the comparison to the unpolarized case, the main information that these responses R^X carry is that corresponding to the *ss* and *dd* contributions and not much more information seems to be gained polarizing the target. It is clear that in these response functions the main observational feature due to deformation is the presence of the two sizeable peaks, one corresponding to the s–wave and the other corresponding to the d–wave. This feature has already been observed to some extent in quasielastic scattering from deformed even–even targets [6-8]. The important difference is that for even–even targets the observation of the effect is associated to lack of resolution, whereas in the case of odd–A target this feature can be observed in a transition to a single state in the residual nucleus, as considered here.

Even more unambiguous evidence on the ℓ–mixing in the deformed orbitals can be gained by measuring the response functions for polarized beam and target, $R^{LT'}$ and $R^{T'}$. As seen in Fig. 6 these response functions are more sensitive to the

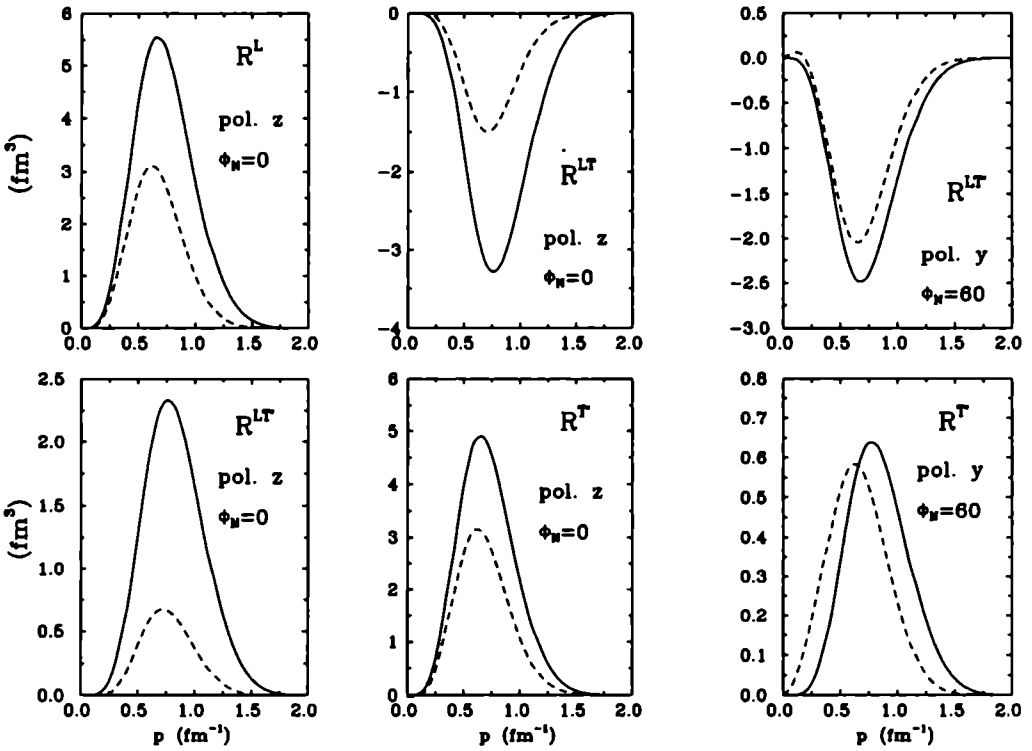

Figure 7: Response functions for $^{37}\overrightarrow{\mathrm{K}}(\vec{e},e'\mathrm{p})^{36}\mathrm{Ar}$ in the spherical limit for different polarization directions and ϕ_N values, calculated in PWIA and in DWIA.

sd interference terms, particularly $R^{LT'}$ whose shape is basically that of the *sd* contribution to the transverse vector momentum distribution (see Fig. 5(d)). Thus the new feature of *sd* interference, a sign of the deformation of the orbital of the struck nucleon, can in principle be detected by measuring the $R^{LT'}$ response at the corresponding kinematics. It should be emphasized that the choices of kinematics and of polarization direction play an important role in dictating which of the response functions ($R^{T'}$ or $R^{LT'}$, or both) is more sensitive to the ℓ–wave interference terms. In Ref. [12] we have carried out a search for the most favorable conditions to detect such *sd*–interference terms for the transitions of our concern here.

To appreciate better the size of the effects of deformation, we compare the results in Fig. 6 with the ones obtained in the spherical limit. It is also important to see whether FSI may produce effects in the response functions and asymmetries comparable to those produced by deformation. For these purposes we present PWIA and DWIA results obtained in the spherical limit, assuming that the struck nucleon is in a $d_{\frac{3}{2}}$ orbital. The DWIA calculations have been made using a relativistic optical potential as described in Ref. [13]. These results are presented in figure 7 where now only the more representative response functions are shown.

The effect of deformation stands out clearly when we compare the PWIA results in Fig. 7 (solid lines) with the corresponding results in Fig. 6 The complex and varied structures of the responses in Fig. 6 disappear in the spherical limit. In this limit the shape of all response functions is similar, and has a single sizeable peak corresponding to that of the $d_{\frac{3}{2}}$ wave function. This dominant feature prevails in the DWIA results (dashed lines).

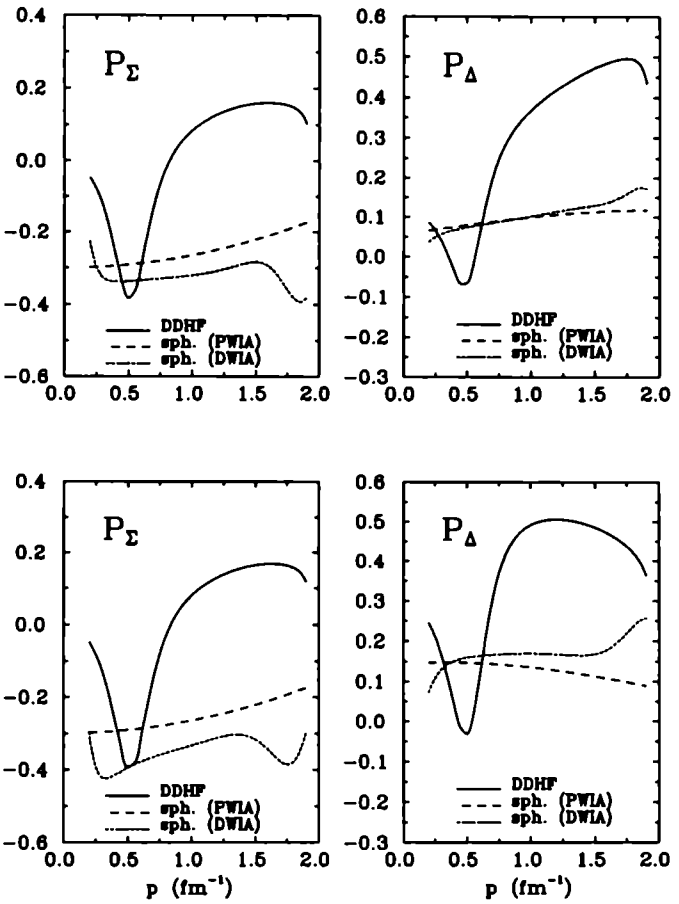

Figure 8: Asymmetries for $^{37}\overrightarrow{K}(\vec{e},e'p)^{36}Ar(2^+)$ (top) and $^{37}\overrightarrow{Ar}(\vec{e},e'n)^{36}Ar(2^+)$ (bottom) calculated with the deformed HF orbital (solid line) and with the spherical orbital in PWIA (dashed line) and DWIA (short-dashed line). The scattering angle is $\theta_e = 30$.

The effect of final state interactions varies depending on the kinematics and on the various response functions, which in some cases can be strongly suppressed. This agrees with the analyses carried out in Ref. [14]. DWIA results in Fig. 7 illustrate that typical FSI effects are quite different from the effects of deformation. This conclusion also emerges from the comparison in figure 8 between the results

for $\mathcal{P}_\Sigma$ and $\mathcal{P}_\Delta$ obtained with the deformed HF solution (solid lines), and the results obtained in the spherical limit in PWIA (dashed line) and in DWIA (short–dashed line). As seen there the DWIA results obtained are very close to the PWIA results over a fairly extended p range. In this range the effects of FSI are qualitatively (and in most cases quantitatively) similar in the polarized and in the unpolarized responses, and therefore, tend to cancel when calculating the asymmetries $\mathcal{P}_\Sigma$ and $\mathcal{P}_\Delta$. On the contrary, the effects of deformation are different in the polarized and in the unpolarized responses, resulting in strong oscillations with p of $\mathcal{P}_\Sigma$ and $\mathcal{P}_\Delta$ that are in contrast with the smooth behaviours observed for the spherical limits. Obviously for comparisons to experimental data it would be desirable to dispose of results that take into account simultaneously both FSI and deformation effects. DWIA calculations using deformed HF solutions for the bound nucleon wave functions, are now in progress. Nevertheless the present results indicate that the effects of deformation encountered here will prevail and be clearly identifiable when more realistic calculations beyond PWIA are made.

This work has been supported in part by DGICYT (Spain) under contract No. PB92/0021-002-01.

References

1. T. de Forest, *Nucl. Phys.* **A392** (1983) 232.
2. J. A. Caballero, T. W. Donnelly and G. I. Poulis, *Nucl. Phys.* **A555** (1993) 709.
3. S. Frullani and J. Mougey, *Adv. in Nucl. Phys.* **14** (1984).
4. A. N. Antonov, P. E. Hodgson and I. Zh. Petkov, "Nucleon Momentum and Density Distributions in Nuclei", *Clarendon, Oxford* (1988).
5. L. Lapikás, *Nucl. Phys.* **A553** (1993) 297c; P. K. A. de Witt Huberts, *J. Phys. G* **G16** (1990) 507.
6. E. Moya de Guerra, J. A. Caballero and P. Sarriguren, *Nucl. Phys.* **A477** (1988) 445.
7. J. A. Caballero and E. Moya de Guerra, *Nucl. Phys.* **A509** (1990) 117; E. Moya de Guerra *et al., Nucl. Phys.* **A529** (1991) 68;
8. J.B.J.M. Lanen *et al., Nucl. Phys.* **A560** (1993) 811.
9. A. S. Raskin and T. W. Donnelly, *Ann. Phys.* **191** (1989) 78, and refs. therein.
10. J.A. Caballero, T.W. Donnelly, G.I. Poulis, E. Garrido and E. Moya de Guerra, *Nucl. Phys.* **A577** (1993) 528.
11. J.A. Caballero, E. Garrido, E. Moya de Guerra, P. Sarriguren and J.M. Udías, *Ann. Phys.* **239** (1995) 351.
12. E. Garrido, J. A. Caballero, E. Moya de Guerra, P. Sarriguren and J.M. Udías, *Nucl. Phys.* **A584** (1995) 256.
13. J.M. Udías, P. Sarriguren, E. Moya de Guerra, E. Garrido and J.A. Caballero, *Phys. Rev.* **C48** (1993) 2731; *Phys. Rev.* **C51** (1995) 3246.
14. S. Boffi, C. Giusti and F.D. Pacati, *Nucl. Phys.* **A476** (1988) 617.

8. METALLIC CLUSTERS

FISSION OF METALLIC CLUSTERS

CARLOS FIOLHAIS

and

ARMANDO VIEIRA

Center for Theoretical Physics, University of Coimbra, 3000 Coimbra, Portugal

ABSTRACT

The fission of sodium clusters is discussed using Nuclear Physics methods. After presenting the Liquid Drop Model for spherical jellium clusters, we introduce shell corrections and compare the obtained energies with self-consistent quantal results. Fission is studied evaluating Q-values and fission barriers, with the shell correction method and the Two Center Shell Model. The threshold of stability with respect to fission is predicted within the Liquid Drop Model.

1. Introduction

Metallic clusters are many-body systems which show striking similarities with atomic nuclei: the valence electrons move in a mean-field as nucleons move in the nuclear mean-field. An important difference is that a part of the mean-field is externally imposed (by the ions) while the whole nuclear mean-field is self-organized by the participants.

Metallic clusters were produced by the middle of the eighties. The static mean field was experimentally identified by a group led by Knight [1]. At the same time but independently, Ekardt [2] predicted the existence of independent particle motion for the valence electrons.

The success in analyzing clusters in the laboratory is due mainly to progresses achieved in the technology of molecular beams. A typical setup consists of a chamber where a metallic sample is vaporized with the aid of a laser. The atoms which are set free may coalesce in clusters, which are transported by a high speed helium beam through an exit channel. The molecular beam is directed to a mass spectrometer. A second laser ionizes the clusters so that they are deviated by a magnetic field and sorted according to its size.

A clear sign for the mean field is the appearance of the magic numbers 8, 20, 40, 58, etc. as peaks in the relative abondances in the mass spectrometer. Another indication comes from the ionization potential, which also shows peaks for clusters with 8, 20, 40, 58, etc. valence electrons. The first two of these magic numers are the same as in atomic nuclei, but the others differ. In fact, the nuclear magic numbers can be well described by a strong spin-orbit splitting, a relativistic effect which is negligicible for clusters. Therefore, a simple Woods-Saxon shape of the mean field, or even a simpler harmonic oscillator for the lightest systems, can explain the correct shell closures in clusters. We can talk about the ubiquity of the shell model, which dominates the structure of atoms, metallic clusters, and nuclei, notwithstanding the fact that there are six orders of magnitude in energy difference between the atomic

and the nuclear domains.

We emphasize that the magic effects in metallic particles arise from the confinement of the electrons and not from the geometrical arrangements of the ions. The physical properties for sp-metals (the only ones which we consider here) are due to the weakly bonded valence electrons and not to the inert cores, which only provide the space where the valence electrons are delocalized. It is difficult to ascertain experimentally (and even theoretically, due to the large number of isomers which differ little in energy) the geometrical disposition of the ions. But it evolves gradually from planar shapes, typical of clusters with up to 4 atoms, to close packed structures. The minimal number of atoms which are necessary to form a piece of material with a given bulk property seems to depend on the particular material and on the particular property.

Clusters are intermediate structures between the atoms and bulk matter in the same way as nuclei are intermediate structures between one nucleon and nuclear matter, which exists in neutron stars. One of the main motivations for studying clusters is precisely the possibility of filling a bridge between the properties of individual atoms and molecules and normal macroscopic matter. In Nuclear Physics, the increase of Coulomb repulsion with the atomic number determines a maximal size for the nuclides. The heavier nuclei decay by spontaneous fission or alpha emission. In spite of that repulsion, one has speculated about the existence of big magic numbers which would give rise to one or more islands of "superheavy nuclei". Cluster physics offers the opportunity to look for similar magic numbers, in large atomic systems, where Coulomb instability is not present.

The theoretical analysis of clusters requires techniques from Solid State Physics as well as from Quantum Chemistry, being Cluster Physics a field where cross fertilization of different methodologies is taking place. Given the analogies between clusters and nuclei, it is natural that concepts and tools from Nuclear Physics disseminate in the new research area. We intend to present here some examples.

In the next section, we sketch the theoretical framework for our approach to clusters, neutral as well as charged. The case is presented for the "import" of the Liquid Drop Model (LDM) and the shell correction method from Nuclear Physics and the possible "export" to Nuclear Physics of some information on the curvature energy of metallic clusters and voids. In section 3, we address the problem of the fission of metallic clusters, considering Q-values and barrier heights obtained with the aid of Kohn-Sham theory, LDM, and the shell correction method. Some general conclusions are drawn at the end.

2. Theoretical tools: self-consistent equations versus the shell-correction method

Density functional methods are very powerful tools in Atomic, Molecular and Condensed Matter Physics. For big enough systems they are the only accurate methods which are feasible.

They are based on an existence theorem due to Hohenberg and Kohn [3,4], according to which the ground-state energy of a many-electron system is a functional of the local electronic density $E = E[n(\mathbf{r})]$. Minimization of this functional with respect to the density would give the exact density and the exact energy if the functional were

known:

$$\frac{\delta E[n]}{\delta n} = 0. \tag{1}$$

The energy is separated in kinetic, electrostatic (Hartree term), exchange and correlation, and the contribution from a local external potential:

$$E[n] = T_s[n] + E_{es}[n] + E_{xc}[n] + \int v_{ext}\, n\, d^3\mathbf{r}. \tag{2}$$

The unknown part is the exchange and correlation piece, $E_{xc}[n]$, for which approximations like the Local Density Approximation (LDA) are mandatory.

A starting point for modelling the ions, which are the source of the external potential felt by the valence electrons, is the so-called jellium approximation [5,6]. The ions are replaced by an uniform distribution of positive charge. This approximation has proved to be useful in the study of bulk and surface properties of simple metals. In the jellium approximation, the electrons interact with the positive background and with themselves.

The radius R of the jellium sphere corresponding to a neutral cluster with N valence electrons goes with the cubic root of N simply due to the neutrality of the cluster:

$$R = r_s N^{\frac{1}{3}}, \tag{3}$$

where r_s is the so-called density parameter, which goes from 1.87 bohr for beryllium to 5.63 bohr for caesium. This is the radius of the sphere occupied by one valence electron. It corresponds in Nuclear Physics to the parameter $r_0 = 1.2$ fm. The density of positive charge is given by a step function:

$$n_+(r) = \overline{n}\, \theta(R - r), \tag{4}$$

with $\overline{n} = (3/4\pi r_s^3)^{-1}$ the average density. The jellium functional has an electrostatic piece which depends on both n and n_+ (including electron-jellium, electron-electron and jellium-jellium interactions):

$$\begin{aligned} E_{jell} &= T_s[n] + E_{es}[n, n_+] + E_{xc}[n], \\ E_{es}[n, n_+] &= \frac{1}{2}\int d^3\mathbf{r} \int d^3\mathbf{r}' \frac{[n(\mathbf{r}') - n_+(\mathbf{r}')]}{|\mathbf{r}' - \mathbf{r}|}[n(\mathbf{r}) - n_+(\mathbf{r})]. \end{aligned} \tag{5}$$

In the jellium model, the energy of a spherical cluster, as a function of N and r_s, can be evaluated solving Eq. (1), called Kohn-Sham equation, within the LDA approximation. That equation reads as (in atomic units):

$$\Big[-\frac{1}{2}\nabla^2 + v_{eff}(\mathbf{r})\Big]\psi_\alpha(\mathbf{r}) = \epsilon_\alpha \psi_\alpha(\mathbf{r}) \ , \tag{6}$$

where α denotes a set of quantum numbers. The effective potential is

$$v_{eff}(\mathbf{r}) = v_+(\mathbf{r}) + \int d^3\mathbf{r}' \frac{n(\mathbf{r}')}{|\mathbf{r} - \mathbf{r}'|} + \mu_{xc}(\mathbf{r}) \quad , \tag{7}$$

with the external (jellium) potential

$$v_+(\mathbf{r}) = \begin{cases} -\frac{N}{2R}\left[3 - \left(\frac{r}{R}\right)^2\right] & (r < R) \\ -\frac{N}{r} & (r > R) \end{cases} , \tag{8}$$

and $\mu_{xc}(\mathbf{r})$ the exchange-correlation potential,

$$\mu_{xc}(\mathbf{r}) = \frac{\delta}{\delta n(\mathbf{r})}\left[n(\mathbf{r})\epsilon_{xc}(\mathbf{r})\right] , \tag{9}$$

with $\epsilon_{xc} = -3k_F/4\pi + \epsilon_c$. The quantity $\epsilon_c = \epsilon_c(r_s)$ is the correlation energy per electron of the uniform electron gas and $k_F = (\frac{4\pi}{3})^{1/3}/r_s$ (we use the Perdew-Wang correlation energy [7]).

The total electronic density is

$$n(\mathbf{r}) = \sum_\alpha |\psi_\alpha(\mathbf{r})|^2 . \tag{10}$$

Once the self-consistent density has been obtained, the total energy is given by the functional:

$$E[n] = \sum_\alpha \epsilon_\alpha - \left[U[n] + \int d^3\mathbf{r}\, \mu_{xc}(\mathbf{r})n(\mathbf{r})\right] + U_B[n_+] + \int d^3\mathbf{r}\, \epsilon_{xc}(\mathbf{r})n(\mathbf{r}) , \tag{11}$$

where

$$U[n] = \frac{1}{2}\int d^3\mathbf{r} \int d^3\mathbf{r}' \frac{n(\mathbf{r})n(\mathbf{r}')}{|\mathbf{r} - \mathbf{r}'|} \tag{12}$$

is the electronic Coulomb repulsion energy and

$$U_B[n_+] = \frac{3}{5}\frac{N^2}{R} \tag{13}$$

is the background Coulomb repulsion.

Fig. 1 shows the results for the selfconsistent density for $N = 42$. We also show the net charge distribution for the double positively ionized system. We see that the excess charge lies mainly in the surface region. The electronic density profile is similar to the corresponding nuclear quantity: the density is constant inside (apart from shell fluctuations) and decreases to zero at the edge. Within our model of metallic clusters, the inner electronic density is determined by the jellium density: it is the same for different clusters of the same metal, but varies from metal to metal. In contrast, the nuclear density is constant for all nuclides, neglecting self-compression effects.

We may think that, given the parentage between nuclei and clusters, a liquid drop formula for the energy of electronic systems is accurate to describe average trends. The energy of a set of neutral clusters of the same element with different number of atoms can indeed be described by a sum of volume, surface and curvature terms. In

the case of charged systems, there is in addition an explicit contribution from the charge.

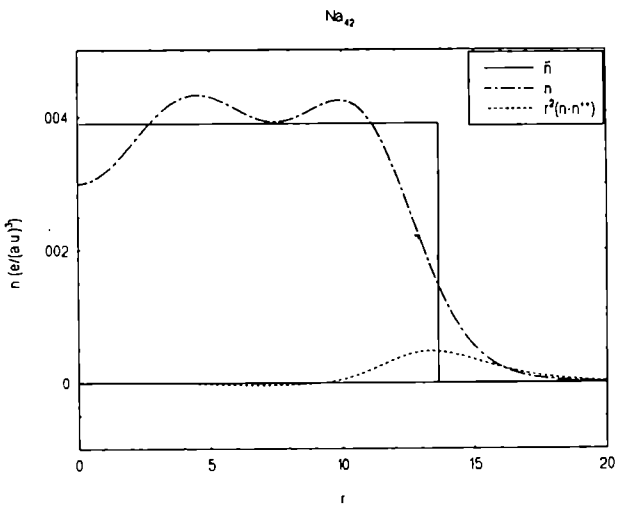

Figure 1: Jellium and valence electronic density $n(r)$ for Na_{42} obtained with the LDA Kohn-Sham method, in the jellium model. The dashed curve represents, in a different scale, the charge difference between the neutral and the double positively ionized system.

Contrary to some widespread belief, the liquid drop formula is not a phenomenological expression but can be derived from first principles with the aid of density functional methods. The energy of a spherical neutral cluster in the so-called leptodermeous expansion [8] (valid for systems with thin skin) can be written:

$$E[n] = E_{LDM} = \sum_{k=0}^{\infty} C_k R^{3-k} = \alpha \frac{4}{3}\pi R^3 + \sigma\, 4\pi R^2 + \gamma\, 2\pi R + ... \qquad (14)$$

The first term is the volume energy, the second is the surface energy, and the third is the curvature energy. The surface tension σ and the curvature energy γ are functionals of the electronic density of the semi-infinite problem [9].

The LDM coefficients obtained within the jellium model for the density of sodium, $r_s = 3.93$ bohr, are: $\alpha = -8.26 \times 10^{-3}$ eV/bohr^3, $\sigma = 2.96 \times 10^{-3}$ eV/bohr^2, and $\gamma = 9.97 \times 10^{-3}$ eV/bohr. The values of σ and γ were evaluated solving the semi-infinite problem (Lang-Kohn calculation [10]).

Let us now consider a spherical jellium cluster with N atoms and net charge Q. The liquid drop energy of this cluster, up to the order $N^{-\frac{1}{3}}$, is the sum of (14) with two charge contributions [11,12]:

$$E_{LDM} = \alpha V + \sigma S + \gamma C + Q(W + \frac{c}{R}) + \frac{1}{2}\frac{Q^2}{R + d_s}, \qquad (15)$$

where V is the cluster volume, S the surface and C the curvature. The quantity $-(W + \frac{c}{R})$ is the chemical potential, with W the work function and c a coefficient which describes a size effect (for sodium, $W = 2.85$ eV, and $c = -2.24$ eV [13]). The last term in Eq. (15) is the classical electrostatic energy, obtained under the assumption that the metal cluster is a perfect conductor and, therefore, the charge lies on the surface. A small spill-out effect due to the accumulation of excess charge on a radial centroid outside the jellium edge is included. The distance $R + d_s$ is the radius of the charge centroid (for sodium, $d_s = 1.1$ bohr).

From Fig. 2 we see that the LDM gives a good average of the Kohn-Sham energies of small spherical jellium clusters, neutral as well as charged. In order to ascertain the relative importance of the curvature energy, the insert shows the liquid drop result with and without the curvature term. We conclude that the curvature contribution plays a role only for very small clusters.

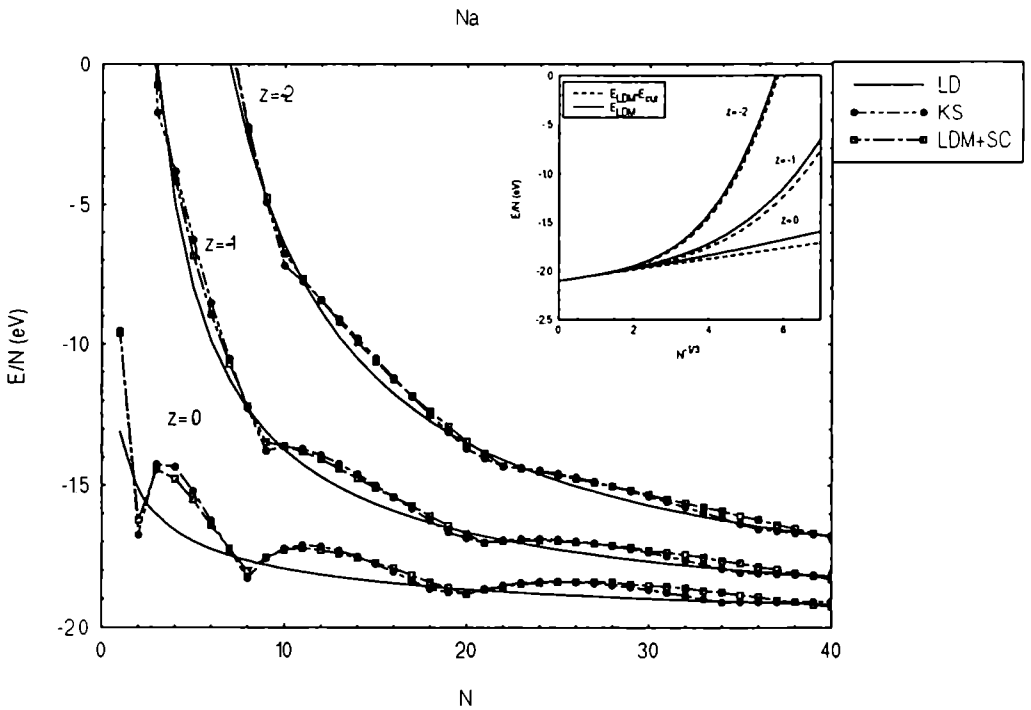

Figure 2: LDM and Strutinsky energies per atom of spherical jellium clusters of sodium, with $Q = 0, +1$ and $+2$ (the number of excess electrons is, respectively, $z = 0, -1$ and -2), in comparison with LDA Kohn-Sham results. In the insert, the LDM energy per atom, with and without the curvature term, is shown as a function of $N^{-\frac{1}{3}}$ for the same systems.

A system which provides a good test of the LDM is a spherical void inside jellium. Fig. 3 shows a comparison of the liquid drop formula with self-consistent calculations for the density $r_s = 2.07$ bohr. The agreement is excellent up to radii smaller than

a monoatomic void. The picture also shows a Padé approximant which has the right asymptotic behaviour for vanishing voids and coincides with the liquid drop formula for large voids [14,15]. A systematic comparison of LDM predictions with experimental void formation energies shows the role of curvature [16].

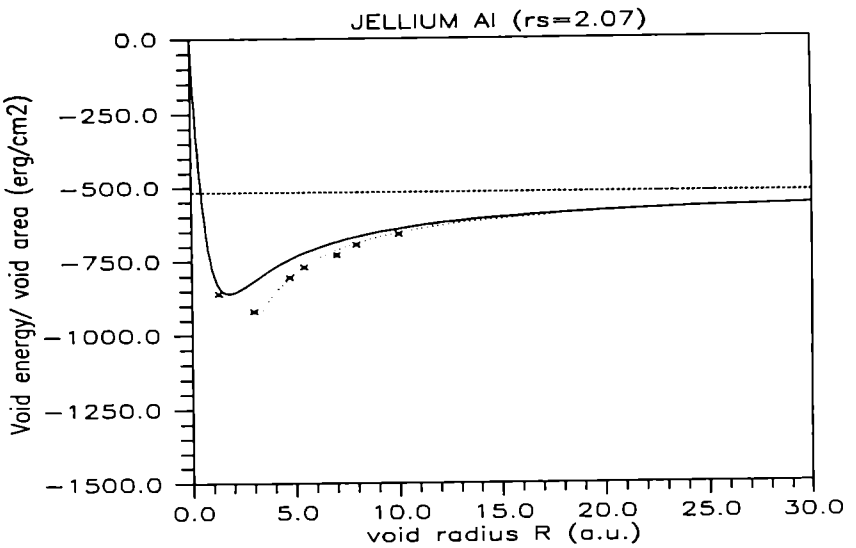

Figure 3: Void formation energies in the jellium model using the LDA Kohn-Sham method (crosses), the LDM (dotted line) and the Padé approximant of Ref. [15] (full line).

The von Weizaecker formula for the nuclear binding energy is well-known. Without the asymmetry term, it reads as

$$E_{LDM}(A,Z) = a_v A + a_s A^{\frac{2}{3}} + a_c A^{\frac{2}{3}} + a_{Coul}\frac{Z^2}{A^{\frac{1}{3}}}, \tag{16}$$

with the coefficients $a_v = -15.85$ MeV, $a_s = 18.34$ MeV, and $a_{Coul} = 0.71$ MeV, A being the mass number and Z the atomic number. There are various theoretical indications that the curvature coefficient is $a_c \simeq 10$ MeV. However, the experimental information on the nuclear binding energies is compatible with zero curvature energy. This is the so-called "curvature energy puzzle" in Nuclear Physics [17]. The success in Metal Physics of the leptodermous expansion is a strong suggestion that the value 10 MeV is right. However, if the leptodermous expansion does not converge quickly enough, higher order terms (which could be accounted for by a Padé formula) may be important and effectively cancel the curvature contribution.

In the Strutinsky shell correction method [18,19], the energy is given by the sum of a LDM term and a shell correction term,

$$E = E_{LDM} + E_{SC}, \tag{17}$$

where the last term may be evaluated as indicated in Ref. [20].

In order to check the validity of the shell correction method, we compare (17) with LDA Kohn-Sham calculations of spherical jellium clusters. Fig. 2 displays the very good agreement of the LDM plus shell corrected energies with the quantal ones. The shell structure is well reproduced with the simple harmonic oscillator up to $N = 42$. A small discrepancy occurs in the region around $N = 34$ (neutral case), where the $1f$ shell is being closed in the Kohn- Sham description, whereas that only happens for $N = 40$ in the case of the harmonic oscillator. We show results for the smallest clusters, keeping the same shell correction parameters, since, remarkably enough, they still compare rather well with the quantal energies.

3. Two Center Shell Model for the fission of charged jellium clusters

Small multiply charged clusters are not observed experimentally. This is due to the fact that charged atomic clusters with less than some critical number of atoms undergo fission, *i.e.*, fragmentation in two or more pieces with smaller charges [21,31]. The preferred decay channel of charged clusters above the critical size is the evaporation of neutral atoms: the heat of evaporation is lower than the fission barrier. In order to learn about cluster stability, it is convenient to have estimates as simple as possible of barrier heights and evaporation energies.

3.1. Quantal and LDM Q-values

An essential limitation on fission arises from the Q-values or heats of reaction, defined as the difference between final and initial energies. A positive heat of reaction means that the reaction can take place on pure energetic considerations but does not assure that the reaction is actually taking place (it is a necessary but not sufficient condition for fission). We consider both Kohn-Sham and LDM Q-values assuming always spherical configurations. Q-values obtained with the shell correction method agree, in general, with the self-consistent ones.

Figs. 4 (a) and (b) shows the Q-values, obtained with the Kohn-Sham method, corresponding to all possible decay channels of single and double positively charged sodium clusters up to $N = 30$. We only find Kohn-Sham solutions with total negative energies when $N > 2$ for single charged clusters and $N > 7$ for doubly charged clusters. The role of shell closures is apparent. Magic mother clusters, as for instance Na_{20}^{++}, are specially stable. On the other hand, final magic daughters, as for instance Na_3^+, are a common outcome.

The Q-values obtained with the LDM are shown in Figs. 4 (c) and (d) . For the single charged system, the asymmetric reaction $Na_N^+ \rightarrow Na_{N-1}^+ + Na_1$ is always preferred since it corresponds to a minimal Coulomb energy of the final configuration. This observation agrees with the Kohn-Sham results of Fig. 4 (a). In contrast, the symmetric channel $Na_N^{++} \rightarrow Na_{N/2}^+ + Na_{N/2}^+$ is preferred by doubly charged sodium clusters up to $N = 28$. A symmetric charge distribution of the fragments lowers indeed the total Coulomb energy for small clusters. This conclusion is not clearly seen in Fig. 4 (b), since shell effects play a major role for small clusters, hiding any smooth trend. However, a central valley is visible for $N > 20$.

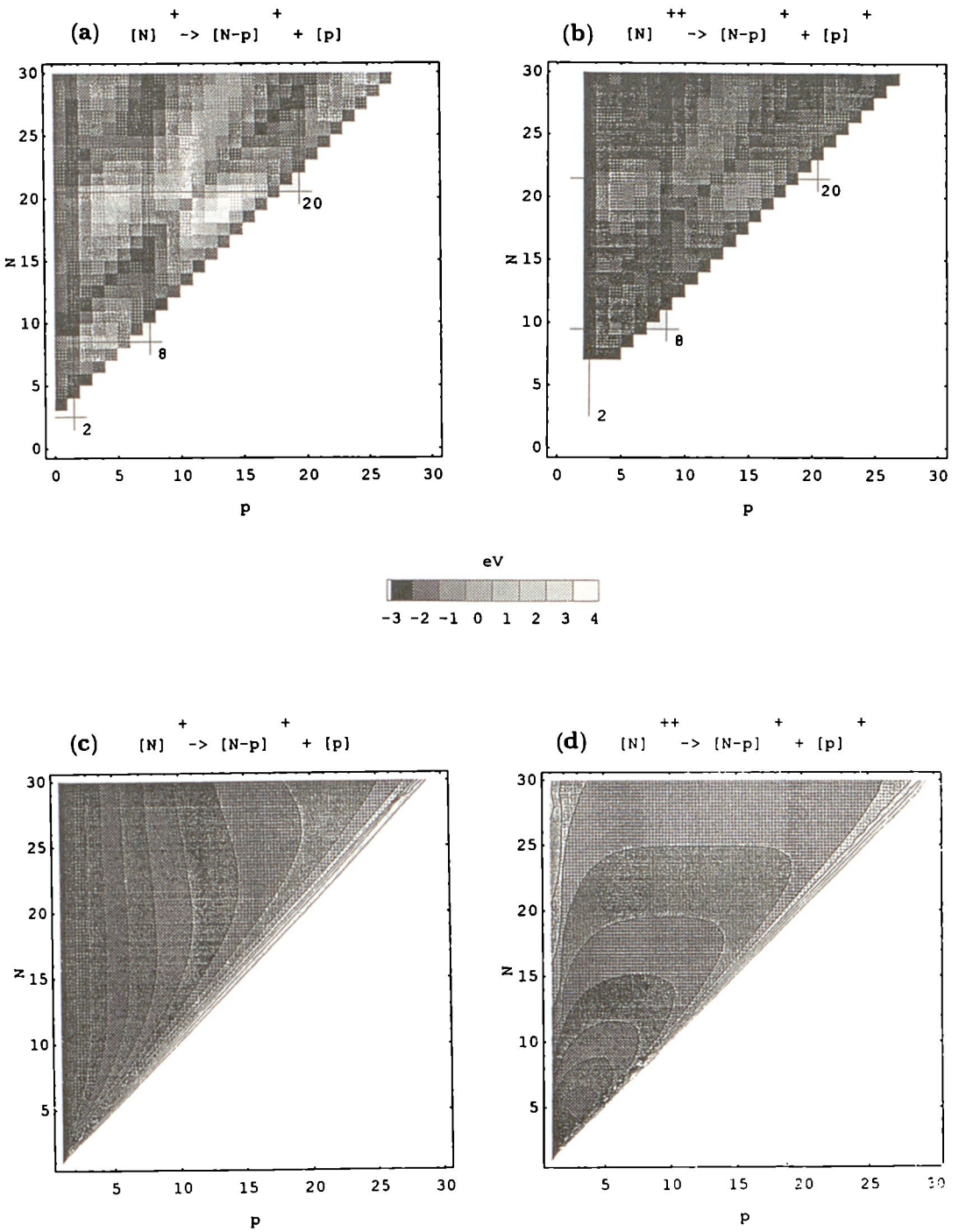

Figure 4: LDA Kohn-Sham Q-values for (a) Na_N^+ and (b) Na_N^{++} for every possible decay channel. Vertical and horizontal lines mark mothers and daughters with magic numbers of atoms. In (c) and (d) same as above but within the LDM.

Fig. 5 displays the Q-values for the most favorable channel obtained by using both the Kohn- Sham and the LDM approaches. We observe that the most favorable channel always has one magic fragment. This agrees with the results obtained in Ref. [22] (see also Ref. [23], which uses the "stabilized jellium model" for aluminium).

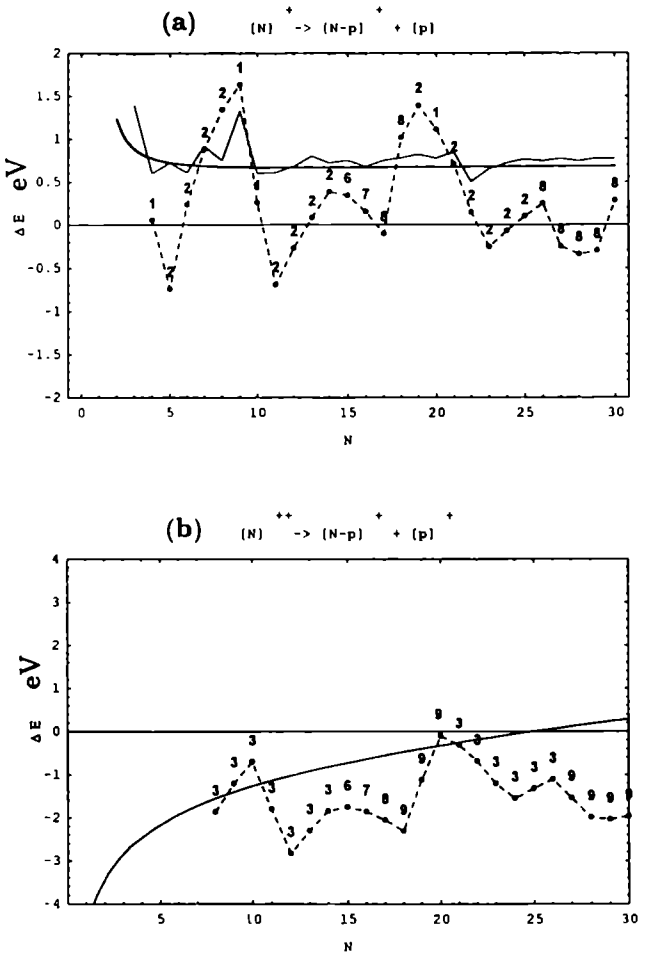

Figure 5: Q-values for the most favored decay channel for (a) Na_N^+ and (b) Na_N^{++}. The smooth line stands for the LDM, while the dots represent quantal results (the numbers above the dots are the values of p). In (a) the experimental results from Ref. [24] are represented by a thin broken line.

Fig. 5 (a) shows experimental results [24] obtained for single charged sodium clusters against our results. The agreement of the LDM with experiment is remarkable. The trends of the experimental results are also well reproduced by the quantal result, although fluctuations are exaggerated in the latter due the imposed sphericity.

In Fig. 5 (b) the two lowest local minima occurs when both fragments are magical: $Na_{12}^{++} \rightarrow Na_9^+ + Na_3^+$ and $Na_{18}^{++} \rightarrow Na_9^+ + Na_9^+$. As expected, the LDM curve goes slightly above the quantal results.

3.2. Deformed LDM and shell corrections

To evaluate the potential energy corresponding to the fission of sodium clusters, using the shell correction method, we need to generalize the LDM to handle deformed systems and to consider a shell model which can describe splitted shapes [25].

We have calculated potential energies for charged clusters which fragment in two pieces, in the framework of the LDM plus shell corrections obtained from the Two Center Shell Model, a double harmonic well which is popular in Nuclear Physics [26,27].

Eq. (17) may be extended to account for deformed clusters with the same volume as a spherical cluster:

$$E_{LDM} = \alpha V + \sigma S + \gamma C + Q(W + \frac{c}{C/2\pi}) + a_{Coul}Q^2, \tag{18}$$

where the surface $S = \int dA$ of the deformed shape and $C = \frac{1}{4}\int \mathcal{R}^{-1} dA$, with $\mathcal{R}$ the local curvature, are evaluated numerically. In the size correction to the chemical potential $C/2\pi$ has replaced R, since this gives the right behaviour for one initial and two final spherical clusters.

The electrostatic energy of a spherical shell is now $a_{Coul}Q^2$, with the coefficient a_{Coul} computed numerically. This is done by minimizing the electrostatic energy under the constraint that the electric potential is constant on the cluster surface [28]. The spill-out effect is included by considering a surface charge which is displaced by d_s with respect to the shape with volume V.

As a set of shapes going from one sphere to two spheres, we select the so-called Blocki's shapes [29], which consists basically of two spheres joined by a smooth neck. This family is described by three parameters: an elongation parameter, a neck parameter and an asymmetry parameter, defined respectively by:

$$\rho = \frac{d}{R_1 + R_2}, \quad \lambda = \frac{l_1 + l_2}{R_1 + R_2}, \quad \Delta = \frac{R_1 - R_2}{R_1 + R_2}, \tag{19}$$

where d is the center to center distance, R_1 and R_2 are the radii of the two fragments, and l_1 and l_2 are the thickness of the lens-shaped piece of the sphere that lies within the matching quadratic surface.

For the path in the (ρ, λ) plane, we assume, based on molecular dynamics results [30], that initially the system does not develop a neck, getting it very quickly in the later stages of fission. Within the liquid drop picture, the energy along the fission line (curve which separates connected from disconnected shapes, given by the equation $\lambda = 1 - 1/\rho$) has a minimum at a saddle point. For obtaining fission barriers, the precise path is unimportant provided it goes through the saddle point.

We are interested not only in evaluating fission barriers but also in comparing them with evaporation energies. We consider the symmetric fragmentation of Na_{18}^{++} and Na_{42}^{++}, for which the final configurations are magic.

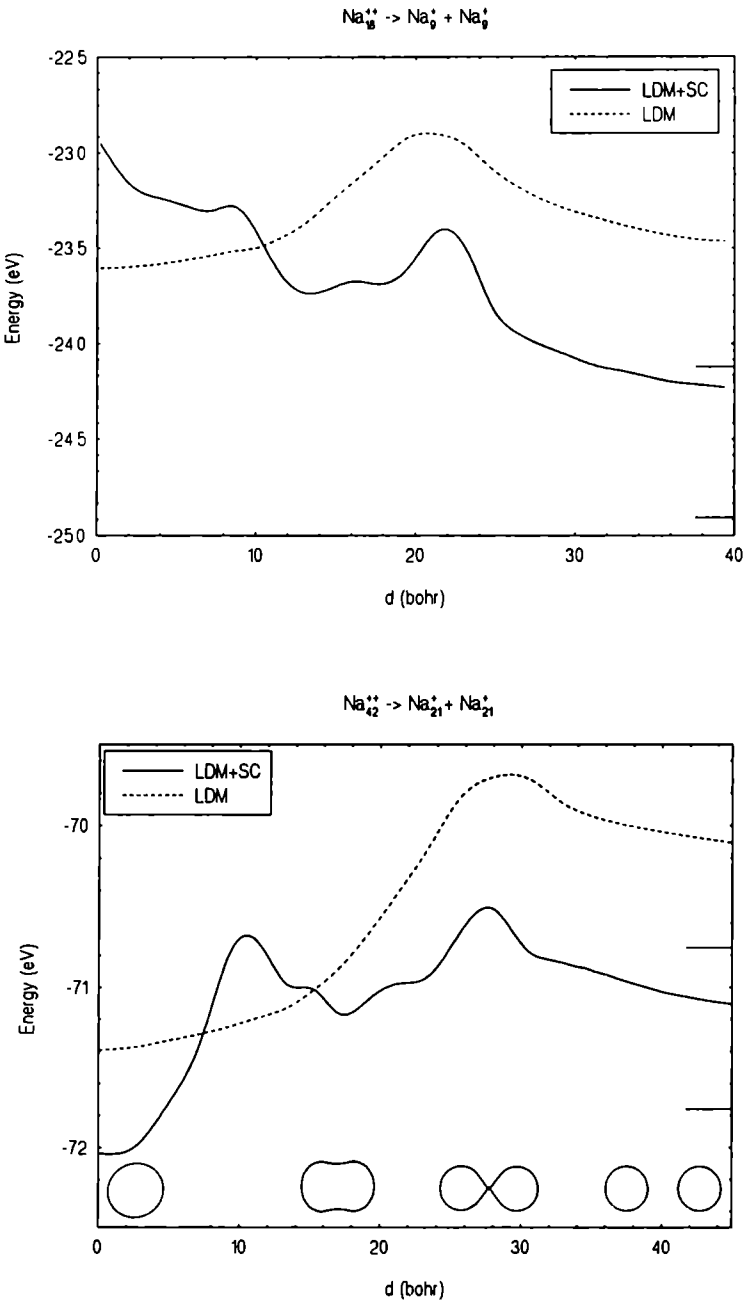

Figure 6: Potential energies for two fission processes using both the LDM and the LDM plus shellcorrections.

Fig. 6 show the potential energy curves for the two reactions along the path described in Ref. [25]. In the case of Na_{18}^{++}, the system shows a well deformed ground state and a small barrier at $d = 20$ bohr, being clearly unstable. In the case of Na_{42}^{++}, the system shows an initial spherical state and a fission isomer at $d = 16$ bohr.

The following Table informs about Q-values, heats of evaporation and fission barriers for the symmetric decays of Na_{18}^{++} and Na_{42}^{++}:

Table: Q-values and heats of evaporation E_{eva}, in the Kohn-Sham method (in brackets the corresponding values using the Strutinsky method). The fission barrier E_b given by the Strutinsky method is also shown. All values are in eV.

Reaction	Q-value	E_{eva}	E_b
$Na_{18}^{++} \rightarrow 2Na_8^+$	-2.05	2.13	
	(-2.06)	(2.19)	(0.53)
$Na_{42}^{++} \rightarrow 2Na_{21}^+$	0.25	1.28	
	(-0.45)	(1.10)	(1.62)

The agreement between the Kohn-Sham and the Strutinsky results is good. The discrepancy for the heat of reaction of Na_{42}^{++} is due to the failure of the harmonic shell correction for clusters around $N = 40$. We note that Na_{42}^{++} can decay symmetricaly on the basis of the Q-value if we calculate it *a la* Kohn-Sham, but the double humped barrier represents a serious hindering of fission. For this system, evaporation is preferred to fission, since $E_{eva} < E_b$.

Finally, we present a LDM estimate of the cluster size, N_c, for which $E_{eva} = E_b$ in the case of doubly charged sodium clusters. We do not make any restrictions on the size of the fission fragments, but for simplicity neglect the curvature term contribution to the barrier. In Fig. 7 we plot the fission barrier height for the most favored channel

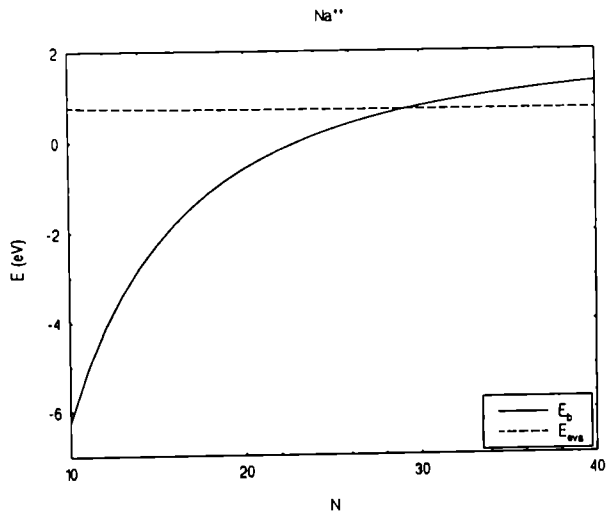

Figure 7: Lowest barrier height in comparison with the evaporation energy, both within the LDM.

together with the evaporation energy (by "most favored" we mean here the channel with the lowest barrier and not that with the lowest Q-value). The fission barrier increases with N, while the evaporation energy is practically constant. The two curves intersect at $N_c = 29$, in good agreement with the experimental number 27 [31]. But shell corrections should have an effect on N_c which remains to be investigated.

4. Conclusions

Nuclear Physics techniques and concepts are being applied to a new and exciting field of Physics. In contrast with Nuclear Physics, in Cluster Physics the exact force is known and systems with any size and charge can be considered.

Notwithstanding the differences in the structure and energy scale, the fission of metallic clusters display similarities with the fission of atomic nuclei. In both cases, fission is determined by the competition between the surface and Coulomb terms. However, the Coulomb term in atomic clusters arises from the surface charge, while in nuclei it is due to the volume charge. Fission occurs for small multiply charged clusters, whose surface tension is unable to sustain the surface Coulomb repulsion.

Shell effects play a major role in shaping fission barriers, changing drastically the liquid drop scenario. We have presented a method to evaluate potential energies of fragmentation processes which is simple but incorporates shell effects with an accuracy which is good enough for many practical purposes.

Acknowledgments

C. F. would like to acknowledge the kind invitation of A. Raduta to present this work at the Predeal school. We are grateful to M. Brajczewska (Coimbra), M. Brack (Regensburg), M. Seidl and J. P. Perdew (New Orleans) for fruitful discussions. This work has been partially supported by the EC- Science project "Study of the stability of charged metal clusters".

References

1. W. D. Knight, K. Klemenger, W. A. De Heer, W. A. Saunders, M. Y. Chou, and M. L. Cohen, *Phys. Rev. Lett.* **52** (1984) 2141.
2. W. Ekardt, *Phys. Rev.* **B31** (1985) 6360.
3. P. Hohenberg and W. Kohn, *Phys. Rev.* **136** (1964) B864.
4. W. Kohn and L. J. Sham, *Phys. Rev.* **140** (1965) A1133.
5. M. Brack, *Rev. Mod. Phys.* **65** (1993) 677.
6. J. P. Perdew, in *Density Functional Theory*, ed. E. K. U. Gross and R. M. Dreizler (Plenum, New York, 1994).
7. J. P. Perdew and Y. Wang, *Phys. Rev.* **B45** (1992) 13244.
8. M. Brack, C. Guet, and H.-B. Hakansson, *Phys. Rep.* **123** (1993) 275.
9. C. Fiolhais and J. P. Perdew, *Phys. Rev.* **B45** (1992) 6207.
10. N. D. Lang and W. Kohn, *Phys. Rev.* **B1** (1970) 4555.

11. J. P. Perdew, in *Condensed Matter Theories*, vol. IV, ed. J. Keller (Plenum, New York, 1989).
12. M. Seidl and M. Brack, *Ann. Phys. (N. Y.)*, in print.
13. E. Engel and J. P. Perdew, *Phys. Rev.* **B43** (1991) 1331.
14. J. P. Perdew, P. Ziesche, and C. Fiolhais, *Phys. Rev.* **B47** (1993) 16460.
15. P. Ziesche, J. P. Perdew, and C. Fiolhais, *Phys. Rev.* **B49** (1994) 7916.
16. J. P. Perdew, Y. Wang, and E. Engel, *Phys. Rev. Lett.* **66** (1991) 508.
17. M. Durand, P. Schuck, and X. Viñas, *Z. Phys.* **A346** (1993) 87.
18. V. M. Strutinsky, *Nucl. Phys.* **A95** (1967) 420.
19. V. M. Strutinsky, *Nucl. Phys.* **A122** (1968) 1.
20. J. R. Nix, *Ann. Rev. Nucl. Sci.* **22** (1972) 65.
21. U. Näher, H. Goehlich, T. Lange, and T. P. Martin, *Phys. Rev.* **B68** (1992) 3416.
22. M. P. Iñiguez, J. A. Alonso, M. A. Aller, and L. C. Balbás, *Phys. Rev.* **B34** (1986) 2152.
23. A. Vieira, M. Brajczewska, and C. Fiolhais, *Int. J. Quantum Chem.*, in print.
24. C. Bréchignac, Ph. Cahuzac, F. Carlier, and M. de Frutos, *J. Chem. Phys.* **93** (1990) 7749.
25. A. Vieira and C. Fiolhais, unpublished.
26. P. Holzer, U. Mosel, and W. Greiner, *Nucl. Phys.* **A138** (1969) 241.
27. D. Scharnweber, W. Greiner, and U. Mosel, *Nucl. Phys.* **A164** (1971) 257.
28. H. Koizumi, S. Sugano, and Y. Ishii, *Z. Phys.* **D28** (1993) 223.
29. J. Blocki, *Journal de Physique* **45 C6** (1984) 489.
30. R. N. Barnett, U. Landman, and G. Rajagopal, *Phys. Rev. Lett.* **67** (1991) 3058.
31. C. Bréchignac, Ph. Cahuzac, F. Carlier, and M. de Frutos, *Phys. Rev. Lett.* **64** (1990) 2893.

9. QUANTUM GROUPS

THE USE OF QUANTUM GROUPS IN NUCLEAR STRUCTURE PROBLEMS

Dennis BONATSOS
ECT, Villa Tambosi, Strada delle Tabarelle 286*
I-38050 Villazzano (Trento), Italy

C. DASKALOYANNIS
Department of Physics, Aristotle University of Thessaloniki
GR-54006 Thessaloniki, Greece

P. KOLOKOTRONIS, D. LENIS
Institute of Nuclear Physics, NCSR "Demokritos"
GR-15310 Aghia Paraskevi, Attiki, Greece

ABSTRACT

Various applications of quantum algebraic techniques in nuclear structure physics, such as the $su_q(2)$ rotator model and its extensions, the use of deformed bosons in the description of pairing correlations, and the construction of deformed exactly soluble models (Interacting Boson Model, Moszkowski model) are briefly reviewed. Emphasis is put in the study of the symmetries of the anisotropic quantum harmonic oscillator with rational ratios of frequencies, which underly the structure of superdeformed and hyperdeformed nuclei, the Bloch–Brink α-cluster model and possibly the shell structure in deformed atomic clusters.

1. Introduction

Quantum algebras [1,2] (also called quantum groups) are deformed versions of the usual Lie algebras, to which they reduce when the deformation parameter q is set equal to unity. Their use in physics became popular with the introduction [3–5] of the q-deformed harmonic oscillator as a tool for providing a boson realization of the quantum algebra $su_q(2)$, although similar mathematical structures had already been known [6,7]. Initially used for solving the quantum Yang–Baxter equation, quantum algebras have subsequently found applications in several branches of physics, as, for example, in the description of spin chains, squeezed states, rotational and vibrational nuclear and molecular spectra, and in conformal field theories. By now several kinds of generalized deformed oscillators [8–12] and generalized deformed su(2) algebras [13–19] have been introduced.

Here we shall confine ourselves to applications of quantum algebras in nuclear structure physics. A brief description will be given of the $su_q(2)$ rotator model [20–25] and its extensions [13,26], of the use of deformed oscillators in the description of pairing correlations [27–29], and of the formulation of deformed exactly soluble models (Interacting Boson Model [30], Moszkowski model [31–33]). The purpose of this short review is to provide the reader with references for further reading. Subsequently, the symmetries of the anisotropic quantum harmonic oscillator with rational ratios of frequencies will be considered in more detail, since they are of current interest [34,35] in connection

with superdeformed and hyperdeformed nuclei [36,37], α-cluster configurations in light nuclei [38–40], and possibly with deformed atomic clusters [41,42].

2. The $su_q(2)$ rotator model

The first application of quantum algebras in nuclear physics was the use of the deformed algebra $su_q(2)$ for the description of the rotational spectra of deformed [20,21] and superdeformed [22] nuclei. The same technique has been used for the description of rotational spectra of diatomic molecules [23]. The Hamiltonian of the q-deformed rotator is proportional to the second order Casimir operator of the $su_q(2)$ algebra. Its Taylor expansion contains powers of $J(J+1)$ (where J is the angular momentum), being similar to the expansion provided by the Variable Moment of Inertia (VMI) model. Furthermore, the deformation parameter τ (with $q = e^{i\tau}$) has been found to correspond to the softness parameter of the VMI model [21].

B(E2) transition probabilities have also been described in this framework [24]. In this case the q-deformed Clebsch–Gordan coefficients are used instead of the normal ones. (It should be noticed that the q-deformed angular momentum theory has already been much developed [24].) The model predicts an increase of the B(E2) values with angular momentum, while the rigid rotator model predicts saturation. Some experimental results supporting this prediction already exist [24].

3. Extensions of the $su_q(2)$ model

The $su_q(2)$ model has been successful in describing rotational nuclear spectra. For the description of vibrational and transitional nuclear spectra it has been found [26] that $J(J+1)$ has to be replaced by $J(J+c)$. The additional parameter c allows for the description of nuclear anharmonicities in a way similar to that of the Interacting Boson Model (IBM) [43,44] and the Generalized Variable Moment of Inertia (GVMI) model [45].

Another generalization is based on the use of the deformed algebra $su_\Phi(2)$ [13], which is characterized by a structure function Φ. The usual su(2) and $su_q(2)$ algebras are obtained for specific choices of the structure function Φ. The $su_\Phi(2)$ algebra has been constructed so that its representation theory resembles as much as possible the representation theory of the usual su(2) algebra. Using this technique one can construct, for example, a rotator having the same spectrum as the one given by the Holmberg–Lipas formula [46]. In addition to the generalized deformed su(2) algebra, generalized deformed oscillators [8–12] have also been introduced and found useful in many physical applications.

4. Pairing correlations

It has been found [27] that correlated fermion pairs coupled to zero angular momentum in a single-j shell behave approximately as suitably defined q-deformed bosons. After performing the same boson mapping to a simple pairing Hamiltonian, one sees

that the pairing energies are also correctly reproduced up to the same order. The deformation parameter used ($\tau = \ln q$) is found to be inversely proportional to the size of the shell, thus serving as a small parameter.

The above mentioned system of correlated fermion pairs can be described *exactly* by suitably defined generalized deformed bosons [28]. Then both the commutation relations are satisfied exactly and the pairing energies are reproduced exactly. The spectrum of the appropriate generalized deformed oscillator corresponds, up to first order perturbation theory, to a harmonic oscillator with an x^4 perturbation.

5. q-deformed versions of nuclear models

A q-deformed version of a two dimensional toy Interacting Boson Model (IBM) has been developed [30], mainly for testing the ways in which spectra and transition probabilities are influenced by the q-deformation. A q-deformed version of the full IBM is under development, while a q-deformed version of the vibron model, which uses the IBM techniques in the case of molecules, has already been developed [47].

Furthermore a q-deformed version of the Moszkowski model has been developed [31] and RPA modes have been studied [32] in it. A q-deformed Moszkowski model with cranking has also been studied [33] in the mean-field approximation. It has been seen that the residual interaction simulated by the q-deformation is felt more strongly by states with large J_z. The possibility of using q-deformation in assimilating temperature effects is under discussion.

6. Anisotropic quantum harmonic oscillator with rational ratios of frequencies

The symmetries of the 3-dimensional anisotropic quantum harmonic oscillator with rational ratios of frequencies (RHO) are of high current interest in nuclear physics, since they are the basic symmetries [34,35] underlying the structure of superdeformed and hyperdeformed nuclei [36,37]. The 2-dimensional RHO is also of interest, in connection with "pancake" nuclei, i.e. very oblate nuclei [35]. Cluster configurations in light nuclei can also be described in terms of RHO symmetries [38,39], which underlie the geometrical structure of the Bloch–Brink α-cluster model [40]. The 3-dim RHO is also of interest for the interpretation of the observed shell structure in atomic clusters [41], especially after the realization [42] that large deformations can occur in such systems.

The two-dimensional [48–53] and three-dimensional [54–60] anisotropic harmonic oscillators have been the subject of several investigations, both at the classical and the quantum mechanical level. These oscillators are examples of superintegrable systems [61]. The special cases with frequency ratios 1:2 [62,63] and 1:3 [64] have also been considered. While at the classical level it is clear that the su(N) or sp(2N,R) algebras can be used for the description of the N-dimensional anisotropic oscillator, the situation at the quantum level, even in the two-dimensional case, is not as simple.

In this section we are going to prove that a generalized deformed u(2) algebra is

the symmetry algebra of the two-dimensional anisotropic quantum harmonic oscillator, which is the oscillator describing the single-particle level spectrum of "pancake" nuclei, i.e. of triaxially deformed nuclei with $\omega_x >> \omega_y, \omega_z$ [35].

6.1. The deformed u(2) algebra

Let us consider the system described by the Hamiltonian:

$$H = \frac{1}{2}\left({p_x}^2 + {p_y}^2 + \frac{x^2}{m^2} + \frac{y^2}{n^2}\right), \tag{1}$$

where m and n are two natural numbers mutually prime ones, i.e. their great common divisor is $\gcd(m,n) = 1$.

We define the creation and annihilation operators [48]

$$\begin{aligned} a^\dagger &= \tfrac{x/m - ip_x}{\sqrt{2}}, \quad a = \tfrac{x/m + ip_x}{\sqrt{2}}, \\ b^\dagger &= \tfrac{y/n - ip_y}{\sqrt{2}}, \quad b = \tfrac{y/n + ip_y}{\sqrt{2}}. \end{aligned} \tag{2}$$

These operators satisfy the commutation relations:

$$[a, a^\dagger] = \frac{1}{m}, \quad [b, b^\dagger] = \frac{1}{n}, \quad \text{other commutators} = 0. \tag{3}$$

Using Eqs (2) and (3) we can prove by induction that:

$$[a, (a^\dagger)^p] = \tfrac{p}{m}(a^\dagger)^{p-1}, \quad [b, (b^\dagger)^p] = \tfrac{p}{n}(b^\dagger)^{p-1},$$

$$[a^\dagger, (a)^p] = -\tfrac{p}{m}(a)^{p-1}, \quad [b^\dagger, (b)^p] = -\tfrac{p}{n}(b)^{p-1}.$$

Defining

$$U = \frac{1}{2}\{a, a^\dagger\}, \qquad W = \frac{1}{2}\{b, b^\dagger\},$$

one can easily prove that:

$$[U, (a^\dagger)^p] = \tfrac{p}{m}(a^\dagger)^p, \quad [W, (b^\dagger)^p] = \tfrac{p}{n}(b^\dagger)^p,$$

$$[U, (a)^p] = -\tfrac{p}{m}(a)^p, \quad [W, (b)^p] = -\tfrac{p}{n}(b)^p.$$

Using the above properties we can define the enveloping algebra generated by the operators:

$$\begin{aligned} S_+ &= (a^\dagger)^m (b)^n, \quad S_- = (a)^m (b^\dagger)^n, \\ S_0 &= \tfrac{1}{2}(U - W), \quad H = U + W. \end{aligned} \tag{4}$$

These genarators satisfy the following relations:

$$[S_0, S_\pm] = \pm S_\pm, \quad [H, S_i] = 0, \quad \text{for} \quad i = 0, \pm, \tag{5}$$

and

$$S_+S_- = \prod_{k=1}^{m}\left(U - \frac{2k-1}{2m}\right)\prod_{\ell=1}^{n}\left(W + \frac{2\ell-1}{2n}\right),$$

$$S_-S_+ = \prod_{k=1}^{m}\left(U + \frac{2k-1}{2m}\right)\prod_{\ell=1}^{n}\left(W - \frac{2\ell-1}{2n}\right).$$

The fact that the operators S_i, $i = 0, \pm$ are integrals of motion has been already realized in [48].

The above relations mean that the harmonic oscillator of Eq. (1) is described by the enveloping algebra of the generalization of the u(2) algebra formed by the generators S_0, S_+, S_- and H, satisfying the commutation relations of Eq. (5) and

$$[S_-, S_+] = F_{m,n}(H, S_0 + 1) - F_{m,n}(H, S_0),$$

$$\text{where} \quad F_{m,n}(H, S_0) = \prod_{k=1}^{m}\left(H/2 + S_0 - \tfrac{2k-1}{2m}\right)\prod_{\ell=1}^{n}\left(H/2 - S_0 + \tfrac{2\ell-1}{2n}\right). \tag{6}$$

In the case of $m = 1$, $n = 1$ this algebra is the usual u(2) algebra, and the operators $S_0, S_\pm$ satisfy the commutation relations of the ordinary u(2) algebra, since in this case one easily finds that

$$[S_-, S_+] = -2S_0.$$

In the rest of the cases, the algebra is a deformed version of u(2), in which the commutator $[S_-, S_+]$ is a polynomial of S_0 of order $m + n - 1$. In the case with $m = 1$, $n = 2$ one has

$$[S_-, S_+] = 3S_0^2 - HS_0 - \frac{H^2}{4} + \frac{3}{16},$$

i.e. a polynomial quadratic in S_0 occurs, while in the case of $m = 1$, $n = 3$ one finds

$$[S_-, S_+] = -4S_0^3 + 3HS_0^2 - \frac{7}{9}S_0 - \frac{H^3}{4} + \frac{H}{4},$$

i.e. a polynomial cubic in S_0 is obtained.

6.2. The representations

The finite dimensional representation modules of this algebra can be found using the concept of the generalized deformed oscillator [8], in a method similar to the one used in Ref. 65 for the study of quantum superintegrable systems. The operators:

$$\mathcal{A}^\dagger = S_+, \quad \mathcal{A} = S_-, \quad \mathcal{N} = S_0 - u, \quad u = \text{ constant}, \tag{7}$$

where u is a constant to be determined, are the generators of a deformed oscillator algebra:

$$[\mathcal{N}, \mathcal{A}^\dagger] = \mathcal{A}^\dagger, \quad [\mathcal{N}, \mathcal{A}] = -\mathcal{A}, \quad \mathcal{A}^\dagger\mathcal{A} = \Phi(H, \mathcal{N}), \quad \mathcal{A}\mathcal{A}^\dagger = \Phi(H, \mathcal{N}+1).$$

The structure function Φ of this algebra is determined by the function $F_{m,n}$ in Eq. (6):

$$\begin{aligned}\Phi(H, \mathcal{N}) &= F_{m,n}(H, \mathcal{N}+u) = \\ &= \prod_{k=1}^{m} \left(H/2 + \mathcal{N} + u - \tfrac{2k-1}{2m}\right) \prod_{\ell=1}^{n} \left(H/2 - \mathcal{N} - u + \tfrac{2\ell-1}{2n}\right).\end{aligned} \tag{8}$$

The deformed oscillator corresponding to the structure function of Eq. (8) has an energy dependent Fock space of dimension $N+1$ if

$$\Phi(E, 0) = 0, \quad \Phi(E, N+1) = 0, \quad \Phi(E, k) > 0, \quad \text{for} \quad k = 1, 2, \ldots, N. \tag{9}$$

The Fock space is defined by:

$$H|E, k> = E|E, k>, \quad \mathcal{N}|E, k> = k|E, k>, \quad a|E, 0> = 0, \tag{10}$$

$$\mathcal{A}^\dagger|E, k> = \sqrt{\Phi(E, k+1)}|E, k+1>, \quad \mathcal{A}|E, k> = \sqrt{\Phi(E, k)}|E, k-1>. \tag{11}$$

The basis of the Fock space is given by:

$$|E, k> = \frac{1}{\sqrt{[k]!}} \left(\mathcal{A}^\dagger\right)^k |E, 0>, \quad k = 0, 1, \ldots N,$$

where the "factorial" $[k]!$ is defined by the recurrence relation:

$$[0]! = 1, \quad [k]! = \Phi(E, k)[k-1]! \quad .$$

Using the Fock basis we can find the matrix representation of the deformed oscillator and then the matrix representation of the algebra of Eqs (5), (6). The solution of Eqs (9) implies the following pairs of permitted values for the energy eigenvalue E and the constant u:

$$E = N + \frac{2p-1}{2m} + \frac{2q-1}{2n}, \tag{12}$$

where $p = 1, 2, \ldots, m$, $q = 1, 2, \ldots, n$, and

$$u = \frac{1}{2}\left(\frac{2p-1}{2m} - \frac{2q-1}{2n} - N\right),$$

the corresponding structure function being given by:

$$\begin{aligned}\Phi(E, x) &= \Phi^N_{(p,q)}(x) = \\ &= \prod_{k=1}^{m} \left(x + \frac{2p-1}{2m} - \frac{2k-1}{2m}\right) \prod_{\ell=1}^{n} \left(N - x + \frac{2q-1}{2n} + \frac{2\ell-1}{2n}\right) \\ &= \frac{1}{m^m n^n} \frac{\Gamma(mx+p)}{\Gamma(mx+p-m)} \frac{\Gamma((N-x)n+q+n)}{\Gamma((N-x)n+q)}.\end{aligned} \tag{13}$$

In all these equations one has $N = 0, 1, 2, \ldots$, while the dimensionality of the representation is given by $N + 1$. Eq. (12) means that there are $m \cdot n$ energy eigenvalues corresponding to each N value, each eigenvalue having degeneracy $N + 1$. (Later we shall see that the degenerate states corresponding to the same eigenvalue can be labelled by an "angular momentum".)

It is useful to show at this point that a few special cases are in agreement with results already existing in the literature.

i) In the case $m = 1$, $n = 1$ Eq. (13) gives

$$\Phi(E, x) = x(N + 1 - x),$$

while Eq. (12) gives

$$E = N + 1,$$

in agreement with Sec. IV.A of Ref. 65.

ii) In the case $m = 1$, $n = 2$ one obtains for $q = 2$

$$\Phi(E, x) = x(N + 1 - x)\left(N + \frac{3}{2} - x\right), \qquad E = N + \frac{5}{4},$$

while for $q = 1$ one has

$$\Phi(E, x) = x(N + 1 - x)\left(N + \frac{1}{2} - x\right), \qquad E = N + \frac{3}{4}.$$

These are in agreement with the results obtained in Sec. IV.F of Ref. 65 for the Holt potential (for $\delta = 0$).

iii) In the case $m = 1$, $n = 3$ one has for $q = 1$

$$\Phi(E, x) = x(N + 1 - x)\left(N + \frac{1}{3} - x\right)\left(N + \frac{2}{3} - x\right), \qquad E = N + \frac{2}{3},$$

while for $q = 2$ one obtains

$$\Phi(E, x) = x(N + 1 - x)\left(N + \frac{2}{3} - x\right)\left(N + \frac{4}{3} - x\right), \qquad E = N + 1,$$

and for $q = 3$ one gets

$$\Phi(E, x) = x(N + 1 - x)\left(N + \frac{4}{3} - x\right)\left(N + \frac{5}{3} - x\right), \qquad E = N + \frac{4}{3}.$$

These are in agreement with the results obtained in Sec. IV.D of Ref. 65 for the Fokas–Lagerstrom potential.

In all of the above cases we remark that the structure function has the form

$$\Phi(x) = x(N + 1 - x)(\lambda + \mu x + \nu x^2 + \rho x^3 + \sigma x^4 + \ldots,$$

which corresponds to a generalized deformed parafermionic algebra [66] of order N, if λ, μ, ν, ρ, σ, ..., are real constants satisfying the conditions

$$\lambda + \mu x + \nu x^2 + \rho x^3 + \sigma x^4 + \ldots > 0, \qquad x \in \{1, 2, \ldots, N\}.$$

These conditions are indeed satisfied in all cases. It is easy to see that the obtained algebra corresponds to this of the generalized parafermionic oscillator in all cases with frequency ratios $1 : n$.

The energy formula can be corroborated by using the corresponding Schrödinger equation. For the Hamiltonian of Eq. (1) the eigenvalues of the Schrödinger equation are given by:

$$E = \frac{1}{m}\left(n_x + \frac{1}{2}\right) + \frac{1}{n}\left(n_y + \frac{1}{2}\right), \tag{14}$$

where $n_x = 0, 1, \ldots$ and $n_y = 0, 1, \ldots$. Comparing Eqs (12) and (14) one concludes that:

$$N = [n_x/m] + [n_y/n],$$

where $[x]$ is the integer part of the number x, and

$$p = \mathrm{mod}(n_x, m) + 1, \quad q = \mathrm{mod}(n_y, n) + 1.$$

The eigenvectors of the Hamiltonian can be parametrized by the dimensionality of the representation N, the numbers p, q, and the number $k = 0, 1, \ldots, N$. k can be identified as $[n_x/m]$. One then has:

$$H \left| \begin{matrix} N \\ (p,q) \end{matrix}, k \right\rangle = \left(N + \frac{2p-1}{2m} + \frac{2q-1}{2n}\right) \left| \begin{matrix} N \\ (p,q) \end{matrix}, k \right\rangle, \tag{15}$$

$$S_0 \left| \begin{matrix} N \\ (p,q) \end{matrix}, k \right\rangle = \left(k + \frac{1}{2}\left(\frac{2p-1}{2m} - \frac{2q-1}{2n} - N\right)\right) \left| \begin{matrix} N \\ (p,q) \end{matrix}, k \right\rangle, \tag{16}$$

$$S_+ \left| \begin{matrix} N \\ (p,q) \end{matrix}, k \right\rangle = \sqrt{\Phi^N_{(p,q)}(k+1)} \left| \begin{matrix} N \\ (p,q) \end{matrix}, k+1 \right\rangle, \tag{17}$$

$$S_- \left| \begin{matrix} N \\ (p,q) \end{matrix}, k \right\rangle = \sqrt{\Phi^N_{(p,q)}(k)} \left| \begin{matrix} N \\ (p,q) \end{matrix}, k-1 \right\rangle. \tag{18}$$

6.3. The "angular momentum" quantum number

It is worth noticing that the operators $S_0, S_\pm$ do not correspond to a generalization of the angular momentum, S_0 being the operator corresponding to the Fradkin operator $S_{xx} - S_{yy}$ [67,68]. The corresponding "angular momentum" is defined by:

$$L_0 = -i\,(S_+ - S_-). \tag{19}$$

The "angular momentum" operator commutes with the Hamiltonian:

$$[H, L_0] = 0.$$

Let $|\ell>$ be the eigenvector of the operator L_0 corresponding to the eigenvalue ℓ. The general form of this eigenvector can be given by:

$$|\ell>=\sum_{k=0}^{N}\frac{i^k c_k}{\sqrt{[k]!}}\left|\begin{array}{c}N\\(p,q)\end{array},k\right\rangle. \tag{20}$$

In order to find the eigenvalues of L and the coefficients c_k we use the Lanczos algorithm [69], as formulated in [70]. From Eqs (17) and (18) we find

$$L_0|\ell>=\ell|\ell>=\ell\sum_{k=0}^{N}\frac{i^k c_k}{\sqrt{[k]!}}\left|\begin{array}{c}N\\(p,q)\end{array},k\right\rangle=$$
$$=\frac{1}{i}\sum_{k=0}^{N-1}\frac{i^k c_k\sqrt{\Phi^N_{(p,q)}(k+1)}}{\sqrt{[k]!}}\left|\begin{array}{c}N\\(p,q)\end{array},k+1\right\rangle-\frac{1}{i}\sum_{k=1}^{N}\frac{i^k c_k\sqrt{\Phi^N_{(p,q)}(k)}}{\sqrt{[k]!}}\left|\begin{array}{c}N\\(p,q)\end{array},k-1\right\rangle$$

From this equation we find that:

$$c_k=(-1)^k 2^{-k/2}H_k(\ell/\sqrt{2})/\mathcal{N},\quad \mathcal{N}^2=\sum_{n=0}^{N}2^{-n}H_n^2(\ell/\sqrt{2})$$

where the function $H_k(x)$ is a generalization of the "Hermite" polynomials (see also [71,72]), satisfying the recurrence relations:

$$H_{-1}(x)=0,\quad H_0(x)=1,$$
$$H_{k+1}(x)=2xH_k(x)-2\Phi^N_{(p,q)}(k)H_{k-1}(x),$$

and the "angular momentum" eigenvalues ℓ are the roots of the polynomial equation:

$$H_{N+1}(\ell/\sqrt{2})=0. \tag{21}$$

Therefore for a given value of N there are $N+1$ "angular momentum" eigenvalues ℓ, symmetric around zero (i.e. if ℓ is an "angular momentum" eigenvalue, then $-\ell$ is also an "angular momentum" eigenvalue). In the case of the symmetric harmonic oscillator ($m/n=1/1$) these eigenvalues are uniformly distributed and differ by 2. In the general case the "angular momentum" eigenvalues are non-uniformly distributed. For small values of N analytical formulae for the "angular momentum" eigenvalues can be found [71]. Remember that to each value of N correspond $m\cdot n$ energy levels, each with degeneracy $N+1$.

In order to have a formalism corresponding to the one of the isotropic oscillator, let us introduce for every N and (p,q) an ordering of the "angular momentum" eigenvalues

$$\ell_m^{L,(p,q)},\quad \text{where}\quad L=N\quad\text{and}\quad m=-L,-L+2,\ldots,L-2,L,$$

by assuming that:

$$\ell_m^{L,(p,q)}\leq\ell_n^{L,(p,q)}\quad\text{if}\quad m<n,$$

the corresponding eigenstate being given by:

$$|L,m;(p,q)\rangle = \sum_{k=0}^{N} \frac{(-i)^k H_k(\ell_m^{L,(p,q)}/\sqrt{2})}{\mathcal{N}\sqrt{2^{k/2}[k]!}} \left| \begin{matrix} N \\ (p,q) \end{matrix} , k \right\rangle . \tag{22}$$

The above vector elements constitute the analogue corresponding to the basis of "spherical harmonic" functions of the usual oscillator.

6.4. Examples

For illustrative purposes, let us discuss a couple of examples in more detail.

i) In the case $m = 1$, $n = 1$ the only (p,q) value allowed is $(1,1)$. In the Cartesian notation $|n_x n_y>$ the lowest energy corresponds to the state $|00>$, the next energy level corresponds to the two states $|10>$ and $|01>$, while the next energy corresponds to the three states $|20>$, $|11>$, $|02>$. In the notation used in Eqs (15)-(18) these states can be written as

$$N(p,q) = 0(1,1), \quad E = 1 \quad \rightarrow \quad |00> = \left| \begin{matrix} 0 \\ (1,1) \end{matrix} , 0 \right\rangle ,$$

$$N(p,q) = 1(1,1), \quad E = 2 \quad \rightarrow \quad \begin{cases} |01> = \left| \begin{matrix} 1 \\ (1,1) \end{matrix} , 0 \right\rangle \\ |10> = \left| \begin{matrix} 1 \\ (1,1) \end{matrix} , 1 \right\rangle , \end{cases}$$

$$N(p,q) = 2(1,1), \quad E = 3 \quad \rightarrow \quad \begin{cases} |02> = \left| \begin{matrix} 2 \\ (1,1) \end{matrix} , 0 \right\rangle \\ |11> = \left| \begin{matrix} 2 \\ (1,1) \end{matrix} , 1 \right\rangle \\ |20> = \left| \begin{matrix} 2 \\ (1,1) \end{matrix} , 2 \right\rangle . \end{cases}$$

From this example it is clear that the irreducible representations (irreps) are characterized by the quantum numbers N and (p,q), while k enumerates the degenerate states within each irrep. The lowest irrep, characterized by $N = 0$ and $(p,q) = (1,1)$, has dimension $d = 1$, while the next irrep has $N = 1$, $(p,q) = (1,1)$ and $d = 2$ and the third one $N = 2$, $(p,q) = (1,1)$ and $d = 3$.

Using the "angular momentum" eigenvalues defined by Eqs (21) and (22) we find:

$$E = 1 \quad \rightarrow \quad |0,0;(1,1)\rangle = |0,0>, \quad \leftarrow \quad \ell_0^{0,(1,1)} = 0,$$

$$E = 2 \quad \rightarrow \quad \begin{cases} |1,-1;(1,1)\rangle = \frac{1}{\sqrt{2}}(|01> + i|1,0>) & \leftarrow \quad \ell_{(-1)}^{1,(1,1)} = -1 \\ |1,+1;(1,1)\rangle = \frac{1}{\sqrt{2}}(|01> - i|1,0>) & \leftarrow \quad \ell_{(+1)}^{1,(1,1)} = 1, \end{cases}$$

$$E=3 \quad \rightarrow \quad \begin{cases} |2,-2;(1,1)\rangle = \frac{1}{2}|0,2> + \frac{i}{\sqrt{2}}|1,1> - \frac{1}{2}|2,0> & \leftarrow \quad \ell^{2,(1,1)}_{(-2)} = -2 \\ |2,0;(1,1)\rangle = \frac{1}{\sqrt{2}}|0,2> + \frac{1}{\sqrt{2}}|2,0> & \leftarrow \quad \ell^{2,(1,1)}_{(0)} = 0 \\ |2,+2;(1,1)\rangle = \frac{1}{2}|0,2> - \frac{i}{\sqrt{2}}|1,1> - \frac{1}{2}|2,0> & \leftarrow \quad \ell^{2,(1,1)}_{(+2)} = +2. \end{cases}$$

We see therefore that the angular momentum eigenvalues l can be used, instead of k, for enumerating the degenerate states within each irrep.

ii) In the case $m = 1$, $n = 2$ the allowed values of (p,q) are $(1,1)$ and $(1,2)$. The lowest irrep is characterized by $N = 0$, $(p,q) = (1,1)$, has dimension $d = 1$ and contains the state $|n_x, n_y> = |00>$, the next irrep is characterized by $N = 0$, $(p,q) = (1,2)$, has $d = 1$ and contains the state $|01>$, the third irrep has $N = 1$, $(p,q) = (1,1)$, $d = 2$ and contains the states $|10>$ and $|02>$, the fourth irrep has $N = 1$, $(p,q) = (1,2)$, $d = 2$ and contains the states $|11>$ and $|03>$, the fifth irrep has $N = 2$, $(p,q) = (1,1)$, $d = 3$ and contains the states $|20>$, $|12>$ and $|04>$, the sixth irrep has $N = 2$, $(p,q) = (1,2)$, $d = 3$ and contains the states $|21>$, $|13>$ and $|05>$. The states are listed in both notations below:

$$E=\frac{3}{4} \quad \rightarrow \quad |00> = \left| \begin{matrix} 0 \\ (1,1) \end{matrix}, 0 \right\rangle, \qquad E=\frac{5}{4} \quad \rightarrow \quad |01> = \left| \begin{matrix} 0 \\ (1,2) \end{matrix}, 0 \right\rangle,$$

$$E=\frac{7}{4} \quad \rightarrow \quad \begin{cases} |02> = \left| \begin{matrix} 1 \\ (1,1) \end{matrix}, 0 \right\rangle \\ |10> = \left| \begin{matrix} 1 \\ (1,1) \end{matrix}, 1 \right\rangle, \end{cases} \qquad E=\frac{9}{4} \quad \rightarrow \quad \begin{cases} |03> = \left| \begin{matrix} 1 \\ (1,2) \end{matrix}, 0 \right\rangle \\ |11> = \left| \begin{matrix} 1 \\ (1,2) \end{matrix}, 1 \right\rangle, \end{cases}$$

$$E=\frac{11}{4} \rightarrow \begin{cases} |04> = \left| \begin{matrix} 2 \\ (1,1) \end{matrix}, 0 \right\rangle \\ |12> = \left| \begin{matrix} 2 \\ (1,1) \end{matrix}, 1 \right\rangle \\ |20> = \left| \begin{matrix} 2 \\ (1,1) \end{matrix}, 2 \right\rangle, \end{cases} \qquad E=\frac{13}{4} \rightarrow \begin{cases} |05> = \left| \begin{matrix} 2 \\ (1,2) \end{matrix}, 0 \right\rangle \\ |13> = \left| \begin{matrix} 2 \\ (1,2) \end{matrix}, 1 \right\rangle \\ |21> = \left| \begin{matrix} 2 \\ (1,2) \end{matrix}, 2 \right\rangle. \end{cases}$$

Using the "angular momentum" eigenvalues defined by Eqs (21) and (22) we find:

$$E=\frac{3}{4} \quad \rightarrow \quad |0,0;(1,1)\rangle = |0,0>, \quad \leftarrow \quad \ell^{0,(1,1)}_{0} = 0,$$

$$E=\frac{5}{4} \quad \rightarrow \quad |0,0;(1,2)\rangle = |0,1>, \quad \leftarrow \quad \ell^{0,(1,2)}_{0} = 0,$$

$$E=\frac{7}{4} \quad \rightarrow \quad \begin{cases} |1,-1;(1,1)\rangle = \frac{1}{\sqrt{2}}(|0,2> + i|1,0>) & \leftarrow \quad \ell^{1,(1,1)}_{(-1)} = -\frac{1}{\sqrt{2}} \\ |1,+1;(1,1)\rangle = \frac{1}{\sqrt{2}}(|0,2> - i|1,0>) & \leftarrow \quad \ell^{1,(1,1)}_{(+1)} = \frac{1}{\sqrt{2}}, \end{cases}$$

$$E=\frac{9}{4} \quad \rightarrow \quad \begin{cases} |1,-1;(1,2)\rangle = \frac{1}{\sqrt{2}}(|0,3> + i|1,1>) & \leftarrow \quad \ell^{1,(1,2)}_{(-1)} = -\sqrt{\frac{3}{2}} \\ |1,+1;(1,2)\rangle = \frac{1}{\sqrt{2}}(|0,3> - i|1,1>) & \leftarrow \quad \ell^{1,(1,2)}_{(+1)} = \sqrt{\frac{3}{2}}, \end{cases}$$

$$E=\frac{11}{4}\rightarrow\begin{cases}|2,-2;(1,1)\rangle=\sqrt{\frac{3}{8}}|0,4>+\frac{i}{\sqrt{2}}|1,2>-\frac{1}{\sqrt{8}}|2,0> & \leftarrow \ell^{2,(1,1)}_{(-2)}=-2\\ |2,0;(1,1)\rangle=\frac{1}{2}|0,4>+\frac{\sqrt{3}}{2}|2,0> & \leftarrow \ell^{2,(1,1)}_{(0)}=0\\ |2,+2;(1,1)\rangle=\sqrt{\frac{3}{8}}|0,4>-\frac{i}{\sqrt{2}}|1,2>-\frac{1}{\sqrt{8}}|2,0> & \leftarrow \ell^{2,(1,1)}_{(+2)}=+2,\end{cases}$$

$$E=\frac{13}{4}\rightarrow\begin{cases}|2,-2;(1,2)\rangle=\frac{\sqrt{5}}{4}|0,5>+\frac{i}{\sqrt{2}}|1,3>-\frac{\sqrt{3}}{4}|2,1> & \leftarrow \ell^{2,(1,2)}_{(-2)}=-\sqrt{8}\\ |2,0;(1,2)\rangle=\sqrt{\frac{3}{8}}|0,5>+\sqrt{\frac{3}{8}}|2,1> & \leftarrow \ell^{2,(1,2)}_{(0)}=0\\ |2,+2;(1,2)\rangle=\frac{\sqrt{5}}{4}|0,5>-\frac{i}{\sqrt{2}}|1,3>-\frac{\sqrt{3}}{4}|2,1> & \leftarrow \ell^{2,(1,2)}_{(+2)}=\sqrt{8}.\end{cases}$$

The following remarks can now be made:

i) In the basis described by Eqs (15)-(18) it is a trivial matter to distinguish the states belonging to the same irrep for any $m:n$ ratio, while in the Cartesian basis this is true only in the 1:1 case.

ii) In the 1:2 case we see that the irreps have degeneracies 1, 1, 2, 2, 3, 3, 4, 4, ..., i.e. "two copies" of the u(2) degeneracies 1, 2, 3, 4, ... are obtained.

iii) In the 1:3 cases the degeneracies are 1, 1, 1, 2, 2, 2, 3, 3, 3, ..., i.e. "three copies" of the u(2) degeneracies are obtained.

iv) It can be easily seen that the 1:n case corresponds to "n copies" of the u(2) degeneracies.

v) Cases with both m, n different from unity show more complicated degeneracy patterns, also correctly reproduced by the above formalism. In the 2:3 case, for example, the degeneracy pattern is 1, 1, 1, 1, 1, 2, 1, 2, 2, 2, 2, 3, 2, 3, 3, ...

vi) The only requirement for each energy eigenvalue to correspond to one irrep of the algebra is that m and n have to be mutually prime numbers. If m and n possess a common divisor other than 1, then some energy eigenvalues will correspond to sums of irreps, i.e. to reducible representations.

vii) The difference between the formalism used here and the one used in [54,56,57,60] is that in the latter case for given m and n appropriate operators have to be introduced separately for each set of (p,q) values, while in the present case only one set of operators is introduced.

6.5. Connection to $W_3^{(2)}$

For the special case $m=1$, $n=2$ it should be noticed that the deformed algebra received here coincides with the finite W algebra $W_3^{(2)}$ [73–76]. The commutation relations of the $W_3^{(2)}$ algebra are

$$[H_W,E_W]=2E_W,\qquad [H_W,F_W]=-2F_W,\qquad [E_W,F_W]=H_W^2+C_W,$$

$$[C_W,E_W]=[C_W,F_W]=[C_W,H_W]=0,$$

while in the $m=1$, $n=2$ case one has the relations

$$[\mathcal{N},\mathcal{A}^\dagger]=\mathcal{A}^\dagger,\qquad [\mathcal{N},\mathcal{A}]=-\mathcal{A},\qquad [\mathcal{A},\mathcal{A}^\dagger]=3S_0^2-\frac{H^2}{4}-HS_0+\frac{3}{16},$$

$$[H, \mathcal{A}^\dagger] = [H, \mathcal{A}] = [H, S_0] = 0,$$

with $S_0 = \mathcal{N} + u$ (where u a constant). It is easy to see that the two sets of commutation relations are equivalent by making the identifications

$$F_W = \sigma \mathcal{A}^\dagger, \qquad E_W = \rho \mathcal{A}, \qquad H_W = -2S_0 + kH, \qquad C_W = f(H),$$

with

$$\rho\sigma = \frac{4}{3}, \qquad k = \frac{1}{3}, \qquad f(H) = -\frac{4}{9}H^2 + \frac{1}{4}.$$

6.6. Summary

In conclusion, the two-dimensional anisotropic quantum harmonic oscillator with rational ratio of frequencies equal to m/n, is described dynamically by a deformed version of the u(2) Lie algebra, the order of this algebra being $m+n-1$. The representation modules of this algebra can be generated by using the deformed oscillator algebra. The energy eigenvalues are calculated by the requirement of the existence of finite dimensional representation modules. An "angular momentum" operator useful for labelling degenerate states has also been constructed. The algebras obtained in the special cases with $1 : n$ ratios are shown to correspond to generalized parafermionic oscillators. In the special case of $m : n = 1 : 2$ the resulting algebra has been identified as the finite W algebra $W_3^{(2)}$.

The extension of the present method to the three-dimensional anisotropic quantum harmonic oscillator is already receiving attention, since it is of clear interest in the study of the symmetries underlying the structure of superdeformed and hyperdeformed nuclei.

7. References

1. V. G. Drinfeld, in *Proceedings of the International Congress of Mathematicians*, ed. A. M. Gleason (American Mathematical Society, Providence, RI, 1986), p. 798.
2. M. Jimbo, *Lett. Math. Phys.* **11** (1986) 247.
3. L. C. Biedenharn, *J. Phys. A* **22** (1989) L873.
4. A. J. Macfarlane, *J. Phys. A* **22** (1989) 4581.
5. C. P. Sun and H. C. Fu, *J. Phys. A* **22** (1989) L983.
6. M. Arik and D. D. Coon, *J. Math. Phys.* **17** (1976) 524.
7. V. V. Kuryshkin, *Annales de la Fondation Louis de Broglie* **5** (1980) 111.
8. C. Daskaloyannis, *J. Phys. A* **24** (1991) L789.
9. M. Arik, E. Demircan, T. Turgut, L. Ekinci, and M. Mungan, *Z. Phys. C* **55** (1992) 89.
10. T. Brzeziński, I. L. Egusquiza, and A. J. Macfarlane, *Phys. Lett. B* **311** (1993) 202.

11. D. Bonatsos and C. Daskaloyannis, *Phys. Lett. B* **307** (1993) 100.
12. S. Meljanac, M. Milekovic, and S. Pallua, *Phys. Lett. B* **328** (1994) 55.
13. D. Bonatsos, C. Daskaloyannis, and P. Kolokotronis, *J. Phys. A* **26** (1993) L871.
14. C. Delbecq and C. Quesne, *J. Phys. A* **26** (1993) L127.
15. C. Delbecq and C. Quesne, *Phys. Lett. B* **300** (1993) 227.
16. C. Delbecq and C. Quesne, *Mod. Phys. Lett. A* **8** (1993) 961.
17. A. Ludu and R. K. Gupta, *J. Math. Phys.* **34** (1993) 5367.
18. C. P. Sun and W. Li, *Commun. Theor. Phys.* **19** (1993) 191.
19. F. Pan, *J. Math. Phys.* **35** (1994) 5065.
20. P. P. Raychev, R. P. Roussev and Yu. F. Smirnov, *J. Phys. G* **16** (1990) L137.
21. D. Bonatsos, E. N. Argyres, S. B. Drenska, P. P. Raychev, R. P. Roussev and Yu. F. Smirnov, *Phys. Lett. B* **251** (1990) 477.
22. D. Bonatsos, S. B. Drenska, P. P. Raychev, R. P. Roussev and Yu. F. Smirnov, *J. Phys. G* **17** (1991) L67.
23. D. Bonatsos, P. P. Raychev, R. P. Roussev and Yu. F. Smirnov, *Chem. Phys. Lett.* **175** (1990) 300.
24. D. Bonatsos, A. Faessler, P. P. Raychev, R. P. Roussev and Yu. F. Smirnov, *J. Phys. A* **25** (1992) 3275.
25. N. Minkov, R. P. Roussev and P. P. Raychev, *J. Phys. G* **20** (1994) L67.
26. D. Bonatsos, C. Daskaloyannis, A. Faessler, P. P. Raychev and R. P. Roussev, *Phys. Rev. C* **50** (1994) 497.
27. D. Bonatsos, *J. Phys. A* **25** (1992) L101.
28. D. Bonatsos and C. Daskaloyannis, *Phys. Lett. B* **278** (1992) 1.
29. D. Bonatsos, C. Daskaloyannis and A. Faessler, *J. Phys. A* **27** (1994) 1299.
30. D. Bonatsos, A. Faessler, P. P. Raychev, R. P. Roussev and Yu. F. Smirnov, *J. Phys. A* **25** (1992) L267.
31. D. P. Menezes, S. S. Avancini and C. Providência, *J. Phys. A* **25** (1992) 6317.
32. D. Bonatsos, L. Brito, D. P. Menezes, C. Providência and J. da Providência, *J. Phys. A* **26** (1993) 895, 5185.
33. C. Providência, L. Brito, J. da Providência, D. Bonatsos and D. P. Menezes, *J. Phys. G* **20** (1994) 1209.
34. B. Mottelson, *Nucl. Phys. A* **522** 1c.
35. W. D. M. Rae, *Int. J. Mod. Phys. A* **3** (1988) 1343.
36. P. J. Nolan and P. J. Twin, *Ann. Rev. Nucl. Part. Sci.* **38** (1988) 533.
37. R. V. F. Janssens and T. L. Khoo, *Ann. Rev. Nucl. Part. Sci.* **41** (1991) 321.
38. W. D. M. Rae and J. Zhang, *Mod. Phys. Lett. A* **9** (1994) 599.
39. J. Zhang, W. D. M. Rae and A. C. Merchant, *Nucl. Phys. A* **575** (1994) 61.
40. D. M. Brink, in *Proc. Int. School of Physics, Enrico Fermi Course XXXVI, Varenna 1966*, ed. C. Bloch (Academic Press, New York, 1966), p. 247.
41. T. P. Martin, T. Bergmann, H. Göhlich and T. Lange, *Z. Phys. D* **19** (1991) 25.
42. A. Bulgac and C. Lewenkopf, *Phys. Rev. Lett.* **71** (1993) 4130.

43. F. Iachello and A. Arima, *The Interacting Boson Model* (Cambridge University Press, Cambridge, 1987).
44. D. Bonatsos, *Interacting Boson Models of Nuclear Structure* (Clarendon, Oxford, 1988).
45. D. Bonatsos and A. Klein, *Phys. Rev. C* **29** (1984) 1879.
46. P. Holmberg and P. Lipas, *Nucl. Phys. A* **117** (1968) 552.
47. R. N. Alvarez, D. Bonatsos and Yu. F. Smirnov, *Phys. Rev. A* **50** (1994) 1088.
48. J. M. Jauch and E. L. Hill, *Phys. Rev.* **57** (1940) 641.
49. Yu. N. Demkov, *Soviet Phys. JETP* **17** (1963) 1349.
50. G. Contopoulos, *Z. Astrophys.* **49** (1960) 273; *Astrophys. J.* **138** (1963) 1297.
51. A. Cisneros and H. V. McIntosh, *J. Math. Phys.* **11** (1970) 870.
52. O. Castaños R. and López-Peña, *J. Phys. A* **25** (1992) 6685.
53. A. Ghosh, A. Kundu and P. Mitra, Saha Institute preprint SINP/TNP/92-5 (1992).
54. F. Duimio and G. Zambotti, *Nuovo Cimento* **43** (1966) 1203.
55. G. Maiella, *Nuovo Cimento* **52** (1967) 1004.
56. I. Vendramin, *Nuovo Cimento* **54** (1968) 190.
57. G. Maiella and G. Vilasi, *Lettere Nuovo Cimento* **1** (1969) 57.
58. G. Rosensteel and J. P. Draayer, *J. Phys. A* **22** (1989) 1323.
59. D. Bhaumik, A. Chatterjee and B. Dutta-Roy, *J. Phys. A* **27** (1994) 1401.
60. W. Nazarewicz and J. Dobaczewski, *Phys. Rev. Lett.* **68** (1992) 154.
61. J. Hietarinta, *Phys. Rep.* **147** (1987) 87.
62. C. R. Holt, *J. Math. Phys.* **23** (1982) 1037.
63. C. P. Boyer and K. B. Wolf, *J. Math. Phys.* **16** (1975) 2215.
64. A. S. Fokas and P. A. Lagerstrom, *J. Math. Anal. Appl.* **74** (1980) 325.
65. D. Bonatsos, C. Daskaloyannis and K. Kokkotas, *Phys. Rev. A* **48** (1993) R3407; **50** (1994) 3700.
66. C. Quesne, *Phys. Lett. A* **193** (1994) 245.
67. P. W. Higgs, *J. Phys. A* **12** (1979) 309.
68. H. I. Leemon, *J. Phys. A* **12** (1979) 489.
69. C. Lanczos, *J. Res. Natl. Bur. Stand.* **45** (1950) 255.
70. R. Floreanini, J. LeTourneux and L. Vinet, *Ann. Phys.* **226** (1993) 331.
71. D. Bonatsos, C. Daskaloyannis, D. Ellinas and A. Faessler, *Phys. Lett. B* **331** (1994) 150.
72. A. A. Kehagias and G. Zoupanos, *Z. Phys. C* **62** (1994) 121.
73. T. Tjin, *Phys. Lett. B* **292** (1992) 60.
74. J. de Boer and T. Tjin, *Commun. Math. Phys.* **158** (1993) 485.
75. T. Tjin, Ph.D. thesis, U. Amsterdam (1993).
76. J. de Boer, F. Harmsze and T. Tjin, SUNY at Stony Brook preprint ITP-SB-95-07, hep-th 9503161.

NUCLEAR β- AND γ- COLLECTIVE BANDS IN THE $SU_q(2)$ ROTATOR MODEL

N. MINKOV, S. B. DRENSKA, P. P. RAYCHEV, R. P. ROUSSEV
Institute for Nuclear Research and Nuclear Energy
72 Tzarigradsko Chaussee Blvd., 1784 Sofia, Bulgaria

D. BONATSOS
European Centre for Theoretical Studies in Nuclear Physics and Related Areas (ECT)*
Strada delle Tabarelle 286, I-38050 Villazzano (Trento), Italy

ABSTRACT

The $SU_q(2)$ rotator model is used for describing the β_1- and γ_1-bands of even-even rare earth and actinide collective nuclei. Good results are obtained in nuclei with valence pair number $N > 10$. It is shown that in the excited bands the violation of the exact SU(2) symmetry is generally stronger than in the ground state bands, indicating the presence of a nonadiabatic perturbation caused by the excited vibrational degrees of freedom. The physical content of the parameter q is discussed. Predictions of the $SU_q(2)$ model for B(E2) intraband transitions in excited bands are presented and the need for specific experimental data is pointed out.

1. Introduction

The quantum algebra $SU_q(2)$[1,2] is a nonlinear generalization (having the structure of a Hopf algebra[3]) of the corresponding Lie algebra SU(2) to which it reduces when the deformation parameter q is set equal to one. It has been found that the $SU_q(2)$ algebra can be used for describing the deviations of rotational spectra of collective nuclei[4-7] and diatomic molecules[8-10] from the rigid rotator symmetry of SU(2), the deformation parameter q being related[5] to the softness parameter of the Variable Moment of Inertia (VMI) model[11]. Furthermore the implications of the $SU_q(2)$ symmetry on B(E2) transition probabilities within the ground state bands (gsb) of deformed nuclei have been considered[12], indicating that the B(E2) values do not saturate but continue to increase with increasing angular momentum I, a result also obtained in the framework of other models[13,14].

So far the $SU_q(2)$ symmetry has been tested only in relation to levels and B(E2) transition probabilities of the ground state band of deformed nuclei. It is the purpose of the present work to examine the applicability of the $SU_q(2)$ symmetry to excited collective bands, the β_1- and the γ_1-band in particular. Such an investigation is naturally motivated by the question: "It is already known that the quantum algebra $SU_q(2)$ is appropriate to characterize nuclear rotations built on the ground state, but what is the q-rotator in the case of a given excited band where besides

the rotational motion there is a presence of other collective (vibrational) degrees of freedom?" In this respect it is interesting to study whether the q-deformation "detects" the presence of the additional nonrotational degrees of freedom. As will be seen below, the study of the energy levels of the excited bands illuminates the above question and leads to interesting conclusions about the physical content of the deformation parameter q, while the study of the intraband B(E2) transition probabilities emphasizes the need for specific experimental data for testing the deviations from the pure SU(2) behavior appearing there.

2. q-rotator definition

The Hamiltonian of the q-rotator model is proportional to the second order Casimir operator $C_2[\mathrm{SU}_q(2)]$ of the quantum algebra $\mathrm{SU}_q(2)$[4]:

$$H = \frac{1}{2\theta} C_2[SU_q(2)] + E_0, \tag{1}$$

where θ is the moment of inertia parameter and E_0 is the bandhead energy (for the gsb $E_0 = 0$). The corresponding energy eigenvalues are:

$$E_I = \frac{1}{2\theta}[I][I+1] + E_0, \tag{2}$$

where I is the angular momentum and the square brackets indicate q-numbers, according to the following definition:

$$[x] = \frac{q^x - q^{-x}}{q - q^{-1}}. \tag{3}$$

In the case of q being a phase ($q = e^{i\tau}$ with τ a real parameter), eq. (2) gives:

$$E_I = \frac{1}{2\theta} \frac{\sin(\tau I)\sin(\tau(I+1))}{\sin^2(\tau)} + E_0 \ . \tag{4}$$

In the limit $\tau \to 0$, the first term in eq. (4) gives the spectrum of the usual SU(2) rigid rotator[15]. It has been proved[5] that the deformation parameter τ is connected to the softness parameter of the VMI model, thus indicating that q-deformation is an alternative way of taking into account nuclear stretching.

3. $\mathrm{SU}_q(2)$ symmetry in exited collective bands

In the case of excited bands one needs an appropriately formulated q-rotator definition which should take into account the circumstance that the rotational energy levels are built on a given excited vibrational state[16]. For this purpose it is convenient to use eq. (4) in the form:

$$\overline{E_I} = E_I - E_0(I_{bh}) = \frac{1}{2\theta} \frac{\sin(\tau I)\sin(\tau(I+1))}{\sin^2(\tau)} \tag{5}$$

with $I > I_{bh}$, where it is supposed that the energy scale of collective rotations has its origin in the bandhead energy $E_0(I_{bh})$, and I_{bh} is the bandhead angular momentum, which is 0 for β-bands and 2 for γ-bands. Thus, after subtracting the bandhead energy we determine the rotational parts of the bandlevels. However, it is important to remark that the so obtained energies are still perturbed by the vibrational motion as far as even in the well deformed nuclei the collective rotations are not separated completely from the vibrational degrees of freedom[16]. Taking into account this nonadiabatic perturbation we suppose that in the excited bands the q-deformations of the SU(2) symmetry should be generally larger in magnitude than the corresponding ones obtained in the gsb's. Hence one could expect that the quantum algebraic parameter τ will be able to indicate the presence of excited vibrational modes. Below it will be seen that the calculations essentially support this supposition.

So, the theoretical predictions (eq. 5) are compared to the experimental quantities $\overline{E_I^{exp}} = E_I^{exp} - E_0(I_{bh})$. For obtaining the fits an autoregularized iterational method of the Gauss-Newton type[17] has been used, the quality of the fits being measured by

$$\sigma = \sqrt{\frac{1}{n} \sum_{I=I_{min}}^{I_{max}} (\overline{E_I^{exp}} - \overline{E_I^{th}})^2}, \tag{6}$$

where n is the number of levels used in the fit and $I_{min} = 2$ for β-bands, while $I_{min} = 3$ for γ-bands. We have included in the fitting procedure rare earth and actinide nuclei in the rotational region (with $3 \leq R_4^g = E_4/E_2 \leq 10/3$) for which at least 5 levels of the β_1- or γ_1-band are known[18,19]. The results for the β_1- and/or γ_1-bands of 28 rare earths and 3 actinides, along with the results for the corresponding gsb are shown in Table 1.

The following comments can now be made:

i) The parameters τ_β and τ_γ generally obtain values in the region 0.03–0.07, close to the typical τ_g values of 0.03–0.06 (see also [4-7]). Nevertheless it is clearly seen that for almost all considered nuclei, the τ values obtained in the excited bands lie above the corresponding gsb values (see also Fig. 1). It turns out that in the excited bands the quantum algebraic parameter τ, which characterizes the deviation of the spectrum from the pure SU(2) symmetry of the rigid rotator[20], indicates the presence of additional nonrotational degrees of freedom. Moreover, some $\tau_\gamma \geq 0.1$ values occur for nuclei with valence pair number N relatively small (10–13), indicating that the rotational character of the γ_1-band is not yet well developed in this N region. So, the sensitivity of the $SU_q(2)$ rotator description to the structure of the different types of bands is obvious.

Table 1. Parameters of the fits of β_1- and γ_1-bands in the rare earth and actinide regions using eq. (5). The deformation parameters τ_β and τ_γ, the quality factors σ_β and σ_γ (in keV) (eq. 6) accompanied by the numbers n_β and n_γ of the experimental levels used in the fit, and the inertial parameters $1/(2\theta_\beta)$ and $1/(2\theta_\gamma)$ (in keV^{-1}) for the β_1- and γ_1-bands respectively are shown. The corresponding deformation parameters τ_g of the ground state band and the valence pair numbers N are also given. The experimental data are taken from [18,19].

Nucleus	N	τ_g	τ_β	τ_γ	$\sigma_\beta[n_\beta]$	$\frac{1}{2\theta_\beta}$	$\sigma_\gamma[n_\gamma]$	$\frac{1}{2\theta_\gamma}$
^{152}Sm	10	0.0622	0.0695	0.1030	22.57[8]	15.39	15.13[8]	21.63
^{154}Sm	11	0.0500		0.1306			1.14[5]	18.67
^{156}Gd	12	0.0521	0.0641	0.0668	5.20[6]	12.36	11.29[10]	14.92
^{158}Gd	13	0.0419		0.1345			4.96[5]	14.87
^{160}Gd	14	0.0392		0.0507			0.31[5]	11.68
^{156}Dy	12	0.0733		0.0727			17.72[11]	18.66
^{160}Dy	14	0.0489		0.0715			0.71[5]	14.24
^{162}Dy	15	0.0368	0.0456	0.0339	7.76[8]	8.56	19.01[13]	12.07
^{164}Dy	16	0.0391		0.0672			3.40[5]	11.70
^{160}Er	12	0.0839		0.1158			4.76[5]	22.53
^{162}Er	13	0.0538		0.0605			12.19[11]	16.39
^{164}Er	14	0.0463		0.0531			19.94[13]	14.49
^{166}Er	15	0.0461	0.0932	0.0520	18.10[7]	12.47	5.97[13]	12.59
^{168}Er	16	0.0353	0.0400	0.0321	0.50[5]	9.79	0.07[7]	12.50
^{170}Er	17	0.0348		0.0438			10.11[6]	13.15
^{166}Yb	13	0.0610		0.0743			8.84[6]	17.18
^{168}Yb	14	0.0499		0.0674			2.20[6]	13.91
^{170}Yb	15	0.0428	0.0577	0.0342	6.49[7]	11.08	11.57[8]	13.13
^{172}Yb	16	0.0327	0.0584		7.75[8]	12.12		
^{172}Hf	14	0.0503		0.0687			9.94[10]	17.55
^{174}Hf	15	0.0496	0.0439		5.07[5]	11.76		
^{176}Hf	16	0.0449	0.0632	0.0673	3.79[6]	12.05	17.17[7]	16.26
^{178}Hf	15	0.0470		0.0867			1.90[5]	16.22
^{180}Hf	14	0.0357		0.0434			2.24[6]	15.15
^{178}W	15	0.0537	0.0545		6.23[8]	13.61		
^{180}W	14	0.0591		0.0883			8.20[7]	18.89
^{182}W	13	0.0607		0.1140			9.70[5]	18.93
^{184}W	12	0.0476		0.0681			1.10[5]	17.22
^{232}Th	12	0.0314	0.0378	0.0424	1.50[8]	7.07	4.80[13]	7.44
^{232}U	12	0.0364	0.0393		0.34[6]	7.15		
^{234}U	13	0.0295	0.0363	0.0514	0.45[5]	6.92	0.29[6]	7.12

ii) It is known[20] that for the ground state bands of the rare earths and the actinides the parameter τ_g decreases with increasing valence pair number N (or, equivalently, with increasing neutron valence pair number N_ν in a given group of isotopes) approximately as

$$\tau = \sqrt{3}(8N^2 + 22N - 15)^{-\frac{1}{2}} \ , \tag{7}$$

indicating that τ_g, as a measure of deviation from the rigid rotator symmetry, indirectly reflects the nuclear shell structure. We remark that the same trend is seen for the τ_γ values, especially in the case of the Er isotopes (shown in Fig. 1) and the Yb isotopes. In the excited bands it is difficult to derive an analytical relation between τ and N, but Fig. 1 clearly shows that such a correlation actually exists. We thus conclude that in the γ-bands the $SU_q(2)$ symmetry quite well characterizes the deterioration of the nuclear rotational properties away from the midshells.

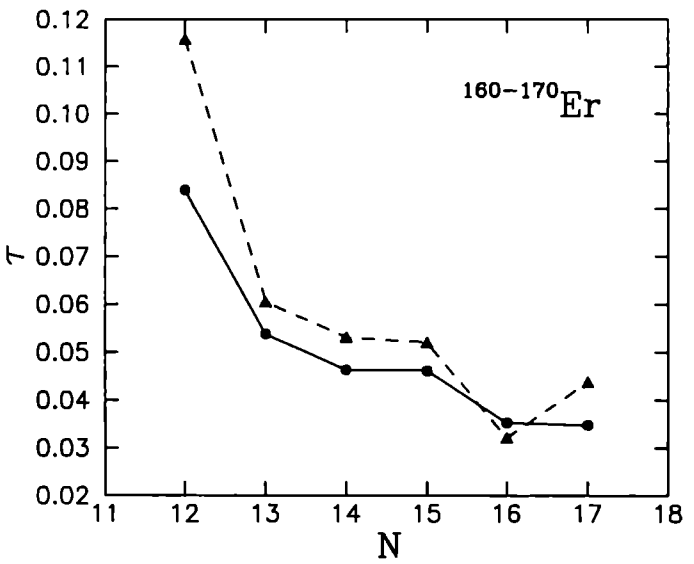

Fig. 1. Deformation parameters τ_g (circles, connected by solid lines) and τ_γ (triangles, connected by dashed lines) for ground state bands and γ_1-bands respectively of Er isotopes (taken from Table 1) are plotted versus the valence pair number N.

iii) we remark that the above behavior of the parameter τ_γ allows one to make some additional conclusions. It has been shown[21] that in the gsb's the correlation between τ and N given approximately by eq. (7) allows one to connect τ with the axial deformation parameter β:

$$\beta \sim \left(B/[3(2B + 60.25)^{1/2} - 22.5]\right)^{1/2} \ , \tag{8}$$

where $B = 1/(1 - \tau \cot \tau)$. Thus it has been obtained that β decreases with the increase of τ and that τ could be considered as a relevant measure of decrease in deformation as well as in rotational collectivity of the nuclei in a given rotational region. Though in the excited bands we have not such analytical estimates, Fig. 1 implies that in the γ-bands the decrease of τ_γ towards the midshells, could be associated similarly with the corresponding increase of nuclear deformation and rotational collectivity. In this case the relevance of the quantum algebraic approach is obvious. The data on β-bands are not enough for drawing any conclusions about the τ_β values.

4. B_q(E2) transitions in the exited bands

We now turn to the study of the B(E2) transition probabilities within β- or γ-bands. In the usual case the B(E2) values are given by

$$B(E2; I_i \to I_f) = \frac{5}{16\pi} {Q_0}^2 |C^{I_i,2,I_f}_{K,0,K}|^2, \tag{9}$$

where Q_0 is the intrinsic quadrupole moment and $C^{j_1,j_2,j}_{m_1,m_2,m}$ are the Clebsch-Gordan coefficients of the Lie algebra SU(2). In the case of $SU_q(2)$ one should use the q-generalized angular momentum theory[22,23,24], in which the irreducible tensor operators for the quantum algebra $SU_q(2)$[23] as well as the q-generalized version of the Wigner-Eckart theorem[24] are available. The q-deformed versions of the Clebsch-Gordan coefficients needed for the q-generalization of eq. (9),

$$B_q(E2; I_i \to I_f) = \frac{5}{16\pi} {Q_0}^2 |{}_qC^{I_i,2,I_f}_{K,0,K}|^2, \tag{10}$$

are also known[22,23,24]. In the case of intraband transitions with $\Delta I = I_i - I_f = 2$ one needs

$${}_qC^{I+2,2,I}_{K,0,K} = q^{-2K} \left(\frac{[3][4][I+K+1][I+K+2][I-K+2][I-K+1]}{[2][2I+2][2I+3][2I+4][2I+5]} \right)^{\frac{1}{2}}, \tag{11}$$

while in cases with $\Delta I = 1$

$${}_qC^{I+1,2,I}_{K,0,K} = -q^{I-2K+2}([I+K]-q^{2I}[I-K]) \left(\frac{[2][3][I+K+1][I-K+1]}{[2I][2I+2][2I+3][2I+4]} \right)^{\frac{1}{2}} \tag{12}$$

is needed, where the square brackets again indicate q-numbers as defined in eq. (3) with $q = e^{i\tau}$.

Therefore in the case of β-bands ($K = 0$) one finds

$$B_q(E2; I+2 \to I) = \frac{5}{16\pi} {Q_0}^2 \frac{[3][4][I+1]^2[I+2]^2}{[2][2I+2][2I+3][2I+4][2I+5]} . \tag{13}$$

In the case of γ-bands ($K = 2$) for $\Delta I = 2$ transitions one has

$$B_q(E2; I+2 \to I) = \frac{5}{16\pi} {Q_0}^2 \frac{[3][4][I-1][I][I+3][I+4]}{[2][2I+2][2I+3][2I+4][2I+5]} , \qquad (14)$$

while for $\Delta I = 1$ transitions one finds

$$B_q(E2; I+1 \to I) = \frac{5}{16\pi} {Q_0}^2 \left([I+2]^2 + [I-2]^2 - 2\cos(2\tau I)[I-2][I+2]\right)$$
$$\frac{[2][3][I+3][I-1]}{[2I][2I+2][2I+3][2I+4]}. \qquad (15)$$

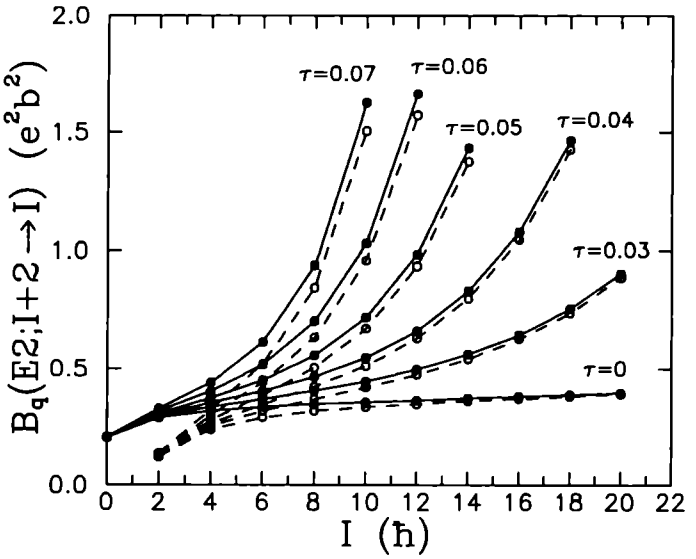

Fig. 2. $B_q(E2; I+2 \to I)$ transition probabilities are plotted as a function of angular momentum I in the cases of β-bands (eq. 13, solid lines) and γ-bands (eq. 14, dashed lines) for some typical values of the deformation parameter τ. The numerical values of $B_q(E2)$ correspond to $\frac{5}{16\pi}Q_0^2 = 1$. The limiting case $\tau = 0$ gives the usual rigid rotator predictions.

On these results the following comments apply:

i) eq. (13), concerning the β-bands, is exactly the same as the one obtained in the case of gsb[4,12]. It has been shown that this equation gives B(E2) values increasing with increasing I, while the corresponding usual SU(2) expression (obtained here for $\tau \to 0$) exhibits saturation with increasing I. This is illustrated in Fig. 2. In the case of gsb's some experimental examples supporting this prediction have been given in [12]. Similar predictions also occur in the framework of other models[13,14]. The existing data for β_1-bands do not suffice for testing this prediction.

ii) eq. (14), concerning $\Delta I = 2$ transitions in γ-bands, gives almost the same behavior as eq. (13), as seen in Fig. 2. It follows that for $\Delta I = 2$ transitions the introduction of q-generalized Clebsch-Gordan coefficients leads to a typical modification of the reduced transition probabilities in all considered bands.

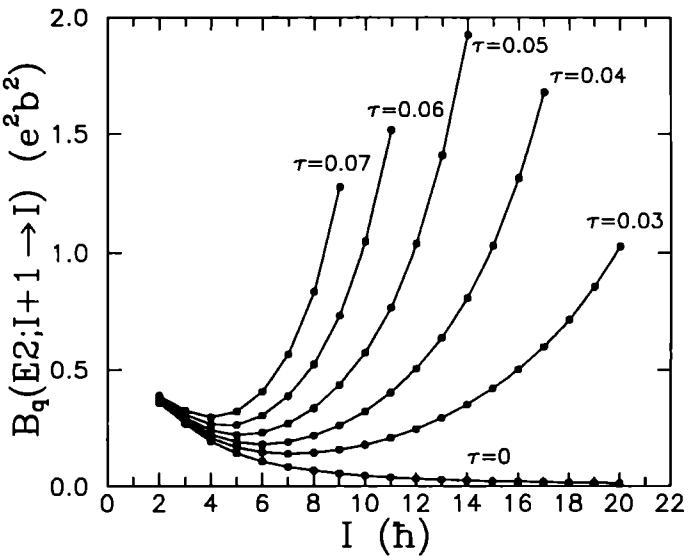

Fig. 3. Same as Fig. 2 but for the case of $B_q(E2; I+1 \rightarrow I)$ transition probabilities in γ-bands.

iii) eq. (15), concerning $\Delta I = 1$ transitions in γ-bands, illustrated in Fig. 3, gives an interesting prediction. For typical τ-values (0.03–0.07) one initially observes a decrease of $B_q(E2; I+1 \rightarrow I)$ with increasing I, but further, after reaching some minimum (for example at $I = 5$ when $\tau = 0.05$), a significant increase of $B_q(E2)$ is observed, while in the rigid rotator limit ($\tau \rightarrow 0$) a continuous decrease down to zero at sufficiently large $I > 12$ is predicted. The available data for $E2$ intraband transitions in the excited bands do not suffice for detailed tests of these predictions, due to the short life times and strong $M1$ mixing observed in these transitions. The need for further experimental data is clear. In particular the observation of any $E2$ transitions with $\Delta I = 1$ at $I > 10 - 12$ in the γ-bands will be useful in testing the predictions of eq. (15).

We now remark that the present investigation outlines the principal limits of the $SU_q(2)$-symmetry approach to the nuclear rotational spectra. It should be emphasized that in the framework of the quantum algebra $SU_q(2)$ as well as in the case of the standard Lie algebra $SU(2)$[25], one is able to provide a consistent description of the physical characteristics of only one given rotational band. This is clearly indicated by the distinctions in the magnitudes of the q-deformation parameter obtained for the different types of bands (see Table 1). It follows that one

should understand the $SU_q(2)$-rotator as a one-band model based on the particular intrinsic state or vibrational mode. Hence the unified description of the different rotational bands including the calculation of the interband transition probabilities is beyond the limits of the quantum algebra $SU_q(2)$. Such an extension could be referred to a model based on the q-deformed algebra $SU_q(3)$ in which the introduction of a bandmixing interaction would be possible. However the realization of such a model is still complicated due to some difficulties in the obtaining of the reduction $SU_q(3) \supset SO_q(3)$ (for example see [26,27]). In this respect the use of the simplest quantum algebra $SU_q(2)$ could be considered as a first approximation in the construction of a more complicated quantum algebraic theory of nuclear collective motion.

5. Conclusion

In conclusion, we have demonstrated the relevance of the $SU_q(2)$ approach beyond the ground state bands, namely in the excited bands of even-even rare earth and actinide nuclei. Good results have been obtained for β_1 and γ_1 bands in nuclei with valence pair number $N > 10$. The quantum algebraic parameter τ fitted in these bands obtains values generally shifted above the corresponding ones in the gsb's. In such a way the q-deformation specifically indicates the presence of a nonadiabatic perturbation caused by the excited vibrational degrees of freedom. The decrease of τ_γ and τ_g with increasing N is in accordance with the interpretation of τ as a measure of deviation from the rigid rotator limit equivalent to the nuclear softness[5,20]. In addition, these correlations (illustrated in Fig. 1) allow one to extend the $SU_q(2)$ symmetry to a wider range of nuclear rotational properties[21]. The predictions of the $SU_q(2)$ rotator model for the $B(E2)$ intraband transition probabilities in the excited bands show modifications in comparison to the SU(2) rigid rotator limit, the experimental data needed for testing these predictions having been identified. It is pointed out that $SU_q(2)$ is a simple one-band model, but it can be considered as the first step in the development of more complicated models based on the q-deformed algebras.

6. References

1. L. C. Biedenharn, *J. Phys.* **A 22** (1989) L873.
2. A. J. Macfarlane, *J. Phys.* **A 22** (1989) 4581.
3. V. G. Drinfeld, in *Proceedings of the International Congress of Mathematicians*, edited by A. M. Gleason (American Mathematical Society, Providence, RI, 1987) p. 798.
4. P. P. Raychev, R. P. Roussev and Yu. F. Smirnov, *J. Phys.* **G 16** (1990) L137.
5. D. Bonatsos, E. N. Argyres, S. B. Drenska, P. P. Raychev, R. P. Roussev and Yu. F. Smirnov, *Phys. Lett.* **B251** (1990) 477.
6. S. Iwao, *Prog. Theor. Phys.* **83** (1990) 363.
7. E. Celeghini, R. Giachetti, E. Sorace and M. Tarlini, *Phys. Lett.* **B280** (1992) 180.

8. D. Bonatsos, P. P. Raychev, R. P. Roussev and Yu. F. Smirnov, *Chem. Phys. Lett.* **175** (1990) 300.

9. Z. Chang and H. Yan, *Phys. Lett.* **A154** (1991) 254.

10. J. G. Esteve, C. Tejel and B. E. Villaroya, *J. Chem. Phys.* **96** (1992) 5614.

11. M. A. J. Mariscotti, G. Scharff-Goldhaber and B. Buck, *Phys. Rev.* **178** (1969) 1864.

12. D. Bonatsos, A. Faessler, P. P. Raychev, R. P. Roussev and Yu. F. Smirnov, *J. Phys.* **A 25** (1992) 3275.

13. M. Mukerjee, *Phys. Lett.* **B251** (1990) 229.

14. J. L. Pin, J. Q. Chen, C. L. Wu and D. H. Feng, *Phys. Rev.* **C 43** (1991) 2224.

15. A. Bohr and B. R. Mottelson, *Nuclear Structure* Vol. II (Benjamin, New York, 1975).

16. J. Eisenberg and W. Greiner, *Nuclear Theory* Vol. I (North-Holland, Amsterdam, 1970).

17. L. Aleksandrov, *Math. Phys. Comput. Math.* **11** (1971) 36.

18. M. Sakai, *At. Data Nucl. Data Tables* **31** (1984) 399.

19. V. M. Belenki and E. P. Grigoriev, *Structure of Even Nuclei* (Energoatomizdat, Moscow, 1987).

20. N. Minkov, R. P. Roussev and P. P. Raychev, *J. Phys.* **G 20** (1994) L67.

21. N. Minkov, P. P. Raychev and R. P. Roussev, *J. Phys.* **G 21** (1995) 557.

22. Yu. F. Smirnov, V. N. Tolstoy and Yu. I. Kharitonov, *Yad. Fiz.* **53** (1991) 959 [*Sov. J. Nucl. Phys.* **53** (1991) 593]; *Yad. Fiz.* **53** (1991) 1746 [*Sov. J. Nucl. Phys.* **53** (1991) 1068].

23. F. Pan, *J. Phys.* **A 24** (1991) L803.

24. A. U. Klimyk, *J. Phys.* **A 25** (1992) 2919.

25. E. Chacón, M. Moshinsky and V. Vanagas, *J. Math. Phys.* **22** (1981) 605.

26. C. Quesne, *Phys. Lett.* **B304** (1993) 81.

27. J. Van der Jeugt, *J. Math. Phys.* **34** (1993) 1799.

10. SHORT COMMUNICATIONS

LIST OF SHORT COMMUNICATIONS

I. Silisteanu (Bucharest): *Similar Alpha and Cluster Decay Properties in the Trans-Tin and Trans-Lead Regions*

V. Baran (Bucharest): *Order and Chaos for Quadrupole Degrees of Freedom*

A. Muzichko (Dubna): *Decay Widths of High Excited Compound Ra Nuclei and Their Description under the Statistical Model*

M. Grigorescu (Bucharest): *Dissipative Decay of the Isomeric States*

C.M. Petrache (Padova): *Exotic High-Spin Excitations in A=130 Mass Region*

M. Avrigeanu (Bucharest): *Interplay of Surface Effects and Gradual Absorbtion in Multistep Reaction Calculations*

V. Avrigeanu (Bucharest): *Level Density Effect on Cold-Fission Yields of* ^{234}U

C. Ur (Bucharest): *Towards $N = Z$ nuclei in $A = 80$ mass region at GASP*

V. Kartavenko (Dubna): *On nonlinear vortex waves*

A.M. Oros (Bucharest): *Crossing of the High Spin Members of the* $3^- \otimes g_{9/2}^{-1}$ *and* $5^- \otimes g_{9/2}^{-1}$ *multiplets in* ^{115}In

D. Rompf (Giessen): *Algebraic Realization of a Coupled Rotor Picture*

A. Florescu (Bucharest): *Alpha and Heavier Cluster Decays in the Region above* ^{100}Sn

Adriana Rãdutã (Bucharest): *The Effect of the Residual Interaction on the Nuclear Level Densities for* ^{40}Ca

C. Alexa (Bucharest): *Lie Symmetry Group for 1+1 Dimensional Ultrarelativistic Fluid Dynamics*

Organising committee

Răduţă A. A.	*Director*
Bucurescu D.	*Director*
Delion D. S.	*Scientific Secretary*
Ursu I. I.	*Scientific Secretary*
Aniţoaie A.	*Technical Secretary*

List of participants

Akkus Baki	*University of Istanbul*
Alexa C.	*Institute of Atomic Physics, Bucharest*
Avrigeanu M.	*Institute of Atomic Physics, Bucharest*
Avrigeanu V.	*Institute of Atomic Physics, Bucharest*
Balbutsev E.	*Joint Institute for Nuclear Research, Dubna*
Bădica T.	*Institute of Atomic Physics, Bucharest*
Băran V.	*Institute of Atomic Physics, Bucharest*
Bonatsos D.	*Institute of Nuclear Physics, Demokritos*
Bordeanu C.	*Institute of Atomic Physics, Bucharest*
Bostan Melik	*University of Istanbul*
Von Brentano P.	*University of Köln*
Bracco A.	*University of Milano*
Bulboacă I.	*Institute of Atomic Physics, Bucharest*
Caballero A.	*University of Madrid*
Calboreanu A.	*Institute of Atomic Physics, Bucharest*
Casten R. F.	*University of Yale*
Chiru S.	*Institute of Atomic Physics, Bucharest*
Constantinescu B.	*Institute of Atomic Physics, Bucharest*
Cârstoiu F.	*Institute of Atomic Physics, Bucharest*
Căta D.	*Institute of Atomic Physics, Bucharest*
Coraggio L.	*University of Napoli*
Covello A.	*University of Napoli*
Di Toro M.	*University of Catania*
Dohotar G.	*Institute of Nuclear Physics, Chişinău*
Drafta G.	*Institute of Atomic Physics, Bucharest*
Dumitrescu O.	*Institute of Atomic Physics, Bucharest*
Fiolhais C.	*University of Coimbra*
Florescu A.	*Institute of Atomic Physics, Bucharest*

Flueraşu D.	*Institute of Atomic Physics, Bucharest*
Gelberg A.	*University of Köln*
Gherman O.	*University of Craiova*
	President of the Romanian Senate
Gizon J.	*University of Grenoble*
Grecu D.	*Institute of Atomic Physics, Bucharest*
Gridnev K. A.	*University of Sankt Petersburg*
Grigorescu M.	*Institute of Atomic Physics, Bucharest*
Gudima K.	*Institute of Nuclear Physics, Chişinău*
Harangozo A.	*Institute of Atomic Physics, Bucharest*
Iacob E.	*Institute of Atomic Physics, Bucharest*
Insolia A.	*University of Catania*
Isar A.	*Institute of Atomic Physics, Bucharest*
Lo Iudice N.	*University of Napoli*
Kartavenko V.	*Joint Institute for Nuclear Research, Dubna*
Khalil H.	*University of Cairo*
Kobayashi T.	*RIKEN, Hirosawa*
Lönnroth T.	*University of Turku*
Ludu A.	*University of Bucharest*
Lunardi S.	*Laboratorio Nationale di Legnaro, Padova*
Mihai I.	*Institute of Atomic Physics, Bucharest*
Mihăilescu D.	*University of Iasi*
Mihuţ I.	*Institute of Atomic Physics, Bucharest*
Minkov N.	*Institute for Nuclear Research, Sofia*
Muzychka Yu.	*Joint Institute for Nuclear Research, Dubna*
Nica N.	*Institute of Atomic Physics, Bucharest*
Oros A.	*University of Köln*
Petrache C.	*Laboratorio Nationale di Legnaro, Padova*
Petraşcu M.	*Institute of Atomic Physics, Bucharest*
Podolyak Z.	*University of Cluj*
Poenaru D.	*Institute of Atomic Physics, Bucharest*
Popescu I.	*Institute of Atomic Physics, Bucharest*
Providencia J. (jr.)	*University of Coimbra*
Puşca S.	*Politechnical Institute, Bucharest*
Răduţă A.	*Institute of Atomic Physics, Bucharest*
Răduţă Al.	*Institute of Atomic Physics, Bucharest*
Rizea M.	*Institute of Atomic Physics, Bucharest*
Rompf D.	*University of Giessen*
Săndulescu A.	*Institute of Atomic Physics, Bucharest*
Scheid W.	*University of Giessen*
Schuck P.	*University of Grenoble*
Shalaby M.	*University of Cairo*

Silişteanu I.	*Institute of Atomic Physics, Bucharest*
Skouras L.	*Institute of Nuclear Physics, Demokritos*
Soloviev V. G.	*Joint Institute for Nuclear Research, Dubna*
Stoica S.	*Institute of Atomic Physics, Bucharest*
Stroe L.	*Institute of Atomic Physics, Bucharest*
Suhonen J.	*University of Jyväskylä*
Ştefănescu E.	*Romanian Academy*
Trache L.	*Texas A & M Univ. Ciclotron*
Ţugulea M.	*University of Bucharest*
Ur C.	*Institute of Atomic Physics, Bucharest*
Vautherin D.	*University of Paris, Orsay*
Vrânceanu D.	*University of Bucharest*
Zamick L.	*University of Rutgers*

INTRODUCTION TO RADIATION PROTECTION DOSIMETRY

by **J Sabol** *(Czech Tech. Univ.)* & **P-S Weng** *(Nat'l Tsing Hua Univ., Taiwan)*

One essential characteristic of life is the exchange of matter and energy between organisms and their environment. Radiation is a form of energy that has always been around in nature and will forever be the companion of human beings throughout life. In order to assess the impact of radiation exposures properly, it is essential to introduce appropriate quantities and units which can then be used for quantification of exposures from various sources. In principle, radiation protection is mainly aimed at controlling radiation exposure, while radiation dosimetry deals primarily with the measurement of relevant radiation quantities especially doses. This book is divided into two parts. The first contains up-to-date definitions of the most significant radiation quantities including their interpretation. In the second part, the exposures of both individuals and population at large to various types of natural and man-made sources are compared and discussed. The concept of quantities and units as well as analysis of exposure due to various sources in our environment is based on the latest, highly regarded authentic sources such as ICRU, ICRP, IAEA and particularly UNSCEAR reports and recommendations. The material reflects the latest review of the current terminology in radiation protection dosimetry and the contemporary assessment of radiation exposures of the population, radiation workers and patients.

Contents: Introduction; Radiation Quantities and Units; Assessment of Exposures from Natural and Man-Made Sources; Instrumentation in Dosimetry and Radiation Protection; Methods of Evaluation and Measurement of Basic Dosimetry and Radiation Protection Quantities.

Readership: Nuclear physicists, radiation physicists and environmentalists interested in radiation exposures and radioactive contamination.

300pp (approx.) *Pub. date: Jun 1995* *981-02-2116-9*

NUCLEAR MOLECULES

by **Walter Greiner** *(Johann Wolfgang Goethe-Univ. Frankfurt am Main)*, **Jae Y Park** *(North Carolina State Univ.)* & **Werner Scheid** *(Justus-Liebig-Univ. Giesson)*

Nuclear molecules are analogous to ordinary electronic molecules. Valence nucleons are circling nuclear cores and thus bind them. They appear in collisions of nuclei on nuclei, and in fission and fusion processes. Here a lively field of research has developed over the past 20 years. Nuclear Molecules are the strongest deformed nuclear complexes and play an important role in nuclear structure (cluster) physics. They are also of considerable interest for the synthesis of elements in astrophysics (cosmology). Most of the various nuclear molecular phenomena are discussed.

This book is the first monograph exclusively written to cover the theoretical aspects of nuclear molecular phenomena in heavy ion collisions. The experimental evidence is presented and confronted with theory.

Readership: Graduate students and active researchers interested in nuclear and heavy ion physics and nuclear astrophysics.

400pp (approx.) *Pub. date: Jun 1995* *981-02-1723-4*

World Scientific
An International Publisher